

Lecture Notes in Electrical Engineering 979

Poonam Singhal
Sakshi Kalra
Bhim Singh
R. C. Bansal *Editors*

Recent Developments in Electrical and Electronics Engineering

Select Proceedings of ICRDEEE 2022

 Springer

Lecture Notes in Electrical Engineering

Volume 979

Series Editors

Leopoldo Angrisani, Department of Electrical and Information Technologies Engineering, University of Napoli Federico II, Naples, Italy

Marco Arteaga, Departament de Control y Robótica, Universidad Nacional Autónoma de México, Coyoacán, Mexico

Bijaya Ketan Panigrahi, Electrical Engineering, Indian Institute of Technology Delhi, New Delhi, Delhi, India

Samarjit Chakraborty, Fakultät für Elektrotechnik und Informationstechnik, TU München, Munich, Germany

Jiming Chen, Zhejiang University, Hangzhou, Zhejiang, China

Shanben Chen, Materials Science and Engineering, Shanghai Jiao Tong University, Shanghai, China

Tan Kay Chen, Department of Electrical and Computer Engineering, National University of Singapore, Singapore, Singapore

Rüdiger Dillmann, Humanoids and Intelligent Systems Laboratory, Karlsruhe Institute for Technology, Karlsruhe, Germany

Haibin Duan, Beijing University of Aeronautics and Astronautics, Beijing, China

Gianluigi Ferrari, Università di Parma, Parma, Italy

Manuel Ferre, Centre for Automation and Robotics CAR (UPM-CSIC), Universidad Politécnica de Madrid, Madrid, Spain

Sandra Hirche, Department of Electrical Engineering and Information Science, Technische Universität München, Munich, Germany

Faryar Jabbari, Department of Mechanical and Aerospace Engineering, University of California, Irvine, CA, USA

Limin Jia, State Key Laboratory of Rail Traffic Control and Safety, Beijing Jiaotong University, Beijing, China

Janusz Kacprzyk, Systems Research Institute, Polish Academy of Sciences, Warsaw, Poland

Alaa Khamis, German University in Egypt El Tagamoa El Khames, New Cairo City, Egypt

Torsten Kroeger, Stanford University, Stanford, CA, USA

Yong Li, Hunan University, Changsha, Hunan, China

Qilian Liang, Department of Electrical Engineering, University of Texas at Arlington, Arlington, TX, USA

Ferran Martín, Departament d'Enginyeria Electrònica, Universitat Autònoma de Barcelona, Bellaterra, Barcelona, Spain

Tan Cher Ming, College of Engineering, Nanyang Technological University, Singapore, Singapore

Wolfgang Minker, Institute of Information Technology, University of Ulm, Ulm, Germany

Pradeep Misra, Department of Electrical Engineering, Wright State University, Dayton, OH, USA

Sebastian Möller, Quality and Usability Laboratory, TU Berlin, Berlin, Germany

Subhas Mukhopadhyay, School of Engineering and Advanced Technology, Massey University, Palmerston North, Manawatu-Wanganui, New Zealand

Cun-Zheng Ning, Electrical Engineering, Arizona State University, Tempe, AZ, USA

Toyoaki Nishida, Graduate School of Informatics, Kyoto University, Kyoto, Japan

Luca Oneto, Department of Informatics, BioEngineering, Robotics and Systems Engineering, University of Genova, Genova, Genova, Italy

Federica Pascucci, Dipartimento di Ingegneria, Università degli Studi "Roma Tre", Rome, Italy

Yong Qin, State Key Laboratory of Rail Traffic Control and Safety, Beijing Jiaotong University, Beijing, China

Gan Woon Seng, School of Electrical and Electronic Engineering, Nanyang Technological University, Singapore, Singapore

Joachim Speidel, Institute of Telecommunications, Universität Stuttgart, Stuttgart, Germany

Germano Veiga, Campus da FEUP, INESC Porto, Porto, Portugal

Haitao Wu, Academy of Opto-electronics, Chinese Academy of Sciences, Beijing, China

Walter Zamboni, DIEM—Università degli studi di Salerno, Fisciano, Salerno, Italy

Junjie James Zhang, Charlotte, NC, USA

The book series *Lecture Notes in Electrical Engineering* (LNEE) publishes the latest developments in Electrical Engineering—quickly, informally and in high quality. While original research reported in proceedings and monographs has traditionally formed the core of LNEE, we also encourage authors to submit books devoted to supporting student education and professional training in the various fields and applications areas of electrical engineering. The series cover classical and emerging topics concerning:

- Communication Engineering, Information Theory and Networks
- Electronics Engineering and Microelectronics
- Signal, Image and Speech Processing
- Wireless and Mobile Communication
- Circuits and Systems
- Energy Systems, Power Electronics and Electrical Machines
- Electro-optical Engineering
- Instrumentation Engineering
- Avionics Engineering
- Control Systems
- Internet-of-Things and Cybersecurity
- Biomedical Devices, MEMS and NEMS

For general information about this book series, comments or suggestions, please contact leontina.dicecco@springer.com.

To submit a proposal or request further information, please contact the Publishing Editor in your country:

China

Jasmine Dou, Editor (jasmine.dou@springer.com)

India, Japan, Rest of Asia

Swati Meherishi, Editorial Director (Swati.Meherishi@springer.com)

Southeast Asia, Australia, New Zealand

Ramesh Nath Premnath, Editor (ramesh.premnath@springernature.com)

USA, Canada

Michael Luby, Senior Editor (michael.luby@springer.com)

All other Countries

Leontina Di Cecco, Senior Editor (leontina.dicecco@springer.com)

**** This series is indexed by EI Compendex and Scopus databases. ****

Poonam Singhal · Sakshi Kalra · Bhim Singh ·
R. C. Bansal
Editors

Recent Developments in Electrical and Electronics Engineering

Select Proceedings of ICRDEEE 2022

 Springer

Editors

Poonam Singhal
J.C. Bose University of Science
and Technology, YMCA
Faridabad, India

Sakshi Kalra
J.C. Bose University of Science
and Technology, YMCA
Faridabad, India

Bhim Singh
Indian Institute of Technology Delhi
Delhi, India

R. C. Bansal
University of Sharjah
Sharjah, United Arab Emirates

ISSN 1876-1100

ISSN 1876-1119 (electronic)

Lecture Notes in Electrical Engineering

ISBN 978-981-19-7992-7

ISBN 978-981-19-7993-4 (eBook)

<https://doi.org/10.1007/978-981-19-7993-4>

© The Editor(s) (if applicable) and The Author(s), under exclusive license to Springer Nature Singapore Pte Ltd. 2023

This work is subject to copyright. All rights are solely and exclusively licensed by the Publisher, whether the whole or part of the material is concerned, specifically the rights of translation, reprinting, reuse of illustrations, recitation, broadcasting, reproduction on microfilms or in any other physical way, and transmission or information storage and retrieval, electronic adaptation, computer software, or by similar or dissimilar methodology now known or hereafter developed.

The use of general descriptive names, registered names, trademarks, service marks, etc. in this publication does not imply, even in the absence of a specific statement, that such names are exempt from the relevant protective laws and regulations and therefore free for general use.

The publisher, the authors, and the editors are safe to assume that the advice and information in this book are believed to be true and accurate at the date of publication. Neither the publisher nor the authors or the editors give a warranty, expressed or implied, with respect to the material contained herein or for any errors or omissions that may have been made. The publisher remains neutral with regard to jurisdictional claims in published maps and institutional affiliations.

This Springer imprint is published by the registered company Springer Nature Singapore Pte Ltd.

The registered company address is: 152 Beach Road, #21-01/04 Gateway East, Singapore 189721, Singapore

Contents

Design and Implementation of Fractional-Order PID Controller for Magnetic Levitation System Using Genetic Algorithm-Based Optimization	1
Nitesh Kumar Soni, Sandeep Bhongade, and R. S. Gamad	
Spin-Transfer Torque MRAM with Emerging Sensing Techniques	15
Seema Kumari and Rekha Yadav	
Optimum Design of Controller Parameters for Automatic Generation Control Employing Hybrid Statistically Tracked Particle Swarm Optimization Algorithm	27
Cheshta Jain Khare, Ujjwala Rai, H. K. Verma, and Vikas Khare	
A Comparative PWM Analysis of MMC	41
Rahul Jaiswal, Anshul Agarwal, Richa Negi, and Komal Agrawal	
An Analytical Study to Evaluate the Performance of Different PV Configurations Under Various Partial Shading Conditions	51
Varun Agarwal, Venkata Madhava Ram Tatabhatla, and Anshul Agarwal	
Detection of Parkinson’s Disease Using Support Vector Machine and Combination of Various Tissue Density Features	65
Reema Ganotra and Shailender Gupta	
Modified Sine Cosine-Based Controller for Microgrid Frequency Regulation	71
Rajendra Kumar Khadanga, Preeti Ranjan Sahu, Amit Kumar, Prakash Kumar Hota, and Sidhartha Panda	
Impact of Different Demand Response Programs on Distribution Network Using Particle Swarm Optimization	85
S. Sharma, Tanuj Rawat, Richa Sharma, and Gulshan Sharma	

Impact of Redox Flow Battery and HVDC Link on Combined ALFC-AVR of a Hydrothermal System Incorporating GTPP Considering Communication Delay	99
Biswanath Dekaraja, Lalit Chandra Saikia, and Satish Kumar Ramoji	
Amalgamated Voltage and Frequency Regulation of an Interconnected Multi-source Power System Using the CFOI-TIDN Controller	117
Satish Kumar Ramoji, Lalit Chandra Saikia, and Biswanath Dekaraja	
Harmonics Mitigation Using Proportional–Resonant Controller-Based DSTATCOM in Distribution System	131
Atma Ram, Paras Ram Sharma, and Rajesh Kumar Ahuja	
Analysis of Z-Source Resonant Converter for Wireless Charging Application	145
Ayush Kumar Srivastava and Narendra Kumar	
Application of a Novel Method to Reduce Congestion in DPS Applying TCSC	155
Anubha Gautam, P. R. Sharma, and Yogendra Kumar	
A Hybrid Approach to PMBLAC Machine for High-Speed Mobility	165
Sumit Kumar Yadav, Shakuntla Boora, and Nitin Goel	
Analysis of DSR Protocol in Varying Network Configurations	179
Sonam Khera, Neelam Turk, and Rohin Rakheja	
A Multilevel Secured Mechanism for Data Protection	191
Anjali Malik, Sunil Jadav, and Shailender Gupta	
Optimal AGC of Two-Area Multi-source Power System Incorporating ES Under Deregulated Environment	201
Sandeep Rangi, Sheilza Jain, and Yogendra Arya	
Real-Time Price-Based Optimal Energy Mix in Smart Distribution Network	211
Raju Wagle, Pawan Sharma, Charu Sharma, and Mohammad Amin	
Path Planning of Quadrotor Using A* and LQR	227
Ritika Thusoo, Sheilza Jain, and Sakshi Bangia	
Studying the Effect of Heating on Synthesis of ZnO Nanoparticles Properties for Electromagnetic Applications	239
Bahareh Dabaghiannejad, Sandeep K. Arya, and Sandeep Kumar	
A Comparative Analysis of Chaotic and Quantum Chaotic Encryption Mechanisms	249
Jitender, Shailender Gupta, and Sangeeta Dhall	

Analyzing Chaos in SMIB Power System 269
 Sheetal and Sanju Saini

Hybrid AC/DC Microgrid Control and Management of Power Using Bidirectional AC/DC Converter by Autonomous Control Mode 277
 S. Mamatha and G. Mallesham

Analysis of Intelligent Control of Irrigation System 291
 Arunesh Kumar Singh and Tabish Tariq

A Recursive CEIEC Technique for Image Enhancement Employing Sharpening Filter 303
 Archana Agarwal, Shailender Gupta, and Munish Vashishath

Short-Term Wind Power Forecast Using Time Series Analysis: Auto-regressive Moving-average Model (ARMA) 319
 Rudresh B. Magadum, Satish Bilagi, Srishtik Bhandarkar, Anchit Patil, and Abhigna Joshi

Design and Analysis of EV Charging Station Using LLC Converter 343
 Nayan M. Kengar, Richa Adlakha, and Ashish Grover

Cascaded Fuzzy and Three-Degree-of-Freedom Controller for Hybrid AGC Considering AC/DC Link 351
 Ashiwani Kumar, Ravi Shankar, and R. K. Mandal

Harmonic Performance Analysis for Different Loads with and Without PV 363
 Aakriti Khanna, Anjali Garg, and Sreedhar Madichetty

Intelligent Planning of Multiple DG with Practical Load Models Using Metaheuristic Methods 375
 Bikash Kumar Saw, Aashish Kumar Bohre, and Tushar Kanti Bera

Modeling and Simulation of a Single-Phase Single-Stage Grid Connected PV System 383
 Rachna Dhir

Grid Integration of 3P3W Single-Stage Solar PV System Using Modified Digital Filter Control 393
 Pushpendra Sharma, Abhishek Kumar, and Rashmi Agarwal

Multi Terrain Motion Control Vehicle 403
 Oomang Bishnoi, Preeti, and Sansh Bir Dagar

Optimal Frequency Control of Micro-Grid System Using IPD-(1 + I) Controller 411
 Yogendra Arya and Kavita Singh

Study of Polarization Effect in WDM Channels Network	421
Vikash Kumar Dahiya and Sandeep K. Arya	
The Accomplishment of Quantum Key Distribution via BB84 Protocol with Optical Simulator	433
Prakash Singh Gill and Sandeep K. Arya	
Grid Fault Ride Through Control of a Permanent Magnet Synchronous Generator based Wind Energy Conversion System	445
Arika Singh and Kirti Pal	
DTMOS Based Squarer Circuit and Its Application in Controllable Gaussian Function Generator	457
Sanjeev Kumar Yadav, Shweta Kumari, Maneesha Gupta, and Ritu Raj Singh	
Low-Voltage Low-Power DTMOS Based Second Generation Voltage Conveyor: Features and Design	469
Dhanuj Kumar Sharma, Shweta Kumari, and Maneesha Gupta	
A Novel Method to Power Losses Reduction in Radial Distribution System: A Multiobjective Generalized Particle Swarm Optimization (MOGEP SO)	479
Sapna Ladwal, Anil Kumar, and Avantika Sethi	
The Uprising of Blockchain Technology in the Energy Market Industry	497
Nishkar R. Naraindath, Ramesh C. Bansal, and Raj M. Naidoo	
Performance of Nichrome/p-Si Schottky Diode	511
Ekta Sharma, Reena Rathi, and Vamshi Krishna Dasarraju	
Behaviour of SiC Schottky Diode Temperature Sensors in 200–600 K	517
Jaya, Bhavya Sinhmar, Vamshi Krishna Dasarraju, and Sudhir Dalal	
Investigation on Trench Edge Termination in SiC Based Power Device	525
Reena Rathi, Ekta Sharma, and Vamshi Krishna Dasarraju	

About the Editors

Poonam Singhal is a professor and chairperson in the Department of Electrical Engineering, J.C. Bose University of Science and Technology, YMCA, Faridabad. She obtained her B.Sc. from REC Rourkela, M.Tech. from YMCAIE, Faridabad, and Ph.D. from J.C. Bose University of Science and Technology, YMCA, Faridabad. Her areas of interest include power systems, FACTS, AI, and microgrids. She has over 30 years of teaching experience.

Sakshi Kalra is an assistant professor in the Department of Electrical Engineering, J.C. Bose University of Science and Technology, YMCA, Faridabad. She obtained her B.E. in instrumentation and control engineering, M.Tech. in power systems and drives, and Ph.D. from Maharishi Dayanand University, Rohtak. Her areas of interest include power systems and drives, control systems, AI, and microgrids. She has over 15 years of teaching experience with several papers published in reputed journals and conferences.

Bhim Singh received his B.E. from the University of Roorkee, India, in 1977 and M.Tech. (Power Apparatus & Systems) and Ph.D. from the Indian Institute of Technology (IIT) Delhi, India, in 1979 and 1983, respectively. Prof. Singh is also a member of Governing Council of Central Power Research Institute. Prof. Singh has guided 101 Ph.D. dissertations and 171 M.E./M.Tech./M.S.(R) theses. He has filed 94 patents. He has executed more than eighty sponsored and consultancy projects. He has co-authored a textbook on power quality: Power Quality Problems and Mitigation Techniques published by John Wiley & Sons Ltd. in 2015. His areas of interest include solar PV grid interface systems, microgrids, power quality monitoring, and mitigation, solar PV water pumping systems, improved power quality ACDC converters, power electronics, electrical machines, drives, flexible alternating transmission systems, and high-voltage direct current systems.

R. C. Bansal is a professor in the Department of Electrical Engineering, University of Sharjah. He obtained his Ph.D. degree in renewable energy/power systems, M.E. in power systems, MBA, Grad Cert in Higher Ed (GCHE). His research areas are

renewable energy and conventional power systems that further include wind, photovoltaics, hybrid power systems, distributed generation, grid integration of renewable energy, power systems analysis, smart grid, and power quality. He has 25+ years of experience in academia, research, and industry. He has over 350 publications in reputed journals, conferences, and edited volumes.

Design and Implementation of Fractional-Order PID Controller for Magnetic Levitation System Using Genetic Algorithm-Based Optimization



Nitesh Kumar Soni, Sandeep Bhongade, and R. S. Gamad

1 Introduction

Magnetic levitation is a most effective and popular contactless and frictionless technique in which a ferromagnetic object is draped in the air with the support of magnetic fields. Use of magnetic fields is to counteract the gravitational force and any other counteracceleration. Magnetic levitation has given frictionless, efficient, and outstanding technologies [1].

In a magnetic levitation system, a steel ball made of ferromagnetic material is levitated against gravity and its levitation position is controlled by electromagnetic force of attraction generated by coil and force is controlled by controlling voltage which is applied to the coil [1]. Due to the absence of mechanical contact the frictional force in magnetic levitation system gets eliminated. This results in improved system efficiency. There are various engineering applications of magnetic levitation technology such as high-speed trains, wind turbine, and personal rapid transit. Position of the suspended object is being measured by the use of optical sensor. Based on the error generated, i.e., difference of desired and actual position of the suspended object, a controller takes action and provides suitable current to electromagnetic coil. It generates a required force which is applied on the ferromagnetic object to control its position and make it stable and able to track a reference signal [2]. Without an efficient controller, Maglev system is inherently unstable.

N. K. Soni (✉) · S. Bhongade · R. S. Gamad
Shri Govindram Seksaria Institute of Technology and Science, Indore, India
e-mail: nitesh@medicaps.ac.in

S. Bhongade
e-mail: sbhongade@sgsits.ac.in

R. S. Gamad
e-mail: rgamad@sgsits.ac.in

The nonlinearity and instability of Maglev makes very challenging system. Most of time traditional controllers are not perfectly able to handle the nonlinearity and instability of system. Generally for controlling of such systems some traditional controllers like PID, PI, fuzzy controller, and other controllers are used [3]. If we use FOPID controller, it is advantageous in that it has two extra tuning parameters (λ and μ) which provides additional degree of freedom for better control, speed in response, flexibility, stability, and better handling of a nonlinear system [4]. Settling time must be decreased to increase the stability, speed of response, and efficiency of the system. Instability and nonlinearity of the open-loop magnetic levitation system are two aspects that are represented by an extremely nonlinear differential equation [5].

In this paper, magnetic levitation system is controlled by FOPID controller which is a nonconventional control technique. Organization of this paper is as follows. Section 2 explains about the mathematical model of the magnetic levitation system. The description of GA algorithm is given in Section 3. FOPID controllers have been introduced and explained in Section 4. Implementation of FOPID controller is shown in Section 5. The results and comparative analysis are shown in Section 6. Finally, Section 7 shows the conclusions and future scope.

2 The Magnetic Levitation System

The block diagram of magnetic levitation system is shown in Fig. 1. Magnetic levitation system consists of an electromagnetic coil along with a pair of infrared transmitter and sensor which can accurately sense the position of the ball [6]. The electromagnetic force exerted by the coil is controlled by controlling the current in the electromagnetic coil. The current is controlled by controller in such a way so that the metal object can float in the air space [7–10]. The electromagnetic force F which is generated by electromagnetic coil and the gravitational force g are opposite which manages to sustain the metal object in the air space. The generated electromagnetic force F by the coil depends on the current I and the air gap X between the metal ball and the electromagnet coil, the generated force F is given by [11–13]

$$F = Mg - K_m \left(\frac{i_m}{x_b} \right)^2 \quad (1)$$

where

i_m = current in electromagnetic coil (Ampere);

x_b = ball distance from the coil (m)

g = gravitational constant (m/s^2);

k_m = magnetic force constant

M = mass of the metal ball (K_g)

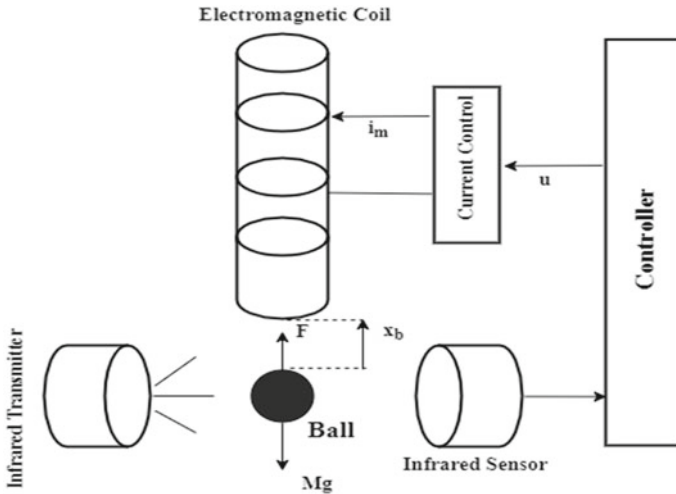


Fig. 1 Magnetic levitation system [14]

The differential equation of the magnetic levitation system is given by Newton's second law of motion as given in Eq. (2):

$$M \frac{d^2 x_b}{dt^2} = Mg - K_m \left(\frac{i_m}{x_b} \right)^2 \quad (2)$$

The metal ball position and value of electromagnetic coil current at the operating point can be derived by putting $\frac{d^2 x_b}{dt^2} = 0$ in Eq. (2) which gives

$$x_{b_{ss}} = \sqrt{\frac{K_m}{Mg}} i_{m_{ss}} \quad (3)$$

where

$x_{b_{ss}}$ = metal ball position; $i_{m_{ss}}$ = electromagnetic coil current.

In theoretical sense, this coil current is sufficient to generate force F to levitate the metal ball to the desired location. But practically there is fair chance to fail due to any variation at operating point which may be caused by external disturbances, uncertainties in parameter, and others. That's why we require an efficient controller which is capable of handling such irregularities of the system. The system linearization can be done by taking the approximates of x_b and i_m as

$$x_b(t) \triangleq \hat{x}_b + x_{b_{ss}} \quad (4)$$

$$i_m(t) \triangleq \hat{i}_m + i_{m_{ss}} \quad (5)$$

where

$x_{b_{ss}}$ = ball position variations; $i_{m_{ss}}$ = coil current variation.

Above variations of ball position and coil current are around the operating point. The dynamic equation of the magnetic levitation system is given by Eq. (6).

$$M \frac{d^2 \hat{x}_b}{dt^2} = Mg - K_m \left(\frac{\hat{i}_m + i_{m_{ss}}}{\hat{x}_b + x_{b_{ss}}} \right)^2 \quad (6)$$

Now, by using Taylor's series expansion method we linearized.

Equation (6) and assuming that $\hat{x}_b \gg x_{b_{ss}}$, $\hat{i}_m \gg i_{m_{ss}}$

$$\frac{d^2 \hat{x}_b}{dt^2} = \frac{1}{M} \left\{ \frac{\partial}{\partial \hat{x}_b} \left(Mg - K_m \left(\frac{\hat{i}_m + i_{m_{ss}}}{\hat{x}_b + x_{b_{ss}}} \right)^2 \right) \Big|_{\hat{x}_b=0, \hat{i}_m=0} \right. \\ \left. \hat{x}_b + \frac{\partial}{\partial \hat{i}_m} \left(Mg - K_m \left(\frac{\hat{i}_m + i_{m_{ss}}}{\hat{x}_b + x_{b_{ss}}} \right)^2 \right) \Big|_{\hat{x}_b=0, \hat{i}_m=0} \right\} \quad (7)$$

Therefore

$$\frac{d^2 \hat{x}_b}{dt^2} = \frac{1}{M} \left(\frac{2K_m i_{m_{ss}}^2}{x_{b_{ss}}^3} \hat{x}_b - \frac{2K_m i_{m_{ss}}}{x_{b_{ss}}^2} \hat{i}_m \right) \quad (8)$$

The Laplace transformation of system is given as

$$G(s) = \frac{\hat{X}_b(s)}{\hat{I}_m(s)} = -\frac{K_2}{s^2 - K_1} \quad (9)$$

where $K_1 = \frac{2K_m i_{m_{ss}}^2}{M x_{b_{ss}}^3}$ and $K_2 = \frac{2K_m i_{m_{ss}}}{M x_{b_{ss}}^2}$

with $M = 0.002kg$; $g = 9.81m/sec^2$.

And the equilibrium point of the feedback system is $[x_{b_{ss}} = -1.5V, i_{m_{ss}} = 0.8A]$. After considering above values, the transfer function of the magnetic levitation system becomes

$$G(s) = \frac{-24.5250}{s^2 + 13.08} \quad (10)$$

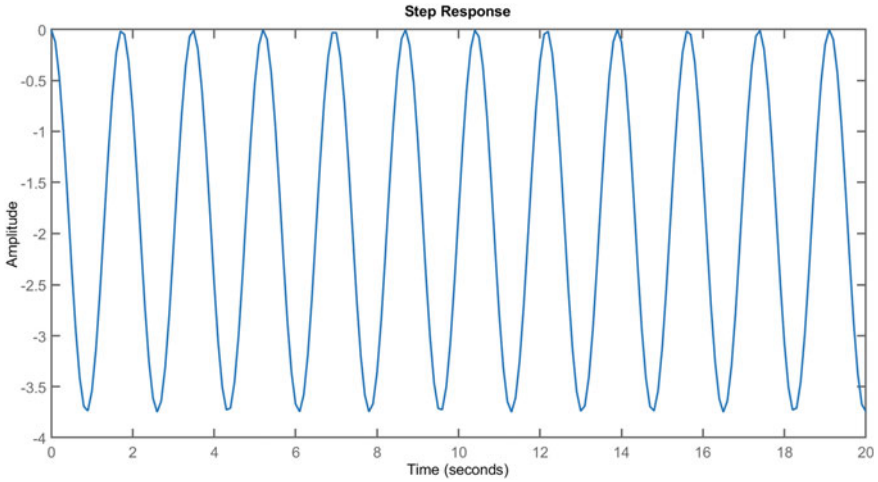
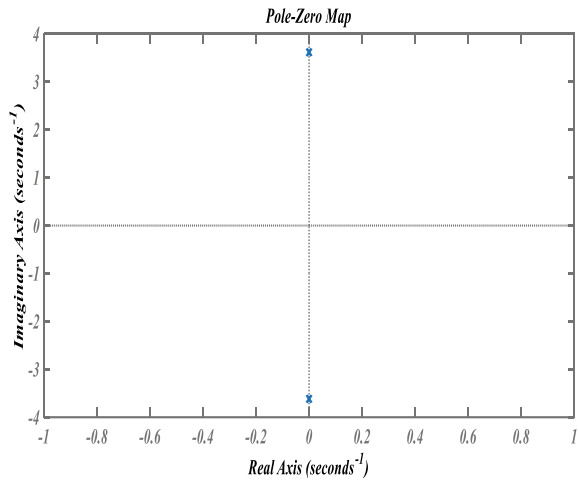


Fig. 2 Step response of open-loop system

Fig. 3 Pole zero plot of open-loop system



The step response and frequency response of the open-loop system are shown in Figs. 2 and 4, respectively. In Fig. 3, we can see that the poles of the open-loop system, which are located on the imaginary axis, i.e., at $s = \pm j3.6166$ which means that the system goes toward instability or having sustained oscillations which can be seen in Fig. 2. When we make this system closed loop the system becomes unstable

as shown in Fig. 5. One of the pole is lying on the right-hand side of the s-plane and the closed-loop poles are located at $s = \pm 3.3823$. Therefore, a controller is required for making closed-loop system stable which can control the position of the metal ball so that it can levitate in the air space.

Fig. 4 Open-loop response of magnetic levitation system

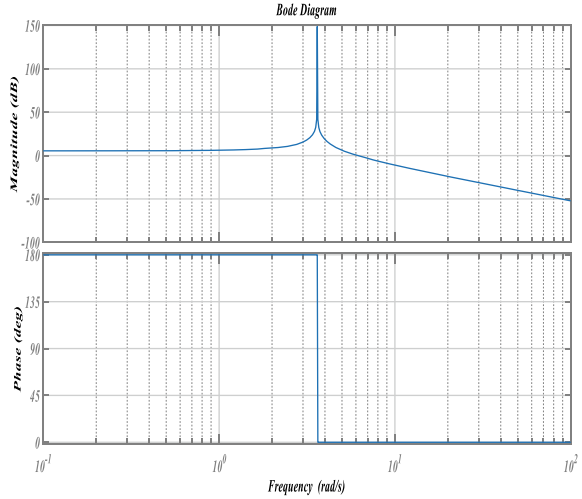
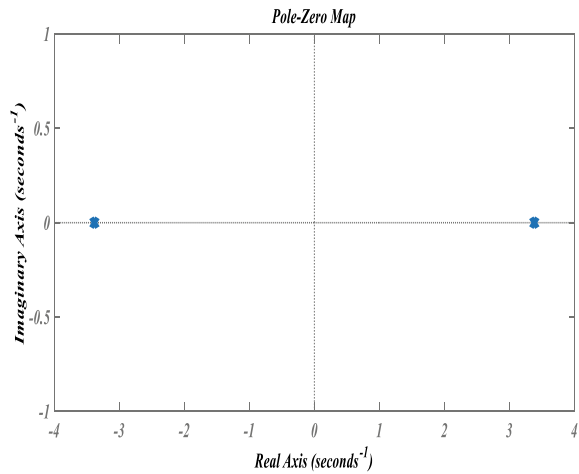


Fig. 5 Pole zero plot of close loop system



3 Description of GA Algorithm

Genetic algorithm is very popular optimization technique to optimize and solve highly nonlinear and complex system problems. In GA probabilistic transition rules are used. It can handle a population of potential solutions which is termed as individuals or chromosomes that are developed in iterative manner. Figure 6 shows the flow diagram of genetic algorithm.

Steps of GA:

Step 1: First initialize all the parameter with population of random solutions.

Step 2: After initialization compute above parameters and then evaluate the best value of the fitness function.

Step 3: Increase crossover, mutation operation, and new cluster.

Step 4: Until we get the best fitness value repeat step 2.

Figure 7 shows the complete block diagram of magnetic levitation system with GA algorithm. Similar block diagram can be there with PID only in place of FOPID, which we avoid showing for brevity. The global optimum solution of the system is determined by supervising the performance index by convergence of the GA algorithm. With each increment of iteration the tuning parameters of both the controller PID and FOPID also get modified so that they can produce optimum value of performance index.

Table 1 shows the different parameters of genetic algorithm which are used for tuning of PID controller. After tuning of PID controller we get the different optimized parameters which are shown in Table 2.

Fig. 6 Genetic algorithm. Flow diagram

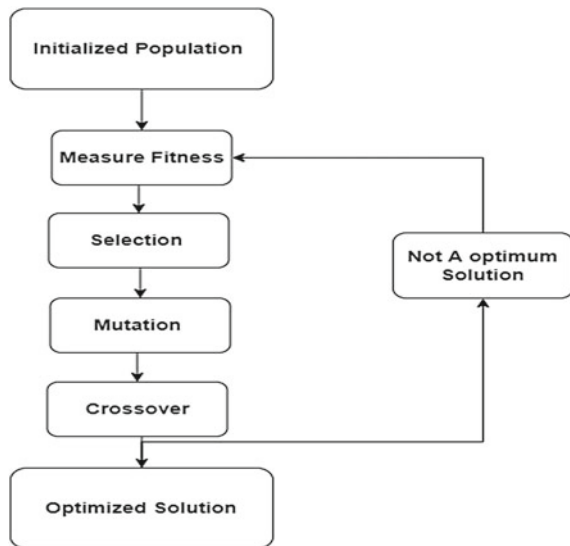


Fig. 7 Block diagram for optimum search using GA

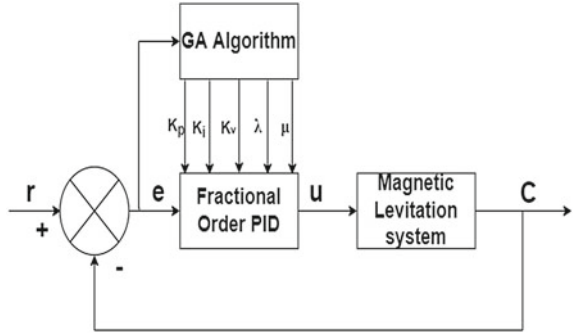


Table 1 GA parameter used for PID tuning

Parameter	Value
Lower bound	[-10 -10 -10]
Upper bound	[10 10 10]
Population size	50
Crossover	Scattered
Crossover fraction	0.8
Mutation fraction	0.011
Iterations	70
Selection	Stochastic Uniform

Table 2 Tuned parameters of PID controller using GA algorithm

Controller	K_p	K_i	K_d
PID	-4.026	-3.862	-0.608

The step response of closed-loop magnetic levitation system with PID controller is shown in Fig. 8. We found that system is stable for the tuned parameter using GA of PID controller. The time response characteristics for step input of considered magnetic levitation system with PID controller tuned by the genetic algorithm is shown in Table 3. It can be noted that PID controller has stabilized and improved performance of system. Now we will implement the FOPID controller for comparison of the performance with PID.

Fig. 8 Step response of ML with PID using GA

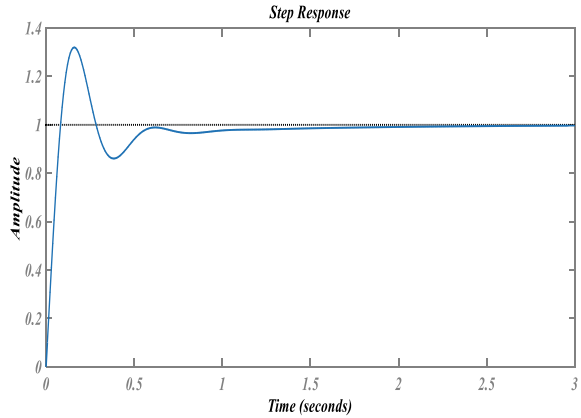


Table 3 Step response characteristics of ML with PID

Specification	PID tuned by GA
Rise time	0.0860 s
Peak overshoot	32.0189%
Settling time	1.1182 s
Steady-state error	0.00

4 Fractional Calculus and FOPID Controller

4.1 Fractional Calculus

It is more than 300-year-old mathematical technique which deals with generalization of integer-order integration and differentiation to non-integer operators ${}_a D_t^\alpha$ that have α fractional number power [15–17]. In the last couple of decades, fractional-order calculus found their applications in control engineering.

There are three most frequently used definitions which are Riemann–Liouville, Grunwald–Letnikov, and Caputo [16]. The most popular and common definition is known as Riemann–Liouville:

$${}_a D_t^\alpha f(t) = \frac{1}{\Gamma(n - \alpha)} \frac{d^n}{dt^n} \int_a^t \frac{f(\tau) d\tau}{(t - \tau)^{\alpha - n + 1}} \tag{11}$$

The second definition is the Grunwald–Letnikov as

$${}_a D_t^\alpha f(t) = \lim_{h \rightarrow 0} \frac{1}{h^\alpha} \sum_{j=0}^{(t-a)/h} (-1)^j f(t - jh) \tag{12}$$

where $\binom{\alpha}{j} = \Gamma(\alpha + 1) / \Gamma(j + 1)\Gamma(\alpha - j + 1)$

The third definition is Caputo expression which is defined as

$${}_a D_t^\alpha f(t) = \frac{1}{\Gamma(n - \alpha)} \int_a^t \frac{f^n(\tau) d\tau}{(t - \tau)^{\alpha - n + 1}} \tag{13}$$

where $n - 1 < \alpha < n$

n and α are an integer number and initial condition, respectively.

4.2 Fractional-Order PID Controller

PID controller [18, 19] has been very popular and widely used controllers, but in the last couple of decades the improvement in fractional calculus in the field of control engineering has introduced new controller which is known as the fractional-order PID controller and it becomes very popular in control applications. Fractional-order $PI^\lambda D^\mu$ controller has two extra parameters λ and μ which makes it complex and also provides extra degree of freedom as compared to integer-order PID controller. Fractional-order $PI^\lambda D^\mu$ controller is described as

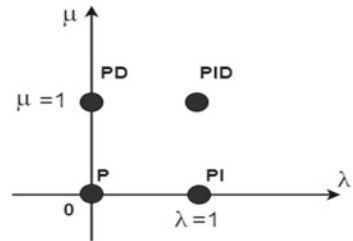
$$u(t) = K_p e(t) + K_I D^{-\lambda} e(t) + K_D D^\mu e(t) \tag{14}$$

The generalization of PID controller can be done for different values of λ and μ in (14) through fractional-order PID controller as shown in Fig. 9. PID ($\lambda = 1, \mu = 1$), PI ($\lambda = 1, \mu = 0$), PD ($\lambda = 0, \mu = 1$), and P ($\lambda = 0, \mu = 0$) are the special cases of $PI^\lambda D^\mu$ controller.

After considering the Laplace transform of Eq. 14, the expression of FOPID controller in s-domain is obtained as

$$C(s) = \frac{U(s)}{E(s)} = K_p + \frac{K_I}{S^\lambda} + K_D S^\mu \tag{15}$$

Fig. 9 Generalization of PID



By taking $\lambda = 1$, $\mu = 1$ in (15), the expression becomes

$$C(s) = \frac{U(s)}{E(s)} = K_p + \frac{K_I}{S} + K_D S \quad (16)$$

PID controller can be implemented by FOPID so that in the present work PID controller is also studied along with the study of $PI^\lambda D^\mu$ controller because PID controller is easily implemented by fractional-order controller. The performance comparison of PID with $PI^\lambda D^\mu$ is carried out on the basis of same design specifications to show that the fractional-order $PI^\lambda D^\mu$ controller has better performance in terms of performance index considered.

The hardware and software realization of FOPID controller is difficult. Therefore, an integer-order approximation method is used for the fractional-order elements [20]. In MATLAB, FOPID controller can be implemented using FOMCOM toolbox [4] where Oustaloup's approximation is realized.

5 Simulation Results

The different parameters of the FOPID controller for magnetic levitation system are tuned and the optimized values of different controller parameters [$K_p, K_i, K_d, \lambda, \mu$] are obtained. The considered performance index is integral time absolute error (ITAE) and it is minimized by use of GA algorithm optimizer toolbox [14].

For fractional-order system, different performance index criterions like ITAE, ISCO, ITSE, etc. can be applied. Different integral performance index criterion has different advantages for every design of PID and FOPID controller. Among them, the ITAE performance index criterion optimizes the absolute error and settling time, which is not possible to achieve by other performance index. From the different literature study, it has been noted that the most popular and commonly used performance index is ITAE for tuning of PID and FOPID controller. In this paper, we considered the same objective function (ITAE) which is minimized using GA and it is given as

$$J = \int_0^{\infty} t |e(t)| dt \quad (17)$$

where $e(t)$ is error signal.

Optimization of controller parameters is done by MATLAB optimization toolbox. The chosen objective function converges to 0.06028 after 100 iterations by optimization and the tuned values of FOPID controller parameters are shown in Table 4 and comparison with PID is also shown in that table; the different parameters which are used to tune the FOPID controller using GA are shown in Table 5.

Figure 10 shows the comparative time response analysis of magnetic levitation system with integer-order PID and fractional-order PID controller for the unit step

Table 4 Parameters of PID and FOPID controller tuned by GA algorithm

Controller	K_p	K_I	K_D	λ	μ
PID	-4.026	-3.862	-0.608	-	-
FOPID	9.135	9.145	9.698	0.054	1.998

Table 5 Parameter of GA used for FOPID tuning

Parameter	Value
Lower bound	[1, 1, 1, 0, 0]
Upper bound	[2, 8]
Size of population	60
Crossover type	Scattered
Crossover fraction	0.8
Mutation fraction	0.01
Iterations	400
Selection	Stochastic uniform

Fig. 10 Step response with PID and FOPID

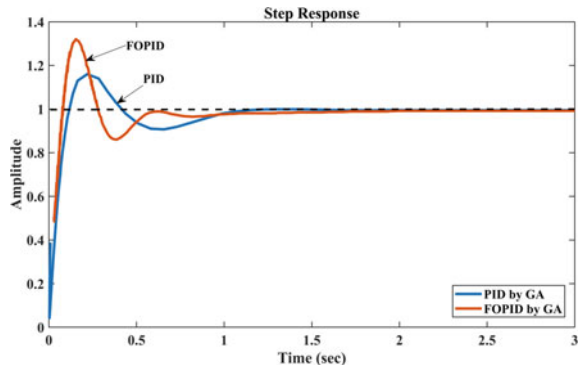


Table 6 Comparison of response characteristics of FOPID and PID

Response	PID controller	FOPID controller
Rise time	0.0860 s	0.0644 s
Peak overshoot	32.0189%	17.5006%
Settling time	1.1182 s	0.9776 s
Steady-state error	0.00	0.00

input in which both FOPID and IOPID controllers are tuned by genetic algorithm and the response graph clearly shows that there is a better improvement in the closed step response with FOPID controller compared to the integer-order PID controller.

The various characteristics of time response of PID and FOPID are shown in Table 6.

It is clearly seen in Table 6 that there is remarkable improvement in system response with FOPID compared to PID for step input in terms of time response characteristics mentioned in Table 6. The response of the system with FOPID controller shows good robustness for step disturbance, and this is due to the two additional parameters of FOPID controller.

6 Conclusions

The controlling of magnetic levitation system is attained successfully using GA-based direct tuning method for PID and FOPID controllers. It has been observed that GA technique for tuning controller parameters provides good convergence toward optimal values of controller parameters. In this paper, two controllers have been designed, one is integer order and other is fractional order. A comparative study of PID and FOPID is also done and it has been found that the results are quite acceptable for both integer-order and fractional-order controllers but the fractional-order controller seems to be better and robust. Therefore, we can conclude that the fractional-order PID controller could be the good replacement for integer-order PID controller in the future. The real-time implementation of fractional-order PID controller for different types of nonlinear systems such as magnetic levitation systems might be the subject of further research.

References

1. Ahmad I, Javaid MA (2010) Nonlinear model & controller design for magnetic levitation system. In: 9th WSEAS international conference on signal processing, robotics and automation. Cambridge, UK
2. Yaghoubi H, Barazi N, Aoliaei MR (2012) "Maglev, ch 6," in Infrastructure design, signalling and security in railway, pp 123–176, InTech, Rijeka, Croatia
3. Podlubny I, Dorcak L, Kostial I (1997) On fractional derivatives, fractional-order dynamic systems and PI λ D μ controllers. In: 36th IEEE conference on decision and control. San Diego, US
4. Tepljakov A, Petlenkov E, Belikov J (2012) A flexible MATLAB tool for optimal fractional-order PID controller design subject to specifications. In: Proceedings of the 31st Chinese control conference, Hefei, Anhui, China, pp 4698–4703
5. Kumar T, Shimi S, Karanjkar D, Rana S (2014) Modeling, simulation and control of single actuator magnetic levitation system. In: 2014 recent advances in engineering and computational sciences (RAECS), pp 1–6. IEEE
6. Knospe CR, Collins EG (1996) Special issue on magnetic bearing control. IEEE Trans Cont Syst Technol 4(5)
7. Rule RG (1980) Combined magnetic levitation and propulsion: the mag-transit concept. IEEE Trans Veh Technol VT 29:41–49
8. Ion B, Trica A, Papusoiu G, Nasar AS (1988) Field tests on a maglev with passive guideway linear inductor motor transportation system. IEEE Trans. Veh Technol VT 38:230–236
9. Yadav S, Tiwari JP, Nagar SK (2012) Digital control of magnetic levitation system using fuzzy logic controller. Int J Comput Appl (0975–8887) 41(21)

10. Yadav S, Verma SK, Nagar SK (2016) Optimized PID controller for magnetic levitation system. *IFAC-PapersOnLine* 49(1):778–782
11. Kumar EV, Jerome J (2013) LQR based optimal tuning of PID controller for trajectory tracking of magnetic levitation system. *Proc Eng* 64:254–264
12. Verma SK, Yadav S, Nagar SK (2015) Optimal fractional order PID controller for magnetic levitation, Presented at 39th NSC-2015, 14th–16th December, Shiv Nadar University, Dadri, India
13. Golob M, Tovornik B (2003) Modeling and control of the magnetic suspension system. *ISA Trans* 42:89–100
14. Yadav S et al (2017) Performance enhancement of magnetic levitation system using teaching learning based optimization. *Alexandria Eng J*
15. Ortigueira MD (2011) *Fractional calculus for scientists and engineers*. Springer, Berlin, Germany
16. Caponetto R, Dongola G, Fortuna L, Petras I (2010) *Fractional order systems: modeling and control applications*, vol. 72 of *World Scientific Series on Nonlinear Science Series A*, world Scientific Publishing, Singapore
17. Baleanu D, Diethelm K, Scalas E, Trujillo JJ (2012) *Fractional calculus models and numerical methods. Nonlinearity and Chaos*, World Scientific Publishing, Singapore, Series on Complexity
18. Ogata K (2002) *Modern control engineering*. Prentice-Hall, Upper Saddle River, NJ, USA
19. Astrom KA, Hagglund T (1995) *PID controller: theory, design and tuning*, Instrument Society of America, Research Triangle Park, NC, USA
20. Outstaloup A, Levron F, Mathieu B, Nanot FM (2000) Frequency-based complex noninteger differentiator: Characterization and synthesis. *IEEE Trans Circuits Syst I: Fundamental Theory Appl* 47(1):25–39

Spin-Transfer Torque MRAM with Emerging Sensing Techniques



Seema Kumari and Rekha Yadav

1 Introduction

Spin-transfer torque MRAM shows fast access speed, excellent endurance, retention, simple cell structure high array density, low-power switching characteristics, and excellent CMOS compatibility and scalability [1–3]. It has been used in embedded systems, last-level cache, a microcontroller unit (MCU), and so on. Data is saved as two or more distinct resistance conditions of an MTJ device in an MRAM bit. Making working memory non-volatile and turning off the power of the memory region in stand-by are effective ways to lower the operational power of computer systems. STT-MRAM is currently the most probable choice for non-volatile working memory in terms of operating parameters such as speed and low-voltage operability. The rise in switching current as the technology shrinks down is one of MRAM's significant drawbacks. The spin-polarized current is applied vertically through the MTJ component in STT-RAM, which overcomes the switching current problem. Unlike CMOS dynamic RAM and static RAM, STT-MRAM is a technology in which there is no leakage current in the data array. A decrease in the access transistor's threshold voltage exhibits two useful effects. First, a small transistor could be used to provide the device with the necessary write current. Another one is the access transistor's resistance is decreased, further improving both the current and voltage sense margins.

S. Kumari (✉) · R. Yadav
Department of ECE, DCRUST Murthal, Murthal, India
e-mail: 19001903905seema@dcrustm.org

R. Yadav
e-mail: rekhayadav.ece@dcrustm.org

© The Author(s), under exclusive license to Springer Nature Singapore Pte Ltd. 2023
P. Singhal et al. (eds.), *Recent Developments in Electrical and Electronics Engineering*,
Lecture Notes in Electrical Engineering 979,
https://doi.org/10.1007/978-981-19-7993-4_2

1.1 Magnetic Tunnel Junction

MTJ is a suitable device for implementing non-volatile memories [1]. These memories can solve the power issues in a nanoscale integrated circuit due to data holding after power shutdown. The MTJ structure is the basic component of the MRAM. MTJs are popular in the market due to their easy integration with the CMOS process and low fabrication cost. The perpendicular spin-transfer torque (p-STT) is preferred for low-power operation and improving scalability. In p-STT, the two FMs' polarization is perpendicular to the MTJ plane, indicating decreased switching current for the same retention time. The main magnetism of MTJs for logic is their non-volatile aspect, which permits in principle instant-on operation and zero leakage (Fig. 1).

An oxide barrier layer separates two ferromagnetic layers in a magnetic tunnel junction (MTJ). The resistance is high or low dependent on whether the ferromagnetic layers are magnetically anti-parallel or parallel as shown in Fig. 2. When both layers have the same directions, it is called the RAP resistance of MTJ. Whereas when the magnetic directions of layers are different it is called anti-parallel resistance of MTJ. To design the STT-RAM, one reference layer's magnetic orientation is fixed whereas the free layer's magnetic orientation can be modified by delivering a switching current polarized by the reference layer magnetization.

The tunneling magnetoresistance ratio (TMR) determined the difference between anti-parallel resistance and parallel resistance in an MTJ.

$$TMR(\%) = (RAP - RP) \times 100/RP$$

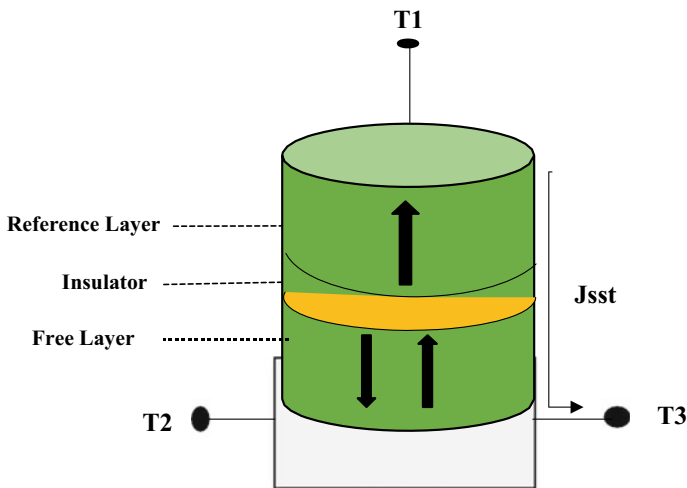
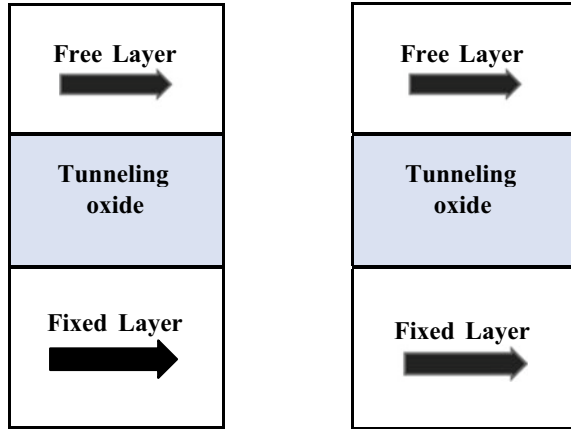


Fig. 1 Magnetic tunnel junction

Fig. 2 MTJ is in a condition of high or low resistance



There are various ways to design MTJs-based logic circuits, but mostly two categories are preferred: in first one MTJs are arranged and used as a 2D memory array, and in another category MTJs are used as a particular switch which is either in parallel/series configuration to keep logic functionality or having the status of register replacement devices.

1.2 MRAM Memory

MRAM is being investigated as a promising contender for next-generation universal memory. One of the most extensively utilized spintronics-based circuits for embedded memory in FPGAs and microprocessors is MRAM (magnetically random-access memory). Because of its non-volatility, intrinsic hardness to radiation effects, and high integration capabilities, MRAMs can be used to replace SRAM memory in these structures.

Because of its great density and speed, MRAM is an excellent substitute for standalone dynamic random-access memory. To store information in MRAM, the direction of magnetization concept is used and fluctuation in resistance with magnetization (magnetoresistance) as info readout. The progression of the MRAM technology assisted greatly in the rapid progress and revolutionary findings in magnetoresistive materials driven by the need to improve magnetic recording areal density.

Advantages of STT-MRAM:

- Suitability for low power and high endurance;
- CMOS compatibility;
- High-speed operation; and
- Fast switching.

2 Techniques for STT-MRAM

The voltage sense amplifier approach improves the bit-error-rate performance significantly. The VSenseAmp is less affected by data and reference cell resistance fluctuations. The VSenseAmp, which uses a single pMTJ cell as a reference, is a viable choice for high-speed, low-power read operations [3].

Convolutional neural networks are popular for deep learning structures. These models are made up of several layers, each with a separate function, that work together to do tasks that are generally difficult for traditional algorithms to complete. To overcome the complexity of metadata management, they proposed a grouping mechanism in which some blocks are combined to further decrease the storage overhead. To solve issues with MLC STT-RAM, including reliability and excessive power consumption, a simple yet effective technique is proposed to concurrently enhance their reliability and degrade power consumption [4]. Toggle Spin Torques (TST)-MRAM is an excellent choice for upper level caches when rapid operation and long write durability are required. The TST mechanism significantly improves the write endurance of the toggle spin-torque MRAM as compared to STT-MRAM. As a result, the TST-MRAM is particularly well suited to ultrafast and long-duration applications like upper level caches. As one of the most important issues in magnetic RAMs, the Spin Hall-assisted STT approach reduces writing energy [5].

To improve the bit error rate (BER) and sensing margin dynamic dual-reference sensing technique (DDRS) is used. If the reference cell maintains the same structure as those of the data cell, then no regularity difficulties exist in the suggested DDRS scheme. In deeply scaled STT-MRAM, read reliability is the main challenge that can be dealt with by using the DDRS technique. The main feature of the suggested DDRS scheme is to enhance the sensing margin without increasing the read disturbance. So that for STT MRAM, the DDRS scheme offers a powerful solution in deep submicrometric skill nodes [6].

Two magneto-tunnel junctions (MTJs) and two transistors make up a non-volatile, dependable static gain cell for cache memory applications. The variation in the gain cell threshold voltage and the wide distribution in MTJs resistance in anti-parallel and parallel states can be overcome by self-reference sensing circuits and connecting two complementary MTJs, respectively. The high voltage is applied across the stack complementary MTJ which enhances the sensing margin. The self-reference sensing structure has a greater ON/OFF ratio as compared to 1T1MTJ STT-MRAM and a smaller cell area as compared to SRAM [7].

2.1 Double-Barrier MTJs: (DMTJs)

The DMTJ consists of two MgO oxide barriers which act as the interference layer. The free layer in DMTJ is sandwiched between two MgO oxide barriers. The reference lines have anti-parallel magnetizations, which increase the total torque acting on the

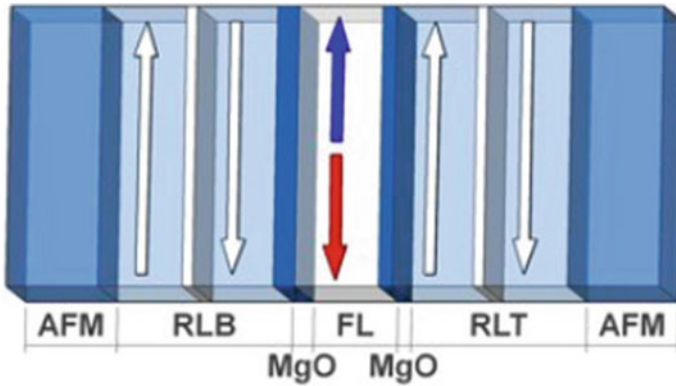


Fig. 3 DMTJ

free layer, therefore leading to decreased switching currents as compared to SMTJ. The bit cells based on DMTJ consume low energy for write operation as compared to SMTJ-based implementations. The STT-MRAM based on DMTJ is more energy efficient for write and read access. As compared to SMTJ, DMTJ is less space-hungry and more efficient in terms of leakage power (Fig. 3).

2.2 *Non-destructive Self-reference Sensing (NSRS) Technique*

NSRS scheme does not require write operation so that it maintains the STT-RAM short read latency and the non-volatility design. This scheme is used to overcome MTJ's resistance variation from bit to bit. The robustness of NSRS can be improved by using three techniques: yield-driven cell current choosing, R-I curve skewing, and ratio matching technique. Theoretical, "R-I curve skewing" and techniques significantly increased the STT-RAM cell current with the least yield-driven cell current choosing impact on memory reliability. By modifying the cell current at the post-manufacture stage, the "ratio matching" technology can balance the process variance in the voltage divider. NSRS can provide superior energy, performance, and yield trade-off. These strategies significantly enhance chip yield by eliminating sensing failures with low-power consumption and a high sense margin, according to measurements on a 16Kb test chip [1] (Fig. 4).

2.4 Dynamic Dual-Reference Sensing Technique (DDRS)

The DDRS scheme has the following features:

- Two reference signals are formed by two reference cells that have the same design as the data cells that are produced by two reference cells that are given to the sensing circuit.
- The reference signals are dynamically determined by the target data cell's content.
- The sensing result is determined by two output signals, which adds redundancy to support SED (self-error detection) ability.

The DDRS technique can increase sensing margin and reduce bit error rate [8].

2.5 Voltage-Driven Non-destructive Self-reference Sensing (VDRS) Scheme

The VDRS scheme increases sense margin in STT-RAM chips, resulting in higher yield. The VDRS technique improves device tolerance while maintaining a low read latency, high sense margin, and power consumption. In comparison to an NSRS technique, the VDRS is more resilient (Fig. 5).

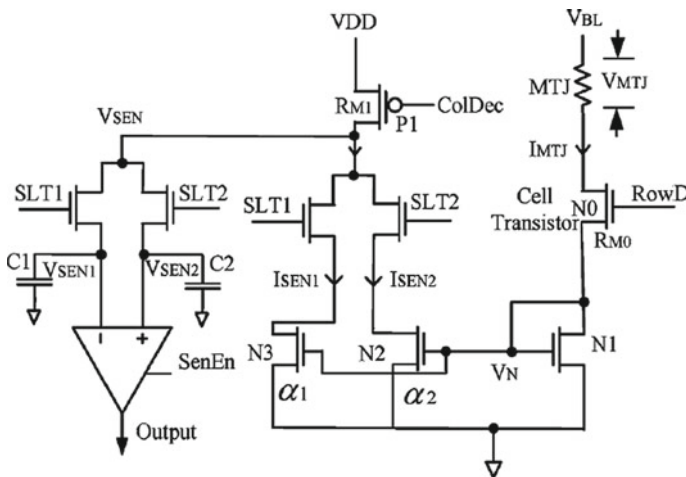


Fig. 5 VDRS scheme [9]

2.6 DMSS (*Dual-Mode Sensing Scheme*)

The main point of DMSS is to identify the exception state without any operational or energy consumption in the normal mode. The data-cell-variation-tolerant DMSS mostly operates in normal mode when appropriate sensing is assured. Non-DCVT-SS can operate in normal mode to achieve high performance and low energy consumption. When correct sensing is uncertain these schemes operate in exception mode. The DMSS can attain the target read yield by using the dual-mode strategy. The target read yield was calculated using the D-SRSS as DCVT-SS in exception mode [10].

2.7 TVS (*Three-Input Voltage Sense Amplifier*) Technique

TVS scheme has two modules:

- (1) One module adds bit lines and two reference MTJ cells to a column of cells to generate two reference voltages.
- (2) TVSA module: this module amplifies the difference in voltage between the read voltage and the two reference voltages.

TVS scheme enhance read speed because there is no need for additional read time. At the same read access, the two reference bit lines and the bit line are read. So that these schemes improve the reliability of the voltage sensing schemes [11].

2.8 *Source-Line-Biasing Technique*

In STT-RAM transistor leakage reduces the sensing accuracy and undesirably impacts on writing current scaling and read margin. To overcome these problems, we can use the dual-SL-biasing technique (DSLBI). DSLBI is preferred for sensing accuracy. These operate at lower read and write current, which improves read margin. This not only degrades the overall energy but also supports continued STT-RAM and MTJ scaling [12].

2.9 *Quantum Well States in MTJs Barrier*

- Quantum well states in barrier improve the spin-transfer torque in MTJ.
- These MTJs can be simply integrated with MOSFETs.
- It decreases resistance area product upholding good TMR as compared to without quantum well states in the barrier.

2.10 Tunnel Magnetoresistive Effect-Based Current Sensors

The electrical current measurement of the device is the main aspect when determining the energy converter's regulation and efficiency. The magnetoresistive-based electrical current sensor is an optimal measurement approach due to the absence of thermal losses, low-power consumption, and isolation. Several microfabricated or commercial prototypes MR current sensors used in instrumentation or industrial application offer different electrical properties.

2.11 MTJ-Based Biosensor

The sensor based on MTJ consists of an MTJ, a gold covering layer right beneath a bio-coating layer, and an isolation layer. The free ferromagnet of the top of the MTJ stack is heated by a current pulse above its blocking temperature. During the cool-down time, the top free magnet takes up its magnetization direction dependent on the externally applied magnetic field.

During the sensing phase, to excite the superparamagnetic bio-labels a vertical excitation is applied. The biosensor design can attain high sensitivity in three distinct ways:

- (1) In the time domain, the electronic readout operation and the magnetic sensing technique are decoupled.
- (2) The binary readout enhances its signal-to-noise ratio substantially.
- (3) The sensor sensitivity can be decoupled by thermally assisted magnetic sensing from the magnetic rigidity of the sensing layer.

To prevent damage to the bio-coating layer, the temperature should be below 50C gold layer's top surface (Table 1).

3 Conclusion

We have discussed the various techniques of STT-RAM. The DMTJ-based STT-MRAM is more energy efficient for write and read access. NSRS scheme does not require write operation so that it maintains the STT-RAM short read latency and the non-volatility design. The source-line-biasing technique operates at a lower read and write current, which improves read margin. TMRAM cells reduce the write energy. The magnetoresistive-based electrical current sensor is an optimal measurement approach due to the absence of thermal losses and low-power consumption. VSenseAmp with a specific reference pMTJ cell is preferred for low-power and high-speed read operations. To decrease the resistance area product upholding good TMR quantum well states are used in the barrier [13–30].

Table 1 Comparative analysis of various techniques

	Process	Supply voltage	Sensing margin	TMR	Read energy/bit	Read time [ns]
Chen et al. [1]	130 nm	–	50.4 mV	–	1.16Pj	15
Cai et al. [2]	28 nm CMOS	0.6 V	High 95 mV	50%	–	–
Seyedfaraji et al. [8]	32 nm CMOS	0.9 V	large	200%	79.0pJ	1.4 ns
Sun et al. [9]	130 nm PTM	–	62.5 mV	–	5.65pJ	15
Na et al. [10]	45 nm CMOS	–	–	100%	0.304pJ	8.7
Wang et al. [11]	28 nm CMOS	1 V	100 mV	120%	0.065pJ	0.7
Kang et al. [6]	40 nm CMOS	1 V	309.8 mV	100%	77.307pJ	–

References

- Chen Y, Li H, Wang X, Zhu W, Xu W, Zhang T (2011) A 130 nm 1.2 V/3.3 V 16 Kb spin-transfer torque random access memory with non-destructive self-reference sensing scheme. *IEEE J Solid- State Circuits* 47(2):560–573
- Cai H, Liu M, Zhou Y, Liu B, Naviner LAB (2020) CSME: a novel cycle-sensing margin enhancement scheme for high yield STT-MRAM. *Microelectron Reliab* 114:113732
- Atasoyu M, Altun M, Ozoguz S (2019) Sensing schemes for STT-MRAMs structured with high TMR in low RA MTJs. *Microelectron J* 89:30–36
- Jasemi M, Hessabi S, Bagherzadeh N (2020) Reliable and energy-efficient MLC state-ram buffer for CNN accelerators. *Comput Electr Eng* 86:106698
- Fiorentini S, Ender J, Selberherr S, de Orio RL, Goes W, Sverdlöv V (2021) Coupled spin and charge drift-diffusion approach applied to magnetic tunnel junctions. *Solid-State Electron* 186:108103
- Kang W, Pang T, Lv W, Zhao W (2016) Dynamic dual-reference sensing scheme for deep submicrometer STT-MRAM. *IEEE Trans Circuits Syst I Regul Pap* 64(1):122–132
- Ryu JW, Kwon KW (2015) A reliable 2T2MTJ nonvolatile static gain cell STT-MRAM with self-referencing sensing circuits for embedded memory application. *IEEE Trans Magn* 52(4):1–10
- Seyedfaraji S, Hajisadeghi AM, Talafy J, Zarandi HR (2020) DYSCO: dynamic stepper current injector to improve write performance in STT-RAM memories. *Microprocess Microsyst* 73:102963
- Sun Z, Li H, Chen Y, Wang X (2011) Voltage-driven non-destructive self-reference sensing scheme of spin-transfer torque memory. *IEEE Trans Very Large-Scale Integr (VLSI) Syst* 20(11):2020–2030
- Na T, Song B, Kim JP, Kang SH, Jung SO (2017) Data-cell-variation-tolerant dual-mode sensing scheme for deep submicrometer STT-RAM. *IEEE Trans Circuits Syst I Regul Pap* 65(1):163–174
- Wang J, Zhang Y, Lian C, Wang G, Zhang K, Wu X, Zhang Y, Zhao W (2019) High speed and reliable sensing scheme with three voltages for STT-MRAM. In: 2019 IEEE/ACM international symposium on nanoscale architectures (NANOARCH). IEEE, pp 1–6

12. Chatterjee S, Salahuddin S, Mukhopadhyay S (2010) Dual-source-line-bias scheme to improve the read margin and sensing accuracy of STTRAM in sub-90-nm nodes. *IEEE Trans Circuits Syst II Express Briefs* 57(3):208–212
13. Ouyang Y, Hu J, He J, Zhao G, Xue F, Wang Z, Wang SX, Yuan Z, Ding Z (2014) Modeling the frequency dependence of packaged linear magnetoresistive sensors based on MTJ. *IEEE Trans Magnet* 50(11):1–4
14. Moinuddin MG, Lone AH, Shringi S, Srinivasan S, Sharma SK (2019) Low-current-density magnetic tunnel junctions for STT-RAM application using MgO tunnel barrier. *IEEE Trans Electron Dev* 67(1):125–132
15. Park J, Zheng T, Erez M, Orshansky M (2015) Variation-tolerant writes completion circuit for variable-energy write STT-RAM architecture. *IEEE Trans Very Large-Scale Integr (VLSI) Syst* 24(4):1351–1360
16. Xu W, Zhang T, Chen Y (2009) Design of spin-torque transfer magnetoresistive RAM and CAM/TCAM with high sensing and search speed. *IEEE Trans Very-Large-Scale Integr (VLSI) Syst* 18(1):66–74
17. Zhao H, Amiri PK, Zhang Y, Lyle A, Katine JA, Langer J, Jiang H, Wang KL, Krivorotov IN, Wang JP (2012) Spin-transfer torque switching above ambient temperature. *IEEE Magnet Lett* 3:3000304–3000304
18. Amiri PK, Alzate JG, Cai XQ, Ebrahimi F, Hu Q, Wong K, Grèzes C, Lee H, Yu G, Li X, Akyol M, Wang KL (2015) Electric-field-controlled magnetoelectric RAM: progress, challenges, and scaling. *IEEE Trans Magnet* 51(11):1–7
19. Wolf SA, Lu J, Stan MR, Chen E, Treger DM (2010) The promise of nanomagnetic and spintronics for future logic and universal memory. *Proc IEEE* 98(12):2155–2168
20. Zeinali B, Esmaili M, Madsen JK, Moradi F (2017) Multilevel SOT-MRAM cell with a novel sensing scheme for high-density memory applications. In: 2017 47th European solid-state device research conference (ESSDERC). IEEE, pp 172–175
21. Barla P, Joshi VK, Bhat S (2020) A novel low power and reduced transistor count magnetic arithmetic logic unit using hybrid STT-MTJ/CMOS circuit. *IEEE Access* 8:6876–6889
22. Arias SIR, Muñoz DR, Cardoso S, Ferreira R, de Freitas PJP (2015) Total ionizing dose (TID) evaluation of magnetic tunnel junction (MTJ) current sensors. *Sens Actuators, A* 225:119–127
23. Chen Y, Li H (2011) Emerging sensing techniques for emerging memories. In: 16th Asia and South Pacific design automation conference (ASP-DAC 2011). IEEE, pp 204–210
24. Bhuin S, Sweeney J, Pagliarini S, Biswas AK, Pileggi L (2017) A self-calibrating sense amplifier for a true random number generator using hybrid FinFET-straintronic MTJ. In: 2017 IEEE/ACM international symposium on nanoscale architectures (NANOARCH). IEEE, pp 147–152
25. Takenaga T, Yoshida C, Yamazaki Y, Hatada A, Nakabayashi M, Iba Y, Takahashi A, Noshiro H, Tsunoda K, Aoki M, Furukawa T, Sugii T (2013) MgO based magnetic tunnel junctions with $\text{Co}_{20}\text{Fe}_{60}\text{B}_{20}$ sensing layer for magnetic field sensors. *IEEE Trans Magnet* 49(7):3878–3881
26. Chang JH, Chang CR (2013) Influence of film thickness on magnetic tunneling junction sensor with in-plane/out-of-plane sensing capabilities. *IEEE Trans Magn* 50(1):1–4
27. Arikan M, Ingvarsson S, Carter M, Xiao G (2013) DC and AC characterization of MgO magnetic tunnel junction sensors. *IEEE Trans Magn* 49(11):5469–5474
28. Patel R, Guo X, Guo Q, Ipek E, Friedman EG (2015) Reducing switching latency and energy in STT-MRAM caches with field-assisted writing. *IEEE Trans Very Large Scale Integr (VLSI) Syst* 24(1):129–138
29. Trinh QK, Ruocco S, Alioto M (2018) Time-based sensing for reference-less and robust read in STT-MRAM memories. *IEEE Trans Circuits Syst I Regul Pap* 65(10):3338–3348
30. Verma S, Kaushik BK (2015) Low-power high-density STT MRAMs on a 3-D vertical silicon nanowire platform. *IEEE Trans Very Large-Scale Integr (VLSI) Syst* 24(4):1371–1376

Optimum Design of Controller Parameters for Automatic Generation Control Employing Hybrid Statistically Tracked Particle Swarm Optimization Algorithm



Cheshta Jain Khare, Ujjwala Rai, H. K. Verma, and Vikas Khare

1 Introduction

Automatic generation control (AGC) is required by power utilities to match precisely the power demand at any time. The AGC system is designed to achieve the short-term reallocation of power to keep the change in system frequency within the set pre-specified limits. System frequency is a good indication of imbalance between power generation and load; further, an imbalance between generated and demanded power will be reflected with change in frequency and this will result in an increase or decrease of speed of turbine-generator set and in turn system frequency will deviate from nominal frequencies [1]. Different controllers can be employed to maintain frequency and tie line power at set values and an inappropriate controller gain value can affect the system performance and even it can become an unstable system. Various control methodologies like auto-tuning, self-tuning, etc. have been proposed by many researchers [2] and these conventional methods have some disadvantages which may be easily overcome by employing different evolutionary algorithms. A suitable distributed control system for an AGC system along with the assessment of generation allocation is analyzed by Raj et al. [3] and, in this paper, algorithms for distribution automation have been implemented and an attempt has been made for better results compared to the other techniques. Further, Sahu et al. [4] analyzed differential evaluation-based parallel two-degree freedom of proportional-integral-derivative (PID) controllers for AGC of power system with effect of governor dead band nonlinearity. This paper shows superiority of the proposed algorithm by comparison with the performance of AGC which is tuned by chaotic PSO algorithm. Jain

C. J. Khare (✉) · U. Rai · H. K. Verma
SGSITS, Indore, India
e-mail: cheshtajain194@gmail.com

V. Khare
STME, NMIMS, Indore, India

et al. [5] illustrated that modern controller is much faster than conventional integral control and gives better results.

The proposed work introduced a new variation in classical PSO in terms of statistical parameters called **hybrid statistically tracked particle swarm optimization (hybrid STPSO)** to search global best value with fast convergence speed. In multi-dimensional shifted, rotated problem, basic PSO may enmesh on local best value and then no further changes are observed in velocity of particles and at this point statistical parameter gives a new path to get global best value. This paper illustrates a statistical-based comparison of six evolutionary algorithms: ant colony optimization [6], chaotic PSO (CPSO) [7, 8], cuckoo search [9, 10], bacteria foraging optimization (BFO) [11, 12], teaching learning-based optimization (TLBO) [13, 14], and hybrid STPSO to find optimal PID controller gains of automatic generation control.

2 Modeling and Problem Formulation

Modeling is the framework, which provide optimum design of any system, which consists of all the essential parameters, which is used for performance enhancement of that system and if a system is modeled out with mathematical equation then it is called the problem formulation of a particular system. Here we are discussing modeling and problem formulation of automatic and generation control system.

The main objectives of automatic generation control (AGC) are

- i. To maintain the frequency within specified limits.
- ii. To control tie-line power flows.
- iii. Distribute the loads among the generating units of multi-area system.

In the present, workload-frequency dynamics are illustrated by developing a mathematical model of the interconnected reheat thermal system in the state variable form and Fig. 1 shows the transfer function model for j th area representation of the reheat thermal system.

- *Effect of governor dead band*

In an electric power system generation can be changed at a maximum rate and therefore dynamic performance of speed governor system is affected by inclusion of dead band. If the change in frequency is much smaller, it will remain in the band; hence speed control will be inactive [1]. Since both linear and nonlinear systems are studied in the proposed paper state space model is suitable for problem formulation. The change in tie-line power can be assumed as an additional disturbance to any j th area. The change in tie-line power can be assumed as an additional disturbance to any j th area. The area-wise state variable is defined as follows [2]:

$$\begin{aligned} X_1 &= \Delta f_j, X_2 = \Delta P_{E,j}, X_3 = \Delta P_{T,j}, X_4 = \dot{X}_3, \\ X_5 &= \Delta P_{tie,j}, X_6 = \Delta P_{C,j} \end{aligned}$$

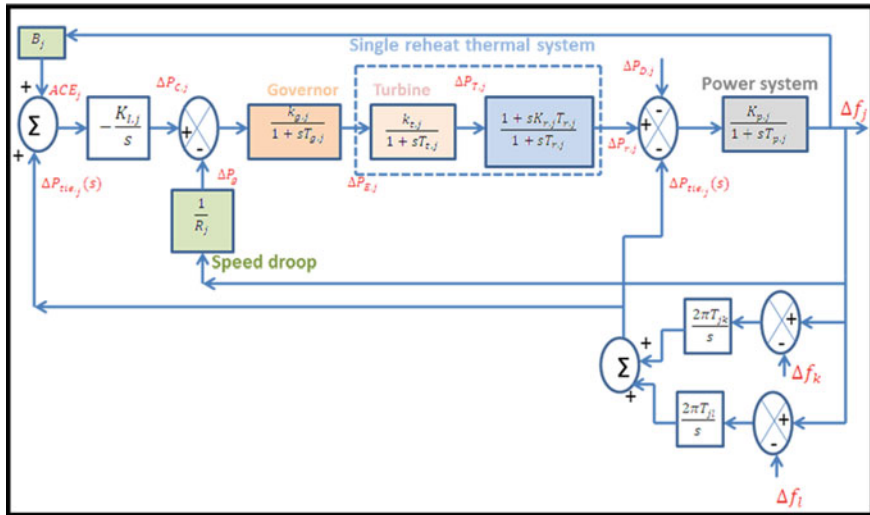


Fig. 1 Block diagram of j th area AGC implies dead band in the speed governing loop

The state space equation of j^{th} area can be written in the following form:

$$\dot{[X]}_j = [A]_j[X]_j + [U]_j, \tag{1a}$$

where $[X]_j^T = [X_1, X_2, X_3, X_4, X_5, X_6]_j$ and $[A]_j$ is the state matrix of j th area which can be written using the state Eq. (1a) of Fig. 1 as follows:

Matrix $[U]_j$ is defined as follows:

$$[A]_j = \begin{bmatrix} \frac{-1}{T_{p,j}} & 0 & \frac{K_{p,j}}{T_{p,j}} & 0 & \frac{-K_{p,j}}{T_{p,j}} & 0 \\ a_{21} & \frac{-1}{T_{g,j}} & 0 & 0 & 0 & \frac{1}{T_{g,j}} \\ 0 & 0 & 0 & 1 & 0 & 0 \\ a_{41} & \left(\frac{1}{T_{i,j} T_{r,j}} - \frac{K_{r,j}}{T_{g,j} T_{r,j}} \right) & \frac{-1}{T_{r,j} T_{i,j}} & - \left(\frac{T_{r,j} + T_{i,j}}{T_{r,j} T_{i,j}} \right) & 0 & \frac{K_{r,j}}{T_{g,j} T_{i,j}} \\ \sum_{\substack{k=1 \\ k \neq j}}^n 2\pi T_{jk} & 0 & 0 & 0 & 0 & 0 \\ -K_{I,j} B_j & 0 & 0 & 0 & -K_{I,j} & 0 \end{bmatrix}$$

$$[U]_j = \begin{bmatrix} -\frac{K_{p,j}}{T_{p,j}} \Delta P_{D,j} & U_{2,j} & 0 & U_{4,j} & - \sum_{\substack{k=1 \\ k \neq j}}^n 2\pi T_{jk} \Delta f_k & 0 \end{bmatrix},$$

where the value of a_{21} , a_{41} , U_2 , and U_4 depends whether the effect of dead band is considered or not. For the linear system (dead band not considered) this values is expressed as [2]

$$a_{21} = -\frac{1}{R_j T_{g,j}} \quad (2a)$$

$$a_{41} = -\frac{K_{r,j}}{R_j T_{g,j} T_{t,j}}. \quad (2b)$$

And U_2, U_4 both are equal to zero.

For nonlinear model (considering dead band) there will be two $[A]$ matrices for each area, one considers operation inside the dead band and the other considers the operation outside the dead band region.

- (i) When operation inside the dead band: there is no signal available corresponding to change in frequency. Hence values of matrix element $a_{21}, a_{41}, U_2,$ and U_4 become zero.
- (ii) Operation outside the band: when deviation in frequency is greater than 0.06% (DB) then the values of elements become [2]:

$$a_{21} = -\frac{1}{R_j T_{g,j}} \quad (3a)$$

$$a_{41} = -\frac{K_{r,j}}{R_j T_{g,j} T_{t,j}}$$

$$U_2 = \frac{DB}{R_j T_{g,j}} \text{sign}(\Delta f_j) \quad (3b)$$

$$U_4 = \frac{K_{r,j}}{R_j T_{g,j} T_{t,j}} DB \text{sign}(\Delta f_j)$$

The proposed research work analyzed four-area systems with and without effect of speed governing dead band of 0.06%.

3 Proposed Methodology Using Hybrid STPSO

Many academics have improved PSO algorithms in recent years, and while all of these changes have helped to speed up convergence, a multidimensional problem still requires a large number of iterations to get an optimal value. The current study uses various statistical parameters as a tracker to get the best global value with less iteration. To generate optimal AGC controller gains, a newly designed hybrid statistically tracked particle swarm optimization (STPSO) method is applied in this study. Basic PSO is a well-known evolutionary method with a random initialization. This algorithm updates particle positions to find the best solution in a given search space. Using the equations below, each particle sets its position and velocity [6]:

$$x_i^k = x_{min} + \text{rand}(N, d) * (x_{max} - x_{min})$$

and

$$v_i^k = v_{i,min} + rand(N, d) \cdot (v_{max} - v_{min}), \quad (4)$$

where N : number of population, d : number of parameters to optimize, k : current iteration count,

x_{min} and x_{max} : minimum and maximum values of particles in search space, and v_{min} and v_{max} : minimum and maximum value velocity vectors.

The velocity and position of each (i th) particle are updated using following equations:

$$v_i^{k+1} = wv_i^k + c_1r_1(\mathbf{pbest}_i^k - x_i^k) + c_2r_2(\mathbf{gbest}^k - x_i^k) \quad (5)$$

$$x_i^{k+1} = x_i^k + v_i^{k+1}, \quad (6)$$

where r_1 and r_2 are two separate random numbers ranging from 0 to 1. The acceleration constants c_1 and c_2 help particles advance toward the best possible value (\mathbf{gbest}^k), which is set to 1.5 and “ w ” is the inertia weight used to balance between best and best value. The weight of inertia changes with each iteration:

$$w = w_{max} - \frac{(w_{max} - w_{min})}{itermax} * iter, \quad (7)$$

where $itermax$ is the maximum number of iterations; w_{max} and w_{min} , the upper and lower limits of inertia weights. In the proposed paper, these values are 0.9 and 0.4 for each benchmark function. In complex multimodal issues, such an inertia weight method may not provide satisfactory results. To update particle velocity, the proposed hybrid STPSO employs the following modified relations:

$$v_{new,i}^{k+1} = wv_i^k + c_1r_1(\mathbf{pbest}_i^k - x_i^k) + c_2r_2(\mathbf{gbest}^k - x_i^k) + \beta^k, \quad (8)$$

where β^k denotes a factor of acceleration based on a statistical characteristic. The mean and standard deviation of the particle locations are used to calculate this factor. Because the mean value updates velocity in the direction of best location by mutual effect of different neighbor particles, and standard deviation utilizes the effect of dispersion around the mean position of the particle, these statistical characteristics are used to improve particle group behavior. The acceleration factor is calculated using the formulae below:

$$\beta^k = rand.(\mathbf{gbest}^k - X_s^k), \quad (9)$$

where $gbest^k$ = position corresponding to the global best value. X_s^k is computed using one of the statistical parameters:

- (1) Mean of particle position:

$$X_s^k = \bar{X} = \frac{\sum X_i}{N}. \quad (10)$$

- (2) Standard deviation of particle position:

$$X_s^k = \sigma_s^k = \sqrt{\frac{\sum (X_i^k - \bar{X})^2}{N - 1}}. \quad (11)$$

The position of the particle is updated using the following equation:

$$x_{new,i}^{k+1} = x_i^k + v_{new,i}^{k+1}. \quad (12)$$

The current study investigates hybrid STPSO by employing two statistical parameters to get an optimum value with increased variety. The mean value (X) of the particle's position is the first parameter, and the standard deviation () is the second. When there is no improvement in the global best value of the basic PSO, statistical tracking based on mean value is used, and when mean tracking becomes slow, standard deviation tracking is used to update particle position.

Now, calculate fitness function value corresponding for $x_{new,i}^{k+1}$. Now particle is selected for next iteration as

$$x_i^{k+1} = \begin{cases} x_{new,i}^{k+1} & \text{if } f(x_{new,i}^{k+1}) \leq f(x_i^k) \\ x_i^k & \text{if } f(x_i^k) < f(x_{new,i}^k) \end{cases} \quad (13)$$

3.1 Computational Algorithm Using Hybrid STPSO Method

- Step 1 Initialize optimization parameters such as population size (N), maximum iteration number (itermax), number of variables (d), search space range (x_{min} and x_{max}), and so on.
- Step 2 Set $i = 1$ and initialize particle's position and velocities using Eq. 4.
- Step 3 Evaluate fitness function of each population and obtain $pbest_{i^k}$ and $gbest^k$.
- Step 4 Modify velocity and position of each particle using relations 5 and 6, respectively.
- Step 5 Obtain fitness function for each updated particles.
- Step 6 Obtain $pbest_{i^{k+1}}$ and $gbest^{k+1}$.

- Step 7 If $|f(gbest^k) - f(gbest^{k+1})| \leq \epsilon$ then go to step-9. Here ϵ is a switch criteria (set at 0.0001) to change tracks from basic PSO to mean.
- Step 8 Increase the generation count $k = k + 1$, and go to step-4.
- Step 9 Calculate mean of particle position \bar{X} and determine the acceleration factor using relations 10 and 9.
- Step 10 Update velocity and position of each particle using relations 8, 12, and 13, respectively.
- Step 11 Calculate fitness function further for updated particles and obtain $pbest_i^k$ and $gbest^k$.
- Step 12 If $|f(gbest^k) - f(gbest^{k+1})| \leq \epsilon$ then go to step 14.
- Step 13 Increment the generation count $k = k + 1$ and go to step 9.
- Step 14 Calculate standard deviation vector σ using relation 11.
- Step 15 σ using relation 11.
- Step 16 Update each particles using relations 12 and 13.
- Step 17 Set $k = k + 1$. If $k \geq itermax$ then stop otherwise repeat from step 11.

In the proposed research, hybrid STPSO is implemented for four-area linear and nonlinear AGC systems as shown in Fig. 2.

The goal of the AGC problem is to find a gain parameter that allows for desired system performance such as lowest overshoot, undershoot, and settling time. To attain the aforesaid objectives, the current study applied the following optimization function [2]:

$$\text{fitness function} = \int_0^t \sum_{j=1}^n (\Delta f_j)^2 + \sum_{j=1}^{n-1} (\Delta P_{tie,j})^2 dt \quad (14)$$

This fitness function is minimized subject to following constraints in state space equation-1-a.

$$\sum_{i=1}^n \Delta P_{tie,i} = 0 \quad (15)$$

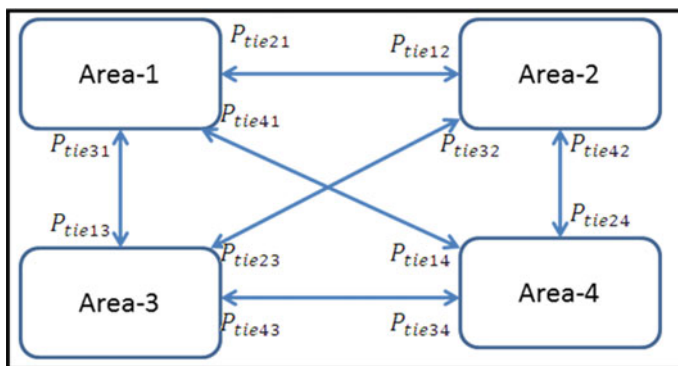


Fig. 2 Schematic diagram of four-area test system

$$\Delta P_{tie,n} = - \sum_{i=1}^{n-1} \Delta P_{tie,i}. \quad (16)$$

Substituting this condition and modifying state matrix of Eq. (1a) as follows:

$$x = \begin{bmatrix} \Delta f_1, \Delta P_{E,1}, \Delta P_{T,1}, \Delta P_{T,1}, \Delta P_{c,1}, \Delta f_2, \Delta P_{E,2}, \\ \Delta P_{T,2}, \Delta P_{T,2}, \Delta P_{c,2}, \Delta f_3, P_{E,3}, \Delta P_{T,3}, \\ \Delta P_{T,3}, \Delta P_{c,3}, \Delta f_4, \Delta P_{E,4}, \Delta P_{T,4}, \Delta P_{T,4}, \\ \Delta P_{c,4}, \Delta P_{tie,1}, \Delta P_{tie,2}, \Delta P_{tie,3}, \Delta P_{tie,4} \end{bmatrix}^T \quad (17)$$

In which $\Delta P_{tie,1}$, $\Delta P_{tie,2}$, $\Delta P_{tie,3}$, and $\Delta P_{tie,4}$ for four-area system can be written as

$$\begin{aligned} \Delta P_{tie,1} &= (2\pi T_{12} + 2\pi T_{13} + 2\pi T_{14})\Delta f_1 - 2\pi T_{12}\Delta f_2 - 2\pi T_{13}\Delta f_3 - 2\pi T_{14}\Delta f_4 \\ \Delta P_{tie,2} &= (2\pi T_{12} + 2\pi T_{23} + 2\pi T_{24})\Delta f_2 - 2\pi T_{12}\Delta f_1 - 2\pi T_{23}\Delta f_3 - 2\pi T_{24}\Delta f_4 \end{aligned} \quad (18)$$

Similarly equation for change in tie-line power for other areas can be written.

4 Results and Discussions

The performance of hybrid STPSO was compared to that of chaotic PSO (CPSO), ant colony, bacterium foraging optimization, cuckoo search, and teaching learning-based optimization (TLBO) algorithms in this section. For the sake of comparison, 100 runs were done for each technique. The proposed hybrid STPSO provides the following benefits.

Convergence profile: Fig. 3 compares the convergence of the best fitness value with the number of iterations for the four-area test system. The hybrid STPSO with mean and standard deviation discovers the best value faster than the other approaches, as seen in this graph.

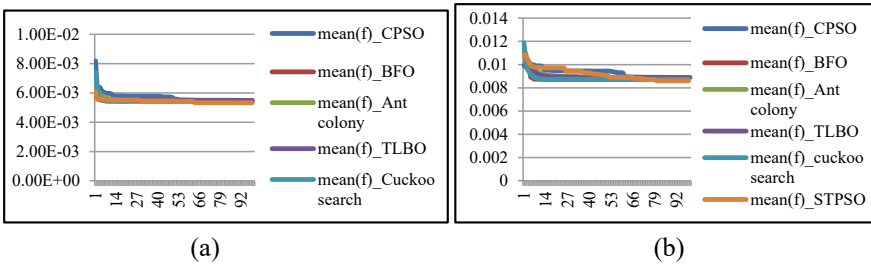


Fig. 3 Convergence profile for four-area (a linear, b nonlinear) AGC system of best mean fitness function value with respect to iteration count

Table 1 a Parameter values for test system without considering dead band. **b:** Parameter values for test system with dead band (nonlinear system)

Test system	Algorithms	Parameters		Fitness function
(a) Parameter values for test system without considering dead band				
Four-area AGC		K_I	B	
	CPSO	0.32203068	0.9660046	0.0054784203
	BFO	0.3515	0.8800	0.0054350498
	Ant Colony	0.3451	0.9000	0.0054300418
	TLBO	0.4239	0.7342	0.0054867217
	Cuckoo Search	0.3580	0.8977	0.0054330442
	Hybrid STPSO	0.3467	0.8993	0.0053300418
(b) Parameter values for test system with dead band (nonlinear system)				
Four-area AGC		K_I	B	
	CPSO	0.2746904	0.87208495	0.0088929749
	BFO	0.2656	0.8086	0.0087297675
	Ant Colony	0.2386	0.8949	0.008708383
	TLBO	0.29568052	0.88709475	0.0088690639
	Cuckoo Search	0.23619314	0.89047862	0.0087363357
	Hybrid STPSO	0.23480	0.8106	0.0086047532

Dynamic performance evaluation of AGC test system: The current study evaluates the best controller for AGC of four-area systems, both with and without nonlinearity, and implements various heuristics algorithms for the test system. When compared to alternative evolutionary algorithms for similar systems, such as CPSO, BFO, ant colony, TLBO, and cuckoo search optimization, the effectiveness of the proposed hybrid STPSO is demonstrated. The integral controller is discussed in this section of the text. The optimum values for test system corresponding to performance indices considered in Eq. 14 are summarized in Table 1a, b.

Dynamic performance

Test system (four-area system) without dead band

Figure 4 shows that in the case of a four-area system without the effect of a dead band hybrid, STPSO still outperforms in terms of maximum overshoot, minimum undershoot, settling time, and steady-state error for changes in frequency of area (area 1 and area 4). In hybrid STPSO, Fig. 4 depicts the area control error of four areas adjusted to zero with decreased settling time.

With effect of dead band: With increased number of area and nonlinearity included in the system, hybrid STPSO performs better and gives a good dynamic response of change in frequency of all areas as shown in Fig. 5. In comparison to other evolutionary algorithms, such as CPSO, BFO, ant colony, TLBO, and cuckoo

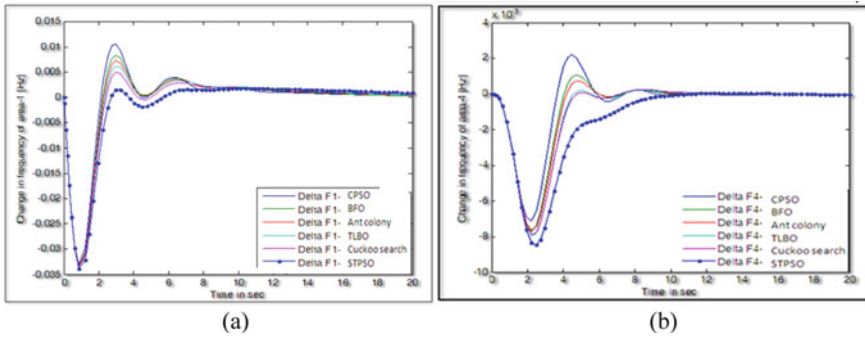


Fig. 4 Comparison of change in frequency of area 1 (a), area 4 (b)

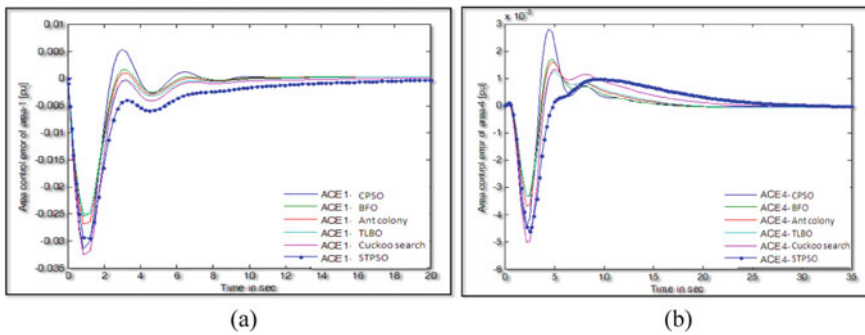


Fig. 5 Dynamic performance evaluation of area control error of area 1 (e), area 4 (f) with respect to time

search, change in tie-line power flow among various areas also gives better performance as shown in Figs. 6 and 7, which depict that area control error of all areas reach desired value faster with hybrid STPSO.

- Comparison based on statistical evaluation:** Table 2 shows the results of a four-area system’s autonomous generation control. In terms of minimum fitness function, the statistical performance of hybrid STPSO is better than that of other heuristic algorithms, as shown in the table (four-area linear: CPSO-0.00547, BFO-0.00545, Ant Colony-0.00545, TLBO-0.00546, Cuckoo search: 0.00543, STPSO-0.00534, four-area nonlinear: CPSO-0.00871, BFO-0.00871, Ant Colony-0.00871, TLBO-0.00881, Cuckoo Search-0.00870, STPSO-0.00861), mean of fitness function, maximum of fitness function, etc.

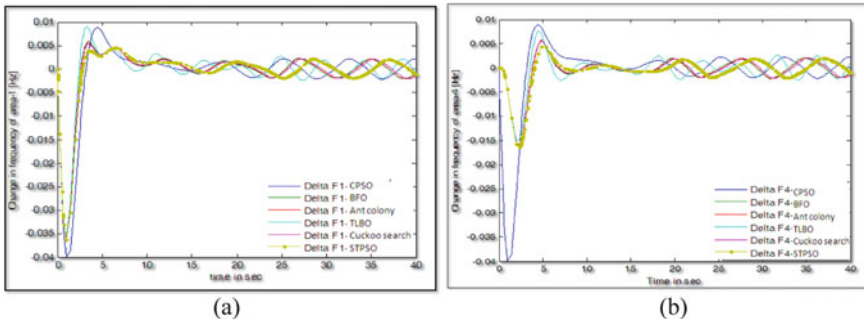


Fig. 6 Comparison of hybrid STPSO with other evolutionary algorithms for change in frequency of area 1 (k), area 4 (l)

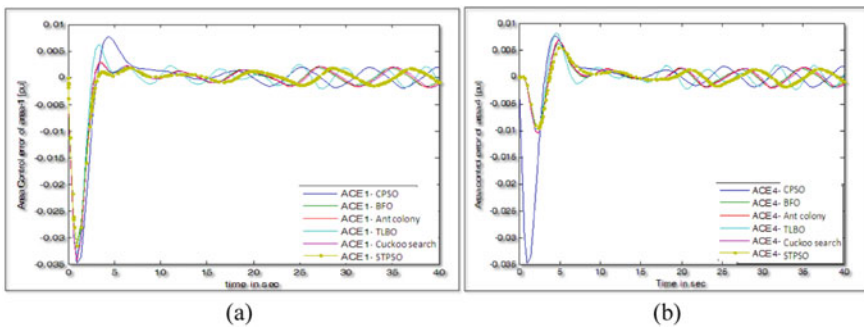


Fig. 7 Comparison of different heuristic algorithms for area control error of area 1(m), area 4(p) w.r.t time

5 Conclusion

A modified PSO algorithm was created in this study by introducing statistical factors to get the global optimal value. Table 2 compares the proposed hybrid STPSO method to existing optimization methodologies such as basic PSO and CPSO in terms of best value, maximum value, standard deviation mean, and other statistical metrics. For linear and nonlinear systems, the performance of hybrid STPSO is compared to BFO, CPSO, ant colony, cuckoo search, and TLBO of autonomous generation control. In terms of convergence profile and statistical parameters, experimental results show that hybrid STPSO performs better for four-area test systems with and without dead band. The proposed technique can successfully prevent the trapping on local best value, according to numerical data.

Table 2 Statistical comparison of four-area (linear and nonlinear) AGC with confidence level 0.95

System	Algorithm	Mean (fbest) (μ)	Median (fbest)	Std (fbest) (σ)	Best value (fbest)	Max. value (fbest)	Freq. of convergence	Standard error of the mean fitness function (ϵ) = $C*\sigma/\sqrt{n}$; n = pop size; C = 97.5th percentile of distribution	Length of confidence $2*C*\epsilon$
Four area (linear)	CPSO	0.00548	0.00542	0.00014	0.00547	0.00585	78	0.0000247	0.0000481
	BFO	0.00544	0.00544	0.00002	0.00545	0.00548	50	0.0000032	0.0000063
	Ant Colony	0.00543	0.00543	0.00000	0.00545	0.00543	77	0.0000000	0.0000000
	TLBO	0.00549	0.00549	0.00001	0.00546	0.00551	65	0.0000018	0.0000036
	Cuckoo Search	0.00543	0.00543	0.00001	0.00543	0.00543	86	0.0000001	0.0000001
Four area (nonlinear)	PSO mean and std (STPSO)	0.00533	0.00535	0.00007	0.00534	0.00537	88	0.0000131	0.0000255
	CPSO	0.00889	0.00893	0.00014	0.00871	0.00913	48	0.00003	0.00005
	BFO	0.00873	0.00872	0.00003	0.00871	0.00886	62	0.00001	0.00001
	Ant colony	0.00871	0.00871	0.00013	0.00871	0.00871	81	0.00002	0.00005
	TLBO	0.00887	0.00885	0.00005	0.00881	0.00894	42	0.00001	0.00002
Cuckoo search	0.00874	0.00874	0.00000	0.00870	0.00874	64	0.00000	0.00000	
PSO mean and std (STPSO)	0.00860	0.00878	0.00010	0.00861	0.00868	83	0.00002	0.00003	

Appendix

System parameter for four area AGC system [2, 4]

$$k_{g,1} = k_{g,2} = k_{g,3} = k_{g,4} = 1,$$

$$T_{g,1} = T_{g,2} = T_{g,3} = T_{g,4} = 0.08,$$

$$k_{t,1} = k_{t,2} = k_{t,3} = k_{t,4} = 1,$$

$$T_{t,1} = T_{t,2} = T_{t,3} = T_{t,4} = 0.3,$$

$$K_{r,1} = K_{r,2} = K_{r,3} = K_{r,4} = 0.5,$$

$$T_{r,1} = T_{r,2} = T_{r,3} = T_{r,4} = 10,$$

$$K_{p,1} = K_{p,2} = K_{p,3} = K_{p,4} = 120,$$

$$T_{p,1} = T_{p,2} = T_{p,3} = T_{p,4} = 20,$$

$$\beta_1 = \beta_2 = \beta_3 = \beta_4 = 0.872,$$

$$R_1 = R_2 = R_3 = R_4 = 2.2568,$$

$$2\pi T_1 = 2\pi T_2 = 2\pi T_3 = 2\pi T_4 = 0.05.$$

Parameters for PSO algorithm:

Initial population = 30; Maximum iteration = 100; $W_{\max} = 0.9$; $W_{\min} = 0.4$; $C_1 = C_2 = 1.5$.

Parameters for CPSO algorithm:

Initial population = 30; Maximum iteration = 100; $W_{\min} = 0.1$

Parameters for DE algorithm:

Initial population = 30; Maximum iteration = 100; $F = 0.5$;

$R = 0.98$;

Parameters for B B-BC algorithm:

Initial population = 30; Maximum iteration = 100; $\beta = 0.7$;

$\alpha = 0.5$

Parameters for TLBO algorithm:

Initial population = 30; Maximum iteration = 100.

References

1. Elgerd OI, Fosha C (1970) Optimum megawatt-frequency control of multiarea electric energy systems. IEEE Trans Power Apparatus Syst PAS-89(4):556–563
2. Sinha N, Lai LL, Rao VG (2008) GA optimized PID controllers for automatic generation control of two area reheat thermal system under deregulated environment. In: Proceedings of the IEEE international conference on electric utilizes deregulation and restructuring and power technologies, 6–9 April, pp 1186–1191
3. Raj H (2006) A distributed algorithm for an AGC in hydrothermal power plant. IFAC Proc Vol 39(7):1–6
4. Sahu R, Panda S, Raut UK (2013) DE optimized parallel 2-DOF PID controller for load frequency control of power system with governor dead-band nonlinearity. Int J Electr Power Energy Syst 49:19–33

5. Jain D, Bhasker MK, Kumar M (2014) Comparative analysis of different methods of tuning the PID controller parameters for load frequency control problem. *Int J Adv Res Electr, Electron Instrument Eng* 3(11):13144–13154
6. Dorigo M, Blum C (2005) Ant colony optimization theory: a survey. *Theoret Comput Sci* 344:243–278
7. Nikabadi A, Ebadzadeh MM, Safabaksh R (2011) A novel particle swarm optimization with adaptive inertia weight. Elsevier, *Appl Soft Comput* 11:8658–3670
8. Gao WF, Liu S-Y, Hauang L-L (2012) Particle swarm optimization with chaotic opposition based population initialization and stochastic search technique. Elsevier 17:4316–4327
9. Payne B (2005) Robert. Oxford University Press, *The Cuckoos*
10. Rajabioun R (2011) Cuckoo optimization algorithm. *Appl Soft Comput* 11:5508–5518
11. Agrawal V, Sharma H, Bansal JC (2011) Bacterial foraging optimization: a survey. In: *The international conference on soft computing for problem solving (SOCPROS)*, pp 227–242
12. Ali ES, Abd-Elazim SM (2011) Bacteria foraging optimization algorithm based load frequency controller for interconnected power system. *Electr Power Energy Syst* 33:633–638
13. Rao RV, Savsaniand VJ, Vakharia DP (2012) Teaching–learning-based optimization: an optimization method for continuous non-linear large scale problems. Elsevier, *Inform Sci* 183:1–15
14. VenkataRao R, Patel V (2012) An elitist teaching-learning-based optimization algorithm for solving complex constrained optimization problems. *Int J Industr Eng Comput* 3:535–560

A Comparative PWM Analysis of MMC



Rahul Jaiswal, Anshul Agarwal, Richa Negi, and Komal Agrawal

1 Introduction

Multilevel converters demonstrated to be extremely prevalent recently, more than over three decades especially for medium- and high-power applications, like distribution, transmission, and generation systems [1–3]. Due to various advantages, the multilevel converters are more efficient as compared to the two-level converter, such as improved harmonic distortions, lower switching losses, lower electromagnetic interference (EMI), and better output waveform, etc. In case, if number of levels increases the quality of output will be improved but the complexity of the multilevel converter has also been increased such as voltage balancing problem, control technique, size of the circuit, etc. [4, 5].

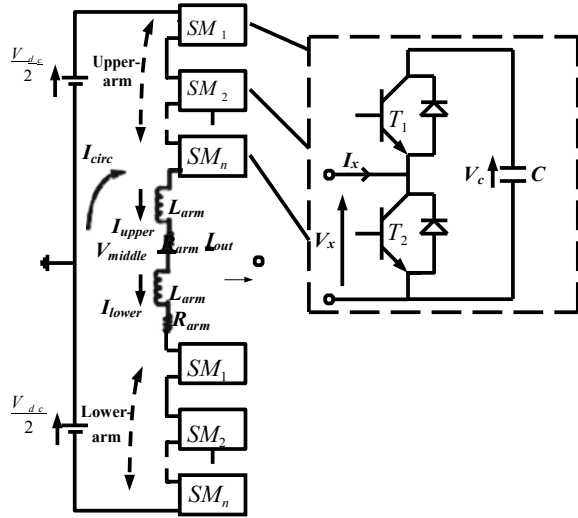
The modular multilevel converter is part of multilevel converters which are defined as a cascaded interconnected submodule. These submodules comprise of power semiconductor devices, capacitance, and diode. Researcher has introduced different type of submodule but most common type of submodules are half-bridge and full-bridge submodule.

The modular multilevel converter has lot of advantages such as lower switching losses, simple voltage balancing problem, scalable up to different power and voltage level and transformerless device. Due to these advantages, a lot of research papers have been published on a modular multilevel converter from the last couple of years [6–11]. The basic feature of single-phase leg modular multilevel converter is depicted in Fig. 1.

R. Jaiswal · R. Negi · K. Agrawal
Department of Electrical Engineering, MNNIT Allahabad, Prayagraj, India

A. Agarwal (✉)
Department of Electrical and Electronics Engineering, NIT Delhi, Delhi, India
e-mail: anshul@nitdelhi.ac.in

Fig. 1 Single-phase leg MMC



In recent years, many challenges have been found like design constraints (reliability, semiconductor losses, size of capacitor, size of inductor), control challenges, capacitor pre-charging, startup, and modeling, etc. The control technique is one of the crucial challenges of MMC and it plays a vital role. The performance of MMC is highly dependent on modulation technique. Abundant research is going on based upon multiple modulation techniques [12, 13].

The control and dynamic analysis of modular multilevel converter has been examined. The average model of this converter has also been studied. The MMC is used for numerous applications such as HVDC, grid system, railway applications, and solar and wind application [14, 15].

In this paper, the performance and analysis of MMC have been done by utilizing various modulation techniques including APOD, CO, and PS modulation strategy. The analysis has been performed at different modulation index and comparative analysis of different modulation techniques has also been examined here.

2 Modular Multilevel Converter (MMC)

The MMC is defined as a series-connected submodule by means of arm inductance and resistance. The submodule is a combination of power semiconductor devices and capacitance. These devices are arranged in a different way to obtain efficient output and improved total harmonic distortions. These arrangements are half-bridge, full-bridge, double clamp submodule, etc. These submodules have own advantages and disadvantages. It has been observed that the half-bridge submodule is one of the best submodules among the other submodule. The half-bridge submodule has higher

efficiency and lower cost as compared to other submodules. So half-bridge submodule is used for numerous applications. The MMC is classified into two parts, the first one is upper arm and another one is lower arm which includes the arm inductance and arm resistance. The arm inductance is used to restrict short circuit current through single-phase leg [8, 16]. The basic feature of single-phase leg modular multilevel converter is depicted in Fig. 1.

3 Control Structure

There is lot of control techniques used for generating pulse signal. The multicarrier PWM technique is used for multilevel converter which is dividing into two parts, first one is level-shifted PWM technique and other one is PS modulation technique. The multicarrier modulation strategy is widely used in various applications due to its simple working principal, and furthermore it tends to be effectively executed in the low-voltage application [12, 17–19]. In general, amplitude modulation index (m_a), and frequency modulation index (m_f) for level shifted and phase shifted are explained below.

The amplitude modulation index (m_a) of level-shifted modulation technique is represented in (1).

$$m_a = \frac{2A_r}{(m-1)A_c} \quad (1)$$

Similarly, amplitude modulation index of phase-shifted modulation technique is represented in (2).

$$m_a = \frac{A_r}{\left(\frac{A_c}{2}\right)} \quad (2)$$

where m is number of level, A_r is reference sine wave amplitude, and A_c is carrier wave amplitude.

The frequency modulation index (m_f) of phase- and level-shifted modulation technique is same which is defined in (3)

$$m_f = \frac{f_c}{f_r} \quad (3)$$

where f_c is frequency of carrier triangular waveform and f_r is frequency of reference sinusoidal waveform.

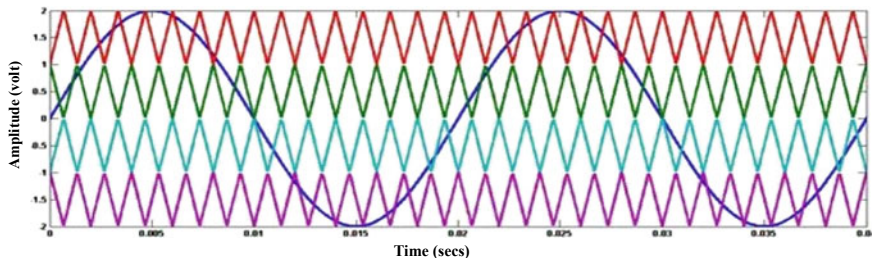


Fig. 2 Alternate phase opposition disposition PWM waveform

4 Alternate Phase Opposition Disposition (APOD)-PWM

In (APOD)-PWM, every carrier waveform is 180 degree in phase opposition with its neighboring carrier wave as shown in Fig. 2. All carrier waveforms are of the same frequency and same amplitude. All odd carrier waveforms are in phase with respect to one another but are in 180-degree out of phase with respect to all even carrier waveforms. The N th number of carrier waveform is compared with single reference waveform which generates $(N+1)$ th level output waveform. Here, the five levels of the modular multilevel converter have been considered, so the four carrier waveforms are analogized with single reference waveform.

In this modulation technique, the $+V_{dc}/2$ voltage will be generated when the sinusoidal waveform is greater than all triangular waveforms. The $+V_{dc}/4$ voltage will be generated when the sinusoidal waveform is lower than the uppermost triangular waveform and greater than all other triangular waveforms. The zero voltage will be generated when the sinusoidal waveform is lower than above zero reference waveform, and greater than below zero reference waveform. Similarly, $-V_{dc}/4$ voltage will be generated when the sinusoidal waveform is greater than the lower most triangular waveform and lower than other carrier waveforms. The $-V_{dc}/2$ voltage will be generated when the sinusoidal waveform is lower than all triangular waveforms.

5 Carrier Overlap-PWM

In this modulation technique, the $(N-1)$ carriers are eliminated such that their bands superimpose one another and $A_c/2$ is the vertical distance between each carrier. The reference waveform is placed in middle of carrier signals as depicted in Fig. 3. The amplitude modulation index pertaining to this case is mentioned in Eq. (4). There are four triangular waveforms which are analogized with the single sinusoidal waveform to generate pulse signal of five levels for MMC.

$$m_a = \frac{A_r}{\left(\frac{m}{4}\right)A_c} \quad (4)$$

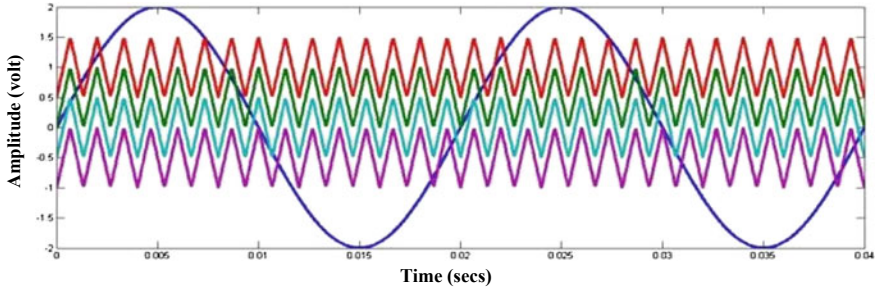


Fig. 3 Carrier overlapping PWM waveform

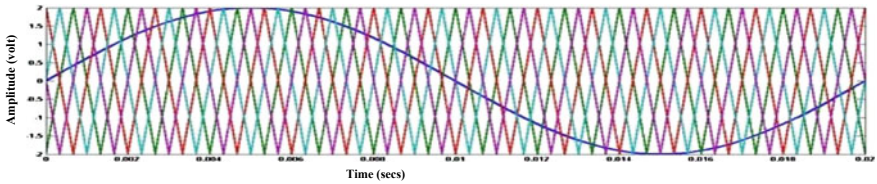


Fig. 4 Phase-shifted PWM waveform

6 Phase-Shifted PWM

In this technique, every carrier waveform possesses identical frequency and amplitude, but is phase shifted with respect to one another as shown in Fig. 4. The phase difference of consecutive waveform is represented in Eq. (5). The output pulse signal has been generated by comparing the sinusoidal waveform with the triangular waveform.

$$\frac{360^\circ}{N} \tag{5}$$

where N denotes number of submodules in one converter arm.

7 Result and Discussion

The analysis and execution of five-level MMC has been examined for R load by using alternate phase opposition disposition (APOD), carrier overlap (CO), and phase-shifted (PS) modulation techniques at different modulation indices. The output voltage waveform and current waveforms have been attained. It is close to sinusoidal nature. All the results have been obtained by using parameters as shown in Table 1.

Table 1 Simulation parameters for the multicarrier PWM

Parameters	Value
V_{dc} , (DC-link voltage)	800 V
R_o , (load resistance)	10 k Ω
D , (duty ratio)	50%
Submodule capacitance, C	100 μ F
(Carrier frequency), f_c	750 Hz
(Fundamental frequency), f_m	50 Hz

The performance and analysis of output current and voltage waveform of five-level MMC have been attained for R load. This analysis is done by using APOD-PWM, CO-PWM, and PS-PWM, respectively, as depicted in Figs. 5, 6, and 7. The output waveform is close to sinusoidal that means losses are very less and the efficiency has been improved.

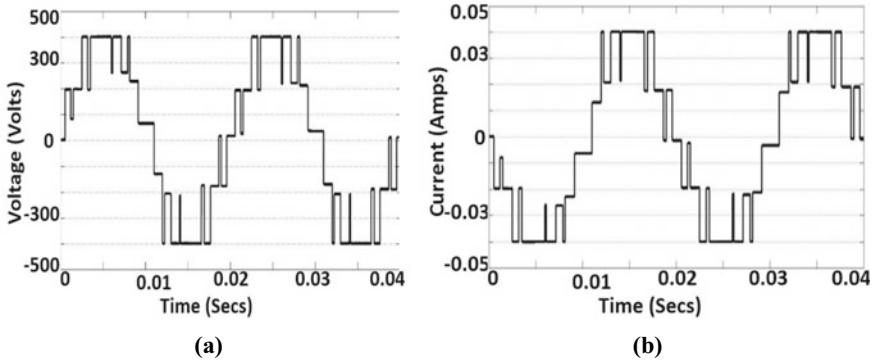


Fig. 5 **a** Output voltage **b** output current for five-level MMC using APOD-PWM

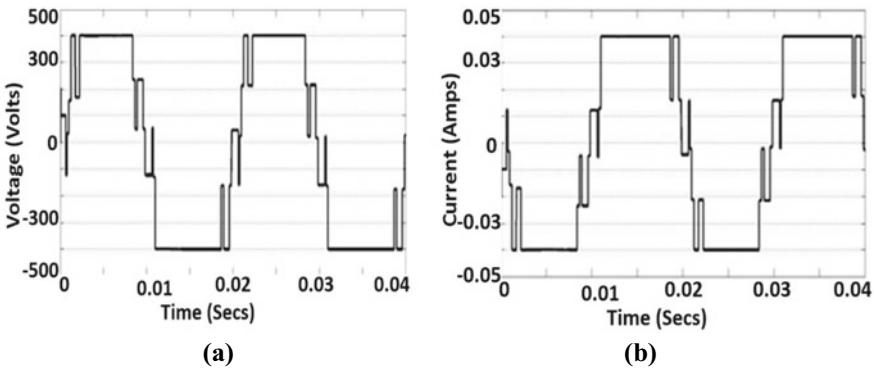


Fig. 6 **a** Output voltage, **b** output current for five-level MMC using carrier overlapping PWM

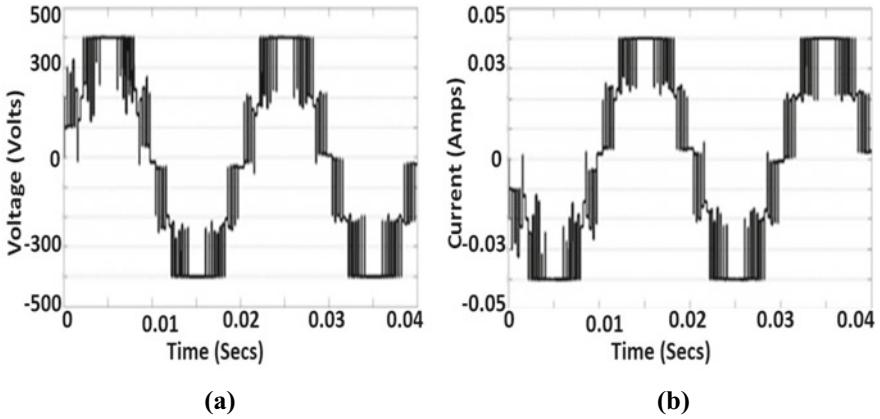


Fig. 7 a Output voltage, b output current for five-level MMC using phase-shift PWM

The THD has been calculated for APOD-PWM, CO-PWM, and phase-shifted PWM technique for R load (five-level MMC) under numerous modulation indices. The harmonic spectra under various modulation techniques for the output voltage are shown in Fig. 8.

The comparisons of THD for APOD-PWM, CO-PWM, and PS-PWM have been calculated at different modulation indices and fixed carrier frequency (750 Hz), as

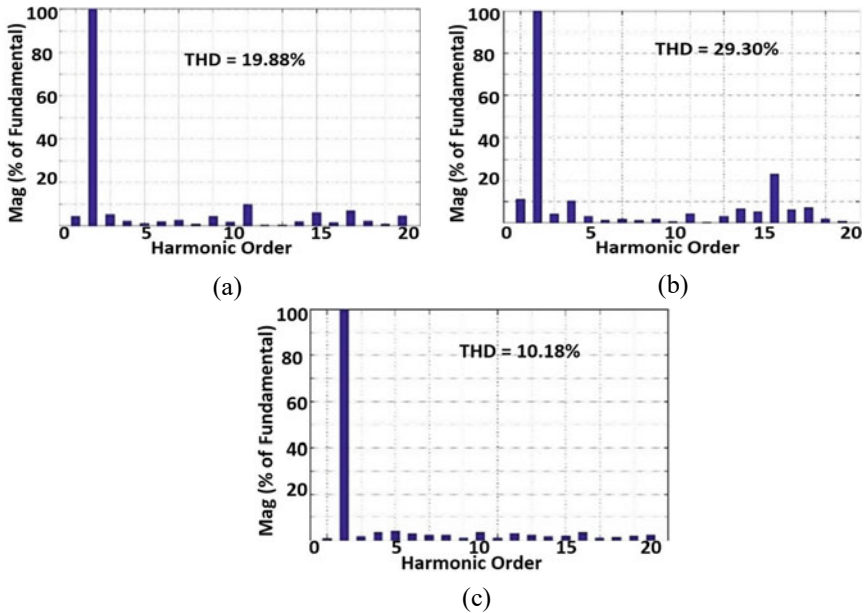


Fig. 8 Harmonic spectra for a APOD-PWM, b CO-PWM, c PS-PWM

Table 2 Comparison for different modulation techniques at different modulation indices and their THD (in percentage)

m_a	<i>APOD</i>	<i>PS</i>	<i>CO</i>
1	19.88	10.18	29.30
0.9	28.74	10.31	35.60
0.8	32.78	12.11	35.41
0.7	32.06	17.39	49.36
0.6	30.17	20.45	51.56

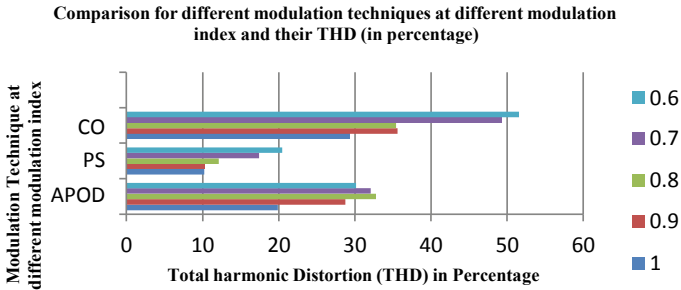


Fig. 9 Comparison of total harmonic distortion (THD)

shown in Table 2. It is evident that THD of PS modulation technique has been lowered as compared to other modulation techniques. Thus the PS-PWM technique is superior. It has also been noticed that the THD will increase when the modulation index is decreased. That means THD and modulation index are inversely proportional to each other. The variation of THD and modulation techniques at different modulation indices has been plotted as shown in Fig. 9.

8 Conclusion

The multicarrier modulation technique manifests as best modulation technique. The accomplishment of APOD-PWM, CO-PWM, and PS-PWM is very similar to each other but the phase-shifted modulation technique is the best technique compared to the rest of the technique. The losses are very low in phase-shifted modulation technique so this technique is more efficient. It has also been inferred that THD is improved at unity modulation index and fixed carrier frequency (750 Hz) in all cases. If the modulation index decreases, the THD will increase. It can be said that the THD is in inverse proportion to the modulation index.

References

1. Parkhideh B, Bhattacharya S (2013) Vector-controlled voltage-source converter-based transmission under grid disturbances. *IEEE Trans Power Electron* 28(2):661–672
2. Jaiswal R, Mittal V, Agarwal A, Agarwal V (2018) Voltage and power balance of a three-phase solid state transformer using a decoupled control strategy for grid-side converter. In: International conference on computing, power and communication technologies (GUCON) 2018, pp 449–454
3. Anese ED, Dhople S, Giannakis G (2014) Optimal dispatch of photovoltaic inverters in residential distribution systems. *IEEE Trans Power Electron* 5(2):487–497
4. Yazdani M, Mehrizi-Sani A (2014) Internal model-based current control of the RL filter-based voltage-sourced converter. *IEEE Trans Energy Convers* 29(4):873–881
5. Rodriguez J, Franquelo LG, Kouro S, Leon JI, Portillo RC, Prats MAM, Perez MA (2009) Multilevel converters: an enabling technology for high-power applications. *Proceedings of the IEEE* 97(11):1786–1817
6. Lesnicar A, Marquardt R (2003) An innovative modular multilevel converter topology suitable for a wide power range. In: presented at the IEEE Bologna Power Tech Conference 2003, Bologna, Italy
7. Naik MD, Agarwal V, Naik MV, Yadav S, Agarwal A, Jaiswal A (2018) Torque ripple reduction of BLDC motor using modular multilevel converter. In: International conference on computing, power and communication technologies (GUCON) 2018, pp 829–833
8. Li Z, Li Y, Wang P, Zhu H, Chu Z, Wang W (2011) Improving the performance of modular multilevel converter by reducing the dead time effect. In: European conference on power electronics and applications, EPE 2011, pp 1–10
9. Tu Q, Xu Z (2011) Impact of sampling frequency on harmonic distortion for modular multilevel converter. *IEEE Trans Power Deliv* 26(1):298–306
10. Ilves K, Antonopoulos A, Harnfors L, Norrga S, Angquist L, Nee HP (2011) Capacitor voltage ripple sharing in modular multilevel converters allowing for operating region extension. *IEEE IECON* 2011, pp 4250–4255
11. Ceballos S, Pou J, Choim S, Saeedifaard M, Agelidis VG (2011) Analysis of voltage balancing limits in modular multilevel converters. *IEEE IECON* 2011:4244–4249
12. Li Y, Wang Y, Li BQ (2016) Generalized theory of phase-shifted carrier PWM for cascaded H-bridge converters and modular multilevel converters. *IEEE J Emerging Selected Topics Power Electron* 4(2):589–605
13. Konstantinou G, Ciobotaru M, Agelidis VG (2011) Analysis of multicarrier PWM methods for back-to-back HVDC systems based on modular multilevel converters. *IEEE IECON* 2011:4238–4243
14. Hagiwara M, Maeda R, Akagi H (2010) Theoretical analysis and control of the modular multilevel cascade converter based on double-star chopper-cells (MMCC-DSCC). International power electronics conference, IPEC, 2010, pp 2029–2036
15. Jaiswal R, Agarwal A, Agarwal V (2018) A comprehensive analysis of delta and adaptive delta modulated modular multilevel converter. In: *Lecture Notes in Electrical Engineering*, Springer
16. Gowaid IA, Adam GP, Massoud AM, Ahmed S, Williams BW (2018) Hybrid and modular multilevel converter designs for isolated HVDC–DC converters. *IEEE J Emerging Selected Topics Power Electron* 6(1):188–202
17. Song S, Liu J, Ouyang S, Chen X, Liu B (2018) Control of direct AC/AC modular multilevel converter in railway power supply system. In: The international power electronics conference 2018, pp 1051–1055
18. Jaiswal R, Agarwal A, Agarwal V (2018) Control strategy of a solid state transformer for the grid-side converter. *Recent Adv Electr Electron Eng* 12(1):1–9
19. Choi J, Han B, Kim H (2016) New scheme of phase-shifted carrier PWM for modular multilevel converter with redundancy submodules. *IEEE Trans Power Del* 31(1):407–409

An Analytical Study to Evaluate the Performance of Different PV Configurations Under Various Partial Shading Conditions



Varun Agarwal, Venkata Madhava Ram Tatabhatla, and Anshul Agarwal

1 Introduction

With rising level of pollution and global warming the world is shifting towards renewable energy sources to meet the ever-growing demand for energy. Out of all available sources of green energy most prominent source is solar energy. Solar energy is helping to shift from fossil-fuel-based economy to carbon-neutral economy. To extract the solar energy, PV cells convert solar irradiance to useful electric energy. Solar PV plants' size varies from few KW to thousands of MW.

Although solar energy is very useful the major drawbacks are due to its dependency on environmental conditions, that is, irregular availability and partial shading. In order to deal with irregular availability energy storage systems are developed [3].

Under the partial shading condition all the panels of the solar array do not get same level of solar irradiance due to which the I-V and P-V characteristic curves show multiple peak values and hence develops difficulty in defining the maximum output power points [9]. There are various conditions which cause shadings such as (i) moving clouds, (ii) dust and wind, (iii) tall hospitals and buildings, (iv) moving aircraft, (v) long tree, and (vi) gases given out by factories [3]. For the shading conditions, the shaded panel generates reduced current which causes reduction in power generated at the output of PV array and also makes the shaded panel to act as load and it starts consuming power. This leads to hot-spot phenomenon. This all limits the reliability of the solar power and hence the power given out of a PV system will also reduce. Therefore, to avoid the ill effects of partial shading condition the bypass diodes are taken into account in shunt to the PV panels [5, 7, 10]. However, this

V. Agarwal · A. Agarwal (✉)
National Institute of Technology Delhi, Delhi, India
e-mail: anshul@nitdelhi.ac.in

V. M. R. Tatabhatla
BMS College of Engineering Bangalore, Bangalore, Karnataka, India

leads to generation of local maximum power point (LMPP) in power against voltage characteristics curve due to mismatch between row currents. This also makes tracking of the global maximum power point (GMPP) difficult for the controller [4, 8, 11].

The significant and effective way to enhance the power is by joining the panels in series connections along with and parallel connections [6]. In this work, we have considered four different types of configurations: Series with Parallel (S-P), Total-Cross-Tied (TCT), Bridge-Tied (BT) and Honeycomb (HC).

To validate the given configurations, it is tested on 36 panels which are connected in 6x6 PV array. The results are obtained for different shading patterns such as Diagonal, Z-shading, Centre and Random shading. The power generated for various configurations is compared under distinct shading conditions to know which configuration gives better power output and reduces row current mismatch.

2 System Configuration

An PV array is the connection of large number of PV cells to produce the optimal power at the output port. A PV array is formed by connections of PV panels in series and parallel depending upon the voltage and current requirement. The simplified electrical equivalent of one-diode PV cell is presented in Fig. 1 [2].

The current given out of the solar cell is presented as (I_{solar}). The diode connected to the circuit produces the reverse current (I_{dio}) and the circuit has two resistors (R_{shunt}) which are connected in shunt to the diode and (R_{series}) which is connected in series to the output terminal. (R_{series}) is used to determine slope near open-circuit condition and (R_{shunt}) is used to determine slope near short-circuit condition in I-V curve.

The generated current at the output is given by

$$I_o = I_{solar} - I_{diode} - I_{shunt}$$

$$I_o = I_{solar} - I \left[\exp\left(\frac{V_o + I_o R_{series}}{A V_t}\right) - 1 \right] - \left(\frac{V_o + I_o R_{series}}{R_{shunt}}\right) \tag{1}$$

where (I_{solar}) represents electric current generated by each solar cell, (I) represents reverse saturation current, (I_{diode}) represents diode saturation current, (I_{shunt}) depicts the current flowing through the shunt path resistor (R_{shunt}), (I_o) and (V_o) represent the

Fig. 1 Single diode equivalent model of the PV cell

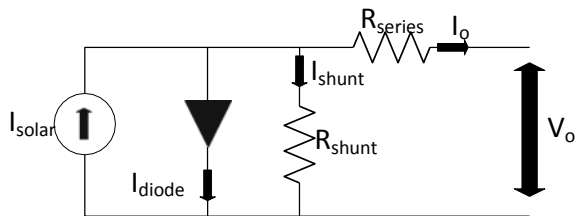


Table 1 PV panel specifications

Pmax	Vmax	I _{max}	V _{oc}	I _{sc}
50.388 W	16.45 V	3.06 A	19.8 V	3.3 A

actual of current and voltage observed at the output terminal that can be utilized by the load, (V_t) gives the voltage across the pins of the diode and ($A = nkT_o / qo$) where (A) gives ideality factor of the diode, (n) gives total cells joined in series fashion, (k) gives Boltzmann constant, (qo) gives the charge, and (T_o) represents the temperature at which the solar cell is working at Standard Test Conditions (STC). The PV panel specifications are mentioned in Table 1.

In this work, 33 solar cells are joined in series fashion to represent the solar panel where all solar cells have same characteristics. Bypass diodes are interlinked to each PV panel in shunt connection to bypass the current through them so that PV panel can supply power even at a decreased voltage rather than supplying no power under shading conditions. It also helps in preventing hot-spot phenomena, whose effect is that it can damage the panels permanently.

3 PV Array Configurations

In order to evaluate different configurations for various shading cases, a total of 36 panels are used which are connected to form a 6x6 PV array. The different configurations under analysis are

- Series with Parallel (S-P).
- Total-Cross-Tied (TCT).
- Bridge-Tied (BT).
- Honeycomb (HC).

The 6x6 array connections for the various configurations are presented in Fig. 2. The various configurations for the PV array such as S-P, BT, and HC are far less superior than TCT. This is due to the fact that TCT has large number of cross-ties which makes TCT rugged and robust compared to other configurations.

3.1 Series with Parallel Configuration

Under the configuration employing the series and parallel combination, the panels are firstly joined in the series form as per the voltage requirement. The series connected panels form the strings. The strings are then attached to each other in parallel connection to get required current level. This configuration is most commonly used due to its simplistic approach to use and implement. In the MATLAB-SIMULINK

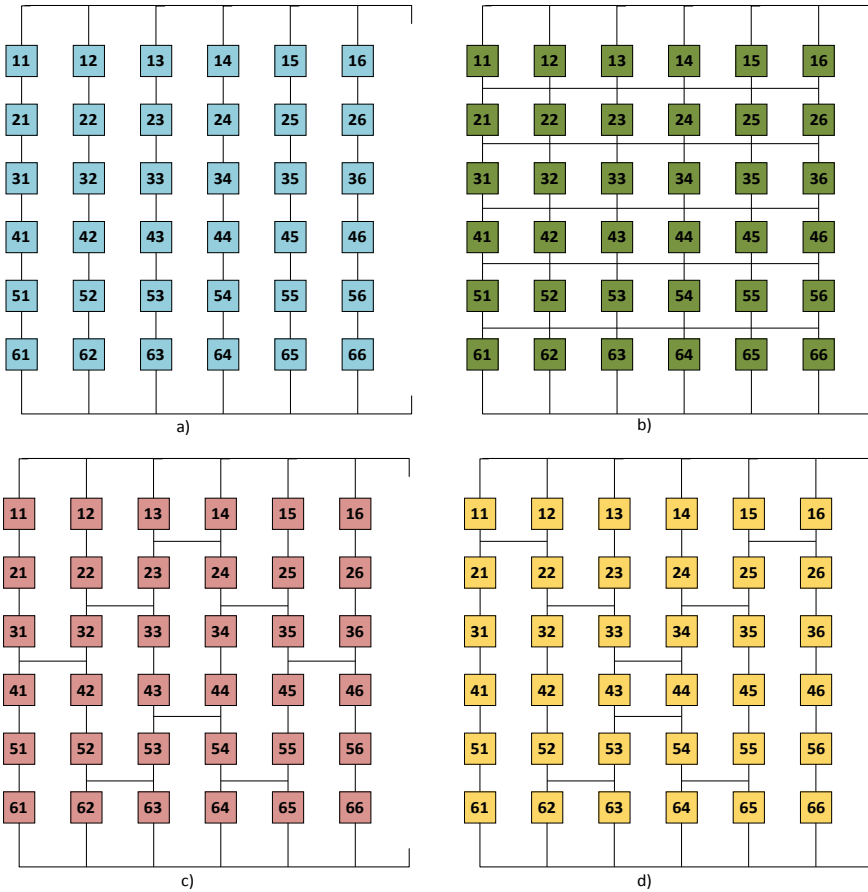


Fig. 2 A 6 × 6 array for different configurations **a** Series with Parallel (S-P) **b** Total-Cross-Tied (TCT) **c** Bridge-Tied (BT) **d** Honeycomb (HC)

model of 6 × 6 array, the maximum output current value is equivalent to the total addition of all the parallel-connected strings and maximum output voltage is same as the addition of voltage of each panel in a string.

Bypass diodes are employed in shunt for each panel so that the PV panels can avoid the danger of hot-spot phenomenon under partial shading conditions.

3.2 Total-Cross-Tied Configuration

In Total-Cross-Tied (TCT) configuration, the panels are first joined in the parallel form. The parallel-connected panels are called tiers. The tiers are then connected in series to get the final configuration. As the number of connections are increased, the

complexity of the configuration increases and the wiring losses also becomes significant. In the MATLAB-SIMULINK model of 6x6 array, the total current generated at the output of the array is equal to the total addition of current generated in parallel-connected panels called tier. The total voltage generated at the output is equivalent to the total addition of voltages of each tier or row.

3.3 Bridge-Tied Configuration

As series connections increase in the configuration, then the mismatch between row current increases under shading cases but as number of parallel ties between panels increases then it helps to balance the row currents and reduces the mismatch current. The Bridge-Tied (BT) configuration is similar to Series with Parallel (S-P) with some panels connected in parallel to form bridge. This helps to reduce mismatch currents. In MATLAB-SIMULINK model of 6x6 array, the panels are joined firstly in the form Series with Parallel (S-P) configuration and then ties are added in between the panels to form bridge.

3.4 Honeycomb Configurations

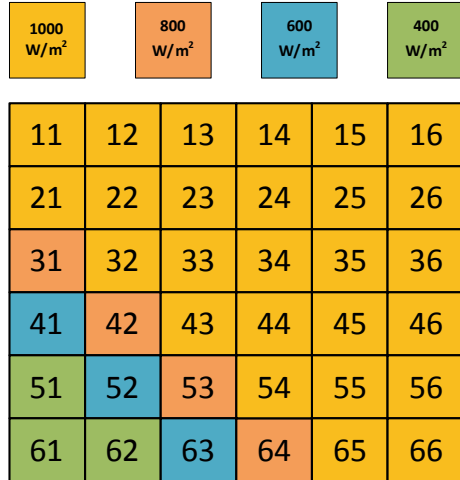
In honeycomb configuration, the connections are made in such a way that it resembles the structure of a honeycomb. It has more parallel connections compared with Series with Parallel (S-P) but less in comparison with Total-Cross-Tied (TCT) and Bridge-Tied (BT) configurations. So, it has greater ability to reduce mismatch current than Series with Parallel (S-P) but lesser than Total-Cross-Tied (TCT) and Bridge-Tied (BT) configurations.

4 Results

For the evaluation of the performance of TCT, S-P, BT and HC, a MATLAB-SIMULINK model was created. In this model, a 6×6 PV array was simulated and was tested for various shading patterns: Diagonal, Z-pattern, Centre and Random shading patterns. The effectiveness of various configurations was evaluated based on maximum output power generated by each configuration under different shading cases.

The shading patten employs various solar irradiance levels of 1000 W/m^2 (uniform irradiance), 800 W/m^2 , 600 W/m^2 and 400 W/m^2 . As different solar irradiance levels are used it helps to better represent the effects of moving clouds over the PV array.

Fig. 3 Diagonal shading pattern



4.1 Diagonal Shading Pattern

For the diagonal shading pattern, bottom left corner panels are receiving lesser solar irradiance. There are four panels getting 800 W/m², three panels are getting 600 W/m² and three panels exposed to 400 W/m². Remaining all panels are receiving a solar irradiance of 1000 W/m². The diagonal shading pattern is presented in Fig. 3.

The GMPPs for S-P, TCT, BT and HC under diagonal shading case are 1335 W, 1415 W, 1380 W and 1375 W which are given at 13.64 A and 103.67 V, 13.02 A and 102.51 V, 13.43 A and 102.8 V and finally 13.36 A and 102.91 V, respectively. It can be seen that there are four LMPPs and one GMPP in all configurations. In TCT, the LMPPs are 536.36 W at 19.15A and 28.02 V, 855.51 W at 17.92 A and 47.96 V, 1122 W at 17.19 A and 65.26 V and 1308 W at 15.72 A and 82.72V. For S-P the LMPPs are at 614.22 W, 939.4 W, 1165 W and 1306 W. For BT the LMPPs are given at 613.4 W, 901.7 W, 1151 W and 1280 W. For the HC case LMPPs are 597.4 W, 926.3 W, 1153 W and 1287 W.

The current against voltage and power against voltage are given in Fig. 4. The TCT shows a power increment of 4.24%, 2.47%, and 2.82% compared with S-P, BT and HC.

4.2 Z-Shading Pattern

Z-shading pattern presents a shading pattern which is of the form of alphabet Z. In this pattern, 7 panels are getting 800 W/m², 7 panels are getting 400 W/m² and 2 panels are getting 600 W/m². The Z-shading pattern is shown in Fig. 5.

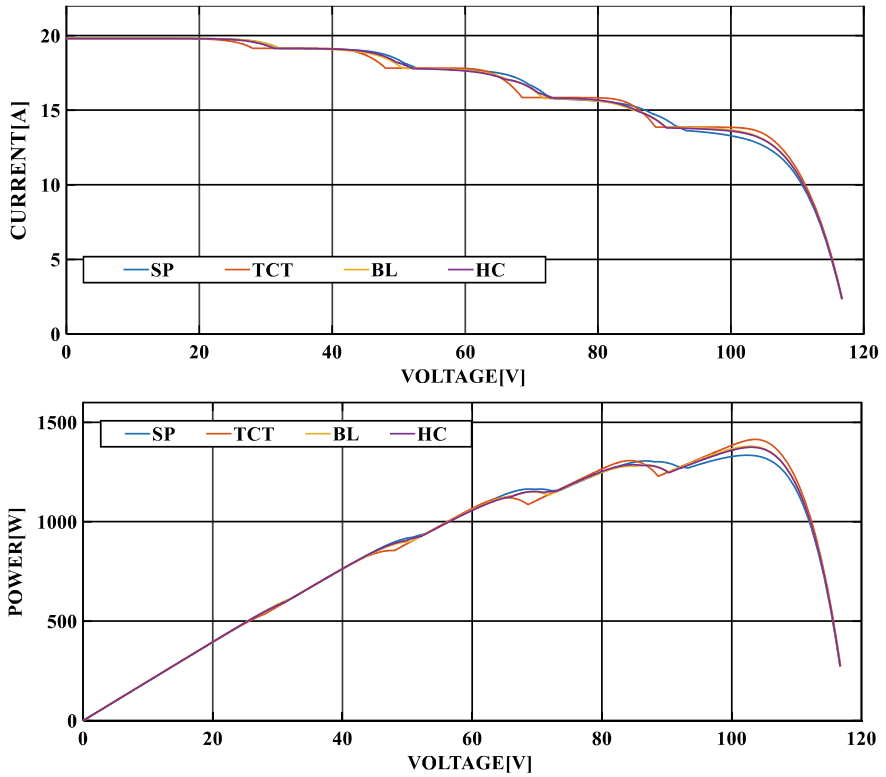
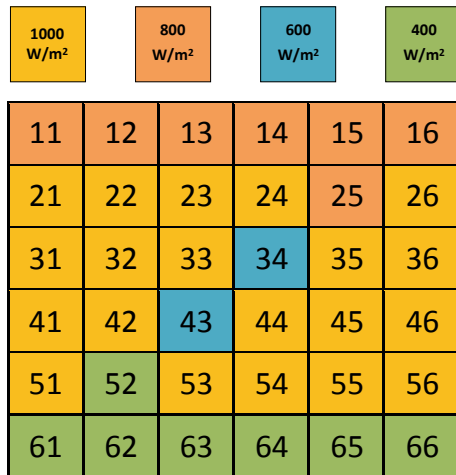


Fig. 4 Characteristics curve (current against voltage and power against voltage) for distinct configurations under diagonal shading pattern

Fig. 5 Z-shading pattern



The GMPPs for S-P, TCT, BT and HC for Z-shading case are 1099 W, 1289 W, 1183 W and 1246 W at 15.46 A and 83.37 V, 12.84 A and 85.59 V, 14.10 A and 83.89 V and for last configurations 15.09 A and 82.54 V. In Z-shading case, there are 4 LMPP and one GMPP. The LMPPs for TCT are 217.62 W at 18.48 A and 11.74 V, 800.86 W at 17.82 A and 44.92 V, 1087 W at 17.14 A and 63.41 V and lastly 842.61 W at 9.04 A and 93.21 V. The LMPPs for S-P are 885.54 W, 1078 W, 998.7 W and 831.2 W. Similarly, the BT has LMPP of 600.5 W, 877.4 W, 1048 W and 838.9 W. For the case of HC, the LMPPs are 249.2 W, 584.6 W, 902.7 W and 840 W.

The current against voltage and power against voltage curve is given in Fig. 6. The TCT shows a power increment of 14.74%, 8.22% and 3.33% compared with S-P, BT and HC. There is slight increase in power in TCT compared with HC.

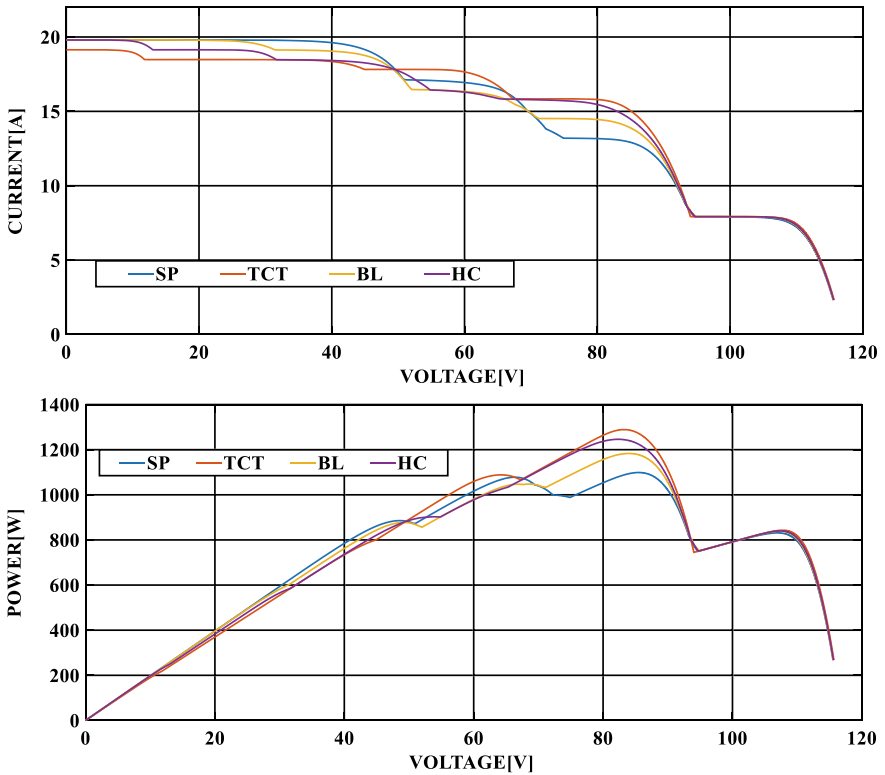
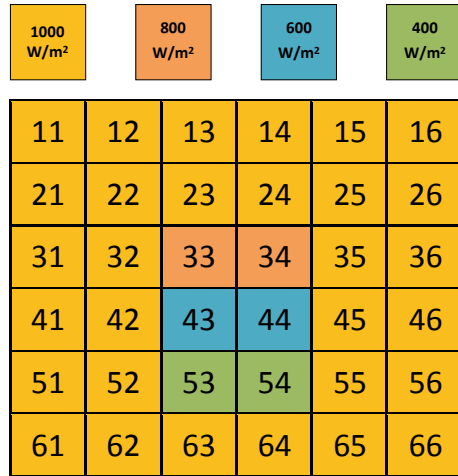


Fig. 6 Characteristics curve (current against voltage and power against voltage) for distinct configurations under Z-shading pattern

Fig. 7 Centre shading pattern



4.3 Centre Shading Pattern

For Centre shading pattern, the shading pattern is concentrated at the centre of the array where 2 panels each are receiving 800 W/m², 600 W/m² and 400 W/m². The Centre shading pattern is shown in Fig. 7.

The GMPPs are 1483 W, 1585 W, 1516 W and 1523 W for Centre shading under S-P, TCT, BT and HC. The GMPPs for S-P, TCT, BT and HC are found at 16.6 A and 89.32 V, 15.53 A and 102.04 V, 14.94 A and 101.42 V and lastly 14.89 A and 102.23 V. The Centre shading conditions have 3 LMPP and 1 GMPP. The LMPPs for TCT are given as 869.84 W at 18.48A and 47.06V, 1154.2 W at 17.72 A and 65.14 V and 1393.4 W at 16.7 A and 83.42 V. The S-P configuration has 940 W, 1247W and 1472W as its LMPP. The BT also has three LMPPs at 902.3 W, 1201 W and 1454 W. Similarly, the HC has LMPP of 893.4 W, 1193 W and 1451 W, respectively.

The current against voltage and power against voltage curve is given in Fig. 8. The power increment in TCT is maximum compared with S-P with 6.43% increase in output power.

4.4 Random Shading Pattern

In random shading pattern, the shading is distributed randomly across the array. In these 4 panels each is receiving 800 W/m² and 600 W/m² and 5 panels are receiving 400 W/m². The random shading pattern is presented in Fig. 9.

The GMPPs are given as 1179 W, 1395 W, 1206 W and 1212 W for S-P, TCT, BT and HC. The GMPPs for S-P, TCT, BT and HC are at 13.84 A and 85.22 V, 13.64 A and 102.28 V, 14.02 A and 85.95 V and for lastly at 13.75 A and 88.08 V. In this

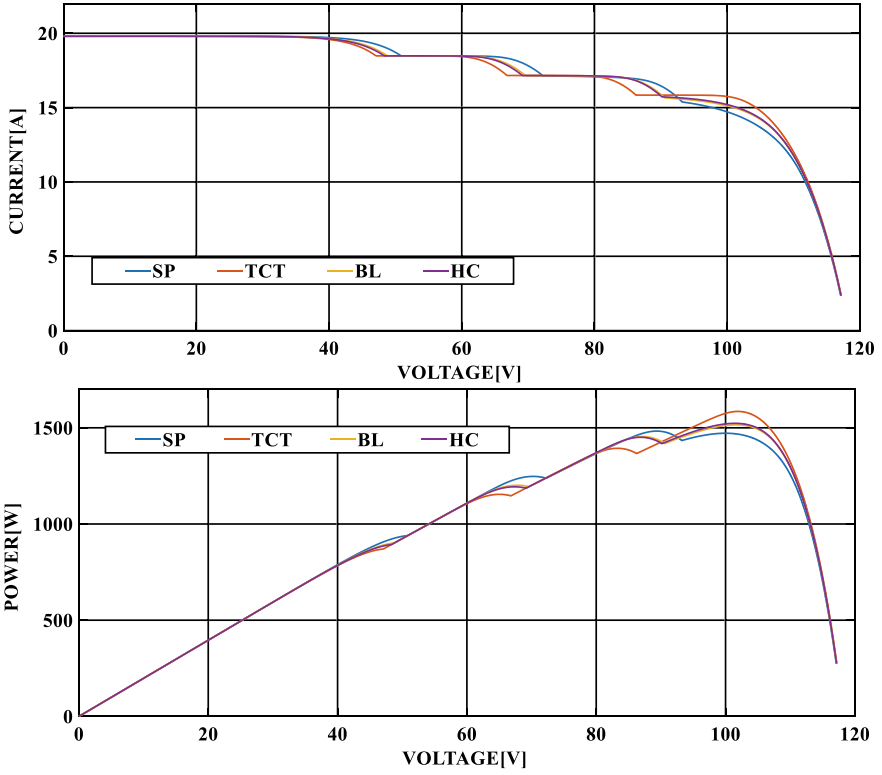
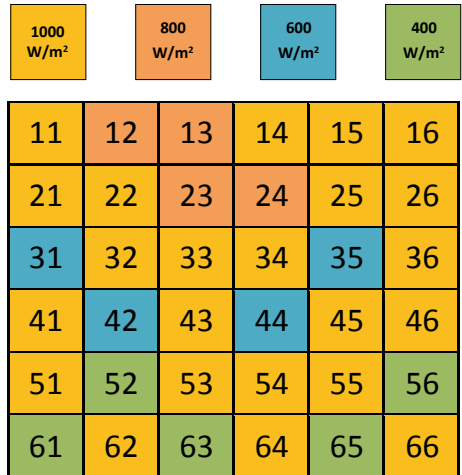


Fig. 8 Characteristics curve (current against voltage and power against voltage) for distinct configurations under Centre shading pattern

Fig. 9 Random shading pattern



case, there are 3 LMPP and 1 GMPP. The LMPP for TCT is found to be 516.13 W at 17.16 A and 30.36 V, 1047 W at 16.07 A and 65.12 V and finally 1272 W at 15.37 A and 82.69V. The LMPPs for S-P are 938.4 W, 1146 W and 906.8W. The BT has LMPPs of 579.1 W, 1074 W and 1198 W. The HC has 583.7 W, 1111 W and 1177 W as its LMPP.

The characteristics curve is given in Fig. 10. In random shading TCT shows an increase in power of 15.48% compared with S-P.

For all the shading cases, the maximum power is depicted in Fig. 11. In all the shading cases, TCT shows an improvement in the power output compared with other configurations.

The mismatch losses under various shading conditions are represented in Fig. 12. The mismatch losses for S-P, TCT, BT and HC under diagonal shading are 479 W, 399 W, 434 W and 439 W, respectively. The mismatch losses obtained for the Z-shading are 715 W, 525 W, 631 W and 568 W for S-P, TCT, BT and HC. The mismatch losses are significantly reduced for TCT compared with S-P under Z-shading. For the Centre shading, the mismatch losses are 331 W, 229 W, 298 W and 291 W for

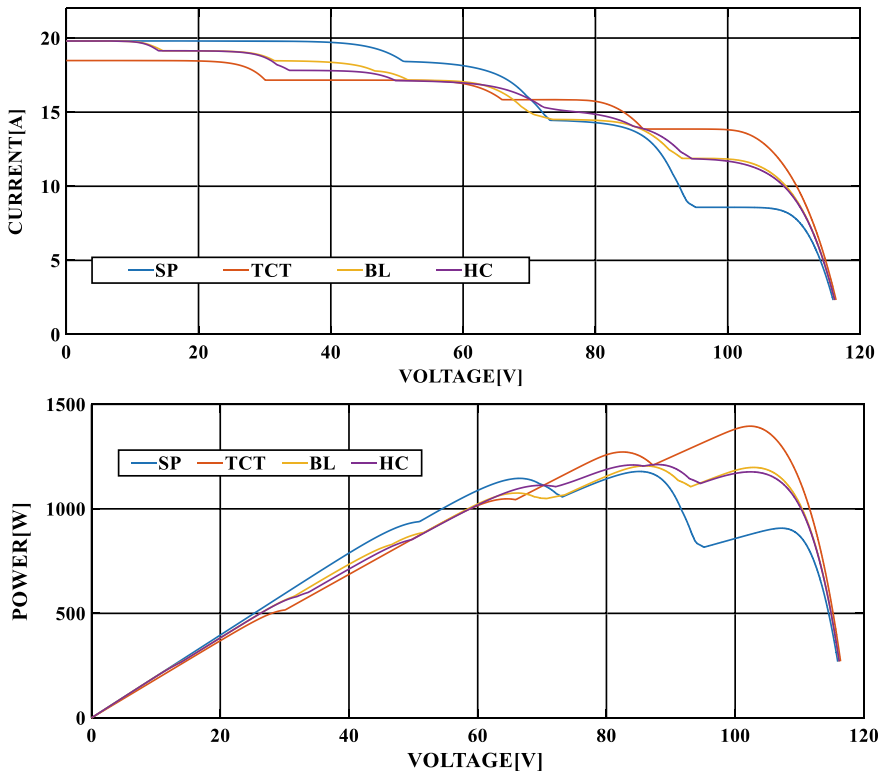


Fig. 10 Characteristics curve (current against voltage and power against voltage) for distinct configurations under random shading pattern

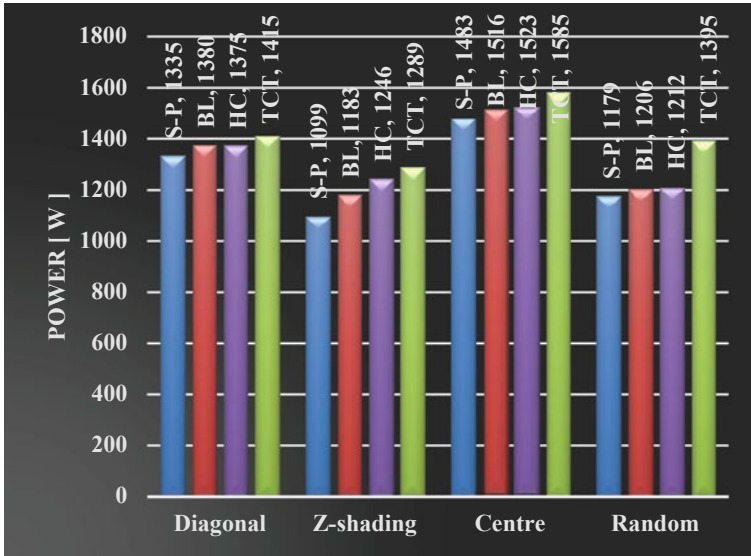


Fig. 11 Maximum power given at the output for various configurations under different shading cases

S-P, TCT, BT and HC. Under the random shading, the TCT has a mismatch loss of 419 W which is much lower than 635 W in case of S-P. The mismatch losses are 608 W and 602 W which is observed for BT and HC under random shading. The reduction in the mismatch losses under TCT configuration is highest compared to other configurations.

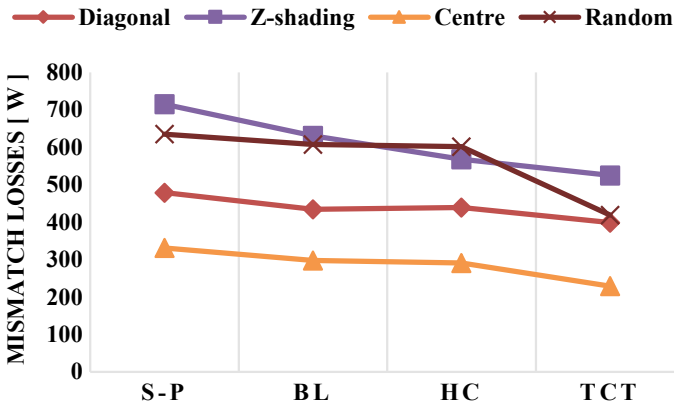


Fig. 12 Mismatch losses of all configurations under different shading cases

5 Conclusion

For this paper, four distinct types of configurations called as Series with Parallel (S-P), Total-Cross-Tied (TCT), Bridge-Tied (BT) and Honeycomb (HC) are analysed for a 6x6 array. The shading patterns considered for the study are Diagonal, Z-shading, Centre and Random. In the Diagonal shading, TCT gave power improvement of 80 W, 35 W and 40 W, respectively, compared with S-P, BT and HC. Under the case of Z-shading pattern the TCT shows a power increment of 14.74%, compared with S-P. The power is improved by 106 W and 43 W for TCT compared against BT and HC under Z-shading. In the Centre shading case, we got power increment of 102 W, 69 W and 62 W for TCT in comparison with S-P, BT and HC. The random shading of the output power level increased by 15.48%, 13.54% and 13.11% for TCT compared with S-P, BT and HC.

From the results, it is observed that TCT gave better results under all shading cases and also reduced the mismatch between row currents. So, it can be said TCT has most rugged configuration for various shading patterns because of its large number of cross-ties.

References

1. Anjum S, Mukherjee V (2022) A novel arithmetic sequence pattern reconfiguration technique for line loss reduction of photovoltaic array under non-uniform irradiance. *J Clean Prod* 331:129822. <https://doi.org/10.1016/j.jclepro.2021.129822>
2. Bharti G et al (2021) Power maximization under partial shading conditions using advanced sudoku configuration. In: Dave M et al (eds) *Paradigms of computing, communication and data sciences*. Springer Nature Singapore, pp 189–205. https://doi.org/10.1007/978-981-15-7533-4_15
3. Deshkar SN et al (2015) Solar PV array reconfiguration under partial shading conditions for maximum power extraction using genetic algorithm. *Renew Sustain Energy Rev* 43(2014):102–110. <https://doi.org/10.1016/j.rser.2014.10.098>
4. Dhanalakshmi B, Rajasekar N (2018) Dominance square-based array reconfiguration scheme for power loss reduction in solar PhotoVoltaic (PV) systems. *Energy Conv Manage* 156:84–102. <https://doi.org/10.1016/j.enconman.2017.10.080>
5. Pendem SR, Mikkili S (2018) Modelling and performance assessment of PV array topologies under partial shading conditions to mitigate the mismatching power losses. *Sol Energy* 160:303–321. <https://doi.org/10.1016/j.solener.2017.12.010>
6. Sahu HS et al (2016) Maximizing the power generation of a partially shaded PV array. *IEEE J Emerging Selected Topics Power Electron* 4(2):626–637. <https://doi.org/10.1109/JESTPE.2015.2498282>
7. Tatabhatla VMR et al (2020) A generalized chaotic baker map configuration for reducing the power loss under shading conditions. *Electr Eng* 4:102. <https://doi.org/10.1007/s00202-020-01016-4>
8. Tatabhatla VMR et al (2019) Improved power generation by dispersing the uniform and non-uniform partial shades in solar photovoltaic array. *Energy Convers Manage* 197:111825. <https://doi.org/10.1016/j.enconman.2019.111825>
9. Tatabhatla VMR et al (2019) Performance enhancement by shade dispersion of Solar photovoltaic array under continuous dynamic partial shading conditions. *J Clean Prod* 213:1–18. <https://doi.org/10.1016/j.jclepro.2018.11.015>

10. Tatabhatla VMR et al (2020) Performance improvement by mitigating the effects of moving cloud conditions. *IEEE Trans Power Electron* 36(4):1–1. <https://doi.org/10.1109/tpe.2020.3020807>
11. Yadav AS, Mukherjee V (2018) Line losses reduction techniques in puzzled PV array configuration under different shading conditions. *Sol Energy* 171:774–783. <https://doi.org/10.1016/j.solener.2018.07.007>

Detection of Parkinson's Disease Using Support Vector Machine and Combination of Various Tissue Density Features



Reema Ganotra and Shailender Gupta

1 Introduction

Parkinson's Disease (PD) is a neurodegenerative disease caused by decreased production of dopamine in region of substantia nigra [1, 2]. PD is characterized by many motor and non-motor symptoms such as tremors, changes in gait, postural deformity, and balancing problems [3, 4]. The increasing number of cases of PD and its socio-economic impact arises the need for early detection of the disease. Researchers have been employing neuroimaging techniques such as structural Magnetic Resonance Imaging (sMRI), Positron Emitting Tomography (PET), and Single Photon Emission Computerized Tomography (SPECT) to detect the disease in its early stages. Further, these techniques combined with machine learning methods are frequently being used to distinguish patients with PD from Cognitively Normal (CN) group [5–9]. In many machine learning approaches, features from neuroimages are obtained using Voxel-Based Morphometry (VBM) and utilized by classifier such as Support Vector Machines (SVM), Naive Bayes, or K-nearest neighbors [10–12]. VBM provides with the tissue density maps for Gray Matter (GM), White Matter (WM), and Cerebrospinal Fluid (CSF). These features obtained through VBM work as marker for detection of the disease and highlight the brain regions affected. Although many pathological studies provide strong evidence that WM and CSF are useful biomarker for identification of PD [1, 13, 14], most of the existing machine learning approaches are focused on GM features alone. Motivated by these facts, we conducted a study to investigate the effect of WM and CSF along with GM features on distinguishing PD and CN subjects. For the purpose, an SVM classifier is employed to discriminate PD and CN classes based on GM, WM, and CSF features and their possible

R. Ganotra (✉) · S. Gupta

J. C. Bose University of Science and Technology, YMCA, Faridabad, India

e-mail: reemaganotra01@gmail.com

combinations. The features are obtained from sMRI image obtained from Parkinson's Progression Markers Initiative (PPMI).

2 Data Acquisition and Preprocessing

All T1-weighted MR images are obtained from baseline assessment of PPMI (www.ppmi.info.org). The dataset comprises 356 PD subjects consisting of 226 males and 130 females within the age range of 38–82.2 years. Similarly, there are 130 CN subjects comprised of 86 males and 44 females within the age range of 30.6 years to 80.9 years. All images are preprocessed prior to classification using Statistical Parametric Mapping (SPM) toolbox v.12 in MATLAB 9.0. In first step of preprocessing, each sMRI image was segmented into GM, WM, and Cerebrospinal Fluid (CSF) tissue probability maps using unified segmentation algorithm. After this, the segmented images are registered to a custom template which is iteratively generated using DARTEL toolbox. These images are then registered to Montreal Neurological Institute (MNI) template and smoothed using 10 mm full width half maximum isotropic Gaussian kernel. In the last step, each image is modulated with Jacobian determinant of its deformation field. After preprocessing, all images are intensity normalized, resampled by 6 mm isotropic kernel, and masked to remove artifacts like air and background.

3 Support Vector Machine

Support Vector Machines (SVM) are one of the most popular supervised machine learning algorithms used for classification purpose. For the present study, let's suppose $(x_1, y_1), (x_2, y_2) \dots (x_n, y_n)$ are the samples that belong to PD and CN classes of subjects. An SVM classifier is built on these samples where x_n represent a sample from class $y_n \in \{-1, 1\}$. The typical hard margin SVM estimates a hyper-plane to separate the samples from the two classes with maximum margin. However, applications of hard margin SVM is limited to classification problems with linearly separable classes. For non-linear problems, a soft margin SVM classifier is employed which relaxes the constraints and imposes a penalty for wrong classification. The objective function for soft margin SVM is given by

$$\omega^*, b^*, \xi^* = \operatorname{argmin}_{\omega, b, \xi} \frac{1}{2} \|\omega\|^2 + C \sum_{i=1}^m \xi_i, \quad (1)$$

where $y_i(\omega^T x_i + b) \geq 1 - \xi_i$; $\xi_i \geq 0$; $i = 1, \dots, m$.

The penalty of misclassification is represented by ξ_i and it is controlled by parameter C . In our study, the value of parameter C is fixed to 1 for all experiments.

4 Experimental Setup

The experiments are built on SVM classifier with linear kernel and verified on fivefold cross validation to remove the effect on any randomness. The computation of results is performed on an Intel core i5 processor with processing speed of 2.50 GHz CPU and 8 GB memory. The implementations for experiments were written using Python 3.7.

5 Result and Discussion

In the proposed work, Experiment 1 depicts classifier result on GM features alone which provide accuracy, sensitivity, and specificity of 77.6, 82.05, and 70.21%. Similarly, Experiments 2 and 3 illustrate classifier results on WM and CSF features alone. All results are summarized in Table 1. It is also shown that best classification results are obtained by classifier built on combination of GM, WM, and CSF features with accuracy, sensitivity, and specificity of 80%, 82.05%, and 76.59%. A graphical comparison of results is shown in Fig. 1. It can be noted that classifier built on combination of GM, WM, and CSF features provides 3% and 6% improvement in classification accuracy and specificity, respectively, than that of classifier built on GM features alone. The improvement in accuracy facilitates better distinction between PD and CN subjects. Similarly, improved specificity signifies the ability of classifier to accurately predict true negative subjects which prohibits false diagnosis of CN subjects.

The results obtained from proposed work are compared to that of recently published approaches as shown in Table 2. As shown in table, Soltaninejad et al [9] and Adeli et al. [5] have reported their results on a dataset containing 341 and 356 PD subjects and 262 and 169 CN subjects, respectively. The number of PD subjects used in proposed work is comparative to these studies, however the number of CN subjects reposted in Adeli et al. [5] is relatively less. On the other hand, Gong et al. [7] reported their results on proportionately small dataset with 76 and 77

Table 1 Accuracy, sensitivity, and specificity obtained by SVM classifier

Experiment	Features	Accuracy (%)	Sensitivity (%)	Specificity (%)
Experiment 1	GM	77.6	82.05	70.21
Experiment 2	WM	73.6	79.48	63.82
Experiment 3	CSF	72	73.07	70.21
Experiment 4	GM + WM	64	67.94	57.44
Experiment 5	WM + CSF	76	80.76	68.08
Experiment 6	GM + CSF	70.4	76.92	59.57
Experiment 7	GM + WM + CSF	80	82.05	76.59

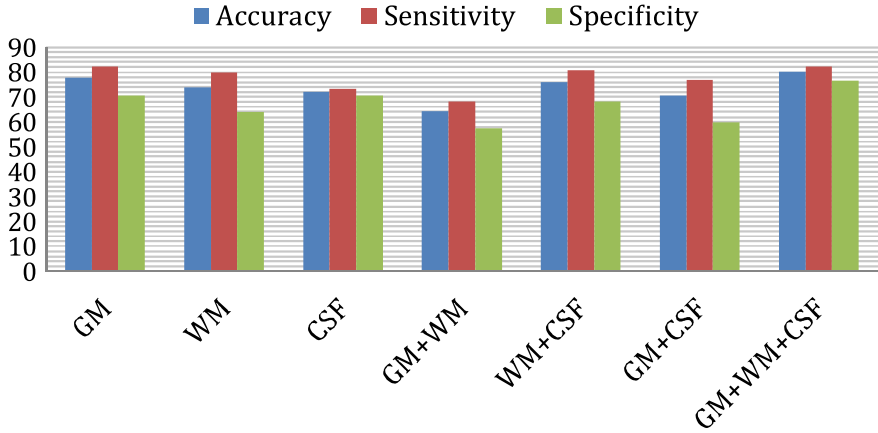


Fig. 1 Comparison of results obtained on GM, WM, CSF, GM + WM, WM + CSF, GM + CSF, and GM + WM + CSF features

Table 2 Comparison of results obtained by proposed work to recent approaches

Author	Imaging	Dataset		Classifier	Accuracy (%)
		PD	CN		
Soltaninejad et al [9]	sMRI	341	262	SVM	70.91
Gong et al. [7]	sMRI	76	77	SVM	75.16
Adeli et al. [5]	sMRI	374	169	SVM	69.1
Proposed work	sMRI	356	226	SVM	80

PD and CN subjects, respectively. This variation in data size is attributable to gathering medical imaging data from different sources. However, it is always desirable to build a classifier on an ample dataset for better generalization of the model. Thus, the proposed work employs comparatively equal or larger dataset to the abovementioned approaches.

For a true comparison, only those approaches are included where SVM classifier is built on the feature obtained from sMRI images. It is shown that the proposed work provides more than 9% improvement in the classifier accuracy when compared to same given in Soltaninejad et al. [9]. Similarly, the proposed work provides improved classification accuracy by 4 and 10% when compared to same provided by Gong et al. [7] and Adeli et al. [5].

References

1. Simunovic F, Yi M, Wang Y, Macey L, Brown LT, Krichevsky AM, Anderson SL, Stephens RM, Benes FM, Sonntag KC (2009) Gene expression profiling of substantia nigra dopamine neurons: further insights into Parkinson's disease pathology. *Brain* 132(7):1795–1809
2. Damier P, Hirsch EC, Agid Y, Graybiel AM (1999) The substantia nigra of the human brain II. Patterns of loss of dopamine-containing neurons in Parkinson's disease. *Brain* 122:1437–1448
3. Sveinbjornsdottir S (2016) The clinical symptoms of Parkinson's disease. *J Neurochem* 139:318–324
4. Redgrave P, Rodriguez M, Smith Y, Rodriguez-Oroz MC, Lehericy S, Bergman H, Agid Y, Delong MR, Obeso JA (2010) Goal-directed and habitual control in the basal ganglia: implications for Parkinson's disease. *Nat Rev Neurosci* 11:760–772
5. Adeli E, Shi F, An L, Wee CY, Wu G, Wang T, Shen D (2016) Joint feature-sample selection and robust diagnosis of Parkinson's disease from MRI data. *Neuroimage* 141:206–219
6. Cigdem O, Beheshti I, Demirel H (2018) Performance analysis of different classification algorithms using different feature selection methods on Parkinson's disease detection. *J Neurosci Methods* 309:81–90
7. Gong B, Shi J, Ying S, Dai Y, Zhang Q, Dong Y, An H, Zhang Y (2018) Neuroimaging-based diagnosis of Parkinson's disease with deep neural mapping large margin distribution machine. *Neurocomputing* 320:141–149
8. Salvatore C, Cerasa A, Castiglioni I, Gallivanone F, Augimeri A, Lopez M, Arabia G, Morelli M, Gilardi MC, Quattrone A (2014) Machine learning on brain MRI data for differential diagnosis of Parkinson's disease and progressive supranuclear palsy. *J Neurosci Methods* 222:230–237
9. Soltaninejad S, Cheng I, Basu A (2018) Towards the identification of Parkinson's disease using only T1 MR images. *Smart Multimedia* 11010:145–156
10. Focke NK, Helms G, Scheewe S, Pantel PM, Bachmann CG, Dechent P, Ebentheuer J, Mohr A, Paulus W, Trenkwalder C (2011) Individual voxel-based subtype prediction can differentiate progressive supranuclear palsy from idiopathic Parkinson syndrome and healthy controls. *Hum Brain Mapp* 32(11):1905–1915
11. Morales DA, Vives-Gilabert Y, Gomez-Anson B, Bengoetxeae E, Larranaga P, Bielza C, Pagonabarraga J, Kulisevsky J, Corcuera-Solano I, Delfino M (2013) Predicting dementia development in Parkinson's disease using Bayesian network classifiers. *Psychiatry Res: Neuroimaging* 213(2):92–98
12. Solana-Lavalle G, Rosas-Romero R (2021) Classification of PPMI MRI scans with voxel-based morphometry and machine learning to assist in the diagnosis of Parkinson's disease. *Comput Meth Programs Biomed* 198:105793
13. Sherbaf FG, Mohajer B, Ashraf-Ganjouei A, Zadeh MM, Javinani A, Moghaddam HS, Shandiz MS, Aarabi MH (2018) Serum insulin-like growth factor-1 in Parkinson's disease; study of cerebrospinal fluid biomarkers and white matter microstructure. *Front Endocrinol* 9:608
14. Maillard P, Fletcher E, Singh B, Martinez O, Johnson DK, Olichney JM, Farias ST, DeCarli C (2019) Cerebral white matter free water: a sensitive biomarker of cognition and function. *Neurology* 92(19):e2221–e2231

Modified Sine Cosine-Based Controller for Microgrid Frequency Regulation



Rajendra Kumar Khadanga, Preeti Ranjan Sahu, Amit Kumar, Prakash Kumar Hota, and Sidhartha Panda

Nomenclature

BESS	Battery energy storage
Δf	Frequency deviation
FC	Fuel cell
FLC	Fuzzy logic controller
FOPD+I	Fractional-order fuzzy PD+I
HAE	Hydro-aqua electrolyzer
IT2FPID	Interval type-2 fuzzy PID
K_{WTG}, T_{WTG}	Gain and time constant of wind turbine
K_{FC}, T_{FC}	Gain and time constant of fuel cell
K_{FESS}, T_{FESS}	Gain and time constant of flywheel energy storage
K_{DEG}, T_{DEG}	Gain and time constant of diesel energy generator
K_{MTG}, T_{MTG}	Gain and time constant of wind microturbine
K_p, T_p	Gain and time constant of power system

R. K. Khadanga (✉)

Department of Electrical and Electronics Engineering, Centurion University of Technology and Management, Bhubaneswar 752050, India

e-mail: rajendra.khadanga@cutm.ac.in

P. R. Sahu

Department of Electrical and Electronics Engineering, NIST Institute of Science and Technology, Berhampur 761008, India

A. Kumar

Department of Electrical and Instrumentation Engineering, Thapar Institute of Engineering and Technology, Patiala 147004, India

P. K. Hota · S. Panda

Department of Electrical Engineering, Veer Surendra Sai University of Technology, Burla 768018, India

LFC	Load frequency control
LMF	Lower membership function
MG	Microgrid
MTG	Microturbine
OGT2FPI	Optimal general type-2 fuzzy PI controller
PV	Photovoltaic panel
RES	Renewable energy sources
T1FPID	Type-1 fuzzy PID controller
UMF	Upper membership function
WTG	Wind turbine

1 Introduction

Recently, the advancement of AC MGs has aided in the provision of electrical power to rural areas where the traditional method of obtaining power from a network is very expensive [1]. The discontinuous nature of regeneration sources, nonlinear structure, instabilities, and dynamic complexity are all essential factors in the real-world operation of an AC MG. If any power mismatch occurs, there is a corresponding divergence in system voltage and frequency, resulting in an MG power outage [2]. Different renewable sources like PV, WTG, FC, FESS, MTG, DEG, and BESS can be used to create an AC MG that maintains a proper power balance between generation and demand [3, 4].

The frequency regulation of an AC MG is a critical aspect in achieving perfect power balancing [5, 6], and a unique technique to achieve this has been proposed in [7, 8]. Variable fuzzy PID as the primary controller with the standard PID as a supplementary controller [9], hPSO-PS-based FLC [10], MHSA-based OGT2FPI [11], and MBHA-tuned FOFPD + I [12] are the distinct H_∞ and μ -synthesis-based controllers explained in [13]. The evolutionary algorithm (EA), which has been effectively used to handle the nonlinear functions related to MG design, is another way to deal with the MG frequency regulation concern [14]. Bat algorithm [15], bacteria foraging optimization [16], PSO [17, 18], CSA [19], GA [20], FA [21], and gravitational search algorithm [22, 23] are some of the numerous applications of EA. These approaches, despite providing superior execution and dealing with compelling LFC structures, also have a slow convergence rate and are always stuck in local optima.

The SCA algorithm is a recently discovered population-based optimization algorithm that solves optimization issues using sine and cosine mathematical functions [24]. The conventional SCA algorithm is unable to meet the stated goal with higher convergence. As a result, the SCA algorithm is upgraded in this paper by introducing various scaling parameters that influence particle movement during the conventional SCA method [25]. As a result, the SCA algorithm is upgraded by incorporating

various scaling parameters that influence particle movement during the conventional SCA method. The originality of this chapter can be summarized as follows:

- To solve the frequency control problem in an AC MG, an IT2FPID controller is proposed.
- A modified Sine Cosine Algorithm (MSCA) is developed by including a scaling factor to the conventional SCA algorithm.
- The efficacy and supremacy of the proposed MSCA-optimized proposed controller is compared with the MSCA-optimized standard controllers such as type-1 fuzzy and recently published SCA.

2 System Understudy

2.1 System Configuration and Design Consideration

The AC MG system layout adopted in this chapter is presented in Fig. 1. Figure 2 shows the corresponding transfer function representation of AC MG. The presented system consists of energy sources PV, WTG, MTG, DEG, FC, and energy storage devices such as BESS and FESS, as well as some AC loads [14]. The AC MG parameters used in this chapter are given in Table 1.

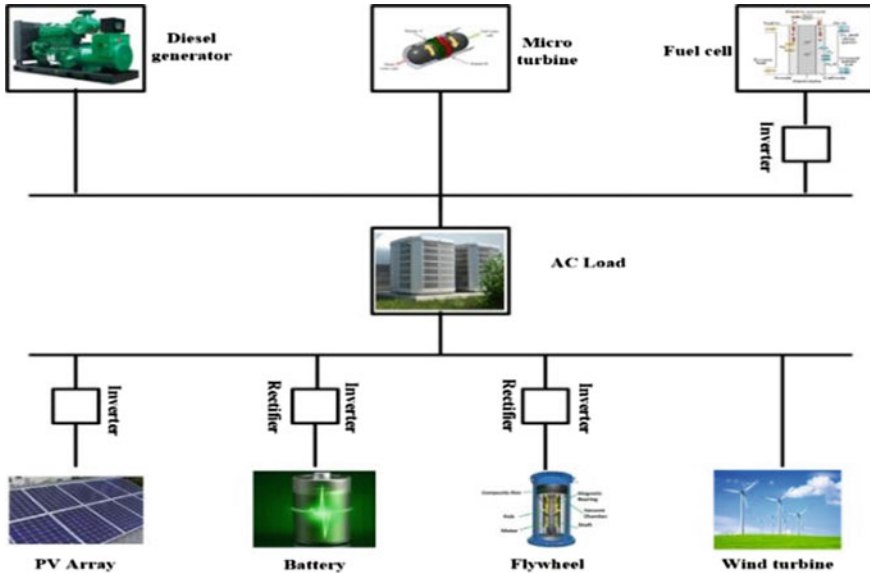


Fig. 1 Islanded MG configuration

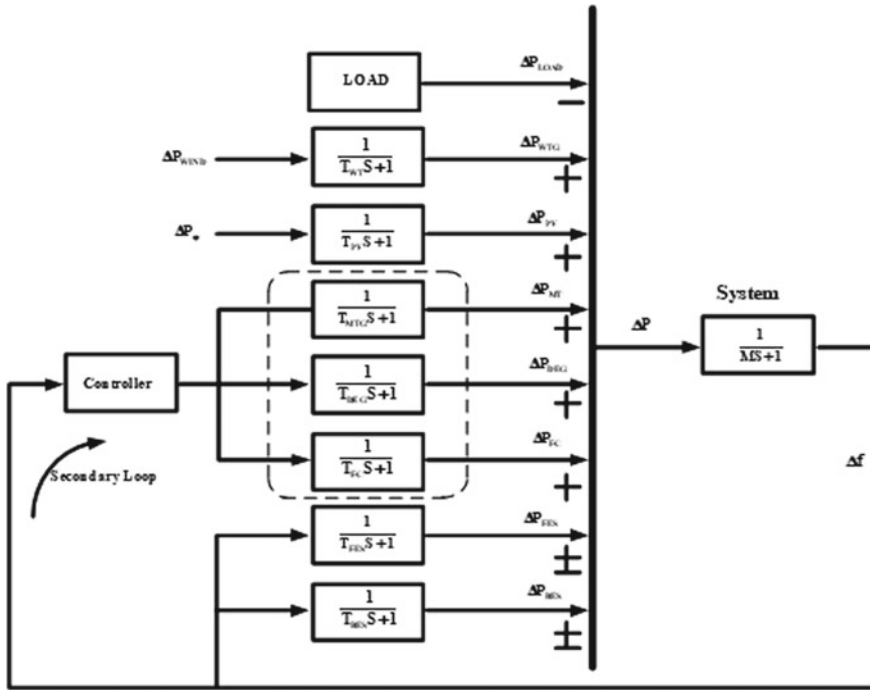


Fig. 2 Proposed transfer function model of MG

Table 1 Characteristics of the AC MG components [14]

Components	Gain (K)	Time constant (T)
WTG	$K_{WTG} = 1$	$T_{WTG} = 1.5$
PV system	$K_{PV} = 1$	$K_{PV} = 1$
FC	$K_{FC} = 0.01$	$T_{FC} = 4$
DEG	$K_{DEG} = 0.003$	$T_{DEG} = 2$
Microturbine	$K_{MTG} = 1$	$T_{MTG} = 1.5$
BESS	$K_{BESS} = -0.03$	$T_{BESS} = 0.1$
FESS	$K_{BESS} = -0.01$	$T_{BESS} = 0.1$
Damping coefficient	$D = 0.03$	
Inertia constant	$M = 0.4$	

A. Mathematical design and modeling of various generating units PV, WTG, DEG, FC, and MTG are [25]

$$G_{WTG}(s) = \frac{K_{WTG}}{1 + ST_{WTG}} \quad (1)$$

$$G_{PV}(s) = \frac{K_{PV}}{1 + sT_{PV}} \quad (2)$$

$$G_{FC}(s) = \frac{K_{FC}}{1 + sT_{FC}} \quad (3)$$

$$G_{DEG}(s) = \frac{K_{DEG}}{1 + sT_{SEG}} \quad (4)$$

$$G_{MTG}(s) = \frac{K_{MTG}}{1 + sT_{MTG}} \quad (5)$$

B. Mathematical modeling of storage unit: The controller's signal energizes the MG's different storage devices, such as BESS and FESS. They function as a source or load, as required, and can be presented as load in the proposed analysis [25]:

$$G_{BESS}(s) = \frac{K_{BESS}}{1 + sT_{BESS}} = \frac{\Delta P_{BESS}}{\Delta U} \quad (6)$$

$$G_{FESS}(s) = \frac{F_{FESS}}{1 + sT_{FESS}} = \frac{\Delta P_{FESS}}{\Delta U} \quad (7)$$

2.2 Proposed IT2FPID Controller

The fuzzy sets used in T2FS are known as secondary MFs. Whenever secondary MFs are converted into unit intervals of the primary MFs, they have named IT2FS. The fuzzy system which uses IT2FS in its rule base is called as IT2 fuzzy logic system (IT2FLS). IT2FLS is already used in some applications and often outperforms their type-1 counterparts when faced with uncertainty. The type-reduction (TR) approach is the most important concept of the IT2FLS controller. The best TR approach can be considered a genuine concern. Control tuning parameters, knowledge-based design, and MF are currently the major steps in constructing IT2FPID. Figures 3 and 4 depict the structure and membership functions of the proposed IT2FPID controller. Membership functions are assigned linguistic variables based on input and output parameters as displayed in Table 2. The said fuzzy set \tilde{A} is characterized as [25]

$$\tilde{A} = \int_{x \in X} \int_{u \in J_x \subseteq [0,1]} 1/(x, u) dx \cdot du = \int_{x \in X} \left[\int_{u \in J_x \subseteq [0,1]} 1/u \right] / x dx \cdot du \quad (8)$$

where the value of $\tilde{A} = 1$.

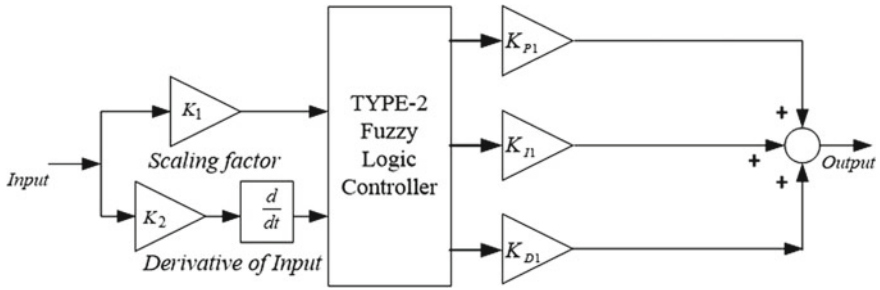


Fig. 3 Proposed T2FPID controller

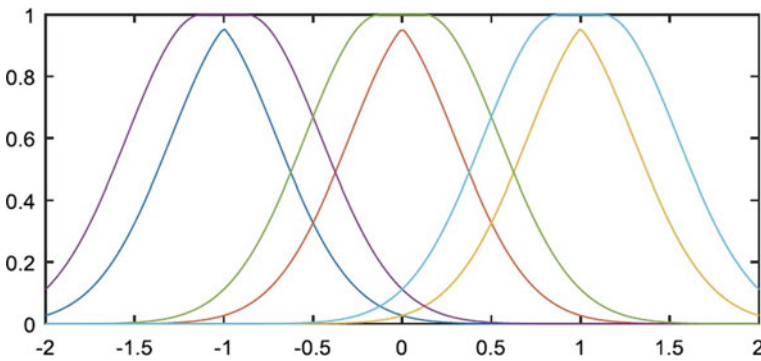


Fig. 4 MF of error for the proposed controller

Table 2 Rule base for three membership functions

Rule number	First input	Second input	Output	Corresponding bi value
1	N	N	P	1
2	N	Z	P	1
3	N	P	Z	0
4	Z	N	P	1
5	Z	Z	Z	0
6	Z	P	N	-1
7	P	N	Z	0
8	P	Z	N	-1
9	P	P	N	-1

2.3 Optimization Problem

The main purpose of the optimization is to minimize the change in frequency deviation in the system during system transients. To do so the objective function adopted

in this paper takes integral square error (ISE) into account. This paper adopts ISE due to its time dependency nature, which is basic in optimization problems [25].

$$\text{ISE} = \int_0^{t_{sim}} (\Delta F)^2 \cdot dt \quad (9)$$

where ΔF represents the frequency error of the AC MG.

With this the formulated objective function to estimate controller parameters is given below:

$$\text{Minimize } J \quad (10)$$

subject to

$$\begin{aligned} K_{P \min} &\leq K_P \leq K_{P \max} \\ K_{I \min} &\leq K_I \leq K_{I \max} \\ K_{D \min} &\leq K_D \leq K_{D \max} \\ K_{1 \min} &\leq n \leq K_{1 \max} \\ K_{2 \min} &\leq n \leq K_{2 \max} \end{aligned} \quad (11)$$

3 Proposed Modified Sine Cosine (MSCA) Algorithm

3.1 SCA Algorithm

The recently proposed SCA optimization technique is fully reliant on the scientific capacities of sine and cosine. The SCA algorithm is modified in two stages [23]. Firstly, the promising region of the exploration stage is reshaped by arranging random solutions at a higher rate, however, in the exploitation stage. Secondly, sine and cosine calculation is acquired by continuously updating the positions of solutions.

$$Y_t^{i+1} = Y_t^i + p_1 \times \sin(p_2) \times |p_3 P_t^i - Y_t^i| p_4 < 0.5 \quad (12)$$

$$Y_t^{i+1} = Y_t^i + p_1 \times \cos(p_2) \times |p_3 P_t^i - Y_t^i| p_4 \geq 0.5 \quad (13)$$

where Y_t^{i+1} represents the updated solution in the t th dimension at i th cycle, Y_t^i is the current position and i th—iteration, and P_t^i is the position of the destination. The parameters p_1 , p , p_3 , and p_4 are constant whose values are random and lie in between [0, 1].

The optimization method must converge to the optimal position in the search space to find out the global solution. To maintain the balance between the global search and local search, the SCA estimate parameter p_1 adaptively is given in (16). The parameter p_1 is again used in (14) and (15) to update the position which ensures a balance between the exploration and exploitation phases of the MSCA algorithm.

$$p_1 = b - i \left(\frac{b}{I} \right) \quad (14)$$

By changing the p_1 linearly as in (16), the number of iterations required to achieve an optimal solution will be high which resulted in an increased computational burden on the system. Furthermore, it reduces the convergence rate of the algorithm. To address these issues, this chapter presents a modified SCA algorithm (MSCA) discussed briefly in the subsequent section.

3.2 Proposed Modified SCA Algorithm (MSCA)

The proposed MSCA algorithm utilizes a sine function to decide the value of the control parameter p_1 instead of using a linear function as in the case of SCA. Using the sine function to estimate control parameter p_1 enables changes in the combined operation of exploration and exploitation stages. In SCA, initially, the best solution is unknown. Therefore, a large step size during the initial stages may result in moving far away from the optimum solution. Hence, in MSCA a scaling factor (SF) is used to control the movement of the search agent in the search process. The MSCA control equations are given in (12) and (13).

$$Y_t^{i+1} = [Y_t^i + p_1 \times \sin(p_2) \times |p_3 P_t^i - Y_t^i|] / SF p_4 < 0.5 \quad (15)$$

$$Y_t^{i+1} = [Y_t^i + p_1 \times \cos(p_2) \times |p_3 P_t^i - Y_t^i|] / SF p_4 \geq 0.5 \quad (16)$$

where

$$SF = 2 - \left(\frac{i}{I} \right) \quad (17)$$

The proposed flowchart of MSCA is displayed in Fig. 5.

Fig. 5 Flow-Chart for the proposed Modified Sine Cosine (MSCA) Algorithm

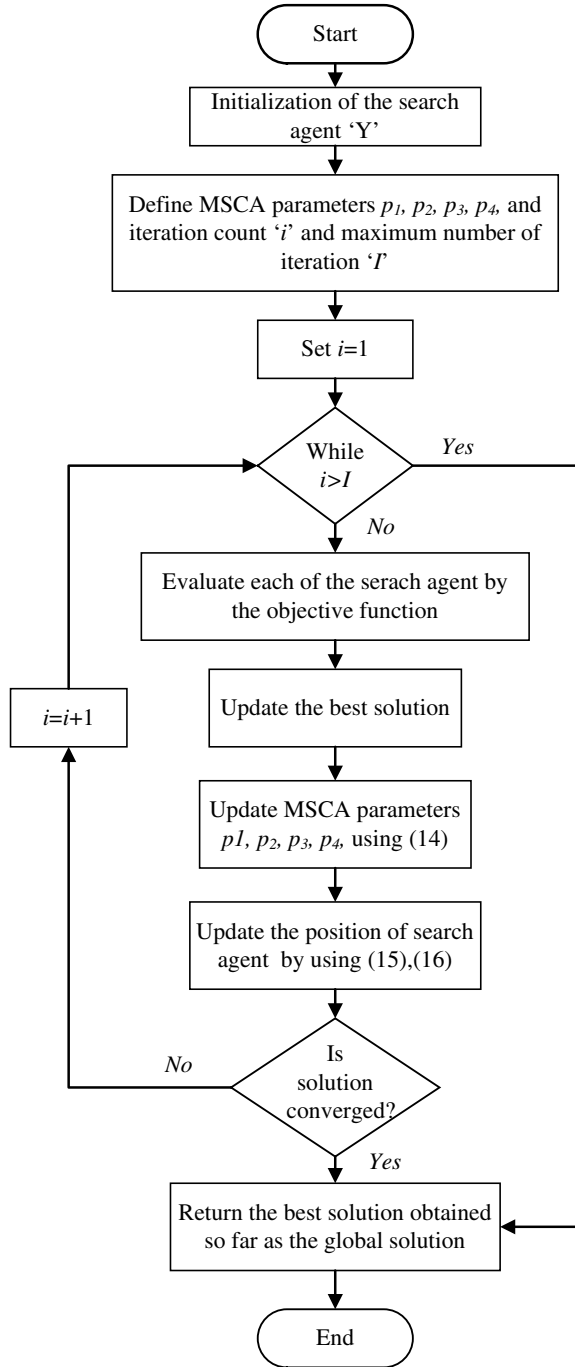


Table 3 Tuned parameters for the AC MG

Parameter	Proposed MSCA-based IT2FPID	MSCA Tuned T1FPID	MSCA-tuned PID	SCA-tuned PID
K_{P1}	0.9998	1.4651	0.7231	0.9821
K_{I1}	0.8383	0.6961	0.8329	0.5028
K_{D1}	0.1092	0.7586	0.8626	0.6375
K_1	0.6826	0.9842	–	–
K_2	0.5378	0.0772	–	–
ISE	0.0368	0.06568	0.07933	0.08302

4 Results and Discussion

4.1 Implementation of Proposed MSCA Algorithm

The simulation of the proposed system is carried out by estimating the objective function by introducing an unsettling disturbance in the system. The proposed controller parameters are estimated by using Eq. (13). The optimized parameters and other conventional controllers used in this chapter are tabulated in Table 3. The obtained results show the proposed MSCA-optimized IT2FPID controller has improved results as compared to the MSCA-optimized T1FPID and conventional controllers. As a result, it is reasonable to conclude that the proposed MSCA technique, when compared to SCA, produces better results for the engineering design problem. The accompanying disruption is considered while evaluating time-domain performance.

4.2 Case 1: During 100% Penetration of Renewal Energy Sources

The typical operation of an AC MG is used as the key example. Figure 6 shows the renewable energy penetration as well as the load pattern. By using the generation and load pattern presented in Fig. 6 power imbalance in AC MG is shown in Fig. 7. The power difference between renewable generation and load demand is negative from 2 to 20S and thus the required load demand is fulfilled by other distribution sources of the system. From the 20S to 40S, the power difference is positive, hence the controller maintains power balance by reducing power demand from generating sources. The power difference again becomes negative from 40 to 60S, hence the controller demand power from other distributed energy sources to fulfill the load demand. The frequency deviation with a different controller is plotted in Fig. 8. The

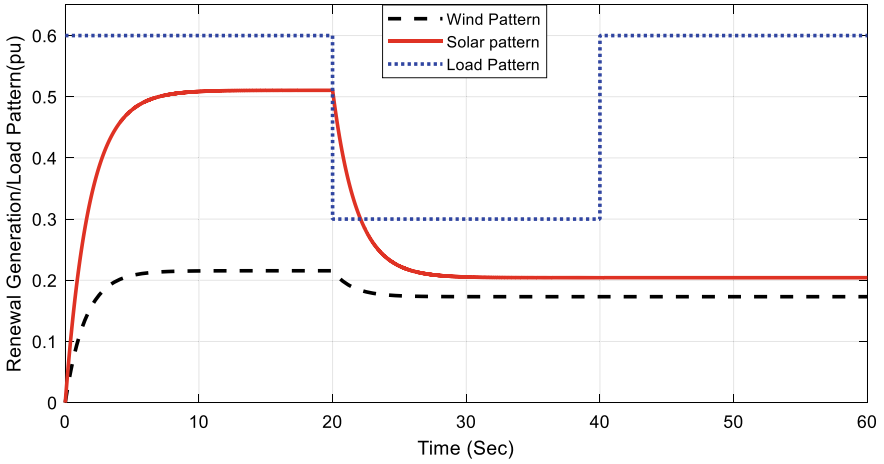


Fig. 6 Renewable energy generation pattern and load demand

proposed MSCA-based IT2FPID shows less deviation in frequency as compared to others.

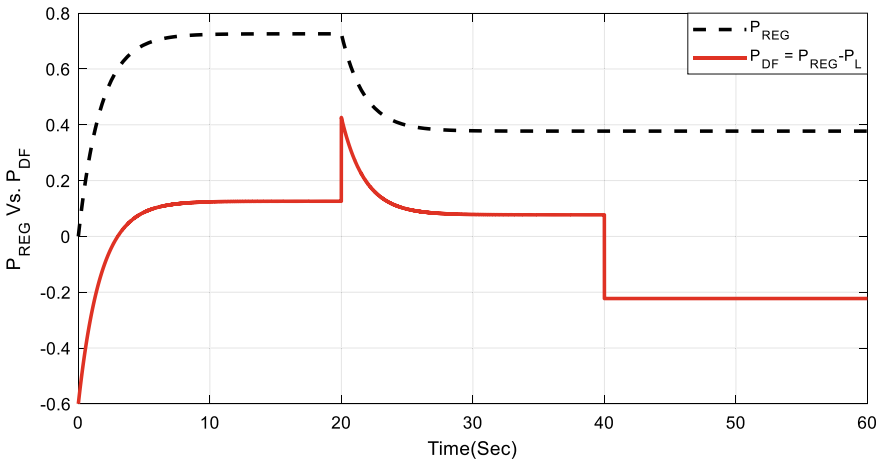


Fig. 7 Renewable power and AC MG power imbalance (Case 1)

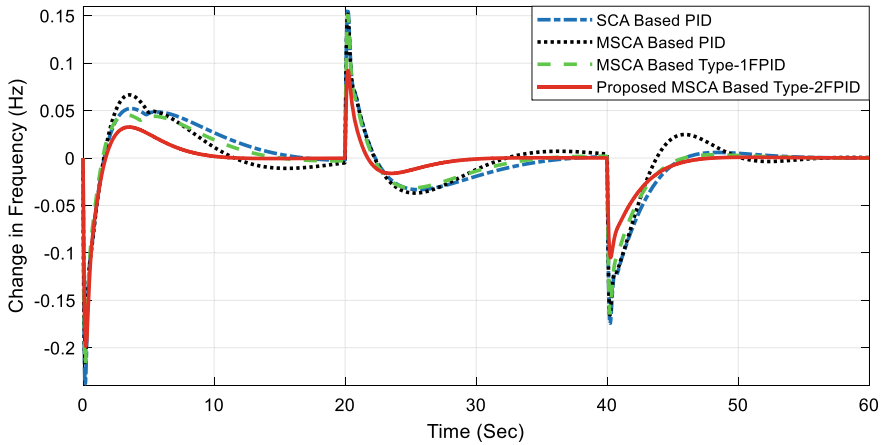


Fig. 8 Response of frequency deviation for Case 1

4.3 Case 2: During 50% Penetration of Renewable Sources

Here, the system is investigated with a 50% increase in solar and wind power. Figure 9 shows total disturbance signal for case 2. It can be observed that the power difference is always positive, hence surplus power is always delivered to the distributed sources. The frequency deviation with the different controllers is plotted in Fig. 10. The proposed MSCA-based IT2FPID controller shows improved performance as compared to another conventional controller.

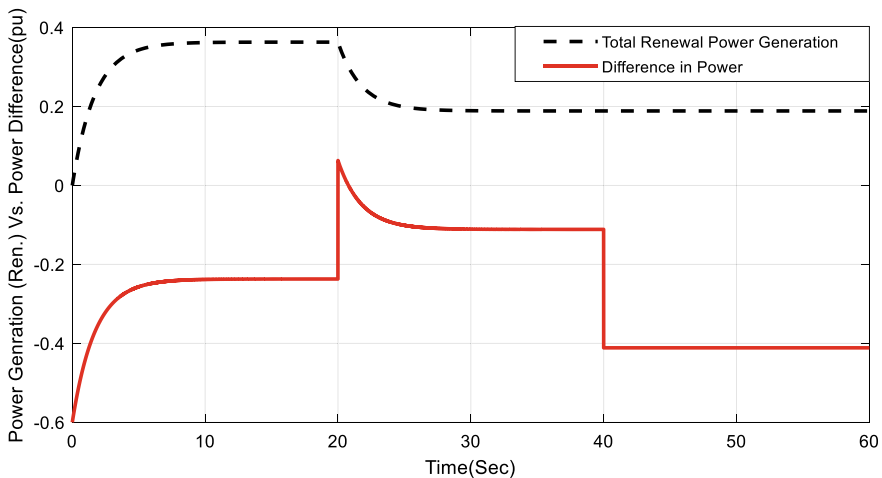


Fig. 9 Renewable energy vs. AC MG power imbalance (Case 2)

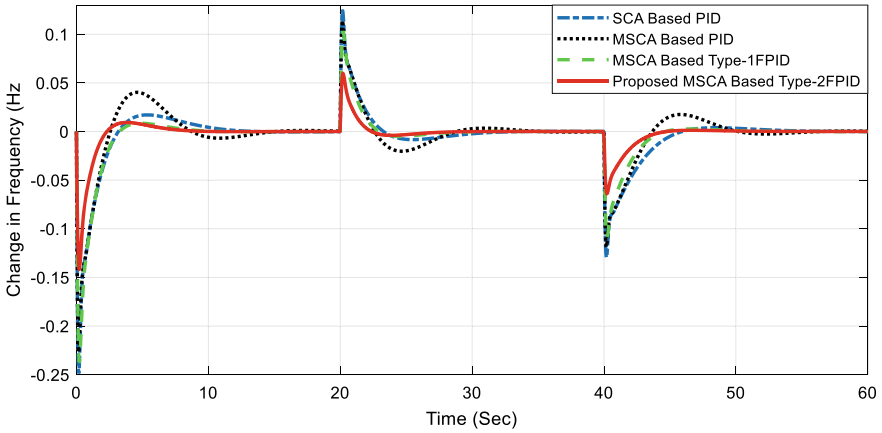


Fig. 10 Response of frequency deviation for Case 2

5 Conclusion

In this chapter, a Modified Sine Cosine Algorithm (MSCA)-based IT2FPID controller is proposed for frequency regulation of an AC MG. The AC MG considered in this chapter consists of renewable sources and storage units, resulting in a novel comparative analysis. The proposed MSCA methodology is used to optimize the IT2FPID controller parameters. The J value with the proposed MSCA-based IT2FPID is improved by 43.97% as compared to MSCA-based T1FPID. Similarly, a comparative result shows the percentage improvements in J value are 53.91% and 55.67% with SCA-based PID and PID controller, respectively. Furthermore, the transient performance of AC MG with the proposed MSCA-based IT2FPID controller in terms of system overshoot, undershoot, and frequency error shows better results as compared to other conventional controllers.

References

1. Alzola JA, Vechiu I, Camblong H, Santos M, Sall M, Sow G (2009) Microgrids project, Part 2: design of an electrification kit with high content of renewable energy sources in Senegal. *Renew Energy* 34(10):2151–2159
2. Jimeno J, Anduaga J, Oyarzabal J, de Muro AG (2011) Architecture of a microgrid energy management system. *Eur Trans Electr Power* 21(2):1142–1158
3. Zheng L, Liu S, Xie X (2015) Frequency domain-based configuration and power follow-up control for power sources in a grid-connected microgrid. *Int Trans Electr Energy Sys Tems* 25(10):2499–2514
4. Guerrero JM, Loh PC, Lee TL, Chandorkar M (2012) Advanced control architectures for intelligent microgrids—Part II: power quality, energy storage, and AC/DC microgrids. *IEEE Trans Industr Electron* 60(4):1263–1270

5. Mehrizi-Sani A, Iravani R (2010) Potential-function based control of a microgrid in islanded and grid-connected modes. *IEEE Trans Power Syst* 25(4):1883–1891
6. Shafiee Q, Guerrero JM, Vasquez JC (2013) Distributed secondary control for islanded microgrids—a novel approach. *IEEE Trans Power Electron* 29(2):1018–1031
7. Zhou Q, Shahidehpour M, Yan M, Wu X, Alabdulwahab A, Abusorrah A (2019) Distributed secondary control for islanded microgrids with mobile emergency resources. *IEEE Trans Power Syst* 35(2):1389–1399
8. Zhao G, Wang J, Li W, Zhu J (2020) Master and auxiliary compound control for multi-channel confluent water supply switching control based on variable universe fuzzy PID. *Appl Sci* 10(22):7983
9. Sahu RK, Panda S, Sekhar GC (2015) A novel hybrid PSO-PS optimized fuzzy PI controller for AGC in multi area interconnected power systems. *Int J Electr Power Energy Syst* 64:880–893
10. Arya Y (2018) Improvement in automatic generation control of two-area electric power systems via a new fuzzy aided optimal PIDN-FOI controller. *ISA Trans* 80:475–490
11. Arya Y (2019) A new optimized fuzzy FOPI-FOPD controller for automatic generation control of electric power systems. *J Franklin Inst* 356(11):5611–5629
12. Bevrani H, Feizi MR, Ataee S (2015) Robust frequency control in an islanded microgrid: $\{H\}_{\infty}$ and μ -synthesis approaches. *IEEE transactions on smart grid* 7(2):706–717
13. Khadanga RK, Kumar A, Panda S (2021) Application of Interval Type-2 Fuzzy PID controller for frequency regulation of AC islanded microgrid using modified equilibrium optimization algorithm. *Arab J Sci Eng* 46(10):9831–9847
14. Khooban MH, Niknam T (2015) A new intelligent online fuzzy tuning approach for multi-area load frequency control: self adaptive modified Bat Algorithm. *Int J Electr Power Energy Syst* 71:254–261
15. Ali ES, Abd-Elazim SM (2013) BFOA based design of PID controller for two area load frequency control with nonlinearities. *Int J Electr Power Energy Syst* 51:224–231
16. Khadanga RK, Satapathy JK (2015) Time delay approach for PSS and SSSC based coordinated controller design using hybrid PSO–GSA algorithm. *Int J Electr Power Energy Syst* 71:262–273
17. Zhang Z, Jiang Y, Zhang S, Geng S, Wang H, Sang G (2014) An adaptive particle swarm optimization algorithm for reservoir operation optimization. *Appl Soft Comput* 18:167–177
18. Abdelaziz AY, Ali ES (2016) Load frequency controller design via artificial cuckoo search algorithm. *Electr Power Compon Syst* 44(1):90–98
19. Daneshfar F, Bevrani H (2012) Multiobjective design of load frequency control using genetic algorithms. *Int J Electr Power Energy Syst* 42(1):257–263
20. Sekhar GC, Sahu RK, Baliarsingh AK, Panda S (2016) Load frequency control of power system under deregulated environment using optimal firefly algorithm. *Int J Electr Power Energy Syst* 74:195–211
21. Wang Y, Yu Y, Gao S, Pan H, Yang G (2019) A hierarchical gravitational search algorithm with an effective gravitational constant. *Swarm Evol Comput* 46:118–139
22. Khadanga RK, Satapathy JK (2015) A new hybrid GA–GSA algorithm for tuning damping controller parameters for a unified power flow controller. *Int J Electr Power Energy Syst* 73:1060–1069
23. Mirjalili S (2016) SCA: a sine cosine algorithm for solving optimization problems. *Knowl-Based Syst* 96:120–133
24. Khadanga RK, Kumar A, Panda S (2021) A novel sine augmented scaled sine cosine algorithm for frequency control issues of a hybrid distributed two-area power system. *Neural Comput Appl* 33(19):12791–12804
25. Khadanga RK, Kumar A, Panda S (2021) Frequency control in hybrid distributed power systems via type-2 fuzzy PID controller. *IET Renew Power Gener* 15(8):1706–1723

Impact of Different Demand Response Programs on Distribution Network Using Particle Swarm Optimization



S. Sharma, Tanuj Rawat, Richa Sharma, and Gulshan Sharma

1 Introduction

The overall power demand of every country increases every year and its effect reflects on the complete power system. Therefore, to bridge the gap between power generation and increasing demand is the primary focus of every distribution network [1]. The smart grid modern technologies such as demand response and its different pricing are the motivation of consumers to alter the demand [2]. The demand control of different types of consumers plays a crucial role in achieving distribution system operator benefits. The residential, agriculture, and commercial consumers are differently assigned to the particular feeders of distribution network in the planning phase. The consideration of multiple load models on the feeders is providing the most practical DR modeling.

In 2021, the Indian power generation reached 375 GW. The vision of the Central Electricity Authority of India is to provide reliable electricity with adequate quality to every single consumer. However, the consumer's demand changes as per the sessions such as winter, summer, weekdays, and holidays [3–5]. Therefore, to manage the adequate power quality and peak demand management is still complicated issues for the system operator [6–8]. Another major issue is to improve the penetration of

S. Sharma (✉)

Department of Electrical Engineering, Graphic Era Deemed to Be University, Dehradun, India
e-mail: sachineesharma@gmail.com

T. Rawat

Department of Electrical Engineering, SKIT Jaipur, Jaipur, India

R. Sharma

Department of Electronics and Communication Engineering, MNIT Jaipur, Jaipur, India

G. Sharma

Department of Electrical Engineering Technology, University of Johannesburg, Johannesburg, South Africa

renewable sources in power sector [9]. The important vision of the Indian power sector is to install 175 GW of renewable sources including 100 GW from solar, 60 GW for wind, and biopower contribution with microhydropower is set to 15 GW. Therefore, high penetration of renewable is again raising some adverse issue in the power system such as supply and demand mismatch. Renewable sources such as photovoltaic and wind are very uncertain in nature. The operational planning of distribution system based on these high penetrated renewables is complex and complicated.

These above issues at glance motivate to incorporate some flexible technologies that reduce the unplanned gap between supply and generation. These unplanned gaps create technical limit violation of the distribution system such as frequency and node voltage violation. The demand response programs incorporation in distribution system reduces such issues up to a certain limit.

In [10], the authors presented the benefits of adopting demand response in the USA by reducing the peak demand. In [11, 12], the authors focused on the different priced-based demand response programs for residential consumers to reduce their peak demands. Some other distributed energy resource incorporations with demand response reduce the above issues of distribution system. The optimal combinations and scheduling of dispatchable distributed generation such as microturbine, flywheel energy storage, battery energy storage, diesel generator, pump hydro storage with renewable resources, and demand response may reduce their uncertainties issues [13].

Furthermore, DR participation in electricity market reduces the risk factor of independent renewable power producers [14]. In [15, 16], the authors proposed the operational optimal scheduling of distributed generation and time of use-based demand response programs for reducing the cost of electric demand consumptions. The demand response is also utilized in the scheduling of electric vehicles as it is a type of controllable load and has great potential in near future to help in reducing the gap between supply and generation [17]. However, only proper scheduling of electric vehicles reduces the system issues; otherwise, it increases the costly peak demand in the distribution system [18]. The minimization of feeder current by incorporation of real-time demand response programs is presented in [19]. In [20], the authors proposed operational strategy including photovoltaic and demand response to minimize the network loss. In [21], the authors proposed the novel pricing strategies to ensure economic benefits with maintaining the technical constraints of distribution network.

In the existing literature, the demand response benefits are reported in many areas such as electric vehicles, planning, and operational problems of distribution systems. Most of the literature proposed the two types of implementation of demand response programs, the first is based on elasticity-based programs, and the second is modeled by non-linear optimization. In elasticity-based demand response, the consumers willing to change the electricity demand with the effect of price is modeled by self- and cross-elasticity. In optimization-based demand response, the controllable demands of the consumers are schedules optimally to achieve the multiple objectives of the distribution system. The previous literature supported the facts that

the controllable demand of consumers of any area having the potential to reduce the technical violations of the distribution system up to a certain extent. However, these consumers benefited from the pricing and incentive for changing their power consumption patterns. Therefore, demand response aggregator collects the data of participated consumers in different types of demand response programs such as mandatory, and voluntary types, and also motivates them by providing the incentives. In this paper, different demand response programs are incorporated by using particle swarm optimization to minimize the network loss and node voltage deviation of the distribution system.

2 Aggregated Demand Considering Residential, Industrial, and Commercial Consumers

In this paper, different types of consumers are dedicated to particular feeders. The distribution planning and its expansion is based on the aggregated load profile. It is analyzed from the previous literature that different consumers having different patterns of power consumption depend on weekdays, holidays, rainy and winter seasons. Moreover, the operation of distribution network such as scheduling of dispatchable distributed generation is based on the hourly load pattern. For more practical analysis, distribution system is assigned by different categories of consumers such as residential, industrial, and commercial. The diversified network feeders are analyzed with incorporation of different demand response programs. Figure 1 shows the peak, off-peak, and low-demand periods of considered consumers.

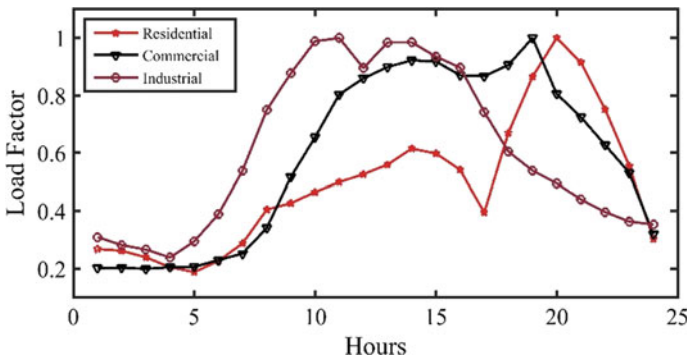


Fig. 1 Energy consumption profile of different consume

3 Problem Formulation

The optimal scheduling of controllable demand of different consumers is determined to minimize the network loss and voltage deviation of every node of distribution network.

3.1 Network Loss

Network loss is a very important objective of the distribution system. Moreover, this network loss is related to the economy. Every loss of power is ultimately the loss of resources that are used to generate the power. In the Indian power system, most of the power generation is dependent on fossil fuels and its wastage is also related to the environment issues. Therefore, network loss minimization is considered as one of the objectives and is defined as [20].

$$OBJ_1 = \sum_{\text{Time}=1}^{24} P_L^{\text{Time}} \quad (1)$$

$$P_L^{\text{Time}} = \sum_{a=1}^A \sum_{b=1}^A \alpha_{ab}^{\text{Time}} (P_a^{\text{Time}} P_b^{\text{Time}} + Q_a^{\text{Time}} Q_b^{\text{Time}}) + \beta_{ab}^{\text{Time}} (Q_a^{\text{Time}} P_b^{\text{Time}} - P_a^{\text{Time}} Q_b^{\text{Time}}) \quad \forall \text{Time} \quad (2)$$

where, $\alpha_{ab}^{\text{Time}} = r_{ab} \cos(\delta_a^{\text{Time}} - \delta_b^{\text{Time}}) / V_a^{\text{Time}} V_b^{\text{Time}}$ and $\beta_{ab}^{\text{Time}} = r_{ab} \sin(\delta_a^{\text{Time}} - \delta_b^{\text{Time}}) / V_a^{\text{Time}} V_b^{\text{Time}}$ where P_L^{Time} , P_a^{Time} , P_b^{Time} , Q_b^{Time} , Q_b^{Time} , V_a^{Time} , V_b^{Time} , r_{ab} , δ_a^{Time} represent the network loss, real and reactive power, magnitude of voltages, resistance between the branches and voltage angle, respectively.

3.2 Magnitude of Voltage Deviation

The aim of the distribution operator is to maintain the magnitude of every node voltage in the permissible limits. Therefore, minimization of voltage deviation is another objective and is considered as a penalty if it violates the limits [21, 22].

$$OBJ_2 = \left(1 + \sum_{\text{Time}=1}^{24} Vol_d^{\text{Time}} \right) \quad (3)$$

$$\text{where, } Vol_d^{\text{Time}} = \begin{cases} |V_{mn} - V_a^{\text{Time}}| & \text{if } V_a^{\text{Time}} < V_{mn}. \\ 0 & \text{if } V_{mn} \leq V_a^{\text{Time}} \leq V_{mx}. \\ \lambda & \text{if } V_a^{\text{Time}} > V_{mx}. \end{cases} \quad (4)$$

here, $\text{Vol}_d^{\text{Time}}$, $V_{\text{mx.}}$, $V_{\text{mn.}}$, V_a^{Time} and λ present the penalty value of voltage, limits of considered voltage, and value of voltage at a particular time and random large number for penalty, respectively.

3.3 Problem Constraints

$$P_a^{\text{Time}} = (P_{\text{Ga}}^{\text{Time}} - P_{\text{Db}}^{\text{Time}}) \forall \text{Time}, a \quad (5)$$

$$P_b^{\text{Time}} = (P_{\text{Gb}}^{\text{Time}} - P_{\text{Db}}^{\text{Time}}) \forall \text{Time}, b \quad (6)$$

$$P_{\text{Da}}^{\text{Time}} = (P_{\text{in},a}^{\text{Time}} + P_{\text{el},a}^{\text{Time}}) \forall \text{Time}, a \quad (7)$$

$$\sum_{a=1}^A \sum_{\text{Time}=1}^{24} (P_{\text{in},a}^{\text{Time}} + P_{\text{el},a}^{\text{Time}}) \times \Delta\text{time} = E_{\text{na}}^{\text{Total}} \quad (8)$$

$$P_{\text{el},i\text{ime}}^{\text{mn}} \leq P_{\text{el},a}^{\text{Time}} \leq \min((C - P_{\text{in},a}^{\text{Time}}), P_{\text{el},a}^{\text{mx.}}) \forall \text{Time} \quad (9)$$

$$P_{\text{el},a}^{\text{mx.}} = \hbar \sum_{\text{Time}=1}^{24} \text{Load}_{\text{d},a}^{\text{Time}} \quad (10)$$

where, $P_{\text{Ga}}^{\text{Time}}$, $Q_{\text{Ga}}^{\text{Time}}$, $P_{\text{Da}}^{\text{Time}}$, $Q_{\text{Da}}^{\text{Time}}$, $P_{\text{in},a}^{\text{Time}}$, $P_{\text{el},a}^{\text{Time}}$, E_a^{Total} , $P_{\text{el},a}^{\text{mn.}}$, $P_{\text{el},b}^{\text{mx.}}$, C , $\text{Load}_{\text{d},a}^{\text{Time}}$ and \hbar are the generation of real and reactive power, consumption of real and reactive power, controllable and non-controllable demand, complete day energy consumption, limits of controllable demand, total demand of the day, and demand response penetration, respectively.

Feeders' current limit constraints

$$I_{\text{ab}}^{\text{Time}} \leq I_{\text{ab}}^{\text{mx.}} \forall \text{Times}, a, b \quad (11)$$

where $I_{\text{ab}}^{\text{Time}}$, $I_{\text{ab}}^{\text{mx.}}$ are the actual and maximum limit of feeders' current, respectively.

Power balance constraints

$$P_a^{\text{Time}} \leq V_a^{\text{Time}} \sum_{b=1}^A V_b^{\text{Time}} Y_{ab} \cos(\theta_{ab} + \delta_b^{\text{Time}} - \delta_a^{\text{Time}}) \forall \text{Time}, a \quad (12)$$

$$Q_a^{\text{Time}} \leq V_a^{\text{Time}} \sum_{b=1}^A V_b^{\text{Time}} Y_{ab} \sin(\theta_{ab} + \delta_b^{\text{Time}} - \delta_a^{\text{Time}}) \forall \text{Time}, a \quad (13)$$

System demand modeling

$$P_{D,a}^{Time} = \kappa_a^{Time} P_{D,a}^{Time} \quad \forall Time, a \quad (14)$$

$$Q_{D,a}^{Time} = \kappa_a^{Time} Q_{D,a}^{Time} \quad \forall Time, a \quad (15)$$

where, $P_{D,a}^{Time}$, $Q_{D,b}^{Time}$ κ_a^{Time} is the power demands and different consumers demand factor.

4 Particle Swarm Optimization for Demand Response

In this paper, particle swarm optimization is developed for implementing the multiple demand response programs for distribution system. The problem framed is a non-linear mixed integer in nature and is solved efficiently by particle swarm optimization. In this optimization algorithm, considered particles are used to optimize the objective by their position in the search space and this particle is changes their position with respect to the neighboring particle to find the global optimum solutions. The solution formed by the effect of neighboring particles with respect to time is G best and it helps in determining the best position. Figure 2 shows the flow chart for particle swarm optimization to solve the considered problem of distribution system.

The steps for determining the best fitness for the considered problem are as follows:

- I. Assign the input data such as permissible voltage limit, different categories of consumers demand, and line data.
- II. Use Newton–Raphson load flow methods to find the network loss of complete days.
- III. Generate the initial population using a random process between the search spaces. The variable considered in this problem is controllable demand of different consumers.
- IV. If the node voltage, feeder current limit, and demand response constraints are in the limit, then determined the network loss by using load flow methods.
- V. Compare the fitness value of every particle and save the best value as P best and G best.
- VI. For every iteration, save the best values.
- VII. Repeat this process for the assigned maximum value of iterations.
- VIII. Save the best minimum network loss values and node voltage of the distribution network.

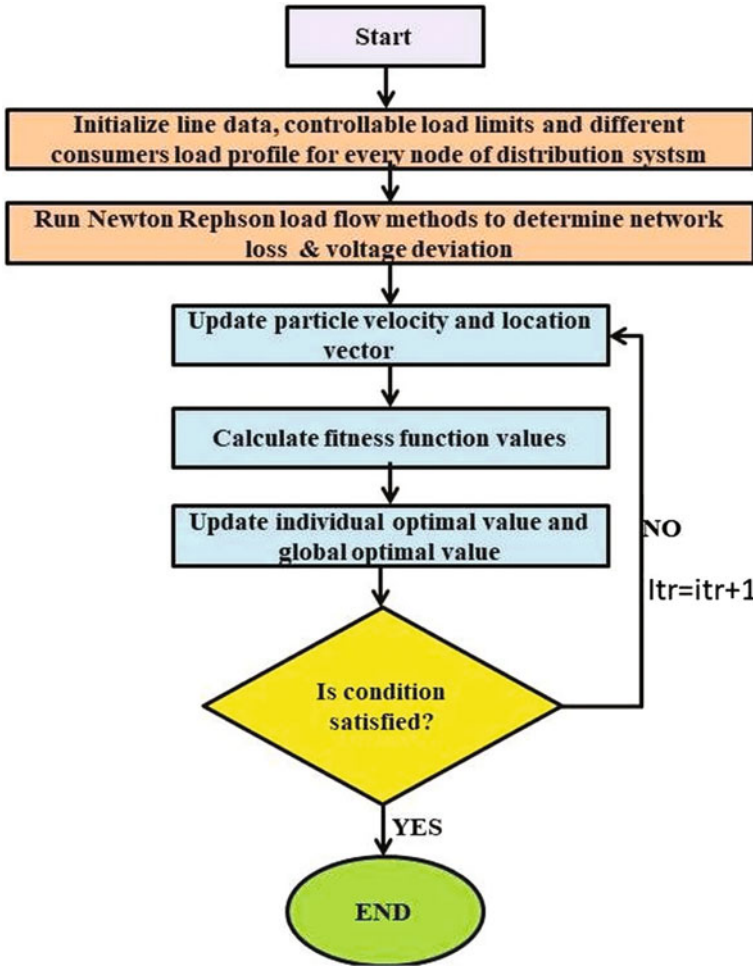


Fig. 2 Flow chart of PSO for solving the considered distribution problem

5 Results and Discussion

In this section, selection of demand response programs problem for different categories of consumers is developed using particle swarm optimization, i.e., Sect. 3. For the efficacy of the results, the framed problem is tested on a standard 33-bus distribution system as presented in Fig. 2. It is a radial network having 12.66 kV with real power and reactive power load is 3715 kW and 2300 kVAr, respectively. The considered electricity rates under different demand response programs and flat rate is presented in Table 1. The dedicated feeders are assigned to the different categories of consumers such as residential consumers, i.e., from 1 to 15 buses, industrial consumers, i.e., from 22 to 29 buses, and commercial consumers, i.e.,

from 16 to 21 and 30 to 33, respectively. For the residential consumers, price-based demand response programs are floated. Moreover, for the industrial and commercial consumers, incentives-based program is floated by the demand response aggregator. Table 2 presents the category-wise supplier revenue and consumer benefits for different demand response programs. In this paper, 15% of the controllable load from total loads are considered for demand response modeling (Fig. 3). The altered demands and node voltage profile after the successful implementation of different demand response programs are presented in Figs. 4, 5, 6, 7, 8, and 9.

Table 1 Pricing of demand response programs

Consumer categories	Demand response programs	Electricity rates (₹/kWh)	Incentives (₹/kWh)	Penalty (₹/kWh)
Residential	Base case	₹5	0	0
	TOU	₹3, ₹5, ₹10 at low period, off-peak and peak periods	0	0
	CPP	₹12 at 20, 21, 22 h	0	0
	RTP	₹1, ₹1, ₹2, ₹3, ₹5, ₹11, ₹4 for different inter-val of 24 h	0	0
Industrial & commercial	Base case	₹6	0	0
	DLC	₹6	19	0
	EDRP	₹6	29	0
	I/C	₹6	14	11

Table 2 Supplier and consumer economic benefits of different consumer groups

Consumers categories	Demand response programs	Electricity consumption cost (₹)	Incentives (₹)	Penalty (₹)	Supplier revenue (₹)	Consumer benefits (₹)
Residential	Base	4091	0	0	4091	–
	TOU	3720.27	0	0	3720.27	370.73
	CPP	3911.28	0	0	3911.28	179.72
	RTP	3059.78	0	0	3059.78	1031.22
Industrial	Base	12,131.5	0	0	12,131.5	–
	DLC	10,287.79	2369.45	0	7918.34	4213.2
	EDRP	10,871.89	5339.29	0	5532.61	6598.9
	I/C	11,075.52	2278.69	798.63	9595.57	2535.9
Commercial	Base	5833.2	0	0	5863.2	–
	DLC	5459.2	1189.4	0	4269.8	1563.4
	EDRP	5271.8	2554.5	0	2717.3	3115.9
	I/C	5334.64	1054.9	396.9	4676.6	1156.6

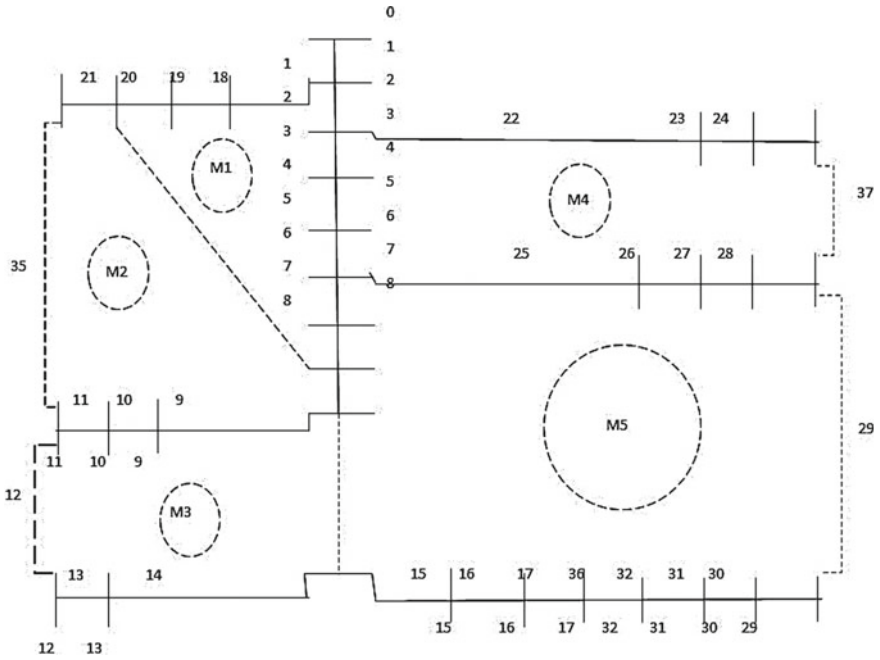


Fig. 3 33-bus distribution system

Fig. 4 Voltage profiles for residential feeder

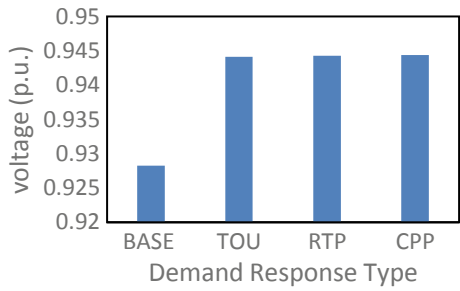
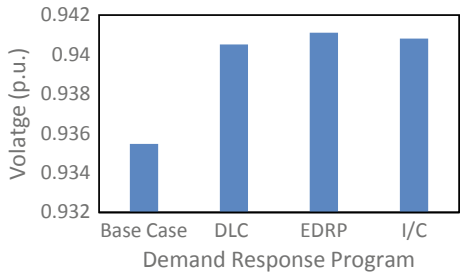


Fig. 5 Voltage profiles for industrial feeder



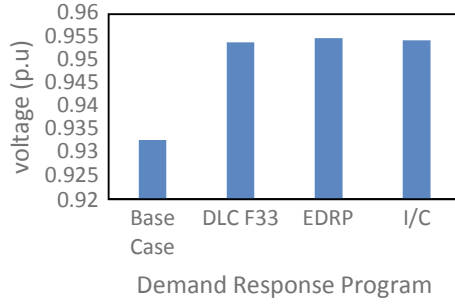


Fig. 6 Voltage profiles for commercial feeder

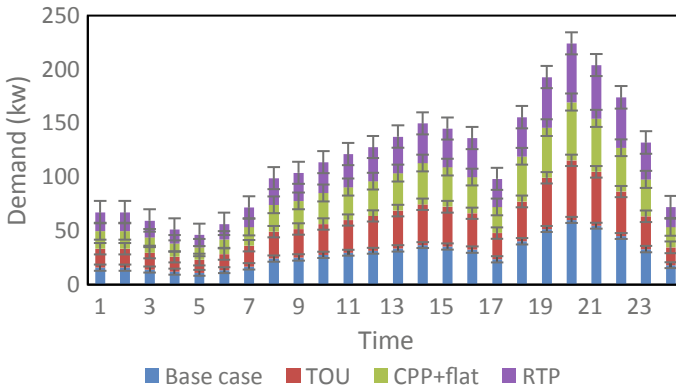


Fig. 7 Load profiles for residential feeder

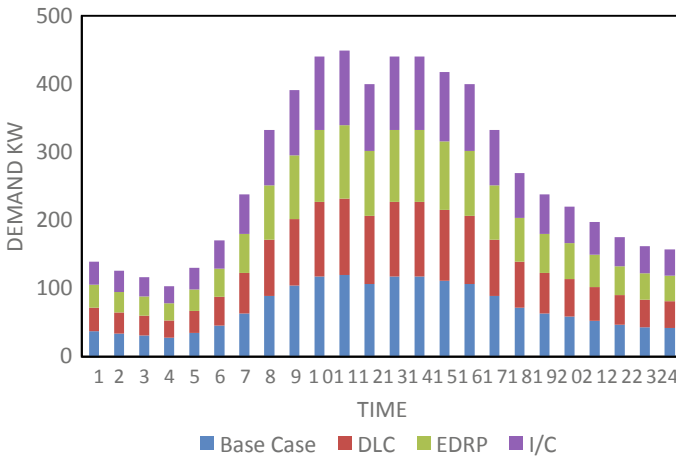


Fig. 8 Load profile for industrial feeder

Case 1:

This is the baseline case, based on the existing pricing mechanisms in several states of the Indian power system, which are primarily concerned with the collection of generating and service costs. Moreover, this subsidized and set rate electricity price does not encourage end users to make optimal use of electricity. Adding a different demand response price component to existing tariffs may motivate the end users to alter their power use to take advantage of lower cost of electricity consumption and even free from the imbalance issues. The supplier revenue and consumption cost of electricity for residential, commercial, and industrial consumers are ₹4091, ₹12131.5, and ₹5833.2, respectively, and are shown in Table 2. In this case, supplier revenue and electricity consumption cost are same. The minimum node voltage of residential, commercial, and industrial feeders is 0.927, 0.936, and 0.932 p.u., respectively, and is presented in Fig. 4, Fig. 5, and Fig. 6, respectively.

Case 2:

This case is dedicated to the residential consumers and assigned to feeders 1–15. The price-based demand response programs are implemented. It is analyzed that minimum node voltage of this feeder is better than the base case, i.e., 0.92–0.94 p.u., respectively, and is presented in Fig. 4. It is concluded that for all the price-based demand response programs, the minimum node voltages are almost same. It is due to the residential consumer participation among all the different demand response programs are same. As per the concern of peak demand, the critical demand response program achieved maximum reduction, i.e., 11% and is shown in Fig. 7. Table 2 presented that real-time pricing-based demand response programs is one of the programs that achieved maximum consumer profit, i.e., ₹1031.22 (Fig. 8).

Case 3:

The mandatory type demand response programs in which incentives and penalty are designated to industrial and commercial consumers. The electricity price for these cases is set to ₹6 and penalty is the main part of mandatory programs. Therefore, incentives are ₹19, ₹29, and ₹14 for direct load control, emergency demand response program, and interrupted and curtailed-based programs, respectively. It is analyzed that minimum node voltage of commercial feeder is better than the base case, i.e., 0.932–0.954 p.u., respectively, and is presented in Fig. 6. The emergency demand response program achieved the maximum peak reduction of 10.2% and is presented in Fig. 9. Table 2 shows that maximum supplier benefits are achieved by emergency demand response program, i.e., ₹6598.9 and least in case of interrupted and curtailed-based program, i.e., ₹2535.9.

The best accomplish demand response program benefits for the above scenarios are applied simultaneously on all the segregated feeders for better network performance. Moreover, it is concluded from the above results that real-time demand response program is best suited for residential consumers and emergency demand response programs for commercial and industrial consumers. It is analyzed that distribution network loss without implementing any demand response is 1738 kW

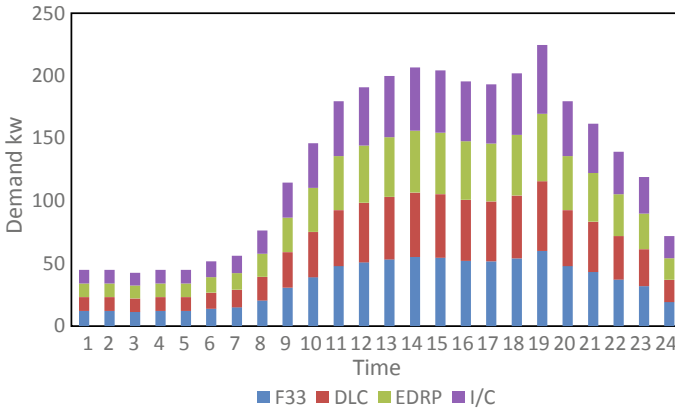


Fig. 9 Load profiles for commercial feeder

and after implementing the above combination of demand response, network losses are 799.5 kW. Moreover, the aforesaid demand response is simply applied in the distribution system, and the system’s minimum node voltage improves from 0.924 to 0.955 p.u.

6 Conclusions

In this paper, different pricing of demand response models using particle swarm optimization to minimize the network loss and deviation in node voltage is investigated. To show the efficacy of successful implementation of different pricing of DR, it is compared with standard distribution network without consideration of DR and within different proposed pricing of DR. In comparison to the base case, the results show that demand response program incorporation reduces the node voltage deviation and peak demand. The residential consumers profit the most in terms of energy consumption costs when they participate more in real-time price-based program, and the same is true for industrial and commercial feeders when they participate more in emergency demand response program. The proposed model also aids in lowering the extra generation limit for supplying peak demand and reducing network congestion. The ability of demand response management to improve voltage and reduce power loss for various dedicated feeders demonstrates that it can do so with a substantial margin.

References

1. ISGAN (2013). Report, dynamic tariff structure for demand side management and demand response. www.iea.isgan.org
2. FERC (2012) Staff report, assessment of demand response and advanced metering. www.FERC.gov
3. Medina J, Muller N, Roytelman I (2010) Demand response and distribution grid operations: opportunities and challenges. *IEEE Transactions on Smart Grid* 1(2):193–198
4. Saele H, Grande OS (2011) Demand response from household customers: experiences from a pilot study in Norway. *IEEE Trans Smart Grid* 2(1):102–109
5. Molina-Garcia A, Kessler M, Fuentes JA, Gomez-Lazaro E (2011) Probabilistic characterization of thermostatically controlled loads to model the impact of demand response programs. *IEEE Trans Power Syst* 26(1):241–251
6. Palensky P, Dietrich D (2011) Demand side management: demand response, intelligent energy systems, and smart loads. *IEEE Trans Industr Inf* 7(3):381–388
7. Safdarian A, Fotuhi-Firuzabad M, Lehtonen M (2014) A distributed algorithm for managing residential demand response in smart grids. *IEEE Trans Industr Inf* 10(4):2385–2393
8. Safdarian A, Fotuhi-Firuzabad M, Lehtonen M (2016) Benefits of demand response on operation of distribution networks: a case study. *IEEE Syst J* 10(1):189–197
9. Haider HT, See OH, Elmenreich W (2016) Review of residential demand response of smart grid. *Renew Sustain Energy Rev* 59:166–178
10. Mohsenian-Rad AH, Leon-Garcia A (2010) Optimal residential load control with price prediction in real-time electricity pricing environments. *IEEE Transactions on Smart Grid* 1(2):120–133
11. Parsa Moghaddam M, Abdollahi A, Rashidinejad M (2011) Flexible demand response programs modeling in competitive electricity markets. *Appl Energy* 88:3257–3269
12. Kirschen DS, Strbac G, Cumperayot P, de Paiva Mendes D (2000) Factoring the elasticity of demand in electricity prices. *IEEE Trans Power Syst* 15(2):612–617
13. Roscoe AJ, Ault G (2010) Supporting high penetrations of renewable generation via implementation of real-time electricity pricing and demand response. *IET Renew Power Gener* 4(4):369–382
14. Heydarian-Forushani E, Parsa Moghaddam M, Sheikh-El-Eslami MK, Shafie-khah M, Catalao J (2016) Risk constrained offering strategy of wind power producers considering Intraday Demand Response Exchange. In: 2016 IEEE/PES Transmission and Distribution Conference and Exposition (T&D), Dallas, TX, pp 1–1
15. Zhang C, Xu Y, Dong ZY, Wong KP (2017) Robust coordination of distributed generation and price-based demand response in microgrids. *IEEE Trans Smart Grid*:1–1
16. Liu Y, Yuen C, Ul Hassan N, Huang S, Yu R, Xie S (2015) Electricity cost minimization for a microgrid with distributed energy resource under different information availability. *IEEE Trans Ind Electron* 62(4):2571–2583
17. Shao S, Pipattanasomporn M, Rahman S (2011) Demand response as a load shaping tool in an intelligent grid with electric vehicles. *IEEE Transactions on Smart Grid* 2(4):624–631
18. Rawat T, Niazi KR (2017) Comparison of EV smart charging strategies from multiple stakeholders' perception. *J Eng* 13:1356–1361
19. Maigha, Crow ML (2017) Cost-constrained dynamic optimal electric vehicle charging. *IEEE Trans Sustain Energy* 8(2):716–724
20. Sharma S, Niazi KR, Verma K, Thokar RA (2019) Bilevel optimization framework for impact analysis of DR on optimal accommodation of PV and BESS in distribution system. *Int Trans Electr Energy Syst* 29(9):2019
21. Sharma S, Niazi KR, Verma K, Meena NK (2019) Multiple DRPs to maximise the techno-economic benefits of the distribution network. *J Eng* 18:5240–5244
22. Charu KM, Thakur P, Ansari MF, Saini P (2021) Pitfalls of conventional MPPT techniques of solar PV. In: IEEE international conference on advances in computing, communication control and networking (ICAC3N), pp 1197–1202

Impact of Redox Flow Battery and HVDC Link on Combined ALFC-AVR of a Hydrothermal System Incorporating GTPP Considering Communication Delay



Biswanath Dekaraja, Lalit Chandra Saikia, and Satish Kumar Ramoji

1 Introduction

Large interconnected power system (PS) networks have numerous utilities which are interconnected via a tie-line between them to exchange power at the scheduled value. When the power imbalance occurs in one control area, the frequency and tie-line power deviate from their nominal values. The automatic load frequency control (ALFC) scheme helps to restore them to their original operating point. ALFC loop comprises two loops, viz. primary and secondary loops. The primary loop tries to alleviate the power mismatch between generation and load demand via the governor mechanism. But, the primary loop may not be able to diminish the power mismatch. Hence, the secondary loop is used to restore the original value of frequency and tie-line power by diminishing the power mismatch. The researchers have designed various control approaches to achieve a robust secondary controller for the ALFC scheme [1]. Various control approaches such as sliding mode [2], model predictive control [3], soft-computing-based methods [4], etc., have been found in the literature for ALFC studies. The power mismatch in the interconnected systems is not only made the frequency and tie-line power deviations but also the voltage deviation occur [5, 6]. This voltage deviation of the power generating unit is controlled by the automatic voltage regulator (AVR). Even though the AVR loop responds faster than the ALFC loop during the large disturbance, there is a weak mutual interaction

B. Dekaraja (✉) · L. C. Saikia · S. K. Ramoji
National Institute of Technology Silchar, Silchar, Assam 788010, India
e-mail: biswaju10@gmail.com

L. C. Saikia
e-mail: lcsaikia@yahoo.com

S. K. Ramoji
e-mail: satish.ramoji@gmail.com

between them for small-signal analysis in power systems [5, 6]. Hence, ALFC studies are needed by considering the AVR loop.

Several articles were published in the last decade on the studies of the ALFC scheme using the AVR loop [7–17]. The authors of [7] studied the AVR loop's impact on the ALFC loop. A single-area thermal system has been considered without any physical constraints for their investigations. They also studied the damper winding impact on their considered system. The authors of [8] studied the impact of AVR on the ALFC loop using a single-area thermal system without physical constraints. The above authors have not included generation rate constraints (GRC) and governor dead-band (GDB) in their investigated system. Both GDB and GRC are equipped with thermal/hydro units to provide a more accurate representation of these units. The authors in [9] studied two-area thermal systems without RGC and GDB. The authors of [10] and [11] investigated the two-area hydrothermal system by taking into account the GRC and the boiler dynamics for the thermal units. They have taken the mechanical governor for the hydro plant. In the modern hydropower plant, the electric governor is equipped with the hydro plant. The performance of the mechanical and electric governors of the hydro unit has not been compared in the literature under the ALFC studies having the AVR loop. The addition of the electric governor to the system that they are considering may affect the system dynamics [10, 11]. Hence, two-area hydrothermal systems with the electric governor of the hydro unit by considering GRC and GDB are needed further investigation. Also, the communication time delay (CTD) is one of the vital issues in the studies of the ALFC scheme. The power generation of the generating units adjusts based on the command signal which is received from the Load Dispatch Center (LDC). The communication between the LDC and the power generating station takes time. No literature has considered the CTD constraints in their investigated systems. Hence, it is needed further investigations.

Non-conventional energy sources (NCES)-based plants have been incorporated into the power grid to decrease global warming. Various researchers have studied the ALFC problem by considering the AVR loop having NCES like wind, dish Stirling solar thermal system, solar thermal power plant, geothermal power plant (GTPP), etc. [12–17]. In the literature, no studies have been found of two-area hydrothermal systems incorporating GTPP by considering physical constraints like GRC, CTD, and GDB. Hence, there is an opportunity to investigate the influence of the GTPP and physical constraints on system dynamics.

A high-voltage direct current (HVDC) link is preferable to an AC transmission line for bulk power exchange between control areas. Using power electronic equipment, the HVDC connection permits greater controllability in PS operation and control. At the sending and receiving ends of the HVDC, a converter and an inverter are used to exchange power flow between the control areas. The authors of [15, 16, 18] utilized the HVDC link in their considered systems. They demonstrated that the addition of the AC/HVDC link improved the system's performance. The HVDC link has only been considered in a few studies of the unified ALFC and AVR model. Hence, there is a scope to explore the same.

For the smooth operation of the ALFC scheme, the secondary controller plays a vital role along with the control approach. Hence, the researchers mainly emphasized designing the secondary controller. Various controllers have been suggested in the literature and performed successfully in the ALFC scheme using the AVR loop. The secondary controller like PID [10], fractional-order (FO) PID [11], FO integral-order double derivative [16], etc. The cascaded controller outperformed the single loop controller in terms of system dynamics criteria. Various cascaded combinations of FO and integer-order controllers like cascade PDN-PIDN [12], cascade FOPDN-FOPIDN [13], and cascade PDN-FOPIDN [15] have been employed successfully in this unified model. The FO controller also yielded better system performance due to its inherent properties [14, 17]. In this work, a novel cascade FO PID with the filter coefficient and PD with filter coefficient called CFOPIDN-PDN controller is proposed. The proposed controller performance will be compared with PIDN and FOPIDN controllers.

The power system network configuration is a huge man-made dynamic system. Hence, the conventional method may not be able to obtain the controller optimal values or may be obtained sub-optimal solutions and also be time-consuming. Many studies have used metaheuristic algorithms to find the best controller parameters in order to overcome these issues. Various metaheuristic optimization techniques such as moth flame optimization [11], lighting search algorithm [16], particle swarm optimization [9], artificial flora algorithm (AFA) [12–15], etc., have been employed. In this study, AFA [19] will be implemented to get the optimal settings for the controller parameters.

Energy storage system (ESS) devices like capacitor energy storage [15], redox flow battery [15, 20, 22], superconducting magnetic ESS [21], and flywheel ESS [15] have been employed successfully in the joined ALFC-AVR model. The authors in [20, 22] investigated the impact of RFB on the system performance for three-area multiunit systems. A few studies have been done in the combined scenario considering RFB. As a result, there is potential for further investigation.

The sensitivity analysis will be performed to certify the controller's sturdiness. Various approaches have been found for controller sensitivity analysis in literature. Some of them are (i) changes in the magnitude of the step load disturbance (SLD), (ii) changes in the position of the SLD, (iii) changed in system loading, etc. In this study, the change in uneven loading of the system will be done.

1.1 Novelty and Main Contribution of This Work

- (a) A two-area hydrothermal system incorporating GTPP is developed for the ALFC studies having an AVR loop in each control area considering the system nonlinearity constraints like GRC, GDB, and CTD.
- (b) A novel CFOPIDN-PDN controller will be implemented for the first time in the ALFC scheme by considering the AVR loop.

- (c) A maiden attempt has been made to apply RFB in each control area of the developed system in (a).
- (d) The influence of the conventional HVDC tie-line on the system performance of the considered system (a) for the first time.
- (e) The effect of CTD on system dynamics in ALFC studies by considering the AVR loop for the first time.
- (f) The proposed controller's robustness will be validated by a sensitivity analysis.

2 Methodology

The methodology section is divided into the system under investigation, modeling of cross-coupling coefficient, modeling of RFB, conventional HVDC link, and proposed controller followed by the optimization technique. Later, the results and analysis are discussed followed by the conclusion.

2.1 System Under Study

Figure 1 shows the TF model of the two-area hydrothermal systems integrating GTPP. The area capacity ratio is considered as 1:2. The area control error (ACE) in each area is shared by each generating unit in each control area and called as ACE participation factor (*apf*). In this study, *apf* is taken as $apf_{11} = apf_{21} = 0.8$, and $apf_{12} = apf_{22} = 0.2$. GRC and GDB are considered as 3% p.u MW/m and 0.06% for the thermal plant [24]. GRC of 270%/min for increasing and 360% /min for decreasing for the hydro plant [23]. GDB is taken as 0.02% for the hydro unit [14]. The RFB is incorporated into all control areas. The system parameter values at nominal system conditions are given in the Appendix. The CTD ($e^{-s\tau_{cd}(t)}$) value is taken as $\tau_{cd}(t) = 0.5$ s as a nominal value. The proposed CFOPIDN-PDN, PIDN, and FOPIDN controllers will be implemented as secondary controllers to find the best one.

2.2 Modeling of Cross-Coupling Coefficients

The power transfer from the synchronous generator to the bus is given in (1) [5]

$$P_e = \frac{|V||E|}{X_s} \sin(\delta) \quad (1)$$

where δ denotes the angle of the rotor, E and V are denoted as the induced emf of the synchronous generator and bus voltage. X_s is the synchronous reactance. The small change in active power (ΔP_e) can be stated in terms of a small change in rotor angle

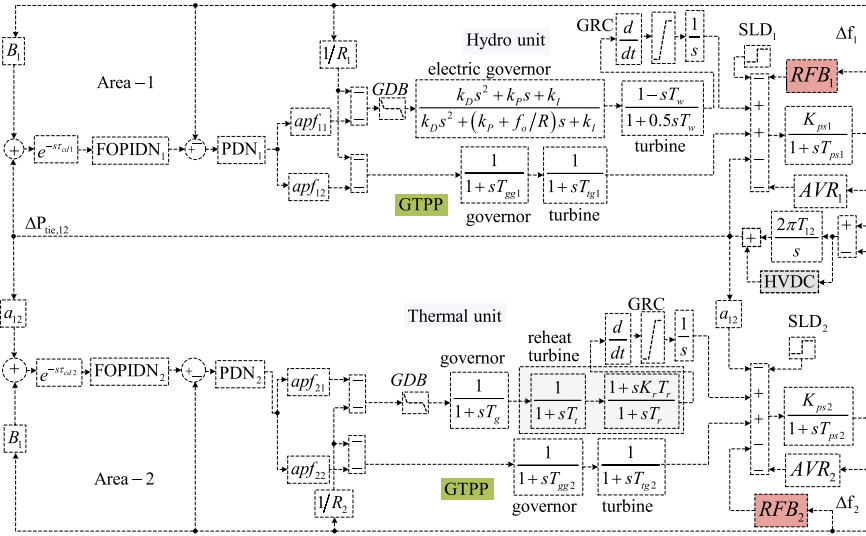


Fig. 1 Transfer function (TF) model for investigated system

($\Delta\delta$) and the small change in induce emf (ΔE) of the synchronous generator and given in (2) [12]

$$\Delta P_e = K_1 \Delta\delta + K_2 \Delta E \tag{2}$$

where K_1 is the synchronizing coefficient and K_2 represents the small change in power w.r.t. small change in emf at a constant rotor angle.

The small change in terminal or bus voltage can be represented in terms of a small change in the rotor and induced emf voltage and given in (3) [12]

$$\Delta V = K_5 \Delta\delta + K_6 \Delta E \tag{3}$$

where K_5 is denoted by ΔV w.r.t. the $\Delta\delta$ at constant emf and K_6 represents the ΔV w.r.t. ΔE at constant rotor angle.

The small change in induce emf can be represented in terms of the synchronous generator field wind and $\Delta\delta$ and given in (4) [12]

$$\Delta E = \frac{K_3 K_f}{1 + sT_{do} T_f} (1 - K_4 \Delta\delta) \tag{4}$$

where K_f and T_f are the generator field winding gain and time constant, respectively. T_{do} is the transient time constant.

K_6 , K_5 , K_3 , and K_1 are the coupling coefficients in the combined system.

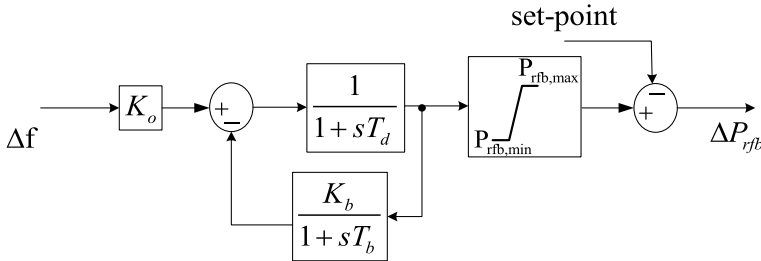


Fig. 2 TF model of the RFB

2.3 Modeling of RFB

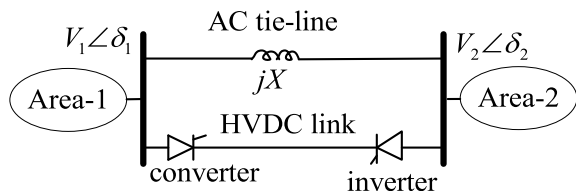
Redox flow batteries (RFBs) use chemical oxidation and reduction reaction processes to store energy in liquid electrolytes. RFB converts chemical energy into electrical energy through the DC–AC converter control mode to the power grid during peak demand. RFB is more efficient than traditional batteries based on design facilities, long lifetime, rapid charging/discharging cycles, high efficiency, simplicity to ship, simplicity of reusing, etc. [4]. RFB can be designed from kW to MW rating and storage time of 3–11 h [4]. TF model of the RFB for the unified ALFC and AVR studies is depicted in Fig. 2 [4].

RFB is operated at the maximum energy storage equal to the maximum permissible energy release. Hence, RFB control is no longer active if the power consumption exceeds the RFB’s rated capacity. Therefore, the maximum ($P_{rfb,max}$) and minimum ($P_{rfb,min}$) have been taken as 0.01 and -0.01 p.u MW, respectively, based on the considered PS. This study uses frequency deviation as an RFB input signal.

2.4 Modeling of AC/HVDC Link

The schematic diagram of two area power systems with parallel AC and HVDC links is shown in Fig. 3. The power exchange between two areas via AC tie-line is represented as (5) [5]

Fig. 3 AC/HVDC link parallel connection between two areas



$$P_{ac,12} = \frac{|V_1||V_2|}{X_{12}} \sin(\delta_1 - \delta_2) \quad (5)$$

The small change in P_{ac12} can be written as (6), where T_{12}^{-*} is the synchronizing coefficient [6].

$$\Delta P_{ac12} = T_{12}^*(\Delta\delta_1 - \Delta\delta_2) \quad (6)$$

Taking Laplace transform in Eq. (6), the following equation is obtained:

$$\Delta P_{ac12}(s) = \frac{2\pi T_{12}^*}{s} (\Delta f_1(s) - \Delta f_2(s)) \quad (7)$$

where $\Delta\delta_1(s) = 2\pi\Delta f_1(s)/s$ and $\Delta\delta_2(s) = 2\pi\Delta f_2(s)/s$.

The conventional HVDC link model is taken as the first-order lag transfer function and given in (8) [15]

$$\Delta P_{dc12}(s) = \frac{K_{dc}}{1 + sT_{dc}} (\Delta f_1(s) - \Delta f_2(s)) \quad (8)$$

where K_{dc} is the gain and T_{dc} is a time constant for the HVDC link model. where $\Delta P_{tie,12} = \Delta P_{ac,12}$.

2.5 Proposed CFOPIDN-PDN Controller

Combined ALFC-AVR system, the secondary controller's main objective is to achieve zero ACE at steady state. The integral (I) controller is used to minimize the ACE at a steady state. I-controller might be produced a slower closed-loop dynamic response time. The PI controller enhances the system dynamics and provides a simple design and low cost when designing a simple linear and stable system. But when the system becomes higher order with nonlinearities, the PI controller is not efficient. To overcome these issues, the PID controller is used. FOPID controller offers superior to PID controller in terms of system dynamics due to its inherent features [13].

Cascade control is another control approach to improve system performance. A cascade controller has more tuning knobs than a standard controller [12]. The proposed CFOPIDN-PDN controller linearized equations are given in (9) and (10)

$$G_{FOPIIDN}(s) = K_P + \frac{K_I}{s^\mu} + \frac{s^\lambda K_D N}{s^\lambda + N} \quad (9)$$

$$G_{PDN}(s) = K_p + \frac{s K_d N_1}{s + N_1} \quad (10)$$

where K_P , K_I , K_D , K_p , and K_d are the proposed controller gains, μ and λ are the FO integral and derivative order, and N and N_1 are the filter coefficients. Nine parameters in each control area need to be optimized.

The CFOPIDN-PDN controller output is given by (11), where $i = 1, 2$.

$$\Delta P_{ci}(s) = \left[\text{ACE}_i \times \left(K_{Pi} + \frac{K_{Ii}}{s^{\mu i}} + \frac{s^{\lambda i} K_{Di} N_i}{s^{\lambda i} + N_i} \right) - \Delta f_i(s) \right] \times \left(K_{pi} + \frac{s K_{di} N_{1i}}{s + N_{1i}} \right) \quad (11)$$

and

$$\left. \begin{aligned} \text{ACE}_1 &= B_1 \Delta f_1 + \Delta P_{\text{tie},12} \\ \text{ACE}_2 &= B_2 \Delta f_2 + \Delta P_{\text{tie},12} \end{aligned} \right\} \quad (12)$$

The governor signal is provided by the controller. The amount of fuel injected into the turbine depends on the controller output signal. To achieve a steady output signal from the controller, it necessities to optimize the parameter. Hence, the design problem is considered a constraints optimization problem and is given by (13) [12], where $i, j = 1, 2, 3$ and $i \neq j$ and $T = 120$ s. Δf = frequency deviation, ΔV = voltage deviation, ΔP_{tie} = Tie-line power deviation.

$$\text{Min } J = \int_{(t=0)}^{(t=T)} (\Delta f_i^2 + \Delta V_i^2 + \Delta P_{(\text{tie},i-j)}^2) dt \quad (13)$$

The Eq. (13) is minimized subjected to

$$\left. \begin{aligned} K_{Pi}^{\min} < K_{Pi} \leq K_{Pi}^{\max}, K_{Ii}^{\min} < K_{Ii} \leq K_{Ii}^{\max}, K_{Di}^{\min} < K_{Di} \leq K_{Di}^{\max}, \\ K_{pi}^{\min} < K_{pi} \leq K_{pi}^{\max}, K_{di}^{\min} < K_{di} \leq K_{di}^{\max}, N_i^{\min} < N_i \leq N_i^{\max}, \\ N_{1i}^{\min} < N_{1i} \leq N_{1i}^{\max}, \mu_i^{\min} < \mu_i \leq \mu_i^{\max}, \lambda_i^{\min} < \lambda_i \leq \lambda_i^{\max}, \end{aligned} \right\} \quad (14)$$

The upper and lower limits of the controller gains are taken as one and zero. The FO integral and derivative operator lower and upper limits are considered as 0.5 and 0.99, respectively. The controller filter coefficient's maximum and minimum values are taken as 100 and 10, respectively.

2.6 Mechanical and Electric Governor for Hydro Unit

The TF model of the mechanical governor ($G_{\text{mech}}(s)$) for the hydro plant is given in (15) [23]

$$G_{\text{mech}}(s) = \frac{1}{R} \frac{1 + sT_{\text{rh}}}{(1 + sT_1)(1 + sT_2)} \quad (15)$$

where T_1 and T_2 are the time constants of the mechanical governor. T_{th} denotes the reset time constant. The TF model of the electric governor or PID governor for the hydro plant is given in (16) [23]

$$G_{P.I.D}(s) = \frac{1}{R} \frac{(k_D s^2 + k_P s + k_I)}{(k_D s^2 + (k_P + \frac{f_o}{R})s + k_I)} \quad (16)$$

where k_D , k_P , and k_I are the gain or tunable parameters of the PID governor. R is the governor's speed regulation.

3 Artificial Flora Algorithm

The authors in [19] proposed the AFA in 2018. AFA can be implemented to solve nonlinear, complex, and discrete optimization problems [19]. Although plants cannot migrate, they may distribute seeds surrounded by a definite range to allow offspring to locate the best habitat for them. Initially, the original plant's locations are generated randomly having propagation distance and positions. The next step is to generate the offspring plant's locations based on the original plant's positions and propagation distance. Finally, based on a selection function like the roulette wheel the best offspring plant is obtained and considered as a new original plant. The iteration process is continued until it hits the best solution. The authors in [19] proved the AFA accuracy and stability against the classical PSO and artificial bee colony algorithms by considering six benchmark functions. The mathematical derivations and flowchart are available in [12].

4 Results and Analysis

4.1 Performance Comparison Among PIDN, FOPIDN, and CFOPIDN-PDN Controllers

In this section, two-area hydrothermal combined ALFC and AVR systems incorporating GTPP with appropriate nonlinearity constraints like GRC and GDB for both hydro and reheat turbine and CTD in each control area is investigated by various secondary controllers such as PIDN, FOPIDN, and CFOPIDN-PDN. The mechanical governor is considered for the hydro unit. AFA has been employed to optimize the various controller parameters by minimizing the integral square error subjected to 1% SLD at $t = 1$ s in Area-1. The optimized controller gains are shown in Table 1. Comparative dynamic responses of PIDN, FOPIDN, and CFOPIDN-PDN controllers are presented in Fig. 4(a)–(d). It is evident from Fig. 4(a) to (d), that

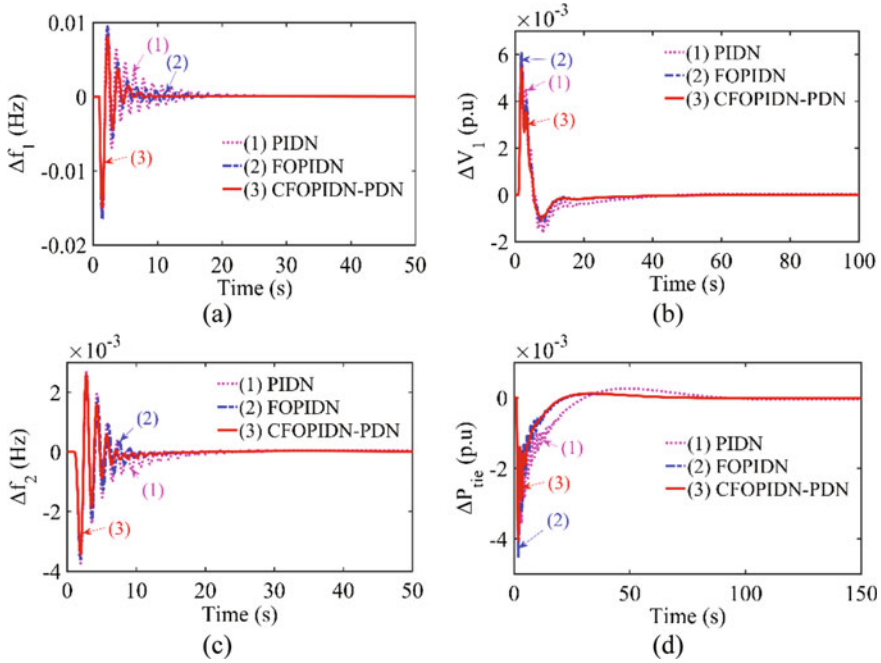


Fig. 4 Dynamic responses comparisons among PIDN, FOPIDN and CFOPIDN-PDN controllers. Deviation of **a** Δf_1 , **b** ΔV_1 , **c** Δf_2 , **d** ΔP_{tie}

the CFOPIDN-PDN controller exhibits superior performance than the FOPIDN and PIDN controllers in terms of peak deviations and settling time. Thus, the subsequent studies will be carried out using the CFOPIDN-PDN controller.

4.2 Performance Comparison Between Mechanical and Electric Governor

The investigated system in Sect. 4.1 has been studied by considering mechanical governor for the hydro unit. To analyze the performance between the mechanical and electric governor of the hydro unit, the mechanical governor is replaced with an electric governor keeping all other system parameters remaining the same as in Sect. 4.1. The proposed CFOPIDN-PDN controller parameters are optimized by the AFA technique and obtained the Δf_1 , Δf_2 , ΔV_1 , and ΔP_{hydro} responses. Figure 5(a)–(c) show the comparisons of the time-domain system dynamic responses between the mechanical and electric governor of the hydro unit. It is clearly seen from Fig. 5(a) to (c) that the system dynamics responses improve significantly in terms of peak deviations, settling time, and oscillations with the electric governor compared to the mechanical governor of the hydro unit. Moreover, Fig. 5(d) shows that the dynamic

Table 1 Optimum value of PIDN, FOPIDN, and CFOPIDN-PDN controller parameters

ALFC/AVR controller	Optimal parameters of the controller
PIDN/PIDN	$K_{P1} = 0.5412, K_{P2} = 0.3254, K_{I1} = 0.2351, K_{I2} = 0.3214, K_{D1} = 0.5124, K_{D2} = 0.6214, N_1 = 63.251, N_2 = 85.362, K_{Pav1} = 0.5841, K_{Pav2} = 0.6254, K_{Iav1} = 0.4621, K_{Iav2} = 0.1842, K_{Dav1} = 0.9614, K_{Dav2} = 0.8436, N_{av1} = 36.5142, N_{av2} = 36.1624$
FOPIDN/PIDN	$K_{P1} = 0.2512, K_{P2} = 0.4264, K_{I1} = 0.5221, K_{I2} = 0.1511, K_{D1} = 0.8122, K_{D2} = 0.7284, N_1 = 73.2951, N_2 = 45.382, \mu_1 = 0.9984, \mu_2 = 0.8995, \lambda_1 = 0.9316, \lambda_2 = 0.8965, K_{Pav1} = 0.8811, K_{Pav2} = 0.9224, K_{Iav1} = 0.1321, K_{Iav2} = 0.1242, K_{Dav1} = 0.6114, K_{Dav2} = 0.7136, N_{av1} = 76.112, N_{av2} = 26.1824$
CFOPIDN-PDN/PIDN	$K_{P1} = 0.8812, K_{P2} = 0.6354, K_{I1} = 0.1841, K_{I2} = 0.1134, K_{D1} = 0.8921, K_{D2} = 0.8914, N_1 = 60.281, N_2 = 75.392, \mu_1 = 0.8984, \mu_2 = 0.9195, \lambda_1 = 0.9916, \lambda_2 = 0.7995, K_{p1} = 0.8121, K_{p2} = 0.9951, K_{d1} = 0.7829, K_{d2} = 0.6854, K_{Pav1} = 0.5341, K_{Pav2} = 0.9454, K_{Iav1} = 0.1671, K_{Iav2} = 0.1232, K_{Dav1} = 0.7514, K_{Dav2} = 0.7936, N_{av1} = 86.556, N_{av2} = 46.1524$

response of the hydro unit with the electric governor is faster than the dynamic response of hydro unit with the mechanical governor. Hence, further case studies, the electric governor will be used for the hydro unit.

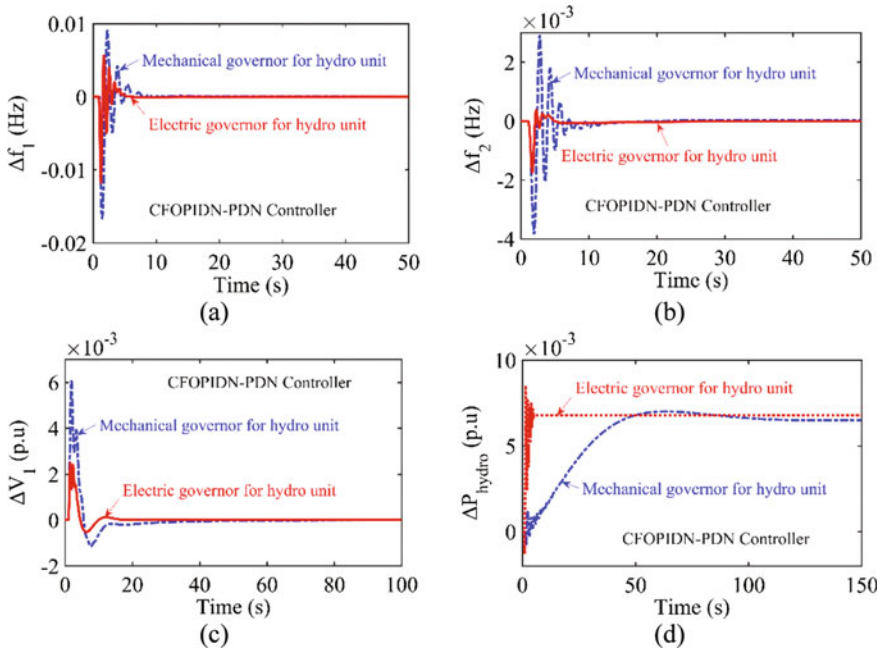


Fig. 5 Dynamic responses comparisons between electric and mechanical governor for the hydro unit. Deviation of **a** Δf_1 , **b** Δf_2 , **c** ΔV_1 , **d** ΔP_{hydro}

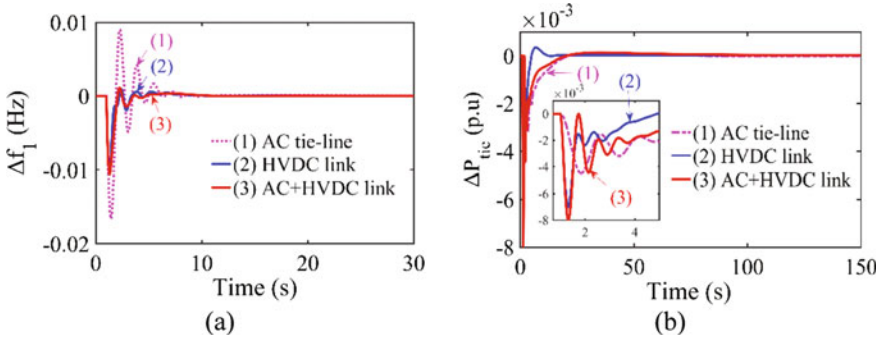


Fig. 6 Dynamic response comparisons among AC, HVDC, and AC + HVDC links. Deviation of **a** Δf_1 , **b** ΔP_{tie}

4.3 Effect of HVDC Transmission Link

The considered system in Sect. 4.2 has been examined having the AC tie-line. In order to study the impact of the HVDC tie-line, in this section, two cases are considered (i) HVDC tie-line alone and (ii) parallel AC and HVDC tie-line. In both cases, the proposed CFOPIDN-PDN controller parameters are optimized by the AFA technique and accordingly obtained the Δf_1 and ΔP_{tie} responses. Here, the controller's optimal parameter values are not provided. Figure 6(a) and (b) show the comparisons between the dynamics responses obtained in this section and the dynamics responses obtained in Sect. 4.2. From Fig. 6(a) and (b), it is clearly examined that the system dynamics enhance drastically with the HVDC tie-line compared to the AC tie-line. Moreover, in both cases ((i) and (ii)), the system dynamics responses are almost the same. Furthermore, it is exhibited that the slower tie-line power response and less deviation with AC tie-line compared to both cases ((i) and (ii)). Further studies were carried out considering case (ii).

4.4 Impact of the RFB on the Considered System Performance

In the previous Sect. 4.3, two-area hydrothermal system with appropriate nonlinearities for hydro and thermal units and CTD incorporating GTPP by considering parallel AC and HVDC links without RFB has been studied. RFB is integrated into both the control areas in order to study the effect of RFB. The CFOPIDN-PDN controller parameters are optimized by the AFA technique and obtained system Δf_1 , ΔV_1 , ΔP_{rfb} , and ΔE_{rfb} responses. The controller's optimum settings are not provided. Comparison of the Δf_1 , ΔV_1 , ΔP_{rfb} , and ΔE_{rfb} responses with and without RFB are presented in Fig. 7(a) and (b). Figure 7(a) and (b) show that RFB makes the system

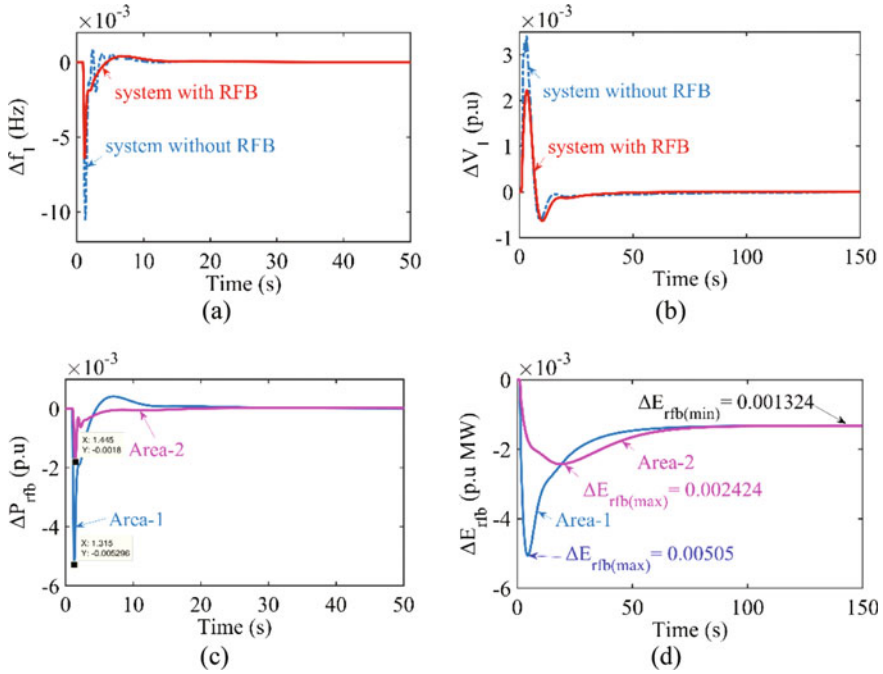


Fig. 7 Dynamic responses comparisons with and without RFB. Deviation of **a** Δf_1 , **b** ΔV_1 , **c** ΔP_{rfb} , **d** ΔE_{rfb}

perform better in terms of peak deviations and oscillations. The settling time is almost the same in both cases. From Fig. 7(c), the rated capacity of the RFB in Area-1 and Area-2 is required 0.005296 p.u. or $0.005296 \times 1000 = 5.296$ MW and 0.0018 p.u or $0.0018 \times 2000 = 3.6$ MW to satisfy the power mismatch for the considered system. Moreover, the MJ capacity in each RFB is obtained from Fig. 7(d).

The MJ capacity is calculated [5] from the energy deviation of the RFB as follows:

$$\Delta E_{rfb} = \int \Delta P_{rfb} dt \quad (17)$$

RFB MJ capacity = $\Delta E_{rfb(max)} - \Delta E_{rfb(min)}$.

From Fig. 7(d), the simulation results show the MJ capacities of the RFB in Area-1 is $0.003726 \times 1000 = 3.726$ MJ and in Area-2 is $0.0011 \times 2000 = 2.2$ MJ. The MJ capacity in Area-1 is more than the Area-2.

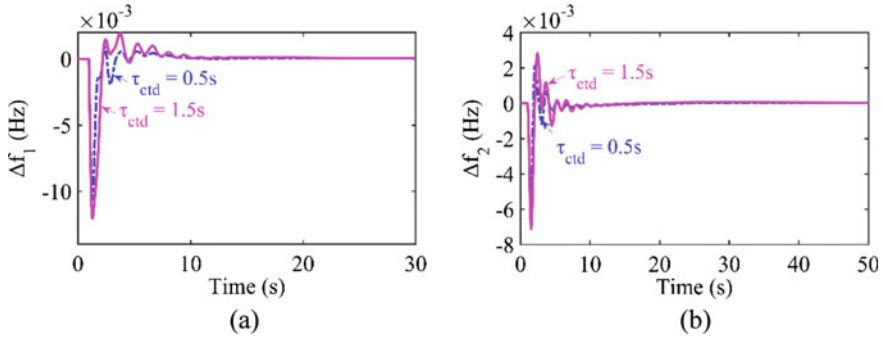


Fig. 8 Dynamics responses comparison at different CTD values. Deviation of **a** Δf_1 , **b** Δf_2

4.5 Effect of the CTD on the Considered System Performance

In Sect. 4.3, two-area hydrothermal system with appropriate nonlinearity constraints for hydro and thermal units incorporating GTPP with parallel AC and HVDC links has been studied at communication time delay (CTD), $\tau_{cd} = 0.5$ s. To study the impact of CTD on the system dynamics, the $\tau_{cd} = 0.5$ value is increased to $\tau_{cd} = 1.5$ s. The proposed CFOPIDN-PDN controller parameters are optimized by the AFA technique at $\tau_{cd} = 1.5$ s keeping all other system parameters remain constant and obtaining the system's dynamic responses. The controller's optimum settings are not provided. Figure 8(a) and (b) show the comparison of the Δf_1 and Δf_2 dynamic responses at two different τ_{cd} values. From Fig. 8, it is seen that the system responses like Δf_1 and Δf_2 degrade with increasing the CTD value.

4.6 Sensitivity Analysis

In Sect. 4.4, two-area hydrothermal systems with suitable system nonlinearity constraints for both hydro and thermal unit incorporating GTPP and the energy storage devices RFB in each control area has been studied at nominal system loading or 50% loading. In order to validate the robustness of the optimized CFOPIDN-PDN controller parameters at 50% loading, the system loading varies $\pm 20\%$ from its nominal loading. The proposed controller parameters are optimized by the AFA technique in both system loading (70% and 30% loading) and obtained accordingly dynamics responses. Figure 9 shows the dynamics responses comparisons between the dynamics responses obtained at changes in the system condition and dynamic responses obtained at changes in the system condition with the optimized controller parameters at nominal conditions. In both systems, dynamic responses are almost the same with higher accuracy. Hence, it is inferred that the optimized CFOPIDN-PDN

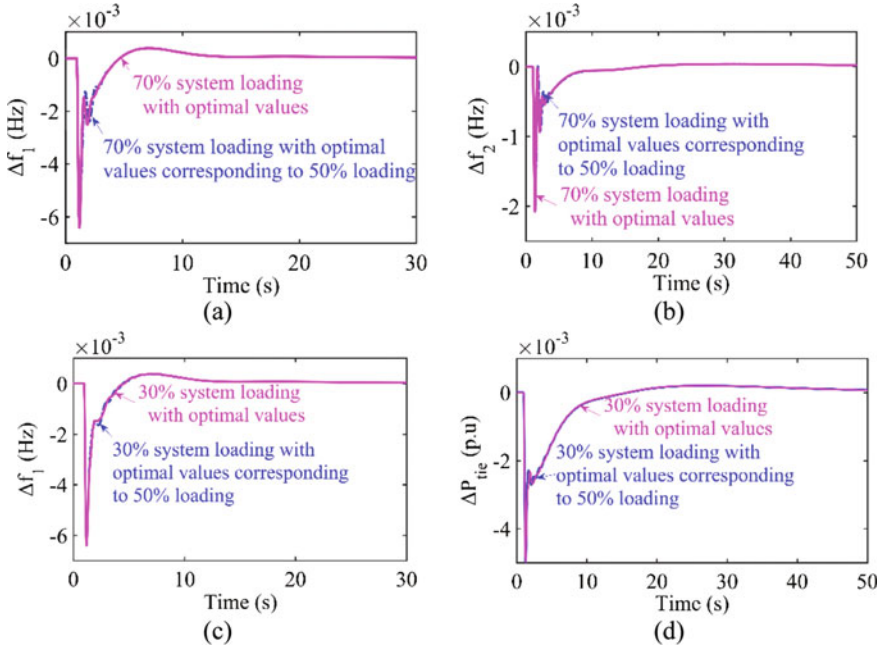


Fig. 9 Dynamic responses comparisons. Deviation of **a** Δf_1 at 70% loading, **b** Δf_2 at 70% loading, **c** Δf_1 at 30% loading, **d** ΔP_{tie} at 30% loading

controller settings are more resilient under nominal conditions, and there is no need to reset again with the wide change in the system conditions.

5 Conclusion

A novel CFOPIDN-PDN controller is suggested to control the frequency and voltage of two-area hydrothermal systems incorporating GTPP. AFA has been employed to optimize the PIDN, FOPIDN, and CFOPIDN-PDN controllers. In terms of maximum overshoot, undershoot, and settling time, the suggested CFOPIDN-PDN controller outperformed the other controllers. Simulation results reveal that the electric governor of the hydro plant is more effective than the mechanical governor. Investigations exhibited that the integration of RFB into the considered system improved the system performance. The analysis reflects that the HVDC link significantly reduced the peak deviation of the frequency in both areas. Moreover, it is inferred that the system performance considerably degraded when the CTD values increased. Finally, the sensitivity analysis shows that the optimum values for the suggested FOPIDN-PDN controller settings under nominal system conditions are resilient and do not repeatedly reset with wide change in system loading.

Appendix

System parameters [23] [24]:

$$K_{ps} = 120 \text{ Hz/p.u MW}, T_{ps} = 20 \text{ s}, B = 0.425 \text{ p.u MW/Hz}, R = 2.4 \text{ p.u MW/Hz},$$

$$a_{12} = -0.5, T_{12}^* = 0.0866,$$

Thermal plant [12]: $K_r = 0.5, T_r = 10 \text{ s}, T_t = 0.3 \text{ s}, T_g = 0.08 \text{ s},$

GTPP [12]: $T_{tgeo} = 0.2 \text{ s}, T_{ggeo} = 0.15 \text{ s},$

Hydro unit [14]: $k_p = 1, k_D = 0.27, k_I = 0.24, T_w = 1 \text{ s}, T_1 = 48.75 \text{ s}, T_2 = 0.513 \text{ s}.$

AVR data are taken from [12].

RFB [12]: $K_o = 0.456 \text{ p.u MW/Hz}, T_d = 0, K_{rb} = 1, T_{rb} = 0.78 \text{ s}.$

HVDC link [16]: $K_{dc} = 1, T_{dc} = 0.2 \text{ s}.$

References

1. Alhelou HH, Hamedani-Golshan ME, Zamani R, Heydarian-Forushani E, Siano P (2018) Challenges and opportunities of load frequency control in conventional, modern and future smart power systems: a comprehensive review. *Energies* 11:1–35
2. Lv X, Sun Y, Hu W, Dinavahi V (2021) Robust load frequency control for networked power system with renewable energy via fractional-order global sliding mode control. *IET Renew Power Gener* 15:1046–1057
3. Elsisli M, Aboelela M, Soliman M, Mansour W (2018) Design of optimal model predictive controller for LFC of nonlinear multi-area power system with energy storage devices. *Electr Power Compon Syst* 46:1300–1311
4. Sharma M, Dhundhara S, Arya Y, Prakash S (2020) Frequency stabilization in deregulated energy system using coordinated operation of fuzzy controller and redox flow battery. *Int J Energy Res* 45:7457–7475
5. Elgerd OI (1982) *Electric energy systems theory: an introduction*, 2nd edn. Tata McGraw Hill, New Delhi
6. Saadat H (1994) *Power system analysis*, 2nd edn. Tata McGraw Hill, New Delhi
7. Rakhshani E, Rouzbehi K, Sadeh S (2009) A new combined model for simulation of mutual effects between LFC and AVR loops. In 2009 Asia-Pacific power and energy engineering conference, pp 1–5
8. Gupta M, Srivastava S, Gupta JRP (2016) A novel controller for model with combined LFC and AVR loops of single area power system. *J Inst Eng (India): Ser B* 97:21–29
9. Sambariya DK, Nath V (2015) Optimal control of automatic generation with automatic voltage regulator using particle swarm optimization. *Univers J Control Autom* 3:63–71
10. Chandrakala KV, Balamurugan S (2016) Simulated annealing based optimal frequency and terminal voltage control of multi-source multi area system. *Int J Electr Power Energy Syst* 78:823–829
11. Lal DK, Barisal AK (2019) Combined load frequency and terminal voltage control of power systems using moth flame optimization algorithm. *J Electr Syst Inf Technol* 6:1–24
12. Dekaraja B, Saikia LC (2021) Combined voltage and frequency control of multiarea multisource system using CPDN-PIDN controller. *IETE J Res*:1–16
13. Dekaraja B, Saikia LC (2021) Performance of redox flow battery in combined frequency and voltage control of multi-area multi-source system using CFOPDN-FOPIDN controller. *Int Trans Electr Energy Syst* 31:1–22

14. Dekaraja, B., Saikia, L. C.: Coordinated control of ALFC-AVR in Multiarea multisource systems integrated with VRFB and TCPS using CFDPN-PIDN controller. *IETE Journal of Research*, pp. 1–17, (2022).
15. Dekaraja B, Saikia LC, Ramoji SK, Behera MK, Bhagat SK (2022) Performance analysis of diverse energy storage on combined ALFC and AVR control of Multiarea multiunit system with AC/HVDC interconnection. *IFAC-PapersOnLine* 55:479–485
16. Rajbongshi R, Saikia LC (2018) Combined voltage and frequency control of a multi-area multisource system incorporating dish-Stirling solar thermal and HVDC link. *IET Renew Power Gener* 12:323–334
17. Dekaraja B, Saikia LC (2021) Impact of energy storage and flexible alternating current transmission devices in combined voltage and frequency regulation of multiarea multisource interconnected power system. *Energy Storage*:1–20
18. Naga Sai Kalyan CH, Sambasiva Rao G (2020) Frequency and voltage stabilization in combined load frequency control and automatic voltage regulation of multiarea system with hybrid generation utilities by AC/DC links. *Int J Sustain Energy* 39:1009–1029
19. Cheng L, Wu X-h, Wang Y (2018) Artificial flora (AF) optimization algorithm. *Appl Sci* 8:1–22
20. Dekaraja B, Saikia LC, Babu NR (2022) Redox flow battery support for combined ALFC-AVR control of multiarea thermal system incorporating renewable energy sources. In *Proceedings of the international conference on computational intelligence and sustainable technologies*. Springer, Singapore, pp 97–110
21. Dekaraja B, Saikia LC, Ramoji SK, Babu NR, Bhagat SK, Behera MK (2020) Coordinated control of voltage and frequency in a three-area multisource system integrated with SMES using FOI-FOPDF controller. In *2020 IEEE 17th India council international conference (INDICON)*, IEEE, pp 1–7
22. Dekaraja B, Bhagat SK, Saikia LC, Behera MK, Ramoji SK (2022) Combined frequency and voltage regulation of a renewable and energy storage integrated multi area systems using cascade controller. In *IEEE Delhi section conference (DELCON)*, pp 1–6
23. Nanda J, Mangla A, Suri S (2006) Some new findings on automatic generation control of an interconnected hydrothermal system with conventional controllers. *IEEE Trans Energy Convers* 21:187–194
24. Dekaraja B, Saikia LC, Ramoji SK, Babu NR, Bhagat SK, Behera MK (2021) Modeling and simulation of a multi-area hydro-thermal interconnected system using FOPI μ controller for integrated voltage and frequency control. In *Modeling, simulation and optimization*. Springer, Singapore, pp 275–285

Amalgamated Voltage and Frequency Regulation of an Interconnected Multi-source Power System Using the CFOI-TIDN Controller



Satish Kumar Ramoji , Lalit Chandra Saikia ,
and Biswanath Dekaraja 

1 Introduction

A modern power system is made up of multiple power generation units that are interconnected to produce high-quality power in response to fluctuating load demand. Cohesive sets of generators called control areas are formed by grouping these generators, as many generators in control areas must operate in unison. Each control area is connected to other control areas by tie-lines, which allow electricity to be exchanged between them. Since the load demand on power system is never stable, the most challenging duty is to preserve system stability, which is contingent on maintaining together frequency and system terminal voltage. Controlling the frequency can be accomplished by curtailing the real power imbalance among demand and generation, which can be accomplished by managing generator speed governor through an ALFC system. The generator AVR regulates system terminal voltage by varying the generator field excitation current. In order to handle the system's frequency, two different control loops are employed. One is the primary loop, which stops the frequency from changing quickly. The other is the ancillary loop, which is also called AGC or LFC, and it is used to cut down on frequency deviations and get the system's frequency back to its ideal value. AVR and ALFC systems are now part of the AGC studies. This is a progressive expansion of the original AGC studies by incorporating the excitation system. AVR systems are more sensitive than ALFC systems because the excitation method has a lower time constant. Although the ALFC and AVR systems function on completely separate time scales, AVR has a substantial influence on the ALFC system, while the ALFC system has no such effect [1, 2]. Because of the frail

S. K. Ramoji (✉) · L. C. Saikia · B. Dekaraja
Department of Electrical Engineering, National Institute of Technology Silchar,
Silchar Assam-788010, India
e-mail: satish.ramoji@gmail.com

© The Author(s), under exclusive license to Springer Nature Singapore Pte Ltd. 2023
P. Singhal et al. (eds.), *Recent Developments in Electrical and Electronics Engineering*,
Lecture Notes in Electrical Engineering 979,
https://doi.org/10.1007/978-981-19-7993-4_10

coupling impact between ALFC and AVR systems, only a few studies have been performed on this amalgamated pattern, demanding further investigation.

The ALFC analyses began with a single area system with primary and secondary LFC [3, 4] and later it is stretched to two area systems with both patterns of LFC [5] in a conventional scenario of operation. Similarly, the AGC or ALFC studies are also explored in a restructured environment of power systems with two area multi-source systems [6, 7]. Many ALFC studies are progressively extended to multi-area- and multi-source-based systems with equal and unequal areas [8–14]. Prelude studies on AGC are explored with multi-area reheat thermal plants with physical constraints such as generation rate constraints [8] and with other plants such as gas turbine plants [9] and hydro plant and gas turbine plants [9, 10]. Many authors also examined the AGC studies of several renewable energy sources such as wind turbine plant, solar photovoltaic plant, geothermal plant [11, 12], and dish Stirling solar thermal plant [12]. Load frequency control studies are investigated using heavy-duty gas turbine plants [13, 14]. The above-mentioned investigations are merely confined to the frequency control aspect which is done by the ALFC systems.

Introductory investigations on AVR systems are based on the practical operation with the use of conventional controllers and classical optimization techniques [15]. To achieve constancy in voltage in different operating scenarios, various control strategies are employed for the AVR system of generators [16, 17].

Gradually, AGC analyses are elongated with the inclusion of excitation mechanisms, which is called amalgamated ALFC and AVR exploration. Preliminary studies of combined ALFC and AVR systems are initiated to explore the mutual effects between these two loops [18] and with single area power system [18, 19]. Many authors are explored the conflated ALFC and AVR structures with equal and unequal areas having various types of renewable and non-renewable sources such as solar thermal power plant, diesel engine [20], combined cycle gas turbine [21, 24], electric vehicles [22], heavy-duty gas turbine [23], and dish Stirling solar thermal [24]. The combination of a thermal-heavy-duty gas turbine-geothermal plant hasn't been looked at yet in the amalgamated ALFC and AVR pattern. According to the extensive literature review, numerous conventional and renewable energy sources have yet to be explored.

The ALFC secondary controller and the AVR main controller are imperative to the effective operation of the power system. Due to the complexity and unpredictability of the system, the standard integral controller wouldn't provide adequate performance. Many studies are explored several controllers in amalgamated ALFC and AVR systems such as Integral (I) and Proportional-Integral (PI) controllers [18], Integral double derivative with derivative filter (IDDF) controllers [20], Tilt-Integral-Derivative with filter (TIDF) controller [21], two degrees of freedom tilt-integral-derivative (2DOFTID) controller [22], and fuzzy logic-based 2DOFTID (F2DOFTID) controller [23]. Several authors investigated cascaded controllers, for example, Proportional-Integral-Derivative with filter cascaded to fractional-order integral (PIDN-FOI) controller [25] and fractional-order integral cascaded to Tilt-Derivative (FOI-TD) controller [26] in only ALFC systems. From the advantages of FOI controller [25, 26] and Tilt-Integral-Derivative with filter (TIDF) controller

[21, 27, 30] a new controller termed as fractional-order integral controller cascaded with tilt–integral–derivative with filter (CFOI-TIDN) controller is proposed for this amalgamated ALFC and AVR study. From the literature, it is perceived that the proposed CFOI-TIDN controller is not yet investigated in amalgamated ALFC and AVR study.

Appropriate tuning of controller parameters is necessary for the power system to operate well. Many authors implemented various metaheuristic optimization techniques such as bacterial foraging optimization (BFO) algorithm [6, 8], binary bat algorithm [10], sine cosine algorithm [11], lightning search algorithm [20], and quasi-oppositional grey wolf optimization algorithm [29] in ALFC and combined ALFC and AVR schemes. A novel algorithm named HHO [27] is available in the literature, which is proposed for the current amalgamated study. A derivative-free, fast-convergence, upfront, and exceptionally efficient method is the HHO approach. On the whole, it depends on the chase pattern and the hawks' accompanying behavior [27].

A thorough assessment of the literature reveals these objectives, such as:

- (a) To design three unequal area power systems by amalgamated ALFC and AVR loops, where Area-1 and Area-2 comprise thermal–thermal–HDGT plant and Area-3 includes thermal–thermal–geothermal plant.
- (b) To obtain the superior controller among FOI, TIDN, and CFOI-TIDN for the system developed in (a) using the HHO algorithm and ISE as the performance measure.
- (c) To study the repercussions of AVR modules and HDGT plants on the amalgamated ALFC and AVR system distinctly.
- (d) To examine the sensitivity study of the superior controller obtained in (b) by varying the loading condition and also by changing the magnitude of the perturbation or the disturbance.

2 Investigated System

The power system suggested in this study is a three-unequal-area multi-sourced system under the conventional scenario. Each area is equipped with its own ALFC and AVR and has an unequal ratio of 1:2:3. Area-1 and Area-2 comprise the thermal–thermal–heavy-duty gas turbine plants, whereas Area-3 has the thermal–thermal–geothermal plant. The three areas are interconnected with their tie-lines. The thermal plants are equipped with a requisite GRC of 3% pu MW/min and GDB of 0.036 Hz. Each unit of every area receives the ACE proportional to their participation factor. The considered apf for apiece unit is $apf_{11} = apf_{12} = apf_{21} = apf_{22} = apf_{31} = apf_{32} = 0.4$, $apf_{13} = apf_{23} = apf_{33} = 0.2$. The transfer function models of the proposed power system and AVR system are portrayed in Fig. 1(a) and Fig. 1(b), respectively.

In this study, three controllers, for instance, FOI, TIDN, and CFOI-TIDN are utilized separately as ALFC loop secondary controller and AVR loop core controller of each area. The HHO technique is used to optimize the controller parameters of

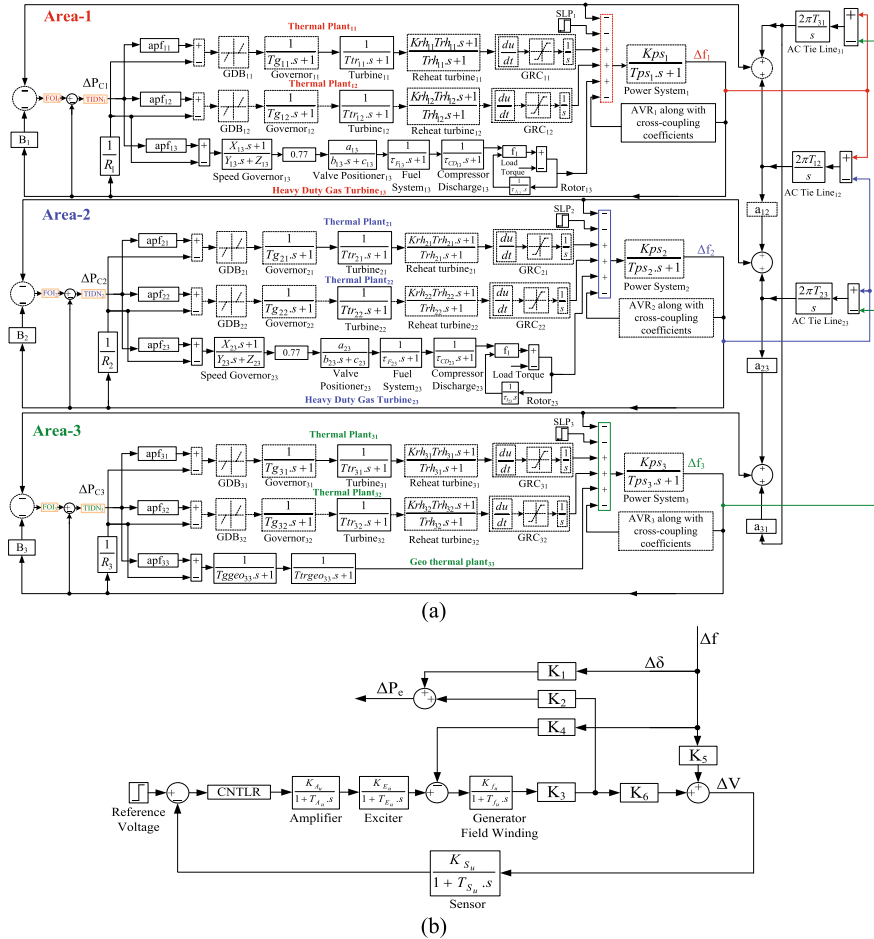


Fig. 1 **a** Transfer function model of proposed power system, **b** transfer function model of AVR module with the cross-coupling constants

each controller. Likewise, the integral square error criterion assesses the system performance with a 1% disturbance at Area-1. The cost function for the deliberated system is set by (1), such as

$$O_{ISE} = \int_0^T (\Delta f_u)^2 + (\Delta V_u)^2 + (\Delta P_{tie_{u-v}})^2 \tag{1}$$

where O_{ISE} is the objective function, simulation time ($T = 100$ s), u and v are the area numbers ($u \neq v$), the frequency deviation (Δf), voltage deviation (ΔV), and deviation in tie-line power between two areas (ΔP_{tie}). The proposed system's required

codes and simulation models are developed in MATLAB platform. The amalgamated analysis of ALFC and AVR modules along with their coupling coefficients are considered from [18–24]. The study of Heavy-Duty Gas Turbine (HDGT) plant is considered from [13, 14, 23].

3 Proposed Controller

Two or more controllers comprise a cascade controller. In this study, a fractional-order integral (FOI) controller is cascaded with a tilt–integral–derivative with filter (TIDN) controller and referred to CFOI-TIDN. The proposed controller is shown in Fig. 2.

The output of FOI controller determines the set point of TID controller. The cascade controller enhances system performance solely by providing additional tuning knobs [25, 26]. The output of FOI controller is given by (2)

$$\Delta P_{\text{set},u} = (K_{I_u} s^{-\lambda_u}) \times \text{ACE}_u \quad (2)$$

$$\text{Where } \text{ACE}_u = B_u \Delta f_u + \Delta P_{\text{tie}_{u-v}} \quad (3)$$

The controller output is given as

$$\Delta P_{C_u} = (\Delta P_{\text{set},u} - \Delta f_u) \left(\frac{K_{t_u}}{s^{n_u}} + \frac{K_{i_u}}{s} + K_{d_u} \left(\frac{N_u s}{s + N_u} \right) \right) \quad (4)$$

The tuning gains are K_{I_u} , K_{t_u} , K_{i_u} , K_{d_u} , and other tuning parameters are λ , n , N . The seven tuning parameters in each control area. The controller gains are limited among 0 and 1. The precincts are $0 < \lambda_u < 1$, $0 < n_u < 3$, and $0 < N_u < 100$. The

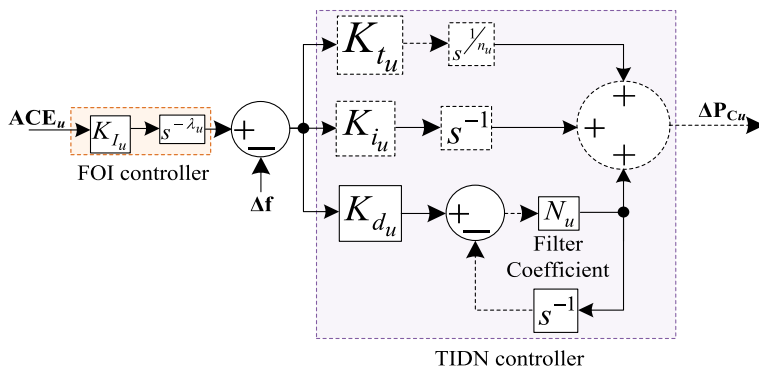


Fig. 2 CFOI-TIDN controller

minimum and maximum edges of controller gains and all tuning parameters are represented as shown below in (5)

$$\left. \begin{aligned} K_{I_u}^{\min} &\leq K_{I_u} \leq K_{I_u}^{\max}, \\ K_{t_u}^{\min} &\leq K_{t_u} \leq K_{t_u}^{\max}, \\ K_{i_u}^{\min} &\leq K_{i_u} \leq K_{i_u}^{\max}, \\ K_{d_u}^{\min} &\leq K_{d_u} \leq K_{d_u}^{\max}, \\ \lambda_u^{\min} &\leq \lambda_u \leq \lambda_u^{\max}, \\ n_u^{\min} &\leq n_u \leq n_u^{\max}, \\ N_u^{\min} &\leq N_u \leq N_u^{\max} \end{aligned} \right\} \quad (5)$$

4 Optimization Technique

The suggested HHO algorithm is a gradient-free, swarm-based optimization method with numerous active and time-varying exploration and exploitation phases. The "surprise pounce" technique, which involves the cooperative behavior of several chase types, is the most significant component of this approach. Depending on the shifting demeanor of circumstances and bunny's evading actions, Harris hawks can use a variety of group quest stratagems. They lurk and pounce as a cluster while the rabbit runs in zig-zag patterns, with more hawks approaching from other locations to contribute to the chaos. The comprehensive HHO algorithm deliberation is referred from [28]. Figure 3 depicts the flow chart for the HHO approach under consideration. Population density, maximum iterations, and escape energy are all tunable factors in this study, and they are 50, 120, and 0.5, respectively, for the HHO approach.

5 Results and Analysis

The system represented in Fig. 1(a) is assessed on behalf of further analysis after the controller values have been optimized using the HHO approach and the ISE as performance index and the addition of 1% SLP to Area-1. Additionally, analyses are conducted under the system's nominal loading state. For ΔV , the reference voltage value is considered as 0.

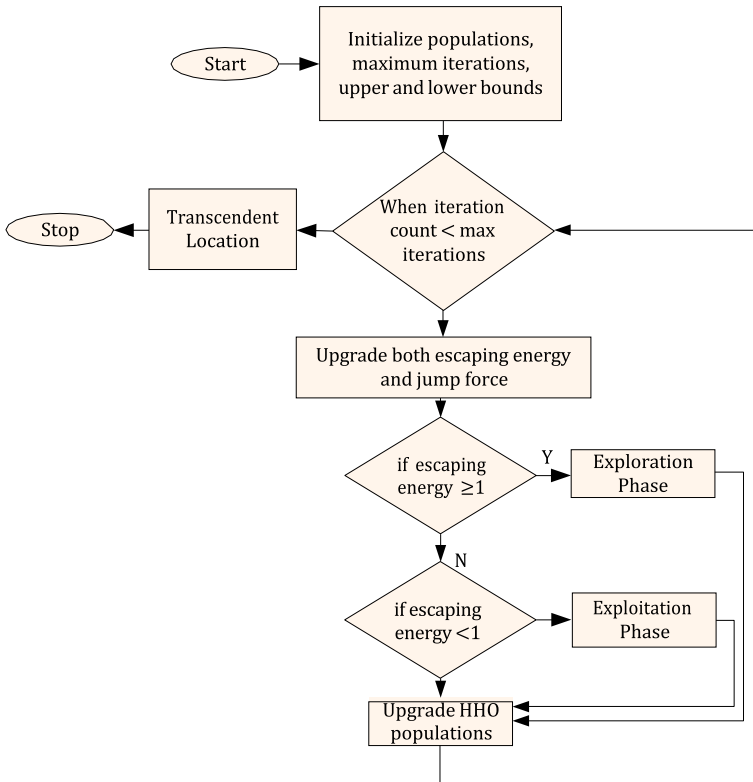


Fig. 3 Flow chart

5.1 Exploration of System Performance by Different Controllers

The amalgamated system described above is observed using different controllers, i.e., FOI, TIDN, and CFOI-TIDN. Each of these controllers acts as a secondary controller for ALFC and a primary controller for the AVR loop of every area. The HHO approach optimizes the parameters of each controller. Table 1 lists the optimal values for each controller. The system responses are achieved by means of the optimal values for each controller, and the results are compared to obtain which controller is the preeminent one by assessing wholly time-domain characteristics. On the basis of time-domain characteristics, i.e., peak overshoot and undershoot, settlement time, oscillation magnitude, etc., it concludes that the CFOI-TIDN controller beats all other controllers. The outcomes are depicted in Fig. 4(a)–(d). Further studies are being done using the proposed CFOI-TIDN controller.

Table 1 Optimal values

Controller	Optimal values
FOI	$K_{I_1}^* = 0.6428, \lambda_1^* = 0.8134, K_{I_{1a}}^* = 0.7035, \lambda_{1a}^* = 0.5132, K_{I_2}^* = 0.8132, \lambda_2^* = 0.9004, K_{I_{2a}}^* = 0.3115, \lambda_{2a}^* = 0.4598, K_{I_3}^* = 0.2119, \lambda_3^* = 0.4531, K_{I_{3a}}^* = 0.9134, \lambda_{3a}^* = 0.5667$
TIDN	$K_{t_1}^* = 0.9436, K_{i_1}^* = 0.1548, K_{d_1}^* = 0.6428, n_1^* = 2.4658, N_1^* = 64.34, K_{t_{1a}}^* = 0.4978, K_{i_{1a}}^* = 0.6147, K_{d_{1a}}^* = 0.5512, n_{1a}^* = 1.9435, N_{1a}^* = 92.64, K_{t_2}^* = 0.6778, K_{i_2}^* = 0.4286, K_{d_2}^* = 0.2456, n_2^* = 1.0255, N_2^* = 94.31, K_{t_{2a}}^* = 0.4546, K_{i_{2a}}^* = 0.2213, K_{d_{2a}}^* = 0.1645, n_{2a}^* = 1.0058, N_{2a}^* = 69.34, K_{t_3}^* = 0.9456, K_{i_3}^* = 0.3421, K_{d_3}^* = 0.8435, n_3^* = 1.6637, N_3^* = 84.38, K_{t_{3a}}^* = 0.8134, K_{i_{3a}}^* = 0.1657, K_{d_{3a}}^* = 0.1924, n_{3a}^* = 2.0084, N_{3a}^* = 79.64$
CFO-TIDN	$K_{I_1}^* = 0.9435, \lambda_1^* = 0.8137, K_{I_1}^* = 1.1918, K_{i_1}^* = 0.5864, K_{d_1}^* = 0.1642, n_1^* = 1.1625, N_1^* = 69.23, K_{I_{1a}}^* = 0.7915, \lambda_{1a}^* = 0.5452, K_{I_{1a}}^* = 0.3745, K_{i_{1a}}^* = 0.1350, K_{d_{1a}}^* = 0.4821, n_{1a}^* = 2.1294, N_{1a}^* = 88.67, K_{I_2}^* = 0.8462, \lambda_2^* = 0.9514, K_{I_2}^* = 1.1948, K_{i_2}^* = 0.576, K_{d_2}^* = 0.154, n_2^* = 1.1815, N_2^* = 91.15, K_{I_{2a}}^* = 0.3695, \lambda_{2a}^* = 0.4798, K_{i_{2a}}^* = 0.376, K_{d_{2a}}^* = 0.145, K_{I_{2a}}^* = 0.4781, n_{2a}^* = 2.1944, N_{2a}^* = 95.32, K_{I_3}^* = 0.2829, \lambda_3^* = 0.4961, K_{I_3}^* = 1.1588, K_{i_3}^* = 0.5640, K_{d_3}^* = 0.1342, n_3^* = 1.1275, N_3^* = 97.67, K_{I_{3a}}^* = 0.9774, \lambda_{3a}^* = 0.5357, K_{I_{3a}}^* = 0.3735, K_{i_{3a}}^* = 0.176, K_{d_{3a}}^* = 0.4381, n_{3a}^* = 2.1724, N_{3a}^* = 75.94$

5.2 Repercussions of AVR and HDGT Plant

In this analysis, the repercussions of AVR system and heavy-duty gas turbine plants on the amalgamated system are observed separately. The repercussion of AVR system is assessed by disconnecting all the three AVRs from the system (described in Sect. 5). In this regard, the controller parameters are tuned in both scenarios, i.e., with and without AVRs in the system, to achieve the best possible performance. The optimal controller values are obtained from both cases and compared. From the comprehensive study of the responses, it's been shown that when the system is provided with AVRs, the system dynamics are greatly enhanced as compared to when system is not equipped with all AVRs. Figure 5(a)–(c) displays the responses of AVR effect.

Likewise, the repercussion of HDGT plants is assessed by disconnecting the two HDGT plants from the system (described in Sect. 5). In this regard, the controller parameters are tuned in both scenarios, i.e., with and without HDGT plants in the system, to achieve the best possible performance. The optimal controller values are obtained from both cases and compared. From the comprehensive study of the responses, it's been shown that when the system is provided with HDGT plants, the system dynamics are significantly affected as compared to when system is not equipped with all HDGT plants. Figure 5(d)–(f) displays the responses of HDGT plant effect.

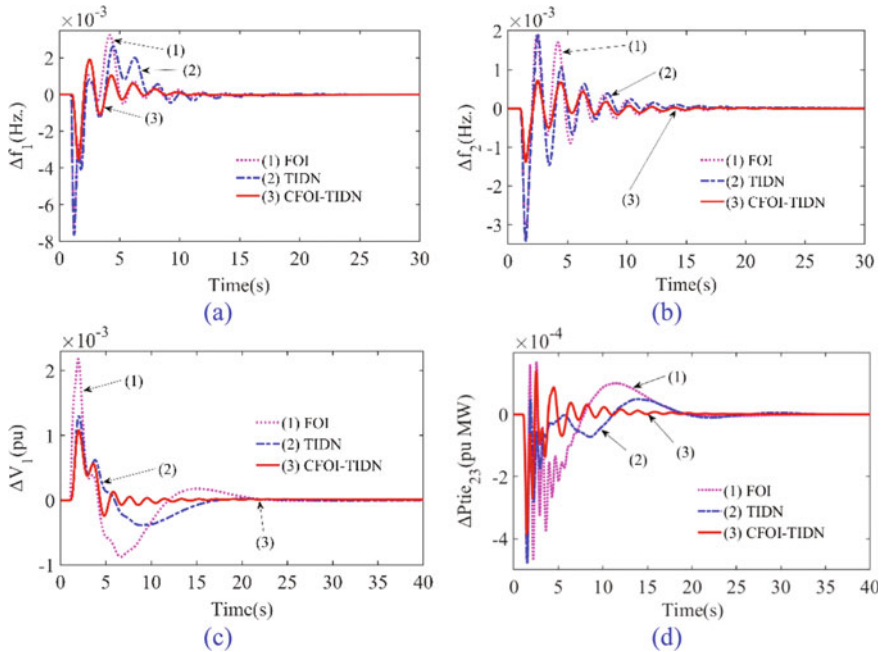


Fig. 4 System performance comparisons vs. time for different controllers **a** Δf of Area-1, **b** Δf of Area-2, **c** ΔV of Area-1, **d** ΔP_{tic} midst Areas 2 and 3

5.3 Sensitivity Analysis

Sensitivity analysis determines a controller’s robustness in numerous ways, such as parameter modifications, changes in system loadings, variations in system nonlinearities, etc. In this analysis, sensitivity exploration is assessed by changing system loading conditions and by changing the magnitude of perturbation. Here, the loading conditions of each area are altered, for instance, Area-1 to 40%, Area-2 to 60%, and Area-3 to 70%. As system loading deviates since its nominal rate in response to changes in the parameters Kps_x , Tps_x , B_x , and D_x , which are deviated. In both cases, controller parameters are optimized using HHO method. In both the cases, system responses are assimilated and compared using their optimal controller values. The comparative responses convey that both the responses are identical. According to the consequences of the detailed analyses of responses, it is manifested, optimal controller values achieved underneath nominal conditions are durable enough to withstand any type of disturbance and do not need to be changed. The system responses are depicted in Fig. 6(a) and (b). Likewise, the magnitude of system disturbance at Area-1 is changed from 1 to 4%. In individual cases, controller parameters are optimized using HHO method. In both the cases, the system dynamic responses are acquired and compared using their optimal controller values. The comparative responses convey that both the responses are identical. According to the consequences of the detailed

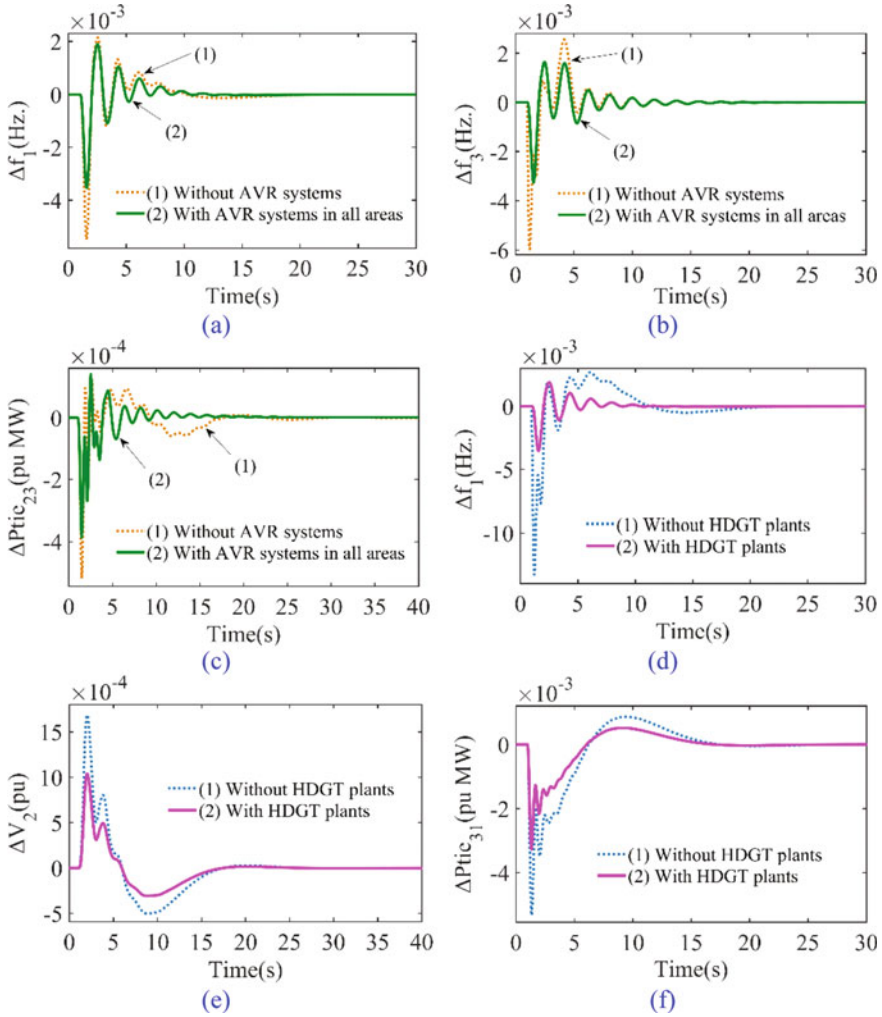


Fig. 5 System performance comparisons vs. time for with and without AVR and HDGT plants **a** delta f in Area-1, **b** delta f in Area-3, **c** delta P_{tie} midst Areas 2 and 3, **d** delta f at Area-1, **e** delta V at Area-2, **f** delta P_{tie} midst Areas 3 and 1

interpretation of responses, it is manifested, the optimal controller values achieved underneath nominal conditions are sturdy enough to withstand any type of disturbance and do not need to be changed. The system responses are depicted in Fig. 6(c) and (d).

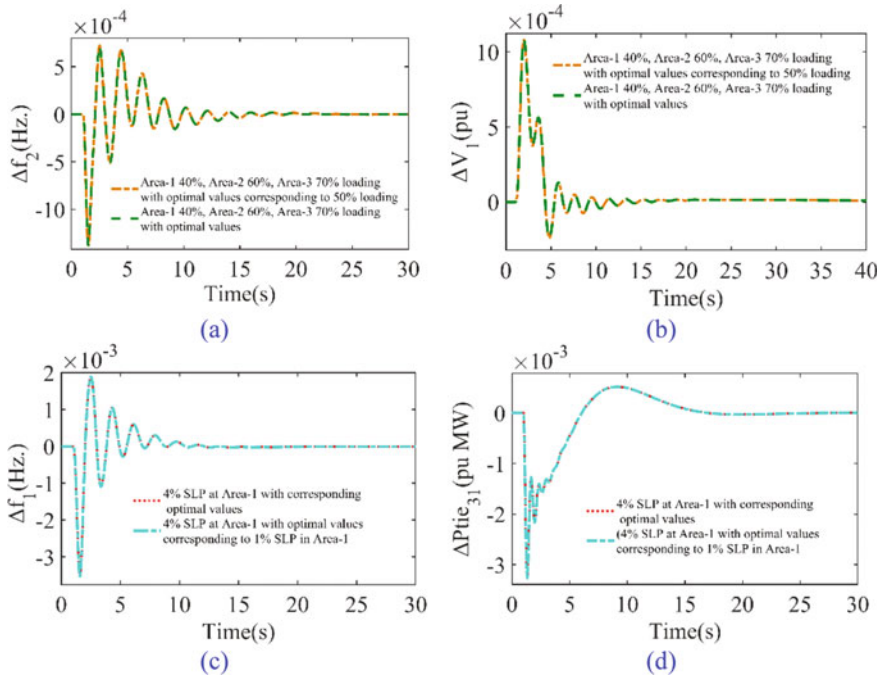


Fig. 6 Sensitivity study vs. time for varying system loading condition and magnitude of perturbation **a** delta f in Area-2, **b** delta V in Area-1, **c** delta f in Area-1, **d** delta P_{tie} among Areas 3 and 1

6 Conclusion

The authors of this study attempted to use a cascaded FOI-TIDN controller in ALFC and AVR systems of a three-unequal-area multi-source interrelated power system. In order to optimize controller parameters and other gains, the HHO technique is being explored for application. The suggested CFOI-TIDN controller outperforms both the FOI and the TIDN controllers in terms of time-domain indices, as discovered by a comparative investigation of system dynamics. Separately, the influence of the AVR system and the HDGT plant has been proven to improve the system's dynamics. The system's sensitivity study demonstrates that controller values obtained under nominal conditions are robust enough to handle any form of disturbance generated by different loading conditions in each area and changes in disturbance magnitudes.

References

1. Bevrani H (2014) Robust power system frequency control, 2nd edn. Springer International Publishing, Switzerland
2. Dixon A (2019) Modern aspects of power system frequency stability and control. Academic Press, Elsevier Science, United Kingdom
3. Pan CT, Liaw CM (1989) An adaptive controller for power system load-frequency control. *IEEE Trans Power Syst* 4(1):122–128
4. Mandal R, Chatterjee K, Patil BK (2018) Load frequency control of a single area hybrid power system by using integral and LQR based integral controllers. In: 2018 20th national power systems conference (NPSC)
5. Alomoush MI (2010) Load frequency control and automatic generation control using fractional-order controllers. *Electr Eng* 91(7):357–368
6. Arya Y, Kumar N, Ibraheem (2015) AGC of a two-area multi-source power system interconnected via AC/DC parallel links under restructured power environment. *Optim Control Appl Methods* 37(4):590–607
7. Arya Y, Kumar N (2017) Design and analysis of BFOA-optimized fuzzy PI/PID controller for AGC of multi-area traditional/restructured electrical power systems. *Soft Comput* 21(21):6435–6452
8. Nanda J, Mishra S, Saikia LC (2009) Maiden application of bacterial foraging-based optimization technique in multiarea automatic generation control. *IEEE Trans Power Syst* 24(2):602–609
9. Arya Y, Dahiya P, Çelik E, Sharma G, Gözde H, Nasiruddin I (2021) AGC performance amelioration in multi-area interconnected thermal and thermal-hydro-gas power systems using a novel controller. *Eng Sci Technol, Int J* 24(2):384–396
10. Guha D, Roy PK, Banerjee S (2019) Binary bat algorithm applied to solve MISO-type PID-SSSC-based load frequency control problem. *Iran J Sci Technol, Trans Electr Eng* 43(2):323–342
11. Tasnin W, Saikia LC (2018) Comparative performance of different energy storage devices in AGC of multi-source system including geothermal power plant. *J Renew Sustain Energy* 10(2):024101
12. Satapathy P, Debnath MK, Mohanty PK, Sahu BK (2019) Participation of geothermal and dish-stirling solar power plant for LFC analysis using fractional-order. In: Innovation in electrical power engineering, communication, and computing technology: proceedings of IEPCCT 630(113):2020
13. Balamurugan S, Xavier RJ, Jeyakumar AE (2009) Control of heavy-duty gas turbine plants for parallel operation using soft computing techniques. *Electr Power Compon Syst* 37(11):1275–1287
14. Balamurugan S, Janarthanan N, Chandrakala KV (2016) Small and large signal modeling of heavy duty gas turbine plant for load frequency control. *Int J Electr Power Energy Syst* 79:84–88
15. Gaing ZL (2004) A particle swarm optimization approach for optimum design of PID controller in AVR system. *IEEE Trans Energy Convers* 19(2):384–391
16. Eke I, Saka M, Gozde H, Arya Y, Taplamacioglu MC (2021) Heuristic optimization based dynamic weighted state feedback approach for 2DOF PI-controller in automatic voltage regulator. *Eng Sci Technol, Int J* 24(4):899–910
17. Veinović S, Stojić D, Joksimović D (2022) Optimized four-parameter PID controller for AVR systems with respect to robustness. *Int J Electr Power Energy Syst* 135:107529
18. Rakhshani E, Rouzbehi K, Sadeh S(2009) A new combined model for simulation of mutual effects between LFC and AVR loops. In 2009 Asia-Pacific power and energy engineering conference. IEEE, pp 1–5
19. Ramoji SK, Saikia LC, Dekaraja B, Behera MK, Babu NR, Bhagat SK (2021) Combined Voltage and Frequency control of a Multi-Area Multi-Source Power System using CFOPI-TIDN Controller. In 2021 international conference on computational performance evaluation (ComPE). IEEE, pp 761–766

20. Ramoji SK, Saikia LC, Dekaraja B, Behera MK, Bhagat SK (2022) Performance Comparison of various tilt controllers in coalesced voltage and frequency regulation of multi-area multi-unit power system. In 2022 IEEE Delhi section conference (DELCON). IEEE, pp 1–7
21. Ramoji SK, Saikia LC (2021) Optimal coordinated frequency and voltage control of CCGT-thermal plants with TIDF controller. IETE J Res:1–18
22. Ramoji SK, Saikia LC (2021) Utilization of electric vehicles in combined voltage-frequency control of multi-area thermal-combined cycle gas turbine system using two degree of freedom tilt-integral-derivative controller. Energy Storage 3(4):e234
23. Ramoji SK, Saikia LC (2021) Maiden application of fuzzy-2DOFTID controller in unified voltage-frequency control of power system. IETE J Res:1–22
24. Ramoji SK, Saikia LC, Dekaraja B, Babu NR, Bhagat SK, Behera MK (2021) Modeling and simulation of an isolated CCGT and DSTS plant using BWO optimized $PI\lambda D\mu$ controller for amalgamated control of voltage and frequency. In Modeling, simulation and optimization: proceedings of CoMSO 2020. Springer Singapore, pp 297–309
25. Arya Y (2018) Improvement in automatic generation control of two-area electric power systems via a new fuzzy aided optimal PIDN-FOI controller. ISA Trans 80:475–490
26. Daraz A, Malik SA, Waseem A, Azar AT, Haq IU, Ullah Z, Aslam S (2021) Automatic generation control of multi-source interconnected power system using FOI-TD controller. Energies 14(18):5867
27. Lurie BJ (1994) National Aeronautics and Space Administration NASA, *Three-parameter tunable tilt-integral-derivative (TID) controller*. U.S. Patent 5,371,670
28. Heidari AA, Mirjalili S, Faris H, Aljarah I, Mafarja M, Chen H (2019) Harris hawks optimization: Algorithm and applications. Futur Gener Comput Syst 97:849–872
29. Guha D, Roy PK, Banerjee S (2016) Load frequency control of large scale power system using quasi-oppositional grey wolf optimization algorithm. Eng Sci Technol, Int J 19(4):1693–1713
30. Kumari S, Shankar G (2018) Novel application of integral-tilt-derivative controller for performance evaluation of load frequency control of interconnected power system. IET Gener Transm Distrib 12(14):3550–3560

Harmonics Mitigation Using Proportional–Resonant Controller-Based DSTATCOM in Distribution System



Atma Ram, Paras Ram Sharma, and Rajesh Kumar Ahuja

1 Introduction

Prospective power electronics devices based nonlinear/unbalanced load are increasing nowadays in distribution system which degrades the power quality of system [1]. Reactive loads like fans, pumps, etc., are consuming a large amount of power because these loads draw lagging currents which increase the reactive power utilization in distribution system. In the case of unbalanced loads, power quality problems become worse. An increase in the demand for load reactive power increases unnecessary, ohmic losses and also reduces the active power capability in distribution system [2]. Active power filters have been proposed for the enhancement of power quality [3, 4]. A numerous standard has been proposed for the measurement of power quality such as IEC 1000-3-2, IEEE Std.141-1993, and IEEE519-1992 [5–7].

Shunt connected compensating device, DSTATCOM is used in distribution system that injects the currents through VSI [8, 9]. It is used for harmonic suppression, load balancing, and power factor improvement. The DSTATCOM performance depends upon the techniques which are used for the computation of reference current. Different control techniques have been presented in literature [10–20]. For computation of PI controller gains, GA and FLC techniques have been presented in [10, 11]. For compensation of load current harmonics, load voltage balance, coupling point voltage regulation, and power factor control, an NN-based technique for DSTATCOM have been proposed [12]. Artificial immune system-based adaptive controller for DSTATCOM has been reported and particle swarm optimization technique is used for the computation of controller parameter [13]. If any unknown and random disturbance is arising in the system parameters of controller are adjusted adaptively. Enhanced phase-locked loop-based technique for DSTATCOM for both (PFC &

A. Ram (✉) · P. R. Sharma · R. K. Ahuja
J.C. Bose University of Science and Technology, YMCA, Faridabad, Haryana 121006, India
e-mail: atma.ram12@gmail.com

ZVR) modes of operation has been implemented for power quality issue mitigation in distribution system [14]. Leaky least mean square (LLMS) control technique has been developed for DSTATCOM and the advantage of this technique is that it gives a superior dynamic response [15].

DSTATCOM control has been implemented based on composite observer technique for reference current extraction and used in distribution system for enhancement of power quality [16, 17]. Adaptive controller based on linear-sinusoidal tracer technique for mitigation of power quality problems has been developed [18]. The proposed control technique has good accuracy, fast dynamic response, and stability performance.

In distribution system, three different control techniques are compared for power quality improvement have been developed [19]. Voltage-controlled oscillator less PLL has been developed using SRFT technique for source reference current computation and power quality problems mitigation in distribution system, which gives faster response than conventional controller [20]. For power quality problem mitigation optimal step, least mean square technique for DSTATCOM has been developed, and active and reactive weights are estimated by using the proposed control technique [21]. Different control algorithms (SRFT, IRPT, and Adeline) are presented and compared for power quality improvement in distribution system [22]. Proportional–Resonant controllers in SRFT technique have been developed and compared with conventional controller for power quality mitigations [23]. In this paper, PR controller-based IRPT technique for DSTATCOM is presented for load balancing, source-side harmonic elimination, and reactive power compensation in distribution system.

2 System Under Study

The proposed distribution system with nonlinear load and DSTATCOM is depicted in Fig. 1, where V_{sa} , V_{sb} , and V_{sc} are the source voltages, $(R_s + L_s)$ is the source impedance, and L_f is the coupling inductor. The output of VSC-based DSTATCOM is passed through coupling inductor and given to distribution system for source-side harmonic elimination which is injected by nonlinear load.

3 Control Technique

3.1 Proportional–Resonant Controller

DC link voltage and AC link voltage are controlled by using PR controller. The overall gain of an ideal PR controller is given by

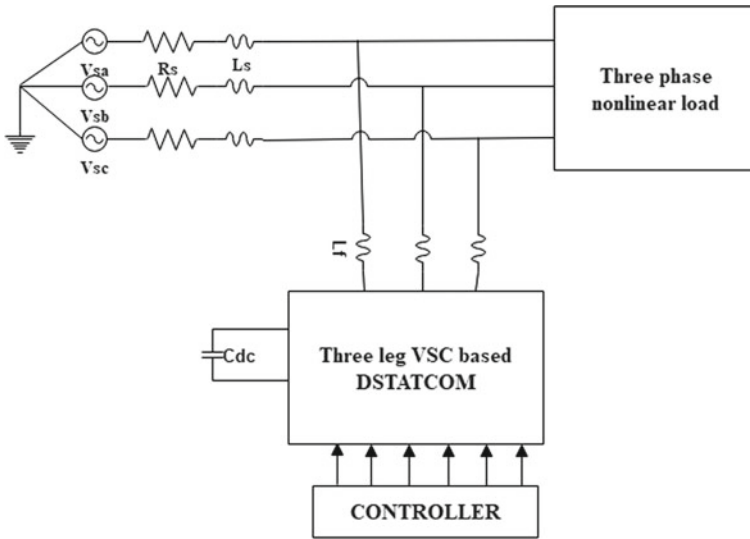


Fig. 1 DSTATCOM in distribution system

$$G_{PR(s)} = K_p + \frac{SK_i}{S^2 + \omega_0^2} \tag{1}$$

where K_p , K_i , and ω_0 are the proportional, integral gain, and fundamental frequency of PR controller. The above-mentioned transfer functions of PR controller with an infinite gain creates stability issues. By adding a damping coefficient in ideal PR controller gain could be made non-ideal to avoid such circumstances which is expressed as

$$G_{PR(s)} = K_p + \frac{2SK_i}{S^2 + 2\omega_c S + \omega_0^2} \tag{2}$$

where ω_c is the cut-off frequency which is approximately equal to resonant frequency ω_0 [24, 25].

3.2 Extraction of Reference Currents

The PR controller-based IRPT-based control for DSTATCOM has been depicted in Fig. 2. Active and reactive power instantaneous values are computed with help of load currents (I_{La} , I_{Lb} , I_{Lc}), ,, and PCC voltages (V_{sa} , V_{sb} , V_{sc}) The PCC voltages (V_{sa} , V_{sb} , V_{sc}) are transformed to (V_α , V_β) by using the following formulation:

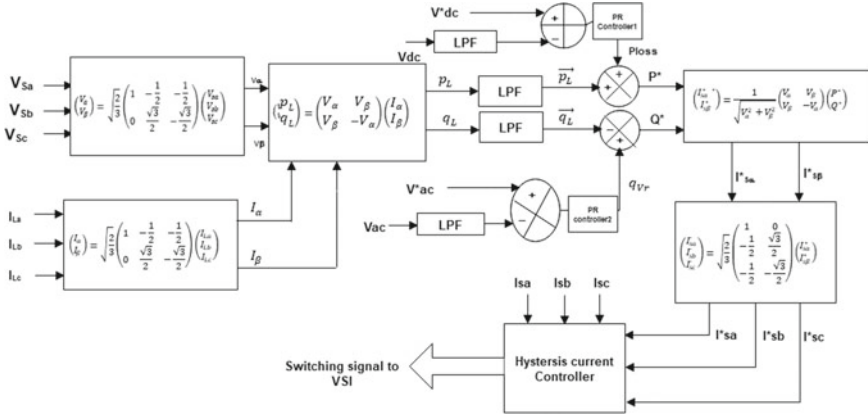


Fig. 2 Extraction of Reference current using the proposed control technique

$$\begin{pmatrix} V_\alpha \\ V_\beta \end{pmatrix} = \sqrt{\frac{2}{3}} \begin{pmatrix} 1 & -\frac{1}{2} & -\frac{1}{2} \\ 0 & \frac{\sqrt{3}}{2} & -\frac{\sqrt{3}}{2} \end{pmatrix} \begin{pmatrix} V_{Sa} \\ V_{Sb} \\ V_{Sc} \end{pmatrix} \tag{3}$$

Load currents (I_{La} , I_{Lb} , I_{Lc}) are converted to (I_α , I_β) by using the following formulation:

$$\begin{pmatrix} I_\alpha \\ I_\beta \end{pmatrix} = \sqrt{\frac{2}{3}} \begin{pmatrix} 1 & -\frac{1}{2} & -\frac{1}{2} \\ 0 & \frac{\sqrt{3}}{2} & -\frac{\sqrt{3}}{2} \end{pmatrix} \begin{pmatrix} I_{La} \\ I_{Lb} \\ I_{Lc} \end{pmatrix} \tag{4}$$

The active power (p_L) and reactive power (q_L) instantaneous values of load side are computed by using Eqs. (3) and (4) as

$$\begin{pmatrix} p_L \\ q_L \end{pmatrix} = \begin{pmatrix} V_\alpha & V_\beta \\ V_\beta & -V_\alpha \end{pmatrix} \begin{pmatrix} I_\alpha \\ I_\beta \end{pmatrix} \tag{5}$$

The p_L & q_L passed through the LPF to extract the DC component $\overline{p_L}$ & $\overline{q_L}$ and remaining ac power \vec{p}_L & \vec{q}_L are computed as

$$\vec{p}_L = p_L - \overline{p_L} \tag{6}$$

$$\vec{q}_L = q_L - \overline{q_L} \tag{7}$$

The DC link voltage V_{dc} is subtracted from V_{dc}^* reference for estimation of error and which is supplied to DC link PR controller. The output power of DC link PR controller is denoted by p_{Loss} .

This active power \vec{p}_L is added to p_{Loss} for computation of the total active power of load.

$$P^* = \vec{p}_L + p_{Loss} \quad (8)$$

AC link voltage magnitude is given by

$$V_{ac} = \sqrt{\frac{2}{3}(V_{sa}^2 + V_{sb}^2 + V_{sc}^2)} \quad (9)$$

This V_{ac} is subtracted from V_{ac}^* for the generation of error for AC link which is given to AC PR controller. The output power of PR controller 2 is denoted by q_{vr} .

The reactive power \vec{q}_L is extracted from q_{vr} for computation of the total reactive power of load.

$$Q^* = q_{vr} - \vec{q}_L \quad (10)$$

The I_{α}^* and I_{β}^* can be obtained by using the following formulation:

$$\begin{pmatrix} I_{s\alpha}^* \\ I_{s\beta}^* \end{pmatrix} = \frac{1}{\sqrt{V_{\alpha}^2 + V_{\beta}^2}} \begin{pmatrix} V_{\alpha} & V_{\beta} \\ V_{\beta} & -V_{\alpha} \end{pmatrix} \begin{pmatrix} P^* \\ Q^* \end{pmatrix} \quad (11)$$

The $I_{s\alpha}^*$ and $I_{s\beta}^*$ currents are converted to three-phase reference source currents (I_{sa}^* , I_{sb}^* and I_{sc}^*) by using the following formulation:

$$\begin{pmatrix} I_{sa}^* \\ I_{sb}^* \\ I_{sc}^* \end{pmatrix} = \sqrt{\frac{2}{3}} \begin{pmatrix} 1 & 0 \\ -\frac{1}{2} & \frac{\sqrt{3}}{2} \\ -\frac{1}{2} & -\frac{\sqrt{3}}{2} \end{pmatrix} \begin{pmatrix} I_{s\alpha}^* \\ I_{s\beta}^* \end{pmatrix} \quad (12)$$

These three reference currents (I_{sa}^* , I_{sb}^* and I_{sc}^*) are deducted from source currents (I_{sa} , I_{sb} and I_{sc}) for computation of error signals. These errors are given to HCC control for the generation of triggering signals for IGBT-based VSC.

4 Results and Discussion

The proposed controller-based IRPT technique is developed in MATLAB using SIM power Toolbox and results are compared with PI-based IRPT for nonlinear load for dynamic conditions in time domain.

4.1 Controller Performance

The performance of PR controller-based IRPT with nonlinear load under dynamic conditions when the load current a phase is out for 0.7 s–0.8 s in terms of source voltages (V_{sabc}), load currents (I_{Labc}), load active voltage (V_{α}), load active current (I_{α}), source reference active current ($I_{s\alpha}^*$), source reference reactive current ($I_{s\beta}^*$), and reference source current (I_{sabc}^*), respectively, depicted in Fig. 3.

4.2 DSTATCOM Performance with Linear Load

DSTATCOM performance with PR controller-based IRPT technique with linear load under dynamic conditions with a phase is out for 0.7 s–0.8 and results are recorded in terms of source voltages (V_{sabc}), source currents (I_{sabc}) load currents (I_{La}, I_{Lb}, I_{Lc}), compensator currents (I_{Ca}, I_{Cb}, I_{Cc}), and DC link voltage (V_{dc}), respectively, depicted in Fig. 4. With the proposed control technique, DSTATCOM

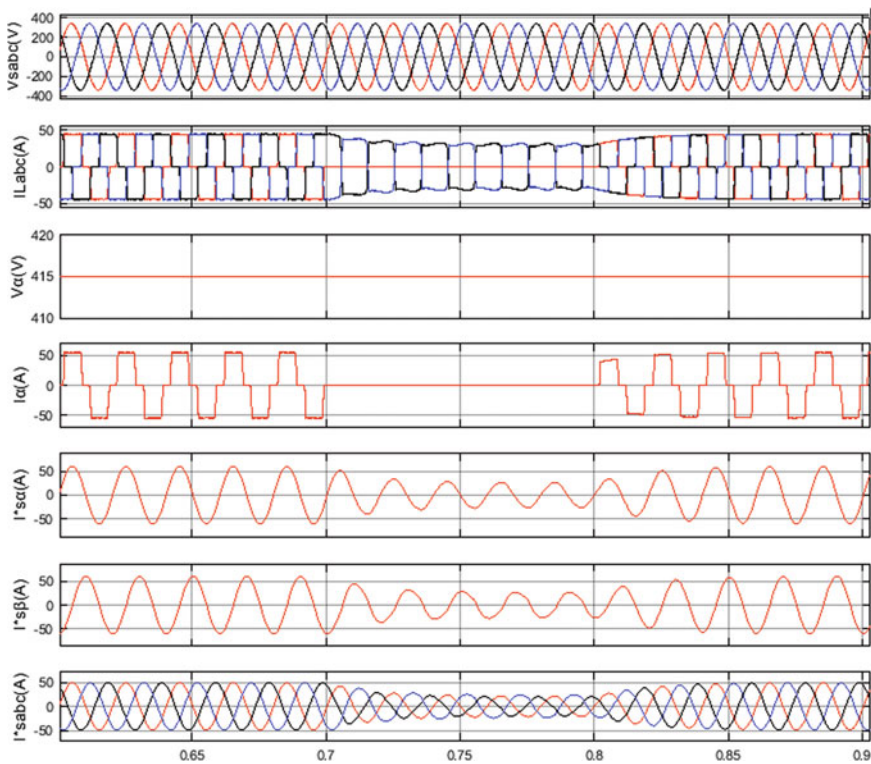


Fig. 3 PR-based controller performance

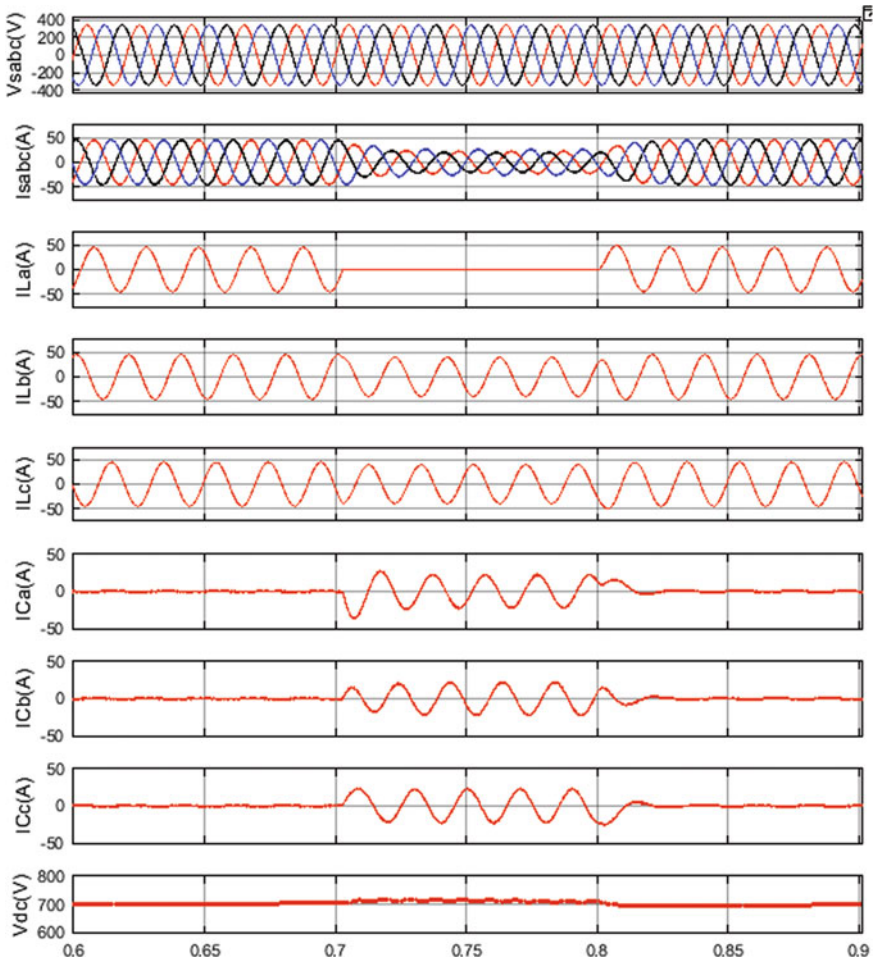


Fig. 4 DSTATCOM performance with PR controller under dynamic linear load

performance is satisfactory for the load balancing, DC link voltage regulation, and power factor improvement achieved in distribution system.

4.3 DSTATCOM Performance with Nonlinear Load

DSTATCOM performance with PR controller-based IRPT technique with nonlinear load under dynamic conditions with a phase is out for 0.7 s–0.8 s and the results are recorded in terms of source voltages (V_{sabc}), source currents (I_{sabc}) load currents (I_{La} , I_{Lb} , I_{Lc}), compensator currents (I_{Ca} , I_{Cb} , I_{Cc}), and DC link voltage (V_{dc}),

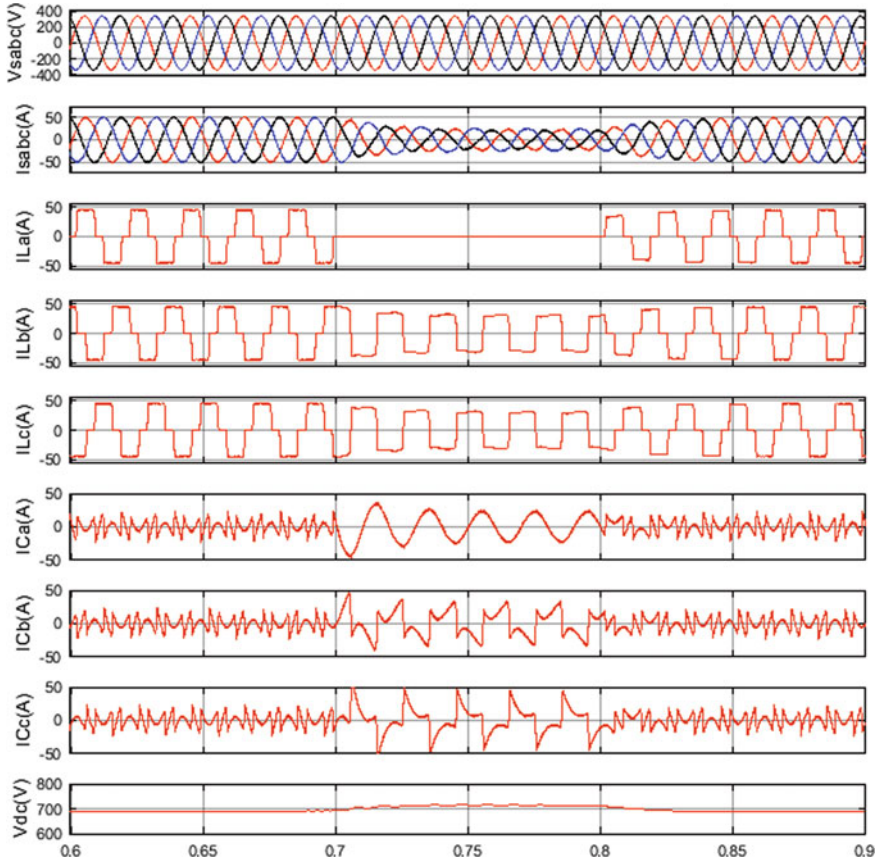


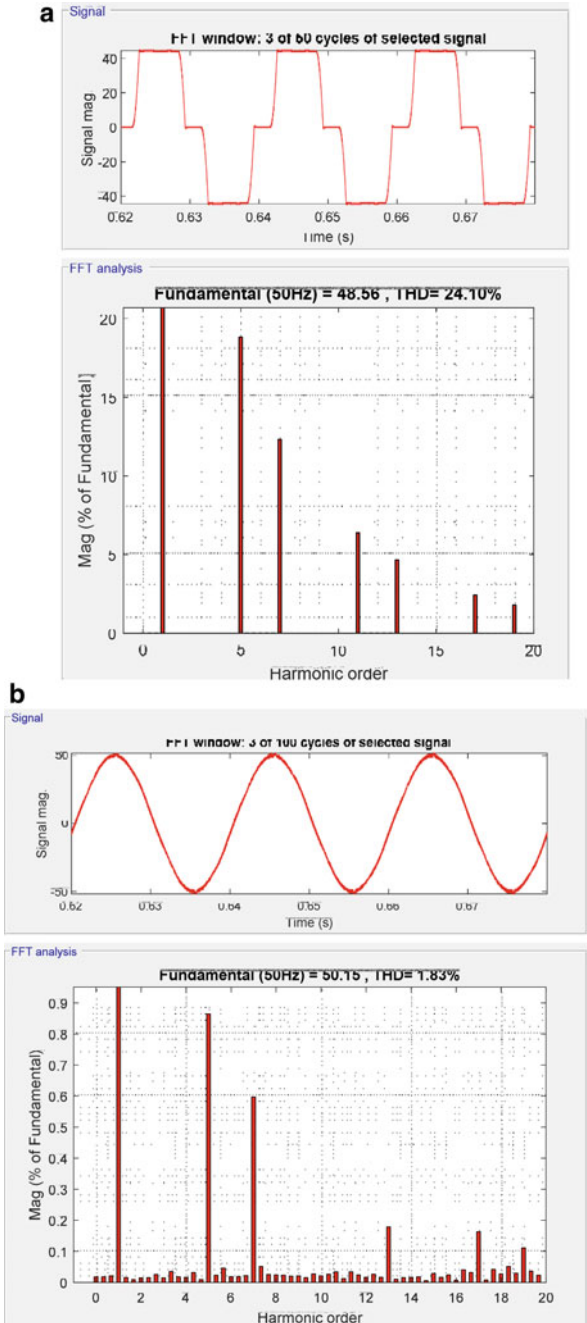
Fig. 5 DSTATCOM performance with PR controller under dynamic nonlinear load

respectively, depicted in Fig. 5. With the proposed control technique, load balancing, DC-link voltage, source current harmonic suppression, and improvement in power factor are achieved in distribution system.

4.4 Harmonic Comparisons

The harmonic spectrum of a phase for source current without controller, source current with PI controller, source current with PR controller, and load current are presented in Fig. 6(a, b, c, and d), respectively. After the comparison of Fig. 6(b) and (c), the PR controller is more accurate and efficient than the PI controller for source-side harmonic suppression. Tables 1 and 2 also show the betterment of the PR controller with DSTATCOM for source harmonic suppression in distribution

Fig. 6 a Source current THD% without any controller. **b** THD% with PI controller for source current. **c** THD% with PR controller for source current. **d** Load current THD%



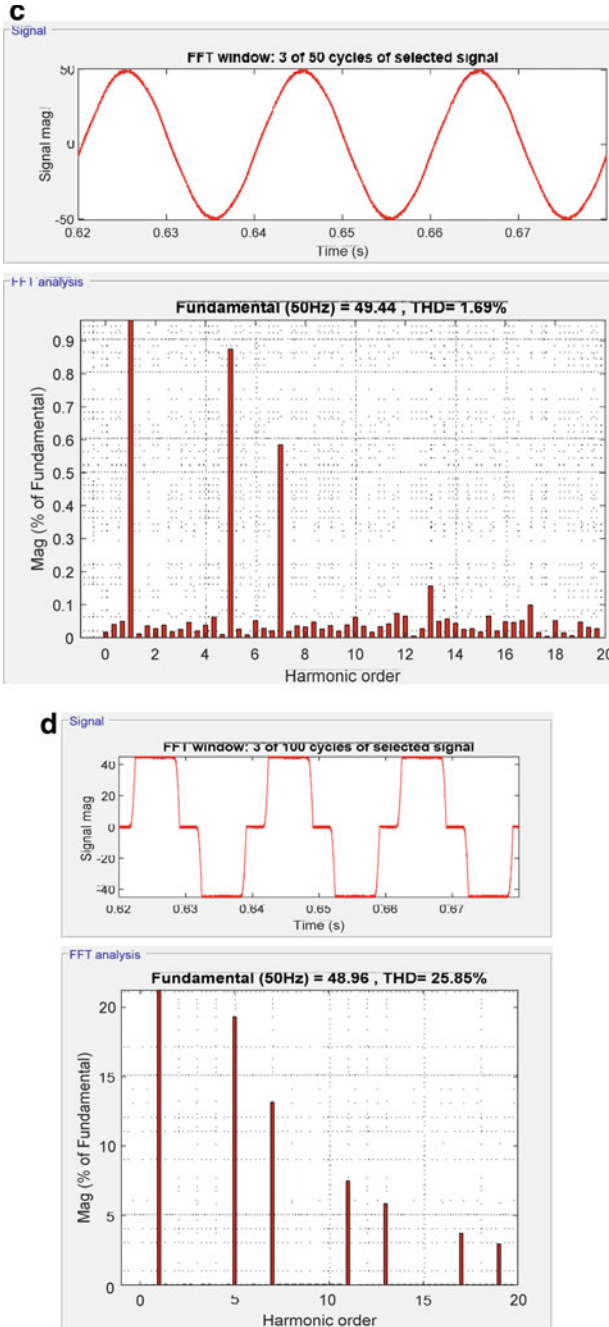


Fig. 6 (continued)

Table 1 Comparisons of each phase source harmonic distribution

Phase	% THD with PI controller (%)	% THD with PR controller (%)
Source current phase a	1.83	1.69
Source current phase b	1.84	1.71
Source current phase c	1.84	1.73

Table 2 Comparisons of source current harmonics

Harmonic order	5th (%)	7th (%)	11th (%)
THD without any controller	18.81	12.32	6.38
A phase THD% order with PI controller	0.87	0.57	0.03
A phase THD order with PR controller	0.0	0.0	0.0

system. Table 1 shows the harmonic % of all phases for PI and PR controllers for the source side and Table 2 shows the % of harmonic order up to 11 orders for source current phase with PI and PR controllers. THD is decreased efficiently with DSTATCOM operation. The 5th-, 7th-, and 11th-order harmonics are suppressed using PR controller.

5 Conclusion

The DSTATCOM control with the proposed PR controller-based IRPT technique is developed for improvement of source-side harmonics in distribution system and compared with the conventional PI-based IRPT technique. The proposed technique is simulated in MATLAB software using PSIM blocks for source-side harmonic suppression, load balancing, and power factor correction with nonlinear dynamic load. The performance of the proposed control technique is improved significantly with PR controller as compared to PI controller. In both the cases the, PR controller is better for harmonics elimination of each phase as well as for the elimination of higher order harmonics of source current in distribution system.

References

1. Bollen M (1999) Understanding Power Quality Problems: Voltage Sags and Interruptions. IEEE Press, New York, NY, USA
2. Moreno-Munoz A (2007) Power Quality: Mitigation Technologies in a Distributed Environment. Springer- Verlag, London, UK
3. Kale M, Ozdemir E (2015) A new hysteresis band current control technique for a shunt active filter. Turk J Elec Eng & Comp Sci 23:654–665

4. Chaoui A, Gaubert JP, Krm F (2010) Power quality improvement using DPC controlled three-phase shunt active filter. *Electr Pow Syst Res* 806:657–666
5. IEEE Std 1531. IEEE Guide for Application and Specification for Harmonic Filters, 2003.
6. IEEE Std 1159. IEEE Recommended Practice for Monitoring Electric Power Quality, 1995.
7. IEEE Std 519. IEEE Recommended Practices and Requirements for Harmonics Control in Electric Power Systems, 1992.
8. Anadol MA, Aydin M, Yalcinoz T (2013) A real-time extraction of active and reactive current using microcontrollers for a multi-pulse STATCOM. *Turk J Elec Eng & Comp Sci* 21:1044–1060
9. Rahbarimaghham H, Maali Amirie E, Vahidi B, Babamalek Gharehpetian G, Abedi M (2015) Superior decoupled control of active and reactive power for three-phase voltage source converters. *Turk J Elec Eng & Comp Sci* 23:1025–1039
10. Jazebi S, Hosseinian SH, Vahidi B (2011) DSTATCOM allocation in distribution networks considering recon configuration using differential evolution algorithm. *Energ Convers Manage* 52:2777–2783
11. Valderrabano A, Ramirez JM (2010) DSTATCOM regulation by a fuzzy segmented PI controller. *Electr Pow Syst Res* 80:707–715
12. Singh B, Jayaprakash P, Kumar S, Kothari DP (2011) Implementation of neural-network-controlled three-leg VSC and a transformer as three-phase four-wire DSTATCOM. *IEEE Ind Applic* 47:1892–1901
13. Mitra P, Venayagamoorthy GK (2010) An adaptive control strategy for DSTATCOM applications in an electric ship power system. *IEEE Power Electron* 25:95–104
14. Singh B, Arya SR (2013) Implementation of single-phase enhanced phase-locked loop based control algorithm for three phase DSTATCOM. *IEEE T Power Deliver* 28:1516–1524
15. Arya SR, Singh B (2013) Performance of DSTATCOM using leaky LMS control algorithm. *IEEE J Sel Top Power Electron* 1:104–113
16. Selvajothi K, Janakiraman PA (2008) Extraction of harmonics using composite observers. *IEEE T Power Deliver* 23:31–40
17. Singh B, Arya SR (2013) Composite observer-based control algorithm for distribution static compensator in four-wire supply system. *IET Power Electron* 6:251–260
18. Singh B, Arya SR (2013) Adaptive theory-based improved linear sinusoidal tracer control algorithm for DSTATCOM. *IEEE Power Electron* 28:3768–3778
19. Sabha Raj Arya, Mittal M. Patel, Sayed JavedAlam, JayadeepSrikakolapu ,Ashutosh K. Giri, Phase lock loop–based algorithms for DSTATCOM to mitigate load created power quality problems. *Int Trans. Electr Energy Syst.* 2019; e12161. <https://doi.org/10.1002/2050-7038.12161>.
20. Ashutosh K. Giri, Sabha Raj Arya , Rakesh Maurya, B. Chitti Babu, VCO-less PLL control-based voltage-source converter for power quality improvement in distributed generation system. *IET Electr. Power Appl.*, 2019, Vol. 13 Iss. 8, pp. 1114–1124. doi: <https://doi.org/10.1049/iet-epa.2018.5827>.
21. Sanjay Kumar Patel, Sabha Raj Arya & Rakesh Maurya, Optimal Step LMS-Based Control Algorithm for DSTATCOM in Distribution System. *Electric Power Components and Systems*, 0(0): 1–17, 2019. ISSN: 1532–5008 print / 1532–5016 online DOI:<https://doi.org/10.1080/15325008.2019.1602797>.
22. Bhim Singh, Jitendra Solanki, A Comparison of Control Algorithms for DSTATCOM. *IEEE transactions on industrial electronics*, Vol. 56, no. 7, July 2009.
23. Mohammad MAHDIANPOOR, Arash KIYOUARS, Mohammad ATAEI, Rahmat Allah HOOSMAND, Houshang KARIMI, A multifunctional DSTATCOM for power quality improvement. *Turk J Elec Eng & Comp Sci*(2017) 25: 172 -183. doi:<https://doi.org/10.3906/elk-1505-260>.

24. Amgad El-Sayed Salem, Omar M. Salim, Shawky I. Arafa, New triple-action controller for inverter power quality improvement. *Computers and Electrical Engineering* 81 (2020) 106543. <https://doi.org/10.1016/j.compeleceng.2019.106543>.
25. Sen Ye, Youbing Zhang, Luyao Xie, Haiqiang, Lu Shunt, Active Power Filter Based on Proportional Integral and Multi Vector Resonant Controllers for Compensating Nonlinear Loads. *Hindawi Journal of Electrical and Computer Engineering* Volume 2018, Article ID 1312064, 11 pages <https://doi.org/10.1155/2018/1312064>.

Analysis of Z-Source Resonant Converter for Wireless Charging Application



Ayush Kumar Srivastava and Narendra Kumar

1 Introduction

An air gap is used in Wireless Power Transfer (WPT) systems to satisfactorily transmit power from a static main coil to a static or moveable secondary coil. Inductive coupling between two items via an air gap is referred to as contactless coupling. The fundamental idea of a WPT system is analogous to that of extremely coupled electrical and electromechanical machines such as transformers and induction motors, which have very low leakage inductance due to high magnetic coupling. WPT systems, on the other hand, have high leakage inductances and minimal magnetic coupling because of the huge air gap they utilize. WPT systems are inefficient in terms of power transfer due to significant leakages and low magnetic coupling. WPT systems are often run at high frequencies to compensate for poor magnetic coupling caused by major magnetic leakages, thereby enhancing the quality factor of WPT transformers.

The system's losses will grow at high frequencies due to the inverter's high switching losses, lowering the system's overall power transfer efficiency. To overcome this disadvantage, compensating capacitors are frequently used in WPT systems to function at resonant frequency. Resonant circuits also reduce reactive power requirements of the system, thereby enhancing total power transfer potentiality and lowering Volt–Ampere (VA) ratings of the system.

Wireless Power Transfer (WPT) methodology transmits power through an electromagnetic field in the absence of any tangible connection between the transmitter and receiver [1, 2]. Latest breakthroughs in this sector have spearheaded more demanding

A. Kumar Srivastava (✉) · N. Kumar
Department of Electrical Engineering, Delhi Technological University, Delhi, India
e-mail: ayusriv08@gmail.com

N. Kumar
e-mail: narendrakumar@dtu.ac.in

design prerequisites being recommended and studied by researchers, such as efficiency gains [3–7], coupling deviation [8, 9], unfamiliar object recognition [10, 11], and regulation at the output end [12–14]. Electronic engineering is important in these studies and drives WPT technology development.

2 Comparison of Conventional & Suggested WPT

2.1 Converters in General

As shown in Fig. 1, a typical battery charger of On-Board Type (OBC) has a structure with two levels containing a PFC unit on the front side and a high-frequency transformer with a DC–DC Converter. This structure has a high overall cost and complexity.

The ZSRC simultaneously performs the PFC on the input side and voltage regulation on the output side as it includes both shoot-through duty cycle (Dst) and active state duty cycle (Dact).

The voltage source inverter (VSI) is an important component of a Wireless Power Transfer (WPT) system since it produces high-frequency AC power for transmitting the power wirelessly. Traditional VSI inverters can only be used in low-voltage or wide-input scenarios since its output voltage is always equal to or less than the input voltage. Front-end converters, such as boost or buck–boost converters, are employed to augment the DC-rail voltage between a DC source and a VSI to overcome this barrier [15, 16]. This, however, necessitates additional room and raises the system's cost. One more heat sink and related drive circuitry must be accommodated in order to add one more IGBT/MOSFET. In the WPT system, the ZSI is a superior alternative to front-end converters because of the additional cost and design complexities.

In contrast to a standard VSI, the ZSI has an input diode and a Z-source network between the DC voltage source and the VSI [13]. The ZSN consists of two alike inductors (L1 and L2) and capacitors created by short-circuiting one or both legs of the back-end inverter bridge (C1 and C2). The shoot-through (ST) state is also referred to as this.

The next sections describe the proposed ZSN-based wireless power transfer system's operating principle, analysis, simulation, and experimental findings.

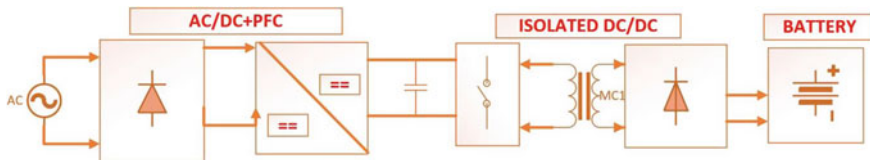


Fig. 1 Block diagram of a conventional OBC

3 Overview of Z-Source-Based Resonant Converter

The Z-source Network (ZSN) is proposed in this paper as a new converter for WPT applications. The ZSN can be inserted in the PFC stage for on-board charging applications, followed by an isolated DC/DC converter, which in this case is a conventional SRC. The term given to the architecture designed by OBC is Z-source resonant converter (ZSRC) (Fig. 2).

In comparison to DC/AC applications, a ZSRC has more states in a single switching cycle. To comprehend the ZSRC, it's critical to clarify all of these states. The ZSN boost ratio is still affected by the overall shoot-through state duty cycle among these states. Using a phase shift control mechanism as an example, the next section describes the ZSRC working principle.

A. ZSRC WPT system operation principle

If the ZSN in Fig. 4 is symmetrical ($C1 = C2 = C$ and $L1 = L2 = L$), then $VC1 = VC2 = VC$ and $VL1 = VL2 = VL$. In addition, the switching frequency in ZSN is 10 times less than the resonant frequency of L and C . As a result, for a single switching cycle, the ZSN inductor current and ZSN capacitor voltage are deemed steady.

The fundamental component of the H-bridge output is in phase with the primary side current at resonance frequency [17], and the total time of shoot-through state (T_{st}) is evenly distributed across one switching cycle.

Active State:

The diagonal switches are ON. The resonant network gets current from both the ZSN inductor and the capacitor. The difference between load current (i_{rp}) and ZSN inductor current (I_L) is created by connecting the two ZSN capacitors in series to the DC source. Only load current travels via the switches (i_{rp}). For this time interval, the ZSN inductor voltage is as follows:

$$V_L = 0.5(|v_{ac}| - v_z) = 0.5(|\hat{v}_{ac} \sin \omega t| - v_z) \tag{1}$$

where \hat{v}_{ac} is the AC input voltage's maximum value, and ω is the line's angular frequency.

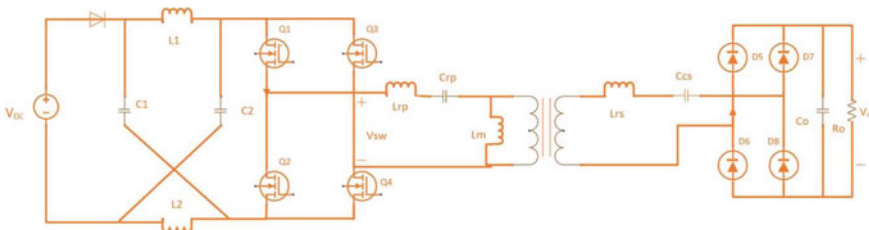


Fig. 2 Z-Source-based Resonant Converter

Shoot-Through State:

Three switches are turned on. The load current is carried by two horizontal switches, while the ZSN inductor current is carried by two switches in one phase leg. As a result, the two currents are carried by a single switch. Since the Z-Source Network (ZSN) current of inductor is always unipolar and the current of load is bidirectional, these two currents whether subtract or add, assist the sum total with their definite values. In the shoot-through state, phase shift control permits only different polarity currents to travel through the same switch. The Z-Source Network (ZSN) capacitors here are used to charge the ZSN inductors (this is how the ZSRC may enhance the voltage). For this time interval, the ZSN inductor voltage is as follows:

$$V_L = V_C \quad (2)$$

Zero State:

Two horizontal switches are ON during the time interval of zero state. The ZSN is not connected to the load in any way. The load current is freewheeling, and the ZSN capacitors are charged by the inductors. For this time interval, the ZSN inductors' voltage is represented as

$$V_L = V_{DC} - V_C \quad (3)$$

The formula for the shoot-through state duty cycle can be obtained by using voltage second balance across the ZSN inductor throughout one switching cycle. As a result of combining (1), (2), and (3), we have

$$\frac{T_{act}}{T_s}(V_{DC} - V_C) + \frac{T_{st}}{T_s}V_C + \left(1 - \frac{T_{act}}{T_s} - \frac{T_{st}}{T_s}\right)(V_{DC} - V_C) = 0 \quad (4)$$

$$V_C = \frac{1 - D_{st}}{1 - 2D_{st}}V_{DC} \quad (5)$$

$$D_{st} = \frac{V_Z - V_{DC}^{st}}{2V_Z} = \frac{V_C - V_{DC}}{2V_C - V_{DC}} \quad (6)$$

$$V_Z = \frac{V_{DC}}{1 - 2D_{st}} \quad (7)$$

The active state duty cycle (D_{act}) acts as a control variable to the system and is the one used for the voltage regulation on the output side. Its command must always match the equation: $D_{act} + D_{st} + D_{zer} = 1$, where $D_{zer} = T_{zer}/T_s$ is the conventional zero state duty cycle.

The voltage on the ZSN capacitor is unrelated to the active state duty cycle D_{act} , according to this relationship in (6).

All of ZSRC’s conceivable states are represented by these three states. Varying load regulation characteristics would result from different allocations of these three states during the course of a switching period (Table 1).

B. Overview of LLC Resonant Converter

Figure 3 depicts a resonant full-bridge LLC DC–DC converter with resonant capacitor, C_r , resonant inductor, L_r , and magnetizing inductor, L_m . It is made up of three parts:

- Square Wave generator: The full bridge generates square wave voltage, VSW, by operating MOSFET switches (Q1,Q2) and (Q3,Q4) alternately with a pulse frequency modulation approach. The power switches are driven by a variable frequency clock, which transfers energy from the input to the output.
- Resonant Network: Resonant capacitor, C_r , resonant inductor, L_r , and magnetizing inductor, L_m , comprise the resonant network. The resonant network circulates the energy and delivers it to the load via the transformer. A bipolar square wave is

Table 1 Table showing switch selection during different states

States	Inverter switches on
Zero	S_2, S_4 or S_1, S_3
Shoot through	S_1, S_2, S_4 or S_1, S_3, S_4 or S_1, S_2, S_3 or S_2, S_3, S_4
Active	S_1, S_4 or S_2, S_3

Fig. 3 Equivalent circuit of LLC resonant converter

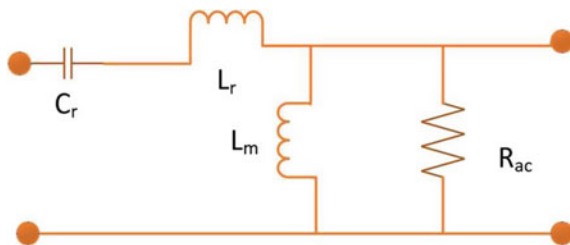
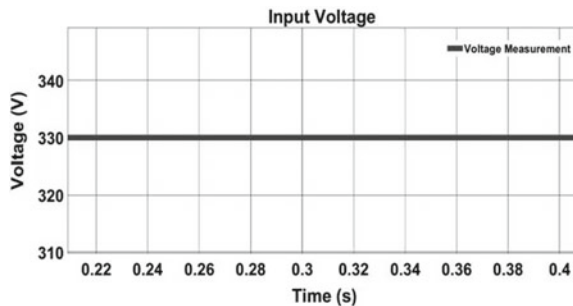


Fig. 4 Input end voltage



received at the transformer's primary side and passed via the secondary winding. Electrical isolation is also provided by the transformer, as well as the required turn ratio for the required output voltage.

- **Rectifier Network:** The rectifier network converts AC voltage to DC voltage using diodes and capacitors. The rectifier network is made up of a complete bridge rectifier with a capacitive output filter.

4 Simulation Results

To validate the analysis, simulations of the proposed system were run at (192 W). The simulation parameters and component values are listed in Table I. The proposed systems have switching frequencies ranging from 100 to 130 kHz [18]. The frequency of 110 kHz was chosen for this study (Tables 2 and 3).

5 Results & Discussion

The circuit modeling of ZSRC WPT system has been introduced. The suitable parameters of switching frequency (f_{sw}), transformer turns ratio (n), L_n (relationship between the magnetizing inductance (L_m) and series resonant inductance (L_r)),

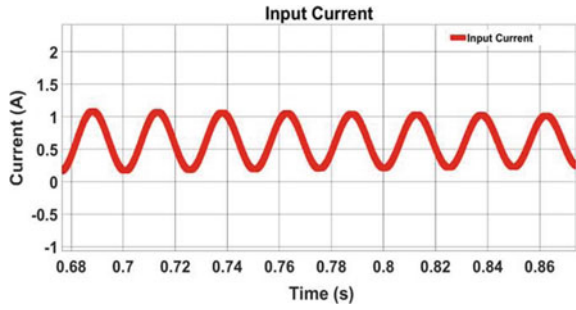
Table 2 Different parameters values

Parameters	Values
Input end voltage (V_{DC})	330 V
Switching frequency	117 kHz
Resonant frequency	110 kHz
Output end voltage (V_O)	24 V
Output end current (I_O)	8 A
Output power	192 W
Turns ratio	13.33:1

Table 3 Different components values

Components	Values
C_1, C_2	0.40 μ F
L_1, L_2	7.81 mH
L_{rp}	80 μ H
C_{rp}	26.2 nF
L_m	400 μ H
C_O	262 μ F
R_O	3 Ω

Fig. 5 Input end current



and quality factor (Q_e) have been chosen to create a full-bridge LLC resonant converter. Figures 4 and 5 show input DC voltage and input current, respectively. Figures 6 and 7 show voltage across Z-source inductor and Z-Source capacitor, respectively. Figures 8 and 9 show input voltage and current across LLC resonant converter, respectively. Figures 10 and 11 show rectified DC output voltage and current, respectively.

Fig. 6 Z-source inductor current

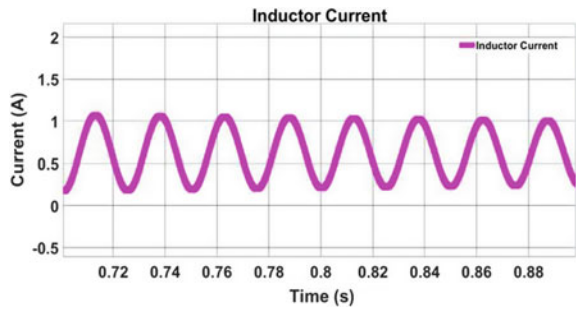


Fig. 7 Z-source capacitor voltage

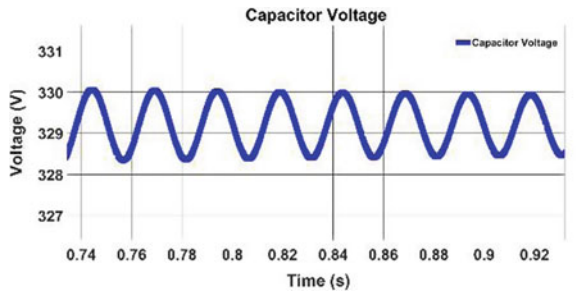


Fig. 8 LLC input voltage

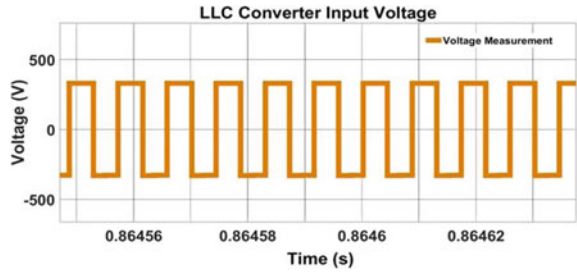


Fig. 9 LLC input current

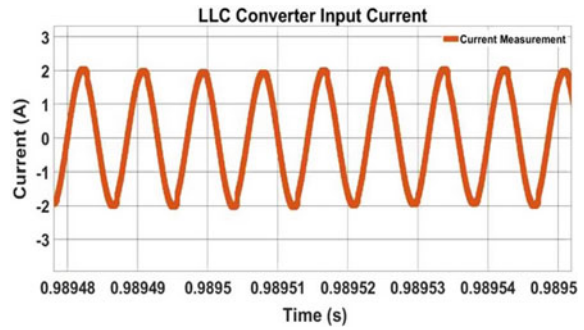


Fig. 10 Output end voltage

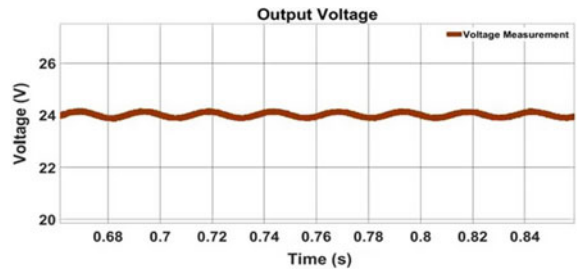
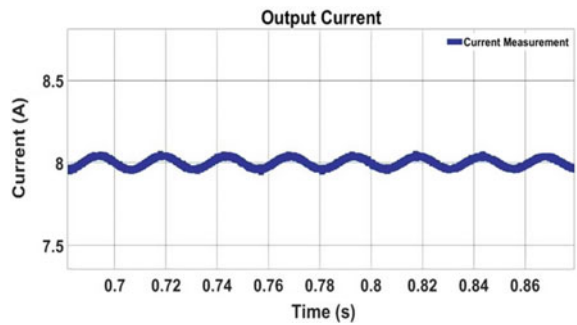


Fig. 11 Output end current



6 Conclusion

This research paper clearly substantiated the role of ZSN for wireless charging applications using a ZSRC WPT system for electric vehicle battery charging. ZSN improves system dependability as it is resistant to shoot-through states. It could also be used for power factor correction by controlling the shoot-through state duty cycle (D_{st}).

This research paper used MATLAB-based simulations to demonstrate the theoretical analysis and it could be utilized for developing an on-board battery charger of 24V and 8A.

Future scope of this control scheme is to reduce harmonic content and implement soft switching to improve system efficiency. In order to implement this research paper into a hardware topology, we need to use a mutual inductor in place of a transformer thereby executing wireless power transfer.

References

1. Boys JT, Covic GA (2015) The Inductive Power Transfer Story at the University of Auckland. *IEEE Circuits Syst Mag* 15(2):6–27
2. Vázquez-Leal H, Gallardo-Del-Angel A, Castañeda-Sheissa R (2012) The phenomenon of wireless energy transfer: experiments and philosophy. In: *Wireless power transfer-principles and engineering explorations*. InTech, Chap 1, pp 1–18
3. Melki R, Moslem B (2015) Optimizing the design parameters of a wireless power transfer system for maximizing power transfer efficiency: a simulation study. In: *Technological advances in electrical, electronics and computer engineering (TAECE)*. pp 278–282
4. Zhang WH, Liu Y (2013) Analysis on the efficiency of magnetic resonance coupling wireless charging for electric vehicles. In: *Cyber technology in automation, control and intelligent systems (CYBER)*. pp 191–194
5. Kanoun KO, Keutel T, Viehweger C (2014) Improvement of the efficiency of MISO configuration in inductive power transmission in case of coils misalignment. In: *Instrumentation and measurement technology conference (I2MTC) proceedings*. pp 856–861
6. Fu M, Zhang T, Ma C, Zhang X (2015) Efficiency and optimal loads analysis for multiple-receiver wireless power transfer systems. *IEEE Trans Microw Theory Techn* 63(3):801–812
7. Low Z, Chinga R, Tseng R, Lin J (2009) Design and test of a high-power high-efficiency loosely coupled planar wireless power transfer system. *IEEE Trans Ind Electron* 56(5):1801–1812
8. Jonah O, Georgakopoulos SV, Daerhan D, Shun Y (2014) Misalignment-insensitive wireless power transfer via strongly coupled magnetic resonance principles. In: *Antennas and propagation society international symposium (APSURSI)*. pp 1343–1344
9. Feng H, Cai T, Duan S, Zhao J, Zhang X, Chen C (2016) An LCC-compensated resonant converter optimized for robust reaction to large coupling variation in dynamic wireless power transfer. *IEEE Trans Ind Electron* 63(10):6591–6601
10. Kuyvenhoven N, Dean C, Melton J, Schwannecke J, Umenei A (2011) Development of a foreign object detection and analysis method for wireless power systems. In: *Product compliance engineering (PSES) proceedings*. pp 1–6
11. Jang G, Jeong S, Kwak H, Rim C (2016) Metal object detection circuit with non-overlapped coils for wireless EV chargers. In: *Southern power electronics conference (SPEC)*. pp 1–6
12. Tan L, Pan S, Xu C, Yan C, Liu H, Huang X (2017) Study of constant current- constant voltage output wireless charging system based on compound topologies. *J Power Electron* 17(4):1109–1116

13. Sun L, Tang H, Yao C (2015) Investigating the frequency for load-independent output voltage in three-coil inductive power transfer system. *Int J Circ Theor Appl* 44(6):1341–1348
14. Zhang L, Yang X, Chen W, Yao X (2010) An isolated soft-switching bidirectional buck-boost inverter for fuel cell applications. *J Power Electron* 10(3):235–244
15. Peng FZ (2003) Z-source inverter. *IEEE Trans Ind Appl* 39(2):504–510
16. Mosobi R, Chichi T, Gao S (2014) Modeling and power quality analysis of integrated renewable energy system. In: National power systems conference (NPSC). pp 1–6
17. Zhang J, Zeng H, Jiang T (2012) A primary-side control scheme for high-power-factor LED driver with TRIAC dimming capability. *IEEE Trans Power Electron* 27(11):4619–4629
18. Keeling NA, Covic GA, Boys JT (2010) A unity-power-factor IPT pickup for high-power applications. In: *IEEE Transactions on Industrial electronics*, vol 57, no 2, pp 744–751

Application of a Novel Method to Reduce Congestion in DPS Applying TCSC



Anubha Gautam, P. R. Sharma, and Yogendra Kumar

1 Introduction

Continuous advancements in technology have resulted in huge power demand. With deregulation in the power system, several generators are utilizing the same transmission lines to supply load [1]. This resulted in overburdening of lines to work at or near their thermal limits. This is the primary cause of congestion. Congestion not only affects system security adversely but also makes the system economically incompetent [2]. Thus, in the literature, several methods are suggested to mitigate congestion. These methods may be broadly classified into technical and non-technical methods [3]. Technical methods involve ways to increase the safety and reliability of systems such as the application of FACTS devices. Non-technical methods see only the economical aspect of the system [4]. TCSC being a versatile FACTS device, is very effective in implementation to mitigate system congestion.

The property to smoothly change line impedance makes TCSC to be chosen above other FACTS devices [5]. However, the implementation of TCSC is very costly. This cost may be recovered in due time if the device is located suitably and sized optimally. Many methods are suggested to search for the most suitable location for TCSC [6]. The sensitivity factor method is one of the best methods to decide on the location of FACTS in contingency conditions [7]. PI sensitivity factors [8], stability margins indicators such as VSM and CTEM [9], over-loading indicative factors such as OLF [10], factors indicative of loss such as congestion rent factors and LSI [11], and LUF-DLUF [12, 13] are some of the most efficient location indicators applied in research. Locating the FACTS device is not sufficient to mitigate congestion. The device

A. Gautam (✉) · P. R. Sharma
Electrical Engineering Department, J C Bose UST, YMCA, Faridabad, India
e-mail: anubhagautam@jcboseust.ac.in

Y. Kumar
Electrical Engineering Department, MANIT, Bhopal, India

must be optimized for its parameters. Several optimization algorithms are proposed and adopted for effective parameter optimization. Detailed comparison of several heuristic methods such as Genetic Algorithm (GA), Evolutionary programming (EP), Tabu search Algorithm (TBA), Fuzzy logic, and SA has been done in [14]. The computational behaviors of Particle swarm optimization (PSO) have been utilized effectively in [15] for parameter optimization of TCSC, SVC, and UPFC. Grey wolf optimization (GWO) has been effectively implemented [16] for optimizing TCSC size for mitigating congestion. Utilizing the prominent features of algorithms, several hybrid algorithms have also been proposed. GA-PSO hybrid [17], DE-CRO hybrid [18], and hybrid fruit fly firefly algorithm [19] have been proposed for optimizing TCSC size.

The novelty of this paper can be indicated as follows:

- A novel method to merge GWO and PSO is proposed to optimize the size of TCSC.
- The method applied here is not used previously for power loss minimization.
- The effectiveness of the proposed method is validated on multiple contingencies.

2 Implemented TCSC Model

The power flow model applied here is based on the theory of change in series reactance which inherently changes the power flow through the line. Figures 1 and 2 present the TCSC model implemented in this study. The TCSC may work in inductive mode or capacitive mode as required by the system.

The impedance of TCSC can be mathematically written as

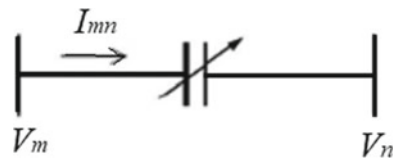
$$Z_{tcsc} = \frac{V_{mn}}{I_{mn}} \quad (1)$$

Transfer admittance matrix of TCSC as shown in Figs. 1 and 2 is presented as

Fig. 1 TCSC in inductive mode



Fig. 2 TCSC in capacitive mode



$$\begin{bmatrix} I_m \\ I_n \end{bmatrix} = \begin{bmatrix} jB_{mm} & jB_{mn} \\ jB_{nm} & jB_{nn} \end{bmatrix} \begin{bmatrix} V_m \\ V_n \end{bmatrix} \quad (2)$$

Change in line admittance due to TCSC:

$$\Delta Y_{mn} = y'_{mn} - y_{mn} \quad (3)$$

where

$$y'_{mn} = G'_{mn} + B'_{mn} \quad (4)$$

$$G'_{mn} = \frac{R_{mn}}{\sqrt{R_{mn}^2 + (X_{mn} + X_{tcsc})^2}} \quad (5)$$

$$B'_{mn} = \frac{-(X_{mn} + X_{tcsc})}{\sqrt{R_{mn}^2 + (X_{mn} + X_{tcsc})^2}} \quad (6)$$

Equations (5) and (6) show the change in TCSC reactance changes the line conductance and susceptance values. This, in turn, changes the net admittance of the line resulting in a changed power flow. The power flow equations can be given as

$$P_{mn} = V_m V_n B_{mn} \sin(\theta_m - \theta_n) \quad (7)$$

$$Q_{mn} = -V_m^2 B_{mm} - V_m V_n B_{mn} \cos(\theta_m - \theta_n) \quad (8)$$

The power flow equations are given in Eqs. (7) and (8) is linearized about the reactance in series and solved iteratively.

3 Sensitivity Factors Applied

This paper uses LUF and DLUF as sensitivity factors to get an optimized location of TCSC. LUF can be calculated as the ratio of the actual MVA flowing through the line and the rated power flow capacity of the line. For line k , between the buses m and n , the LUF can be given as

$$\text{LUF}_k = \frac{\text{MVA}(\text{actual})_{mn}}{\text{MVA}(\text{rated})_{mn}} \quad (9)$$

LUF values for all the lines are calculated and then the lines are sorted and indexed in terms of congestion. Most congested lines are determined and then DLUF values are calculated. DLUF is the disparity line utilization factor, calculated for the lines

connected to a common bus at which the congested line is connected. DLUF can be given by

$$DLUF_{ij,iq} = \{ |LUF_{ij}| - |LUF_{iq}| \} \quad (10)$$

4 Problem Formulation

The objective function here is the minimization of active power loss:

$$f_x = \min P_L \quad (11)$$

The power loss in Eq. (11) can be given by

$$\begin{aligned} P_L = & \{ |V_m^2|G_{mn} - |V_m||V_n|[G_{mn} \cos\theta_{mn} + B_{mn} \sin\theta_{mn}] \\ & - |V_m||V_{snmn}|[G_{mn} \cos\theta_{snmn} + B_{mn} \sin\theta_{snmn}] \} \\ & + \{ |V_n^2|G_{mn} - |V_m||V_n|[G_{mn} \cos\theta_{nm} + B_{mn} \sin\theta_{nm}] \\ & - |V_n||V_{snmn}|[G_{mn} \cos\theta_{snmn} + B_{mn} \sin\theta_{snmn}] \} \end{aligned} \quad (12)$$

4.1 Constraints

- (a) Equality constraints $\begin{cases} P_G - P_D - P_i(V_i, \theta_i) = 0 \\ Q_G - Q_D - Q(V_i, \theta_i) = 0 \end{cases}$
- (b) Inequality constraints $\begin{cases} P_G^{\min} \leq P_G \leq P_G^{\max} \\ Q_G^{\min} \leq Q_G \leq Q_G^{\max} \\ V_{i,\min} \leq V_i \leq V_{i,\max} \end{cases}$
- (c) The range of TCSC considered here is

$$-0.8X_L \leq X_{\text{tcsc}} \leq 0.2X_L$$

5 HGWOPSO Algorithm

The proposed algorithm is a merger of two well-established optimization techniques PSO and GWO. In order to implement PSO, three parameters inertial weight factor (w) and the acceleration coefficients $c1$ and $c2$ are to be tuned. These factors decide the convergence of the solution. Similarly, in the case of GWO, coefficient vectors A and C are to be tuned for desired convergence (Fig. 3).

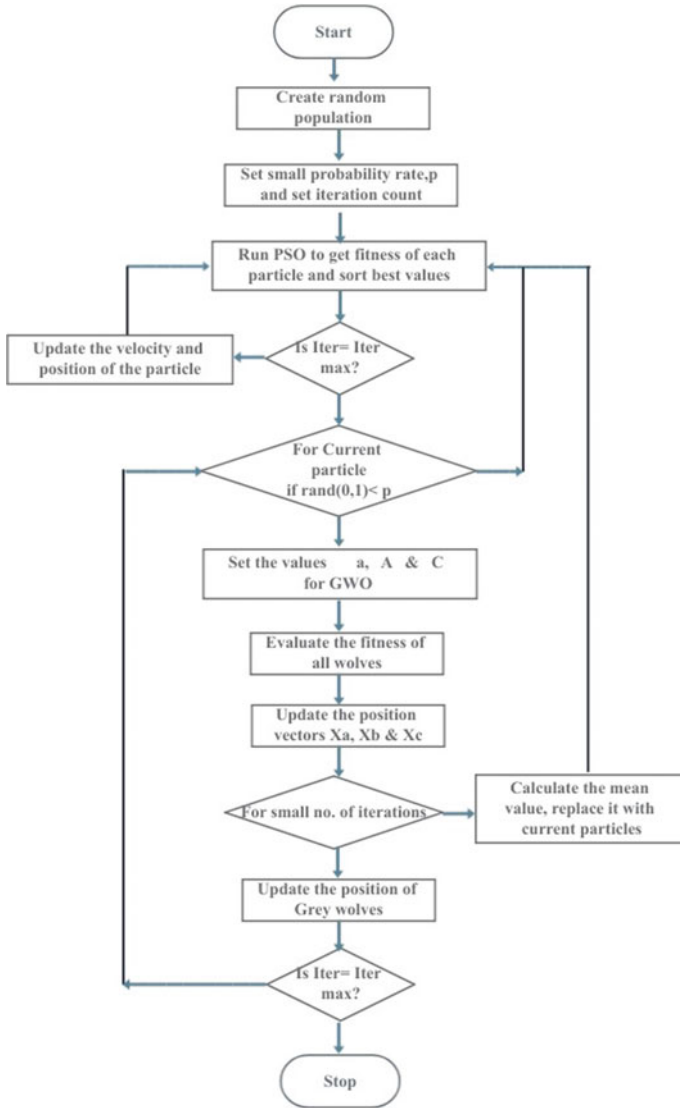


Fig. 3 Flowchart of proposed HGWOPSO algorithm

6 Result Analysis

The proposed algorithm is validated on the IEEE 30Bus system as shown in Fig. 4. N-1 contingency is created by out-aging the line between buses 6 and 10.

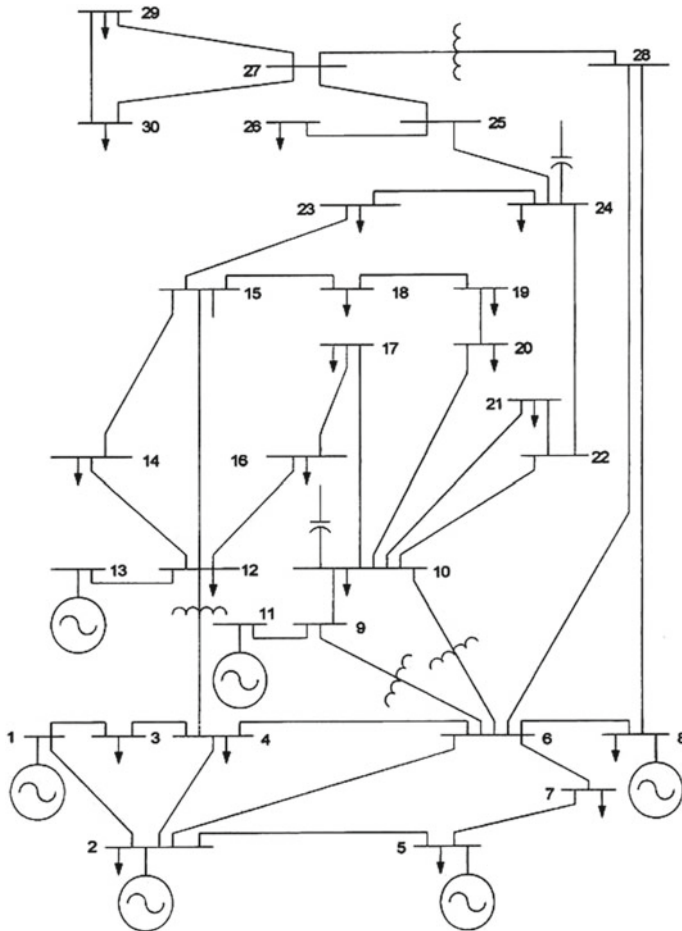


Fig. 4 Standard IEEE 30Bus system [20]

6.1 LUF Redistribution

The LUF values for all lines are calculated and then indexed to get the congested lines. Table 1 gives the details of the lines which get congested after a 6–10 line outage.

From Table 1, it can be observed that with N-1 contingency and without TCSC line number 1, 2, 3, 4, 5, 6, 7, 14, 18, and 27 gets congested. When PSO-optimized TCSC is applied, lines number 4, 18, and 27 remained congested. TCSC optimized with GWO line numbers 3, 4, 18, and 27 remained congested. HGWOPSO-optimized TCSC relieves congestion in all the lines. Here, it can also be observed that there is a redistribution of active power in the lines, to utilize the lines securely.

Table 1 LUF redistribution with HGWOPSO optimized TCSC

Line no	LUF redistribution			
	W/O TCSC	With TCSC		
		PSO	GWO	HGWO-PSO
1	1.08	0.249	0.536	0.794
2	1.13	0.586	0.689	0.45
3	1.05	0.951	1.01	0.826
4	1.04	1.04	1.02	0.854
5	1.13	0.738	0.784	0.753
6	1.48	0.303	0.454	0.138
7	1.36	0.985	0.964	0.962
14	2.41	0.851	0.904	0.564
18	1.36	1.25	1.42	0.764
27	1.36	1.22	1.25	0.379
41	1.02	0.984	0.782	0.765

Table 2 Consolidated results for TCSC location and optimized size

Measured quantities		System states	
		Normal	N-1 contingency
LUF (max.)		0.699	2.41
Most Cong. line		NC	14
DLUF		0.03254	0.08429
TCSC location		16	16
TCSC size	PSO	-0.4587	-0.3458
	GWO	-0.1254	-0.4561
	HGWOPSO	-0.3568	0.4587

Table 2 presents the comparison of TCSC location and optimized size at normal and N-1 contingency conditions with PSO, GWO, and proposed HGWOPSO.

6.2 Power Loss Minimization

Power loss minimization obtained by the proposed optimization technique is presented in Fig. 5.

It can be observed that the reduction in active power loss during normal conditions with PSO and GWO-optimized TCSC is 6.05 MW and 5.85 MW, respectively. This is approximately 11.7 and 14.6% reduction in active power loss, respectively.

While, in the case of HGWOPSO-optimized TCSC, the power loss reduces to 5.25 from 6.85 MW which is approximately 23.4%. Similarly, when there is N-1

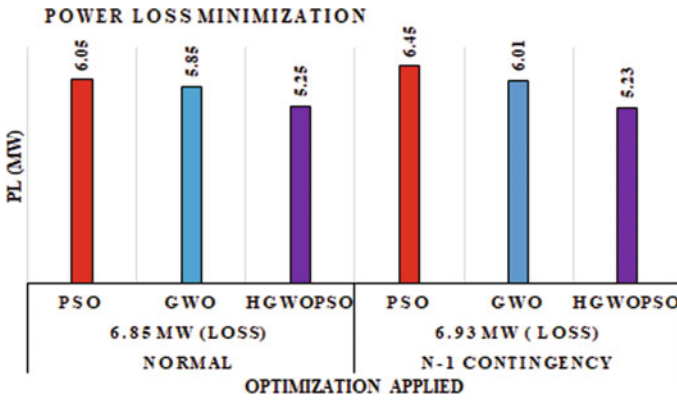


Fig. 5 Power loss minimization

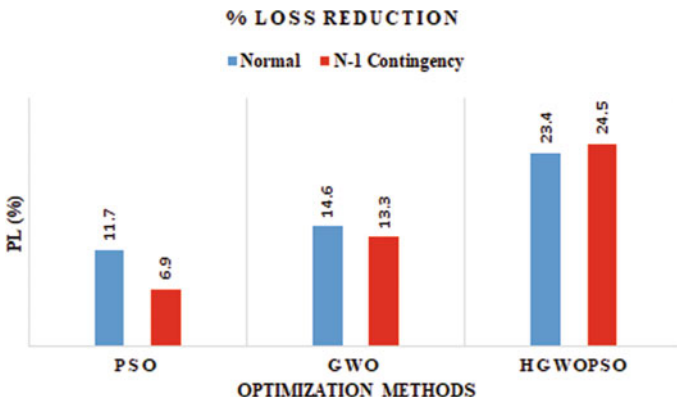


Fig. 6 Percentage loss reduction

contingency, the power losses are 6.45, 6.01, and 5.23 MW by PSO, GWO, and HGWOPSO-optimized TCSCs. Here, the power loss is also reduced by 24.5% with the application of HGWOPSO-optimized TCSC.

Figure 6 illustrates the comparison of the percentage of power loss reduction by HGWOPSO with the well-established PSO and GWO.

7 Conclusions

In this paper, congestion management by applying LUF and DLUF as sensitivity factors are carried out. The sensitivity factors are applied here to get the most suitable location for TCSC. An algorithm is proposed here to optimize the TCSC size to mitigate congestion created due to N-1 contingency. The algorithm is a hybrid of two

well-established algorithms, i.e., PSO and GWO. A novel method is implemented here to merge GWO and PSO to give hybrid GWO-PSO and HGWOPSO. LUF and DLUF located the TCSC precisely and then HGWOPSO is applied to get optimized size. The implemented algorithm reduced the active power losses by 24.5% which is significantly higher as compared to that obtained by GWO and PSO. Moreover, the active power is redistributed and the congestion in the lines is relieved. The proposed algorithm is validated on the standard IEEE 30Bus system applying MATLAB@2016 software.

References

1. Lo KL, Yuen YS, Snider LA (2000) Congestion management in deregulated electricity Markets. In: International conference on electrical utility deregulation and restructuring and power technologies. City University, London
2. Srinivulu G, Pamulaparthi B, Sharma A (2019) Review of Congestion management methods from conventional to smart grid scenario. *Int J Emerg Electr Power Syst* 20
3. Yusoff NI, Zin AAM, Khairuddin AB (2017) Congestion management in power system: a review. In: 2017 3rd international conference on power generation systems and renewable energy technologies (PGSRET). pp 22–27
4. Gupta M, Kumar V, Banerjee GK, Sharma NK (2017) Mitigating congestion in a power system and role of facts devices. *Adv Electr Eng* 1–7
5. Kang T, Yao J, Duong T, Yang S, Zhu X (2017) A hybrid approach for power system security enhancement via optimal installation of flexible AC transmission system (FACTS) devices. *Energies* 10(9):1305
6. Sundar K, Ravikumar HM (2012) Selection of TCSC location for secured optimal power flow under normal and network contingencies. *Int J Electr Power Energy Syst* 34:29–37
7. Samimi A, Golkar MA (2012) A novel method for optimal placement of facts based on sensitivity analysis for enhancing power system static security. *Asian J Appl Sci* 5:1–19
8. Taher SA, Besharat H (2008) Transmission congestion management by determining optimal location of FACTS devices in deregulated power systems. *Am J Appl Sci* 5(3):242–247
9. Esmaili M, Shayanfarand HA, Moslemi R (2014) Locating series FACTS devices for multi-objective congestion management improving voltage and transient stability. *Eur J Oper Res* 236(2):763–773
10. Rajalakshmi L, Suganyadevi MV, Parameswari S (2010) Congestion management in deregulated power system by locating series FACTS devices. *Int J Comput Appl* 13. <https://doi.org/10.5120/1801-2404>
11. Acharya N, Mithulananthan N (2007) Locating series facts devices for congestion management in deregulated electricity markets. *Electr Power Syst Res* 77:352–360. 10.1016
12. Ahamed AA, Sirjani R (2020) Optimal placement and sizing of multi-type FACTS devices in power systems using metaheuristic optimization techniques: an updated review. *Ain Shams Eng J* 11(3):611–628
13. Gautam A, Ibraheem S, Sharma G (2021) Security margin enhancement in deregulated power system implementing TCSC. In: 4th international conference on recent developments in control, automation and power engineering (RDCAPE). pp 127–132
14. Jordehi AR, Jasronita J (2011) Heuristic methods for the solution of the facts optimization problem in power systems. In: Proceedings of 2011 IEEE student conference on research and development, SCORed. pp 30–35
15. Hashemzadeh H, Hosseini SH (2009) Locating series facts devices using line outage sensitivity factors and particle swarm optimization for congestion management. In: IEEE power and energy society general meeting. pp 1–6

16. Gautam A, Sharma PR, Kumar Y (2020) Sensitivity based congestion management in a deregulated power system by optimal allocation and parameter setting of TCSC using grey wolf optimization. *Int J Electr Eng Inform* 12(4)
17. Debasish M, Chakrabarti A, Aparajita S (2012) Optimal placement and parameter setting of SVC and TCSC using PSO to mitigate small signal stability problem. *Int J Electr Power Energy Syst* 42:334–340
18. Sakr WS, Sehiemy RA, Azmy AM (2016) Optimal allocation of TCSCs by adaptive DE algorithm. *IET Gener Transm Distrib* 10(15):3844–3854
19. Naraina A, Deepa SN (2016) Optimal location of TCSC and SVC using hybrid fruit fly firefly optimization algorithm in transmission system. *Asian J Inf Technol* 15:2863–2872
20. Fattah AA, Turki A, Yusuf M, Abdullah A (2012) Optimal power flow using adapted genetic algorithm with adjusting population size. *Electr Power Compon Syst* 40. <https://doi.org/10.1080/15325008.2012.689417>

A Hybrid Approach to PMBLAC Machine for High-Speed Mobility



Sumit Kumar Yadav, Shakuntla Boora, and Nitin Goel

1 Introduction

To promote the overall electric transportation, countries are providing incentives to scrap their vehicles by leveraging the consumer in taxes like in India where FAME (Faster Adoption and Manufacturing of hybrid and electric vehicles) was launched back in 2015 to boost the electric vehicles. Later FAME-II was launched as a progression to it. Other countries provide different rebates like in parking fees, rebate in environment cess, road tax, etc.

The basic difference between an EV and Hybrid EV is that in the former the power is drawn from the batteries and in the latter the power is drawn from both the IC (internal combustion) engine with batteries as well. The power is optimally delivered among them by switching circuits driven by algorithms.

The HEVs are of two types:

Series—In this type, the power is drawn by the motors from the batteries directly which were charged by the engine.

Parallel—In this type, the power is delivered to the motors by the cumulative contribution of battery and IC engine. Net torque is the sum of motor and engine [1].

Both of the aforementioned systems are capable of regeneration when deaccelerating (Table 1).

S. K. Yadav · S. Boora (✉) · N. Goel
Department of Electrical Engineering, JC Bose University of Science and Technology, YMCA,
Faridabad, India
e-mail: shakuntla@jcboseust.ac.in

Table 1 A table showing various research papers available in the literature and a comparison is made based on their work

Reference No.	Author	Key findings	Validation of proposed scheme	Techniques used
[2]	Affanni A. Bellini A. Franceschini G. Guglielmi P Tassoni C	This paper implemented SoC and SoH monitoring along with charge equalization to gain maximum energy during EV braking	Simulations and hardware prototyping	Neural Network is implemented for journey estimation and ProFET is used for cell equalization
[4]	Christopher H.T. Lee James L. Kirtley Jr M. Angle	The authors performed an analysis of double stator SRM	Simulations in commercial JMAG Software	Finite Element Method (FEM)-based approach for electromagnetic analysis
[6]	Ranjan Kumar Rajendra Murmu	Speed control of PMSM drives using FOC (Field Oriented Control) method	Simulations in MATLAB/Simulink	A PID controller is used
[7]	Jose Andres Santisteban Richard M Stephan	This paper illustrates about various control techniques for IMs and implementation of Vector Control	Simulations	A general classification with analytical methods using PI controller
[8]	Chau K.T Chan CC Liu Chunhua	This paper gives Information regarding PMBL Drives, their overview, control strategies and machine topologies	Simulations	Different techniques viz. Fuzzy controller, lookup tables and current control loops are deployed
[9]	Jinyun Gan K. T. Chau C. C. Chan J. Z. Jiang	The authors prototyped a Hybrid PMBLDC motor drive	Simulations and Hardware prototyping	Using FEM for electromagnetic analysis and experimental verification
[10]	Djamel Eddine Beladjine, Djamel Boudana, Abdelhafidh Moualdia, Mohamed Hallouz, Patrice Wira	Authors have compared the conventional PI controller and the ANN-based BLDC controller	Simulations	An analytical comparison is made between PI control and ANN control using Simulink

(continued)

Table 1 (continued)

Reference No.	Author	Key findings	Validation of proposed scheme	Techniques used
[14]	Prof. Prem Prakash Anjali Kumari Hemant Sharma Imroz Khan	This paper gives insights about Supercapacitors, their structure and classifications, as hybrid battery and in charging of EVs	Theoretical aspects covered	
[16]	Kun-Che Ho Yi-Hua Liu Song-Pei Ye	This paper has proposed Switched	–	Simulations in MATLAB
	Guan-Jhu Chen Yu-Shan Cheng	Capacitorbased on mathematical modes of various Battery Equalizers (BE) and their energy transferred through them per cycle		
[18]	Chikhi F El Hadri A Cadiou J.C	In this paper, the author presented wheel-slip characteristics for ABS	Simulations	

2 Components of an EV

2.1 Battery

Batteries are the tank of an EV. They provide power not only for traction but also for various electronic equipment viz. lights, wipers, sensors, active suspension systems and other intelligent controls. It’s the batteries that drive the popularity of EV. The battery parameters SoC and SoH need to be monitored due to asymmetric charge and discharge cycles causing safety issues. For cell voltage monitoring it has a voltage divider resistor and a precise temperature reference by the manufacturer. All the signals are sent to the DSP (Digital Signal Processor) for tuning of the voltage profile, i.e., during overvoltage, the DSP must start a constant voltage charge and in undervoltage, it must reduce the current required by the user. In cell equalization, a ProFET (Protected Field Effect Transistor) is shunted with each cell which diligently drains the voltage across itself during overvoltage and stops the charging of the cells when voltage comes in a range (4.15–4.25) V. All the outputs are fed to the trained Neural Network to estimate the SoC and consequently Kms to go [2].

Typically Lead-Acid batteries are used in automobiles as they are economically viable as compared to other ones. Now as EVs are attracting momentum more and more alternatives are taken to be in consideration as Aluminium Batteries in which an Al rod/substrate will serve the purpose of fuel and will be replaced after degradation, i.e.,



These batteries are quite popular for their covert nature as they are silent and due to which they find applications in military instalments, remote telecom towers, etc.

Lithium-ion batteries gained popularity as they have a stable life cycle and a large number of charging and discharging cycles. It seems that the life of LiFePO₄ is the most stable and inherently safe. LiCoO₂, LiMn₂O₄ and Li(Ni_{1/3}Mn_{1/3}Co_{1/3})O₂ have overcharge and thermal concerns [3].

Recently Cobalt-free batteries are proposed to take over conventional Li-ion batteries due to the poisonous nature of Co and RoHS has also stopped the use of the NiCd (Nickel Cadmium) batteries to save the environment. MIT showed a crystal structure that allows to charge the batteries 100 times faster than the conventional Li ones.

2.2 Motor

- **Switched Reluctance Motor**

The switched reluctance motors have variable reluctance and also have a greater ability to tolerate the faults as all of the windings are decoupled from each other. The windings are connected in a flyback circuit style. Since the reluctance of the magnetic flux varies as per rotor-stator position, in this the author did work on Double Stator Structure to utilize the inner spacing for torque production. In this, the power is transferred to the rotor from the two stators which produces greater torque as compared to single stator SR Drive [4].

- **Permanent Magnet Synchronous Motor**

This motor has a construction similar to the conventional Induction motor but the rotor has permanent magnets mounted on it which contribute to air gap field. The PMSM Drives are used with current-controlled VSI (Voltage Source Inverter) providing constant power and constant torque region of operation. This has further two types IPM (Interior Permanent Magnet) mounted and SPM (Surface Permanent Magnet) mounted. The SPM has a smooth torque profile over the IPM machine as it uses less magnets and less harmonic components of flux linkage that makes it easier to produce sinusoidal MMF (Magneto Motive Force).

IPM machines are capable of large inductances, torque and suspension forces [5].

In FOC (Field Oriented Control), the stator current is split into two components the d-axis (for flux production) and the q-axis control (for torque production) and they can be controlled independently. In this literature, the authors presented the FOC technique to achieve speed control above the base speed of the PMSM drive by flux weakening method. The air gap flux is weakened to gain speed than the base speed providing a constant torque region of operation and the enhancement of the air gap flux makes the drive to run below base speed under constant power region. A d- axis current is controlled by using the PI controller [6].

- ***Induction Motor***

It is a very popular machine used in various applications and also gained popularity in the EV segment due to its high torque capability. Generally, these motors are considered for than 5 kW ratings with a Vector Drive deployed to control speed and torque of the motor.

The basic difference between scalar and vector method of control is in Scaler control or FOC which was proposed by Blaschke, and based on reference frame theory, it considers only the steady state and irresponsive in transients but in Vector control of Induction machines it considers both of the scenarios. In this literature, the generalized D-Q notation by De Doncker and Novotny has chosen arbitrary reference frame theory and is not restricted to just constant values [7].

- ***BLDC (Brushless Direct Current) Motor***

In conventional DC machines, the high-power winding rotates and the lower one is kept stationary, which makes them mechanically worst.

In BLDC machine the concept is reverse as the high-power winding is kept stationary and low powered field of permanent magnets is utilized for rotor part, i.e., “it’s turned inside out”. This configuration makes them free from brushes and mechanical wear and tear [8].

There are two types of PM Brushless Drives; one is the PMBLAC (Permanent Magnets Brushless AC Synchronous Drive) in which sinusoidal AC is fed to its stator and makes it PMAC Drive and the other one is PMBLDC (Permanent Magnets Brushless DC Drive) in which the rectangular signal is fed to its Stator. To enhance their speed range in constant power mode of the region, the FOC technique is deployed, and for the above base speed, a current Vector control method is utilized. As the permeability of the magnets is nearly equal to air consequently a large d-axis current is required to demagnetize the air gap flux to achieve speed above the base one. A PMBLDC machine has more torque and power density than the PMBLAC machine due to the product of rectangular flux and current is higher in PMBLDC than the product of sinusoidal flux and current. This is why BLDC machines have higher torque and power density. The author had tried to hybridize a PMBLDC machine with the features of both the DC Series motor and flux regulated BLDC Drives which leads to a machine with higher starting torque, higher efficiency and a wider range of constant power region using the cumulation of fluxes of Permanent Magnets and two-phase stator currents [9].

A machine implemented through an ANN (Artificial Neural Network) controller has a low transitional peak area and faster response time over a PI-controlled machine and can cope with the modern era of FOCs (Field Oriented Control) [10].

2.3 Ultra Capacitors

Ultracapacitors are nowadays gaining popularity due to their inherited property of holding a charge larger than the conventional ones as they have higher energy density. Graphene-based supercaps are a step ahead in this field. They are static and have no chemical reaction required to store energy (as in Li-ion or Pb acid).

These are also considered as an additional battery source that can be added to the battery bank to enhance its capacity and reduce the thermal stress caused by frequent charging-discharging cycles which consequently has less heating loss, better efficiency and life of the bank. So, it could be benevolent in storing transient energy at a much faster rate.

Supercapacitors have the capacitance in the magnitude of Farads (F) which is larger than the values for regular capacitors and act as a constant current source. Supercapacitors can provide bursts of energy as they can charge and discharge rapidly [11].

A typical table is been presented to check different parameters of an Ultracapacitor module (Table 2).

2.4 Charging System

In an EV both fast and trickle charging are required that can handle high power as well. In this paper, the author tried to present some advantages of H-Bridge converters for power conversions as losses are very less in this topology [13].

Table 2 160 V 8F (Farad) module [12]

Parameters	Symbol	Ratings
Maximum string voltage for series of modules	V	800 V
Maximum rated voltage	VR	160 V
PEAK maximum peak current	I	200 A
Stored energy	EMAX	26.6 W
Operating temperature cell case temperature	TA	[-40 65] °C
Thermal capacitance	CTH	5,500 J/°C
Mass	M	6.0 kg

The Ultracapacitor-based charging has a Depth of Discharge (DOD) of 100% whereas in batteries it's only 25% as supercaps provide a burst of energies. The authors of this literature tried to provide a brief view around the dark conditions of power shortages during the conversion of power from one level to another [14].

A Centre-tapped configuration can be implemented as its connections are internal and away from the user giving higher efficiencies over isolated configuration where the transformer is used [15].

A combination of series and parallel cells makes a battery. In order to maintain a good battery health, its current, voltage and temperature must be monitored and controlled that can be done by Battery Management Systems (BMS). Two parameters provided by this system are SoC (State of Charge) and SoH (State of Health).

A SoC is a measure to determine how much charge is available or left in percentile (%) terms in our battery system similar to a battery indicator in our smartphones.

A SoH is a measure to check the ageing or health of the battery system also available in percentile (%) terms which is a typical indicator that shows how much charge it can retain as compared to its nominal value.

To avoid overload conditions, a Cell Balancer or Battery Equalizer is required to ensure that each cell operates under the same conditions and regulation techniques by discharging them from time to time using bleeding resistors. No sensing or closed-loop control is required. Hence, the balancing current is low and the balancing speed as well [16]. The rate of transfer of charge in the equalization process was assumed to be constant throughout [17].

2.5 Braking

During braking, the power generated is fed back to the battery bank and it works when the motor terminal voltage is greater than the source voltage.

The brake pedal should be integrated with mechanical as well as electrical brakes. First, the electrical brakes should be applied and then the mechanical ones as during deceleration the regenerative power is fed back to the bank. When we need full brakes then pressing the pedal slightly harder also engages the mechanical (Disk/Drum) brakes completely causing the vehicle to stop instantaneously with a shorter duration of regenerative power. In this scenario, the slip between the vehicle and the road can be controlled by the ABS (Anti-Lock Braking System). The author simulated the braking and presented the dependence of braking properties on the wheel slip and the road conditions [18].

Table 3 Three-phase source parameters

Source impedance	X/R ratio
Short-circuit power level	1e6 VA
Source X/R ratio	15
Parasitic parallel conductance	1e-6 S

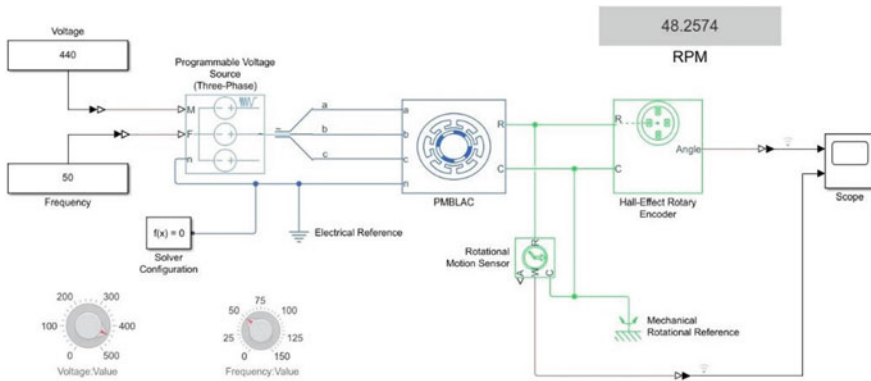


Fig. 1 MATLAB schematic diagram of PMBLAC Drive in Simscape environment

3 Schematic Diagram of PMBLAC Drive

It has been always an area of interest for high-speed machines without having a compromise with torque generation. This gives us a hint to further develop a machine which further gives a boost to this conventional PMBLAC machine or PMBL Synchronous Machine.

In this manuscript, a small hybrid model of this configuration in which a MATLAB model in a complete Simscape environment. A programmable three-phase source is used for variable frequency, and the variable magnitude of the voltage applied is fed to the PMBL machine (Table 3).

A Hall-Effect Rotary Encoder is used to measure theta (θ) and rotational motion sensor to measure the motor RPM and acceleration. A brief work is being shown here in which a PMBLAC drive is implemented as Variable Frequency Drive.

Supporting MATLAB simulations is shown here (Fig. 1 and Table 4).

4 Simulated Outcomes

The model is simulated for infinite time period and it has been observed that when the machine is being run at rated voltage (440 V, 50 Hz) there are some oscillations in after some time they settle down. With the increase in frequency above the rate

Table 4 PMBLAC machine configuration parameters

Winding	Wye
Back EMF profile	Perfectly trapezoidal
Max. PM flux linkage	0.03 Wb
No. of pole pairs	6
Stator d-axis inductance (Ld)	0.00022 H
Stator q-axis inductance (Lq)	0.00022 H
Stator per phase resistance	0.013 Ω
Stator zero-sequence inductance	0.00016 H
Rotor inertia	0.01 kgm ²

of up to 150 Hz, its speed increases with increased oscillations as well. Initially, the machine runs at 50 Hz as we increase the frequency to 75 Hz and there is a considerable increase in the drive speed (RPM) with the least oscillations; further, we step up the frequency by 25–100 Hz, this time oscillations are maximum, which means the output of the machine is not stable. Further increase in this caused the machine to fail and come to almost a halt with some considerable oscillations (Figs. 2 and 3).

This proves that a PMBLAC machine can be implemented as a VFD (Variable Frequency Drive) in order to get higher speeds at constant power. This will find considerable applications in racing or speed arenas and can act as a kind of boost above the base speed. Analytical test results are being shown underneath (Fig. 4).

Three phase shifts (0°, 60°, 120°) are compared and it has been found that at the phase shift of 60° there are minimum oscillations and the least settling time and gives an optimum boost to the speed of the drive. In theta which measures the position of the rotor again misaligns completely with the other comparisons as it takes more time

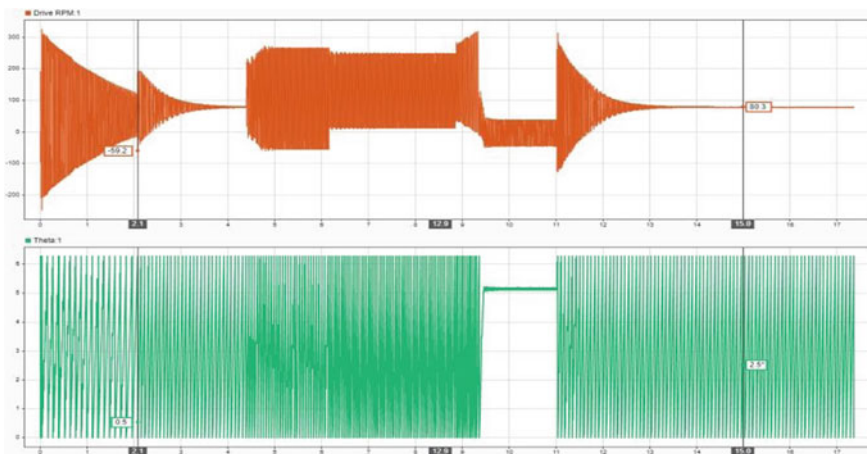


Fig. 2 Response of drive along variation in theta (θ)

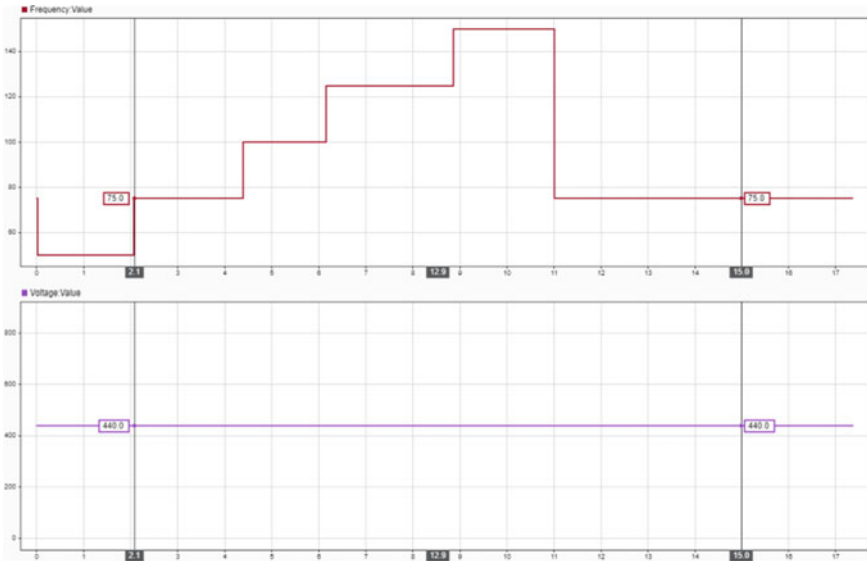


Fig. 3 Simulations for a drive at variable frequency

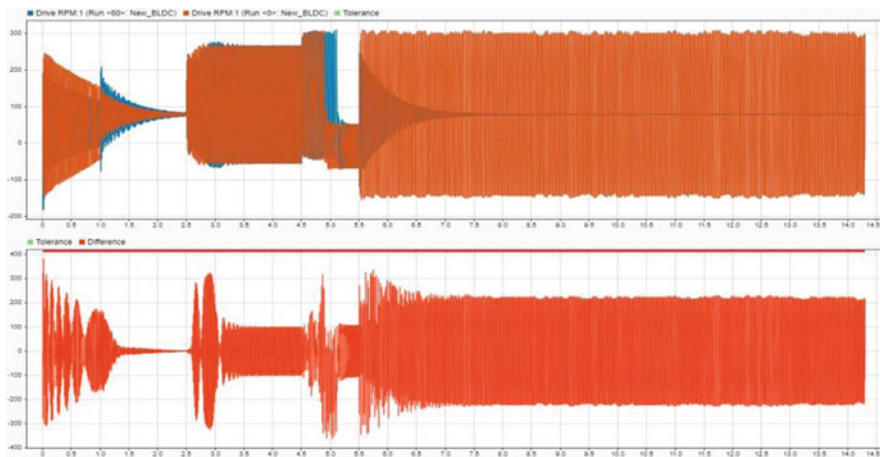


Fig. 4 A comparison in RPM between two scenarios at 0 and 60°

to align with the initial position with the increase in the phase shift. A stimulatory comparison is being shown here underneath, (a green line shows zero tolerance or aligned whereas a red line in the comparison table shows not aligned to the base) (Figs. 5, 6 and 7).

This drive can also be deployed in combination with other drives for higher-speed applications.

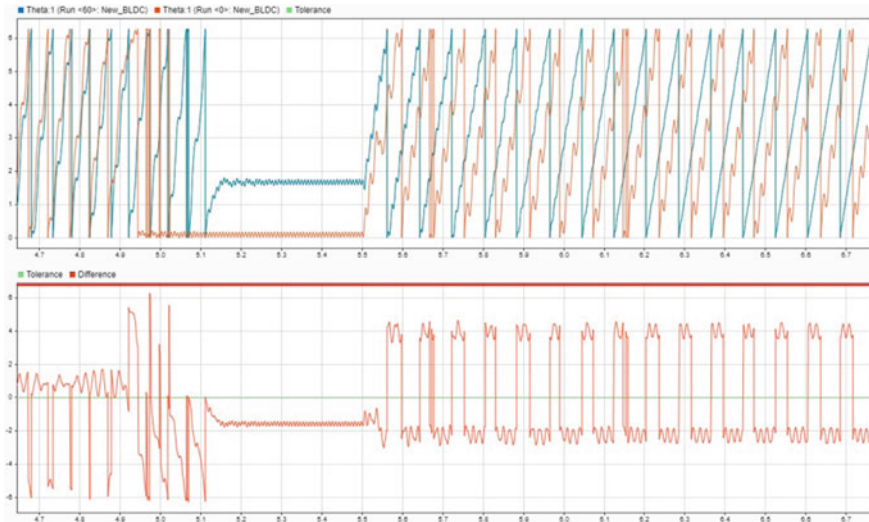


Fig. 5 A comparison in theta between two scenarios at 0 and 60°

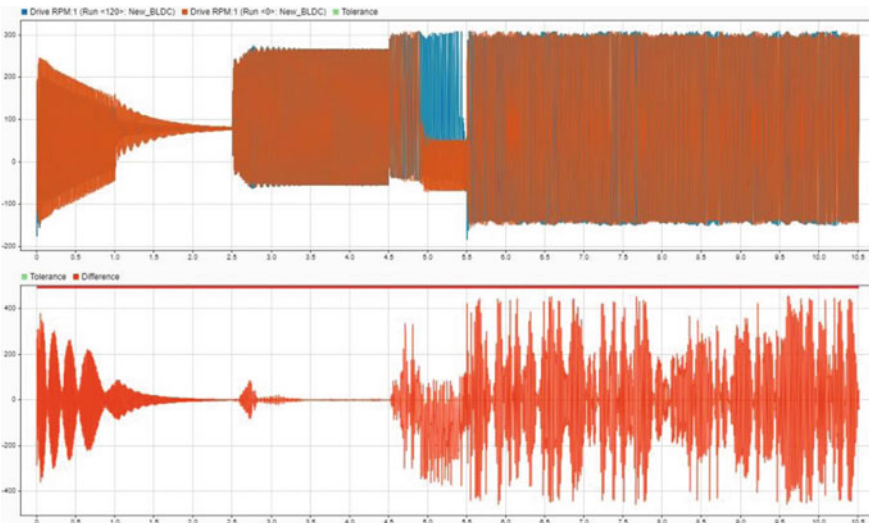


Fig. 6 A comparison in RPM between two scenarios at 0 and 120°

5 Conclusion

This paper gives a terse of literature regarding the components of an electric vehicle, alternatives for conventional power storage, braking, a brief introduction to charging system and more focused towards various control techniques being used for drives associated with it.

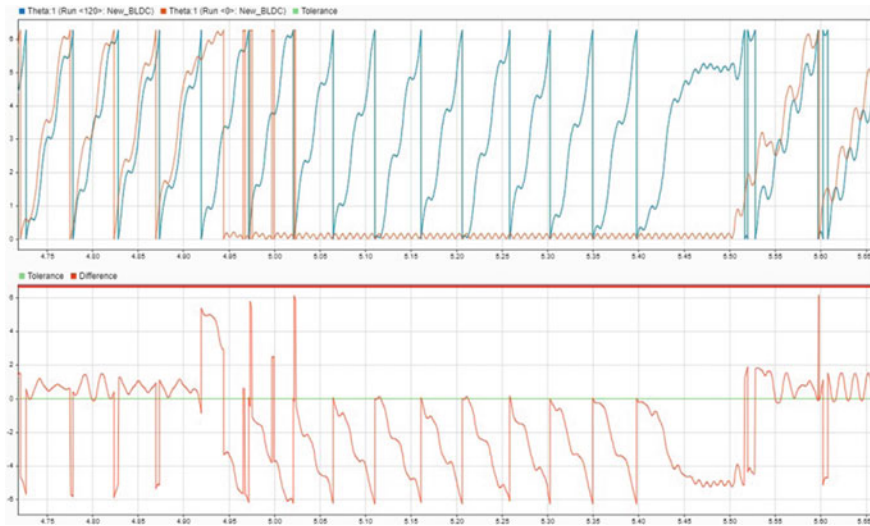


Fig. 7 A comparison in theta between two scenarios at 0 and 120°

This paper discussed the PMBLAC machine and a concept is introduced to utilize the constant power region for higher speed in it for speedy applications, and its fair conditions and complete analytical research for the frequency range have been discussed and plotted. It can serve as a potent system for totally brushless action for modern EV or HEV propulsion systems and also present a blueprint for potential readers to develop a keen interest in the design and development of PMBLAC machines.

References

1. Cheng KWE (2009) Recent Development on Electric Vehicles, s.l. IEEE, 3 international conference on power electronics systems and applications
2. Affanni A, Bellini A, Franceschini G, Guglielmi P, Tassoni C (2005) Battery choice and management for new-generation electric vehicles, s.l. IEEE 52(5):1343–1349
3. Chan CC (2005) The present status and future trends of electric vehicles. Sci Technol Rev 23
4. Lee CHT, Kirtley JL Jr, Angle M (2017) Switched reluctance motor drives for hybrid. Electr Veh 6
5. IPM & SPM Motors. Volcano Electric (2021) (Online) https://www.volcanomotor.com/news/ipm_and_spm_motor-en.html
6. Kumar R, Murmu R (2020) Performance analysis of permanent magnet synchronous motor, s.l. : www.ijert.org. Int J Eng Res Technol (IJERT) 8. ISSN :2278-0181.
7. Santisteban JA, Stephan RM (2001) Vector control methods for induction machines: an overview, s.l. IEEE. IEEE Trans Educ 44
8. Chau KT, Chan CC, Liu C (2008) Overview of permanent-magnet brushless drives for electric and hybrid electric vehicles, s.l.. IEEE, Trans Ind Electron 55:2246–2257

9. Gan J, Chau KT, Chan CC, Jiang JZ ((2000)) A new surface-inset, permanent- magnet, brushless DC motor drives for EVs, s.l.: IEEE Trans Magn 36:3810–3818
10. Beladjine DE, Boudana D, Moualdia A, Hallouz M, Wira P ((2021)) A comparative study of BLDC motor speed control using PI and ANN regulator, s.l. IEEE 18
11. Ultracapacitors (2021a) (Online) Mathworks (2022). <http://www.mathworks.com>
12. Downloads. Maxwell Technologies (2022) (Online) https://maxwell.com/wp-content/uploads/2021/08/3002971-EN.1_160V8F-Module_ds_20191127.pdf
13. Lu Y, Cheng KWE, Ho SL, Pan JF (2005) Passivity-based control of phaseshifted resonant converter, s.l. IEEE 152(6):1509–1515
14. Prakash P, Kumari A, Sharma H, Khan I (2021) Super-capacitor based electric vehicle charging, s.l. Int J Eng Res Technol (IJERT) 10:975. www.ijert.org. ISSN: 2278-0181
15. Cheng KWE (2006) Tapped inductor for switched-mode power converters. In: 2nd International conference on power electronics systems and applications. pp 14–20
16. Ho KC, Liu YH, Ye SP, Chen GJ, Cheng YS, Chin CS (eds) (2021) Mathematical modeling and performance evaluation of switched-capacitor-based batter equalization systems, s.l. MDPI.
17. Chen H, Zhang LH (2014) System-theoretic analysis of a class of battery equalization systems: Mathematical modeling and performance evaluation. 64:1445–1457
18. Chikhi, F El Hadri, A Cadiou, JC (2005) ABS control design based on wheel-slip peak localization. Fifth international workshop on RobotMotion and control. pp 73–77

Analysis of DSR Protocol in Varying Network Configurations



Sonam Khera , Neelam Turk, and Rohin Rakheja

1 Introduction

The path selection in DSR protocol is based on using control messages which are flooded in the entire network. By reducing the overhead (number of packets required for network communication), we can greatly enhance the performance of a routing protocol. However, we would first need to understand the characteristics of the selected protocol to ensure that the reliability and security can be maintained. Before making changes to the header or the routing mechanism, we need to make sure that the protocol can still accommodate the various types of payloads, options and adopt to fragmented or dynamic networks. The sensor nets can be deployed in different configurations depending upon the application. For example:

- The sensors are randomly deployed in a wide area. These are generally used for monitoring an ecosystem or a habitat. The sensors are not attached to the actual targets but are monitored using the data from the entire network. This technique requires additional computations to eliminate the irrelevant data recorded by such a large network [1].
- Another method is targeted sensing where different sensors that record specific parameters from the target are used. It requires deploying the sensors in a planned manner with careful precision. This method is generally used in industries to monitor potential failures, in medical equipment to constantly monitor the health of a patient and has also found uses in robotics and automation of tasks [1].

S. Khera (✉) · N. Turk · R. Rakheja
Department of Electronics Engineering, J.C.Bose University of Science and Technology, YMCA,
Faridabad, Haryana, India
e-mail: sonamkhattar@yahoo.co.in

The major energy components of a wireless network are *Transmission Energy (Tx)*, *Reception Power (Rx)*, *Idle Power (Pi)*, *Overhearing Power (Pover)* [2], *Sleep Power*, *Transition Power and Transition time* [3].

NS2 is a network simulation tool. The architecture of NS2 can be divided into two parts. The network simulation part can also be considered the front end. In this, we can set up the simulation parameters, design network conditions and set the number of nodes, connection types, connection assembly, event scheduling, etc. All this can be done using a scripting language called OTcl. The second part is the internal mechanism of NS2 which consists of distributed C++ scripts that are used as instructions [4]. These scripts guide the NS2 to perform the tasks required by the simulation such as providing the mechanism of the specified routing protocol or implementing certain objects. For example, the functionality of receiving a data packet can be defined using a C++ object but the source and destination of the packet need to be specified while designing the network, i.e. using a OTcl script [5]. NS2 may declare procedures and variables that are not pre-defined members to facilitate the interaction. The member procedures defined in the OTcl domain are called instance procedures (instprocs) and the variables are defined as instances variables (instvars) [2, 3, 6]. The motivation behind this paper is to study the DSR protocol in a large-scale simulated mobile sensor network to identify the possibilities enabling faster route discovery and increase network lifetime and reliability by analyzing the results.

The remaining part of this paper is organized as follows: Sect. 2 covers the dynamic source routing (DSR). Sect. 3 discusses in detail the simulation scenarios undertaken during the research work. In Sect. 4, the simulation results have been discussed. The research work has been concluded in Sect. 5.

2 Dynamic Source Routing

DSR can be broadly categorized as a reactive protocol. It can discover routes as and when needed. It can be used in networks that do not have a fixed infrastructure or where the network topology changes frequently. It can organize and configure itself without the requirement of manual repairs or administrator interference. This makes it suitable for WSNs. It mainly employs the route discovery and route maintenance mechanisms.

Route Maintenance: Each node has a route cache which contains previously learned routes. A source route is selected and included in the header of the packet originated by the source node. This header now contains the sequence of the hops required for it to reach the desired destination [7].

Route Discovery: DSR uses control messages for finding new routes. If a route is not found in the route cache of the source node it floods the network with a RREQ (route request) message. When the destination node receives the RREQ message it forms a RREP (route reply) message. The destination node then searches its route cache for a route to deliver the RREP message found for the source in the cache, and

it will use the address in the header of the RREQ message to traverse a reverse path [7] (Figs. 1, 2, 3 and 4).

The following diagrams illustrate these mechanisms:

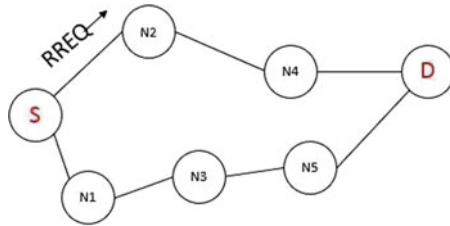


Fig. 1 RREQ message initiated by source

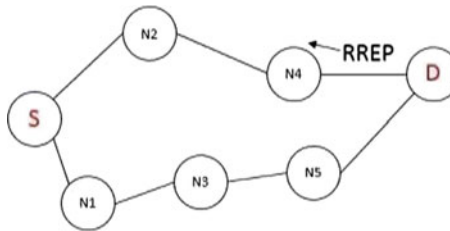


Fig. 2 RREP message initiated by destination

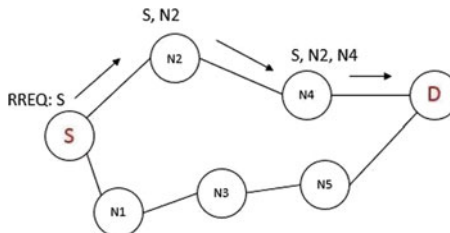


Fig. 3 RREQ header updates

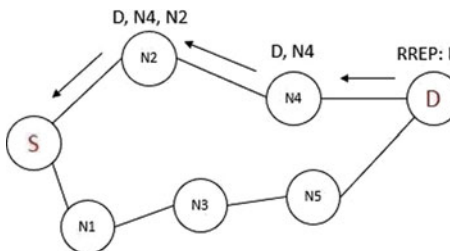


Fig. 4 RREP header updates

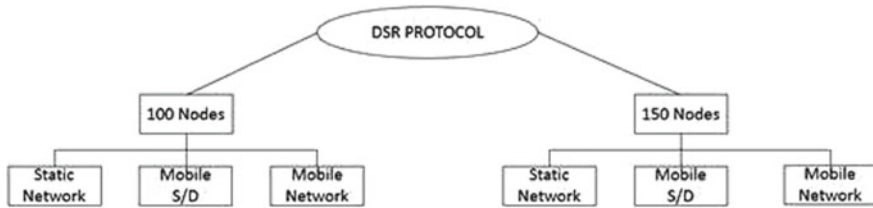


Fig. 5 Simulation scenarios covered under the research work

3 Simulation Scenarios

For understanding the performance metrics under various circumstances, we have simulated two networks consisting of 100 and 150 nodes, respectively, under similar energy models and network parameters. Three scenarios are considered for each network.

Scenario 1 is a non-mobile wireless network with two source and destination nodes. This is similar to a common MANET network.

In Scenario 2, Four nodes are moving toward a fixed destination. This configuration tries to replicate the method of using cluster heads in WSNs. While all the nodes have transmission and reception capabilities, only the mobile nodes act as the sender and the recipient. If considered to be cluster heads their destination can be modified with respect to the base stations. Scenario 3 considers a network with random mobility from all nodes. This scenario simulates the modern applications of wireless sensor networks. For example a network of smart vehicles moving randomly while simultaneously communicating with each other. The simulation run time is 60 s; the traffic begins at 1.0 s and stops at 61.0 s. The maximum movement speed of all nodes is limited to 10 m/s in each scenario. Various parameters are recorded from the trace files generated by NS2 using data manipulation scripts. Figure 5 below demonstrates the simulation scenarios undertaken for the research work.

4 Performance Analysis

The simulation values have been defined as per the commonly used methodologies. For each of the scenarios, the performance has been measured by studying the trace files generated. The Network Animation tool (nam) is used to view the network layout and mobility pattern of the nodes. Variations can be made to the source files included in the package to change the protocol behavior and routing mechanism. However, the NS2 package has a distributed file structure making it difficult to introduce changes and successfully compile them.

While studying the performance of a network protocol it is crucial to ensure that the simulation parameters are similar for different scenarios [8]. The performance of a protocol can be affected by the number of nodes, the grid size, the transmission

Table 1 Simulation parameters

Parameter	Simulation value
Total number of nodes	100/150
Number of source/destination nodes	2/2
Number of mobile nodes	0
Transmission range	250 m
Packet size	1500 Bytes
Propagation model	Two ray ground
Queue type	Drop-tail/Pri Queue/CMU Pri Queue
Antenna type	Omni Antenna
Max packets in queue	50
Frequency	2.47 GHz
Bandwidth (channels)	11 Mb
Routing protocols	DSR
Duration	60 s
Connection type	FTP/TCP
Grid type (topography)	2D (X*Y)
Grid parameters	1000*1000
<i>Energy model</i>	
Initial energy	100 J
Transmission power	0.9 J
Reception power	0.5 J
Idle power	0.45 J
Sleep power	0.05 J

range of the nodes, traffic type, etc. Hence, for comparative study under different network conditions, we may require more than one simulation. As the speed of the mobile nodes increases, it is advisable to read the trace data with fixed time intervals rather than for every second. Data manipulation scripts become necessary to read the trace files as the network becomes larger and more mobile. The graphs have been plotted using the open-source software GNUplot [9] (Table 1).

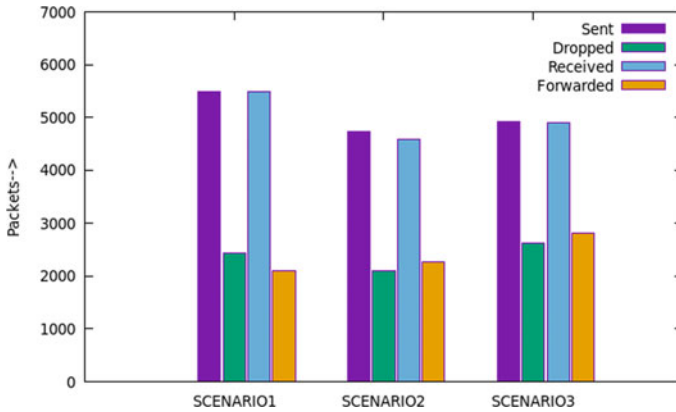
5 Results

A. Network 1

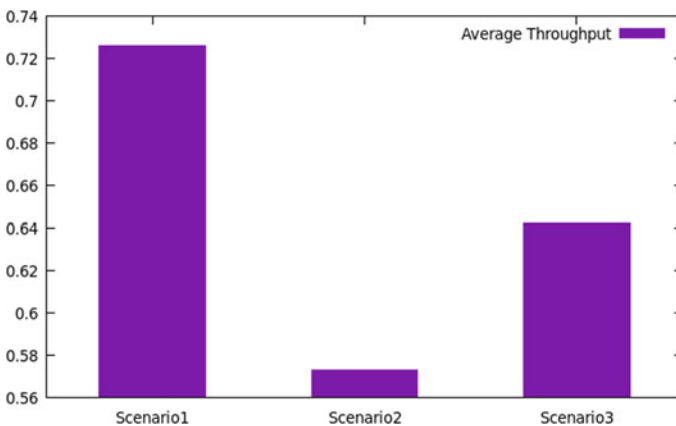
See Plots 1, 2, 3, 4, 5, 6.

B. Network 2

See Plots 7, 8, 9, 10, 11, 12.



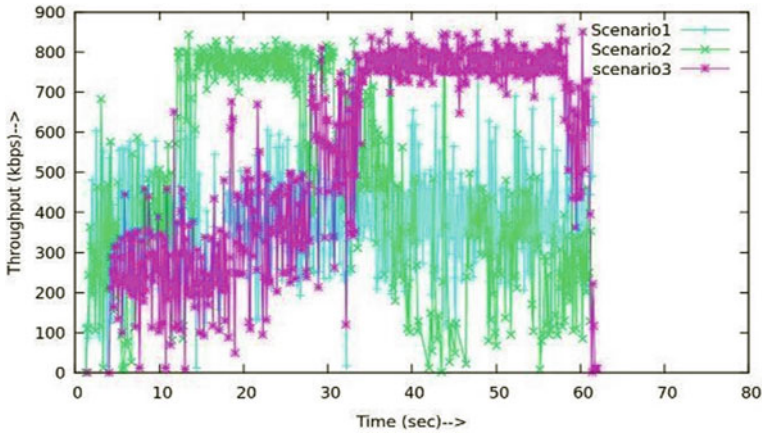
Plot 1 Bandwidth consumption



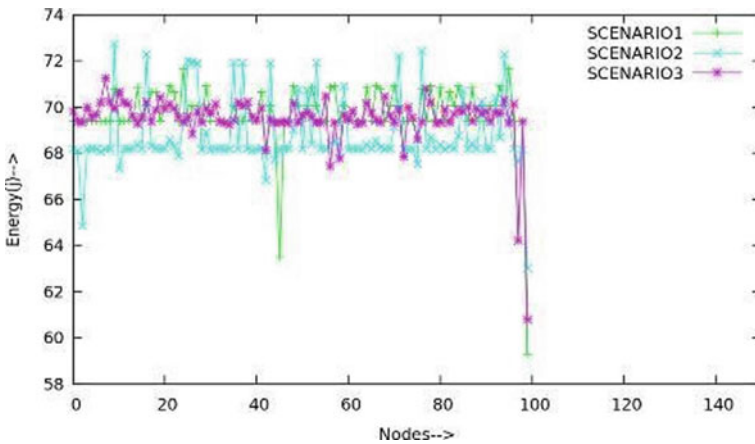
Plot 2 Average throughput (Kbps)

The graphical-based comparison enables easier visualization of the performance of the DSR protocol in the two networks. Plot 1 presents the consumption of bandwidth during the simulation. It takes into consideration the packets which are being generated in the network. Congested networks result in the deterioration of the performance but may be unavoidable due to the limitations of the sensor nodes. Plots 2 and 3 represent the throughput values as recorded during the test. If we divide the total number of packets received successfully over the entire session by the total time, we obtain the average throughput. The time can be calculated by using the difference in times stamps of the first and last transmitted packet.

Plot 4 is the graphical representation of the energy consumption of each node. Plot 5 compares the residual energy of the entire network for the duration of this simulation. Plot 6 is the illustration of the packet drop rate of the two networks in



Plot 3 Instant throughput (Kbps)

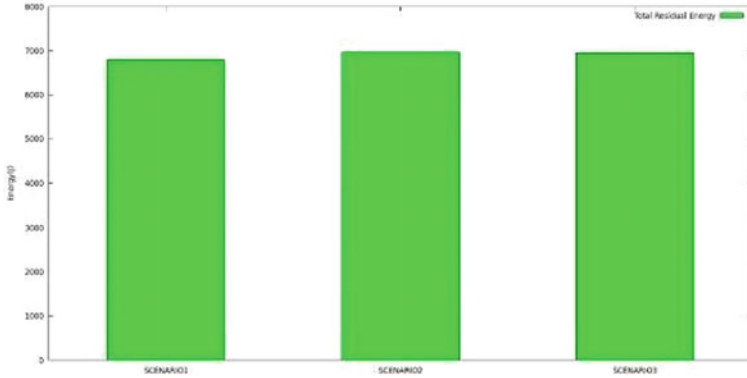


Plot 4 Residual energy of each node

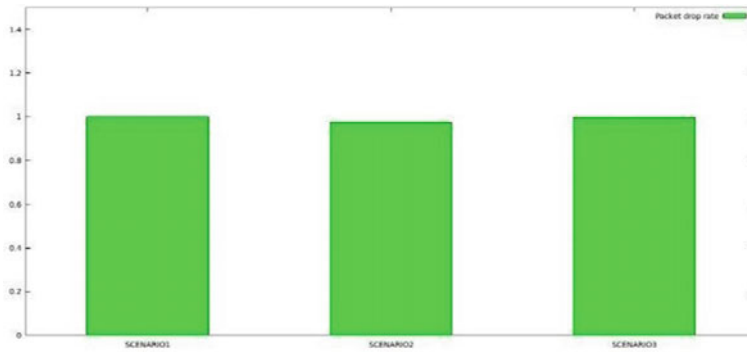
each of the scenarios. It is similar to the packet delivery rate which can be determined as the ratio of data packets received by the destinations to those generated by the sources [6].

6 Conclusion and Future Scope

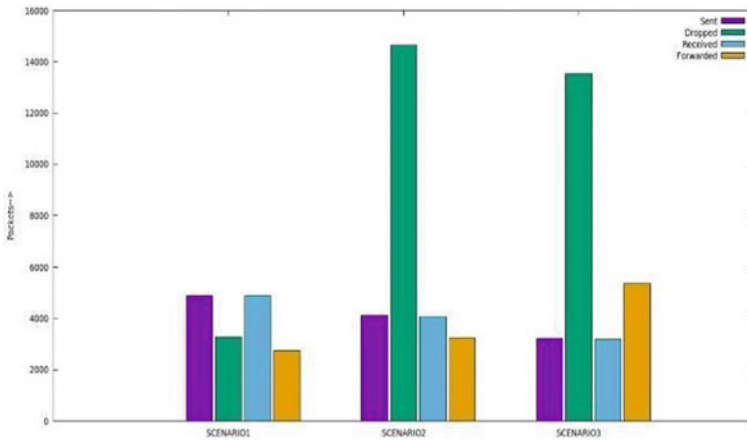
A static network achieves a higher packet delivery rate as the previously established routes are less prone to failure. The control overhead and congestion in the network are lower which leads to lower bandwidth consumption since less packets are generated for delivering a similar payload.



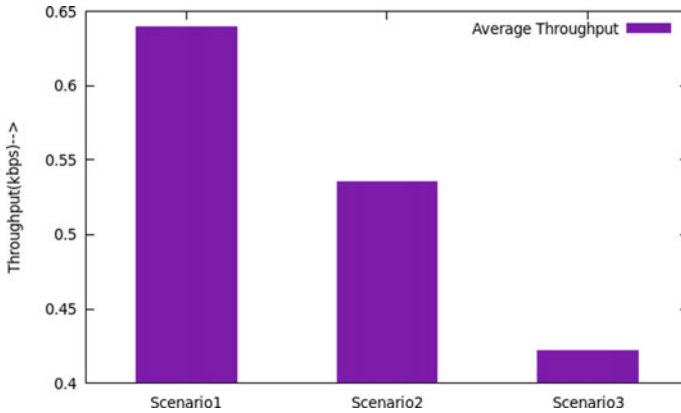
Plot 5 Residual energy of the network



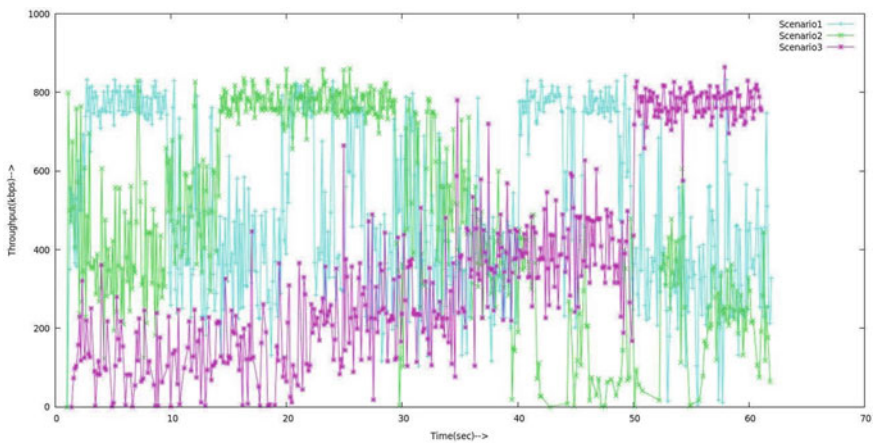
Plot 6 Packet drop rate



Plot 7 Bandwidth consumption



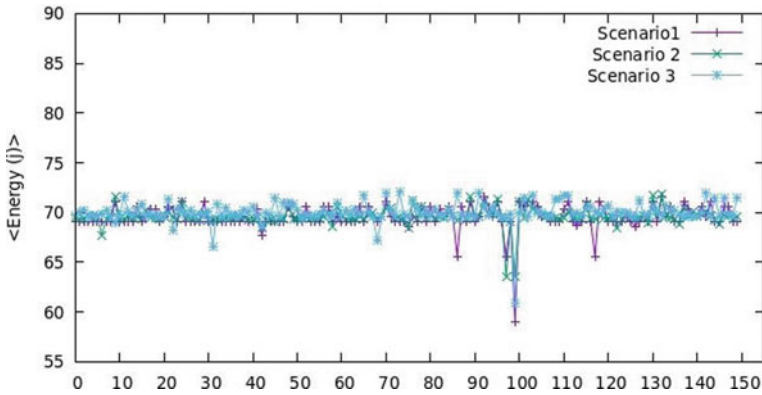
Plot 8 Average throughput (kbps)



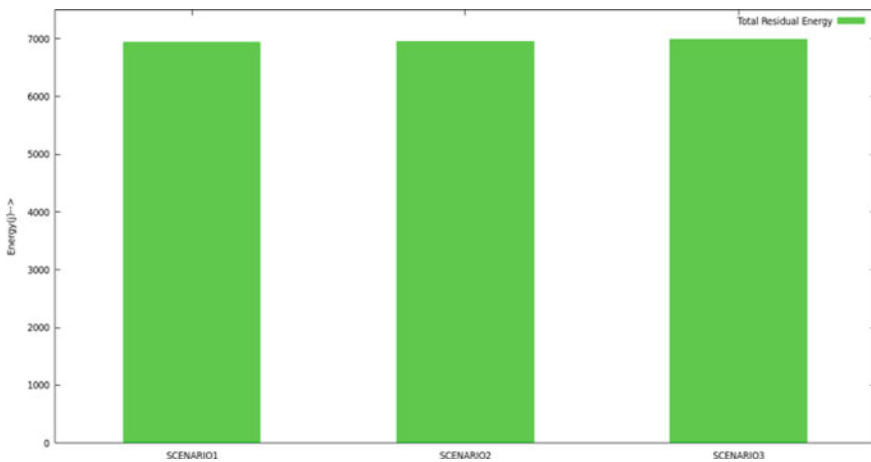
Plot 9 Instant throughput (Kbps)

The clustering technique achieves higher overall network energy efficiency but also suffers from an increased packet drop rate. This is due to the constantly changing position of the source/destination with respect to their neighbors. The bandwidth consumption is higher due to the larger number of packets generated. In network 1, the average throughput decreases drastically for scenario 2. This shows that the positioning of the cluster heads in the network can greatly affect the overall performance.

Even though DSR is completely on-demand and reactive it needs some modification to better fit the needs of a completely mobile autonomous wireless sensor network. Our results for Scenario 3 in Network 2 show that the average throughput decreases considerably with the increase in the number of mobile nodes. Some header information is necessary for route discovery and maintenance and options may be



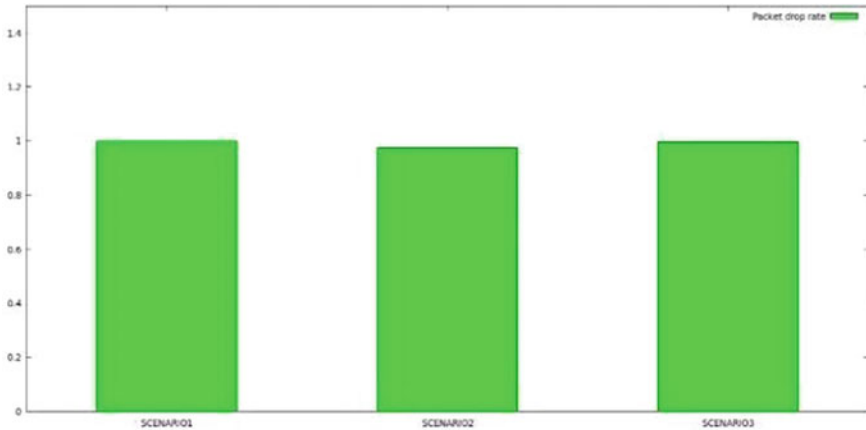
Plot 10 Residual energy of each node



Plot 11 Residual energy of the network

used for the security and reliability of the network. Energy efficiency in WSNs can be achieved by using smart sleep/wake algorithms; however, in a network of randomly moving nodes, this becomes increasingly difficult.

The simulations show that if network deployment conditions necessitate mobility, better performance can be achieved if cluster heads can be assigned. As the network becomes more mobile, the average throughput decreases since it is dependent on the network traffic and the changes in the network topology. Thus, using a cluster head-based technique is preferable if the application allows it. It reduces the changes in network topography and also helps conserve the energy of the nodes. Cluster heads can be changed depending upon the residual energy of the nodes and their position in the network. Parameters such as the pattern of movement and the number of interactions with the neighbors can also be considered.



Plot 12 Packet drop rate

The movement speed of the nodes also affects the performance of the network as the routing protocol needs to update the route cache more frequently due to the position of the neighboring nodes changing rapidly. Reducing overhead in network, reusing already known hierarchically estimated junctions and limiting the number of dropped acknowledgment packets can greatly improve the performance of the routing protocol in future applications of mobile sensor networks.

References

1. <http://www.ee.oulu.fi/~carlos/WSNPapers/AK02.pdf>
2. Issariyakul T, Hossain E (2012) Introduction to network simulator 2 (NS2). In: Introduction to network simulator NS2. Springer, Boston, MA
3. <https://www.tutorialsweb.com/ns2/NS2-1.htm>
4. www.isi.edu/nsnam/ns/doc
5. Issariyakul T, Hossain E (2008) Linkage between OTcl and C++ in NS2. First Online: 20 Sept
6. <https://www.nsnam.org/releases/ns-3-30>
7. <https://www.rfc-editor.org/info/rfc4728>
8. Verma AK, Sadawarti H (2010) Performance analysis of AODV, DSR and TORA routing protocols. IACSIT 2(2): 226–231. ISSN: 1793-8236
9. http://www.gnuplot.info/docs_5.2/Gnuplot_5.2.pdf

A Multilevel Secured Mechanism for Data Protection



Anjali Malik, Sunil Jadav, and Shailender Gupta

1 Introduction

With the advancements in the technology, there is a significant role of information security in our day-to-day life. The advancements in technologies have forced to develop secure mechanism for data communication. So, to provide data security, cryptography and steganography mechanisms are used. Cryptography converts the data from one form to another that is not understood by the intruder [1]. The data sent through this process is in unreadable form so that if any unauthorized user has access to it, it still can't understand. This mechanism involves encryption and decryption processes.

Steganography is the process in which the user hides the data into text files, audio, video or an image [2].

The intruders can expose the data, alter the data or may distort the data. But steganography or cryptography alone fails to provide security to the data. However, the combination of the two is a more reliable and strong mechanism. So to solve this problem, the cryptography and steganography mechanisms are used in combination. The data is first encrypted using the encryption process and then it is embedded into an image. Figure 1 shows the basic block diagram of the multilevel security mechanism.

The combination of the two mechanisms improves the overall security of the system as well as fulfill some desirable features such as memory usage, security and strength for sensitive information transmission across an open channel.

This paper proposes a multilevel security mechanism for data communication by involving both cryptography and steganography mechanisms to incorporate high-level security to the data and for large-area applications. Also, we have incorporated

A. Malik (✉) · S. Jadav · S. Gupta
J.C. Bose University of Science and Technology, YMCA, Faridabad 121006, India
e-mail: anjalimalik@jcboseust.ac.in

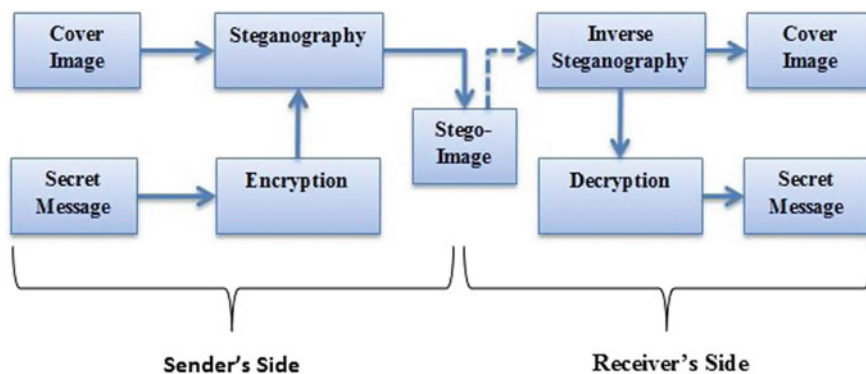


Fig. 1 Basic block diagram of multilevel security mechanism

Huffman compression to enhance the security as well as to increase the data embedding capacity. The data is first encrypted using a qubit encryption mechanism. It is then compressed using Huffman compression for embedding in the cover image. The rest of the paper is organized as follows: Sect. 2 gives the literature survey. The proposed mechanism is shown in Sect. 3. Section 4 provides the setup parameters. A thorough analysis of results is done in Sect. 5 followed by conclusion and references.

2 Literature Survey

Table 1 given below provides the literature survey used till date.

Table 1 shows that the various multilevel techniques available in the literature use various encryption and steganography mechanisms to enhance the security of the data. But very few techniques use compression techniques in their proposed mechanism. Also, very few researchers have worked on the pseudo random LSB approach to embed the data in an image. Thus, our proposed technique aims not only at increasing the embedding capacity but also at securing the data to great extent.

3 Proposed Mechanism

The proposed mechanism involves three stages: Encryption, Compression and Embedding.

Encryption

Figure 2 shows the detailed encryption process used in the proposed mechanism. It involves substitution, permutation and diffusion processes. Each of them involves

Table 1 Literature survey

Proposed by	Cryptography technique used	Steganography technique Used	Compression
Masud Karim et al. [3]	Encryption using secret key	Modified LSB	Huffman compression
Gokul et al. [4]	Visual cryptography	LSB (Least significant Bit)	–
Shailender Gupta et al. [5]	RSA + Diffie Hellman	LSB	–
Mohammad et al. [6]	Diffie Hellman	LSB	–
Nivedhitha et al. [7]	DES	LSB	–
Ramakrishna Mathe et al. [8]	Diffie Hellman	LSB	–
Md. Rashedul Islam et al. [9]	AES	LSB using Status bit	–
Aung et al. [10]	AES	DCT	–
Shingote Parshuram et al. [11]	AES	LSB	–
Sangeeta Dhall et al. [12]	Vigenere	Pseudo random LSB	Huffman compression
Mohamed Elhoseny et al. [13]	AES + RSA	DWT	–
Ashrafal Tauhid et al. [14]	AES	LSB + DWT	–
Nabanita Mukherjee et al. [15]	Dynamic Pairing function	PVD (Pixel Value Difference)	–

the use of a key generated from the quantum logistic map to make the encryption key-dependent process for a highly secured mechanism.

The quantum chaotic map with the lowest order quantum corrections is followed [15]. The $x(i)$, $y(i)$ and $z(i)$ values are taken as keys to make the encryption process unique. Even for single bit of change in key or initial conditions makes up a unique encryption process.

The data is passed through the substitution block where the values of the data are replaced with the new values using a dictionary. The dictionary contains a new value for possible values which is dependent on the key. For different keys, the dictionary to be used is unique. Then the substituted data is passed to the permutation block, where the data is shuffled. The unique positions at which data is to be shuffled are generated for the key. Then the shuffled data is further changed in the diffusion block. In this block, the data is XORed with the sequence of key of the same size as of data to get the encrypted data.

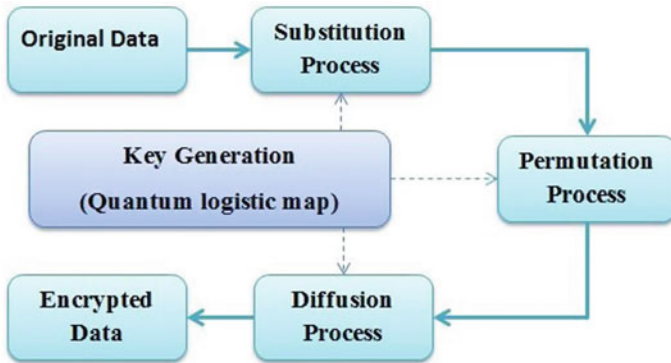


Fig. 2 Block diagram of encryption process used in proposed security mechanism

SUBSTITUTION PROCESS
<pre> Input: a=original data; anew= substituted data [m n]= size(a); s=uint16(randperm(256)); s=s(1:256)-1; %s(256)=0; for i=1:1:m for j=1:1:n b=a(i,j); anew(i,j)=s(b+1); end end </pre>
PERMUTATION PROCESS
<pre> Input: ip=randperm(length(anew)); ip1= permuted data for(i=1:length(anew)) b1=ip(i); ip1(b1)=anew(i); end </pre>
DIFFUSION PROCESS
<pre> Input:X2=(randi([0,255], length(a))); diff= diffused data for(i=1:length(a)) diff(i)=bitxor(ip1(i),X2(i)); end </pre>

Compression

Now to further increase the security of the mechanism and also to increase the embedding capacity as faced by other researchers available in the literature, data is compressed. The Huffman compression is used to compress the data as it requires less storage space and its lossless behavior [16].

The compressed data is now to be embedded in the cover image.

Embedding

Figure 3 shows the detailed embedding process used in the proposed mechanism.

Now for the embedding process first the edges present in the image are detected. This is due to the fact that the change in data of the edges cannot be visually detected.

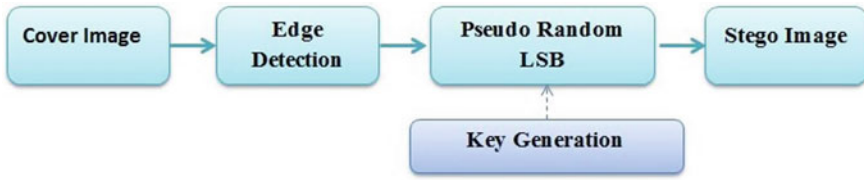


Fig. 3 Block diagram of embedding process used in proposed security mechanism

The edges are detected using the canny edge detection filter. This improves the anti-noise ability and keeps the edge image more clearly [17].

The position of edges is detected where the data in the LSB of the pixels need to be embedded. The positions are scrambled using the quantum map to make the data scrambled and increase the security of data. The data is then embedded in the LSB positions of the edges randomly.

The process to retrieve the data at the receiver’s end is just the reverse of the encryption process.

EMBEDDING PROCESS
<pre> Input:hcode= compressed data; pos1= edge position in R channel of cover image; pos2= edge position in G channel of cover image; pos3= edge position in B channel of cover image; for(i=1:length(hcode)) if(i<=length(pos1)) abc=(de2bi(R(pos1(i)),8))'; abc(8)=hcode(i); EORG1(pos1(i))=uint8(bi2de(abc')); elseif((i>length(pos1)) && (i<=length(pos2))) abc=(de2bi(G(pos2(i-length(pos1))),8))'; abc(8)=hcode(i); EORG2(pos2(i-length(pos1)))=uint8(bi2de(abc')); else abc=(de2bi(B(pos3(i-length(pos2)+length(pos1))),8))'; abc(8)=hcode(i); EORG3(pos3(i-length(pos2)+length(pos1)))=uint8(bi2de(abc')); end end </pre>

4 Setup Parameters

Table 2 provides simulation setup parameters used, while performing different experiments using the proposed mechanism.

Table 2 Simulation setup parameters

Processor	1.50 GHz Intel Core i3
Operating system	Windows 8
Image type	.jpg, .jpeg
Simulation tool	MATLAB version: R2014a serial update 2
Image type	RGB

5 Result

The MATLAB version R2014a software is used to simulate all the results. The simulation results of the proposed mechanism demonstrated below are the average for 10 different images for the below-mentioned performance matrices:

Visual Perceptibility Analysis

For the desired multilevel security mechanism, the distortions introduced in the cover image because of the data embedding process must not be recognized by human eyes as shown in Fig. 4.

It can be observed from Fig. 4 that the proposed technique does not show a perceivable change in the image.

Quantitative Analysis

The embedding process introduces distortion and noise in the cover image. It is essential to measure quantitative measures related to the quality.

Bit Error Rate (BER): For desirable mechanism, BER must be low [15]. Table 3 provides the BER of the proposed technique to the other techniques available in the literature.



Fig. 4 Visual perceptibility of the proposed technique

Table 3 BER of the proposed technique to the other techniques available in the literature

References	BER
[14]	1.54
[15]	1.47
Proposed	0.01019

Table 4 MSE of the proposed technique to the other techniques available in the literature

References	MSE
[14]	0.0339
[15]	2.08
Proposed	3.067

Mean Square Error (MSE): For a desirable mechanism, MSE value must be low [15]. Table 4 provides the MSE of the proposed technique to the other techniques available in the literature.

Peak Signal to Noise Ratio (PSNR): For a desirable mechanism, PSNR must be high [15]. Table 5 provides the PSNR of the proposed technique to the other techniques available in the literature.

Universal Image Quality Index (UIQI): For a desirable mechanism, UIQI must be close to 1 showing similarity in the cover image and corresponding stego image [15]. Table 6 provides the UIQI of the proposed technique to the other techniques available in the literature.

Structural Similarity Index Metric (SSIM): For a desirable mechanism, SSIM must be close to 1 showing similarity in the cover image and corresponding stego image [15]. Table 7 provides the SSIM of the proposed technique to the other techniques available in the literature.

Table 5 PSNR of the proposed technique to the other techniques available in the literature

References	PSNR (dB)
[14]	62.89
[15]	41.59
Proposed	55.66

Table 6 UIQI of the proposed technique to the other techniques available in the literature

References	UIQI
[14]	0.9054
[15]	0.9663
Proposed	0.9857

Table 7 SSIM of the proposed technique to the other techniques available in the literature

References	SSIM
[14]	0.93415
[15]	0.9972
Proposed	0.9985

6 Conclusion

In the proposed model, we have incorporated an encryption process which involves key-dependent substitution, permutation and diffusion blocks. This makes the mechanism more secured. Also, we have enhanced the embedding capacity of the model by involving the Huffman compression mechanism which is lossless in nature. Hence, the data can be completely restored. Also, the LSB steganography technique involved in the proposed model is not only randomized in nature but also the embedding is done in the edges present in the cover image. This helps in the visual perceptibility of the data that cannot be seen by the human eye. Experimental results depict that the proposed model shows the best results in BER, UIQI, SSIM and visually as compared to other latest techniques available in the literature. Our model shows comparable results in terms of PSNR and MSE.

References

1. Cryptography and Network Security principles and practices. William Stallings, pearsons education, first Indian reprint 2003
2. Pooja KM, Kumar A (2010) Steganography—a data hiding technique. *Int J Comput Appl* 9(7). ISSN 0975-8887
3. Masud Karim SM, Rahman MS, Hossain MI (2011) A new approach for LSB based image steganography using secret key. In: *Proceedings of 14th international conference on computer and information technology*, pp 22–24
4. Gokul M, Umeshbabu R, Vasudevan, SK, Karthik D (2012) Hybrid steganography using visual cryptography and LSB encryption method. *Int J Comput Appl* 59(14):5–8
5. Gupta S, Goyal A, Bhushan B (2012) Information hiding using least significant bit steganography and cryptography. *Int J Mod Educ Comput Sci* 4(6):27
6. Mohammad AA, Abdel Fatah MA (2012) Public-key steganography based on matching method. *Eur J Sci Res* 223–231
7. Nivedhitha R, Meyyappan DT, Phil M (2012) Image security using steganography and cryptographic techniques. *Int J Eng Trends Technol* 3(3):366–371
8. Mathe R, Atukuri VRR (2012) Devireddy SK Securing information: cryptography and steganography. *Int J Comput Sci Inf Technol* 3(3):4251–4255
9. Islam MR, Siddiqa A, Uddin MP, Mandal AK, Hossain MD (2014) An efficient filtering based approach improving LSB image steganography using status bit along with AES cryptography. In: *Proceedings of 3rd international conference on informatics, electronics and vision*, pp 1–6
10. Aung PP, Naing TM (2014) A novalsecure combination technique of steganography and cryptography. *Int J Inf Technol Model Comput* 2(1):55–62
11. Shingote Parshuram N, Hussain SA, Bhujbal PM (2014) Advanced security using cryptography and LSB matching steganography. *Int J Comput Electron Res* 3(2):52–55

12. Dhall S, Bhushan B, Gupta S (2016) An improved hybrid mechanism for secure data communication. *Int J Comput Netw Inf Secur* 8(6):67
13. Elhoseny M, Ramírez-González G, Abu-Elnasr OM, Shawkat SA, Arunkumar N, Farouk A (2018) Secure medical data transmission model for IoT-based healthcare systems. *IEEE Access* 6:20596–20608
14. Tauhid A, Tasnim M, Noor SA, Faruqui N, Yousuf MA (2019) A secure image steganography using advanced encryption standard and discrete cosine transform. *J Inf Secur* 10(3):117–129
15. Akhshani A, Akhavan A, Lim SC, Hassan Z (2012) An image encryption scheme based on quantum logistic map. *Commun Nonlinear Sci Numer Simul* 17(12):4653–4661
16. Kumar R, Malik A, Singh S, Chand S (2016) A high capacity email based text steganography scheme using Huffman compression. In: 3rd international conference on signal processing and integrated networks (SPIN). IEEE, pp 53–56
17. Xuan L, Hong Z (2017) An improved canny edge detection algorithm. In: 8th IEEE international conference on softwareengineering and service science (ICSESS), pp 275–278. <https://doi.org/10.1109/ICSESS.2017.8342913>

Optimal AGC of Two-Area Multi-source Power System Incorporating ES Under Deregulated Environment



Sandeep Rangi, Sheilza Jain , and Yogendra Arya 

1 Introduction

In modern restructured electrical power systems, automatic generation control (AGC) is indispensable as it provides regulation and services by offering a balance in-between total load demand plus power losses during transmission and total generated power. If the balance among generating company (GENCO) total power generated and distribution company demand plus losses is impeded, the power of tie line and area frequency, which are reliant on the system's active of GENCO, deviate from their desired value [1]. An AGC scheme's two objectives are to keep area frequency and power of tie line within prescribed limits [2]. In restructured framework, DISCO have the alternative to negotiate a power agreement with possible GENCO present in its own or alternative area for power transactions, resulting in a competitive atmosphere and enabling DISCOs to purchase power at lower rates. By overseeing all power exchanges between DISCOs and GENCOs, independent service operator (ISO) helps to ensure a secure and dependable operation. It offers a variety of additional functions, and load frequency regulation is one among them, which is also known as AGC. The use of an AGC control strategy has a big impact on the performance of the system. In an open market scenario, Donde et al. [3] investigated a two-area system having a thermal generating unit. Arya et al. [4] later presented AGC of a two-area multi-source system having thermal reheat, diesel, hydro, and gas, which provides a

S. Rangi · S. Jain (✉) · Y. Arya
Department of Electronics Engineering, J.C. Bose University of Science and Technology, YMCA,
Faridabad, Haryana 121006, India

S. Rangi
e-mail: rangi44sandeep@gmail.com

Y. Arya
Department of Electrical Engineering, J.C. Bose University of Science and Technology, YMCA,
Faridabad, Haryana 121006, India

more realistic perspective of the system. As a result, the redesigned power system's study is limited to non-renewable energy-generating sources, while the utilization of renewable energy (RE) sources might open up various research gates. Modeling of RE sources like solar energy [5] and wind [6] is discussed in a variety of literature. Geothermal energy (GE) is another RE source that is a viable solution for medium and relatively larger-level electricity and space heating generation around the world. GE is a type of heat energy that the earth spontaneously retains within itself and hence derives directly from the crust [1]. However, GE is a unique method of generating power, and it has been incorporated into AGC research by very few [1]. Researchers have introduced various classical and smart ways to cope with AGC issues, i.e., to optimize controller gains in the restructured system but in contrast to other approaches, optimal control approaches used on restructured power systems exhibit excellent and robust in terms of dynamic performance [4, 7–11].

Aside from control strategies incorporating the energy storage (ES) device in restructured power systems, it impacts the system performance significantly. As a result, energy storage elements RFB [1, 4, 9, 12–15] have been included to make sure that power is consistently reached load while retaining the system cost modestly.

In the context of the foregoing, the primary objectives for the study can be stated as follows:

- (a) The optimal controller has been implemented on two-area restructured system comprising thermal-GTPP and diesel-GTPP GENCOs.
- (b) The efficiency of the OC is validated for system parameter variation and different scenarios of power transactions.
- (c) The role of RFB has been explored in order to boost the studied system's dynamic performance in restructured interconnected power system.

2 System Models

In a deregulated power environment, a two-area system with the same capacity is proposed for study. There are basically two systems considered for the study. The first system is (i) two-area multi-source containing one thermal unit and GTPP unit in area 1 and a diesel unit and GTPP unit in area 2: (ii) The same system as (i) along with RFB incorporated in each area which can be seen in Fig. 1.

3 State Space Modeling

The following state space differential equation describes the state space model of two-area multi-source restructured system [16, 17]:

$$X = AX + BU + \Gamma P_D \quad (1)$$

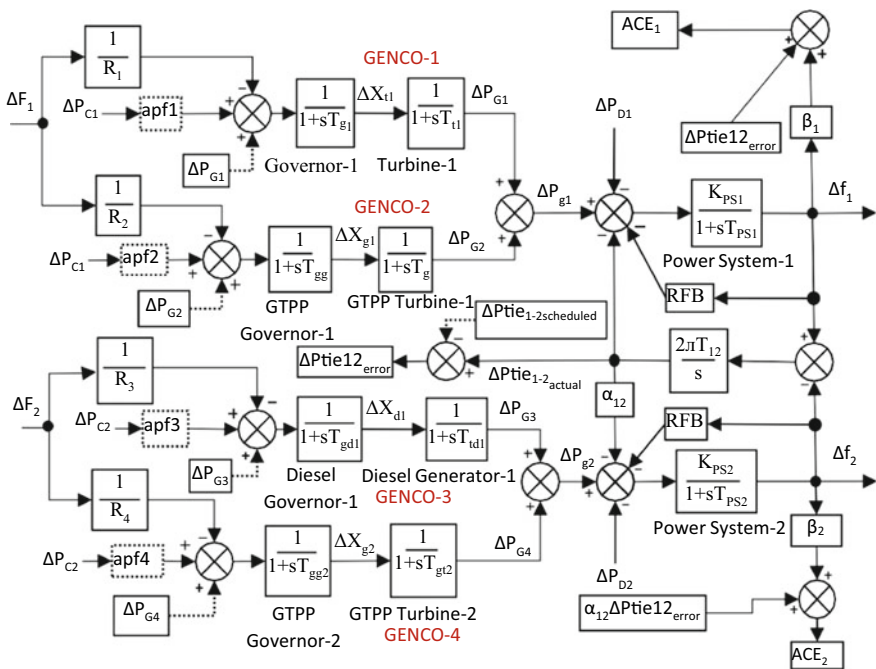


Fig. 1 Block diagram of the interconnected two-area multi-source power system having Thermal-GTPP-Diesel-GTPP

$$Y = CX \tag{2}$$

where X is the state vector matrix with dimension 13×1 , Γ is the disturbance vector matrix with dimension 6×1 , Y is the typical output vector matrix with dimension 13×1 , and U are control vectors with matrix dimensions 2×1 for the two-area system. Where A is system B is output matrix of dimension both have dimension 13×13 , B is the input distribution of dimension 13×2 , and Γ is the disturbance distribution having dimensions of 13×6 for the system.

$$[X] = \left[\Delta f_1 \Delta f_2 \Delta P_{G1} \Delta X_t \Delta P_{G2} \Delta X_{g1} \Delta X_d \Delta P_{G4} \Delta X_{g2} \Delta P_{tie12_actual} \int ACE_1 dt \int ACE_2 dt \right]^T$$

Disturbance vectors:

$$[P_D] = [\Delta P_{L1} \Delta P_{L2} \Delta P_{UC1} \Delta P_{L3} \Delta P_{L4} \Delta P_{UC2}]^T$$

Control vectors:

$$[U] = [\Delta PC1 \Delta PC2]^T$$

and

ΔPC denotes the area control signal, while power demand for DISCO is denoted by ΔPL and ΔPUC for the uncontracted power demand of that control area.

4 Simulation Results and Analysis

The performance of OC is evaluated using three different power exchange scenarios in an open market environment.

Scenario 1: Poolco-Based Transactions—DISCOs deal with GENCOs which are present inside the same control area for power transactions in this scenario [8, 13]. Only DISCOs from the same control area GENCOs are intended to demand the load. Let the power demand of DISCOs for this scenario is equal to 0.2 puMW. The relative DISCO participation matrix (DPM) for the scenario is given as

$$DPM = \begin{bmatrix} 0.6 & 0.5 & 0 & 0 \\ 0.4 & 0.5 & 0 & 0 \\ 0 & 0 & 0.7 & 0.6 \\ 0 & 0 & 0.3 & 0.4 \end{bmatrix} \quad (3)$$

The DPM elements cpf_{13} , cpf_{14} , cpf_{23} , and cpf_{24} are set to zero because DISCOs of any area are not permitted to seek power from GENCOs present in different areas. ACE participation factors for GENCOs for the first control area are considered as $apf_1 = 0.55$ and $apf_2 = 0.45$, and for DISCOs of area-2 $apf_3 = 0.5$ and $apf_4 = 0.5$ in all three scenarios. For poolco-based scenario, Ptiescheduled and steady-state power generation equations will be adjusted as follows:

$$\Delta P_{tie1-2\text{ scheduled}} = - \left((cpf_{31} + cpf_{41})\Delta P_{L1} + (cpf_{32} + cpf_{42})\Delta P_{L2} \right) \\ (cpf_{13} + cpf_{23})\Delta P_{L3} + (cpf_{14} + cpf_{24})\Delta P_{L4} \quad (4)$$

$$\Delta P_{Gi} = cpf_{i1}\Delta P_{L1} + Cpf_{i2}\Delta P_{L2} + cpf_{i3}\Delta P_{L3} + cpf_{i4}\Delta P_{L4} \quad (5)$$

Considering Eqs. (4)–(5), in steady state GENCOs need to generate powers $\Delta PG1 = 0.22$ puMW, $\Delta PG2 = 0.18$ puMW, $\Delta PG3 = 0.26$ puMW, and $\Delta PG4 = 0.08$ puMW. $\Delta P_{tie1-2\text{ scheduled}} = 0$ puMW. Since only GENCOs in that area can satisfy the demands of power for DISCOs in that area $\Delta P_{tie1-2\text{ scheduled}}$ will be 0 puMW.

Scenario 2: Poolco-Bilateral Transactions—In this power transaction case, DISCOs do have the liberty to negotiate for power transaction with their very own control area GENCOs as well as GENCOs of other control areas [8, 9, 13]. For this case, the electrical power needed for all the DISCOs is equal to the power demand that is presumed identical, i.e., 0.5 puMW. The relative DPM for scenario is given below

$$\text{DPM} = \begin{bmatrix} 0.2 & 0.4 & 0.3 & 0.3 \\ 0.3 & 0.3 & 0.3 & 0.2 \\ 0.2 & 0.2 & 0.2 & 0.3 \\ 0.3 & 0.1 & 0.2 & 0.2 \end{bmatrix} \quad (6)$$

Considering Eqs. (4)–(5) GENCOs need to generate power as per contract as $\Delta\text{PG1} = 0.6$ puMW, $\Delta\text{PG2} = 0.55$ puMW, $\Delta\text{PG3} = 0.45$ puMW, $\Delta\text{PG4} = 0.40$ puMW, $\Delta\text{Ptie1-2}$ scheduled = 0.15 puMW according to the above-considered DPM. The simulated response from MATLAB Fig. 2h–l is used to validate the ΔPtie12 scheduled, ΔPtie12 actual, ΔPtie12 error, and GENCO outputs. Because of the combined effect of power demands from the load of all areas, scenario 2 has a large undershoot Fig. 2a–l and more settling time than the first scenario.

Scenario 3: Contract Violation—In some situations, DISCOs may infringe agreement by requesting additional load demand than is mentioned in the contract [8, 9, 13].

As this increased power demand of DISCO is not contractual, it had to be satisfied completely by GENCOs that serve the very same geographic area in which DISCO is present.

For this case, scenario 2 is considered but DISCO-1 demand 0.1 puMW and DISCO-3 demand 0.2 puMW more power than mentioned in the contract, i.e., PUC1 = 0.1 puMW and PUC2 = 0.2 puMW, respectively. Because of the higher power demands in both areas, the steady-state generation power output level of GENCOs for area-1 and area-2 will differ from what it was in scenario 2, and uncontracted load will be now shared according to apf1 and apf2 values in area-1, while for area-2 it will be determined by apf3 and apf4. Therefore, $\Delta\text{PG1, CV} = 0.6 + (0.55 \times 0.1) = 0.655$ puMW and $\Delta\text{PG2, CV} = 0.55 + (0.45 \times 0.1) = 0.595$ puMW. Similarly, $\Delta\text{PG3, CV} = 0.55$ puMW and $\Delta\text{PG4, CV} = 0.50$ puMW; (Fig. 2a–f) however, ΔPtie12 scheduled value during steady state will be same as in scenario 2.

4.1 Comparison of System Performance with RFB

In this section, scenario 2 of the restructured multi-source system is considered for the study, with energy storage devices RFB one in each area. OC is used to simulate the system model. The system model is first simulated without an ES device after that the dynamic response has been compared with the same system model when RFB is installed, illustrated in Fig. 3a–f. With RFB installed along with OC system shows better dynamic response with small undershoot/overshoot as well as when comes to settling time and size of oscillations compared to those of the system without ES devices.

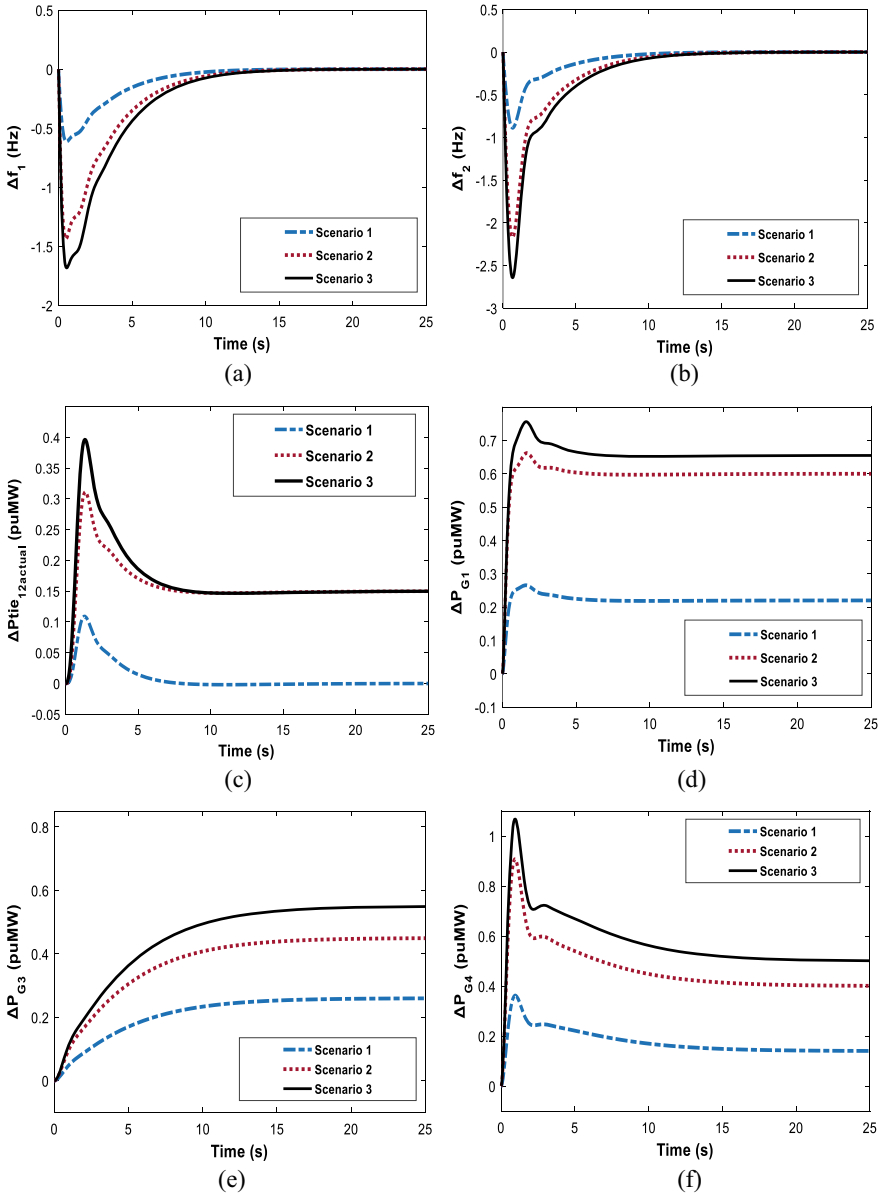


Fig. 2 Dynamic responses of Thermal-GTPP-Diesel-GTPP system with OC for various market transaction scenarios **a** Δf_1 , **b** Δf_2 , **c** $\Delta P_{tie12actual}$, **d** ΔP_{G1} , **e** ΔP_{G3} , and **f** ΔP_{G4}

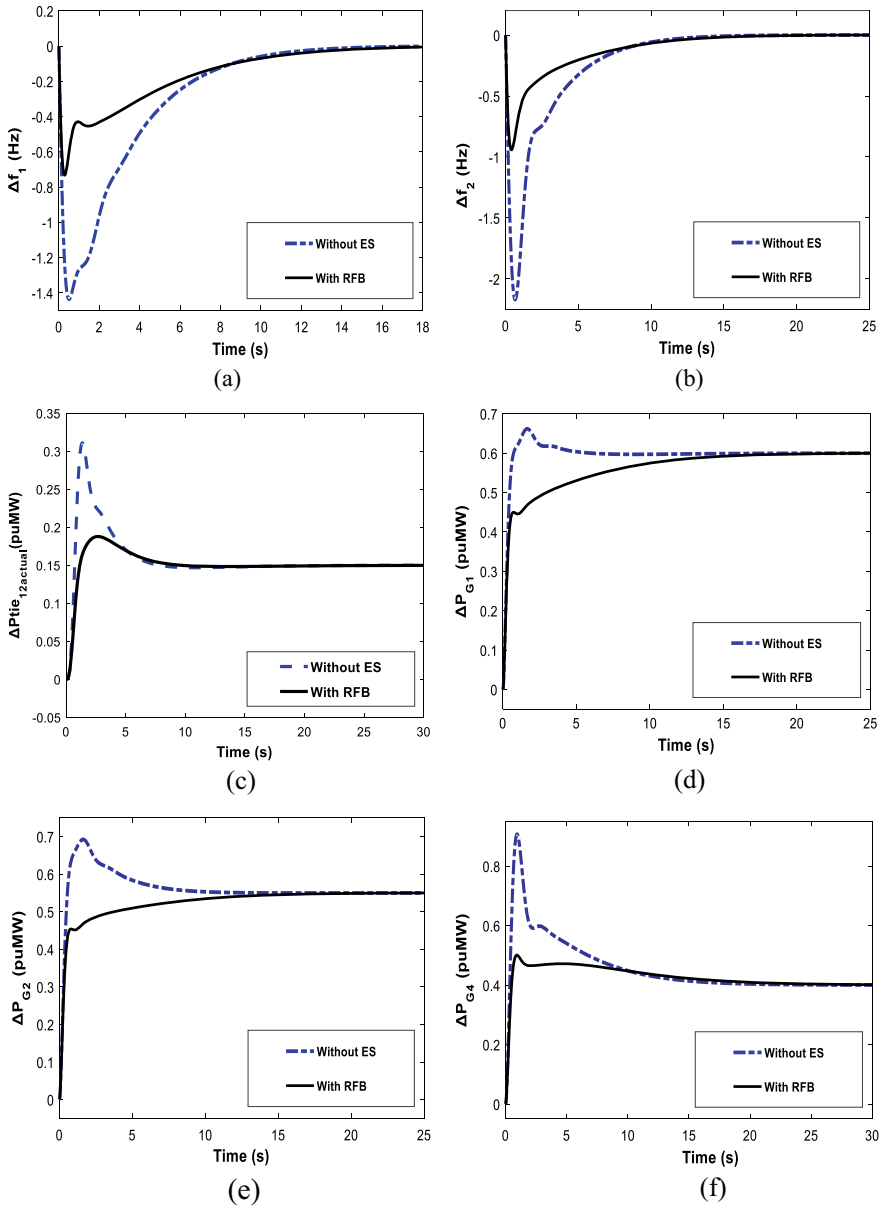


Fig. 3 Dynamic performance of OC on Thermal-GTPP-Diesel-GTPP system without ES and with RFB **a** Δf_1 , **b** Δf_2 , **c** $\Delta P_{tie12actual}$, **d** ΔP_{G1} , **e** ΔP_{G2} , and **f** ΔP_{G4}

5 Conclusion

The efficacy of ES device RFB on AGC performance enrichment of restructured power systems combining thermal, GTPP, and diesel units is studied in a deregulated electricity environment. The optimum control strategy is being utilized to conduct the simulations. The optimal controller's (OC) resiliency is demonstrated for a variety of market transactions. For various market transaction scenarios, the efficiency of OC has been proved as simulation results are smooth and consistent reactions with low settling time. Furthermore, RFB enhances overall performance when compared to a system without energy storage devices by assisting immediate power when load demand increases. The dynamic responsiveness associated with RFB was shown to be significantly superior to the system without the ES device in the study. It has been shown that AGC requirement has been satisfied by OC as in all possible market transaction scenarios the frequency of both areas settled to zero in steady state, as well as values of scheduled tie-line powers of GENCOs matched from simulated values derived under various situations. The simulation results showed that OC is efficient for different possible market transactions and has a minor impact on system performance.

References

1. Tasnin W, Saikia LC (2018) Performance comparison of several energy storage devices in deregulated AGC of a multi-area system incorporating geothermal power plant. *IET Renewab Power Gener* 12(7):761–772
2. Selvaraju RK, Somaskandan G (2016) Impact of energy storage units on load frequency control of deregulated power systems. *Energy J* 97:214–228
3. Donde V, Pai MA, Hiskens IA (2001) Simulation and optimization in an AGC system after deregulation. *IEEE Trans Power Syst* 16(3):481–489
4. Arya Y, Kumar N, Gupta SK (2017) Optimal automatic generation control of two- area power systems with energy storage units under deregulated environment. *Renew Sustain Energy Rev* 9(6):064105
5. Saha A, Saikia LC (2017) Utilisation of ultra-capacitor in load frequency control under restructured STPP-thermal power systems using WOA optimised PIDN- FOPD controller. *IET Gener Transm Distrib* 11(13):3318–3331
6. Saha D, Saikia LC (2017) Performance of FACTS and energy storage devices in a multi area wind-hydro-thermal system employed with SFS optimized I-PDF controller. *J Renew Sustain Energy* 9(2):024103
7. Ibraheem, KP, Hasan N, Singh Y (2012) Optimal automatic generation control of interconnected power system with asynchronous tie-lines under deregulated environment. *Electr Power Compon Syst* 40(10):1208–1228
8. Arya Y, Kumar N (2016) AGC of a multi-area multi-source hydrothermal power system interconnected via AC/DC parallel links under deregulated environment. *Int J Electr Power Energy Syst* 75:127–138
9. Arya Y (2019) Effect of energy storage systems on automatic generation control of interconnected traditional and restructured energy systems. *Int J Energy Res* 43(12):6475–6493
10. Tyagi B, Srivastava SC (2005) A LQG based load frequency controller in a competitive electricity environment. *Int J Emerg Electr* 2(2)

11. Arya Y, Kumar N (2016) Optimal AGC with redox flow batteries in multi-area restructured power systems. *Int J Eng Sci Technol* 19(3):1145–1159
12. Sharma M, Dhundhara S, Arya Y, Prakash S (2021) Frequency stabilization in deregulated energy system using coordinated operation of fuzzy controller and redox flow battery. *Int J Energy Res* 45(5):7457–7475
13. Dhundhara S, Verma YP (2020) Grid frequency enhancement using coordinated action of wind unit with redox flow battery in a deregulated electricity market. *Int Trans Electr Energy Syst* 30(3)
14. Alotto P, Guarnieri M, Moro F (2014) Redox flow batteries for the storage of renewable energy: a review. *Renewab Sustainab Energy Rev* 29:325–335
15. Arya Y (2017) AGC performance enrichment of multi-source hydrothermal gas power systems using new optimized FOFPID controller and redox flow batteries. *Energy* 127:704–715
16. Hakimuddin N, Nasiruddin I, Bhatti TS, Arya Y (2020) Optimal automatic generation control with hydro, thermal, gas, and wind power plants in 2-area interconnected power system. *Electr Power Compon Syst* 48(6–7):558–571
17. Dahiya P, Mukhija P, Saxena AR, Arya Y (2016) Comparative performance investigation of optimal controller for AGC of electric power generating systems. *Automatika* 57(4):902–921

Real-Time Price-Based Optimal Energy Mix in Smart Distribution Network



Raju Wagle, Pawan Sharma, Charu Sharma, and Mohammad Amin

1 Introduction

Global awareness about environmental concerns, economic challenges, and increased energy demand have encouraged power system operators to incorporate more renewable energy [1] in the power system. The transmission system operators (TSOs) focus more on reduced inertia [2] due to the large volume of DERs interfaced through a static conversion system. However, the distribution system operators (DSOs) have problems like terminal voltage rise, reverse power flow, thermal over the limit of cables, [3] and obtaining an optimal energy balance in the network. The technical impacts due to the increased integration of distributed energy resources (DERs) at distribution network can be addressed by the transition of conventional operational and management approaches to the smart distribution network (SDN) paradigm [4].

During recent years substantial explorations have been accompanied on the topics of optimal operation of SDN, and diverse techniques have been demonstrated in the literature [5–8]. Most of the previous studies in SDN cover identifying optimal allocation and optimal sizing of DERs [9–12]. In [9], the authors present a robust approach using Jaya Algorithm for optimal placement of DERs in radial distribution

R. Wagle (✉) · P. Sharma · C. Sharma
UiT The Arctic University of Norway, Lodve Langesgate 2, 8514 Narvik, Norway
e-mail: raju.wagle@uit.no

P. Sharma
e-mail: pawan.sharma@uit.no

C. Sharma
e-mail: charu.sharma@uit.no

M. Amin
Department of Electric Power Engineering, Faculty of Information Technology and Electrical Engineering, NTNU Gløshaugen, 7491 Trondheim, Norway
e-mail: mohammad.amin@ntnu.no

networks to minimize the load demand. The optimum penetration level of augmented distributed generations is studied in [10]. In [11], allocation of fixed and portable energy storage devices (ESDs) is proposed to mitigate the uncertainties of critical DERs for alleviating voltage unbalance in the system. In [12], the uncertainty of multiple RESs is handled in SDN by considering total energy procurement cost as an objective function.

Most of the research in smart distribution networks covers congestion management [13, 14] loss payment minimization [15]. In [13], scheduling flexible energy resources of prosumers for reducing network congestion is done considering iterative distribution locational marginal price. Author [14] demonstrates implementation of the market-based approach in handling the congestion in the distribution network. The authors in [15] propose an appropriate way for reducing the losses payment considering a day-ahead energy market price in a distribution system with energy storage systems and demand response.

In [16], the author presents economic environmental energy-saving day-ahead scheduling problem of power systems considering wind generation (WG) and demand response (DR) using multi-objective dynamic optimal power flow (MDOPF) to minimize fuel cost, carbon emission, and active power losses. An attempt to reduce the operating cost based on the local transactive market is analyzed for a radial distribution system in [17].

In this paper, an optimal energy mix is obtained based on the day-ahead RTP by formulating a mixed integer linear program to compute the optimization problem. The main contribution made by the authors in this article are:

1. Develop a MILP to compute the optimization problem for a system with distributed generations (PVs and Wind), energy storage, and Microhydro Plants (MHPs).
2. Obtain the optimal scheduling of charging and discharging of ESSs and generation schedule of MHPs based on real-time pricing.
3. The efficacy of the proposed method is validated by achieving the energy balance by proper scheduling and reducing the power exchange from the upstream network.

Section 2 describes the problem formulation approaches, especially the mathematical modeling of system components, objective functions, and operating constraints. Simulation Requirements, system data, cases, obtained results after simulation, and discussion is described in Sect. 3. Finally, the last section concludes the main contribution of the work done in this analysis.

2 Problem Formulation

In this paper, an approach for optimal energy mix among PVs, WTs, ESS, MHP, and power exchanged from the upstream network are explored. In this section, for modeling of the system components, especially ESS and MHP, the main objective function to be fulfilled and corresponding operating constraints are discussed.

2.1 Modeling of System Components

In this subsection, the mathematical modeling of the system under consideration is described. Mainly, the mathematical modeling of controllable sources energy storage system and MHP is highlighted. PV and Wind are considered as unregulated renewable energy sources for this analysis and hence a detailed description of them is left behind.

2.1.1 Modeling of ESS

ESS is modeled based on the linearized power output [15] between $\pm P_{rated}^{ESS}$. where P_{rated}^{ESS} is the rated power output of ESS. The power output from the ESS for i number of setpoint is given by

$$P_{out}^{ESS}(i) = \frac{P_{rated}^{ESS} - (-P_{rated}^{ESS})}{N_{setpoint}^{ESS} - 1} * (i - 1) - P_{rated}^{ESS}, \text{ for } i = 1, 2, \dots, N_{setpoint}^{ESS} \quad (1)$$

where, $P_{out}^{ESS}(i)$ is the output power from ESS at i^{th} setpoint. P_{rated}^{ESS} is the rated power of ESS. $N_{setpoint}^{ESS}$ is the number of setpoint level of ESS. The ESS can operate at one setpoint at a time. This defines a constraint for the ESS setpoint.

Relative change of ESS state of charge (SOC) level due to ESS operation at a time is defined as the ratio of power output at that time to rated energy of the ESS E_{rated}^{ESS} . The relative change in SOC is given by Eq. (2).

$$\Delta SOC_t^{ESS} = \pm \frac{t}{E_{rated}^{ESS}} * P_{out}^{ESS}(t), \quad t \in T \quad (2)$$

The SOC of ESS at a particular time is the sum of relative change in SOC and the SOC of ESS at an instant prior to that particular instant. Equation (3)

$$SOC_t^{ESS} = SOC_{t-1}^{ESS} + \Delta SOC_t^{ESS} \quad (3)$$

the state of charge of ESS is limited to minimum and maximum values defined before the optimization process. This will define a constraint for the operation of ESS.

$$SOC_{minimum}^{ESS} \leq SOC_t^{ESS} \leq SOC_{maximum}^{ESS} \quad (4)$$

The charging and discharging power can be obtained by considering the output power from the ESS. If the power output is less than zero, then the charging action is performed in ESS, while if the power output is higher than one, then the discharging action is performed. Equations (5) and (6) are the conditions for the ESS to be in charging or discharging mode based on the SOC and power output from ESS.

Table 1 Technical characteristics and operational limit of ESS [15]

Parameter	Value	Unit
P_{rated}^{ESS}	0.6	MW
E_{rated}^{ESS}	1	MWh
$SOC_{initial}^{ESS}$	0.2	–
$SOC_{minimum}^{ESS}$	0.1	–
$SOC_{maximum}^{ESS}$	0.9	–
$N_{setpoint}^{ESS}$	4	–

$$P_{Charging}^{ESS} = P_{out}^{ESS}, \text{ if } P_{out}^{ESS} < 0 \tag{5}$$

$$P_{discharging}^{ESS} = P_{out}^{ESS}, \text{ if } P_{out}^{ESS} > 0 \tag{6}$$

Table 1 lists out the technical and operational limits of ESS considered in this analysis.

2.1.2 Modeling of MHP

MHPs are small hydropower plants [18], especially designed to fulfill the local power demand in a small community. Normally, the MHPs are only operated when they are to fulfill the minimum amount of load demand to make the operation economical. In this analysis, MHP is designed as linearized power output between the minimum and maximum power outputs for a specific level of operational setpoints. Equation (7) gives the linearized output of the power output from MHP.

$$P^{MHP}(i) = \frac{P_{max}^{MHP} - P_{min}^{MHP}}{N_{setpoint}^{MHP} - 1} * (i - 1) + P_{min}^{MHP}, \quad i = 1, 2, \dots, N_{setpoint}^{MHP} \tag{7}$$

To optimize the power output from MHP, a new binary optimization variable is y introduced. y check the suitable power output from MHP for the economic operation of MHP. The power output of MHP is given by Eq. (8).

$$P_{out}^{MHP} = \sum y * P^{MHP} \tag{8}$$

However, this power output P_{out}^{MHP} is desired to be operated at a range of minimum and maximum set values. This defines two operational constraints Eqs. (9) and (10).

$$P_{out}^{MHP} \geq P_{minimum}^{MHP} \tag{9}$$

$$P_{out}^{MHP} \leq P_{maximum}^{MHP} \tag{10}$$

Table 2 Technical characteristics and operational limit of MHP [18]

Parameter	Value	Unit
$\rho_{\text{maximum}}^{\text{MHP}}$	0.8	MW
$\rho_{\text{minimum}}^{\text{MHP}}$	0.2	MW
<i>Fixed cost</i>	0.0315	Eur/MW
<i>Operational Cost</i> $_{\text{limit}}^{\text{MHP}}$	0.5	Eur/day
$N_{\text{setpoint}}^{\text{MHP}}$	4	–

MHP is designed to operate at a limited operational cost due to the limitation of operating manpower in remote isolated areas and to minimize the losses incurred during the operation. Equation (11) gives the expression for operation cost at a particular setpoint of operation. Fixed cost in the expression is a factor that is required just to operate the MHPs.

$$\text{Operational Cost}_{\text{setpoint}}^{\text{MHP}} = \text{Fixed Cost} * P_{\text{out}}^{\text{MHP}}(i), i = 1, 2, \dots, N_{\text{setpoint}}^{\text{MHP}} \quad (11)$$

The total operational cost given by Eq. (12) is defined as the cost of operation for a particular level of operation of MHP

$$\text{Total Operational cost} = \sum y. * \text{Operational Cost}_{\text{setpoint}}^{\text{MHP}} \quad (12)$$

where y is the binary optimization variable to check the level of the setpoint of operation of MHP. The total operational cost is limited by a constraint to manage the economics of the MHP operation. Equation (13) gives the constraint to limit the operational cost of MHP.

$$\text{Total Operational cost} \leq \text{Operational Cost}_{\text{limit}}^{\text{MHP}} \quad (13)$$

Table 2 lists out the technical and operational limits of MHP considered in this analysis.

2.1.3 Modeling of Power Balance

In order to balance the supply and demand of energy in the SDN, the following power flow constraints and operational limits [15] should be satisfied. The fundamental concept behind this is to fulfill the power demand by power production from available different sources. Equations (14) and (15) give the power balance equation for the study.

Table 3 Power import and export limit of SDN

Parameter	Value	Unit
P_{import}	0.8	MW
P_{export}	0.8	MW

$$PT_t + P_t^{wind} + P_t^{PV} - PD_t + P_t^{ESS} + P_t^{MHP} = 0 \quad (14)$$

$$QT_t + Q_t^{wind} + Q_t^{PV} - QD_t + Q_t^{MHP} = 0 \quad (15)$$

where

PT_t and QT_t are the net active and reactive powers transferred from the upstream network. P_t^{PV} , P_t^{wind} , PD_t , P_t^{ch} , P_t^{dch} , P_t^{MHP} , Q_t^{wind} , QD_t , and Q_t^{MHP} are the active and reactive power generation and demand from PV, wind, battery, load, and MHP, respectively. However, in this analysis, only active power balance is considered as a part of optimization approach.

To use the DERs as a first priority source of a generation when the power import and export from the upstream network is limited to some power import and power export limit. The power will be exported from the SDN if their excess power generation from DERs and will be imported from the upstream network if there is local generation that may not fulfill the load demand. These imports and exports are defined as the power exchange.

$$PT_t = P_t^{wind} + P_t^{PV} - PD_t + P_t^{ESS} + P_t^{MHP} \quad (16)$$

The power transferred can be defined as import or export depending on the following cases

$$PT = \begin{cases} P_{import} & \text{if } PT < 0 \\ P_{export} & \text{if } PT > 0 \end{cases} \quad (17)$$

The import and export limits are given by Eqs. (18) and (19) (Table 3)

$$P_{export} \leq PT_{limit} \quad (18)$$

$$P_{import} \geq -PT_{limit} \quad (19)$$

2.2 Objective Function

The main objective of the proposed method is to provide the optimal energy mix for DERs, especially ESS and controllable MHP in order to maximize the profit from optimal energy sharing from different energy sources. The following optimization problem is solved:

$$Profit = \sum_{t \in \Omega_T} EC_t \quad (20)$$

$$EC_t = \sum_{i \in n} [P_i^{ESS} - P_i^D] * poolprice_i + \sum_{i \in n} [P_i^{MHP} + P_i^{wind} + P_i^{PV}] * average(poolprice) \quad (21)$$

where *Profit* is the total profit obtained while balancing the energy supply and demand and EC_t is the hourly cost of energy at time t . The hourly energy price for wind, PV, and power from the MHP is considered the average of the pool price. Proper allocation of energy from ESS controllable MHP will increase the profit from the total cost paid for the energy balance.

2.3 Operating Constraints

Some of the operating constraints that have to be fulfilled are described below. Constraints are Eqs. (4), (9), (10), (13), (18), and (19).

3 Simulation Results and Discussion

3.1 Overall Methodology

The block diagram shown in Fig. 1 describes the overall methodology of obtaining optimal energy mix in SDN. Initially, the load data and the generated data from DERs (PV and Wind) are measured/predicted for a period of 24 hour and stored in a database. Mathematical models of ESS and MHP are developed with their operational conditionals and constraints. Then the processed data and the models are fed to an optimization block. The optimization block performs optimization based on the objective function described in Eq. (21). The optimization process is executed until the optimal solution fulfilling all the requirements described in Sect. 2.3. Finally, an appropriate energy management system is achieved for optimal energy mix in SDN by scheduling the operation of ESS and MHPs in an optimal fashion.

3.2 System Data

Figure 2 shows the layout of the considered system. The distribution network considered is a network with 30 numbers of households. For now, the network configuration and network parameters are not considered in this analysis. The load data in the network are measured and accumulated on an hourly basis and fed into the optimization

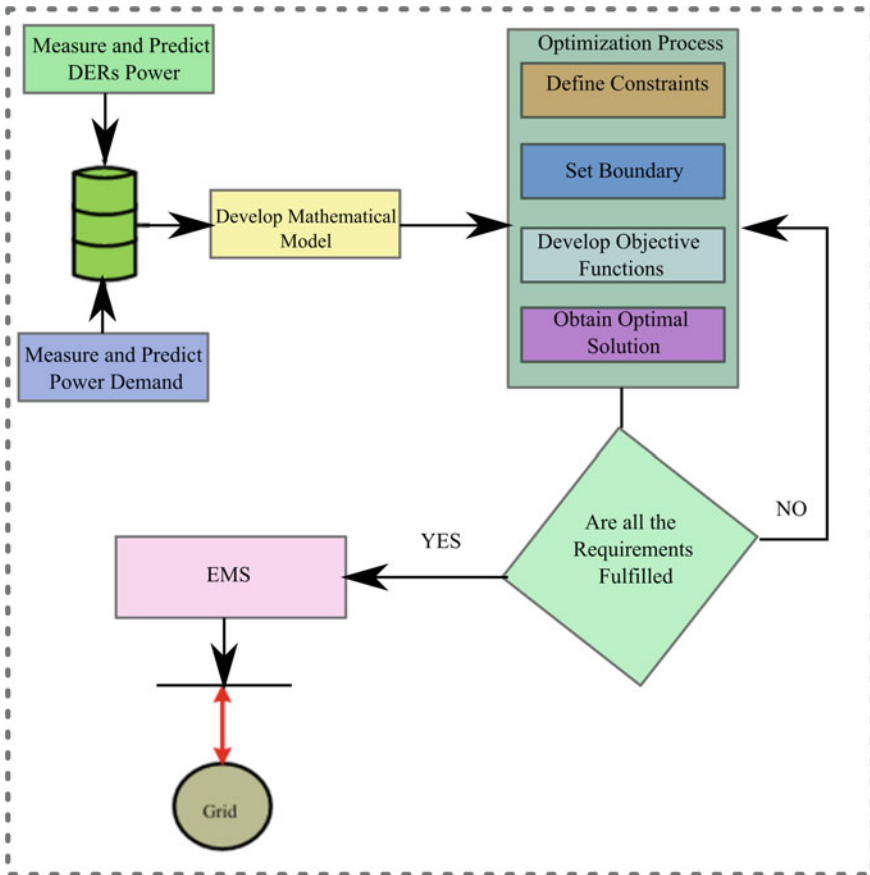


Fig. 1 The overall process of obtaining optimal energy mix

model as a single load profile. Table 4 shows the data [12] for load demand, forecasted PV, and wind generation. The electricity price of the network is taken from [22] and is shown together with hourly load and generation profile of PV and wind in Fig. 3. The energy price from the DERs (PV and wind) are taken as the average of the pool price to maintain constancy in the price paid to the prosumers [21].

3.3 Simulation Studies

The proposed optimization algorithm is implemented in a MATLAB environment running on Intel (R) Core (TM) i5-8265U CPU@1.60GHz 8GB ram and 64-bit operating system. An optimization is performed for the given system data described in the previous section. Figure 4 shows the state of charge and charging and discharging

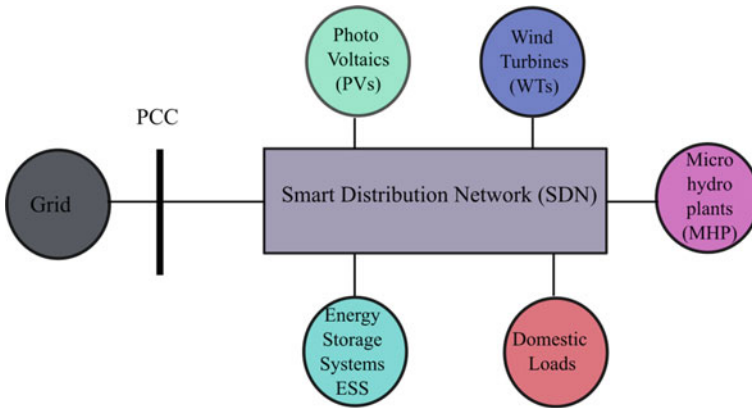


Fig. 2 System layout of SDN distribution network

Table 4 Forecasted hourly demand, the output power of wind turbine, and PV

Hour of day	Total load demand[15]	P_t^{Wind} [19]	P_t^{PV} [20]
1	1.0785	0.3260	0
2	1.0110	0.3520	0
3	0.9360	0.3544	0
4	0.8820	0.3520	0
5	0.8730	0.3524	0
6	0.8820	0.3524	0
7	0.9000	0.3812	0
8	0.9495	0.3948	0.008
9	0.9660	0.3940	0.050
10	1.0950	0.3848	0.125
11	1.1895	0.4000	0.418
12	1.2660	0.3916	0.511
13	1.3125	0.3780	0.516
14	1.3020	0.3104	0.475
15	1.2765	0.2692	0.418
16	1.3125	0.2364	0.254
17	1.4265	0.1948	0.050
18	1.5000	0.1864	0
19	1.4715	0.1492	0
20	1.4229	0.1356	0
21	1.3500	0.1356	0
22	1.3125	0.1488	0
23	1.2015	0.1572	0
24	1.0830	0.1356	0

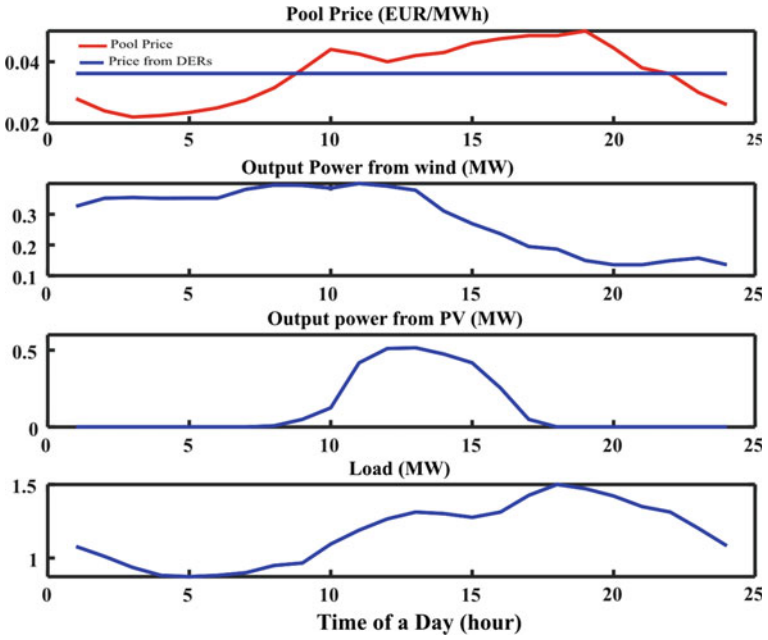


Fig. 3 Day-ahead tariff from Nord Pool [22], output power from wind, PV, and variation in load

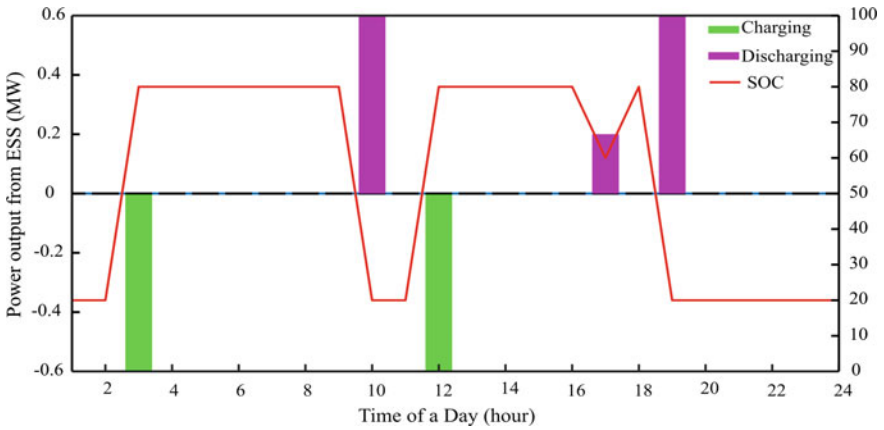


Fig. 4 State of charge of ESS

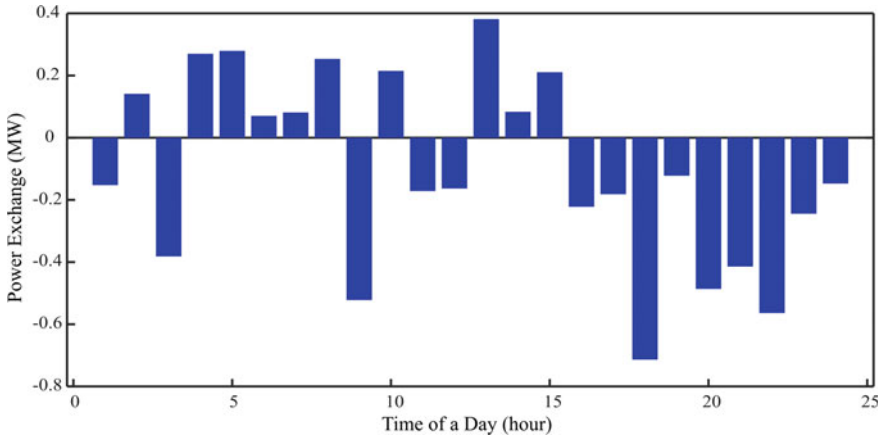


Fig. 5 Power exchange profile

profile of ESS. ESS is charged when the energy price from the upstream network is lower and discharged to supply the energy at a higher price.

Similarly, Fig. 5 shows the power exchange profile between the SDN and the upstream network. Positive values of power exchange indicate that power is exported to the upstream network. In contrast, the negative value indicates that the power is imported to the SDN to balance the energy demand. If we analyze the power profile, then SDN tries to export the power when energy price from the upstream network is higher than the energy price from the available DERs, ESS, and MHPs.

Figure 6 shows the power production schedule from the MHP. MHP operates first to fulfill the local demands first. Two case study figures are presented here to show how the generation profile changes with the change in the price of the power production from the MHPs. When the price is lower for MHPs, they operate for more time than when the price is higher.

To check the effectiveness of the proposed energy mix methodologies following two cases are studied. In the first analysis, the energy price from DERs is considered the average of the energy price from the upstream network. The total power export from SDN to the upstream network is evaluated in this condition. A similar analysis with reduced energy price from DERs (20 % below the average energy price in this case) is performed, and the total power export from SDN is obtained. Table 5 shows the comparison of power export from the SDN to the upstream network in these two scenarios. When the energy price from the available DERs is lower, DERs will first fulfill the energy demand for loads and then start producing more power to export energy to the upstream network. From Table 5, it is also observed that energy export at a reduced price is more.

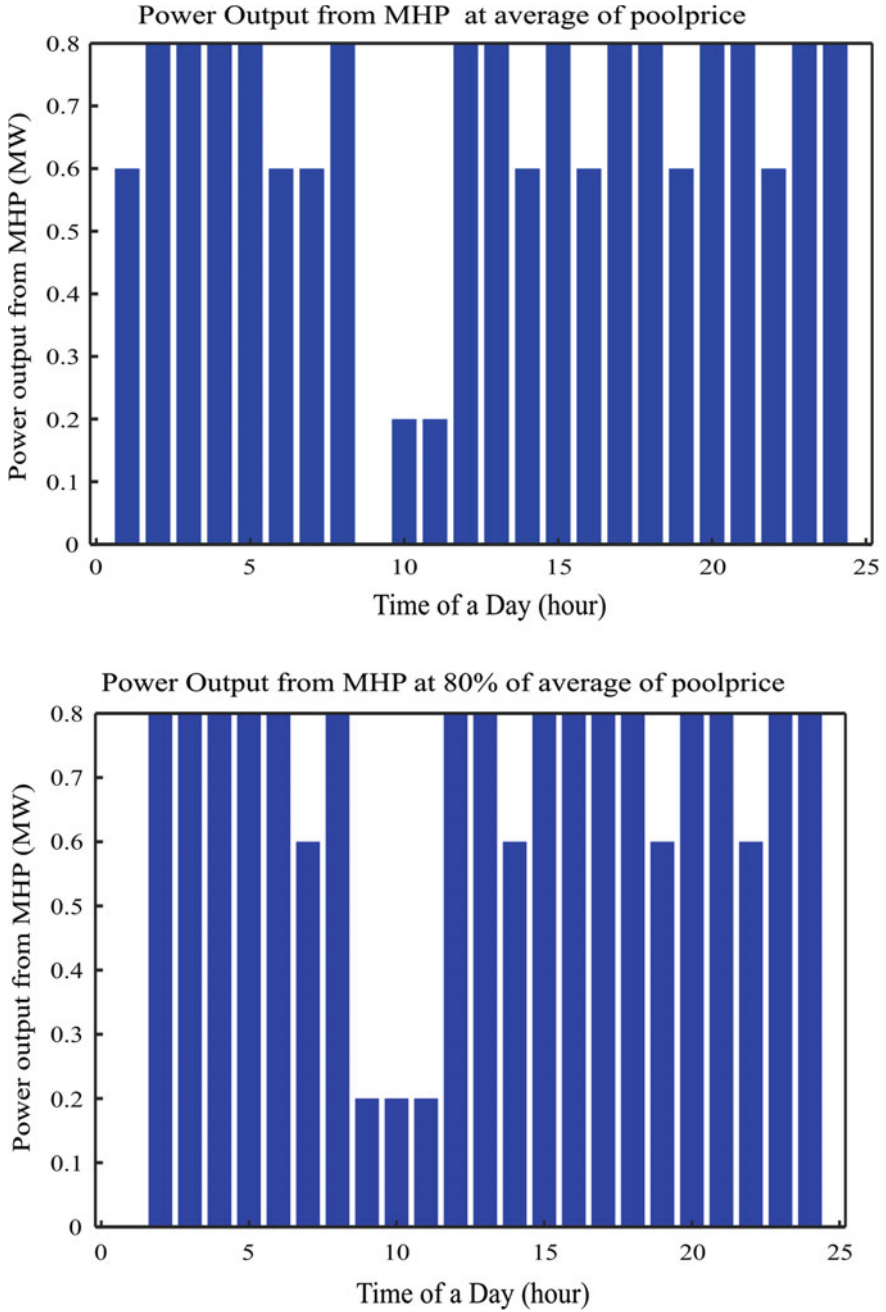


Fig. 6 Power output from MHP

Table 5 Energy export from SDN

Energy price from DERs	Energy export	Unit
At average of pool price	1.9857	MWh
At 20% below of average of pool price	2.1857	MWh

3.4 Discussion

From the analysis, we observed that the load demand is fulfilled first from DERs as the energy price from DERs is lower than that of the upstream network. With the increase in generation from DERs, the power exchanged is reduced. The charging of the ESS is performed when the energy price from the upstream stream is lower and is discharged to fulfill the load demand (not covered by DERs) when the pool price is higher. Similarly, MHPs operate in those instances when the energy price is lower than the energy price from the upstream network. The MHPs are only operated either to produce power at/above minimum setpoint value or to stop production for making the operation economical. Depending on the energy requirement, the MHPs are operated at different setpoints. However, MHPs also produce more energy when their operation makes the energy cheaper than buying from the upstream network.

4 Conclusion

This paper presents the optimal energy mix in a smart distribution network considering the day-ahead real-time energy price of the network. Optimal scheduling of charging and discharging of the ESS and local generation MHP to maximize the profit by optimal scheduling of ESS and MHP in the distribution network is observed. This method can achieve the energy balance by utilizing energy sources that can produce energy at a lower price. Also, we will achieve cost-effective management of energy resources in a smart distribution network. The distribution system operator can plan for scheduling generation from DERs and order the deficit amount of energy from the upstream network in an optimal way using this approach. Future research in this orientation can be the implementation of regulated DERs considering network configuration and parameters of the SDN.

Acknowledgements The authors are very grateful to the Arctic Centre for Sustainable Energy (ARC) (project number 740108), UiT The Arctic University of Norway, Norway, for providing an environment to do this work.

References

1. Chen S, Liu P, Li Z (2020) Low carbon transition pathway of the power sector high penetration of renewable energy. *Renew Sustain Energy Rev* 130:109985. <https://doi.org/10.1016/j.rser.2020.109985>
2. Tamrakar U, Shrestha D, Maharjan M, Bhattarai BP, Hansen TM, Tonkoski R (2017) Virtual inertia: current trends and future directions. *Appl Sci* 7(7):1–29. <https://doi.org/10.3390/app7070654>
3. Anastasiadis AG, Kondylis GP, Vokas GA (2019) Effect of augmented distributed generation in distribution networks. *Energy Rep* 6:177–187. <https://doi.org/10.1016/j.egy.2019.10.036>
4. Ghiani E, Pisano G (2018) Impact of renewable energy sources and energy storage technologies on the operation and planning of smart distribution networks. In: *Operation of distributed energy resources in smart distribution networks*, pp 25–48. Academic Press, chap. 2. <https://doi.org/10.1016/B978-0-12-814891-4.00002-3>
5. IRENA (2019) Innovation landscape brief: future role of distribution system operators. International Renewable Energy Agency, Abu Dhabi
6. Tan S, Xu JX, Panda SK (2013) Optimization of distribution network incorporating distributed generators: an integrated approach. *IEEE Trans Power Syst* 28(3):2421–2432. <https://doi.org/10.1109/TPWRS.2013.2253564>
7. Srivastava A et al (2019) A DSO support framework for assessment of future-readiness of distribution systems: technical, market, and policy perspectives. In: *25th International conference on electricity distribution*, pp 3–6. <https://doi.org/10.34890/832>
8. Alam MS, Arefifar SA (2019) Energy management in power distribution systems: review, classification, limitations and challenges. *IEEE Access* 7:92979–93001. <https://doi.org/10.1109/ACCESS.2019.2927303>
9. Kumawat M et al (2020) Jaya algorithm based optimal allocation of distributed energy resources. In: *Intelligent computing techniques for smart energy systems*, pp 805–814. Springer, Singapore. https://doi.org/10.1007/978-981-15-0214-9_85
10. Anastasiadis AG, Kondylis GP, Vokas GA (2019) Effect of augmented distributed generation in distribution networks. *Energy Rep* 6:177–187. <https://doi.org/10.1016/j.egy.2019.10.036>
11. Shahidehpour M et al (2020) Optimal energy storage allocation for mitigating the unbalance in active distribution network via uncertainty quantification. *IEEE Trans Sustain Energy*. <https://doi.org/10.1109/TSTE.2020.2992960>
12. Hooshmand E, Rabiee A (2019) Robust model for optimal allocation of renewable energy sources, energy storage systems and demand response in distribution systems via information gap decision theory. *IET Gener Transm Distrib* 13(4):511–520. <https://doi.org/10.1049/iet-gtd.2018.5671>
13. Hu J, Wu J, Ai X, Liu N (2020) Coordinated energy management of prosumers in a distribution system considering network congestion. *IEEE Trans Smart Grid* 3053:1–1. <https://doi.org/10.1109/TSG.2020.3010260>
14. Fotouhi Ghazvini MA et al (2019) Congestion management in active distribution networks through demand response implementation. *Sustain Energy Grids Netw* 17:100185. <https://doi.org/10.1016/j.segan.2018.100185>
15. Soroudi A, Siano P, Keane A (2016) Optimal DR and ESS scheduling for distribution losses payments minimization under electricity price uncertainty. *IEEE Trans Smart Grid* 7(1):261–272. <https://doi.org/10.1109/TSG.2015.2453017>
16. Ma R, Li X, Luo Y, Wu X, Jiang F (2019) Multi-objective dynamic optimal power flow of wind integrated power systems considering demand response. *CSEE J Power Energy Syst* 5(4):466–473. <https://doi.org/10.17775/CSEEJPES.2017.00280>
17. Haghifam S, Zare K, Abapour M, Munoz Delgado G, Contreras J (2020) A stackelberg game-based approach for transactive energy management in smart distribution networks. *Energies* 13(14):3621. <https://doi.org/10.3390/en13143621>
18. Harvey A (1993) *Micro-hydro design manual : a guide to small-scale water power schemes*. Intermediate Technology Publications, London

19. Soroudi A, Rabiee A, Keane A (2017) Information gap decision theory approach to deal with wind power uncertainty in unit commitment. *Electr Power Syst Res* 145:137–148. <https://doi.org/10.1016/j.epsr.2017.01.001>
20. Chen C, Duan S, Cai T et al (2011) Smart energy management system for optimal microgrid economic operation. *IET Renew Power Gener* 5(3):258–267. <https://doi.org/10.1049/iet-rpg.2010.0052>
21. Gabash A, Li P (2012) Active-reactive optimal power flow in distribution networks with embedded generation and battery storage. *IEEE Trans Power Syst* 27(4):2026–2035. <https://doi.org/10.1109/TPWRS.2012.2187315>
22. Day-ahead Price, NordPool (2020) <https://www.nordpoolgroup.com/Market-data1/Dayahead/Area-Prices/ALL1/Hourly/?view=table>

Path Planning of Quadrotor Using A* and LQR



Ritika Thusoo, Sheilza Jain, and Sakshi Bangia

1 Introduction

Unmanned Aerial Vehicles (UAVs) are aerial robots which can be controlled autonomously or remotely by a pilot at the ground station. The UAVs can be classified as rotor-type or fixed wing type according to their wing type [1]. Multirotor such as Quadrotors are categorized as rotor type UAVs. Hexacopter and Octacopter are also rotor-type UAVs. The Quadrotors have gained popularity in recent years as they are employed for aerial mapping and surveying, post-disaster administration, examination of crops, medicine delivery [2], border patrolling and surveillance. Many universities and companies are working on different types of UAVs to make our lives better, like Amazon is working on 30 min aerial delivery using drones known as Amazon Prime Air [3]. Quadrotors can take-off without a runway and land in uncertain terrains. Simple design and ease of manufacturing are some other features of Quadrotors.

Control and Path planning are two very important problems of any UAV. The control of Quadrotor is based on designing a control mechanism which will help it to remain in air and move from one place to another without crashing. There are various types of control techniques mentioned in the literature. A non-linear control law is applied to control the designed Quadrotor model. Equations known as Newton–Euler equations are applied to get the dynamic model of Quadrotor. Backstepping control law is intended to control the position (translational motion) and attitude angles (roll, pitch and yaw angles) which are responsible for the motion of Quadrotor. The method uses Lyapunov's theory of stability to obtain a stable system of Quadrotor [4]. To overcome any external disturbances that might affect the stability of the quadrotor system a new nonlinear robust controller is determined

R. Thusoo (✉) · S. Jain · S. Bangia
Department of Electronics Engineering, J.C. Bose UST, YMCA, Faridabad, India
e-mail: ritikathusoo@gmail.com

known as saturation integral backstepping control (SIBC) [5]. A cascade controller *P-PID* is executed to achieve stability in indoor and outdoor flights. The designed controller was tested on a real-mode and the desired flying performance was achieved [6].

The Path planning problem involves designing an algorithm which enables the Quadrotor to reach from one source to destination without crashing into any obstacles [7]. The trajectories followed by the Quadrotors must be smooth and dynamic. Path planning algorithm can be categorized as: Graph-search method and sampling-based methods. Algorithms, such as Dijkstra, D star (D^*) algorithm, and A star (A^*) algorithm, use graphs to seek out a collision-free shortest path in two-dimensional space. These methods provide an optimal solution with increased computational effort. They are useful when the map size is less whereas for searching in maps with higher size, Sampling-based methods are used [8].

A survey was done on the various path following methods which focused primarily on Quadrotors. The techniques used on the Quadrotor model were the Backstepping control algorithm and Feedback Linearization method, and Non-Linear Guidance Law (NLGL) and Carrot-Chase algorithm. The efficiency of these techniques was tested on a Quadrotor system [9].

Quadrotor system dynamics are controlled using PID and LQR technique. The path planning algorithm used to control the system is A star and the algorithm used to track a defined path is done using the LQR Algorithm [10].

This paper is focused on the path planning of a Quadrotor model which is simulated in a Simulink model. The control mechanism implemented for the Quadrotor is the Backstepping control technique which is mentioned in Sect. 2. The path planning implementation on the system is discussed in the 3rd section. The results and discussion are mentioned in Sect. 4 whereas Sect. 5 talks about the conclusion of this paper and its future scope.

2 Backstepping Control of Quadrotor

Quadrotor has four equidistant rotors attached on all the edges of a 'X' frame. The Flight controller (FC) such as PixHawk FC, Naza FC, KK2.5.5 and microcontroller-based FC (Arduino or Raspberry Pi micro controller) is placed at the center of the Quadrotor Frame. The frame material can be plastic, carbon fiber or epoxy glass. The dynamics of the Quadrotor can be simulated using software like MATLAB and Simulink. The Newton–Euler equation can be used to design a Simulink model of the Quadrotor. Figure 1 shows the diagram of the Quadrotor Frame in 'X' configuration [11]. The other configuration that can be used to design a Quadrotor frame is '+' configuration. The pair of rotors 1 and 3, rotate in the right-handed direction and the pair of rotors 2 and 4 rotates in the left-handed direction. A Brushless DC (BLDC) motor helps the four rotors to generate adequate thrust for lift-off. The thrust produced by each motor is depicted as, F_1 , F_2 , F_3 and F_4 in Fig. 1.

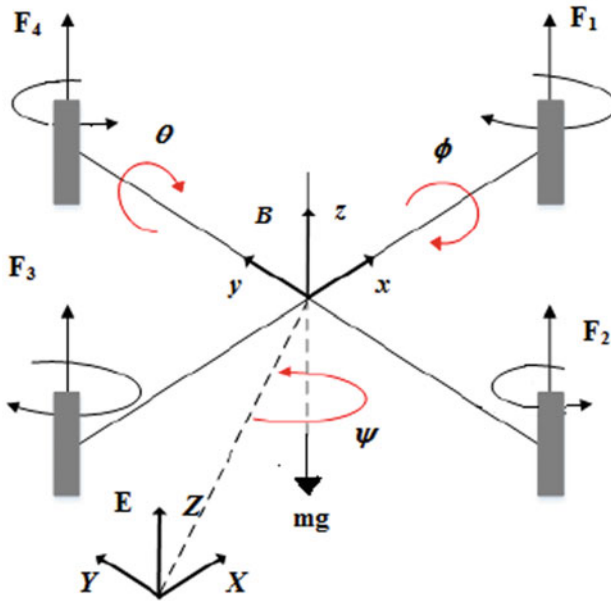


Fig. 1 Diagram of quadrotor

Quadrotor system is a rigid body [12] which is described in the inertial frame(E) with respect to Earth and body frame(B). The body frame is presumed to be affixed to the frame of the Quadrotor system [13]. This is represented in Fig. 1.

The rotational angles of Quadrotor are roll angle, pitch angle and yaw angle. They are denoted by the symbols as: φ (phi) for roll angle, θ (theta) for pitch angle and ψ (psi) for yaw angle. The motion in x, y and z directions in 3D space is known as translational motion. Newton–Euler equations can be used to denote the equations of motion for a Quadrotor system, and they can be represented by the following set of Eqs. (1)–(6):

$$\theta'' I_{xx} = (-F_1 - F_2 + F_3 + F_4) * d_{arm} \tag{1}$$

$$\varphi'' I_{yy} = (-F_1 + F_2 + F_3 - F_4) * d_{arm} \tag{2}$$

$$\psi'' I_{zz} = (T_{m1} - T_{m2} + T_{m3} - T_{m4}) * d_{arm} \tag{3}$$

$$x'' = \frac{1}{mass_{Quad}} * \sum_1^4 F_i [(\sin(\varphi) * \sin(\psi)) + (\cos(\varphi) * \cos(\psi) * \sin(\theta))] \tag{4}$$

$$y'' = \frac{1}{mass_{Quad}} * \sum_1^4 F_i [(\sin(\psi) * \sin(\theta) * \cos(\varphi)) - (\cos(\psi) * \sin(\varphi))] \quad (5)$$

$$z'' = (\frac{1}{mass_{Quad}} * \sum_1^4 F_i [\cos(\varphi) * \cos(\theta)]) - g \quad (6)$$

where F_i the thrust of the motors 1–4, d_{arm} denoted the Quadrotor arm length, T_m describes torque that will be generated by a BLDC motor. There are four motors that are attached at the end of each propeller. I_i signifies the moment of inertia with respect to each axis and $mass_{Quad}$ represents the Quadrotor mass.

In Eqs. (1)–(6), the system of equations derives equations for the following parameters: phi, theta, psi, x, y and z. These equations are further solved to obtain the Quadrotor model as designed in paper [4] which is taken as a reference. Based on these equations a Quadrotor model is designed in Simulink as shown in Fig. 2. The parameters depicted in this figure such as: X_d , Y_d , Z_d , Φ_{i_d} , θ_{i_d} and Ψ_{i_d} denote the desired input values of the parameters: x, y, and z (these describe the translational motion), and roll, pitch and yaw angles (these describe the rotational motion, also known as attitude).

The Simulink model for the Quadrotor system is divided into two parts. The inner subsystem and outer subsystem. In the inner system, the height (motion in z-direction) and rotational angles (or attitude angles) are controlled using PID control law. The PID controller gains are adjusted by means of an inbuilt feature of PID block in Simulink, known as PID Tuner. Since, the system displays non-linear characteristics, feedback linearization control technique can result in the elimination of beneficial nonlinearities. Subsequently, the backstepping control technique [14] has more flexibility than the feedback linearization method [15]. This is done by obtaining “Virtual controls” or “pseudo controls” [16] which act as the inputs for the inner subsystem. They are denoted by ϕ_{i_d} and θ_{i_d} which is the desired roll angle and desired pitch angle. The relation between ϕ_{i_d} and θ_{i_d} virtual inputs

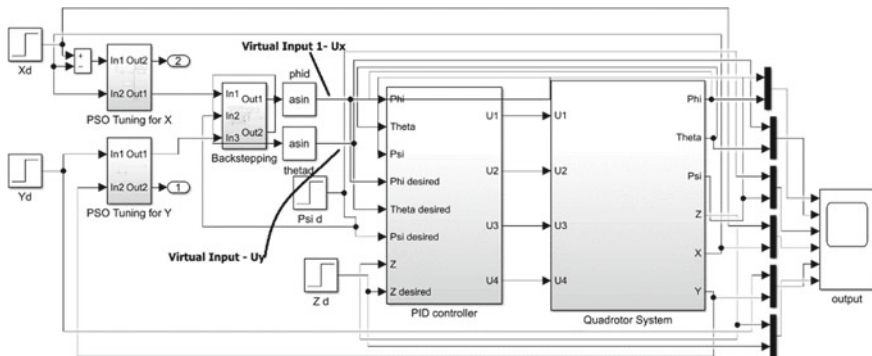


Fig. 2 Simulink model of quadrotor using backstepping control

U_x and U_y are given below in Eqs. (7) and (8) [4]. The virtual inputs for the inner subsystem are the outputs obtained for the outer subsystem.

$$\varphi^d = \arcsin((U_x * \sin(\psi^d)) - (U_y * \cos(\psi^d))) \quad (7)$$

$$\theta^d = \arcsin\left(\frac{((U_x * \cos(\psi^d)) + (U_y * \sin(\psi^d)))}{\cos(\varphi^d)}\right) \quad (8)$$

3 Path Planning of Quadrotor

The Quadrotor model designed in Sect. 2 mimics a physical Quadrotor system which uses the control technique to stabilize its motion once in flight. The system after successful take-off needs to move from one place to another. This can be done either manually by using a remote control or by automatically by a path planning algorithm code on-board where information of the environment may or may not be known to the Quadrotor system. The Quadrotor in Sect. 2 is assumed to have successfully taken-off and provide its current location to our path planning algorithms. There are numerous techniques mentioned in the literature for path planning. Two such algorithms are Astar search Algorithm and Linear Quadratic Regulator (LQR) algorithm.

A star

A Star search algorithm is an expansion of the Dijkstra technique that has a superior computational capability. It is a type of greedy algorithm [17]. It forms search tree diagram by using priority search to find the optimal solution. An evaluation function determines the cost of all the nodes to the destination node [18]. It is represented by Eq. (9) where $F(n)$ is the evaluation function. $G(n)$ is cost of the lowest cost from source S to destination N. $H(n)$ is the lowest cost between the current node under evaluation to destination. Among two adjacent nodes, the node that has the lowest cost is selected next and the current node is updated. The process is imitated until the shortest path to the target is obtained.

$$F(n) = G(n) + H(n) \quad (9)$$

The current location of the Quadrotor model is given as the starting point location of the A star Algorithm. The algorithm then searches the shortest path to the target in the map. Some obstacles are also considered in the map which test the algorithm for our designed systems.

Linear Quadratic Regulator (LQR) algorithm.

LQR-based path planning algorithm computes control u optimally. Control u is the command given to the system to change its direction angle to reach the destination

on a predefined path. The LQR algorithm is represented as shown in Eq. (10):

$$u = \left[\left(\sqrt{\left| \frac{d_b}{(d_b - d)} \right|} \right) * d + \sqrt{2 * \left(\sqrt{\left| \frac{d_b}{(d_b - d)} \right|} \right) + (q_{22} * v_d)} \right] \quad (10)$$

where d_b is the confined zone along the defined path and $V_d = v * \sin(\varphi - \theta)$ is the cross trail error velocity [19]. The matrix Q is given by

$$Q = \begin{bmatrix} q_{11} & q_{12} \\ q_{21} & q_{22} \end{bmatrix}$$

where $q_{12} = q_{21} = 0$ and $q_{11} = \left| \frac{d_b}{d_b - d} \right|$. The path planning performance can be varied by choosing appropriate d_b and q_{22} . A set of waypoints is given to the system and the current location of the quadrotor is given as the starting location of the quadrotor for the path planning algorithm.

4 Results and Discussion

First, a Simulink model of the Quadrotor system is designed. This model is developed using a set of equations that are derived using the concept of Newton–Euler equations of motion. The designed model is controlled for its six parameters namely, roll, pitch, yaw and translational motion along x, y and z axis. A technique known as the Backstepping control is used to obtain the desired output responses. The Fig. 3 shows the response of all six parameters for flight control using the Backstepping control technique. These parameters are known as roll (phi angle), pitch (theta angle), yaw (psi angle), altitude and motions along x and y axis.

The result of this simulation is then given as the current location of the Quadrotor, in terms of x and y. This x and y are used in the A star search algorithm. As shown in Fig. 4, Fig. 5 and Fig. 6 the target and obstacles are changed in every case and with different starting points.

Since, the location of target and obstacles is varied for each case and is used defined, there is difference in the execution time of around 29.396, 18.4122 and 23.0539 s for case 1, 2 and 3, respectively.

Several waypoints are defined for the Quadrotor system in LQR and the starting location of the designed Quadrotor system as coordinates for (x, y) to the LQR algorithm. The responses for varied starting locations are shown in Fig. 7, Fig. 8 and Fig. 9. The system is made to track a set of waypoints. The path tracked is depicted with pink line and the desired path is shown with black dotted lines. The time taken by the algorithm to execute the tracking of the waypoints for different starting locations is given in Table 1.

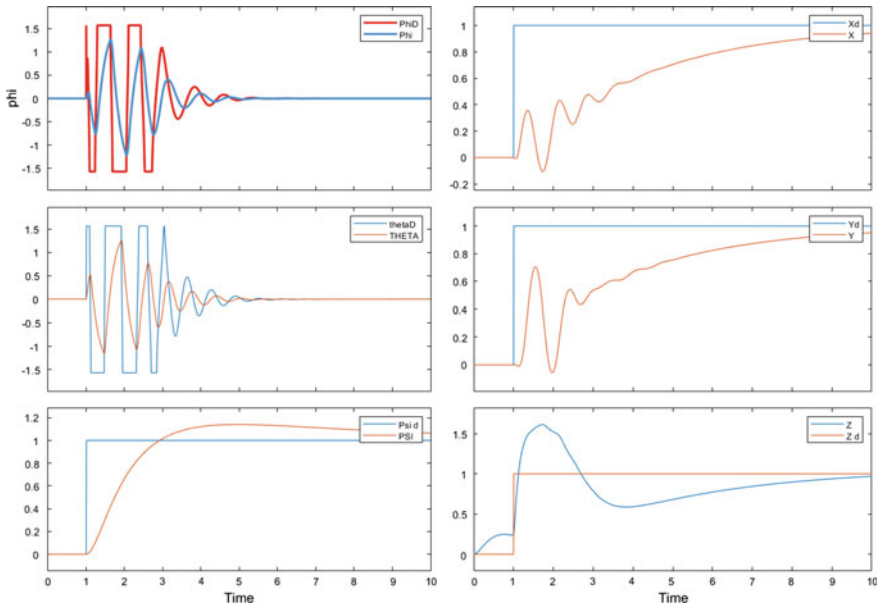


Fig. 3 Output Response of Quadrotor using Backstepping control

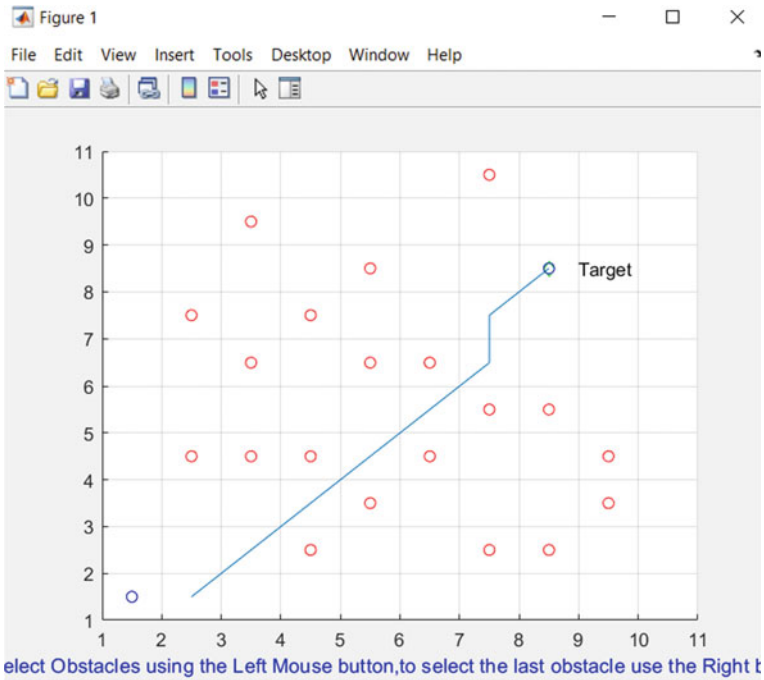


Fig. 4 Output Response of a star search algorithm-case 1

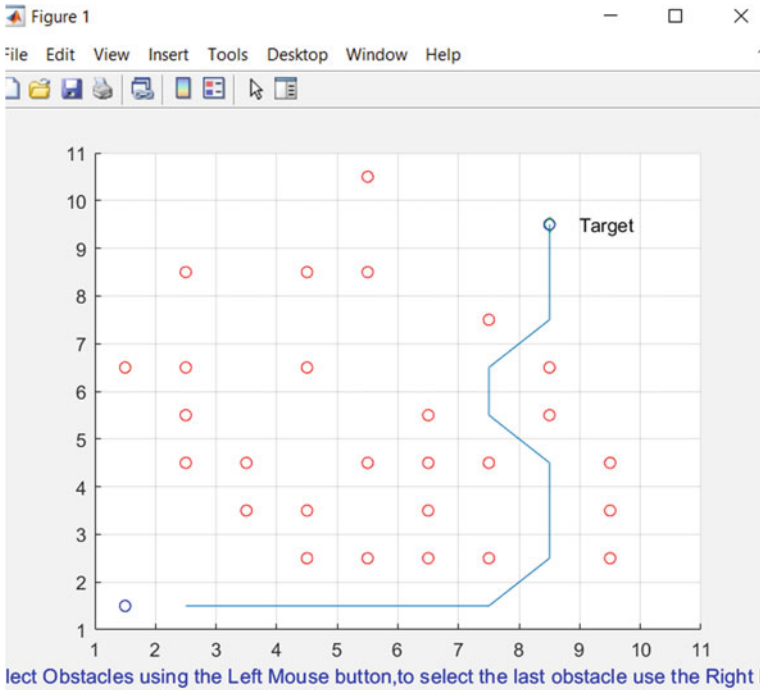


Fig. 5 Response of a star search algorithm-case 2

5 Conclusion and Future Scope

A Mathematical model Quadrotor using equations of motion (based on Newton–Euler equations) is developed in Simulink. The model dynamics such as altitude angles, position and the altitude is controlled in two subsystems, inner and outer subsystem. The attitude (rotational) angles and the altitude is controlled by PID control law. The outer subsystem which contains the control of the dynamics of the system for motion in x and y direction is done using Backstepping control. The output of this outer subsystem acts as virtual inputs (desired inputs) for roll angle and pitch angle. The response of the complete system to step change in input is obtained and displayed graphically. This system’s current location is then given as a starting point to the path planning algorithm which are implemented. The Path planning algorithms implemented are A star search algorithm and LQR algorithm. Two techniques are used: A star path planning Algorithm and LQR algorithm. The A* (A star) algorithm is implemented in the presence of obstacles and the location of the obstacles and target is varied in each case. The algorithm was able to successfully obtain path planning results in less time. There was some delay due to the human interaction with the system to select the obstacle every time. The technique implemented next

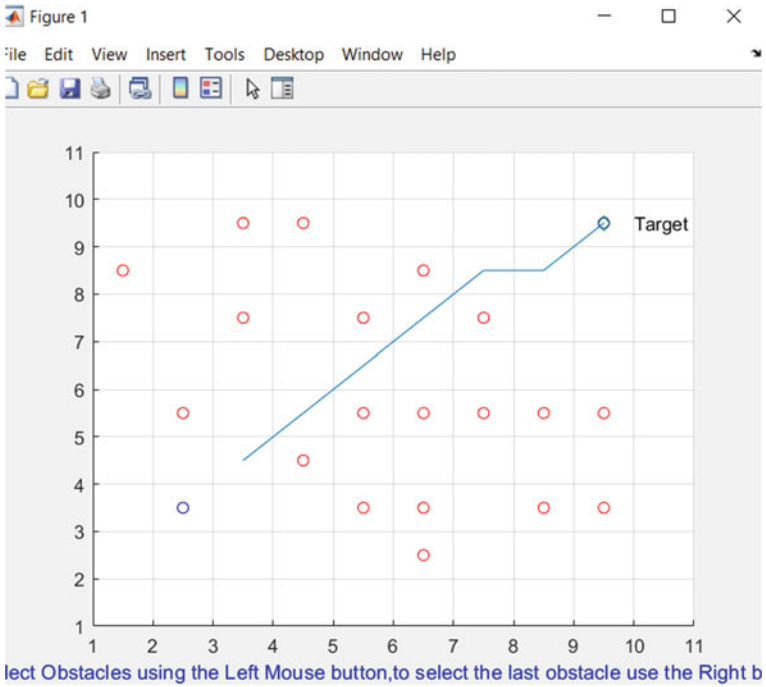


Fig. 6 Response of a star search algorithm-case 3

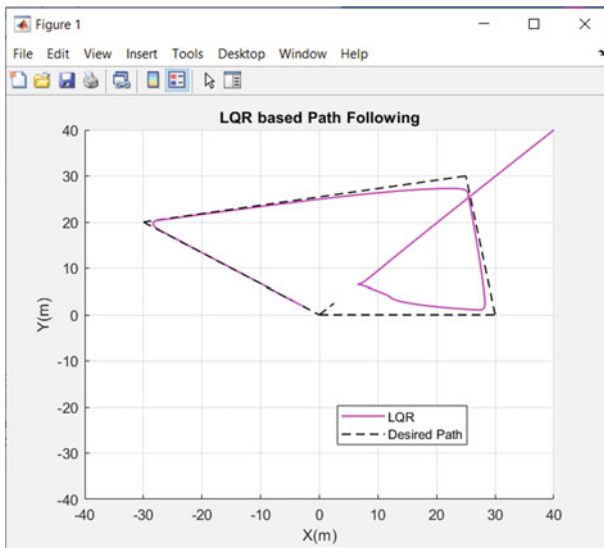


Fig. 7 Output Response of LQR algorithm ($x = 6.5, y = 6.5$)

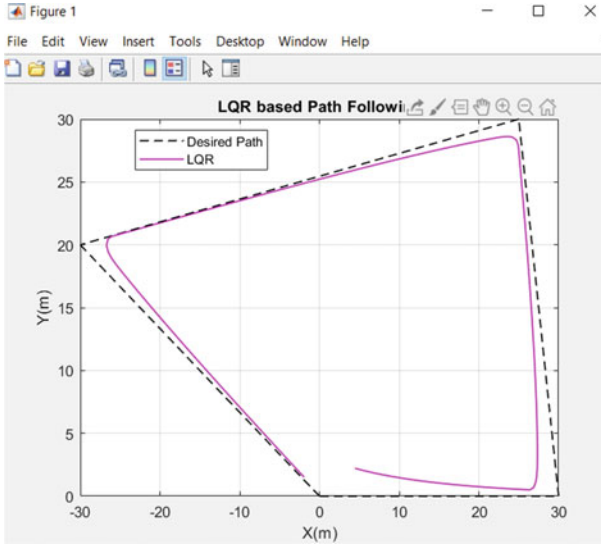


Fig. 8 Output Response of LQR algorithm ($x = 2.5, y = 2.5$)

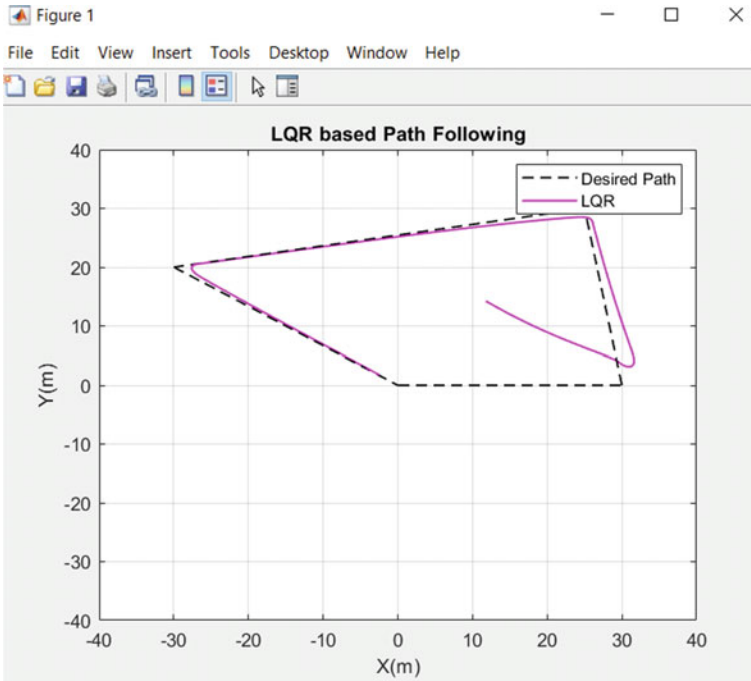


Fig. 9 Output Response of LQR algorithm ($x = 10, y = 15$)

Table 1 Execution time of different starting points

Starting location (x, y)	Execution time (in seconds)
(6.5,6.5)	7.001200
(2.5,2.5)	3.493455
(10,15)	2.506267

was the LQR algorithm in which obstacles were not considered but the execution time obtained was less than the A star algorithm.

The techniques implemented in this paper are 2D in nature. In the future, 3D path planning techniques will be implemented on the Quadrotor model. Path planning techniques which are more computationally faster, and complex would also be implemented to test the efficacy of the designed Quadrotor system.

References

1. Boon MA, Drijfhout AP, Tesfamichael S (2017) Comparison of a fixed-wing and multi-rotor UAV for environmental mapping applications: a case study. *Int Arch Photogramm Remote Sens Spa. Inf Sci-ISPRS Arch* 42: 47–54. <https://doi.org/10.5194/isprs-archives-XLII-2-W6-47-2017>
2. Kim J, Gadsden SA, Wilkerson SA (2020) A comprehensive survey of control strategies for autonomous quadrotors. *arXiv* 43: 3–16. <https://doi.org/10.1109/CJECE.2019.2920938>
3. Motlagh NH, Bagaa M, Taleb T (2017) UAV-based IoT platform: a crowd surveillance use case. *IEEE Commun Mag* 55:128–134. <https://doi.org/10.1109/MCOM.2017.1600587CM>
4. Matouk D, Gherouat O, Abdessemed F, Hassam A (2017) Quadrotor position and attitude control via backstepping approach. *Proc 2016 8Th Int Conf Model, Identif Control, ICMIC 2016*. 73–79. <https://doi.org/10.1109/ICMIC.2016.7804228>
5. Zhou L, Zhang J, She H, Jin H (2019) Quadrotor uav flight control via a novel saturation integral backstepping controller. *Automatika*. 60:193–206. <https://doi.org/10.1080/00051144.2019.1610838>
6. Burggräf P, Pérez Martínez AR, Roth H, Wagner J (2019) Quadrotors in factory applications: design and implementation of the quadrotor’s P-PID cascade control system: modeling and implementation. *SN Appl Sci* 1:1–17. <https://doi.org/10.1007/s42452-019-0698-7>
7. Jamshidi V, Nekoukar V, Refan MH (2021) Real time UAV path planning by parallel grey wolf optimization with align coefficient on CAN bus. *Cluster Comput* 24:2495–2509. <https://doi.org/10.1007/s10586-021-03276-6>
8. Zhou C, Huang B, Fränti P (2021) A review of motion planning algorithms for intelligent robots. *J Intell Manuf* 33:387–424. <https://doi.org/10.1007/S10845-021-01867-Z/FIGURES/29>
9. Rubí B, Pérez R, Morcego B (2020) A survey of path following control strategies for UAVs focused on quadrotors. *J Intell Robot Syst Theory Appl* 98:241–265. <https://doi.org/10.1007/s10846-019-01085-z>
10. Taoudi A, Luo C (2019) Obstacle avoidance for a quadrotor using a* path planning and lqr-based trajectory tracking. *AIAA Scitech 2019 Forum*. <https://doi.org/10.2514/6.2019-1566>
11. Wang P, Man Z, Cao Z, Zheng J, Zhao Y (2016) Dynamics modelling and linear control of quadcopter. *Int Conf Adv Mechatron Syst ICAMechS 0*: 498–503. <https://doi.org/10.1109/ICA MechS.2016.7813499>
12. Cárdenas R, César A, Morales CAC, Ospina JP, Sánchez JF, Caro-Ruiz C, Grisales VH, Ariza-Colpas P, De-la-Hoz-Franco E, González RER (2020) Mathematical modelling and identification of a quadrotor. *Lect. Notes Comput. Sci. (including Subser. Lect. Notes Artif.*

- Intell. Lect. Notes Bioinformatics). 12249 LNCS: 261–275. https://doi.org/10.1007/978-3-030-58799-4_19.
13. Tewari A (2011) Advanced control of aircraft, Spacecraft and Rockets - A& #46. Tewari (Wiley, 2011) BBS.pdf
 14. Mohd Basri MA, Husain AR, Danapalasingam KA (2014) Enhanced backstepping controller design with application to autonomous quadrotor unmanned aerial vehicle. *J Intell Robot Syst* 2014 792 79: 295–321. <https://doi.org/10.1007/S10846-014-0072-3>
 15. Xu LX, Ma HJ, Guo D, Xie AH, Song DL (2020) Backstepping sliding-mode and cascade active disturbance rejection control for a quadrotor UAV. *IEEE/ASME Trans Mechatronics* 25:2743–2753. <https://doi.org/10.1109/TMECH.2020.2990582>
 16. Raptis Ia, Valavanis KP, SpringerLink (Online service) (2011) Linear and nonlinear control of small-scale unmanned helicopters. <https://doi.org/10.1007/978-94-007-0023-9>
 17. Tseng FH, Liang TT, Lee CH, Chou L Der, Chao HC (2014) A star search algorithm for civil UAV path planning with 3G communication. *Proc-2014 10th Int Conf Intell Inf Hiding Multimed Signal Process, IIH-MSP 2014 2000*: 942–945. <https://doi.org/10.1109/IIH-MSP.2014.236>
 18. Fu Z, Yu J, Xie G, Chen Y, Mao Y (2018) A heuristic evolutionary algorithm of UAV path planning. *Wirel Commun Mob Comput* 2018. <https://doi.org/10.1155/2018/2851964>
 19. Sujit PB, Saripalli S, Sousa JB (2013) An evaluation of UAV path following algorithms. *Control Conf.* 3332–3337

Studying the Effect of Heating on Synthesis of ZnO Nanoparticles Properties for Electromagnetic Applications



Bahareh Dabaghiannejad, Sandeep K. Arya, and Sandeep Kumar

1 Introduction

Since nanotechnology was introduced to the world it has become a hotspot and center of attraction for researchers in various fields. As a very powerful human accomplishment it brings lots of changes and remarkable features in the physical and chemical properties of materials. Changing the size of a material from its bulk form to the particles of micrometer to hundreds of nanometer and to less than 100 nanometers alters the behavior of material drastically [1, 2]. One of the achievements of nanotechnology is the enhancement in the surface area of produced material. As the size of particles goes down the surface area increases which means there are more atoms available at the surface level to interact with the outside environment and that results in significant changes in all kinds of properties such as electrical, optical, mechanical, etc. associated with a specific substance [2].

Nanoparticles with their modified properties, due to size reduction, react significantly different in compare to their bulks and as a result, they are used in many different ways and their applications become more diverse. Ranging from electronics/electrical/mechanics industry to biomedical studies, food and cosmetics, nanotechnology is rooting.

Semiconductor nanomaterials [3] and Metal Oxide nanoparticles (MONPs) have unique properties that make them widely used in various industries. Among them

B. Dabaghiannejad (✉) · S. K. Arya

Department of Electronics and Communication Engineering, Guru Jambheshwar University of Science and Technology, Hisar, Haryana 125001, India
e-mail: b.dabaghian@gmail.com

S. Kumar

Department of Bio and Nano Technology, Guru Jambheshwar University of Science and Technology, Hisar, Haryana 125001, India

owning both chemical and physical prominent properties Zinc Oxide (ZnO) nanoparticles have grown a great amount of attention. ZnO is a white powder that has many applications in various industries such as cosmetics [4], rubber [5], textile industry [6] drug delivery [7] etc.

There are several techniques to synthesize zinc oxide nanoparticles in which the parameters of material quantity, reaction time, temperature, etc. can be controlled, and these changes affect the size, morphology and therefore different properties of the particles produced. ZnO nanoparticles can exist in one, two or three dimensional [8]. In recent years, ZnO nanoparticles have been synthesized with diverse morphologies such as, brush-like [9], cone-shaped [10], flower-like [11], nanorod [12] and to obtain these different synthesis methods have been used. Combustion synthesis [13], thermal decomposition [14], chemical vapor synthesis [15], flame spray pyrolysis [16], sol-gel [17], hydrothermal method [18] and chemical precipitation [19, 20] are some of the common synthesis methods used to achieve different particle sizes and morphologies. However most of the methods used have disadvantages such as high cost, high temperature, complex tools and toxicity. Chemical precipitation is a facile, cost effective, low temperature method easily available. The variables of this methods including time of reaction and stirring speed have influence on the particles prepared. This method is often performed at room temperature. In this study we have explored the effect of heating during stirring with only two precursors. By following three different protocols using different precursors and dividing each in to two experiments—one at room temperature and one with heating- we have added heat while stirring to each method to see if high temperature changes the properties of the final outcome. To the best of our knowledge this is the first time this experiment is done, however in another study Kiomarsipour et al [18] used hydrothermal method to study the effect of heating. They prepared 5 samples and the results showed the agglomeration of particles while increasing the temperature.

2 Materials and Methods

For this study to prepare zinc oxide nanoparticles three different starting materials were used and a total of 6 tests were conducted. Starting materials were Zinc Sulphate heptahydrate (M.W.: 287.54, CDH), Zinc Acetate dihydrate (M.W.: 219.50, HIMEDIA), Zinc Nitrate hexahydrate (M.W.: 297.49, CDH), potassium hydroxide pellets (M.W.: 56.11, CDH) and sodium hydroxide pellets (M.W.: 40.00, HIMEDIA). Methanol and double distilled water (DDW) were used as solvents during different experiments. All materials were used as purchased without further purification.

2.1 Sample Preparation

Each experiment was divided into two parts which were performed simultaneously, one at room temperature (RT) and one by heating.

2.1.1 Experiment #1, 2

The solutions of 0.4 g NaOH in 100 ml DDW were added drop wise to the solutions of 0.72 g zinc sulphate in 50 ml DDW. Both samples were stirred at 600 rpm for 16 h. One sample was stirred at 70 °C.

2.1.2 Experiment #3, 4

For this experiment we used methanol as the solvent preparing 0.55 g zinc acetate in 25 ml methanol and 2.8 g KOH in 50 ml methanol solutions. The solutions of KOH were added drop wise to zinc acetate solutions and stirred for 3 hours at 700 rpm. The temperature of heated sample was kept at 60 °C during stirring.

2.1.3 Experiment #5, 6

2.975 g zinc nitrate in 50 ml DDW and 1.12g KOH in 50 ml DDW were prepared and KOH solutions were drop wise added to the ZnNO₃ solutions. Samples were stirred at 500 rpm for 18 h. The heated sample was stirred at 80 °C.

All six samples after stirring were washed 3 times with double distilled water and one time with absolute ethanol and dried in oven at 70 °C over night. After drying samples were crushed manually for 5 mins using pestle mortar and dried again for 4 hrs.

Table 1 shows a summary of the experiments and their naming.

3 Characterization

For the purpose of X-ray diffraction characterization of NPs a Rigaku Multiflex-II with CuK α radiation ($\lambda = 1.5406 \text{ \AA}$), 30 kV, 15 mA, angles varying from 10 to 80 deg with steps of 0.02 deg. was used to study the crystal structure. A JEOL brand, model JSM, 7610 FPLUS Schottky Field Emission Scanning Electron Microscope was used for the investigation of the morphology and size. To study the IR response a PerkinElmer Spectrum IR Version 10.6.2 was used. Finally the ultra violet and visible light absorption spectra were performed with a Shimadzu UV2450 UV-Vis.

Table 1 Summary of experiments

Experiment	Material	Solvent	Stirring time (hr)	Stirring speed (rpm)	Temperature	Sample name
1	Zinc sulphate, NaOH	DDW	16	600	Room Temp	S1
2					70 °C	S2
3	Zinc acetate, KOH	Methanol	3	700	Room Temp	S3
4					60 °C	S4
5	Zinc nitrate, KOH	DDW	18	500	Room Temp	S5
6					80 °C	S6

4 Results and Discussion

It is quite worth noting that before any characterization and while crushing samples manually S2, S4 and S6 showed finer texture that was clearly noticeable compared to samples synthesized at room temperature.

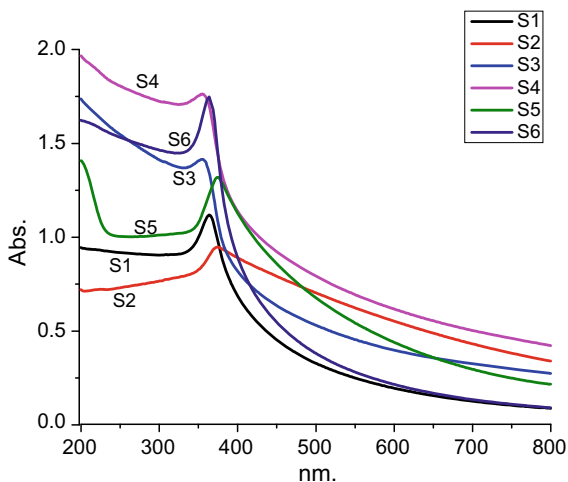
4.1 Ultra Violet and Visible Light Absorption (UV-Vis)

For optical properties of the samples UV-Vis absorptions were studied and for that a solution of 0.01 g in 10 mL DDW was prepared for each sample and sonicated for 90 mins. Sample S1 showed high absorbance of UV radiation at 364 nm while for S2 the absorption peak occurred at 374 nm which can be interpreted as a slight red-shift as the S2 particles were smaller in average. S3 and S4 showed their peaks very close to each other which were at 351 and 355 nm respectively indicating that heat did not affect the optical properties as it did not affect the size of these two samples as well. However for S5 and S6 a slight blue-shift was observed since the peak shifted from 375 nm for S5 to 364 nm for S6 however since sample S6 showed smaller particles; a blue-shift was expected. The UV-Vis absorption spectrum of all samples is shown in Fig. 1. Since we have used different protocols for synthesis comparing each two resulted in different outcomes, therefore a single conclusion cannot be decided based on the obtained data.

4.2 Fourier Transform Infrared (FTIR)

FTIR is a valid method to identify the compositions in the product. Generally the band frequencies less than 800 cm^{-1} indicate the presence of inorganic elements. As for pure ZnO different peaks have been reported by different studies [21, 22] and that

Fig. 1 The UV–Vis absorption spectrum for S1–S6



is due to the fact that methods and conditions of experimental work strongly affect the final product and can position weaker bands. Fig. 2. shows the peaks received from each sample. According to the functional groups wave numbers, the ones above 3200 cm^{-1} represent the O-H stretching vibration which is presented in all samples. Other peaks between 600 cm^{-1} and 3200 cm^{-1} show the presence of other bonds such as N-H, C-C and etc. As for ZnO the peaks occurring at 539.9, 435.03, 449.8, 451.43, 475.09 and 478 for S1 to S6 respectively declare the presence of Zn-O bond. The variation between the results proves the high sensitivity of FTIR to size and morphology of the products.

4.3 Scanning Electron Microscopy (SEM)

To find out information about the particles' morphology and size, scanning electron microscope is a very effective characterization tool since it uses the electron beams which are much smaller than light particles. The SEM characterization of S1 and S2 showed both samples with flake-like shapes as in Fig. 3. with size variations of 15–40 nm and 18–25 nm respectively which indicates that the sample with heating in average has obtained slightly smaller size particles.

As Fig. 3. also shows, both S3 and S4 resulted in spherical shape and similar sizes ranging from 10–15 nm. Therefore as a result, heat had no significant effect on the shape or size of the material.

On the other hand a very significant difference was observed between S5 and S6 in size and shape. Even though they both appeared in volumetric polygons, S6 showed more cube-like (regular polygon) while S5 was seen as irregular ones. Also the sizes obtained from S5 were more than 90 nm whereas sizes of 20–50 nm were observed

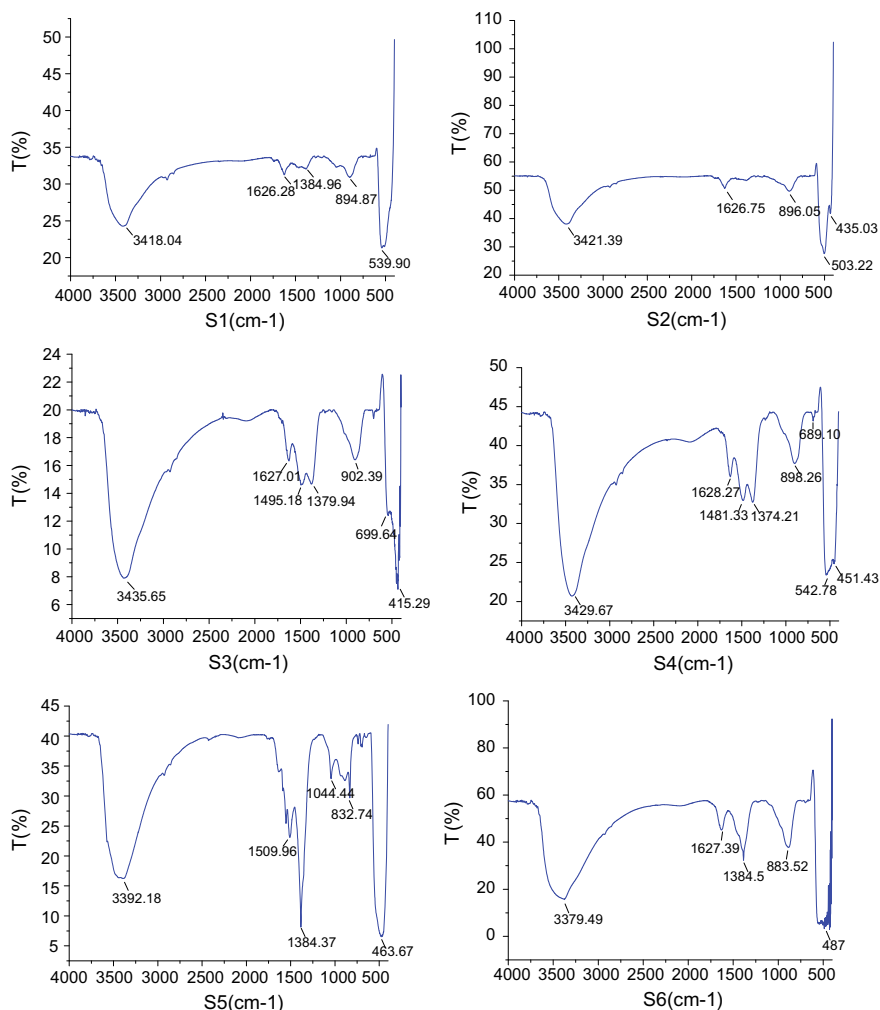


Fig. 2 The FTIR spectrum of S1 to S6

for S6. As the data show, the methods involving double distilled water resulted in comparatively smaller sizes.

4.4 X-Ray Diffraction Studies (XRD)

X-Ray diffraction as a robust nondestructive method was used to ensure that the crystal structure of the prepared materials is following the reported data for ZnO. All six samples showed a hexagonal Wurtzite structure which indicates the formation

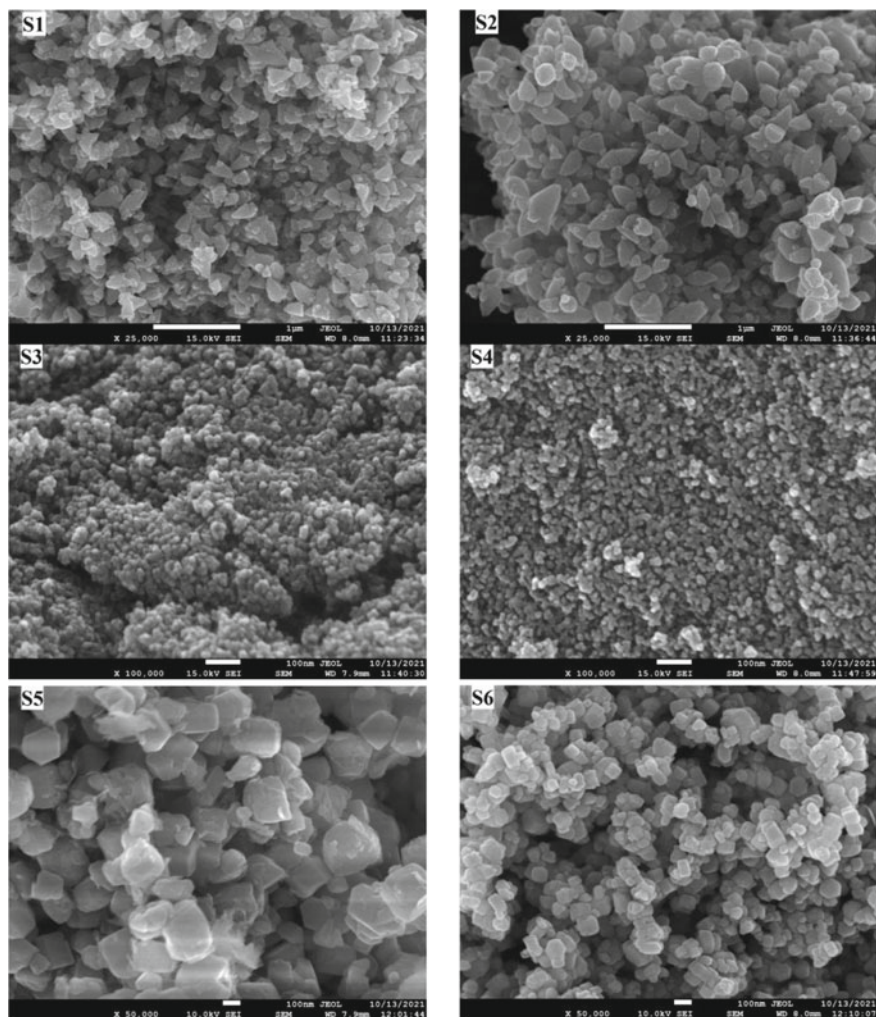
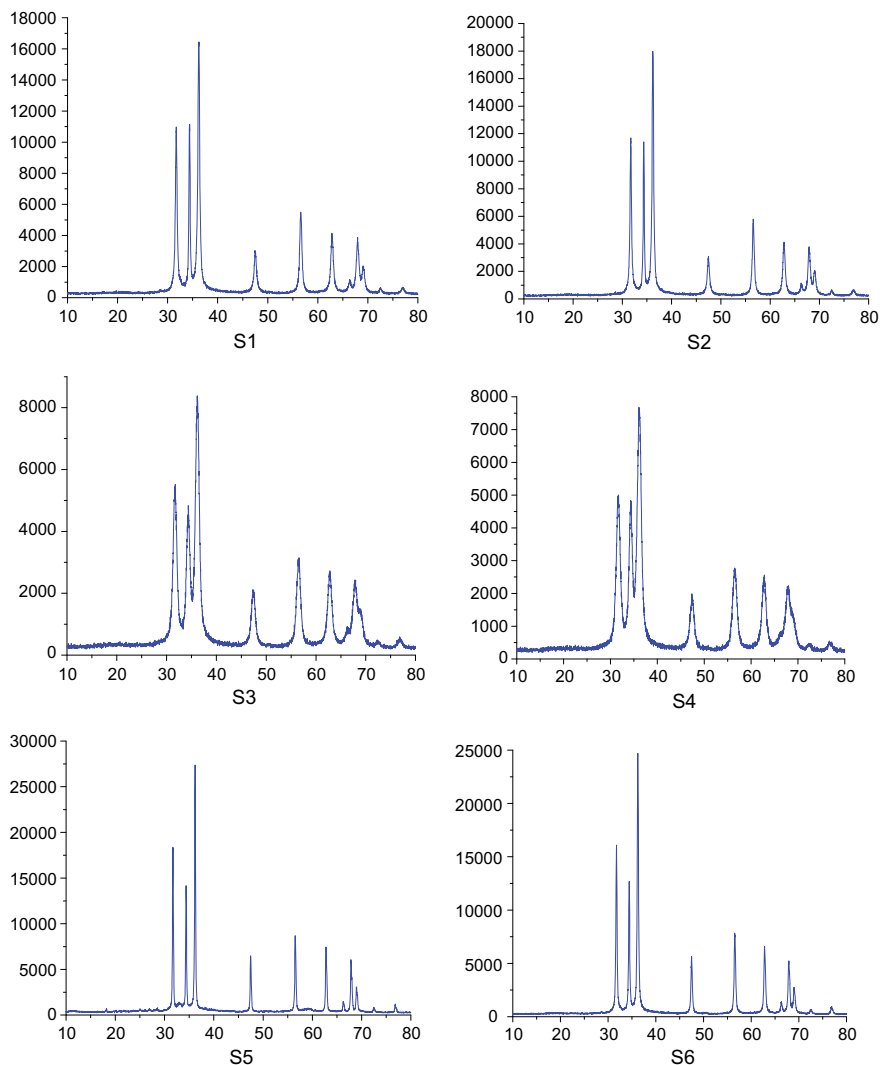


Fig. 3 The SEM characterization of S1 to S6

of ZnO crystals and our data is in conformity with JCPDS PDF no 36–1451 (Joint Committee on Powder Diffraction Standards) which ensures the purity of the product as well. The results of all 6 samples show the peaks corresponding to lattice planes (100), (002), (101), (102) and (110) are all very close to the JCPDS and around 31.4, 34.4, 36.2, 47.4 and 56.5 respectively. Table 2 represents the data collected from our XRD characterization in comparison with JCPDS data. Fig. 4 shows the XRD plot related to each sample.

Table 2 XRD peaks in comparison with JCPDS data

XRD peak	$2\theta^\circ$ from JCPDS	$2\theta^\circ$ of S1	$2\theta^\circ$ of S2	$2\theta^\circ$ of S3	$2\theta^\circ$ of S4	$2\theta^\circ$ of S5	$2\theta^\circ$ of S6
1 0 0	31.770	31.74	31.74	31.74	31.72	31.72	31.78
0 0 2	34.422	34.42	34.38	34.36	34.36	34.4	34.44
1 0 1	36.253	36.26	36.22	36.16	36.1	36.22	36.24
1 0 2	47.539	47.46	47.5	47.36	47.38	47.48	47.52
1 1 0	56.603	56.58	56.58	56.48	56.48	56.52	56.56

**Fig. 4** The XRD characterization of S1 to S6

5 Conclusion

Our aim in this study was to fabricate zinc oxide nanoparticles and investigate the effect of heat on the properties of the products for future use in electromagnetic applications. Six different samples of ZnO nanoparticles were synthesized by simple precipitation method. Zinc sulphate heptahydrate, zinc acetate dihydrate, zinc nitrate hexahydrate, potassium hydroxide pellets and sodium hydroxide pellets were used as precursors in different experiments with methanol and double distilled water as solvents. One set of experiments were done at room temperature and the other set at higher temperatures. All samples were examined by UV-Vis, FTIR, SEM and XRD characterization methods. Samples S1 and S2 showed flake-like morphology in SEM characterization with size ranges of 15–40 nm and 18–25 nm respectively indicating that heating had a slight effect on reducing the size of the particles in average. In UV-Vis analysis a red shift was observed from 364 nm for S1 to 374 nm for S2 indicating the effect of size on UV absorption. S3 and S4 appeared in spherical shape with average size of 15 nm for both, also showed almost same absorption around 351 nm and 355 nm respectively since they had same morphology and size; therefore the effect of heating is negligible on the size and morphology of these samples. However S5 and S6 came with irregular and regular polygon shapes and a big difference in sizes that went from 90 nm for S5 to less than 50 nm for S6 and resulted in a blue-shift in the UV absorption from 375 nm to 364 nm respectively inferring the effect of morphology as another important parameter in UV absorption. FTIR peaks occurring around 539.9, 435.03, 449.8, 451.43, 475.09 and 478 for S1 to S6 respectively proved the existence of ZnO nanoparticles with good purity. XRD of all the samples showed Wurtzite crystal structure as a proof of the formation of ZnO nanoparticles and the results for (100), (002), (101), (102) and (110) were around 31.7, 34.4, 36.2, 47.4 and 56.5 respectively and close to JCPDS PDF no 36–1451. Therefore simple precipitation method can give acceptable results for making ZnO in order to use for electromagnetic applications like photovoltaic cells, UV detectors, optoelectronic and photodetectors.

References

1. Sirelkhatim A, Mahmud S, Seeni A, Mohamad KNH, Ann LC, Mohd Bakhori SK, Hasan H, Mohamad D (2015) Review on zinc oxide nanoparticles: antibacterial activity and toxicity mechanism. *Nano-Micro Lett* 7: 219-242
2. Pal S, Tak YK, Song JM (2007) Does the antibacterial activity of silver nanoparticles depend on the shape of the nanoparticle? a study of the gram-negative bacterium *escherichia coli*. *Appl Environ Microbiol* 73:1712–1720
3. Jiang J, Pi J, Cai J (2018) The advancing of zinc oxide nanoparticles for biomedical applications. *Bioinorg Chem Appl* 2018:1062562
4. Santos AC, Morais F, Simoes A, Pereira I, Sequeira JAD, Pereira-Silva M, Veiga F, Ribeiro A (2019) Nanotechnology for the development of new cosmetic formulations. *Expert Opin Drug Deliv* 16:313–330

5. Kołodziejczak-Radzimska A, Jesionowski T (2014) Zinc oxide—from synthesis to application—a review. *Materials* 7:2833–2881
6. Hatamie A, Khan A, Golabi M, Turner APF, Beni V, Mak WC, Sadollahkhani A, Alnoor H, Zargar B, Bano S, Nur O, Willander M (2015) Zinc oxide nanostructures modified textile and its application to biosensing, photocatalytic and as antibacterial material. *Langmuir* 31:10913–10921
7. Xiong HM (2013) ZnO nanoparticles applied to bioimaging and drug delivery. *Adv Mater* 25:5329–5335
8. Mohan AC, Renjanadevi B (2016) Preparation of zinc oxide nanoparticles and its characterization using scanning electron microscopy (SEM) and X-Ray diffraction(XRD). *Procedia Technol* 24:761–766
9. Zhang Y, Xu J, Xiang Q, Li H, Pan Q, Xu P (2009) Brush-like hierarchical ZnO nanostructures: synthesis, photoluminescence and gas sensor properties. *J Phys Chem C* 113:3430–3435
10. Ren X, Han D, Chen D, Tang F (2007) Large-scale synthesis of hexagonal cone-shaped ZnO nanoparticles with a simple route and their application to photocatalytic degradation. *Mater Res Bull* 42:807–813
11. Zou X, Ke J, Hao J, Yan X, Tian Y (2021) A new method for synthesis of ZnO flower-like nanostructures and their photocatalytic performance. *Phys B Condens Matter* 624:413395
12. Bai S, Liu X, Li D, Chen S, Luo R, Chen A (2011) Synthesis of ZnO nanorods and its application in NO₂ sensors. *Sensors Actuators B-chem* 153:110–116
13. Sharma SK, Pitale SS, Manzar MM, Dubey RN, Qureshi MS, Ojha S (2010) Influence of fuel/oxidizer ratio on lattice parameters and morphology of combustion synthesized ZnO powders. *Phys B Condens Matter* 405:866–874
14. Lin C-C, Li Y-Y (2009) Synthesis of ZnO nanowires by thermal decomposition of zinc acetate dihydrate. *Mater Chem Phys* 113:334–337
15. Reuge N, Bacsá R, Serp P, Caussat B (2009) Chemical vapor synthesis of zinc oxide nanoparticles: experimental and preliminary modeling studies. *J Phys Chem C* 113:19845–19852
16. Hembram K, Sivaprakasam D, Rao TN, Wegner K (2013) Large-scale manufacture of ZnO nanorods by flame spray pyrolysis. *J Nanoparticle Res* 15:1461
17. Rani S, Suri P, Shishodia PK, Mehra RM (2008) Synthesis of nanocrystalline ZnO powder via sol–gel route for dye-sensitized solar cells. *Sol Energy Mater Sol Cells* 92:1639–1645
18. Kiomarsipour N, Shoja Razavi R (2014) Hydrothermal synthesis of ZnO nanopigments with high UV absorption and vis/NIR reflectance. *Ceram Int* 40: 11261–11268
19. Ghorbani HR, Parsa Mehr F, Pazoki H, Mosavar Rahmani B (2015) Synthesis of ZnO nanoparticles by precipitation method. *Orient J Chem* 31: 1219-1221
20. Rajagopalan N, Khanna AS (2013) Effect of size and morphology on UV-blocking property of nanoZnO in epoxy coating. *Int J Sci Res Publ* 3:1–14
21. Sowri BK, Ramachandra RA, Sujatha C, Venugopal RK, Mallika AN (2013) Synthesis and optical characterization of porous ZnO. *J Adv Ceram* 2:260–265
22. Sharma D, Jha R (2017) Analysis of structural, optical and magnetic properties of Fe/Co co-doped ZnO nanocrystals. *Ceram Int* 43:8488–8496

A Comparative Analysis of Chaotic and Quantum Chaotic Encryption Mechanisms



Jitender, Shailender Gupta, and Sangeeta Dhall

1 Introduction

Technology has increased to a great degree in the last decades and reached new milestones of advancement. It has provided a great benefit to us in approx. all the fields whether it is health, education etc. With this advancement the computer capabilities especially, the speed have also increased to a great extent which enables us to enjoy faster communication and other advanced services. But this advancement also provided a great advantage to the intruders to track the activities, data and access of private information which in term increased the hacker capabilities as well [1].

The data such as images, sounds, figures or maps etc. nowadays can be assessed easily in digital form due to the advancement of the internet and digital technology. Once the data is digitalized, the contents of all the data are equivalent and they can be misused, modified and malformed by anyone. Various types of cryptography algorithms are developed by researchers and among these algorithms, the algorithms which are proven and ensure security have been recognized for the development in their fields of existence. Image encryption is used to convert an image into an unrecognized form that can be transmitted through a medium. A basic block diagram of the cryptography process is shown in Fig. 1. The block diagram consists of the transformation of the plain image into a cipher image and key, at the receiver side decryption is used to transform the encrypted image into the original image [2]. When they travel through a medium, it suffers different kinds of noises such as Gaussian noise, which can change data, the cropping attack can change media which in terms results in a change in information. So, it is also required to provide safety against these attacks and noise over the transmission media.

Jitender (✉) · S. Gupta · S. Dhall
JC Bose University of Science and Technology (YMCA), Faridabad, Haryana, India
e-mail: 20001505002@jcbouseust.ac.in

© The Author(s), under exclusive license to Springer Nature Singapore Pte Ltd. 2023
P. Singhal et al. (eds.), *Recent Developments in Electrical and Electronics Engineering*,
Lecture Notes in Electrical Engineering 979,
https://doi.org/10.1007/978-981-19-7993-4_21

249

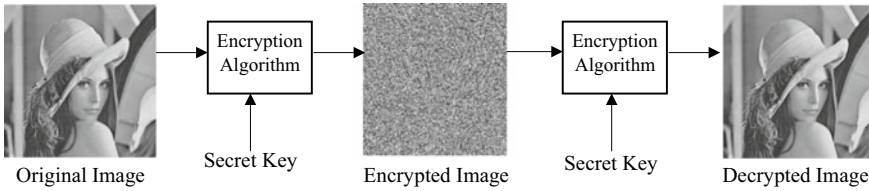


Fig. 1 Block diagram for basic cryptography

Data breaches are increasing day by day. The statistic revealed in Report on “India 3rd in data breaches till Nov” [3] shown in Fig. 2 presents the data breach record till Nov. This report is generated by ‘The Times of India’. India has come to the third spot, after US and Iran in a data breach. India faced a total of 86.6mn data breaches. The affected accounts showed an increase of 356% from last year’s 19mn [3]. On average the companies that spend on malware attacks are around 2.4 million dollars [4]. The fact shows that insecurities are the major issue. Some good encryption schemes are listed below.

Resistance to probable noises and geometric attacks: It is a huge boundary to assess the encryption strategy, and it very well may be processed by considering the clearest commotions like Gaussian, Salt and pepper, Dot, Poisson’s, alongside turn and flip assaults. The PSNR and BER are its measures.

Disassociation: This boundary is utilized for factual examination of the systems and describes the resemblance between the original and cipher image data. Relationship coefficient and histograms are best factors for its calculation.

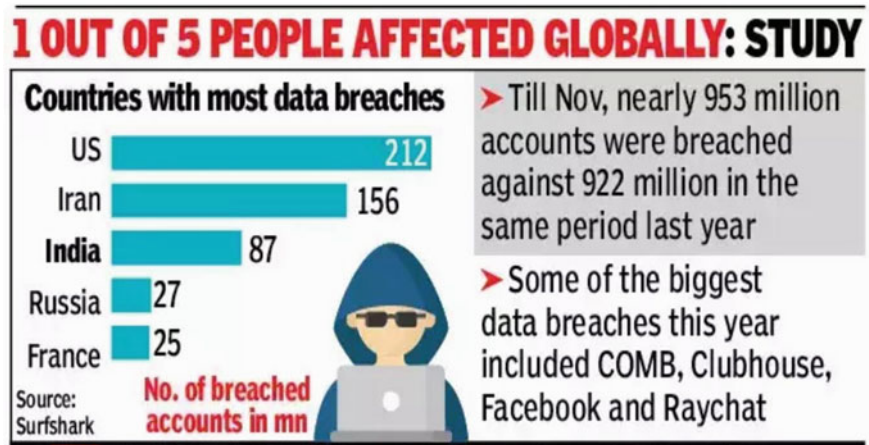


Fig. 2 Data breaches till Nov.21

Imperceptibility: It assesses the nature of the encoded picture, after the execution of cryptographic algorithm on it. Visual review or subjective examination of depictions of pictures when the applied method is the proportion of this property. For a proficient technique output must be exceptionally vague.

Key Space: The key space parameter is used to verify that the encode key by which the image or data is encrypted can't be detected by any other cryptanalyst. The large size of the key is used to resist the brute force attack.

If the above constraints are having optimal values for the original image and encrypted image, then the method is said to be secured. In this paper survey is performed for encryption techniques including traditional, chaotic and quantum chaotic based techniques with and without possible intimidations and it has a thorough examination i.e., Imperceptibility, statistical, brute force search attack and run-time based on numerous constraints mentioned above. The best approaches have recognized comparing the outputs obtained in both conditions i.e., availability and unavailability of intimidations.

The structure of the paper is designed as follows:

Section 2 represents the Motivation and contribution by the author, Sect. 3 shows the enlightenment of several cryptography approaches with suitable figures. Section 4-represents the performance metrics of the approaches, Sect. 5 tells the set-up constraints trailed by Sect. 6 which indicates the results of various approaches. Section 7 represents the results tailed by reference.

2 Motivation and Contribution

Continuous enhancement is going on the getting better solutions for protecting the information that can be in the form of data or images. As a result, ample research and survey papers are available in the literature with distinctive encoding approaches under the impact of outbreaks. Many of them are only theoretical analyses and many are experimental. They are listed as follows:

Mandeep Kaur et.al has surveyed four types of spatial domain techniques. In this paper [5], systems are measured on a theoretical basis with the performance metrics- key space analysis, histogram analysis, information entropy. Also, the author provided the noise attack analysis but more attacks need to be considered. The paper [6], includes the RC4 algorithm and its optimization and the comparative analysis is provided in the paper for the method with the help of various constraints such as the KS test, Correlation, and Chi-square test. In the third paper [7], the HVC method is shown and explained with the help of a flow chart and diagram, also the input and outputs at different phases are compared but no performance metrics have been displayed for comparative analysis. The paper [8] of FIPS on DES describes the DES algorithm with the example and steps involved in it in brief. It also includes

the optimized version of DES which is TDES (triple DES) along with the primitive functions for the algorithm but no comparison is provided. S. Arivazhagan et.al represent the mixed chaotic function in their paper [9]. He explained the types of maps and the constraints that are used by them to generate the secret key with the maps. The author used 3 maps for a different purposes to encrypt the data. Also, the output is considered on various images with the help of several constraints. In paper [10], a method is introduced for chaotic encryption with a 2d-chaotic map. Here the values for the maps are provided for the secret key generation and a single map is used to carry the whole encryption and decryption. A comparative analysis of various images is provided in the paper with several performance metrics. The paper [11] introduces the Lorentz equation followed by a substitution box for the data encryption. The S-Box is used to provide an extra advantage to the security. In this paper, the equation is provided in the polynomial form to develop the Lorentz system and further, the solution is provided to obtain the values of x, y and z for the system. The generated keys are the secret keys that are used for encryption/decryption of data followed by the S-Box. The author also showed the noise attack analysis and cryptanalysis in the paper. The next paper [12], represents an encryption mechanism for encrypting the images with the 2D-Henon map. The zigzag scan pattern is first implemented to break the entropy of the pixels of the image, after that a secret key is generated with the Henon map and an encryption process is carried out. The chaotic stream cipher for enhancing the data encryption is represented theoretically on paper. In this paper, the author uses data ciphering with LSB steganography for the key secrecy. Although the author didn't provide any kind of comparison based on performance metrics in the paper. Ahmed A. et.al in their paper [13], discussed the encryption of images with the quantum-chaotic method. The author uses a 1-D discrete chaotic map, grey code and controlled not operations to obtain the final ciphered image. Various constraints are also provided by the author to compare such as histogram analysis, Shannon entropy analysis, and key sensitivity analysis. The succeeding paperwork [14], shows the quantum color image encryption based on multiple discrete chaotic systems. In this paper, the author described the chaotic system and several maps, the logistic map and asymmetric tent map are used in the paper with the log Chebyshev map to generate the secret key for encryption. Three constraints are generated with these maps and further diffusion and controlled not operations are performed on the image to obtain the ciphering image, The author showed correlation for the comparison of the output. In the paper [15], Priyadharshini A et.al implemented a medical image securing method, where the author compares the output using numerous performance matrices such as histogram analysis, MSE and PSNR.

The above analysis is either theoretical or practical. The experimented approaches are implemented on MATLAB. In this paper, the approaches will be implemented on Python 2.8 because python is open source and lightweight. Availability of open-source IDE along with various features such as debugger inbuilt console, terminal

console variable management space etc. The fast edit-test-debug cycle makes this simple approach very effective.

As per the above analysis, it came into the limelight that from the several available techniques only a few papers in the literature draw an evaluation of almost all the conventional and updated encryption approaches. It shows that prevailing papers provide partial information about cryptography approaches without taking into account the applied case of many noises and outbreaks. Hence, this paper aims to provide:

- The important ciphering approaches include traditional, chaotic and quantum-chaotic for examination.
- Analysis is performed thoroughly by bearing in mind comprehensive performance constraints.
- Frequent performance metrics are used for separate kinds of analysis to obtain the best method.

3 Cryptography Techniques

For the thorough inquiry of ciphering approaches all the traditional, chaotic and quantum-chaotic algorithms are considered for execution. The traditional approaches are the straight approaches that use substitution or shifting methods. The chaotic algorithm is more advance than the traditional technique as a number of functions such as initial conditions, cyclicity and the highly arbitrary system are used in the algorithm that increases the confusion and diffusion process to original data to obtain the ciphered image. Due to the confusing assembly and more randomness, the chaotic method is safer than the conventional method because they are developed by keeping in mind the keyspace and constraints of the suitable period. But the foremost apprehension about this method is the quantization of the orthodox chaotic system.

The quantum-based encryption approaches are drawn attention in the recent era. These approaches are the advancement of the chaotic approaches. In this method quantum version of an orthodox chaotic system is introduced which is used to increase the randomness of the existing method which in terms also increases the key size. This method includes very complex and highly random sequences which are generated by various kinds of maps. In addition, these maps provide high sensitivity, which means a small change in initial and control conditions can result in a very different mechanism and key.

The clarification of the above approaches calculated in the study is depicted below:

Chaotic Scheme 1: New cryptographic algorithm via a two-dimensional chaotic map

In this paper [10], Aesha Elghandour et al. explicated the behavior of a 2-D chaotic map and used the relation for encryption process in creating confusion of image pixels, Two-dimensional piecewise smooth nonlinear chaotic map (2DPSNCM) and

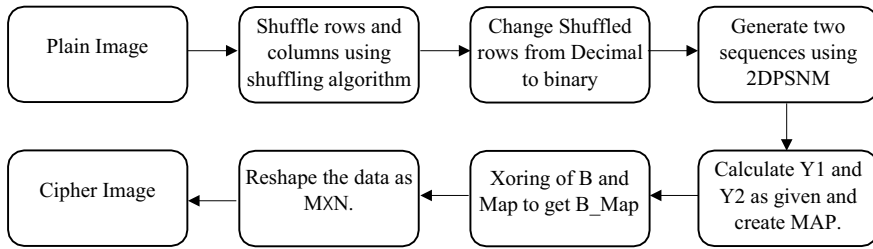


Fig. 3 Block diagram chaotic scheme 1

exoring the 2-pixel values found by a secret key generated and confusion values obtained. The figure below shows the block diagram Fig. 3 for chaotic scheme 1.

The process for the data encryption depicted in the paper is:

- The random number is generated with the help of a chaotic map.
- The change of pixels of the plain should happen according to the new indices obtained.
- Change the pixel values from decimal to binary.
- Generate two sequences of value using 2DPSNCM and convert to Y1 and Y2 form.
- Convert Y1, Y2 to binary form and perform the bitwise ex-or of the confused pixels and values obtained with 2DPSNCM.
- Change the values to decimal vector.

3.1 Chaotic Scheme 2: Mixed Chaotic Maps Based Ecrption for High Crypto Secrecy

This chaotic encryption system [9] is based on mixed chaotic maps for the encryption of data. The author S. Arivazhagan et al., in this paper, introduce two types of chaotic maps. The first is substitution based and the second is transposition-based. The combination of the substitution and transposition map is used to encrypt images and the author showed the results of different experiments through various performance metrics such as NPCR, UACI and visual analysis. In this method, the original image has to be converted to a one-dimensional binary string first. Then ex-or is performed for the binary string and the string is obtained with a chaotic map. Figure 4 represents the mechanism of the method.

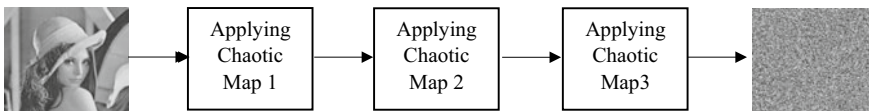


Fig. 4 Block diagram chaotic scheme 2

The process used in the map is as follows:

- Convert the binary image to one-dimensional string of length l.
- Form a binary sequence w using different chaotic maps such that:

$$w_n = \begin{cases} 0, & x_i > c \\ 1, & x_i \leq c \end{cases} \tag{1}$$

where $c = 0.505$

- XOR both the strings obtained.
- Then shuffle the values on the basis of values obtained by the chaotic map.

3.2 Chaotic Scheme 3: A Image Encryption Algorithm Based on Chaotic Lorenz System and Novel Primitive Polynomial S-boxes

This paper uses the Lorenz system followed by an S-Box to perform the encryption. In this paper [11] Temadher. A et al. introduce a chaotic Lorenz system to generate the secret key that will carry the encryption process further. With the help of the chaotic system 3 series named x, y and z are obtained as the secret key utilizing the Lorenz system. The plain image changes into a 1-D vector, then the confusion and diffusion sequences are obtained. Then the sequences are ex-or to obtain the cipher image. After that to add one extra layer to security, an S-box is introduced to make it more complex to breach the security. Figure 5 represents the technique:

The procedure followed to obtain the cipher image is:

- Obtain the values of x, y, z using Lorenz system equations.
- Develop a new chaotic sequence (ki) combining x, y and z in respective order.
- Convert the plain image to a One-dimensional vector.
- Now shuffle the pixels using the new values obtained.
- Define a new sequence with an element based on the new chaotic sequence (ki) obtained.

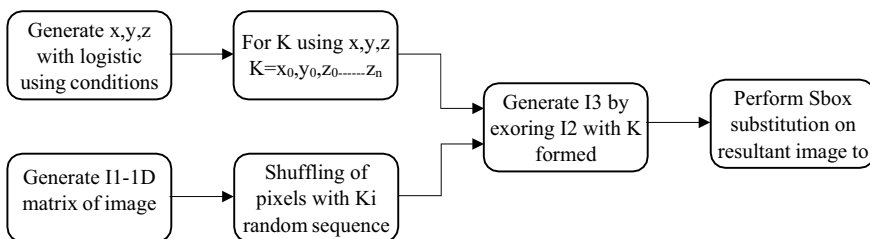


Fig. 5 Block diagram chaotic scheme 3

- Now ex-or the new sequence obtained with the sequence obtained after shuffling of plain image pixels.
- Now convert the pixel values in binary form of 8 bits. Take decimal value of four LSBs as the column and 4 MSBs as row and substitute the values as per given in the S-Box.
- The process will be repeated for all the pixels.

3.3 Chaotic Scheme 4: Chaotic Based Lightweight Image Encryption Algorithm for Real-Time Application Systems

2-D Henon map is introduced by Aguru Aswani et al. in this paper [12]. The 2-D Henon map is used to generate the secret key for this method. The initial constraints are provided in the paper to generate the key sequence using the map. The system proposed uses a 192-bit symmetric key to encrypt each pixel of the image. The key is produced by the chain of six 32-bit inputs in IEEE754 form. The confusion of pixels first takes place in a zigzag pattern to break the entropy after that the encryption process is carried out in the method. The method can be easy with the help of Fig. 6.

The steps involved in the process are:

- Choose the floating points.
- Concatenate the 32-bit IEEE754 illustration of these to get a 192-bit proportional key.
- Obtain values of X and Y using a 2-D Henon map.
- Obtain the shuffling positions b diving mantissa field of X and Y.
- Exor the shuffled pixels with the previously transformed pixels.

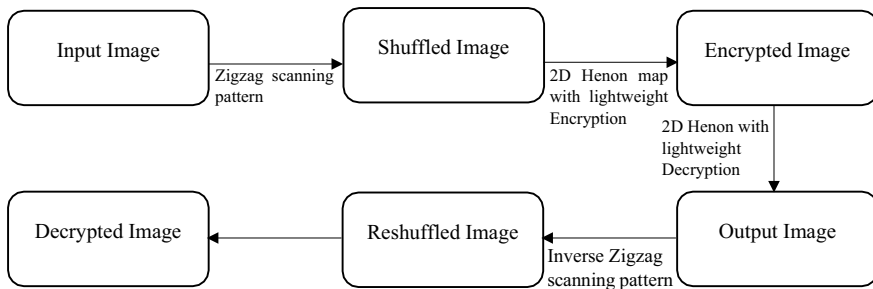


Fig. 6 Clock diagram chaotic scheme 4

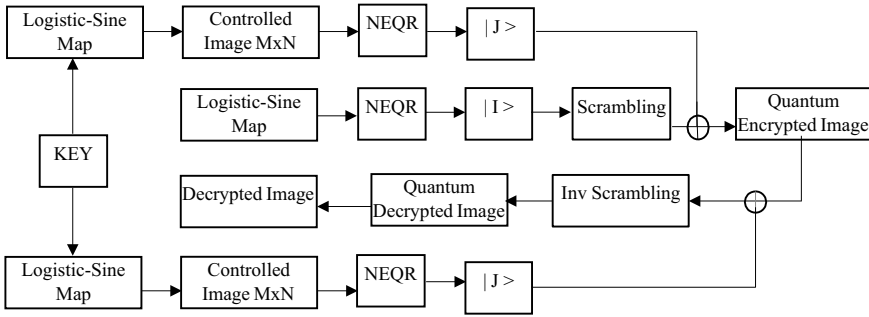


Fig. 7 Quantum chaotic scheme-1

3.4 Quantum-Chaotic Scheme 1: Robust Encryption of Quantum Medical Images

In this Quantum chaotic scheme published in paper [13], a Chaotic map is used to generate key sequences. The random key generated is then transformed to quantum images using NEQR. After that, the original image is quantized and after that, the image is scrambled, and then a controlled not operation is applied to get the ciphered image. Figure 7 given below better describe the process:

The process to obtain the ciphered image with the method is:

- Determine the initial constraints of the map.
- Transmute the sequence into a quantum representation with NEQR.
- Transmute the image in the quantum sequence.
- Scramble the transmute of the image.
- Carry the controlled-NOT operation on scrambled image and transmutation of the sequence generated.

3.5 Quantum Chaotic Scheme-2: Quantum Color Image Encryption Based on Multiple Discrete Chaotic systems

The paper is based on Quantum encryption based on multiple chaotic systems. The author Li Li et al., in the paper [14], use 3 maps to generate secret key sequences for the encryption. The logistic map is used to obtain the X sequence, the Y sequence is obtained by the asymmetric tent map and the Chebyshev map is utilized to obtain the Z sequence. Then the three sequences are transformed into a quantum color image. After that, the obtained quantum image is ciphered with the quantized original color image with a controlled-not operation. The author also compared the output by using performance metrics like- histogram analysis, correlation and keyspace. Figure 8 is used for ease of understanding of the method:

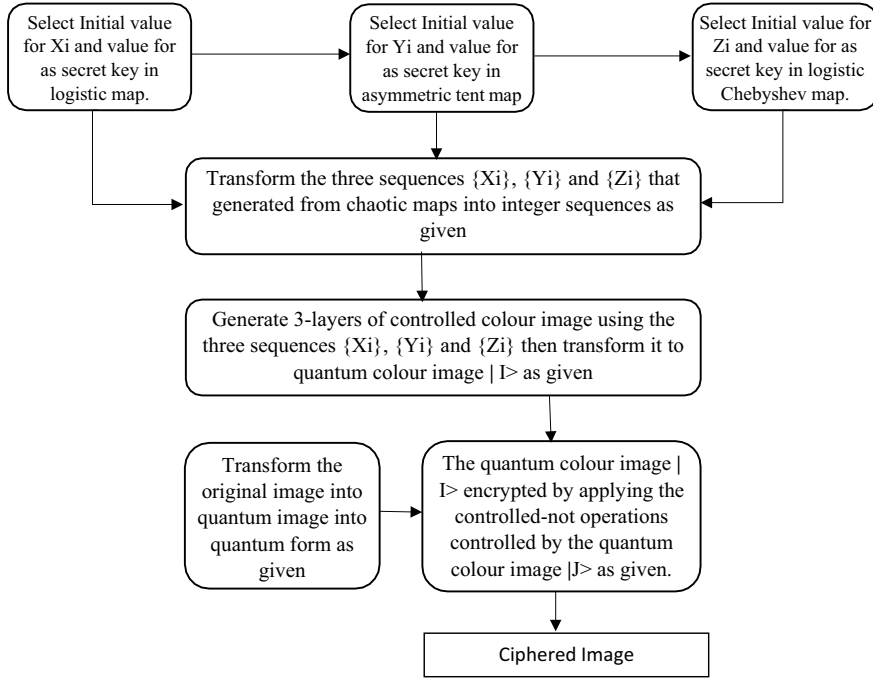


Fig. 8 Quantum chaotic scheme-2

The procedure for the ciphering is:

- Generate the X, Y and Z sequence with Logistic map, Asymmetric tent map and Chebyshev map respectively.
- Transform the sequence into integer form and form a quantum color image.
- Transform the original image into quantum form.
- Obtain the cipher image by applying the generated quantum image and original transformed quantum image.

4 Performance Metrics

The following constraints can be used for mathematical analysis as follows:

- **Visual Assessment**

The encrypted image must be highly distorted such that none of the information would be visually recognized by any intruder. This will be observed by taking snapshots. It can be analyzed by appearance of an image.

- **Key-space Analysis**

The keys used make brute-force attacks infeasible. Larger the key size larger will be the time taken for decoding for image encryption that must be very sensitive and the key space should be large enough to the key. The key space for a good encryption mechanism must be $>2^{100}$.

- **Histogram Analysis**

The histogram of an image is the frequency description of each pixel value. The histogram of encrypted images should be completely different from the original images. For the technique, a direct command is used, for good results, and encrypted images should have uniform histograms. The histogram of the encrypted image should be more random.

- **Correlation Coefficient**

An image when encoded ought to have no connection between the nearby pixels. Any relationship present can be utilized by an unapproved client to reproduce a piece of an image, or more awful the total unique image itself. A zero (0) correlation value represents that no relation is present among the variables. Correlation 1 depicts there is perfect correlation among variables and -1 indicates that variables are related inversely.

- **Number of Pixel Change Rate (NPCR)**

The NPCR measures the change rate of the number of pixels of the cipher-image on single bit change of key.

$$NPCR = \frac{\sum_{i,j} D(i,j)}{M \times N} \times 100\% \tag{2}$$

where, M and N are the width and height of two random images

$$D(i,j) = \begin{cases} 1, & \text{if } C_1(i,j) \neq C_2(i,j) \\ 0, & \text{otherwise} \end{cases} \tag{3}$$

- **Unified Averaged Changing Intensity (UACI)**

The UACI measures the average intensity of two, one or less bit changed cipher-images.

$$UACI = \frac{1}{M \times N} \left[\sum_{ij} \frac{C_1(i,j) - C_2(i,j)}{255} \right] \times 100 \tag{4}$$

where, C1 and C2 are two ciphered images. UACI value for the image must be near 33%.

- **Information Entropy Analysis**

Information entropy interpreted as the degree of disorder or randomness of an image. The entropy $H(S)$ for a given message with symbols S_i whose probabilities are $P(S_i)$ defined as:

$$H(s) = \sum_{i=0}^{n-1} P \left(S_i \log_2 \frac{1}{P(S_i)} \right) \quad (5)$$

For example, if there are 256 possible aftermaths of the message S with equal probability, then it is randomly considered. In this case, $H(S) = 8$, is an ideal value. The value of entropy close to value 8 signifies that the encryption algorithm is secure against entropy attacks.

- **Mean Squared Error (MSE)**

The MSE measures the mean squared value between the encrypted image and the original image. The mean square error of the image should be zero.

- **Peak Signal to Noise Ratio (PSNR)**

Consider original image as the signal and encrypted image as the noise. PSNR measures the presence of amount of original image in the cipher image.

- **Computational Time**

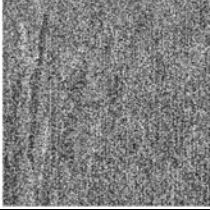
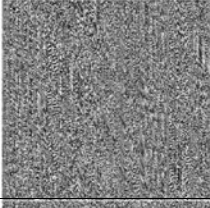
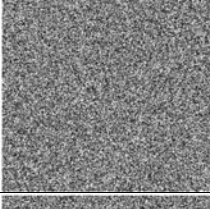
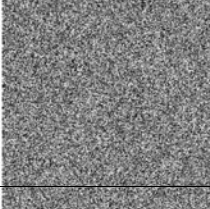
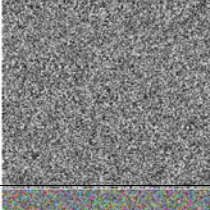
The computational time of an algorithm measures the amount of time taken by an algorithm to run as a function of the length. The encryption mechanism should be fast and consume less processing time as the images are of larger length, and the encryption at the sender and decryption at the receiver may consume a large time. The computation time for any algorithm should be as least as possible.

5 Set-Up Constraints

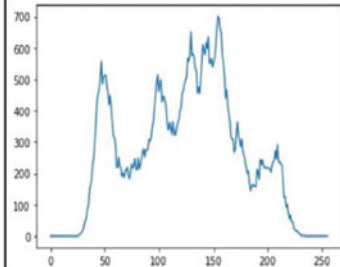
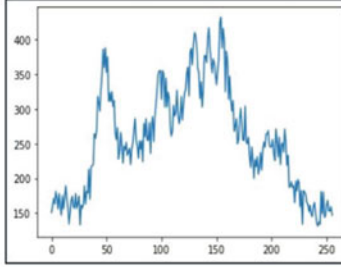
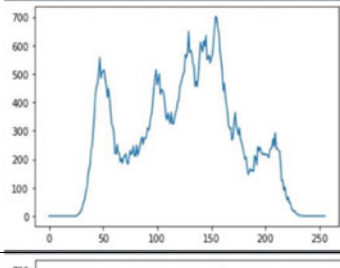
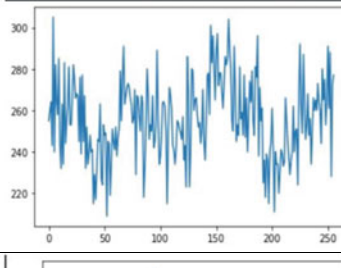
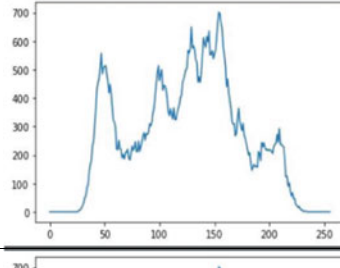
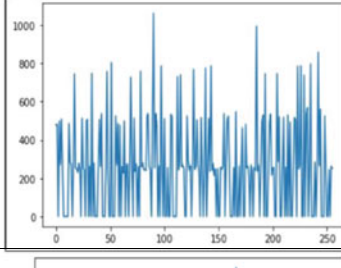
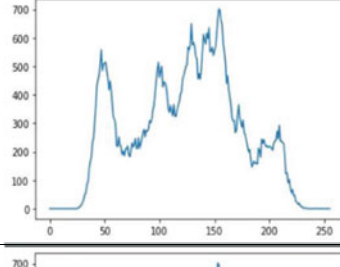
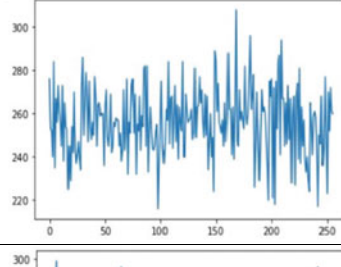
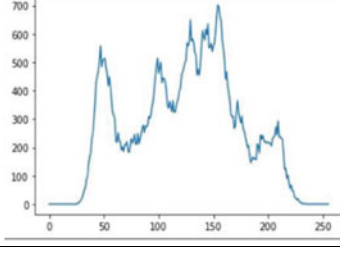
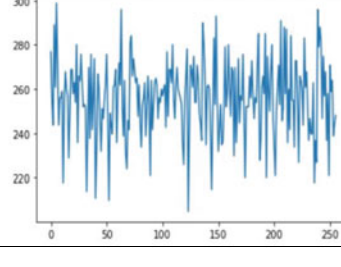
The analysis of various ciphering techniques is performed on image sizes 256*256, and 512*512. The types of images used are .jpg, .jpeg, .png and .tif that are colored or Greyscale. The processing is done on a 2.00 GHz Intel Core i3 processor with Windows 10 Home operating system. Python version 3.8.8 was used with anaconda version 4.11.0 to compile the results depicted in Section VI. For different algorithms, different constraints are used as per suggested by the papers. The performance metrics described in the previous section are used to compare the results.

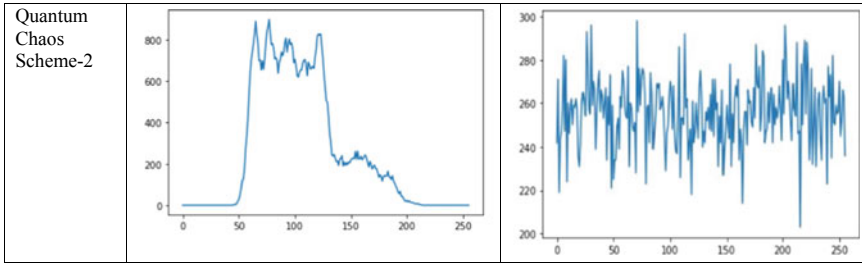
6 Results

6.1 Visual Assessment

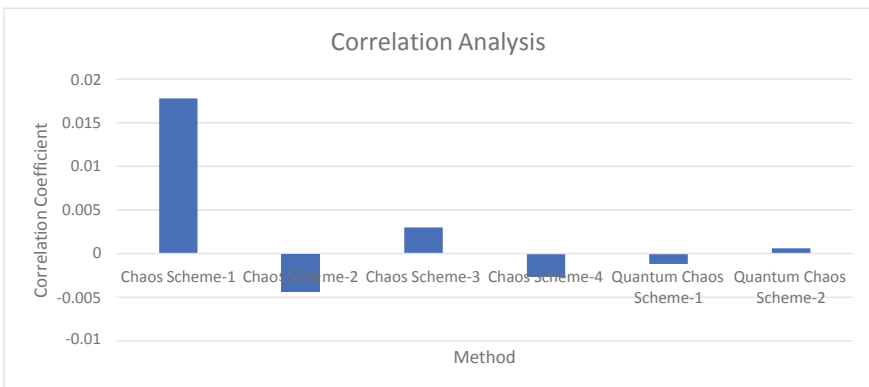
Technique	Original Image	Encrypted Image	Decrypted Image
Chaos scheme-1			
Chaos Scheme-2			
Chaos Scheme-3			
Chaos Scheme-4			
Quantum Chaos Scheme-1			
Quantum Chaos Scheme-2			

6.2 Histogram Analysis

Technique	Original Image	Encrypted Image
Chaos scheme-1	 A line graph showing the histogram of the original image for Chaos scheme-1. The x-axis represents pixel intensity from 0 to 255, and the y-axis represents frequency from 0 to 700. The curve shows a bimodal distribution with peaks around 50 and 150.	 A line graph showing the histogram of the encrypted image for Chaos scheme-1. The x-axis represents pixel intensity from 0 to 255, and the y-axis represents frequency from 150 to 400. The curve shows a bimodal distribution similar to the original image but with a lower frequency range.
Chaos Scheme-2	 A line graph showing the histogram of the original image for Chaos Scheme-2. The x-axis represents pixel intensity from 0 to 255, and the y-axis represents frequency from 0 to 700. The curve shows a bimodal distribution with peaks around 50 and 150.	 A line graph showing the histogram of the encrypted image for Chaos Scheme-2. The x-axis represents pixel intensity from 0 to 255, and the y-axis represents frequency from 220 to 300. The curve shows a noisy, irregular distribution.
Chaos Scheme-3	 A line graph showing the histogram of the original image for Chaos Scheme-3. The x-axis represents pixel intensity from 0 to 255, and the y-axis represents frequency from 0 to 700. The curve shows a bimodal distribution with peaks around 50 and 150.	 A line graph showing the histogram of the encrypted image for Chaos Scheme-3. The x-axis represents pixel intensity from 0 to 255, and the y-axis represents frequency from 0 to 1000. The curve shows a noisy, irregular distribution.
Chaos Scheme-4	 A line graph showing the histogram of the original image for Chaos Scheme-4. The x-axis represents pixel intensity from 0 to 255, and the y-axis represents frequency from 0 to 700. The curve shows a bimodal distribution with peaks around 50 and 150.	 A line graph showing the histogram of the encrypted image for Chaos Scheme-4. The x-axis represents pixel intensity from 0 to 255, and the y-axis represents frequency from 220 to 300. The curve shows a noisy, irregular distribution.
Quantum Chaos Scheme-1	 A line graph showing the histogram of the original image for Quantum Chaos Scheme-1. The x-axis represents pixel intensity from 0 to 255, and the y-axis represents frequency from 0 to 700. The curve shows a bimodal distribution with peaks around 50 and 150.	 A line graph showing the histogram of the encrypted image for Quantum Chaos Scheme-1. The x-axis represents pixel intensity from 0 to 255, and the y-axis represents frequency from 220 to 300. The curve shows a noisy, irregular distribution.

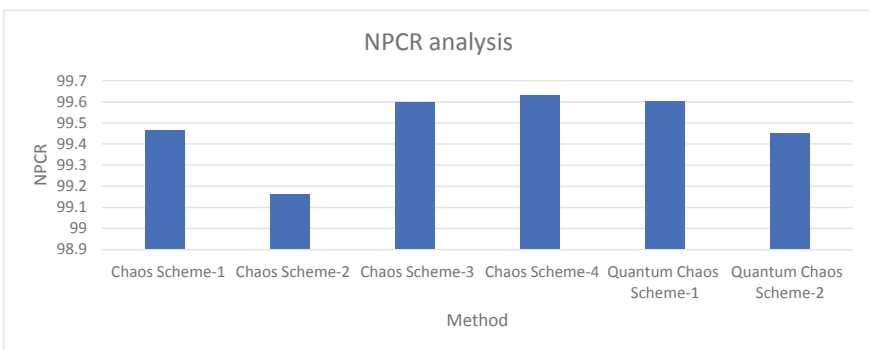


6.3 Correlation Coefficient



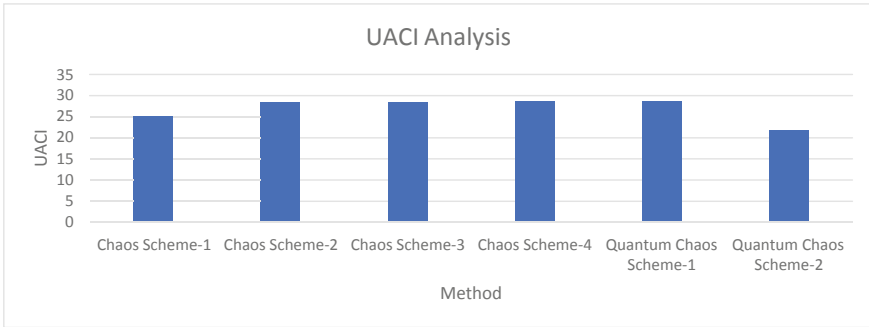
Conclusion: The Quantum scheme-2 represents the best correlation value among all approaches.

6.4 Number of Pixel Change Rate (NPCR)



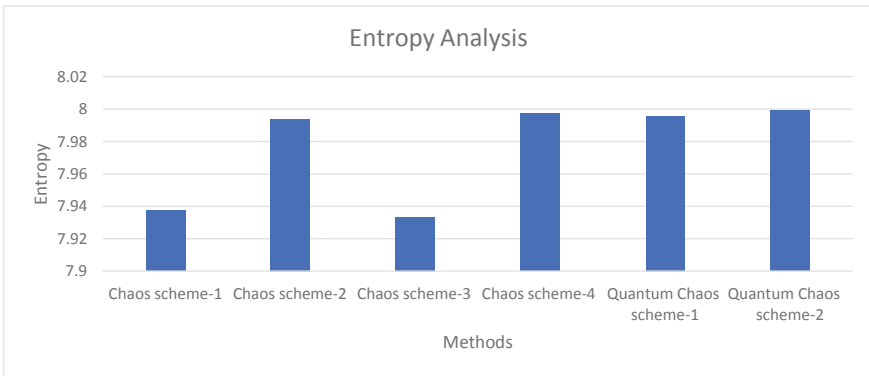
Conclusion: Chaos scheme-4 has highest PSNR among all approaches.

6.5 Unified Averaged Changing Intensity (UACI)



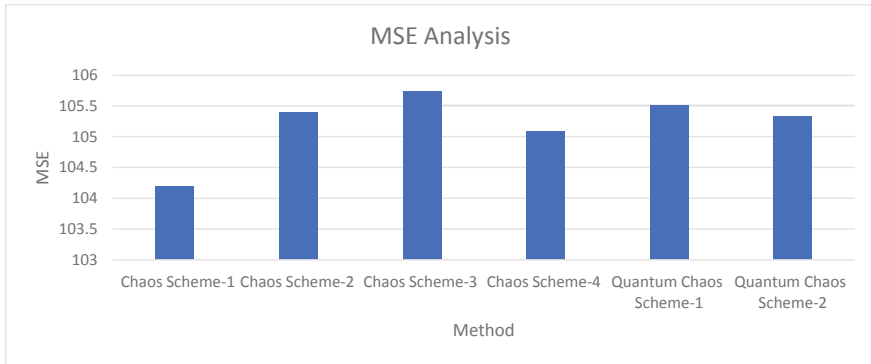
Conclusion: The above figure shows that Quantum chaos scheme-1 has highest UACI.

6.6 Information Entropy Analysis



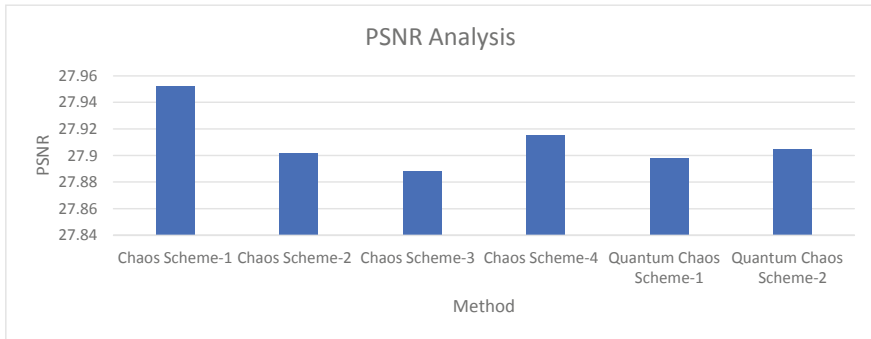
Conclusion: On the basis of the above result it can be concluded that Quantum Scheme-2 has highest Entropy.

6.7 Mean Squared Error (MSE)



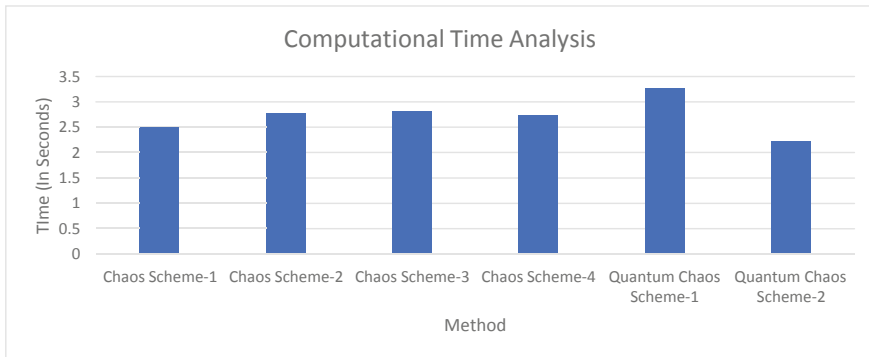
Conclusion: Chaos scheme-3 has highest MSE among all approaches.

6.8 Peak Signal to Noise Ratio (PSNR)



Conclusion: As shown by above figure chaos scheme-3 is good in lowest PSNR.

6.9 Computational Time



Conclusion: The quantum chaos scheme-2 is best because of low computational time.

7 Conclusion and Future Scope

On the basis of above performance metrics, it can be concluded that Quantum scheme has major advantage and, in most constraints, it leads the other. So, this method can be considered good based on above data.

References

1. Mishra KK, Misra AK, Mueller P, Martinez Perez G, Bhatia SK, Wang Y (2014) 'Recent advancements in computer & software technology'. *Sci World J* 2014: 1–1. doi: <https://doi.org/10.1155/2014/609512>
2. Danti A, Nayak R 'Data encryption by excluding repetitive character in cipher text'. 7
3. 'India 3rd In Data Breaches Till Nov | India Business News-Times of India'. <https://timesofindia.indiatimes.com/business/india-business/india-3rd-in-data-breaches-till>. Accessed 03 Apr 2022
4. 'Eighth Annual Cost of Cybercrime Study | Accenture'. <https://www.accenture.com/us-en/insights/security/eighth-annual-cost-cybercrime-study>. Accessed 03 Apr 2022
5. Kaur M, Singh S, Kaur M (2021) Computational image encryption techniques: a comprehensive review. *Math Probl Eng* 2021:1–17. <https://doi.org/10.1155/2021/5012496>
6. Jindal P, Singh B (2014) 'Performance analysis of modified RC4 encryption algorithm'. In: International Conference on Recent Advances and Innovations in Engineering (ICRAIE-2014), Jaipur, India, 1–5. doi: <https://doi.org/10.1109/ICRAIE.2014.6909247>
7. Patel T, Srivastava R (2016) 'Hierarchical visual cryptography for grayscale image'. In: 2016 Online International Conference on Green Engineering and Technologies (IC-GET), Coimbatore, India, 1–4. doi: <https://doi.org/10.1109/GET.2016.7916685>

8. National Bureau of Standards (1993) 'Federal information processing standards publication: data encryption standard (DES)'. National Institute of Standards and Technology, Gaithersburg, MD, NIST FIPS 46-2. doi: <https://doi.org/10.6028/NIST.FIPS.46-2>
9. Arivazhagan S, Jebarani WSL, Kalyani SV, Deiva Abinaya A (2017) 'Mixed chaotic maps based encryption for high crypto secrecy'. In: 2017 Fourth International Conference on Signal Processing, Communication and Networking (ICSCN), Chennai, India, 1–6. doi: <https://doi.org/10.1109/ICSCN.2017.8085697>
10. Elghandour A, Salah A, Karawia A (2022) A new cryptographic algorithm via a two-dimensional chaotic map. *Ain Shams Eng J* 13(1):101489. <https://doi.org/10.1016/j.asej.2021.05.004>
11. Al-Maadeed TA, Hussain I, Anees A, Mustafa MT (2021) A image encryption algorithm based on chaotic lorenz system and novel primitive polynomial S-boxes. *Multimed Tools Appl* 80(16):24801–24822. <https://doi.org/10.1007/s11042-021-10695-5>
12. Devi AA, Ramana AV (2019) 'Chaotic based lightweight image encryption algorithm for real-timeapplication systems'. 7(6): 6
13. Abd El-Latif AA, Abd-El-Atty B, Talha M (2018) 'Robust encryption of quantum medical images'. *IEEE Access* 6: 1073–1081. doi: <https://doi.org/10.1109/ACCESS.2017.2777869>
14. Li L, Abd-El-Atty B, El-Latif AA, Ghoneim A (2017) 'Quantum color image encryption based on multiple discrete chaotic systems'. pp. 555–559. doi: <https://doi.org/10.15439/2017F163>
15. Priyadharshini A, Umamaheswari R, Jayapandian N, Priyananci S (2021) 'Securing medical images using encryption and LSB steganography'. In: 2021 International Conference on Advances in Electrical, Computing, Communication and Sustainable Technologies (ICAECT), Bhilai, India, 1–5. doi: <https://doi.org/10.1109/ICAECT49130.2021.9392396>

Analyzing Chaos in SMIB Power System



Sheetal and Sanju Saini

1 Introduction

Power system chaos has been observed for a wide range of loadings. Power system chaos leads to harmful and undesirable effects in power systems. The growing power demand drives the system to operate at boundary conditions with trivial stability margins. A chaotic nature can be increased because of unexpected disturbances in the operating conditions. Chaos leads to voltage collapse which results in voltage instability, a kind of power system instability. The power system experiences voltage collapse when subjected to heavy reactive loads causing excessive reactive power (Lagging VAR) demands. Voltage collapse is realized when the system's operational point gradually changes, following the growing reactive power demand that causes decay in voltage magnitude at a steady rate until a stage reached when a steeper voltage drop occurs. Catastrophic blackouts can be occurred because of voltage collapse. Hence a satisfactory control of the system is required for alleviating and controlling chaos in power systems. Chaos control is all about suppressing and alleviating the chaotic oscillations when they are harmful [1–3]. In recent times chaos has been proven useful in several areas span power systems to biomedical engineering [4]. Therefore chaos control and its generation (chaotification) have drawn the attention of several researchers in recent years [5–8].

Sheetal (✉) · S. Saini

Department of Electrical Engineering, Deenbandhu Chhotu Ram University Of Science & Technology, Sonapat, Haryana, India
e-mail: Sheetal08041988@gmail.com

S. Saini

e-mail: Sanjusaini.ee@dcrustm.org

Sheetal

Department of Electrical and Electronics Engineering, KIET Group of Institutions, Ghaziabad, Uttar Pradesh, India

The power system and its complexities are growing day by day. The recent advancements in software technology and non-linear mathematical theories enable us to analyze and understand the core complexities of modern power systems. Several state-of-the-art studies in the domain propose different theories and methodologies in this context.

Many researchers proposed several control strategies for suppressing chaos and enhancing voltage stability in the power systems. Neural and fuzzy control methods were studied. The development of linear and nonlinear state feedback controllers have been proposed for controlling bifurcation in power systems. A passivity-based adaptive control technique has been deployed to mitigate the chaos in power systems.

In [9], authors detected chaos in a two-degree freedom swing equation using Melnikov's method. The chaotic behavior of a SMIB system using the perturbation technique is discussed and presented in [10]. The power system non-linear dynamics using Hopf bifurcation is discussed in [11]. The steady-state stability and voltage collapse has been discussed in [12] with static bifurcations.

This paper analyzes the chaos in SMIB power systems using Lyapunov exponents and Poincare maps. The remaining article is presented as: Sect. 2 presents the SMIB modeling and analyzes chaos using a bifurcation diagram, Poincare's map, and phase trajectory. The conclusion of the work is presented in Sect. 3 followed by justified references.

2 The SMIB Modeling and Chaotic Analysis

Figure 1 portrays a standard SMIB power system in which a generator is supplying bulk power to the load connected at the infinite bus. The swing equation (Eq. 1) governing the conventional SMIB power system is discussed and presented in [13].

$$M\ddot{\theta} + D\dot{\theta} + P_{\max} \sin \theta = P_m \quad (1)$$

where

M-Moment of inertia,

D-Damping constant,

P_m -Machine's Power,

P_{\max} -Generator's maximal power.

$$\text{Here, } P_m = A \sin \omega t. \quad (2)$$

Hence, the motion equation in the 1st-order form can be presented by Eqs. 3 and 4.

$$\begin{cases} \dot{x}_1 = x_2, \\ \dot{x}_2 = -cx_2 - \beta \sin x_1 + f \sin \omega t, \end{cases} \quad (3)$$

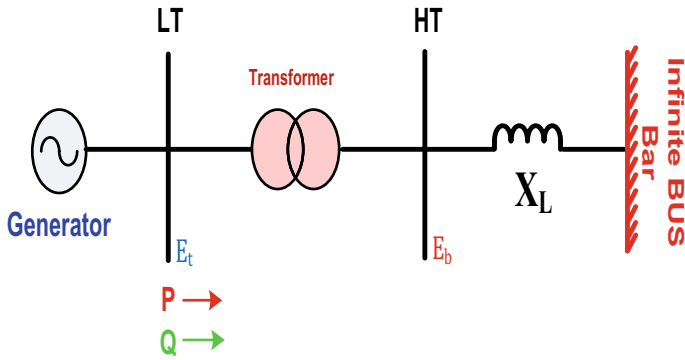


Fig. 1 Standard SMIB system

where,

$$x_1 = 0, x_2 = \dot{\theta}, c = \frac{D}{M}, \beta = \frac{P_{max}}{M}, f = \frac{A}{M}. \tag{4}$$

Using the Lyapunov direct technique, this section describes the system’s local stability. At the start, the fixed points of the system have been examined with the Lyapunov stability analysis [14]. It has been observed (A) $x_1 = x_2 = 0$ and (B) $x_1 = \pi, x_2 = 0$ are the fixed points \forall values of parameter for an autonomous system (as $A = 0$).

For stability analysis, For a fixed point (A) $(x_1, x_2) = (0, 0)$, let the disturbance of motion be represented by Eq. 5

$$\begin{cases} x_1 = \xi_1, \\ x_2 = \xi_2, \end{cases} \tag{5}$$

We get the disturbance equation on substituting Eq. (5) in (3), as represented by Eq. 6

$$\begin{cases} \dot{\xi}_1 = \xi_2, \\ \dot{\xi}_2 = -c\xi_2 - \beta \sin \xi_1. \end{cases} \tag{6}$$

Considering Lyapunov function in the form of Eq. 7

$$V(\xi_1, \xi_2) = \frac{1}{2}\xi_2^2 + \frac{\beta}{2}(1 - \cos \xi_1). \tag{7}$$

This is evident that it is positive definite with derivative given in Eq. 8.

$$-\dot{V}(\xi_1, \xi_2) = c\xi_2^2 \tag{8}$$

The function $-V$ is semi-positive definite. Following the Lyapunov stability theory, $(x_1, x_2) = (0, 0)$ is the stable equilibrium. For studying stability for the fixed point (B) $(x_1, x_2) = (\pi, 0)$, let the disturbed motion is represented by Eq. 9.

$$\begin{cases} x_1 = \pi + \xi_1, \\ x_2 = \xi_2, \end{cases} \tag{9}$$

Substituting Eq. (9) in (3), we have

$$\begin{cases} \dot{\xi}_1 = \xi_2, \\ \dot{\xi}_2 = -c\xi_2 + \beta\xi_1 - \frac{1}{6}\beta\xi_1^3 + O(\xi_i)^5, \end{cases} \tag{10}$$

where $O(\xi_i)^5$ is the higher order term. V , expressed as Eq. (11)

$$V(\xi_1, \xi_2) = \xi_1\xi_2 \tag{11}$$

The total derivative of $-V$ is

$$-\frac{dV}{dt} = \beta\xi_1^2 - \xi_2^2 - c\xi_1\xi_2 + O(\xi_i)^3 \tag{12}$$

The requirements for $-V$ is given in Eq. (13)

$$c^2 > 4\beta, \quad i.e., \quad D^2 > 4MP_{max}. \tag{13}$$

Following Lyapunov theory, Eq. (13) completely describes the instability of system and the fixed point $(x_1, x_2) = (\pi, 0)$, at unstable equilibrium. This establishes stability and instability. The present study numerically integrates the nonlinear motion Eq. (3). While ascertaining the dynamics of power system, it is evident, that several parameters like continuous spectrum, bounded trajectory, strange attractor, fractional dimensions, etc. characterize the chaotic characteristics of power system. Examining the graph of $\dot{\theta}(x_2)$ wrt the f (normalized amplitude) for specified values of β , c , and, ω (the sinusoidal wave frequency) readily detects the bifurcation in SMIB systems.

The 4-th order Runge–Kutta numerical method with twenty initial conditions helps in obtaining the bifurcation. For each value of the normalized amplitude, f ($=M/A$) (of the sinusoidal wave), first 300 points (of the Poincare map) have been removed, excluding the transient state. Following this, the system is assumed in a steady state and velocity for the next few points ($= 200$ here) is shown on the bifurcation diagram. Figure 2 portrays the bifurcation diagram for a particular set of values ($\beta = 1, c = 0.5$, and, $\omega = 1$).

The period-doubling bifurcation phenomenon can be easily observed. The Poincare map and phase trajectories for $f = 2.34$ have been shown in Fig. 3a and b.

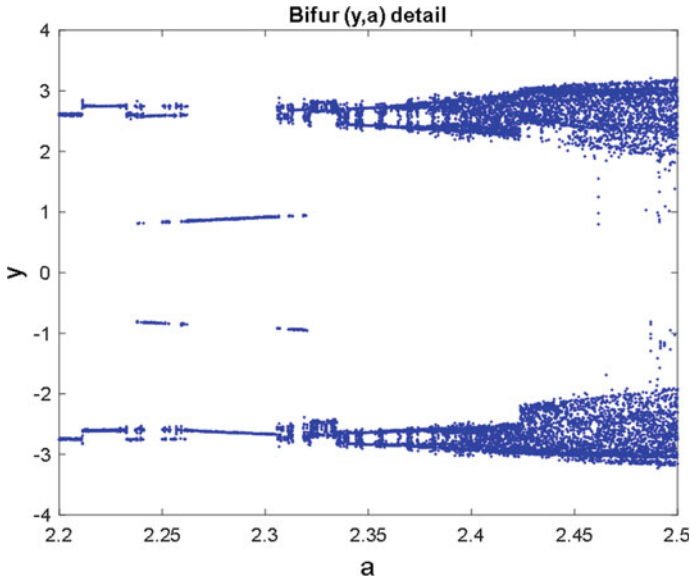


Fig. 2 Bifurcation diagram of x_2 against f for ($\beta = 1, c = 0.5$ and $\omega = 1$)

Phase trajectory and Poincare’s map for $f = 2.41$ have been portrayed in Fig. 4a and b. Figure 5 portrays the 3-D image of the SMIB-attractor for ($\beta = 1, c = 0.5$ and, $\omega = 1$), which also exhibits the chaotic behavior of the system.

3 Conclusion

This study examines the nonlinear/chaotic behavior of a SMIB power system. The chaotic motions of the system have been analyzed and shown using a Poincare map and bifurcation diagrams. The overall motion equation is by nature highly nonlinear and non-autonomous. The Lyapunov direct method hinders getting the positive definite Lyapunov function. The difficulty has been overcome in Sect. 2. Here the Lyapunov direct method has been deployed while getting the conditions (sufficient) for the system stability. Parameter-dependent system’s bifurcation has been numerically investigated.

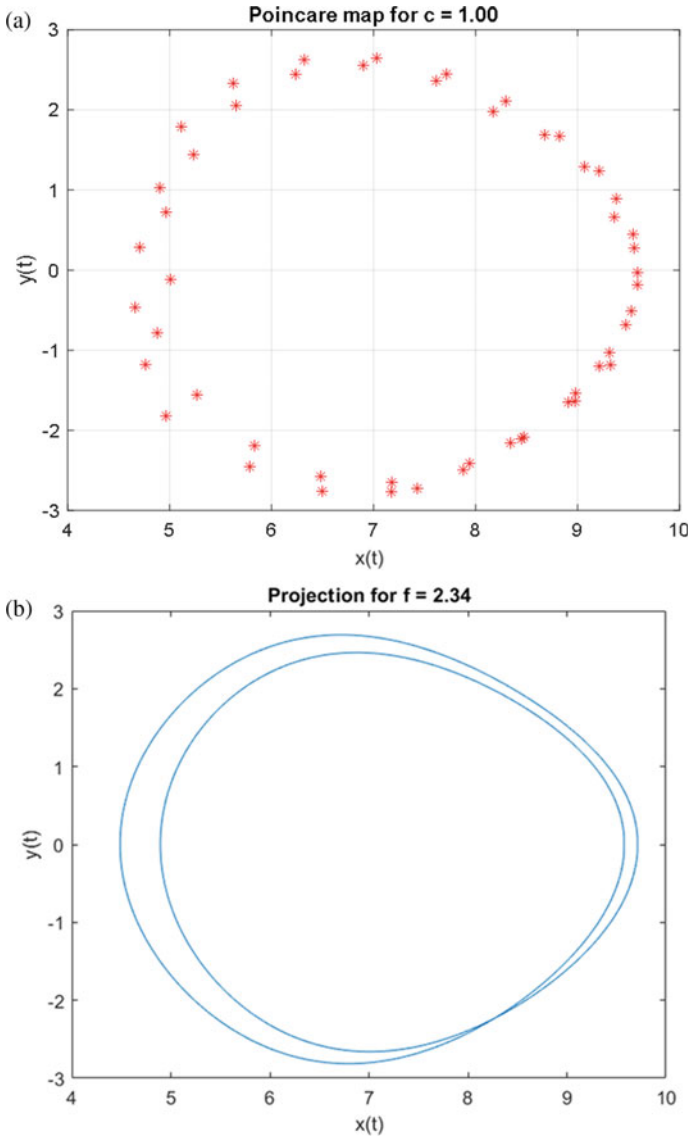


Fig. 3 a The poincare map ($f = 2.34$) ($2-T$ periodic) b Phase trajectory ($f = 2.34$) ($2-T$ periodic)

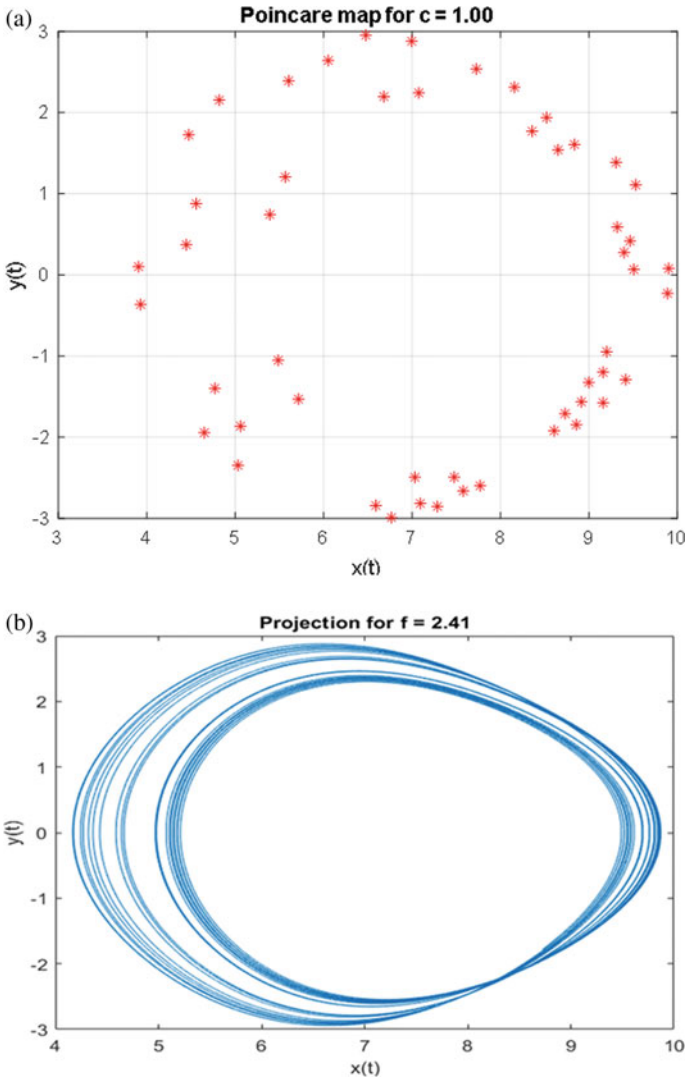


Fig. 4 a Poincare map ($f = 2.41$) (chaotic) b Phase trajectory ($f = 2.41$) (chaotic)

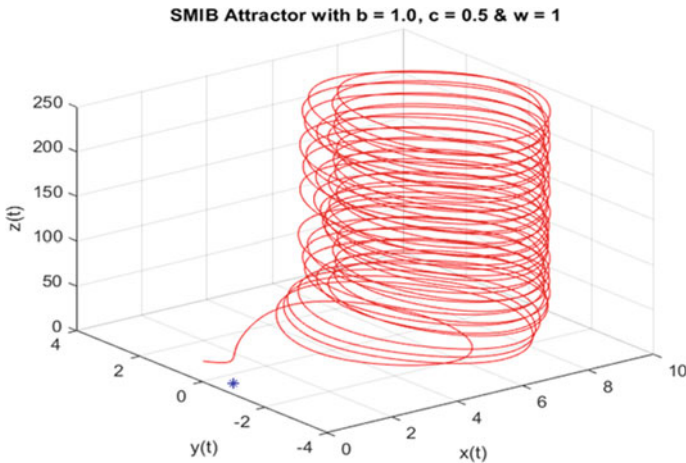


Fig. 5 3D image of SMIB-attractor ($\beta = 1$, $c = 0.5$, and $\omega = 1$)

References

1. Ott E, Grebogi C, Yorke JA (1990) Controlling chaos. *Phys Rev Lett* 64:1196–1199
2. Kapitaniak T (1992) Controlling chaotic oscillations without feedback. *Chaos, Solitons Fractals* 2:519–530
3. Chen G (ed) (1999) Controlling chaos and bifurcation in engineering system. CRC Press, Boca Raton
4. Chen G, Dong X (1998) From chaos to order: methodologies, perspectives and applications. World Scientific, Singapore
5. Chen G, Lai D (1998) Anticontrol of chaos via feedback. *Int J Bifurcat Chaos* 8:1585–1590
6. Chen G, Starkov K (2004) Chaotification of polynomial continuous-time systems and rational normal forms. *Chaos, Solitons Fractals* 22:849–856
7. Wang XF, Chen G, Yu X (2000) Anticontrol of chaos in continuous-time systems via time-delay feedback. *Chaos* 10:771–779
8. Chen HK, Lee CI (2004) Anti-control of chaos in rigid body motion. *Chaos, Solitons Fractals* 21:957–965
9. Kopell N, Washburn RB (1982) Chaotic motions in the two-degree-of-freedom swing equations. *IEEE Trans Circ Syst CAS-* 29:738–746
10. Nayfeh MA, Hamdan AMA, Nayfeh AH (1990) Chaos and instability in a power system-primary resonant case. *J Non-linear Dyn.* 3:313–339
11. Abed EH, Varaiya PP (1984) Nonlinear oscillations in power system. *Int J Electr Power Energy Syst.* 6:37–43
12. Kwatny HG, Bahar LY, Pasrija AK (1986) Static bifurcation in electric power networks: loss of steady-state stability and voltage collapse. *IEEE Trans CAS* 33:981–991
13. Yamayee ZA, Bala JL (1990) Electromechanical energy devices power systems. John Wiley & Sons, New York
14. Vidyasagar M (1993) Non-linear system analysis. Prentice-Hall, London

Hybrid AC/DC Microgrid Control and Management of Power Using Bidirectional AC/DC Converter by Autonomous Control Mode



S. Mamatha and G. Malleshham

1 Introduction

According to the Central Electricity authority of India, total power consumption in India has increased from 914 Kwh in 2012 to 1280 Kwh in 2020.

Total installed capacity in India is 3,93,389.46 MW, out of this from coal 2,09,809.5 MW is generated, from gas 24,899 MW is generated, from diesel 509.71 MW is generated, from nuclear resources 6780 MW is generated, from hydro resources 46512.22 MW is generated and from RES 104878.53 MW is generated. According to the CEA, the total energy share by the fossil fuel such as coal, gas, nuclear energy is 73%. These realities are causing a rapid depletion of the conventional resources needed to keep the current energy system running, and they are a significant source of CO₂ emissions into the atmosphere.

The power consumption scenario we can observe in developing countries like India as increasing. As the conventional energy sources are decreasing day by day to meet the increasing power demand in India the installation of renewable energy systems (RES) into the existing power system is taking place in an Indian power system [1–13]. To overcome the rapid increase in power demand Microgrid is the best solution. In this paper an AC microgrid is modeled using a Wind energy system, fuel cell and a supercapacitor which are included for the purpose of storage of energy generated from RES connected at the AC microgrid [12–15]. As generated power from the RES is DC we will use an inverter to change the power from dc to ac. The DC microgrid is modeled using RES such as PV, and Wind and battery are used for storage and discharge of power according to the load demand. The interlinking converter [1–15], will take the responsibility of exchange of power between AC and DC microgrids [15–30].

S. Mamatha · G. Malleshham (✉)
Electrical Engineering, Osmania University, Hyderabad, India
e-mail: gm.eed.cs@gmail.com

2 Introduction to Microgrid

A Microgrid is collection of different loads such as ac loads and dc loads, respectively, and distributed energy resources (DERs) such as solar, wind, fuel cell etc., that function as a unique structure, contain well-defined electrical parameter limitations. Microgrid structure is shown in Fig. 1. A Microgrid is a distribution network with self-regulation capabilities and control entities, such as RES, power conversion devices and load management.

New models are being developed, and they have been fairly accustomed to these new techniques to dispersed production and they have been envisioned for future periods. By interpreting the microgrids at remote locations and islands could be the best solution to reach the power demand. Because of the near proximity of electricity sources to various users, costs and losses are kept to a minimum. When the utility grid accessibility is down, MG's outstanding particular operating ability has gained high dependability measures in providing power requirements. To make the hybrid system to function in both connected mode and as well as in islanded mode, a microgrid can connect to the main grid and disengage to the main grid. If managed and coordinated properly, the functioning of micro sources in the network can boost the overall system performance. Scheduled maintenance, reduced deficit in the main grid, failures in the local sub grid, or economic considerations may lead a microgrid to switch between these two modes.

Smart grids are the advancement to the electrical power system network. Smart grids are those where Microgrids especially DG's are interconnected. Distributed generators means power generation from renewable energy systems such as PV, Wind, Biomass, Fuel cell etc., will generate clean energy. Smart grids will help in modernizing the existing power system network by the use of digital communication and new control technologies which can improve the Security, reliability and efficiency of the electric grid. Grid operations and resources are dynamically optimized, with comprehensive cyber-security. Smart metering, grid operations and

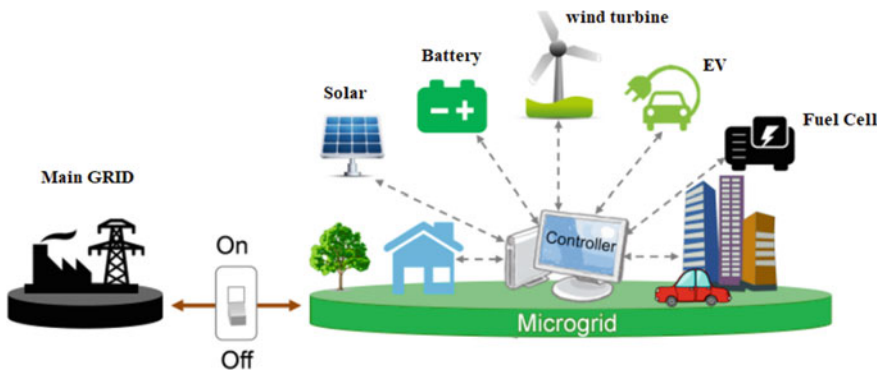


Fig. 1 Microgrid architecture

status messaging, and distribution automation technologies are being developed. Advanced power storage and peak-shaving technologies are being implemented and integrated, including plug-in hybrid and electric cars, as well as thermal storage air conditioning. Identifying and eliminating arbitrary or ineffective barriers to the adoption of smart grid technology, techniques, and services is done. To develop a smart grid, innovative goods and services are integrated with intelligent monitoring, control, communication, and self-healing technology.

3 Introduction to AC Microgrid

In AC microgrid various distributed generation sources and storage elements are connected to the bus through suitable and feasible conversion devices. The AC microgrid architecture is shown in Fig. 2. The DC power generated from Solar system, fuel cell etc. has to be converted into AC using dc to ac power converters, then the DG will be connected to the main AC bus. AC microgrids have the advantage that they can utilize the existing infrastructure of existing ac power grids as well as its standards and control strategies. AC microgrids need to take care of power factor and synchronization.

4 Introduction to DC Microgrid

In recent times, DC microgrids have increased attention due to Renewable Energy Systems such as Photo Voltaic systems, Fuel cell, Wind energy systems etc, which generate DC power. DC microgrid architecture is shown in Fig. 3. Due to the increase in present DC loads such as hybrid and electric vehicles, communication and data

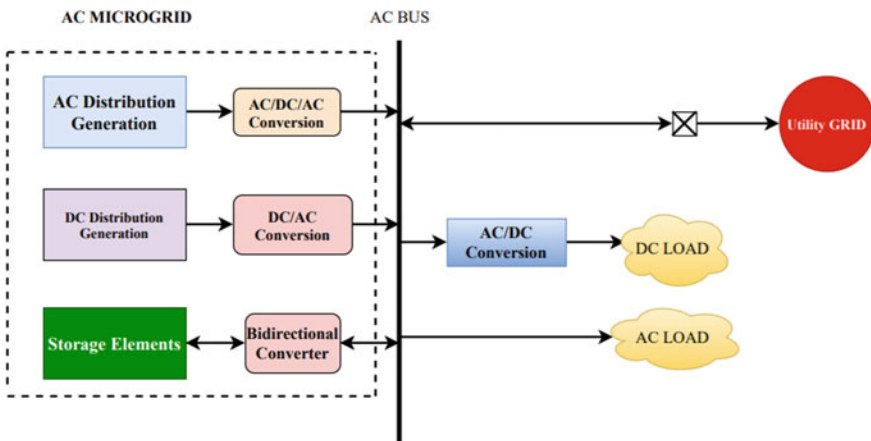


Fig. 2 AC microgrid architecture

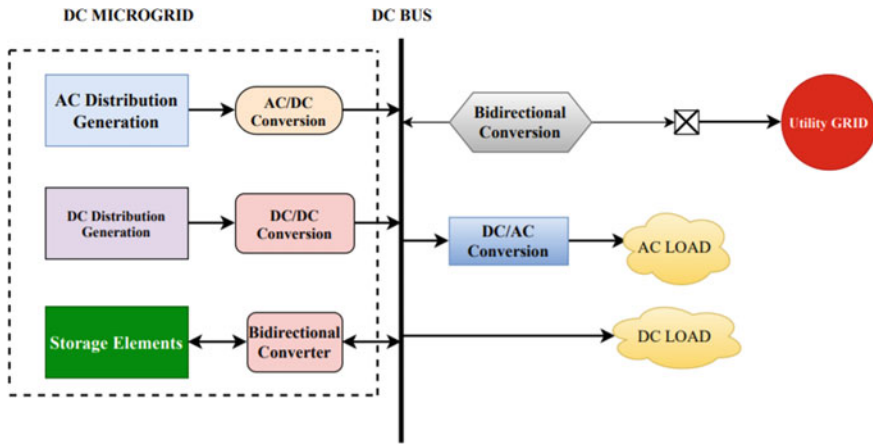


Fig. 3 DC microgrid architecture

centers, printers, laptops etc. DC microgrids have gained much attention. In reality, dc microgrids can readily integrate the dc power provided by most DERs, in addition to providing high power quality and transformer-less voltage levels, resulting in increased distribution network efficiency, with reduced size, and cost. On the other side, power electronic devices are required to feed existing ac loads. Furthermore, there are additional issues associated with the deployment and operation of dc grids that need to be explored in order to make dc microgrids technology more accessible.

5 Hybrid AC-DC Microgrid

A Hybrid ac/dc microgrid [1–39] has recently been proposed as an emerging architecture in future power networks to incorporate the benefits of both the dc microgrid and ac microgrid. Hybrid ac-dc microgrid architecture is shown in Fig. 4. Hybrid ac/dc microgrid consists of both the AC microgrid and DC microgrid separately which are interconnected with each other using an interlinking converter which is also called the bidirectional converter which is having the feasibility of exchange of power between the two grids depending on the load demand. In general, a hybrid structure is defined as having both dc and ac main power sources [11, 12, 30–37].

This hybrid layout will improve the complex structure efficiency as it consists of many RES, decreases the overall system cost due to less conversion stages and loads fed with concerned power generating buses. Although the notion of an ac–dc-coupled hybrid structure is enticing, significant study and development is required, especially in terms of energy and power management. Both dc and ac bus voltage regulation, balancing of powers between the dc and ac subsystems, must be considered in the management of such a system. Controllers of hybrid power systems and power balancing systems are the most important aspects in the operation of the hybrid

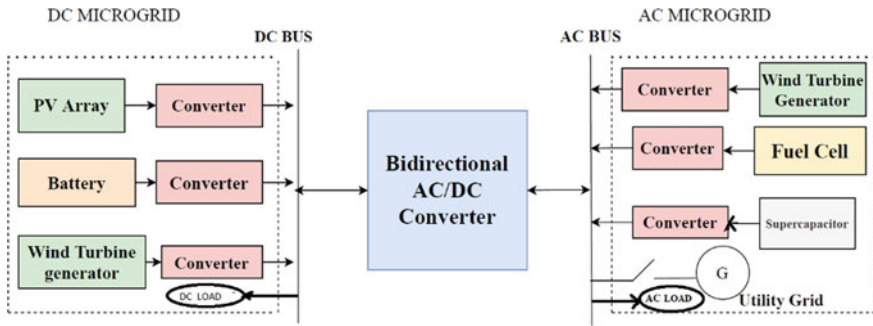


Fig. 4 AC/DC microgrid architecture

system. Power management systems will control the voltage and frequency as well as the output active and reactive power of Distributed Generators and Storage Elements. The above mentioned hybrid structure consists of multiple RES, Storage elements are connected to the dc bus and ac bus. As a result, greater coordination between the ac bus and dc bus is required. For controlling the hybrid structure, for better power management and control there is a necessity of controlling of voltage and balancing of power between the ac microgrid and dc microgrid is essential. The power and voltage in the hybrid ac/dc microgrid must be controlled by the bidirectional AC/DC converter, which is connected between the ac and dc microgrids.

6 Proposed System Modeling

Modelling the proposed hybrid system involves modelling of AC microgrid, modelling of DC microgrid and designing the interlinking converter with autonomous control. The proposed system architecture is shown in Fig. 5.

7 Modeling of the AC Microgrid

The AC microgrid is based on the wind turbine generator, Fuel cell and super capacitor. According to the aerodynamic characteristics of wind turbine

$$P_m = 0.5 \rho A C_P V^3 \tag{1}$$

where, ρ : air density (Kg/m^3)

A: Swept area

C_p : Power coefficient of wind turbine

V: Wind speed

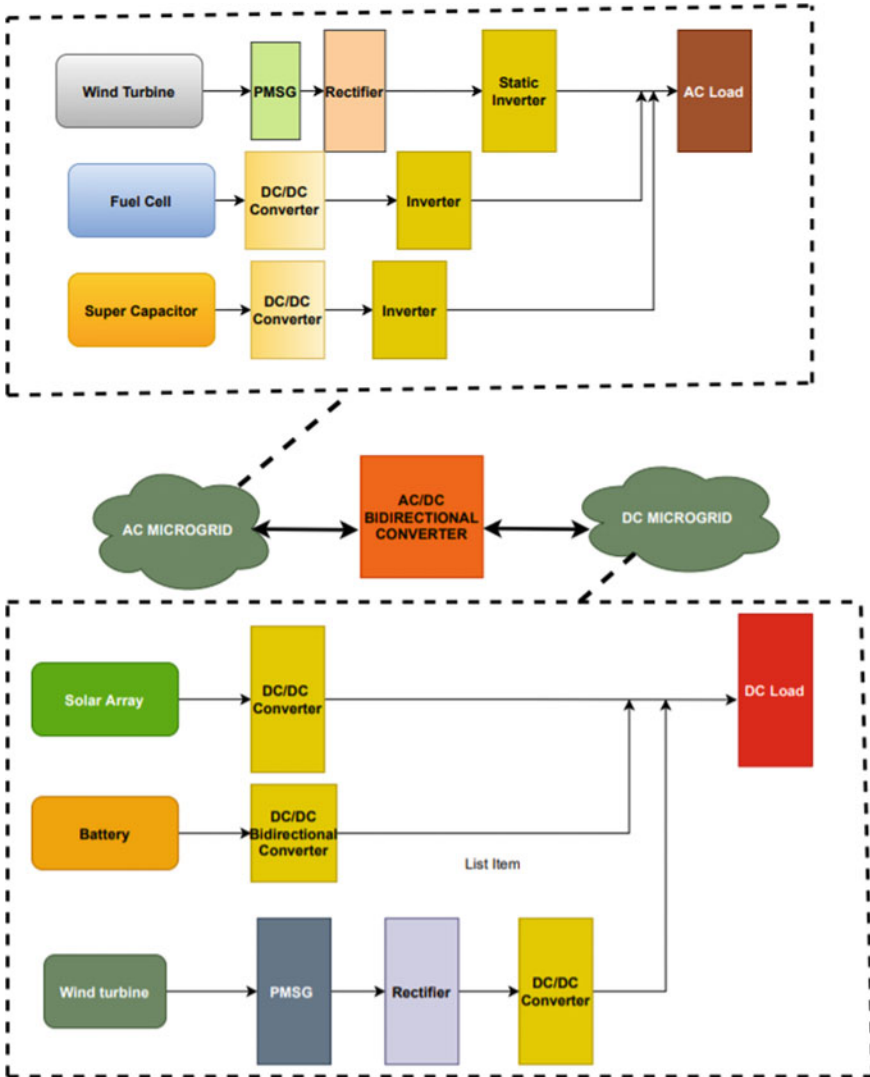


Fig. 5 Proposed hybrid AC/DC microgrid architecture

Therefore, if the air density, swept area, and wind speed are constant the output power of the turbine will be a function of power coefficient of the turbine. In addition, the wind turbine is normally characterized by its C_p -TSR curve; where, TSR, tip-speed rate

$$TSR = \frac{\omega R}{V} \tag{2}$$

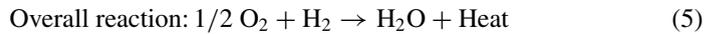
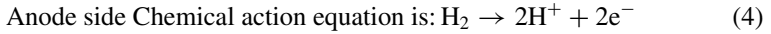
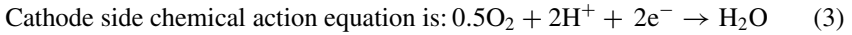
In the above equation ω is turbine speed in “rad/sec”,

R is the radius blade in “m”,

V is the wind speed “m/s”, respectively.

Among the RES, the Fuel cell is also a power generating source with neat and clean energy.

The Basic structure of fuel cell is with electrochemical reaction is as follows



Super capacitor is a high capacity capacitor which also called ultra capacitor. It can tolerate many charge and discharge cycles just like the battery.

8 Modeling of DC Microgrid

DC microgrid in the proposed system consists of a PV system, Wind turbine, and battery

PV system:

Photovoltaics are materials or technologies that can convert the energy contained in photons of light into voltage and current. Photovoltaic systems use semiconductor materials to convert sunlight into power.

V–I characteristic curve for p–sn junction diode is described by the following equation. V–I characteristics are shown in Fig. 6.

$$I_d = I_0(e^{qV_d/kT} - 1). \quad (6)$$

9 Operation of Bidirectional AC/DC Converter

Bidirectional AC/DC converter is used to couple the AC microgrid and DC microgrid for power management between AC/DC microgrid. Control Block diagram of the proposed controller is shown in Fig. 7. For maintaining the power balance between the two buses, an autonomous control scheme is considered. The difference between the Per-Unit (P.U.) values of the dc bus voltage and ac bus frequency is utilized to alter the power requirement of the Inter Linking Converter for DC MG or AC MG support in this method [1–3].

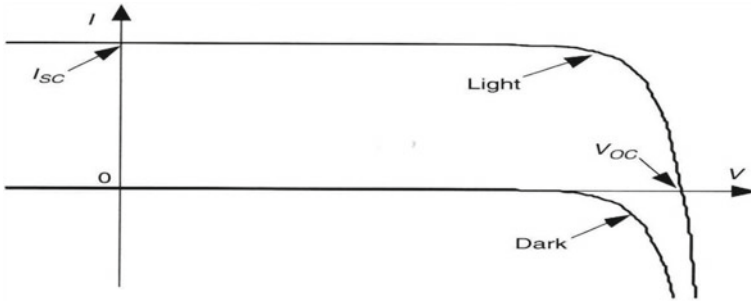


Fig. 6 V-I characteristics

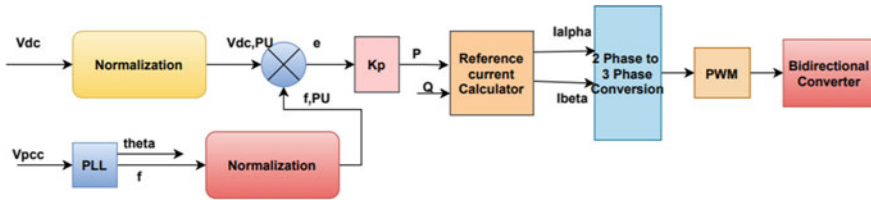


Fig. 7 Control block diagram of bidirectional AC/DC converter (ILC)

The block schematic of a stand-alone hybrid microgrid with ac–dc coupling is displayed and the control of the bidirectional converter is shown in the above Fig. 7. For better operation of the bidirectional ac/dc converter normalization of DC voltage and AC frequency has to be done. Equations (7) and (8) will give the formulae for normalization.

$$f_{PU} = \frac{[f - \{0.5\} \times (f_{max} + f_{min})]}{[0.5 \times (f_{max} - f_{min})]} \tag{7}$$

$$V_{dc.PU} = \left(\frac{V_{dc} - 0.5 \times (V_{dc \max} + V_{dc \min})}{0.5 \times (V_{dc \max} - V_{dc \min})} \right) \tag{8}$$

ILC will operate in the power control mode after identifying the reference active power and reactive power, regulating the outputs to their reference values and then it will regulate the concerned bus voltages [9, 38, 39].

10 Simulation Results

Simulation results for the proposed Hybrid system in Islanding Mode of operation is shown in the Figs. 8, 9, 10, 11 and 12. The bidirectional converter will Convert the AC power and DC power according to the Load demand of the AC microgrid and

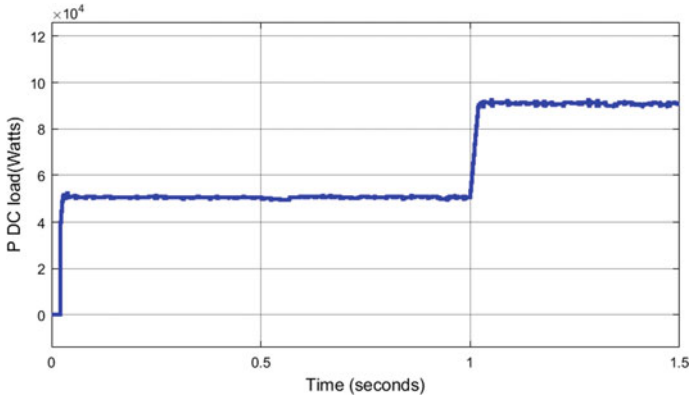


Fig. 8 Simulation results of DC load power

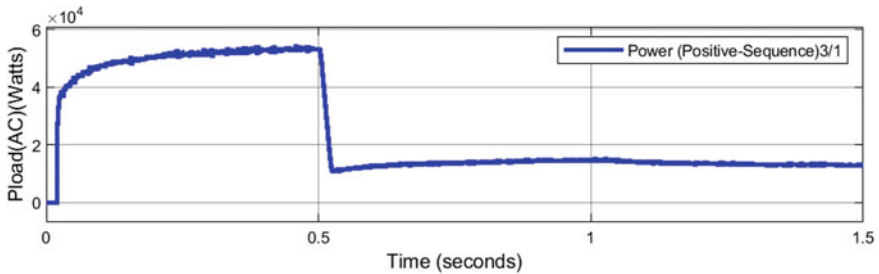


Fig. 9 Simulation results of AC load power

DC microgrid. Table 1 shows the balance between AC load and DC load using the Bidirectional AC/DC converter or Interlinking converter (ILC). For simulating the proposed structure MATLAB software version 2018 is used.

11 Comparison of Existing System with References

In the reference paper [1], DC microgrid, AC microgrid are considered as sources, No renewables are considered for forming AC and DC microgrids. In this paper RES is considered in DC and AC microgrids for generation of power. DC microgrid/subsystem voltage is considered in the reference paper [1] which is 150 V, AC supply frequency is considered as 60 Hz, and ILC power varied from 0 , 300 and 150 W depending on load demand.

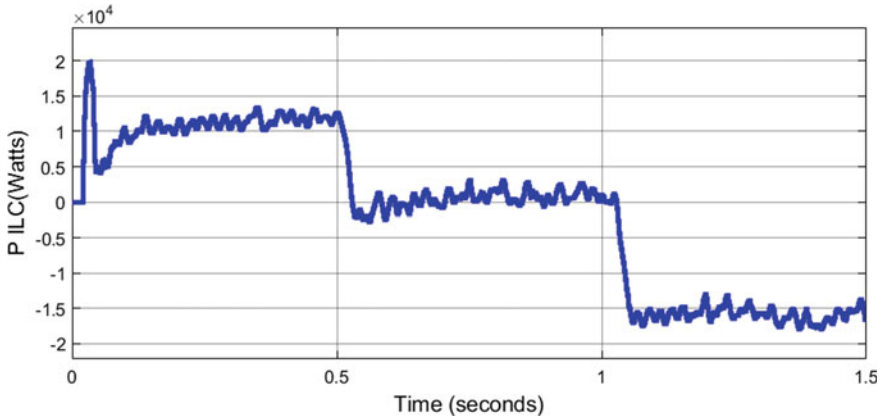


Fig. 10 Simulation results of bidirectional converter power exchange between DC microgrid and AC microgrid

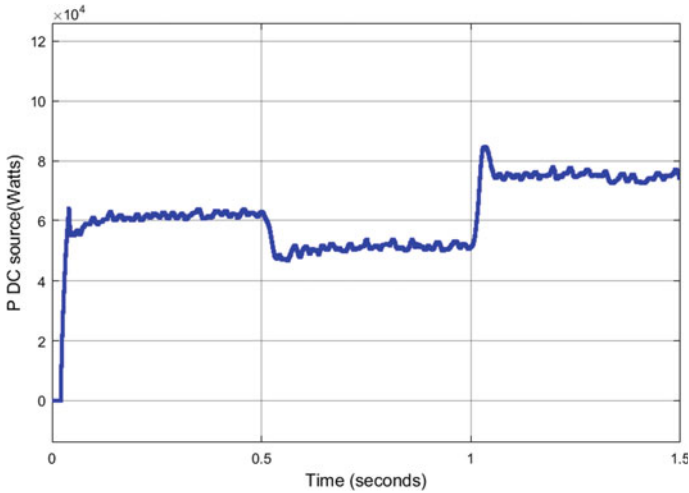


Fig. 11 Power at DC microgrid

12 Conclusion

Power systems with ac have served the globe for more than a century, according to the user's convenience. However, because the type of load utilized by the power consumer changes day by day, there is quick development and improvement in modern civilization. Because of the high load demand, many electrical experts are working to design a user-friendly hybrid power system. One of the Hybrid AC/DC microgrid architectures is covered in this chapter, along with its power management and control technique.

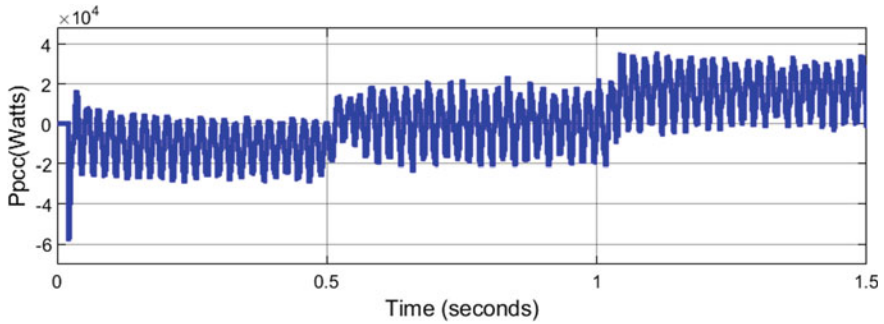


Fig. 12 AC power at point of common coupling

Table 1 Output power management between source and load

Time	0–0.5 s	0.5–1 s	1–1.5 s
Ppv	21 kW	21 kW	21 kW
Pwf (DC)	20 kW	20 kW	20 kW
Pbat	20 kW	10 kW	35 kW
Pwf (AC)	19 kW	14 kW	18 kW
Pfc	10 kW	0 kW	5 kW
Psc	10 kW	0 kW	5 kW
Pdc load	50 kW	50 kW	90 kW
Pac load	50 kW	10 kW	10 kW
P ILC	10 kW (Dc to AC)	0 kW	–15 kW (AC to DC)

References

1. Nejabatkhah F, Wei Y (2015) Overview of power management strategies of hybrid AC/DC Microgrid. *IEEE Trans Power Electron* 30(12)
2. Reza Ahrabi R, Li YW, Nejabatkhah F (2021) Hybrid AC/DC network with parallel LCC-VSC interlinking converters. *IEEE Trans Power Electron* 36(1)
3. Nejabatkhah F, Li YW, Tian H (2019) Power quality control of smart hybrid AC/DC microgrids: an overview. *IEEE Access* 7
4. Ma T, Cintuglu MH, Mohammed OA (2017) Control of a hybrid ac/dc microgrid involving energy storage and pulsed loads. *IEEE Trans Ind Appl* 53(1):567–575
5. Liu Y, Hou X, Wang X, Lin C, Guerrero JM (2016) A coordinated control for photovoltaic generators and energy storages in low-voltage ac/dc hybrid microgrids under islanded mode. *Energies* 9(8):651
6. Hamad AA, Azzouz MA, El-Saadany EF (2016) A sequential power flow algorithm for islanded hybrid ac/dc microgrids. *IEEE Trans Power Syst* 31(5):3961–3970
7. Davari M, Mohamed YARI (2013) Robust multi-objective control of vsc-based dc-voltage power port in hybrid ac/dc multi-terminal microgrids. *IEEE Trans Smart Grid* 4(3):1597–1612
8. Eghtedarpour N, Farjah E (2014) Power control and management in hybrid ac/dc microgrid. *IEEE Trans. Smart Grid* 5(3):1494–1505

9. Eajal AA, Saadany EFE, Ponnambalam K (2016) Equal power sharing in islanded ac/dc hybrid microgrids. In: Proceedings of 2016 IEEE electrical power and energy conference (EPEC), Ottawa, ON, Oct, pp 1–6
10. Zhang J, Guo D, Wang F, Zuo Y, Zhang H (2013) Control strategy of interlinking converter in hybrid ac/dc microgrid. In: Proceedings of 2013 international conference on renewable energy research and applications (ICRERA). Madrid, pp 97–102
11. Davari M, Mohamed YARI (2013) Robust multi-objective control of vsc-based dc-voltage power port in hybrid ac/dc multi-terminal microgrids. *IEEE Trans Smart Grid* 4(3):1597–1612
12. Bahrami S, Wong VWS, Jatskevich J (2014) Optimal power flow for ac-dc networks. In: Proceedings of 2014 IEEE international conference on smart grid communications (SmartGridComm). Venice, pp 49–54
13. Wang P, Jin C, Zhu D, Tang Y, Loh PC, Choo FH (2015) Distributed control for autonomous operation of a three-port ac/dc/ds hybrid microgrid. *IEEE Trans Ind Electron* 62(2):1279–1290
14. Liu X, Wang P, Loh PC (2011) A hybrid ac/dc microgrid and its coordination control. *IEEE Trans Smart Grid* 2(2):278–286
15. Unamuno E, Barrena J (2015) Hybrid ac/dc microgrids—part i: review and classification of topologies. *Renew Sustain Energy Rev* 52:1251–1259
16. Unamuno E, Barrena JA (2015) Hybrid ac/dc microgrids—part ii: review and classification of control strategies. *Renew Sustain Energy Rev* 52:1123–1134
17. Rahman M, Hossain M, Lu J (2016) Coordinated control of three-phase ac and dc type ev-esss for efficient hybrid microgrid operations. *Energy Convers Manage* 122:488–503
18. Manshadi SD, Khodayar M (2016) Decentralized operation framework for hybrid ac/dc microgrid. In: Proceedings of 2016 North American power symposium (NAPS). Denver, CO. pp 1–6
19. Unamuno E, Barrena JA (2015) Primary control operation modes in islanded hybrid ac/dc microgrids. In: Proceedings of IEEE EUROCON—international conference on computer as a tool (EUROCON). Salamanca, pp 1–6
20. Caramia P, Carpinelli G, Mottola F, Russo G (2016) An optimal control of distributed energy resources to improve the power quality and to reduce energy costs of a hybrid ac-dc microgrid. In: Proceedings of 2016 IEEE 16th international conference on environment and electrical engineering (EEEIC). Florence, pp 1–7
21. Guo W, Han X, Ren C, Wang P (2015) The control method of bidirectional ac/dc converter with unbalanced voltage in hybrid microgrid. In: Proceedings of 2015 IEEE 10th IEEE conference on industrial electronics and applications (ICIEA). Auckland, pp 381–386
22. Dheer DK, Doolla S, Rathore AK (2016) Small signal modeling and stability analysis of a droop based hybrid ac/dc microgrid. In: Proceedings of IECON 2016—42nd annual conference of the IEEE industrial electronics society. Florence, pp 3775–3780
23. Jin C, Wang J, Hai KL, Hoong CF, Wang P (2016) Coordination secondary control for autonomous hybrid ac/dc microgrids with global power sharing operation. In: Proceedings of IECON 2016—42nd annual conference of the IEEE industrial electronics society. Florence, pp 4066–4071
24. Sun K, Wang X, Li YW, Nejabatkhah F, Mei Y, Lu X (2017) Parallel operation of bidirectional interfacing converters in a hybrid ac/dc microgrid under unbalanced grid voltage conditions. *IEEE Trans Power Electron* 32(3):1872–1884
25. Loh PC, Li D, Chai YK, Blaabjerg F (2013) Autonomous control of interlinking converter with energy storage in hybrid ac-dc microgrid. *IEEE Trans Ind Appl* 49(3):1374–1382
26. Zhang L, Gao F, Li N, Zhang Q, Wang C (2015) Interlinking modular multilevel converter of hybrid ac-dc distribution system with integrated battery energy storage. In: Proceeding of 2015 IEEE energy conversion congress and exposition (ECCE). Montreal, QC, pp 70–77
27. Xiao H, Luo A, Shuai Z, Jin G, Huang Y (2016) An improved control method for multiple bidirectional power converters in hybrid ac/dc microgrid. *IEEE Trans Smart Grid* 7(1):340–347
28. Wang P, Liu X, Jin C, Loh P, Choo F (2011) A hybrid ac/dc microgrid architecture, operation and control. In: Proc. 2011 IEEE power and energy society general meeting. San Diego, CA, pp 1–8

29. Loh PC, Li D, Chai YK, Blaabjerg F (2013) Autonomous operation of ac-dc microgrids with minimised interlinking energy flow. *IET Power Electron* 6(8):1650–1657
30. Eghtedarpour N, Farjah E (2014) Power control and management in a hybrid ac/dc microgrid. *IEEE Trans. Smart Grid* 5(3):1494–1505; Davari M, Mohamed YARI (2013) Robust multi-objective control of vsc-based dc-voltage power port in hybrid ac/dc multi-terminal microgrids. *IEEE Trans Smart Grid* 4(3):1597–1612
31. Radwan AAA, Mohamed YARI (2012) Assessment and mitigation of interaction dynamics in hybrid ac/dc distribution generation systems. *IEEE Trans Smart Grid* 3(3):1382–1393
32. Abdelsalam A, Gabbar H, Sharaf A (2014) Performance enhancement of hybrid ac/dc microgrid based d-facts. *Int J Elect Power and Energy Syst* 63:382–393
33. Jiang Z, Yu X (2009) Power electronics interfaces for hybrid dc and ac-linked microgrids. In: *Proceedings of 2009 IEEE 6th international power electronics and motion control conference. Wuhan*, pp 730–736
34. Liu Y, Escobar-Mejía A, Farnell C, Zhang Y, Balda JC, Mantooth HA (2014) Modular multilevel converter with high-frequency transformers for interfacing hybrid dc and ac microgrid systems. In: *Proceedings of 2014 IEEE 5th international symposium on power electronics for distributed generation systems (PEDG). Galway*, pp 1–6
35. Loh PC, Li D, Chai YK, Blaabjerg F (2013) Autonomous operation of hybrid microgrid with ac and dc subgrids. *IEEE Trans Power Electron* 28(5):2214–2223
36. Che L, Shahidehpour M, Alabdulwahab A, Al-Turki Y (2015) Hierarchical coordination of a community microgrid with ac and dc microgrids. *IEEE Trans Smart Grid* 6(6):3042–3051
37. Xia Y, Peng Y, Yang P, Yu M, Wei W (2017) Distributed coordination control for multiple bidirectional power converters in a hybrid ac/dc microgrid. *IEEE Trans Power Electron* 32(6):4949–4959
38. Eajal AA, El-Saadany, EF, Ponnambalam K (2016) Inexact power sharing in ac/dc hybrid microgrids. In: *Proceedings of 2016 Canadian conference on electrical and computer engineering (CCECE). Vancouver, BC*, pp 1–5
39. Hart PJ, Lasseter RH, Jahns TM (2016) Symmetric droop control for improved hybrid ac/dc microgrid transient performance. In: *Proceedings of 2016 IEEE energy conversion congress and exposition (ECCE). Milwaukee, WI*, pp 1–8

Analysis of Intelligent Control of Irrigation System



Arunesh Kumar Singh  and Tabish Tariq

1 Introduction

Agriculture is an important aspect of the economy in rising countries, and it is regarded as the economic system's backbone. For decades, agriculture has been related to the production of critical food crops. To create a profitable crop, one must consider the irrigation procedure as well as the amount of water used. Only the amount of water required by the plants should be used. The idea of automatic irrigation is not new; mankind has long used automated and drip irrigation systems to irrigate enormous areas of foliage. There are currently no effective, automatic irrigation systems that can irrigate plants to the effective level and provide those plants with only the required amount of water for regular absorption of growth of plants. If developed, these methods have the potential to reduce the wastage of water for irrigation. The controller for irrigation serves as the "brain" of an irrigation system. It controls the flow of water to irrigate the plants, allowing the farmers or gardeners to achieve the best and most fruitful possible results. We should use water properly because it is one of our most valuable resources. In this paper, analysis is done for the design of different control systems based on control techniques such as algorithmic, linear programming and interpolation, PID, artificial neural network, and fuzzy logic that after considering different factors decide how much water should be given to the crop, and a successful crop is produced if the right amount of water is supplied, not too much and not too little.

A. K. Singh · T. Tariq (✉)

Department of Electrical Engineering, Jamia Millia Islamia A Central University, New Delhi, India

e-mail: er.tabish@gmail.com

A. K. Singh

e-mail: asingh1@jmi.ac.in

2 Implementation of Automatic Irrigation Control System

The irrigation control system can be automated by implementing various techniques like PID, Algorithmic technique, ANN, Fuzzy Logic, etc. Most of the techniques use the design of specific controllers (with or without feedback control) for their system depending upon user requirements. Some techniques based on microcontrollers use predefined algorithms to automate the irrigation control system using sensors to get field data and then based on that data, the algorithm decides what to do like controlling water flow valves, switching on/off pumps, etc. Some use intelligent controllers like artificial neural network or fuzzy logic to make decisions. Using these techniques a smart irrigation control system can be implemented and resources can be saved and used wisely. The intelligent control of the irrigation system is analyzed based on the algorithms, ANN, PID, IoT, etc.

2.1 Algorithm-Based Irrigation Control System

This type of irrigation control system is the simplest of all the different types of systems developed. In this system, a microcontroller is fed with inputs from the field like soil moisture, temperature, humidity, etc. and based on the predefined algorithm, it controls the flow of water or switches on/off the pump.

The system developed in [1] employs soil moisture sensors and a microprocessor to automatically provide plants with water based on their needs without the need for a farmer's intervention. An intelligent irrigation system would automatically control the flow of water for irrigation into the field in the required ratio desired by the plants, thereby maintaining turf. Soil moisture sensors (S1, S2, S3) are used to monitor the water level in the farm, solenoid valves (P1, P2, P3) are used to manage water flow to the farm, and a microcontroller is used to process data and control all operations. The algorithmic irrigation control system is shown in Fig. 1.

The water is distributed to the various fields via several pipes. When a field reaches its required moisture level, the control valve for that field is closed, and if watering is required again, the valve is opened. The system is configured to turn off the main engine once all of the fields have sufficient water levels. The system developed in [2] is almost similar to the system discussed above as it also takes in soil moisture values from soil moisture sensors and controls the solenoid valves based on the moisture value.

To further improve this type of system, a Raspberry Pi computer can be used as discussed and implemented in [3]. Raspberry Pi is a single-board computer with a size comparable to a credit card as shown in Fig. 2; with the help of a camera module and Wi-Fi technology (both of them being supported by Raspberry Pi), the live feed for the irrigation and monitoring of the field can be done; it can also replace the microcontroller used in [1, 2, 3], and a lot more capabilities can be added to the system like controlling the devices connected with a relay that is connected to

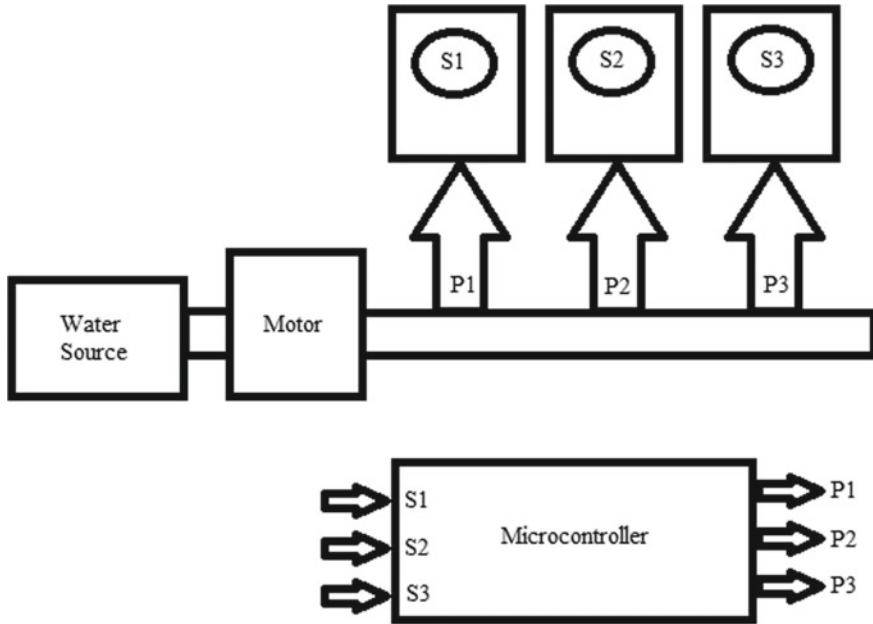


Fig. 1 A simple algorithm-based irrigation control system

the Raspberry Pi through the Internet from anywhere around the world. Important data like water usage and electricity consumption can be saved to a cloud database. Instead of using Raspberry Pi, an Arduino microcontroller with a Wi-Fi shield [4] can also be used when the algorithmic need for more CPU power is less as Arduino is just a simple microcontroller capable of doing simple tasks, whereas Raspberry Pi is a full-featured computer. So depending on the system needs, one of the two devices can be selected.

Mr. Shiraz Pasha incorporated the use of solar panels [5] to make this type of system standalone and environment friendly; a solar PV array is used to charge the battery that powered the whole system (Fig. 3). By making use of this, the whole control system can run anywhere around the earth where there is sunlight. In places where there is a shortage of electricity, this system would be a great fit. The system is further improved by implementing machine learning algorithms like support vector classification [6] to determine soil type as the type of soil also affects how much water should be given to the plants, and implementing this will result in properly irrigated soil. Soil is regarded as a significant natural resource, with soil pH describing the amount of acidity or basicity which affects nutrient availability and, ultimately, plant growth. By implementing a Raspberry Pi camera module and image processing, the soil pH can be determined [7]. The Pi camera is used to take the photographs, and after analyzing the obtained image, the pH value of the soil is computed, and crops or plants that can be planted in that field are advised. This technology will inform farmers about the crops to grow in their specific fields.



Fig. 2 Raspberry Pi single-board computer

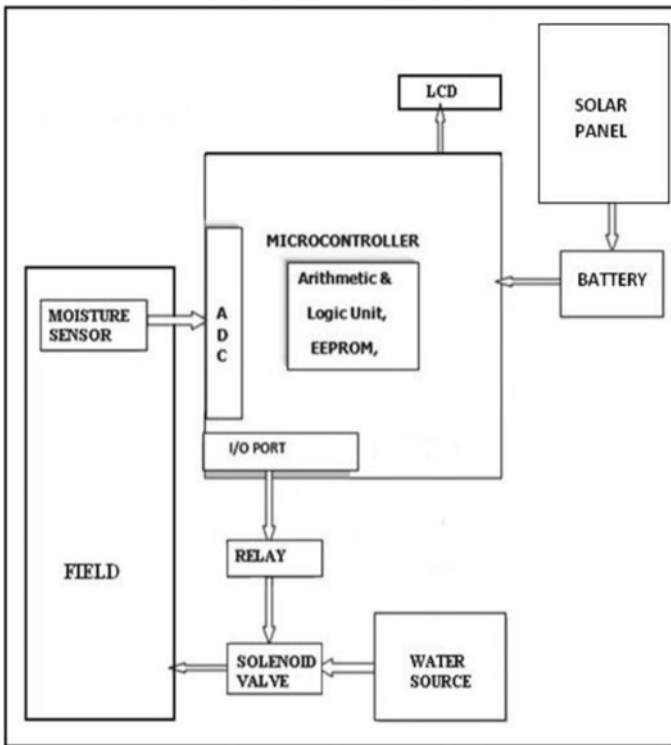


Fig. 3 An algorithm-based irrigation control system powered by a solar panel

2.2 Use of Linear Programming and Interpolation Methodology for Drip Irrigation System

It is not possible to operate a conventional automated drip irrigation system based on several decisions; it can only work based on single soil parameters such as soil moisture, pH, temperature, and light. If simply a soil moisture sensor is used to control automatic drip irrigation, and after that whenever the soil moisture level drops, the Valve Unit is instructed to change its position from OFF to ON, and when the level of soil moisture returns to the right pre-set level, the system is immediately shut off. The traditional technique does not monitor for water availability or the precise amount of water required by the crop. However, this system checks that and operates on that basis. The linear programming approach as discussed in [8, 9, 10] is used for this purpose to make proper use of available water for all available crops in the field or farm where this system is implemented to maximize profit, and it also easily identifies available water and required water for the crops with the help of linear programming. This system consists of a personalized PC and microcontrollers connected with ADCs to gather soil humidity levels from sensors. Following the input of these sensor values into the PC-based algorithm, linear programming is used to build an optimal watering plan, from which drip control commands are formed and then transferred to the hardware parts. The hardware part is entirely controlled over a wireless network. WSN allows a computer to communicate with a hardware device. Figure 4 shows the block diagram of this type of Irrigation Control System. To further improve this system temperature, sensors can also be used to take in temperature values and consider both soil moisture and temperature to give better results as implemented in [11].

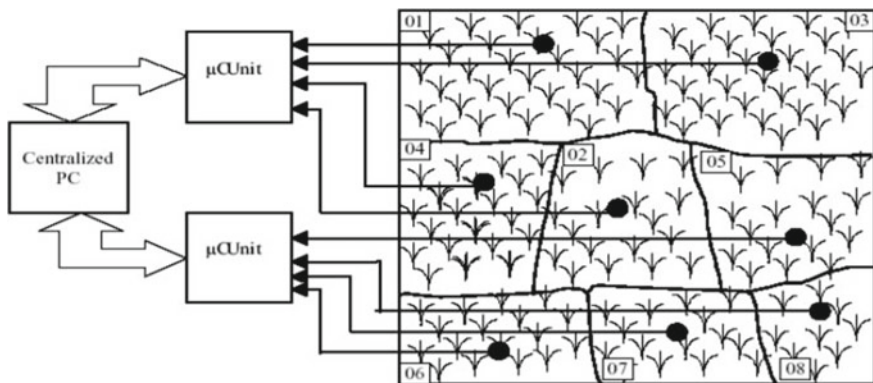


Fig. 4 Block diagram of intelligent drip irrigation system

2.3 PID Controller-Based Irrigation Control System

In this type of control system [12], the integral function has been constrained to values comparable to volumes of positive water application (within the range of zero to zero point five required daily water), while the proportional and derivative functions work as they will be working in a traditional proportional-integral-derivative controller. In this method, the integral function responds to varying water demand in a usual way (as a single-input single-output process), but if a big rainfall event occurs, the integral function is bound to maintain a value point which is comparable to zero volume of water application. Thereafter, if the soil moisture decreases to the reference point, then the integral function begins at a repetitive known point rather than soil moisture level and a time that is windup level-dependent. As a result, a proportional-integral-derivative controller with a limited integral function can more reliably regain soil moisture control following a rainstorm event without a major delay in dead time. The major goal of that system is to show how a limited integral function can be used to apply the benefits of PID control to precision irrigation applications and plant science research. This type of PID controller-based Irrigation System is shown in Fig. 5.

Further improvements in PID control of irrigation systems are discussed in [13]. An Arduino is used to integrate the PID controller, and four inputs are taken in through sensors as follows. Soil moisture is taken as a set point of reference. These four sensors, temperature, humidity, radiation, and wind speed, work in various ratios based on the proportional-integral-derivative and Penman evapotranspiration models. A Pb-acid battery powers the system that can be recharged by a solar PV array. These four selected sensors collect field conditions data and simultaneously transfer data to a monitoring device at a remote location with an LCD through wireless communication.

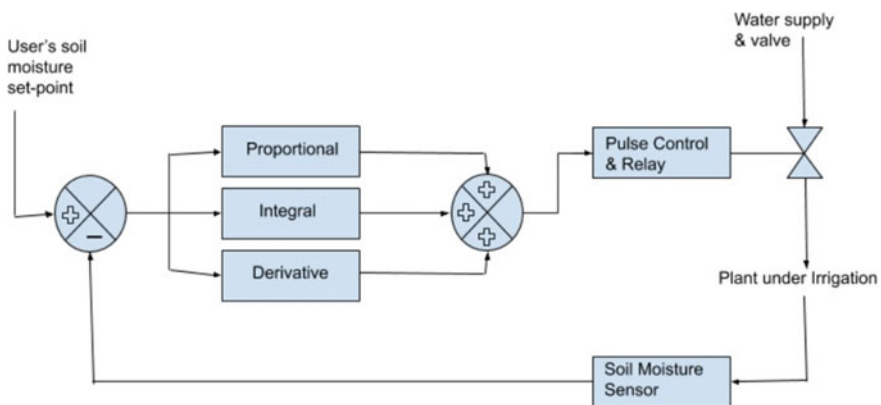


Fig. 5 PID controller-based automatic irrigation system

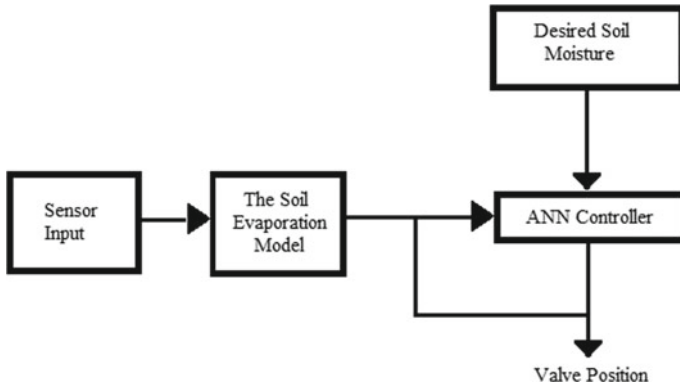


Fig. 6 ANN-based irrigation control system

2.4 ANN-Based Irrigation Control System

The Artificial Neural Network Controller of the system developed in [14] is based on a closed-loop controller design. The Penman-Monteith equation is used to generate a soil model, and the desired soil moisture is provided to the controller together with the current sensor values to control the water pump valve based on the ANN controller output (Fig. 6).

This control system is made up of four stages that are all linked together:

- **Sensor input:** At this stage, several characteristics such as radiation, soil moisture, air humidity, and wind speed are gathered. These variables are then supplied as input to the following stage.
- **This stage turns four input factors into actual soil moisture using the evapotranspiration model.**
- **Soil moisture required:** This contains information about the amount of water plants need to thrive properly.
- **ANN controller:** At this point, the soil moisture requirement is compared to the actual soil moisture, and on a basis dynamic decision is given.

2.5 Irrigation Control System Using Fuzzy Logic

The Fuzzy Logic-based Irrigation Controller system is based on a closed-loop controller design. A soil model is designed in Simulink to find the actual soil moisture using the water flow rate, and it is then compared with the desired soil moisture level using the fuzzy logic controller that takes the difference between the actual moisture of soil and desired moisture and then gives the output to control how much the valve should be open based on the predefined fuzzy rules [15]. A fuzzy model (Fig. 7) is made using the Mamdani model of inference. The fuzzy controller rules

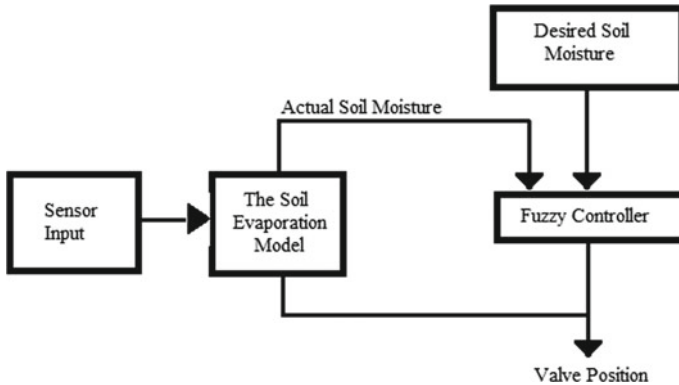


Fig. 7 Irrigation control system using fuzzy logic

are produced for this model. The 5 rules (one input one rule) are made, i.e. large negative, small negative, equal, large positive, and small positive, for the difference between the desired moisture and actual moisture of soil, and the valve will open accordingly.

The system developed in [16] also uses fuzzy logic-based control of irrigation, but instead of defining rules based on soil moisture difference as discussed above they had defined different membership functions for different inputs and outputs that are ground moisture, temperature, humidity, and servo valve. Servo valve is the output variable. Each input and output variable is defined with the help of 3 linguistic variables such as dry, normal, and wet for soil moisture and so on. On the basis of these combinations the valve is closed or open.

2.6 Irrigation Control System Using PLC

The PLC-based system developed in [17] takes soil moisture as input from the soil moisture sensor and water pump that will be switched on and off automatically using the programmable logic controller SIEMENS LOGO 230 RC. The programmer is programmed in order to control the master valve and zonal valve's opening and closing. The water pump is switched on and switched off. The moisture sensor value is set manually to 22 for turning ON and 55 for turning OFF. The PLC-based system is effective for irrigating the plants for taking various environmental conditions (Fig. 8).

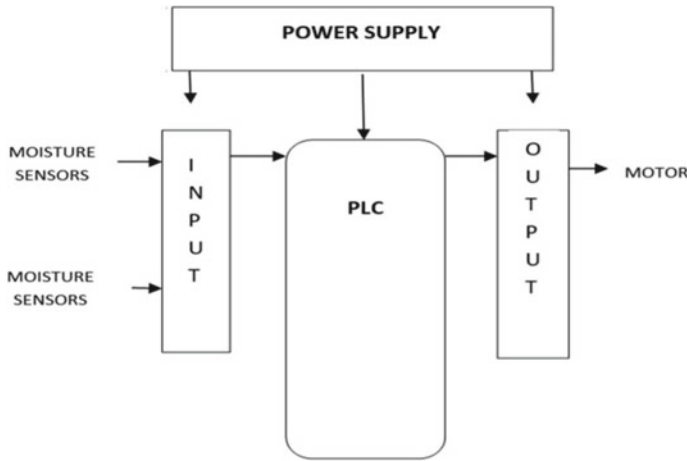


Fig. 8 Irrigation control system using PLC

2.7 *IoT and WSN Network-Based Irrigation Control System*

IoT, Internet of Things, is defined as the network of physical devices that are connected to each other with the Internet and wireless sensor network (WSN); as the name implies, it is the network of sensors connected without using wires to collect field data such as soil moisture from soil moisture sensors placed very far apart from each other. IoT and WSN are some technologies that are heavily implemented, while designing automatic irrigation control systems as large fields requires a large number of sensors to collect data and connecting them using wires will not be feasible and easy [18–22]. Some systems based on IoT and WSN are discussed in detail. Different types of controllers are used such as Arduino with a Wi-Fi shield to make it connect to the Internet and implement remote functionality in the system; some use Raspberry Pi single-board computer where there is a need for heavy computational requirements and the onsite solution is required. If a Simulink model is needed for the system to run, then also Raspberry Pi can be used for data acquisition using Wi-Fi technology. All the sensors can be connected to the Internet by implementing WSN. Serial communication can also be used to transfer data from Arduino or Raspberry Pi to the Simulink or Matlab model [23–29].

The controller can be designed using any of the above techniques such as algorithm-based controller, PID, ANN, and fuzzy logic and incorporated into Arduino or Raspberry Pi.

3 Conclusion

The intelligent controllers for irrigation systems have been analyzed. Using the various control techniques for the irrigation control system, a lot of electricity and water can be saved. These techniques can be further improved by adding new variables as per the requirement of the crop or plant as inputs to get a better and fruitful output. New algorithms can be designed based on these techniques and can be used in combination or simultaneously.

References

1. Kumar ND, Pramod S, Sravani C (2013) Intelligent irrigation system. *Int J Agric Sci Res (IJASR)* 3(3):23–30
2. Selvaperumal A, Muthuchamy I (2017) Irrigation automation using resistive soil moisture sensor. *Int J Agric Sci Res (IJASR)* 7(1):143–148
3. Chate BK, Rana JG (2016) Smart irrigation system using Raspberry Pi. *Int Res J Eng Technol* 3(05):247–249
5. Vagulabranan R, Karthikeyan M, Sasikala V (2016) Automatic irrigation system on sensing soil moisture content. *Int Res J Eng Technol (IRJET)* 3(03):206–208
5. Shiraz Pasha BR, Yogesha DB (2014) Microcontroller based automated irrigation system. *Int J Eng Sci (IJES)* 3(7):06–09
6. Priyanka M, Gajendra RB, Amravati P (2021) Smart irrigation system using machine learning. *Zeich J* 7(6):18–25
7. Kumawat S, Bhamare M, Nagare A, Kapadnis A (2017) Sensor based automatic irrigation system and soil pH detection using image processing. *Int Res J Eng Technol*
8. Wavhal DN, Giri M (2014) Intelligent drip irrigation system using linear programming and interpolation methodology. *Int J Comput (IJC)* 13(1):1–11
9. Giri M, Wavhal DN (2013) Automated intelligent wireless drip irrigation using linear programming. *Proceedings of the special interest group on management of data record. Int J Adv Res Comput Eng Technol* 2(1).
10. Bharathy ML Microcontroller based automation of drip irrigation system S. Mahendra.
11. Prathyusha K, Suman MC (2012) Design of embedded systems for the automation of drip irrigation. *Int J Appl Innov Eng Manag* 1(2):254–258
12. Goodchild MS, Kühn KD, Jenkins MD, Burek KJ, Button AJ (2015) A method for precision closed-loop irrigation using a modified PID control algorithm. *Sens Transducers* 188(5):61
13. Sheikh, S.S., Javed, A., Anas, M. and Ahmed, F., 2018, September. Solar based smart irrigation system using PID controller. In *IOP Conference Series: Materials Science and Engineering* (Vol. 414, No. 1, p. 012040). IOP Publishing.
14. Umair SM, Usman R (2010) Automation of irrigation system using ANN-based controller. *Int J Electr Comput Sci IJECS-IJENS* 10(02):41–47
15. Hussain MH, Min TW, Siraj SF, Rahim SRA, Hashim N, Sulaiman MH (2011) Fuzzy logic controller for automation of greenhouse irrigation system. In: *Conference: 3rd CUTSE international conference*. At Miri, Sarawak, Malaysia
16. Kokkonis G, Kontogiannis S, Tomtsis D (2017) A smart IoT fuzzy irrigation system. *Power (mW)* 100(63):25
17. Imam MA, Francis MS (2021) PLC based automated irrigation system. *Int J Res Appl Sci Eng Technol (IJRASET)* 9(VIII):1519–1525
18. Vij A, Vijendra S, Jain A, Bajaj S, Bassi A, Sharma A (2020) IoT and machine learning approaches for automation of farm irrigation system. *Procedia Comput Sci* 167:1250–1257

19. Naik P, Kumbi A, Katti K, Telkar N (2018) Automation of irrigation system using IoT. *Int J Eng Manuf Sci* 8(1):77–88
20. Kumar MK, Ravi KS (2016) Automation of irrigation system based on Wi-Fi technology and IOT. *Indian J Sci Technol* 9(17):1–5
21. Sadiq MT, Hossain MM, Rahman KF, Sayem AS (2019) Automated irrigation system: controlling irrigation through wireless sensor network. *Int J Electr Electron Eng* 7(2):33–37
22. Rajeshkumar N, Vaishnavi B, Saraniya K, Surabhi C (2019) Smart crop field monitoring and automation irrigation system using IoT. *Int Res J Eng Technol (IRJET)*. 7976–7979
23. Pawar SB, Rajput P, Shaikh A (2018) Smart irrigation system using IOT and raspberry pi. *Int Res J Eng Technol* 5(8):1163–1166
24. Akter S, Mahanta P, Mim MH, Hasan MR, Ahmed RU, Billah MM (2018) Developing a smart irrigation system using arduino. *Int J Res Stud Sci Eng Technol* 6(1):31–39
25. Ashok G, Rajasekar G (2016) Smart drip irrigation system using Raspberry Pi and Arduino. *Int J Sci Eng Technol Technol*
26. Mane SS, Mane MS, Kadam US, Patil ST (2019) Design and development of cost effective real time soil moisture based automatic irrigation system with GSM. *IRJET* 6(9):1744–1751
27. Jain R, Kulkarni S, Shaikh A, Sood A (2016) Automatic irrigation system for agriculture field using wireless sensor network (WSN). *Int Res J Eng Technol (IRJET)* 3(04):1602–1605
28. Derib D (2019) Cooperative automatic irrigation system using Arduino. *Int Res J Eng Technol (IJSR)* 6(3):1781–1787 (Mar 2017)
29. Debo-Saiye Y, Okeke HS, Mbamaluikem PO (2020) Implementation of an Arduino-based smart drip irrigation system. *Int J Trend Sci Res Dev (IJTSRD)* 5(1):1130–1133

A Recursive CEIEC Technique for Image Enhancement Employing Sharpening Filter



Archana Agarwal, Shailender Gupta, and Munish Vashishath

1 Introduction

The images obtained from various sources, i.e. digital sensors, cameras and satellites, suffer degradation in the visual quality on various accounts, for instance, glitches or washing out. CE [1] is the technique employed to overcome such degradation in the images. This process adjusts the relative brightness and darkness of the image resulting in an improved image in terms of perceived quality and information content. As seen in Fig. 1a, the thumbprint image is having low contrast, while Fig. 1b shows the enhanced version of the same after applying the CE technique to it. These CE techniques find application in various areas for image enhancement such as forensic science, oceanography and satellite pictures.

There are 2 main categories of CE techniques, which are Global and Local Contrast Enhancement techniques. The Global CE techniques work globally on the whole image rather than working on minute details of the image as in local CE techniques. In addition, global CE techniques are better in terms of processing speed, while the latter are best in terms of visual quality [28]. Also, the global techniques are not suitable for images that differ continuously from one locale to another of the same image. The global techniques do similar transformation functions on every pixel of low contrast image and include histogram enhancement methods such as histogram equalization-related techniques [3–7]. The local techniques choose small windows of the image that traverse through each and every pixel of an input image consecutively such as Adaptive Histogram Equalization (AHE) and Contrast Limited Adaptive Histogram Equalization (CLAHE) [15, 16]. So, if the image is enhanced using the global technique, locally traversing through the image provides better results as they

A. Agarwal (✉) · S. Gupta · M. Vashishath
JC Bose University of Science and Technology, YMCA, Faridabad, Haryana, India
e-mail: archana_aggrawal@yahoo.co.in



Fig. 1 a Original image b Enhanced image

enhance the image even on local details. This feature is exploited in this paper for image enhancement.

Another important parameter for image enhancement is entropy. The more is the entropy, the higher is the information content in the image. Therefore, the proposed technique uses a sharpening filter as a pre-processing step for CEIEC to enhance the information content of the image. The rest of the paper is organized as mentioned. Section 2 contains the literature survey; Sect. 3 explains the proposed model along with corresponding descriptions and algorithms; Sect. 4 presents the experimental results and their discussions, and Sect. 5 recapitulates the main conclusion followed by references.”

2 Literature Review

Table 1 below gives a short description of various contrast enrichment techniques available in the literature.

Numerous local and global approaches are available in the literature for contrast enhancement. In this paper, a hybrid approach is developed exploiting the advantages of both: global and local CE schemes.

3 Proposed Model

The hallmarks of the proposed scheme are

- The Sharpening filter is used in the pre-processing of an image as it improves the entropy of the image by defining the edges, using a mask window.

Table 1 Survey of available techniques

Name of the paper	Year	Features	Disadvantages
Histogram equalization (HE) [3]	1987	Improve contrast of the images	Unnatural images are created
Dualistic sub-image histogram equalization(DSIHE) [5]	1997	Based on the median of the image, the histogram is divided into two sub histograms	Fake images are created. Over illumination in some parts of image
Brightness preserving Bi-histogram equalization(BBHE) [4]	1997	The original picture based on its mean, is split into 2 sub-images on whom HE is then separately applied, which reduces the average mean brightness error (AMBE)	This technique results in low average information content (AIC) and artificial effects are introduced
Fast image contrast enhancement based onweighted threshold HE. (FWTHE) [6, 7]	1999	Histogram is modified on the basis of probability distribution function values to eliminate the unnatural look	The color and contrast of the images are not significantly changed
Adaptive histogram equalization (AHE) [15]	2000	Adaptively enhance the contrast of the images	Not suitable for RGB and leads to loss of information content
Recursive mean separate histogram equalization (RMHE) [8]	2003	In order to create a naturally enhanced image, the RMHE histogram on the basis of its mean	Requires large computation time and processing overhead
Minimum mean brightness error Bi-histogram equalization (MMBEBHE) [9]	2003	Calculate minimum brightness error between BBHE and input	Requires large computation time
Recursive Dualistic Sub-Image Histogram Equalization (RDSHE) [10]	2007	divides histogram of image on the basis of median and clip off both histograms then HE is applied independently	Not preferable for RGB images
Dynamic quadrants histogram equalization plateau limit (DQHEPL) [12]	2010	Divide the histogram into four segments based on RDSH+G13E S+G13standard. HE is then performed on cut histograms and redesigned picture is gained	Less entropy preservation & high mean brightness slip ups

(continued)

Table 1 (continued)

Name of the paper	Year	Features	Disadvantages
Non-parametric Modified Histogram Equalization(NPMHE) [14]	2013	The enrichment is obtained by modified probability distribution function which is calculated using clipped histogram and measure of un-equalization	Performance metrics indicate that its performance is not too good
Contrast limited adaptiv+E15e histogram equalization (CLAHE) [16]	2013	CLAHE operates on minute tiles of image. It prevents over amplification of the image using a clip limit which leads to its genuineness	Have to find appropriate transform function
Image enhancement based on equal area dualistic sub-image histogram equalization method [5]	2014	Works on four subhistograms and improve the contrast	Relative distribution of color channel changes leading to artificial effects in the image
A novel adaptive cuckoo search algorithm for contrast enhancement of satellite+E26 images [19, 20]	2008	This technique works on threshold limit of the image intensity	No significant enhancement in contrast
Contrast limited adaptive discrete wavelet transform histogram equalisation(CLDWT) [17]	2015	Combination of CLAHE and discrete wavelet transform	Low contrast images can't be enhanced up to the preference
Image contrast enhancement Based on intensity expansion compression (CEIEC) [22]	2017	First expansion of histogram then compression is finished	Significantly changes the pixel values leading to darkening of image
Gradient guided color image contrast and saturationenhancement [24]	2017	It enhances the color and contrast of an image	The overall performance metrics are good but its performance can be further enhanced
Contrast enhancement of brightness-distorted images by improved adaptive gamma correction [27]	2017	It enhances the most darkest images	The overall performance metrics are good but its performance can be further enhanced using Machine learning approaches
Contrast enhancement technique based on Lifting wavelet transf orm [26]	2018	LWT leads to low and high recurrence parts. The previous parts that hold majority of the data are upgraded utilizing CLAHE calculation whereas the last parts are kept unmodified	The results are good but still performance can be enhanced using machine learning approach

- A recursive approach is applied to enhance the image by choosing a small window in an image and traversing it through the complete image. This enhances the local contrast of the image pixels.

The proposed systems take a low-contrast image and apply a Sharpening filter as a pre-processing step to enhance the information content (entropy). In addition, the Recursive approach-based method is used on chosen windows of image traversing through the complete image so as to amplify the local contrast of the original picture. The CEIEC method is applied on each small-size window traversing through the complete image. This proposed technique surpasses the other techniques in terms of increasing the entropy and gradient of the image. Figure 2 depicts the block diagram of the same. The following subsection gives attributes of sharpening and recursive approaches.

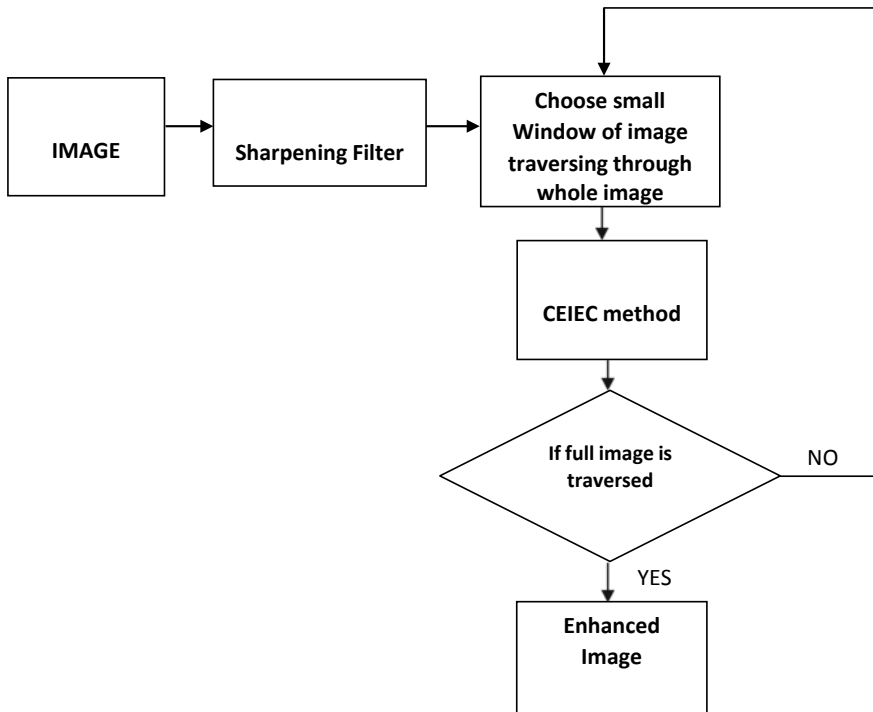


Fig. 2 Block diagram of the proposed technique

3.1 Sharpening Filter

Human observation is exceptionally touchy to edges and fine subtleties of a picture, and since they are created fundamentally by high recurrence components, the visual nature of a picture can be enormously degraded if the high frequencies are weakened or completely evacuated. Conversely, upgrading the high-frequency segments of a picture prompts an improvement in the visual quality. Picture sharpening [29] refers to any improvement system that features edges and fine subtleties in a picture as shown in Fig. 3. It is broadly utilized in printing and photographic businesses for expanding the nearby contrast and sharpening the pictures. As shown in Fig. 4, it can be seen that on applying a Sharpening filter, performance parameters such as Entropy, Gradient and Contrast are improved.

On a fundamental level, sharpening comprises adding a signal corresponding to a high-pass filter version of the original image [31]. Figure 5 represents this methodology, frequently referred to as un-sharp concealing on a one-dimensional signal. As shown in Fig. 5, the image is primarily passed through a high-pass filter which extricates the high-recurrence segments, after which a scaled variant of the

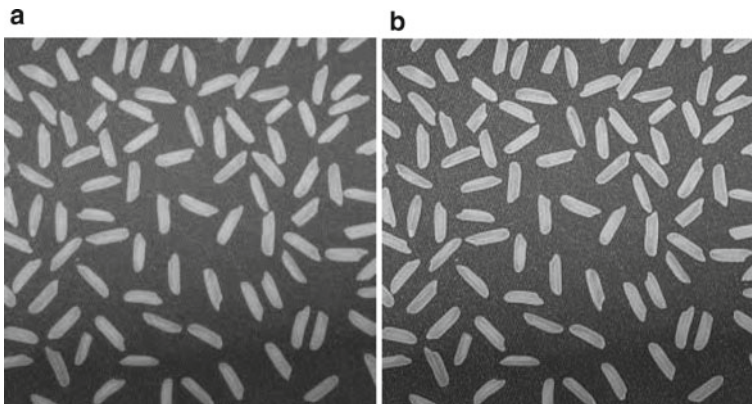
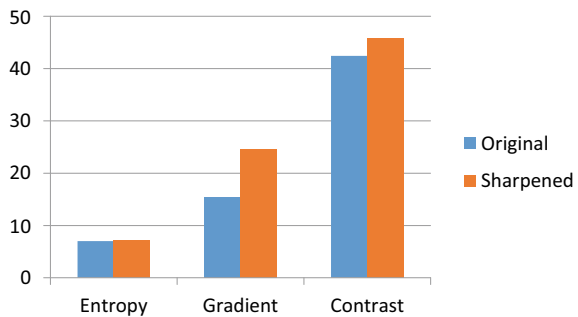


Fig. 3 a Original image b Sharpened image

Fig. 4 Graph between original and sharpened image



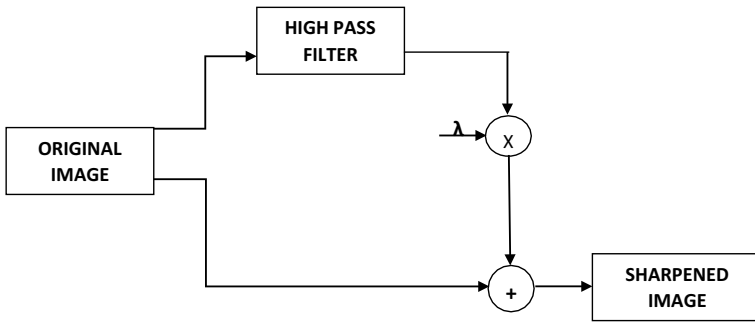


Fig. 5 Methodology of sharpening filter

high-pass channel yield is attached to the input image along these lines, creating a sharpened image. The homogeneous regions of the signal, i.e. where the signal is steady, stay unchanged. The sharpening function is represented as

$$Y(i, j) = x(i, j) + \lambda F(x(i, j))$$

where

$x(i, j)$ is the pixel value of the original image at position (i, j) , $\lambda = 0.25$ is a tuning parameter, $F(\cdot)$ is the high pass filter and $Y(i, j)$ is the sharpened pixel value at position (i, j) .

The salient element in the viable sharpening procedure indwells in the decision of the high-pass filtering task. Customarily, linear filters have been utilized to execute high-pass filtering; in any case, linear techniques can prompt inadmissible outcomes if the first picture is degraded with noise. A commutation between noise attenuation and edge featuring can be acquired if a weighted median filter with suitable weights is employed. To represent this, contemplate a weighted median filter connected to a grayscale picture where the accompanying filter mask is utilized:

$$W = \frac{1}{3} \begin{bmatrix} -1 & -1 & -1 \\ -1 & 8 & -1 \\ -1 & -1 & -1 \end{bmatrix}$$

3.2 *Local-Level Image Contrast Enhancement Based on Intensity Expansion-Compression (CEIEC)*

CEIEC methodology works on expanding and compressing the pixel intensity dynamic range [22]. By amplifying the intensity as per the extremity of neighborhood edges, a halfway picture of the persistent intensity range is obtained. At that point, by compressing this image to the permitted intensity dynamic range, an increment in information substance is guaranteed. The blend of edge-guided expansion with compression additionally empowers the protection of sheer subtleties contained in the information of the image.

In the proposed scheme, the CEIEC scheme is used as local-level enhancement technique. The SHARP_IMG acquired after the sharpening filter is applied to the input image is enhanced by using a window of size $(M/2, N/2)$ where, M , N and L are the dimensions of the input image. On this window, CEIEC is applied to get the contrast-improved image, and the window selected is traversed on the complete image. The algorithm for the same is shown below. The next section gives the details of simulation setup parameters used to evaluate the effectiveness of the proposed scheme.

Algorithm for Recursive CEIEC

```

STEP 1. [M N L]= SIZE(SHARP_IMG)
STEP 2. ENHIMG=SHARPIMG
STEP 3. CHOOSING SMALL WINDOWS OF IMAGE TRAVERSING THROUGH WHOLE IMAGE
FOR I=1: (M/2) +1
FOR J=1: (M/2) +1
    WINDOW= SHARPIMG (I: (M/2) +I-1, J: (N/2)+J-1, :);
    C= CEIEC_FUNCTION (WINDOW);
    ENHIMG (I: (M/2) +I-1, J: (N/2) +J-1, :) =C
END
END

```

4 Simulation Setup Parameters

Table 2 gives the simulation setup parameters for assessing the performance of the proposed scheme.

5 Performance Analysis

The below-mentioned performance metrics are used for the analysis of the efficacy of the proposed scheme:

Table 2 Setup parameters

Processor	Intel(R) core(TM) i3 CPU
Memory	2 GB
Operating system	Windows 7
Image type	.jpg
Simulation tool	MATLAB version: R2015 serial update 2
Color type	RGB
Window of high-pass filter (W)	$\frac{1}{3} \begin{bmatrix} -1 & -1 & -1 \\ -1 & 8 & -1 \\ -1 & -1 & -1 \end{bmatrix}$
Tuning parameter (λ)	0.25

- **Absolute Mean Brightness Error (AMBE):** It is the contrast between the mean of the original and of the upgraded picture. This parameter gives the measure of splendor saved. Least estimation of AMBE is best.
- **Contrast Improvement Index (CII):** So as to assess the intensity of the diverse difference upgrade methods, the most outstanding benchmark is Contrast Improvement Index. This is the proportion of progress in the complexity when contrasted with the information picture. CII must be high for a proficient differentiation improvement plot.
- **Degree of Entropy Unpreserved (DEU):** This parameter is utilized to quantify the measure of data misfortune in a picture after the utilization of the Contrast Enhancement strategy. The estimations of DEU ought to be as low as could reasonably be expected.
- **Structural Similarity Index (SSIM):** SSIM is a metric to estimate the likeness between the two given images. The comparison is performed on the basis of 3 features: Luminance, Contrast and Structure.
- **Expected Measure of Enhancement by Gradient (EMEG):** It is a proportion of the found middle value of the proportion of square-based least total subsidiary to the most extreme outright subordinate. This criterion estimates the picture’s sharpness yet in addition touchy to speckle noise.
- **Quality-aware Relative Contrast Measure (QRCM):** It utilizes pixel slopes to measure the picture quality. The point when QRCM is near unity speaks to all the more likely picture quality.
- **Entropy:** It is a numerical proportion of the measure of data conveyed in a picture. It relies upon the appropriation of forces in the picture. Higher entropy esteem will be acquired when the permitted powers are completely utilized and equally disseminated in the dynamic range.
- **Contrast:** It demonstrates the spread of intensities as for their average magnitudes. This measurement is defined as per human visual discernment, where a bigger variation in intensity is required for perceptible changes in high-intensity locales.

- **Gradient:** It measures the neighborhood sharpness and is arrived at the center of overall pixels in the picture. The gradient of a pixel is the difference between an adjacent pixel and the current pixel.

6 Results

The following are the simulation results of the proposed mechanism for the above-mentioned performance metrics: (Fig. 6)

- **Visual Assessment:**
- **Entropy:**

Figure 7 shows the entropy comparison against the techniques CEIEC, CEIEC_DoG, CEIEC_Laplacian, CEIEC_Prewitt, CEIEC_Sobel, GGCSE, IAGC, CLDWT, CETLWT and Proposed. Owing to the use of a Sharpening filter, the best results with respect to entropy are obtained by the proposed technique. For good contrast

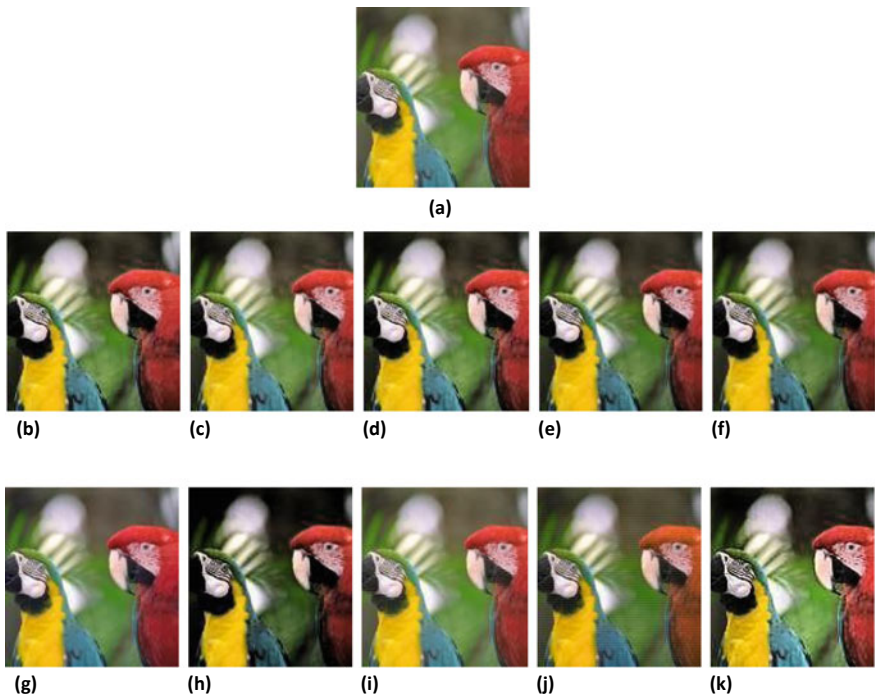


Fig. 6 Results of test image: **a** Input, **b** CEIEC, **c** CEIEC_DoG, **d** CEIEC_Laplacian, **e** CEIEC_Prewitt, **f** CEIEC_Sobel, **g** GGCSE, **h** IAGC, **i** CLDWT, **j** CETLWT and **k** Proposed

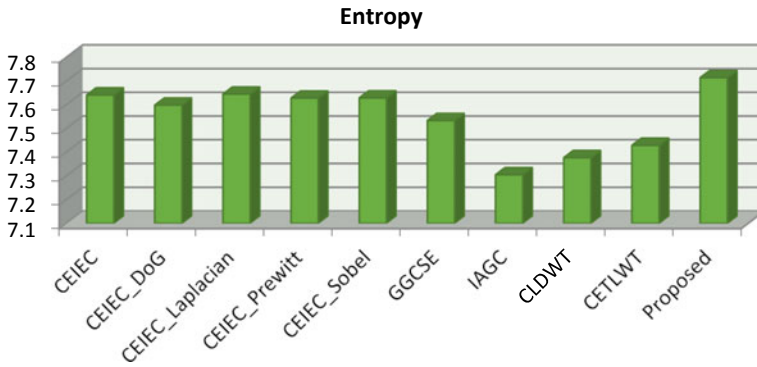


Fig. 7 Graph of different techniques for entropy

enhancement, the entropy value must be high. So, the proposed technique is best in terms of entropy.

- **AMBE:**

Absolute mean brightness error (AMBE) gives the measure of brightness saved. Figure 8 shows the AMBE comparison; it shows that the put-forward technique shows supreme results when compared to CEIEC and IAGC but slightly lesser values in comparison to GGCSE, CLDWT and CETLWT techniques. Lower values of AMBE suggest that brightness is better preserved.

- **DEI:**

Figure 9 shows the DEI comparison; the result shows that the proposed technique obtains the best results when set against CEIEC techniques but is not good in comparison to GGCSE, CLDWT and CETLWT techniques. For good contrast enhancement the DEI value must be low.

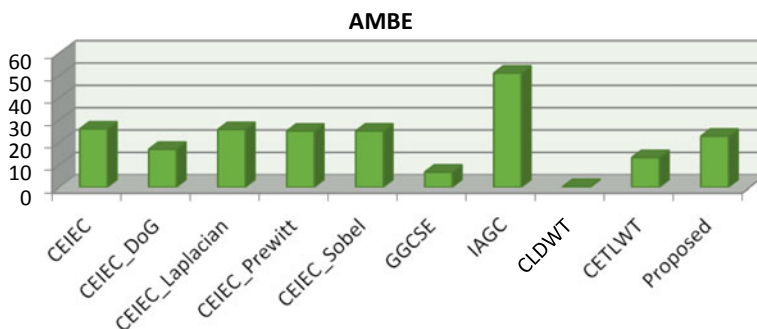


Fig. 8 Graph of different techniques for AMBE

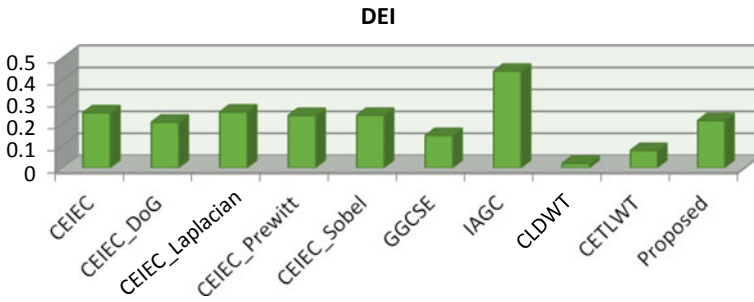


Fig. 9 Graph of different techniques for DEI

• **GRADIENT:**

Figure 10 illustrates the gradient correlation of the proposed with other techniques in the literature. The result shows that the proposed technique is best among all due to the usage of a sharpening filter.

• **CONTRAST:**

Figure 11 shows the contrast comparison; it shows that the proposed technique offers the best outcomes as opposed to other techniques, except for IAGC for which results are comparable.

• **CII:**

Figure 12 shows the CII collation between the put-forward technique and the former techniques. The graph depicts comparable results.

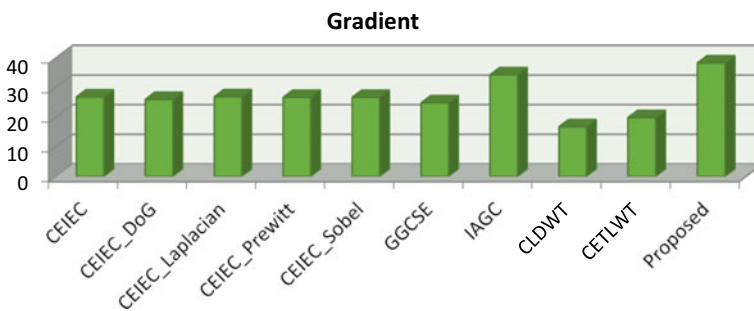


Fig. 10 Graph of different techniques for gradient

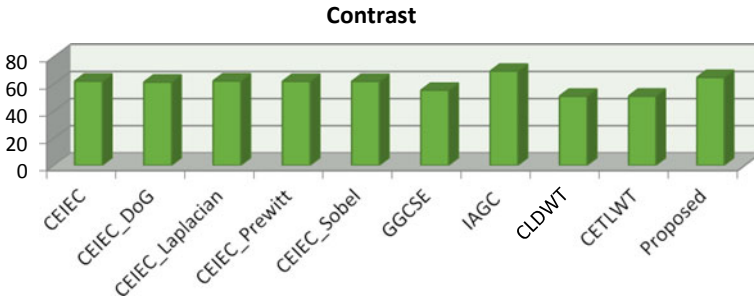


Fig. 11 Graph of different techniques for contrast

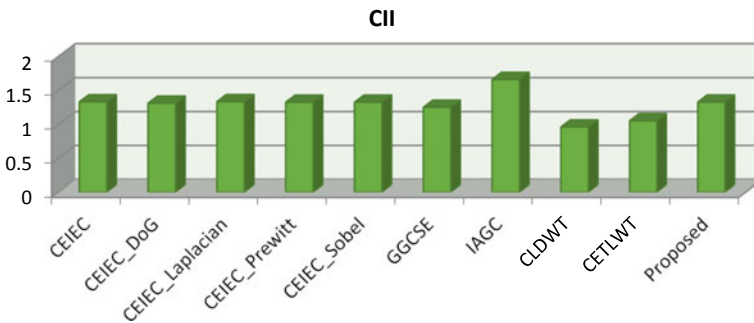


Fig. 12 Graph of different techniques for CII

• **EMEG:**

Figure 13 shows the EMEG comparison. Equivalent results are seen with the proposed technique when compared to other techniques.

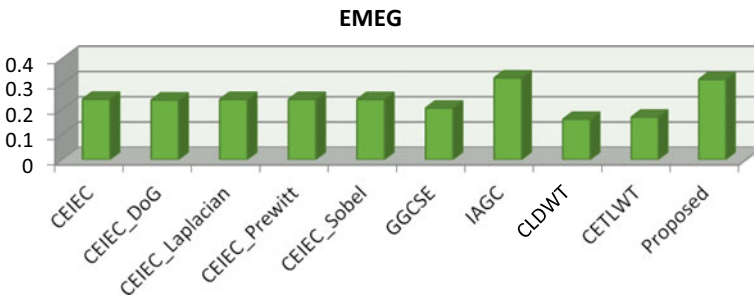


Fig. 13 Graph of different techniques for EMEG

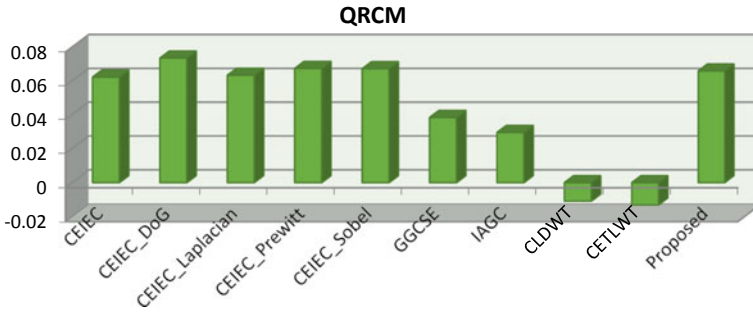


Fig. 14 Graph of different techniques for QRCM

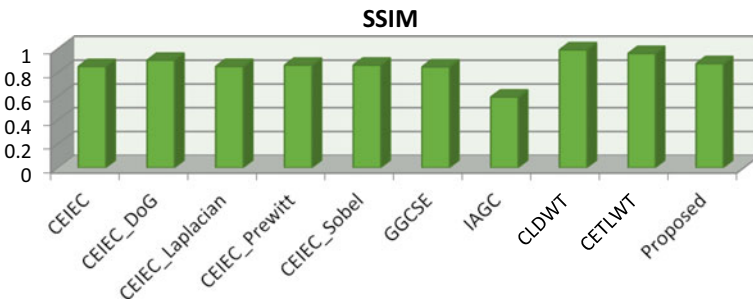


Fig. 15 Graph of different techniques for SSIM

• **QRCM:**

Figure 14 shows the comparison of the given technique with the other techniques, with respect to QRCM. The proposed technique results in a good-quality image, by giving the best results when compared with other techniques.

• **SSIM:**

Figure 15 delineates that comparable outcomes are obtained by the proposed technique when set against CEIEC and GGCSE techniques, but shows inferior values in comparison to CLDWT and CETLWT. The proposed technique shows the best result in comparison to the IAGC technique.

7 Conclusion

In search for an improved contrast enhancement technique, numerous techniques have been proposed and implemented. This paper proposes a technique which shows the best results in comparison to others in the literature. After the assessment of techniques, results are calculated which wrap up to the following inferences:

- The proposed technique shows the best results with reference to visual quality, Entropy, Gradient and Contrast.
- The proposed technique exhibits comparable results in terms of QRCM, SSIM and CIL.
- The proposed technique is shown to preserve maximum information with minimal losses, owing to its highest entropy values among the other techniques.
- In terms of various performance matrices, all the techniques including the proposed one show different optimization results. But none show the foremost results in all of them. Therefore, to get the best results out of all performance matrices, further refinements have to be made.

References

1. Suresh S, Lal S, Reddy CS, Kiran MS (2017) A novel adaptive cuckoo search algorithm for contrast enhancement of satellite images. *IEEE J Sel Top Appl Earth Obs Remote Sens* 10(8):3665–3676
2. Rafeal C, Gonzalez RE, Woods SL, Addins, “Digital image processing using MATLAB”, 2nd Edn. Chapter 6, *Color Image Processing*, pp 194–213
3. Pizer SM, Amburn EP, Austin JD, Cromartie R, Geselowitz A, Greer T, ter Haar Romeny B, Zimmerman JB, Zuiderveld K (1987) Adaptive histogram equalization and its variations. *Comput Vis, Graph, Image Process* 39(3):355–368
4. Kim YT (1997) Contrast enhancement using brightness preserving bi-histogram equalization. *IEEE Trans Consum Electron* 43(1):1–8
5. Wang Y, Chen Q, Zhang B (1999) Image enhancement based on equal area dualistic sub-image histogram equalization method. *IEEE Trans Consum Electron* 45(1):68–75
6. Wang Q, Ward RK (2007) Fast image/video contrast enhancement based on weighted thresholded histogram equalization. *IEEE Trans Consum Electron* 53(2):757–764
7. Jabeen A, Riaz MM, Iltaf N, Ghafoor A (2016) Image contrast enhancement using weighted transformation function. *IEEE Sens J* 16(20):7534–7536
8. Chen SD, Ramli AR (2003) Contrast enhancement using recursive mean-separate histogram equalization for scalable brightness preservation. *IEEE Trans Consum Electron* 49(4):1301–1309
9. Chen SD, Ramli AR (2003) Minimum mean brightness error bi-histogram equalization in contrast enhancement. *IEEE Trans Consum Electron* 49(4):1310–1319
10. Sim KS, Tso CP, Tan YY (2007) Recursive sub-image histogram equalization applied to gray scale images. *Pattern Recognit Lett* 28(10):1209–1221
11. Singh K, Kapoor R (2014) Image enhancement using exposure based sub image histogram equalization. *Pattern Recognit Lett* 36:10–14
12. Ooi CH, Kong NSP, Ibrahim H (2009) Bi-histogram equalization with a plateau limit for digital image enhancement. *IEEE Trans Consum Electron* 55(4):2072–2080
13. Wang S, Gu K, Ma S, Lin W, Liu X, Gao W (2015) Guided image contrast enhancement based on retrieved images in cloud. *IEEE Trans Multimed* 18(2):219–232
14. Poddar S, Tewary S, Sharma D, Karar V, Ghosh A, Pal SK (2013) Non-parametric modified histogram equalisation for contrast enhancement. *IET Image Process* 7(7):641–652
15. Fazli S, Samadi S, Nadirkhanlou P (2013) A novel retinal vessel segmentation based on local adaptive histogram equalization. In: 2013 8th Iranian conference on machine vision and image processing (MVIP). IEEE, pp. 131–135

16. Muniyappan S, Allirani A, Saraswathi S (2013). A novel approach for image enhancement by using contrast limited adaptive histogram equalization method. In: 2013 Fourth International Conference on Computing, Communications and Networking Technologies (ICCCNT). IEEE, pp. 1–6
17. Lidong H, Wei Z, Jun W, Zebin S (2015) Combination of contrast limited adaptive histogram equalisation and discrete wavelet transform for image enhancement. *IET Image Process* 9(10):908–915
18. Arici T, Dikbas S, Altunbasak Y (2009) A histogram modification framework and its application for image contrast enhancement. *IEEE Trans Image Process* 18(9):1921–1935
19. Suresh S, Lal S, Reddy CS, Kiran MS (2017) A novel adaptive cuckoo search algorithm for contrast enhancement of satellite images. *IEEE J Sel Top Appl Earth Obs Remote Sens* 10(8): 3665–3676
20. Suresh S, Lal S (2016) An efficient cuckoo search algorithm based multilevel thresholding for segmentation of satellite images using different objective functions. *Expert Syst Appl* 58:184–209
21. Gu K, Zhai G, Lin W, Liu M (2015) The analysis of image contrast: from quality assessment to automatic enhancement. *IEEE Trans Cybern* 46(1):284–297
22. Liu S, Rahman MA, Lin CF, Wong CY, Jiang G, Kwok N, Shi H (2017) Image contrast enhancement based on intensity expansion-compression. *J Vis Commun Image Represent* 48:169–181
23. Winkler S (2012) Analysis of public image and video databases for quality assessment. *IEEE J Sel Top Signal Process* 6(6):616–625
24. Shi H, Kwok N, Fang G, Lin SCF, Lee A, Li H, Yu YH (2017) Gradient-guided color image contrast and saturation enhancement. *Int J Adv Robot Syst* 14(3):1729881417711683
25. Hou X, Harel J, Koch C (2011) Image signature: highlighting sparse salient regions. *IEEE Trans Pattern Anal Mach Intell* 34(1):194–201
26. Goyal M, Bhushan B, Gupta S, Chawla R (2018) Contrast enhancement technique based on lifting wavelet transform. *3D Res* 9(4): 50
27. Cao G, Huang L, Tian H, Huang X, Wang Y, Zhi R (2018) Contrast enhancement of brightness-distorted images by improved adaptive gamma correction. *Comput & Electr Eng* 66:569–582
28. Celik T (2014) Spatial entropy-based global and local image contrast enhancement. *IEEE Trans Image Process* 23(12):5298–5308
29. “Discrete Laplacian Operators” in module 5.8 of Nptel courses Chapter 8. https://nptel.ac.in/courses/117104069/chapter_8/8_32.html
30. Suganya P, Gayathri S, Mohanapriya N (2013) Survey on image enhancement techniques. *Int J Comput Appl Technol Res* 2(5):623–627
31. Somvanshi SS, Kumar P, Tomar S, Singh M (2017) Comparativestatistical analysis of the quality of image enhancement techniques. *Int J Image Data Fusion*

Short-Term Wind Power Forecast Using Time Series Analysis: Auto-regressive Moving-average Model (ARMA)



Rudresh B. Magadum, Satish Bilagi, Srishtik Bhandarkar, Anchit Patil, and Abhigna Joshi

1 Introduction

Wind power is one of the highest raising energy sources in present electric power systems, and the overall worldwide installed facility of wind power by the end of the year 2021 is about 743 GW [1]. The installation of worldwide wind turbines has augmented yearly at a rate of approximately 40% for the eight-year period 2012–2020 [2]. The drastic increase in wind energy application in power systems is mainly motivated by governmental incentives put in place to address environmental concerns. In spite of the intermittent nature of wind power, the energy content in the wind is massive and pollution free [3]. The electricity production cost from wind is dilapidated with the constant development in wind technology, as compared to the cost of the electricity generated from conventional sources because of ever-rising fuel costs [4].

The Indian wind energy sector has an installed capacity of 38.789GW (as on February 2021). Renewable energy sources currently account for 38% of India's overall power generation capacity with an installed capacity of 136 GW as on March 2020 (IEA report-2020). The incorporation of wind energy sources in an electrical network leads to more difficulties in the system's reliability [5]. Power system security is usually attained by spinning reserve provisions, use of quick start units and making arrangements for interruptible load if the latter is acceptable by mutual economic benefits [6, 7]. Precise analysis of spinning reserve requirements is advantageous from both system reliability and economic points of view [8]. Over-scheduling and under-scheduling are not enviable and are directly related to system reliability and economy [9].

R. B. Magadum (✉) · S. Bilagi · S. Bhandarkar · A. Patil · A. Joshi
E&E Department, KLS GIT, Belagavi, India
e-mail: rbmagadum@git.edu

The accurate wind power forecasting is one of the great challenges; the objective of this work is to develop one module for the analysis and forecasting of wind power generation [10]. It is seen from the literature survey that numerous models have been developed for short-term wind power forecasts. From the literature results, the conclusion can be drawn that similar techniques might be better than the others in diverse conditions, i.e. one approach might gain the least prophecy error for one time point, and another might for another time point [11]. The selection of a superior method or the combination of different methods for various conditions becomes necessary [12]. This present work “short-term wind power forecast for using time series analysis” addresses the accurate short-term wind power forecast by using the time series ARMA model for secure and economical operation of power systems.

2 Time Series Analysis

Qualitative forecasting techniques normally use the outlooks of professionals to predict future values instinctively [13]. Such methods are helpful for past data that are not available. These methods include subjective technological comparisons and curve fittings. Quantitative methods include exponential smoothing, decomposition methods, Box-Jenkins techniques and regression analysis [14].

2.1 AR: Auto-Regressive

In the AR method, the present value Z_t of the time series is represented linearly in terms of its past values Z_{t-1}, Z_{t-2} and a white noise $\{a_t\}$ with zero average and variance σ^2 .

$$Z_t = \phi_1 Z_{t-1} + \phi_2 Z_{t-2} + \dots + \phi_p Z_{t-p} + a_t \tag{1}$$

By introducing the backward shift operator B that denotes $Z_{t-1} = BZ_t$, and accordingly $Z_{t-m} = B^m * Z_t$, Eq. (1) can be written in the form:

$$\phi(B)Z_t = a_t \tag{2}$$

where

$$\phi(B) = 1 - \phi_1 B - \phi_2 B^2 - \dots - \phi_p B^p \tag{3}$$

The AR approach has a similar form to the numerous linear regression forms. The variation is that in regression, the variable of importance is regressed to a linear function of other known variables, but Z_t is articulated as a linear function of its individual precedent values thus the ‘auto-regressive’. As the values of Z_t at p previous times

are involved in the model, it is said to be an AR approach. It is necessary to compute the parameters ϕ_i for prediction. The two techniques are used: maximum possibility inference and least squares estimation. To compute the least squares estimators, it is necessary to play down the following equation (for $p = 2$) with respect to ϕ_1 and ϕ_2 :

$$\sum_{t=1}^N (Z_t - \phi_1 Z_{t-1} - \phi_2 Z_{t-2})^2 \tag{4}$$

But because of the lack of information for $t = 1$ or $t = 2$, a hypothesis is made here that X_1 and X_2 are constant, and apart from the first two terms from the addition of squares. It is given by

$$\sum_{t=3}^N (Z_t - \phi_1 Z_{t-1} - \phi_2 Z_{t-2})^2 \tag{5}$$

Auto-regressive parameters in terms of auto-correlation: Yule-Walker equations:

$$r_1 = \phi_1 + \phi_2 r_1 + \dots + \phi_p r_{p-1} \tag{6}$$

$$r_2 = \phi_1 r_1 + \phi_2 + \dots + \phi_p r_{p-2} \tag{7}$$

In general,

$$r_p = \phi_1 r_{p-1} + \phi_2 r_{p-2} + \dots + \phi_p \tag{8}$$

If the order of the AR model $p = 2$, the equations for calculating AR coefficient are derived from Eq. (8):

$$r_1 = \phi_1 + \phi_2 r_1 \tag{9}$$

$$r_2 = \phi_1 r_1 + \phi_2 \tag{10}$$

Solving Eqs. (9, 10), we will get AR coefficient as

$$\phi_1 = \frac{(1 - r_2) * r_1}{1 - r_1^2} \tag{11}$$

$$\phi_2 = \frac{r_2 - r_1 * r_1}{1 - r_1^2} \tag{12}$$

Example 2: If the order of the AR model $p = 3$, the equations for calculating AR coefficient are derived from Eq. (3.8):

$$r_3 = \emptyset_{31}r_2 + \emptyset_{32}r_1 + \emptyset_{33} \tag{13}$$

$$r_2 = \emptyset_{31}r_{21} + \emptyset_{32} + \emptyset_{33}r_1 \tag{14}$$

$$r_1 = \emptyset_{31} + \emptyset_{32}r_1 + \emptyset_{33}r_2 \tag{15}$$

The calculation of the AR coefficient of order 3 is calculated by using the previous order coefficient, i.e. $\emptyset_{21}, \emptyset_{22}$:

$$\emptyset_{33} = \frac{r_3 - \emptyset_{21}r_2 - \emptyset_{22}r_1}{1 - \emptyset_{21}r_1 - \emptyset_{22}r_2} \tag{16}$$

$$\emptyset_{31} = \emptyset_{21} - \emptyset_{33}\emptyset_{22} \tag{17}$$

$$\emptyset_{32} = \emptyset_{22} - \emptyset_{33}\emptyset_{21} \tag{18}$$

In general, the higher order Auto-regressive coefficients are calculated by

$$\emptyset_{p+1,p+1} = \frac{r_{p+1} - \sum_{j=1}^p r_{p+1-j} * \emptyset_{pj}}{1 - \sum_{j=1}^p r_j * \emptyset_{pj}} \tag{19}$$

$$\emptyset_{p+1,j} = \emptyset_{pj} - \emptyset_{p+1,p+1}\emptyset_{p,p-j+1} \tag{20}$$

where $j = 1, 2, \dots, p$.

2.2 Moving-Average (MA)

In the MA model, the present value of the time series Z_t is represented linearly in terms of present and preceding values of a white noise series a_t, a_{t-1}, \dots . This noise series is created from the predicted errors or residuals when load information is presented.

The order of the progression depends on the previous noise value at which Z_t is regressed. For a MA model order q , this technique can be written as

$$Z_t = a_t - \theta_1 a_{t-1} - \dots - \theta_q a_{t-q} \tag{21}$$

Some application of the backward shift operator on the white noise series would allow Eq. (21) to be written as

$$Z_t = \theta(B)a_t \tag{22}$$

Where, $\theta(B) = 1 - \theta_1 B - \theta_2 * B * B \dots - \theta_q B^q$

The moving-average coefficient is calculated by

$$\text{When } q = 1, \theta_1 = \frac{-1 + \sqrt{1 - 4r_1^2}}{(2r_1)} \tag{23}$$

In general, the higher order moving-average coefficient is calculated by

$$r_k = \frac{-\theta_k + \theta_1\theta_{k+1} + \dots + \theta_{q-k}\theta_q}{1 + \theta_1^2 + \dots + \theta_q^2} \tag{24}$$

$$k = 1, 2, 3 \dots q$$

Example: For the MA model of order $q = 2$,

$$r_1 = \frac{-\theta_1(1 - \theta_2)}{1 + \theta_1^2 + \theta_2^2} \tag{25}$$

$$r_2 = \frac{-\theta_2}{1 + \theta_1^2 + \theta_2^2} \tag{26}$$

2.3 Arma Model

The combining of MA and AR models together becomes a wider class of techniques, i.e. Auto-Regressive Moving-Average (ARMA) model and is represented as

$$Z_t = \phi_1 Z_{t-1} + \phi_2 Z_{t-2} + \dots + \phi_p Z_{t-p} + a_t - \theta_1 a_{t-1} - \dots - \theta_q a_{t-q} \tag{27}$$

That is, $(1 - \phi_1 B - \phi_2 B^2 - \dots - \phi_p B^p)z_t = (1 - \theta_1 B - \theta_2 B^2 - \dots - \theta_q B^q)a_t$
 $\phi(B)Z_t = \theta(B)a_t$ (28)

where ϕ_p and θ_q are called the AR and MA parameters correspondingly. A methodology for ARMA (p, q) models was developed mainly by Box and Jenkins.

Example: If the ARMA (4, 3) is selected for the forecasting, then Eq. (27) reduces to

$$Z_t = \phi_1 Z_{t-1} + \phi_2 Z_{t-2} + \phi_3 Z_{t-3} + \phi_4 Z_{t-4} + a_t - \theta_1 a_{t-1} - \theta_2 a_{t-2} - \theta_3 a_{t-3} \tag{29}$$

The ARMA coefficient of order (p, q) is calculated by

$$\emptyset_{p+1,p+1} = \frac{r_{p+1} - \sum_{j=1}^p r_{p+1-j} * \emptyset_{pj}}{1 - \sum_{j=1}^p r_j * \emptyset_{pj}} \tag{30}$$

$$\emptyset_{p+1,j} = \emptyset_{pj} - \emptyset_{p+1,p+1}\emptyset_{p,p-j+1} \tag{31}$$

where j = 1,2,3.....p

$$r_k = \frac{-\theta_k + \theta_1\theta_{k+1} + \dots + \theta_{q-k}\theta_q}{1 + \theta_1^2 + \dots + \theta_q^2} \tag{32}$$

where k = 1, 2, 3...q.

2.4 Importance of RMSE Values (Order Selection)

The aim of the Root Mean Square Error (RMSE) study is to develop advanced wind power forecasting technology to perk up the accuracy of prediction systems using a variety of methods and to investigate the role of advanced wind power forecast techniques in grid and market integration.

RMSE is calculated by squaring the difference between the predicted wind power and actual wind power generated from the wind farm on an hourly basis, and then taking the square root of the mean to the rated wind power generation. The MAE and RMSE values are given by Eqs. (33, 34):

$$MAE = \frac{\sum_1^N |W_{PF} - W_{PA}|}{W_{PR}} \tag{33}$$

$$RMSE = \frac{\sqrt{\sum_1^N (W_{PF} - W_{PA})^2}}{W_{PR}} \tag{34}$$

The wind Forecast accuracy achieved by short-time range can be improved by utilizing power feedback from the site. The accuracy of wind forecast depends on the decrease in the value of RMSE value.

2.5 Forecasting

Projecting is the inference of the value of a number of variables at a particular future point in time. The wind energy generation predicting setback is closely linked to the problem of projecting the deviation of specific atmospheric conditions over short time intervals for a variety of time horizons. In order to comprehend the special issues involved in wind energy, estimating it is useful to segregate the problem into

four different time scales: long term (24 h to a few days), medium term (6 to 24 h ahead), short term (30 mins to 6 h) and very short term (few seconds to 30 mins).

The forecasting of future values of short-term forecasts after selecting the order of the model at lead times 1, 2, ..., l is presented below. It is necessary to compute the φ weights for forecasting the values of the φ 'S may be obtained by For AR model,

$$\begin{aligned} \varphi_0 &= 1 \\ \varphi_1 &= \vartheta_1 \\ \varphi_2 &= (\vartheta_1 * \varphi_1) + \varphi_2 \\ \varphi_3 &= (\vartheta_2 * \varphi_2) + (\vartheta_1 * \varphi_1) + \varphi_0 \end{aligned}$$

In broad φ equations for the AR model is represented by

$$\varphi_j = \vartheta_1\varphi_{j-1} + \dots + \vartheta_p\varphi_{j-p} \tag{35}$$

For the ARMA model

$$\begin{aligned} \varphi_0 &= 1 \\ \varphi_1 &= \vartheta_1 - \theta_1 \\ \varphi_2 &= (\vartheta_1 * \varphi_1) + \varphi_2 - \theta_2 \\ \varphi_3 &= (\vartheta_2 * \varphi_2) + (\vartheta_1 * \varphi_1) + \varphi_0 - \theta_3 \end{aligned}$$

In general, φ equations for the ARMA model are given by

$$\varphi_j = (\varphi_{j-1} * \vartheta_1) + \dots + (\varphi_{j-p} * \vartheta_p) - \theta_j$$

By taking these values generating the forecast $z_{t+1}(l)$ and $z_t(l+1)$ of the future observation z_{t+1+1} ended at origins $t+1$ and t :

$$\begin{aligned} z_{t+1}(l) &= \varphi_1 a_{t+1} + \varphi_{l+1} a_t + \varphi_{l+2} a_{t-1} + \dots \\ z_{t+1}(l) &= z_t(l+1) + \varphi_1 a_{t+1} \end{aligned} \tag{36}$$

Precisely, the t -origin forecast of z_{t+1+1} can be updated to become the $t+1$ origin forecast of the same z_{t+1+1} , by adding a constant multiplier of the one-step-ahead forecast error a_{t+1} , with multiplier φ_1 .

2.6 Flow Charts

The historical wind data is used for time series analysis to the calculation of mean, auto-covariance, auto-regressive coefficient are used to model formulation as shown

Fig. 1. Depending on the selection of models like AR, MA and ARMA, the calculation of the coefficient for further analysis will be calculated. The AR coefficient calculations depending on the order are shown in Fig. 2. Similarly, the MA and ARMA coefficient calculations are shown in Figs. 3 and 4, respectively.

The orders of the particular model selection play a very important role in the forecasting of future values. The lower value of RMSE values of the order will be chosen for the accurate forecasting values. The calculation of RMSE values is shown in Fig. 5. The calculation of φ weights for forecasting 1, 2, l lead times is shown in Fig. 6. By using φ weights for the generation of ' l ' lead time, future values are shown in Fig. 7.

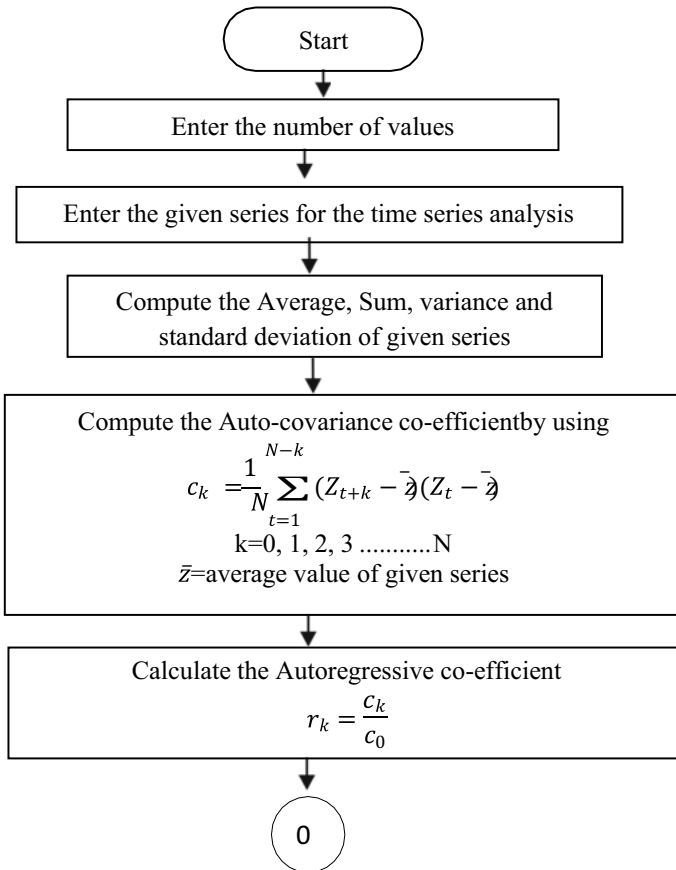


Fig. 1 Flow chart for the formulation of the time series model

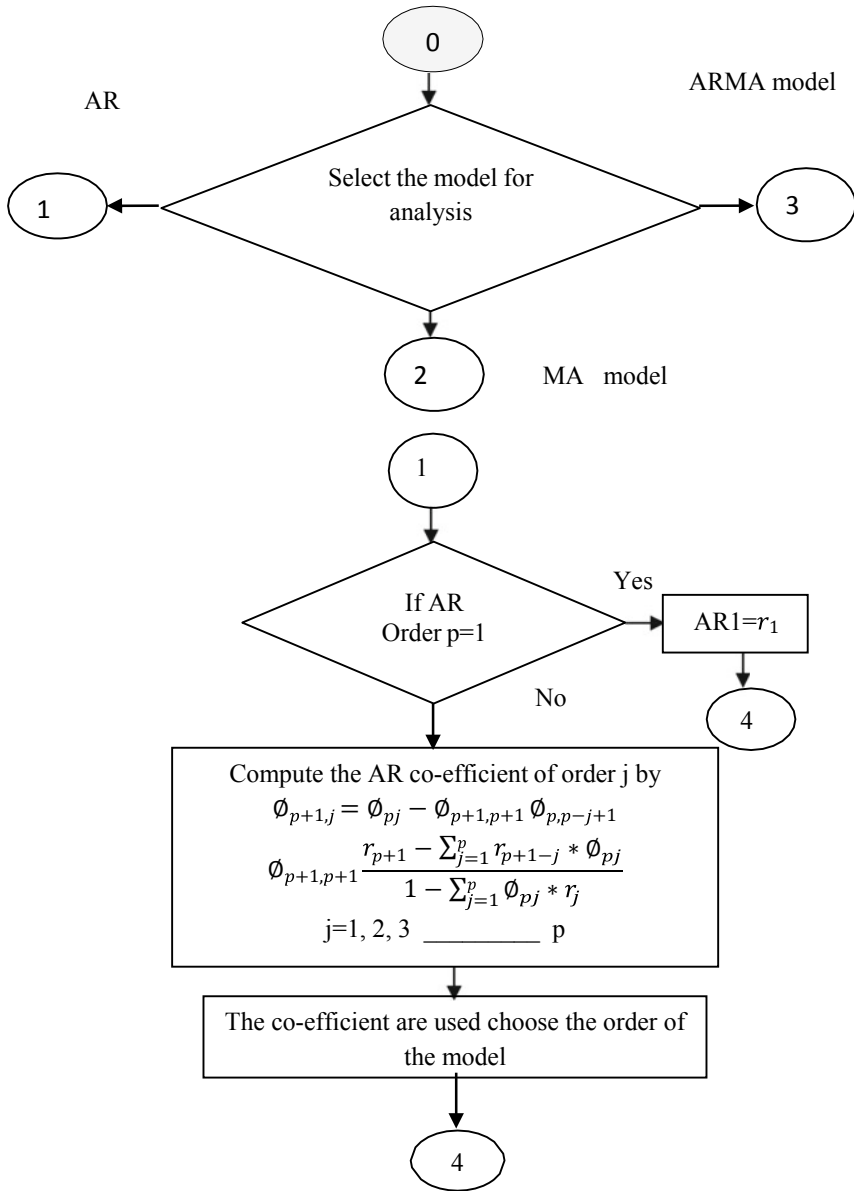


Fig. 2 Flow chart for estimation of AR coefficient

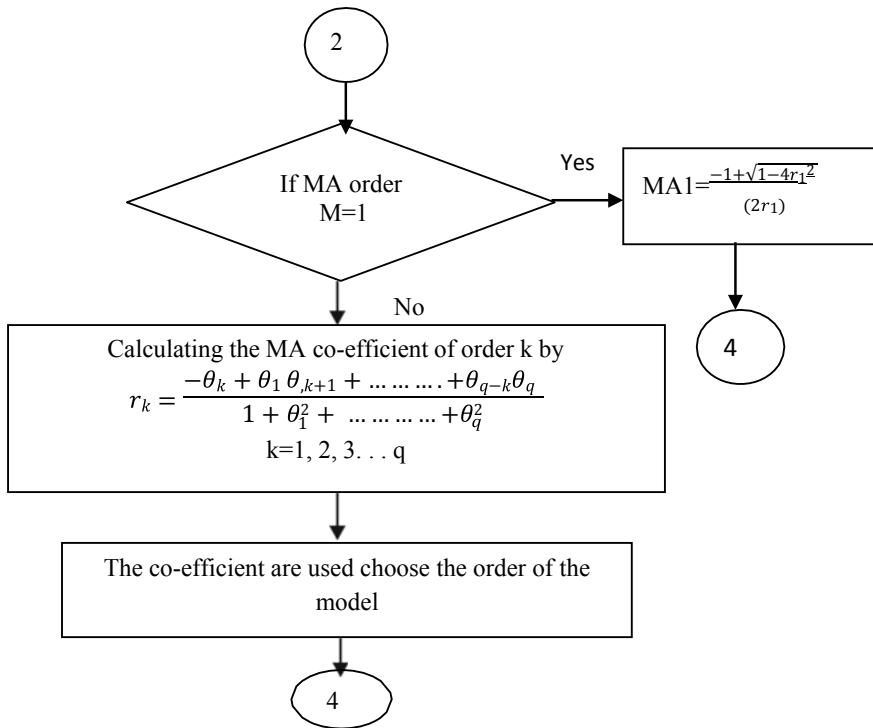


Fig. 3 Flow chart for estimation of MA coefficient

3 Results and Discussions

The accurate short-term wind power forecast plays an important role in the scheduling of conventional generating units. In this chapter, a few case studies are presented to check the performance of the implemented module.

3.1 Case Study 1: Considering One-Week Wind Power Data

The one-week wind power has been considered for the estimation of AR, MA and ARMA coefficient as shown in Fig. 8. The comparison of AR, MA and ARMA coefficient of the implemented module with ‘PAST’ software is shown in Tables 1, 2 and 3, respectively.

Forecasting of wind power

The one-week wind data is considered for forecasting the 1, 2...l step ahead hours, and the results are shown in Tables 4 and 5 for AR and ARMA models, respectively.

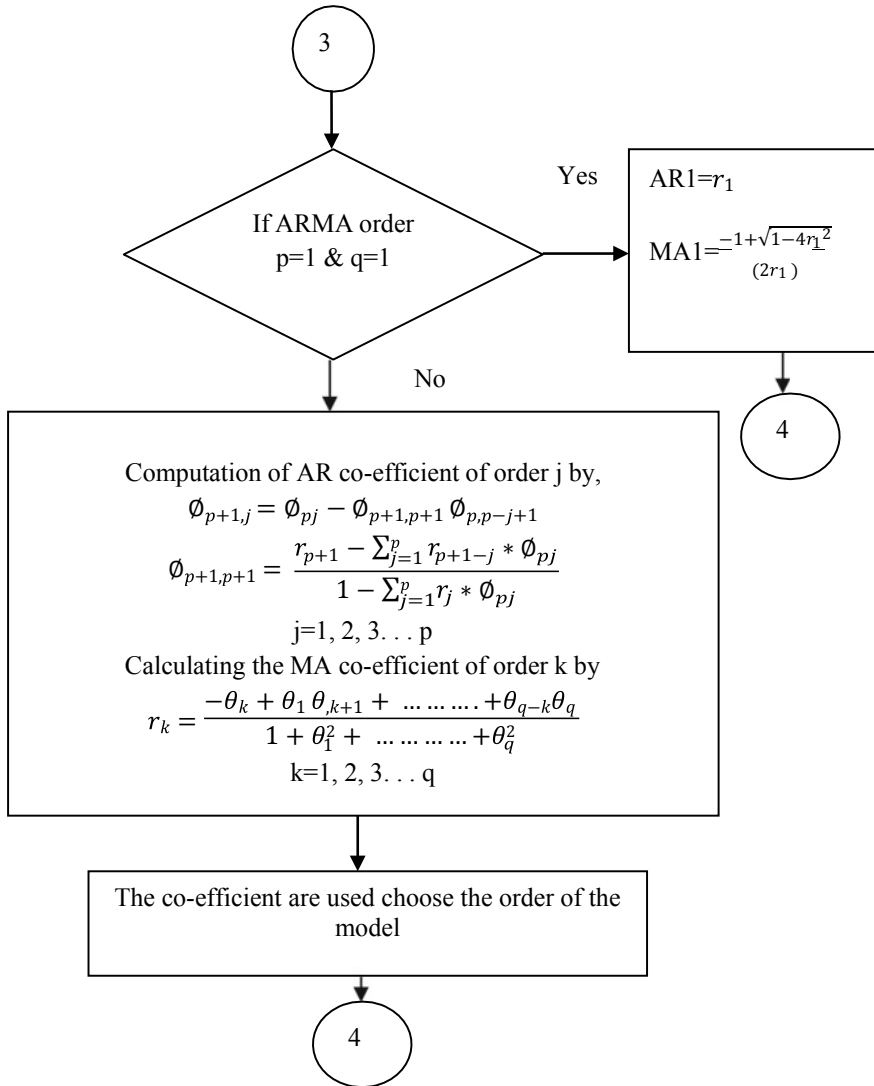


Fig. 4 Flow chart for estimation of ARMA coefficient

From Fig. 9, ARMA (4, 3) gives more accurate forecast values compared to AR (4), hence ARMA (4, 3) is used for forecasting future values.

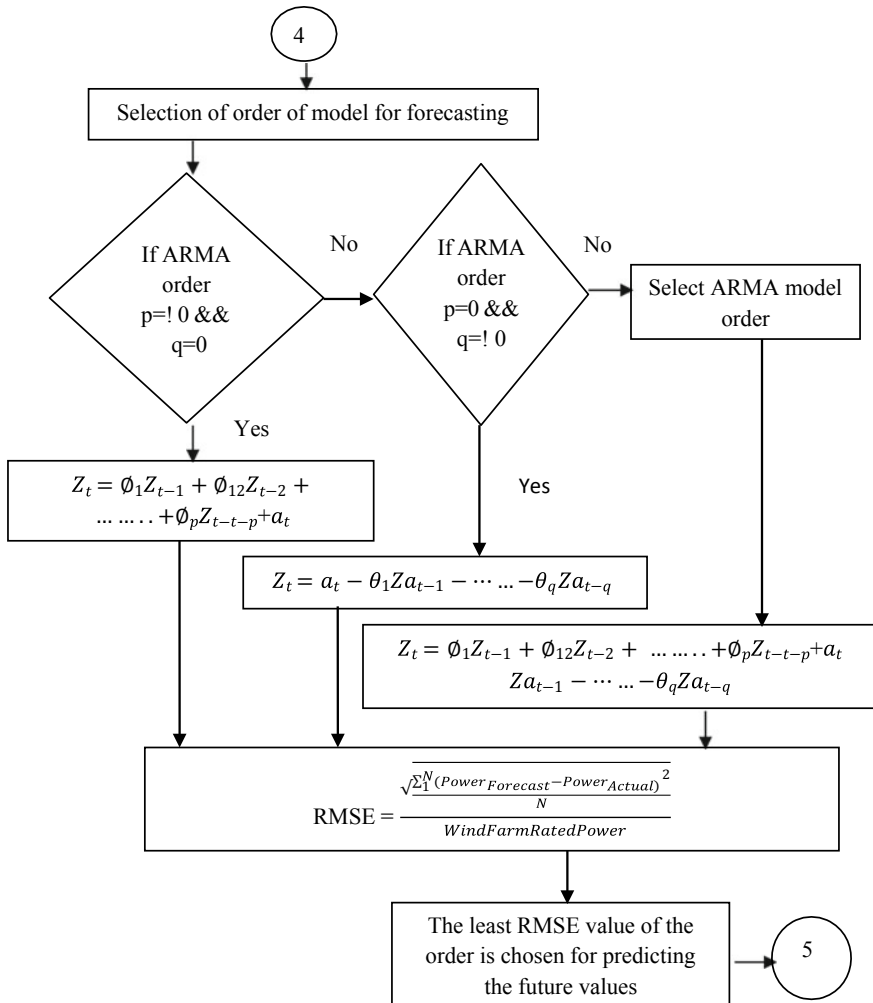


Fig. 5 Flow chart for order of the model selection by RMSE calculation

3.2 Case Study 2: Considering Two-Month Wind Power Data

The two-month wind power has been considered for the estimation of AR, MA and ARMA coefficient as shown in Fig. 10. The comparison of AR, MA and ARMA coefficient of the implemented module with ‘PAST’ software is shown in Tables 6, 7 and 8, respectively.

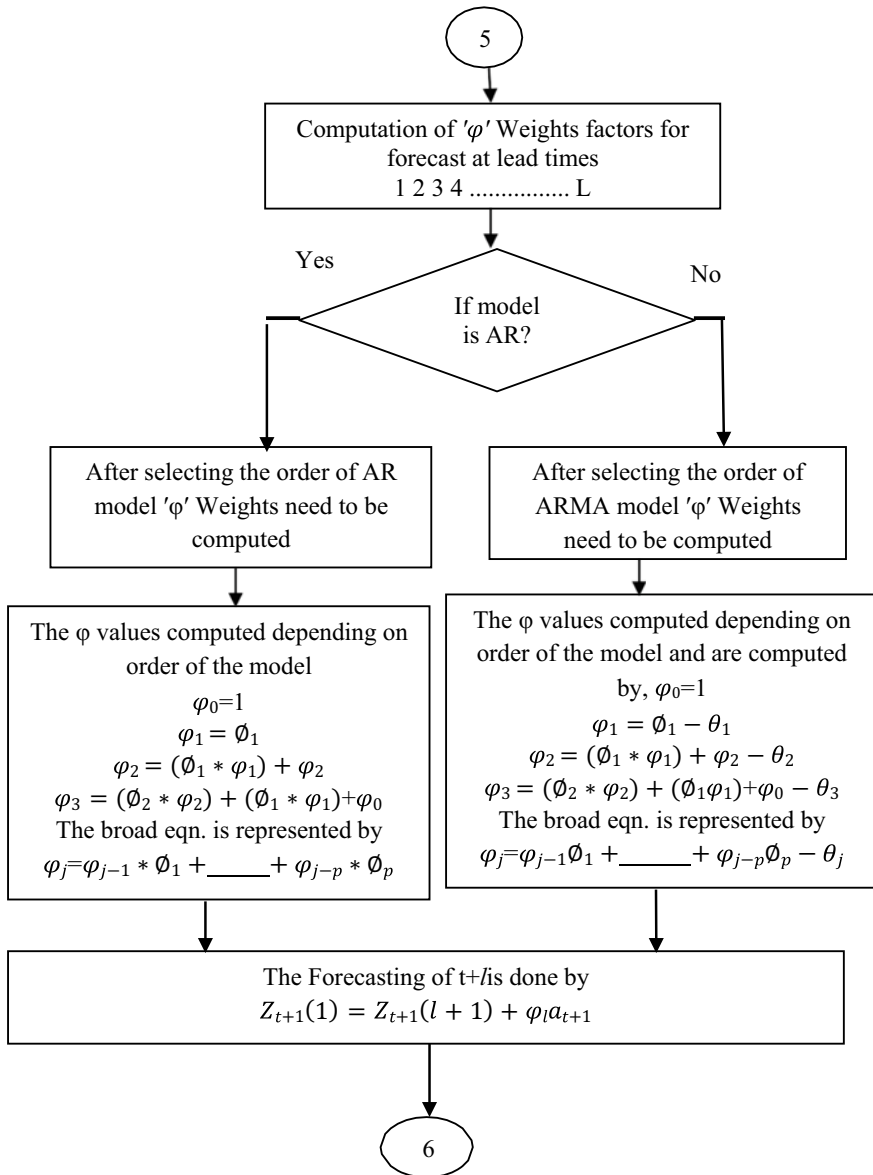


Fig. 6 Flow chart for estimation of ϕ weights for forecasting

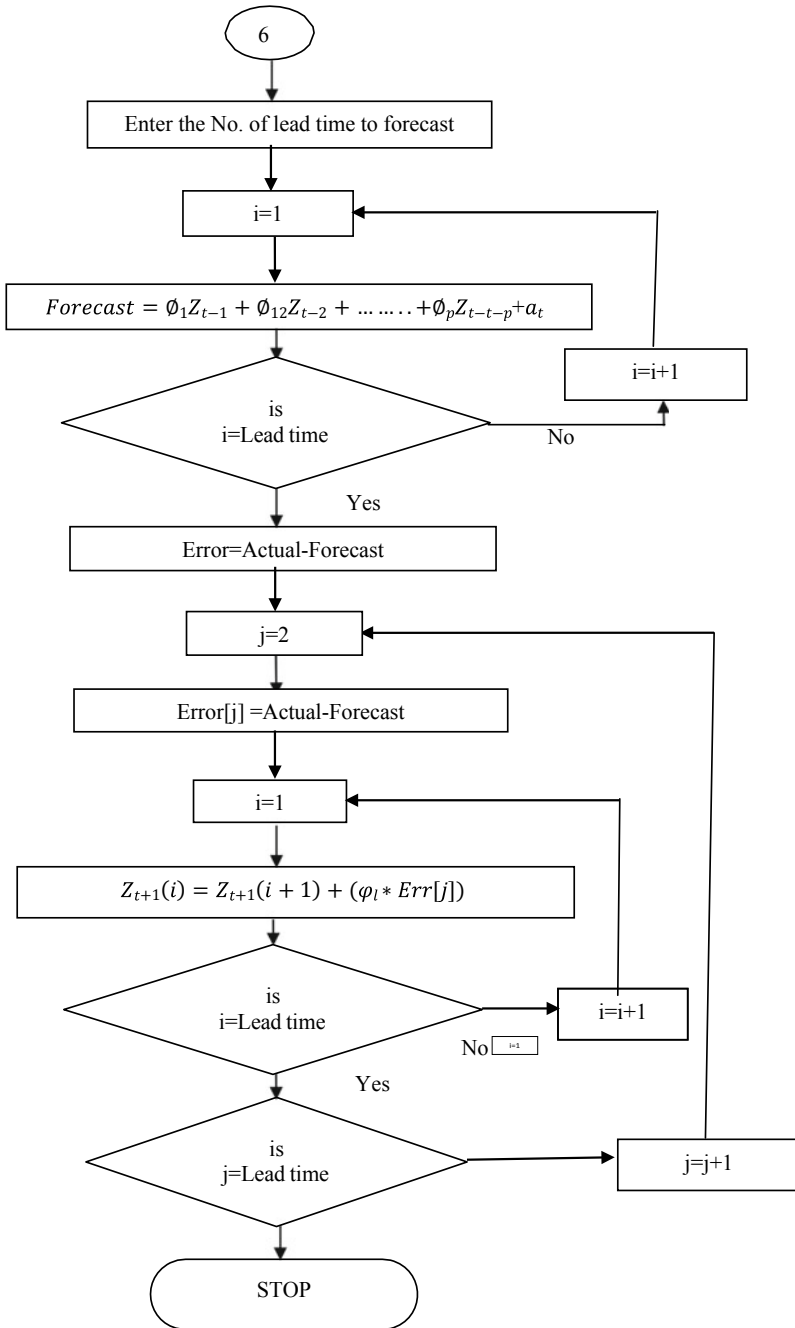


Fig. 7 Flow chart for generating the future values

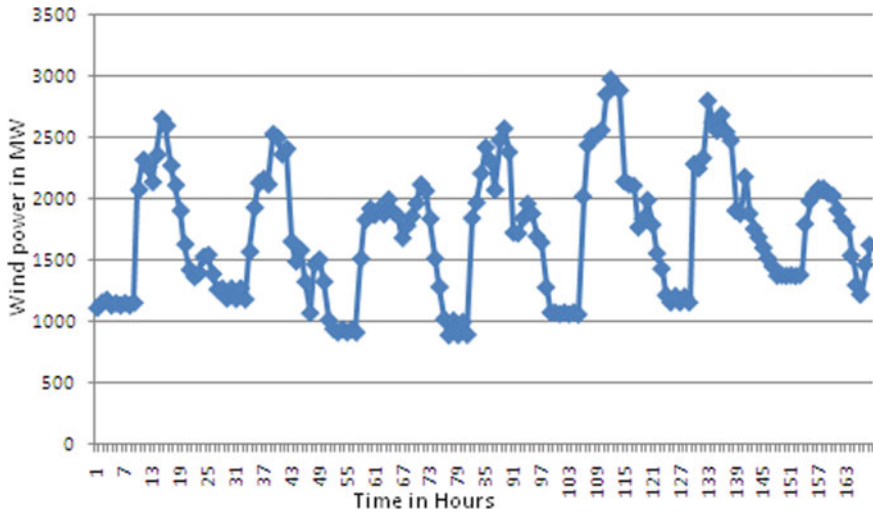


Fig. 8 Wind power versus time in hours

Table 1 Comparison of AR coefficient proposed method with PAST software results

Implemented module results		'PAST' software results	
AR coefficient when order P = 1			
AR.1	0.880454	AR.1	0.8835
AR coefficient when order P = 2			
AR.1	1.100864	AR.1	1.12
AR.2	-0.25034	AR.2	-0.26686
AR coefficient when order P = 3			
AR.1	1.079325	AR.1	1.0976
AR.2	-0.15562	AR.2	-0.15862
AR.3	-0.08604	AR.3	-0.08248
AR coefficient when order P = 4			
AR.1	1.061913	AR.1	1.0807
AR.2	-0.18711	AR.2	-0.2095
AR.3	0.132369	AR.3	0.13754
AR.4	-0.20236	AR.4	-0.2001

Forecasting of wind power

The one-week wind data is considered for forecasting the 1, 2,...l step ahead hours, and the results are shown in Tables 9 and 10 for AR and ARMA models, respectively. The comparison of AR and ARMA models is shown in Fig. 11.

Table 2 Comparison of MA coefficient implemented with PAST software results

Implemented module results		'PAST' software results	
MA coefficient when order P = 1			
MA-1	0.762904	MA-1	0.76061
MA coefficient when order P = 2			
MA-1	1.0847	MA-1	1.0501
MA-2	0.426218	MA-2	0.43043
MA coefficient when order P = 3			
MA-1	0.969679	MA-1	0.9782
MA-2	0.702666	MA-2	0.75694
MA-3	0.340974	MA-3	0.33569

Table 3 Comparison of ARMA coefficient implemented with PAST software resultss

Implemented module results		'PAST' software results	
ARMA coefficient when order (1,1)			
AR-1	0.880454	AR-1	0.88350
MA-1	0.762904	MA-1	0.76061
ARMA coefficient when order (2,2)			
AR-1	1.100864	AR-1	1.1201
AR-2	-0.25034	AR-2	-0.26686
MA-1	1.08471	MA-1	1.05010
MA-2	0.426218	MA-2	0.43043
ARMA coefficient when order (4,3)			
AR.1	1.061913	AR.1	1.0807
AR.2	-0.18711	AR.2	-0.2095
AR.3	0.132369	AR.3	0.13754
AR.4	-0.20236	AR.4	-0.2001
MA.1	0.969679	MA.1	0.9782
MA.2	0.702666	MA.2	0.75694
MA.3	0.340974	MA.3	0.33569

Table 11 shows the comparison of actual with forecasted wind power taking one-week and two-month data for AR (4) and ARMA (4, 3). The ARMA (4, 3) gives better results compared to the AR model for two-month wind power.

Wind power is dispatched whenever there is sufficient wind and used to replace the conventional plants. Based on the availability of wind power, the decision is taken as to which thermal unit should be operated to meet the demand. Table 12 shows the scheduling of conventional power plants to meet the load with available wind power. The scheduling of conventional power depending on the availability of wind power is shown in Fig. 12.

Table 4 Forecasting the wind power considering actual data by AR (4) model

Lead times			0	1	2	3	4	5	6	7
φ Weights of AR (4)			1	1.0793	1.0093	0.8354	0.652	0.487	0.352	0.248
Hrs	Actual	Error	Forecast							
0	2046.19	-26.4	2072.6							
1	2025.59	-18.5	2044.1	2031.8						
2	1910.71	-115.2	2025.9	1923.6	2039.9					
3	1822.03	-85.4	1907.4	1865.1	1951.4	2047.7				
4	1769.93	-61.4	1831.4	1845.8	1907.8	1979.2	2054.3			
5	1538.55	-260.3	1798.8	1836.6	1896.4	1947.8	2003.4	2059.5		
6	1299.43	-265.4	1564.8	1633.7	1827.9	1941.3	1981.4	2022.9	2063.5	
7	1223.56	-123.6	1347.2	1455.6	1586.4	1800.75	1977.8	2007.7	2037.8	2066.4

Table 5 Comparison of actual with forecasted wind power by using ARMA (4, 3)

Lead times			0	1	2	3	4	5	6	7
φ Weights of ARMA (4,3)			1	0.2941	0.4813	0.4979	0.4502	0.384	0.3182	0.2597
Hrs	Actual	Error	Forecast							
0	2046.19	-49.3	2095.5							
1	2025.59	27.1	1998.4	2033.5						
2	1910.71	-102.5	2013.2	1748.6	2059.2					
3	1822.03	19.1	1802.8	1787.4	1734.5	2072.4				
4	1769.93	-18	1787.9	1792.8	1842.5	1785	2081.3			
5	1538.55	-211.9	1750.5	1655.1	1842.9	1896.9	1846.4	2086.9		
6	1299.43	-59.1	1358.5	1100.7	1661.8	1899.6	1947	1906	2090.5	
7	1223.56	86.5	1136.9	1452.9	1214.2	1655.7	1949.4	1987.9	1956.5	2092.6

4 Conclusion

Environment concerns and energy security are the major motivations for increasing renewable energy, out of all; wind energy is a key resource in non-conventional energy technology. The necessity for wind forecast precision is elevated leading to significant augmentation in wind power across the globe. Wind power forecasts can be classified into short term and long term by diverse time scales. A number of physical and statistical models have been used on a daily basis, weekly basis and monthly basis time series, which belong to long-term wind power forecast. Various types of forecasting in terms of long- or short-time scale will make advantages to generation units in electrical network and system security can be assured. Projecting accurate wind power leads noteworthy in reducing the overall costs of the power system. The approach used to forecast short-term future wind power probability distributions is presented in this thesis by using the time series ARMA model. The proposed technique is based

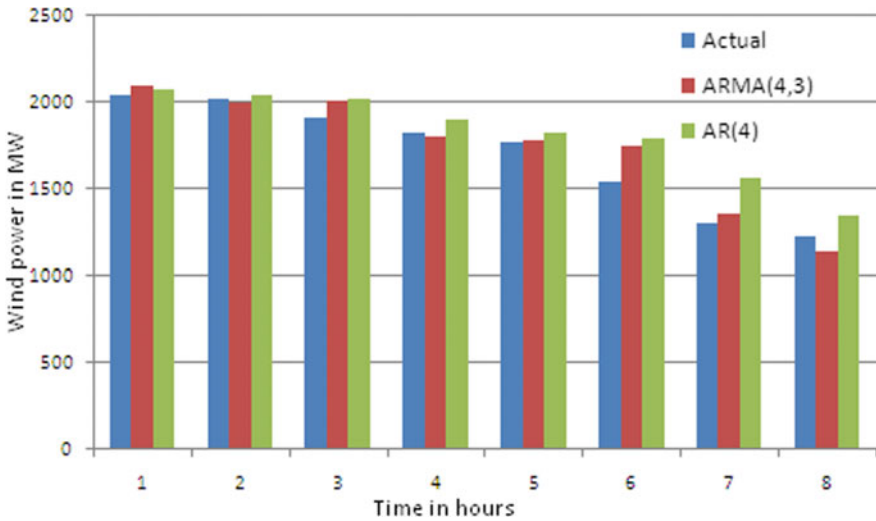


Fig. 9 Comparison of wind power with AR (4) and ARMA (4, 3) taking one-week data

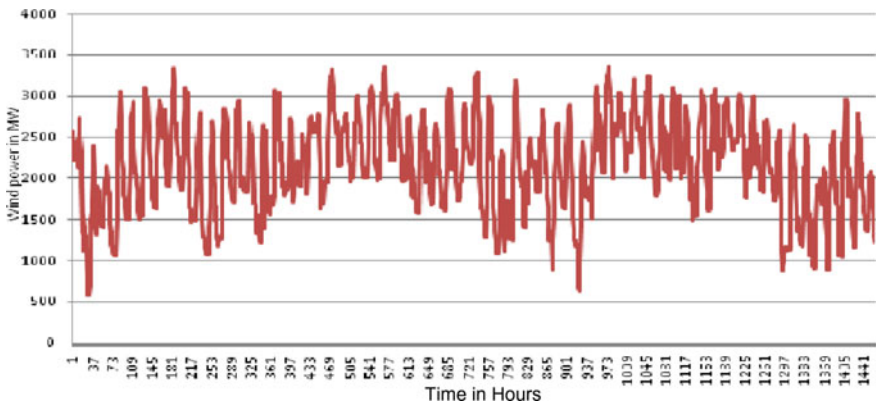


Fig. 10 Wind power versus time in hours

on the ARMA model and depends on historical wind generation data. An accurate short-term forecast of wind generation will facilitate the system operators to schedule conventional generation and meet the demand securely and economically. The estimation of the optimum spinning reserve can reduce the requirement for balancing energy and spinning reserve requirements, which are required to put together wind power into the balancing of demand and supply in the electricity supply system; i.e. to optimize the power plant scheduling. The results obtained using time series analysis gives higher accuracy of wind prediction. Hence, it can be used effectively for scheduling conventional power plants depending on the wind power availability 4-5 h ahead.

Table 6 Comparison of AR coefficient implemented module with PAST software results

Implemented module results		'PAST' software results	
AR coefficient when order P = 1			
AR.1	0.927821	AR.1	0.92838
AR coefficient when order P = 2			
AR.1	1.163871	AR.1	1.1654
AR.2	-0.25441	AR.2	-0.25524
AR coefficient when order P = 3			
AR.1	1.132922	AR.1	1.1332
AR.2	-0.11283	AR.2	-0.10986
AR.3	-0.12165	AR.3	-0.1244
AR coefficient when order P = 4			
AR.1	1.120813	AR.1	1.121
AR.2	-0.12406	AR.2	-0.12148
AR.3	-0.00887	AR.3	-0.01097
AR.4	-0.09954	AR.4	-0.09962

Table 7 Comparison of MA coefficient implemented with PAST software results

Implemented module results		'PAST' software results	
MA coefficient when order P = 1			
MA1	-0.80301	MA1	-0.8008
MA coefficient when order P = 2			
MA1	-1.09202	MA1	-1.0934
MA2	-0.5705	MA2	-0.58862
MA coefficient when order P = 3			
MA1	-1.15869	MA1	-1.1697
MA2	-0.92558	MA2	-0.9112
MA3	-0.4004	MA3	-0.41755

Table 8 Comparison of ARMA coefficient implemented with PAST software results

Implemented module results		'PAST' software results	
ARMA coefficient when order (1,1)			
AR1	0.927821	AR1	0.92838
MA1	-0.80301	MA1	-0.8008
ARMA coefficient when order (2,2)			
AR1	1.163871	AR1	1.1654
AR2	-0.25441	AR2	-0.25524
MA1	-1.09202	MA1	-1.0934
MA2	-0.5705	MA2	-0.58862
ARMA coefficient when order (4,3)			
AR1	1.120813	AR1	1.121
AR2	-0.12406	AR2	-0.12148
AR3	-0.00887	AR3	-0.01097
AR4	-0.09954	AR4	-0.09962
MA1	-1.15869	MA1	-1.1697
MA2	-0.92558	MA2	-0.9112
MA3	-0.4004	MA3	-0.41755

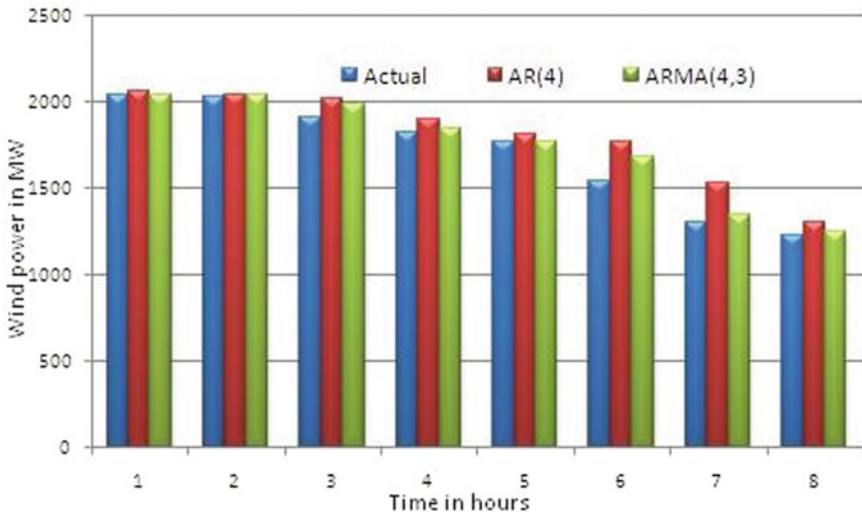


Fig. 11 Comparison of wind power with AR (4) and ARMA (4, 3) taking two-month data

Table 9 Forecasting of the wind power considering actual data by AR (4) model

Lead times			0	1	2	3	4	5	6	7
φ Weights of AR (4)			1	1.119	1.131	1.122	1.008	0.869	0.727	0.587
Hrs	Actual	Error	Forecast							
0	2046.19	-26.4	2059.75							
1	2025.59	-18.5	2038.58	2023						
2	1910.71	-115.2	2023.17	1898	2025					
3	1822.03	-85.4	1897.17	1818	1903	2028.8				
4	1769.93	-61.4	1813.44	1786	1836	1919.9	2033.4			
5	1538.55	-260.3	1768.93	1555	1816	1864.3	1940.1	2037.9		
6	1299.43	-265.4	1528.54	1334	1593	1851.2	1895.1	1960.5	2042.3	
7	1223.56	-123.6	1298.42	1314	1398	1655.3	1887.6	1925.5	1980.2	2046.2

Table 10 Forecasting the wind power considering actual data by ARMA (4, 3) model

Lead times			0	1	2	3	4	5	6	7
φ Weights of ARMA (4,3)			1	0.29	0.4813	0.498	0.4502	0.384	0.3182	0.259
Hrs	Actual	Error	Forecast							
0	2046.19	-49.3	2043							
1	2025.59	27.1	2037	2006						
2	1910.71	-102.5	1988	1896	2007.9					
3	1822.03	19.1	1846	1782	1901.5	2012				
4	1769.93	-18.0	1772	1735	1800.4	1919	2016.5			
5	1538.55	-211.9	1681	1513	1764.6	1829	1939	2021.1		
6	1299.43	-59.1	1343	1245	1550.9	1800	1859.8	1959.4	2025.5	
7	1223.56	86.5	1249	1128	1309.8	1614	1836.7	1890.2	1979.1	2029.4

Table 11 Comparison between forecasted wind power values considering one-week and two-month data

Considering one-week wind data					Considering two-months wind data			
Actual	ARMA (4,3)	%Er r	AR (4)	%Er r	ARMA (4,3)	%Er r	AR (4)	%Er r
2046.1	2095.5	-2.41	2072.6	-1.29	2042.91	0.161	2059.749	-0.66
2025.5	1998.4	1.342	2044.1	-0.91	2037.45	-0.59	2038.579	-0.64
1910.7	2013.2	-5.36	2025.9	-6.03	1987.85	-4.04	2023.169	-5.89
1822	1802.8	1.055	1907.4	-4.69	1846.21	-1.33	1897.172	-4.12
1769.9	1787.9	-1.02	1831.4	-3.47	1771.56	-0.09	1813.439	-2.46
1538.5	1750.5	-13.8	1798.8	-16.9	1680.59	-9.23	1768.928	-15
1299.4	1358.5	-4.55	1564.8	-20.4	1342.56	-3.32	1528.538	-17.6
1223.5	1136.9	7.083	1347.2	-10.1	1248.56	-2.04	1298.4244	-6.12

Table 12 Scheduling of Conventional power plants

Forecasted load	Wind power forecasted	Scheduling of conventional plants
8809.767	2042.900	6766.867
8584.033	2037.450	6546.583
8822.867	1987.856	6835.011
8594.300	1846.200	6748.101
8837.067	1771.560	7065.507
9064.700	1680.590	7384.110
9410.617	1342.561	8068.057
9333.250	1248.562	8084.691

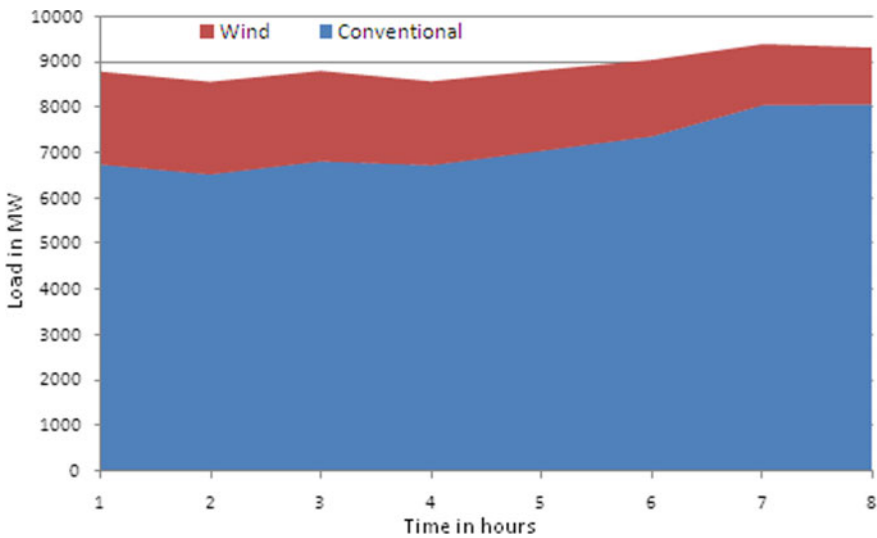


Fig. 12 Scheduling of thermal power plants

References

1. He J, Xu J Ultra (2019) “Short-term wind speed forecasting based on support vector machine with combined kernel function and similar data”. *J Wireless Com Network* 248
2. Chaudhary A, Sharma A, Kumar A, Dikshit K, Kumar N (2020) Short term wind power forecasting using machine learning techniques. *J Stat Manag Syst* 23(1):145–156
3. Daniel LO, Sigauke C, Chibaya C, Mbuva R (2019) Short-term wind speed forecasting using statistical and machine learning methods. *Algorithms* 13(6):132
4. Zhang L, Dong Y, Wang J (2019) “Wind speed forecasting using a two-stage forecasting system with an error correcting and nonlinear ensemble strategy”. *IEEE Access* 7: 176000–176023
5. Fang S, Chiang H (2017) “A high-accuracy wind power forecasting model”. *IEEE Trans Power Syst* 32(2): 1589–1590
6. Ahmadi A, Nabipour M, Mohammadi-Ivatloo B, Amani AM, Rho S, Piran MJ (2020) Long-term wind power forecasting using tree-based learning algorithms. *IEEE Access* 8:1511–1522

7. Zhang Z, Zhang Y, Huang Q, Lee W (2018) Market-oriented optimal dispatching strategy for a wind farm with a multiple stage hybrid energy storage system. *CSEE J Power Energy Syst* 4(4):417–424
8. Cui M, Zhang J, Wang Q, Krishnan V, Hodge B (2019) A data-driven methodology for probabilistic wind power ramp forecasting. *IEEE Trans Smart Grid* 10(2):1326–1338
9. Srivastava T, Vedanshu, Tripathi MM (2020) Predictive analysis of RNN, GBM and LSTM network for short-term wind power forecasting. *J Stat Manag Syst* 23(1): 33–47
10. Toubeau JF, Dapoz PD, Bottieau J, Wautier A, De Grève Z, Vallée F (2021) Recalibration of recurrent neural networks for short-term wind power forecasting. *Electr Power Syst Res* 190:106
11. Liu J, Wang X, Lu Y (2017) “A novel hybrid methodology for short-term wind power forecasting based on adaptive neuro-fuzzy inference system.” *Renew Energy* 103:620–629
12. Kim J-M, Jung H (2018) Time series forecasting using functional partial least square regression with stochastic volatility, GARCH, and exponential smoothing. *J Forecast* 37(3):269–280
13. Wei W, Wu J, Yu Y, Niu T, Deng X (2021) Uncertainty quantification analysis of wind power: A data-driven monitoring-forecasting framework. *IEEE Access* 9:84403–84416
14. Box GEP, Jenkins GM, Reinsel GC (2015) “Time series analysis: Forecasting and control”, 5th edn. Wiley publications

Design and Analysis of EV Charging Station Using LLC Converter



Nayan M. Kengar, Richa Adlakha, and Ashish Grover

1 Introduction

As per today's need for eco-friendly vehicles, hybrid and electric vehicles are now in demand. Hybrid vehicles are a better alternative, but the users of electrical vehicles are still more. The main problem with electric vehicles is the travelling range. Most people choose internal combustion vehicles over electric because of this. But to counter this problem, many charging stations are being developed around the globe. Also, as per the development in technology, better battery systems and charging systems are being developed. The charging time and effective charging are other factors that affect the choice of the customer. As per the charging of the battery, it requires the DC supply to charge. But DC supply cannot be transferred to long distance. Hence, the AC supply is used [1]. This AC supply is then converted into the DC to charge the battery. Now, this conversion circuit should be effective and with less losses. In the following paper, such a circuit of an EV charging station is described with the input voltage current waveform and the output voltage current waveform. The presented circuit is developed and simulated in the PSim software. This software is used to develop, test and simulate the electric circuit. For this circuit, Vienna rectifier and LLC bridge converter are used in series for effective conversion.

2 Types of Chargers

On the basis of supplied AC, there are three types of chargers. Three types of EV chargers are as follows:

N. M. Kengar (✉) · R. Adlakha · A. Grover
Department of Electrical and Electronic Engineering, MRIIRS, Faridabad, India
e-mail: Nayanmahadevkengar007@gmail.com

- Level 1:

In this type of charger, single-phase AC supply of 120 volts and 12 to 16A current are being converted. This level of charger is inexpensive because it takes 12h to charge the EV which is completely discharged having a battery capacity of 24 kWh.

- Level 2:

In this type of charger, polyphase AC supply is used. The value of the current is 15–80A and the voltage is 208–240V. As an increase in the current and voltage it reduces the time of charging. It can charge the EV in 7 hours.

- Level 3:

In this type of charger, large voltage AC supply is used. The range of voltage is 300V to up to 920V and the current can be up to 500A. The design of this type of charger is more expensive and complex compared to Level 1 and Level 2. Due to this type of charger, it is possible to charge the EV within 10 to 30 minutes based on the energy of the battery.

3 Vienna Rectifier

Hence, as per the time required for charging, the EV is less in the level three charger. It is most suitable for charging the EV. A Vienna rectifier is used in this type of charger. The rectifier used is a three-phase one. It is a unidirectional rectifier with three-phase pulse width modulation (PWM). It is more effective than the boost-type PWM rectifier. In the Vienna rectifier, multilevel switching is used which is three levels. It reduces the inductance value requirement. It also reduces the voltage stresses developed on the switches by half; because of this, it improves efficiency and power density (Fig. 1).

The efficiency of this type of rectifier is 99%. The Vienna rectifier is more complex in design when we use hysteresis-based controllers. Due to the recent development in the technology, it is shown that sine triangle-based PWM can be used for control. But with this, development in the technology of this type of control is still complex to design and develop as they need fine-tuning, high-frequency switching and multiple loop executions (Figs. 2, 3).

4 Input to Vienna Rectifier

For the presented system, we use three-phase AC supply of 660 Volts. As AC supply is being provided for the charging station of EV. As per the three-level charger is requirement we choose these input values (Fig. 4).

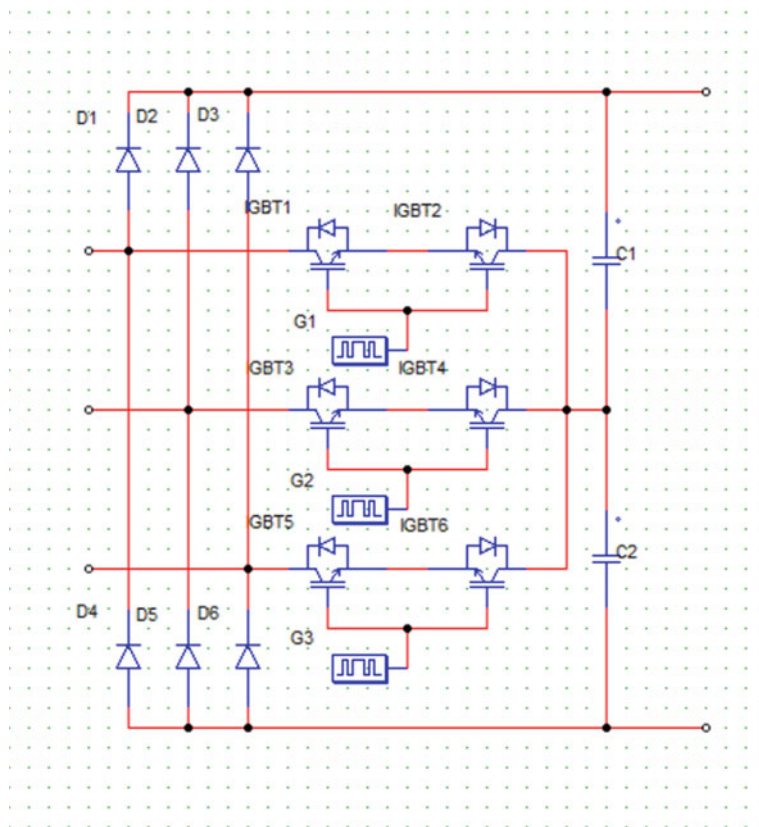


Fig. 1 Vienna rectifier

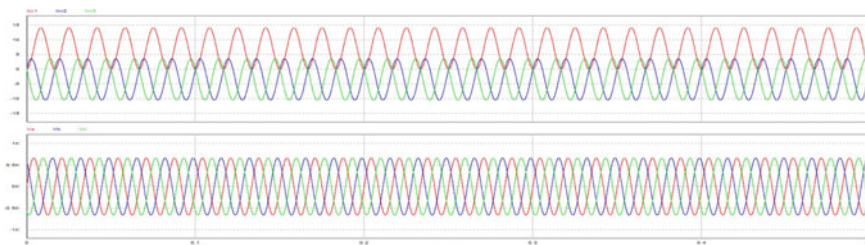


Fig. 2 Input current and voltage waveform of the system

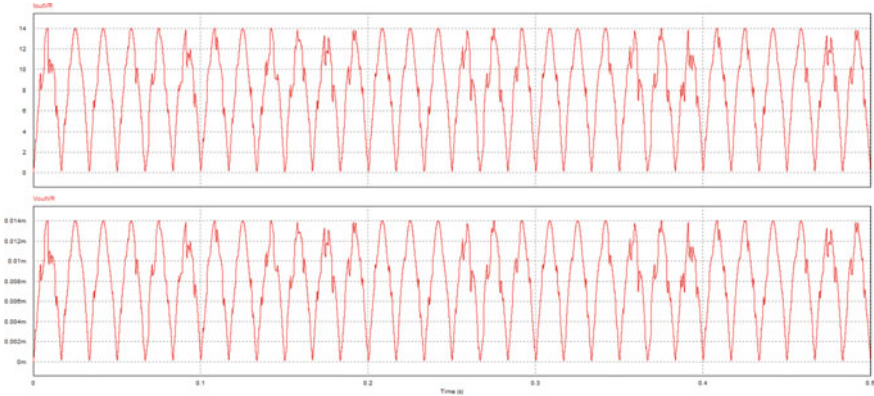


Fig. 3 Output waveform of current and voltage of vienna rectifier

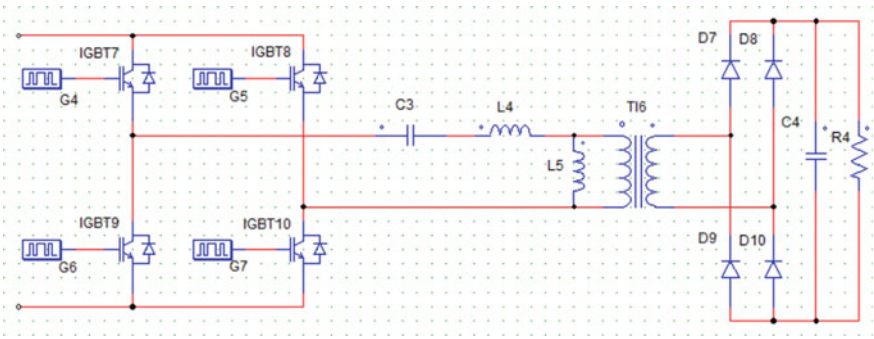


Fig. 4 LLC bridge converter

5 Output of Vienna Rectifier

As per the output of the Vienna rectifier, we get pulsating DC voltage. The current is also pulsating. We use this as input for further conversion and to get the final required current and voltage of the system.

6 Full Bridge LLC Converter

Nowdays, various combined charging systems are used [2, 3]. To meet these requirements, LLC bridge is used. Its performance in terms of efficiency and power density meets the requirement [4]. This converter can be used for the power class of range 300–1000V.

7 Construction of LLC Converters

Junming Zeng [5, 6] It consists of four IGBT switches named IGBT7, IGBT8, IGBT9 and IGBT10, a gating block, capacitor, inductors, transformer, diodes and resistor. The IGBT switches 7, 9 and 8, 10 are connected in series, while each pair is connected to other parallels. This circuit is further connected to the transformer for step-up or step-down purposes. Then again four diodes named D7, D8, D9 and D10 are used. The diodes 7, 9 and 8, 10 are connected in series, while each pair is connected to other parallels. The converter is a DC-to-DC converter [4, 7] It is preferred for high-power applications.

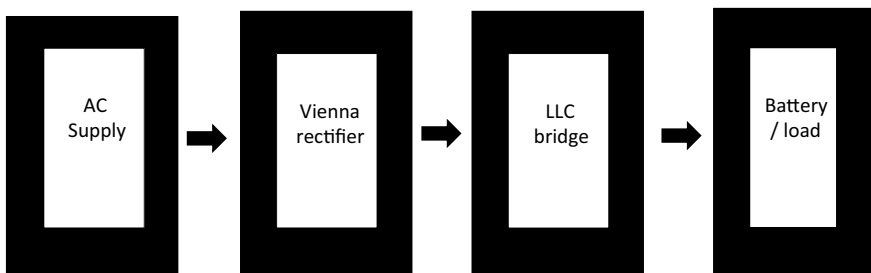
8 LLC's Converters Used in Industry

- Half-bridge LLC converter;
- Full-bridge LLC converter;
- TL-LLC converter.

9 Advantages of LLC Bridge Converter

- Electrical isolation;
- Magnetic integration;
- A wide output ranges;
- Low voltage stresses;
- High efficiency;
- High energy density;
- Low EMI and harmonic pollution;
- Zero-current switching turn-off;
- Zero-voltage switching turn-on.

10 Block Diagram



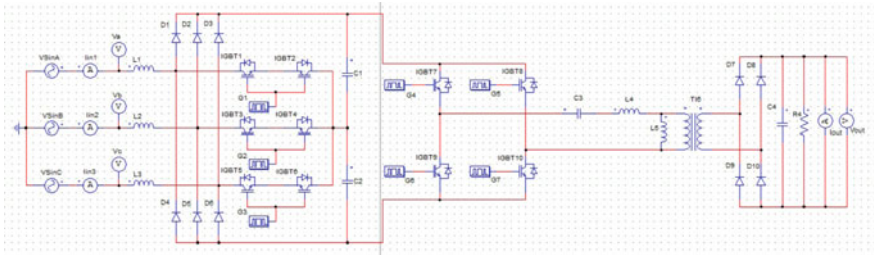


Fig. 5 Circuit of EV charging station

11 Proposed Design

The presented design consists of a Vienna rectifier and an LLC bridge converter. They are connected in series. It is a level three charger. It can be used for the range of 300–930V. This circuit is connected to the three-phase AC supply. It converts AC into DC. The values of each component are decided based on the supply we have provided. Its efficiency and power density are high as we have used the LLC bridge and Vienna rectifier (Fig. 5).

12 Results

As the result, we get the pulsating DC of the desired voltage. The graphs we get from the software about the current and the voltage are the same. The conversion of AC to DC takes place as per the requirement of the charging of the electric vehicle with a time of 25–35 minutes depending upon the capacity of the battery (Fig. 6).

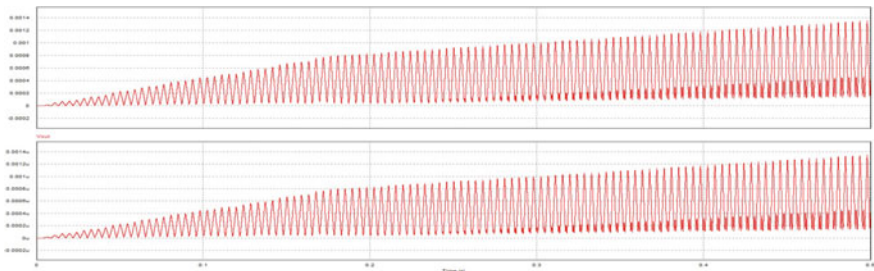


Fig. 6 Output current and voltage of the system

13 Conclusion

By using the level three charger, we reduce the charging time to 30 mins. By changing the value of the capacitors of the system, we can get a more stable output. The LLC bridge and Vienna rectifier can be used to achieve higher efficiency in the EV charging application. In this paper, we have come across the study of types of chargers. Their efficiency, characteristics, input supply and working. Each type of charger has its own working requirement and applications out of which, we can conclude that the level three charger is more suitable for the effective and fast charging of Electric vehicles.

References

1. Singh B, Singh BN, Chandra A, et al. (2003) A review of single-phase improved power quality AC-DC converters. *IEEE Trans Ind Electron*
2. Rivera S, Wu B, Kouro S, et al. (2015) Electric vehicle charging station using a neutral point clamped converter with bipolar DC bus. *IEEE Trans Ind Electron*
3. Li Z, Wu T, Zhan G, et al. (2018) Hybrid modulation method combining variable frequency and double phase- shift for a 10 kW LLC resonant converter. *IET Power Electron*
4. Liu R, Lee CQ (2018) Analysis and design of LLC-type series resonant converter. *Electron Lett*
5. Zeng J, Zhang G, Yu SS, Zhang B, Zhang Y (2020) LLC resonant converter topologies and industrial applications—A review. *Chin J Electr Eng* 6(3)
6. Li G, Xia J, Wang K, et al. (2019) Hybrid modulation of parallel-series LLC resonant converter and phase shift full-bridge converter for a dual-output DC-DC converter. *IEEE J Emerg Sel Top Power Electron*
7. Zhang G, Li Z, Zhang B, et al. (2018) Power electronics converters: Past, present and future. *Renew Sustain Energy Rev*
8. Chon S, Bhardwaj M, Nene H (2018) Maximizing power for Level 3 EV charging stations

Nayan Mahadev Kengar is currently pursuing M. Tech First year degree in robotics and automaton associated with Mitsubishi Electrics from Manav Rachna International Institute of Research and Studies, Faridabad

Richa Adlakha has completed her Ph.D. in Power Electronics. She is currently working as Assistance professor in Department of Electrical and Electronics Engineering in the Manav Rachna International Institute of Research and Studies, Faridabad.

Ashish Grover has completed her Ph.D. in Sustainable Energy Sources. She is currently working as Assistance professor in Department of Electrical and Electronics Engineering in the Manav Rachna International Institute of Research and Studies, Faridabad.

Cascaded Fuzzy and Three-Degree-of-Freedom Controller for Hybrid AGC Considering AC/DC Link



Ashiwani Kumar, Ravi Shankar, and R. K. Mandal

1 Introduction

In the power system, AGC is very significant. AGC's main purpose is to keep frequency variation to a minimum following any disruption. Many writers have investigated the effects of nonlinearities like GRC and GDB in [1]. If not addressed effectively, communication delay (CD) can cause system instability. Nonlinearity like GRC, GDB, BD, and CD has been tested in [2]. Aqua Electrolyzer (AE), Solar Photovoltaic (SPV), Wind Turbine System (WTS), Battery Energy System (BES), Diesel Engine Generator (DEG), and Fuel cell (FC) are the most common components of DG [3]. Renewable energy, particularly solar and wind energy, will play an essential role in the future power system due to its low cost and technological improvement. The only issue with renewables is that they are inherently probabilistic [4]. This problem can be solved if renewable energy is hybridized with better battery energy storage. Deregulation was implemented in the power sector to increase competition and provide customers with lower cost, higher quality electricity. Following deregulation, the electricity sector saw massive investment, and the quality of the power supply increased as well. Following deregulation, only three types of transactions are permitted: polco, bilateral, and contract-violation transactions [5]. Electric vehicles (EV) have been used to meet the extra demand of DISCO in [6, 7]. The single electrical vehicle has an energy capacity of 10–30 KW, so a single EV is not suitable for AGC. For AGC, we need thousands of EVs connected together [8]. EV fleet, along with conventional sources like thermal, gas, and hydro, is used in [9]. In this article, the proposed controller is used to regulate conventional sources and the EV fleet. The response in the presence of an EV fleet is much better. In order to control load frequency, EV is used in [10, 11].

A. Kumar (✉) · R. Shankar · R. K. Mandal
Department of Electrical Engineering, NIT, Patna, Bihar, India
e-mail: ashwani@nitp.ac.in

Electricity demand is increasing every year as a result of the rising population and industrialization. To meet increasing electricity demand, all regional grids are connected, so cheap electricity can be transferred from one region to another. For transmitting power from one control region to another, we use tie-lines, which have now reached their maximum limit, so their capacity needs to be increased. In the long AC lines, there is the problem of the Ferranti effect, stability, and synchronization. To satisfy rising power demand, the ideal way is to build HVDC tie-lines in parallel with existing AC tie-lines [12]. HVDC stored energy is used in conjunction with AC/DC tie-lines in [13, 14] for interconnected power systems.

In the literature, many cascaded and fractional controllers were utilized, with better results than typical classical techniques [15]. Researchers have been interested in fractional-order controllers in recent years because they have more tuning parameters and produce better results than traditional controllers [16, 17]. For load frequency control, a two-degree-of-freedom controller is used in [18, 19], and results are better when compared with the conventional controller like I, PI, and PID, [19]. Three-degree-of-freedom controller is used in [20] and the results are encouraging.

The controller's parameters must be fine-tuned in order for it to function properly. In recent years, many meta heuristic techniques for controller tuning have evolved. The cascaded PI-PID controller is optimized by the bat algorithm, and its result is far superior to the classical controller like I, PI, and PID [21]. Gases Brownian motion optimization is used to optimize fractional-order PID controllers in [22], and the findings are promising for AGC. To optimize the parameters of a fractional-order PID controller for AVR control, the chaotic ant swarm technique is applied [23]. PID controllers for AVR control are tuned using teaching-learning-based optimization (TLBO) [24]. TLBO optimized sliding mode control is employed in the AGC of multi-connected power systems [25]. For the proposed power AGC, the Fruitfly approach [26] is utilized to optimize the PIDN controller parameters. The PI controller for AGC is tuned using a hybrid Bacterial foraging optimization technique [27]. Water wave optimization is used in [28] to tune the cascaded controller for AGC.

Maziar Yazdani proposed the Lion Optimization Algorithm (LOA) in 2016 [29]. LOA is the most recent optimization algorithm that focuses on a lion's ability to find its prey and maintain a healthy lifestyle. In LOA, along with a normal lion, a quasi-opposition-based lion is also used to find the right solution, which needs a compact search space. Therefore, the solution achieved by initialization is closer to the optimum solution because the almost quasi-opposite number is used instead of a pseudo-random number. Consequently, the number of iterations needed for the ideal solution is smaller than the other initialization method.

2 System Investigated

The proposed test system consists of sources like biogas, thermal, DG, and EV in both areas. Figure 1 depicts the proposed evaluated power system network. Solar photovoltaic (SPV), diesel engine generator, wind turbine system (WTS), battery energy storage system (BESS), aqua electrolyzer (AE), fuel cell (FC), and flywheel energy storage system (FESS) are all components of the DG. In area -1 , the participation factors for thermal, DG, and gas are 0.5, 0.3, and 0.2, respectively, while in area -2 , the participation factors are 0.5, 0.3, and 0.2, respectively. When EV is fully charged, it can act as a source, and charged below a certain value, it can act as a load. Due to the increasing interconnection of the control area and increasing power demand, tie-line power transfer capability needs to be increased. Adding an AC-line or HVDC line in parallel to the existing AC-line can improve tie-line power capabilities. It is better to go for an HVDC tie-line, as it is more economical and has less technical issues. Using INEC, the HVDC tie-stored line's energy can be used for frequency adjustment. In this paper, HVDC stored energy has been used for frequency regulation. In order to improve competition in the power sector, deregulation was undertaken. Following deregulation, the energy system received a substantial amount of private investment, resulting in better power quality. An Independent system operator (ISO) manages all transactions between GENCO and DISCO. The proposed controller consists of a fuzzy controller cascaded with $(3-DOF-PI-FOPIDN)$. Three-degree-of-freedom controller means three inputs are given to the controller to make the decision, and they are area control error (ACE), frequency deviation, and disturbance instead of ACE in a normal controller. First, the ACE signal and its derivative are given to the fuzzy controller, and the fuzzy controller output is fed to the fractional controller.

3 Proposed Controller

A fuzzy controller in cascade with classical is the recommended controller. Table 1 introduces the fuzzy membership rule base, and Fig. 2 shows the membership function. Figure 3 depicts the fuzzy cascaded controller. The recommended cascaded controller is shown in (Figs. 4 and 5).

4 Result and Analysis

The suggested test system is run in a restructured power condition using the MATLAB/Simulink toolbox. A GDB of 0.0006 pu is utilized in the suggested test system, and 10% of GRC is used to raise generation in the thermal power system. Two possibilities have been considered in this suggested AGC system inquiry. In the

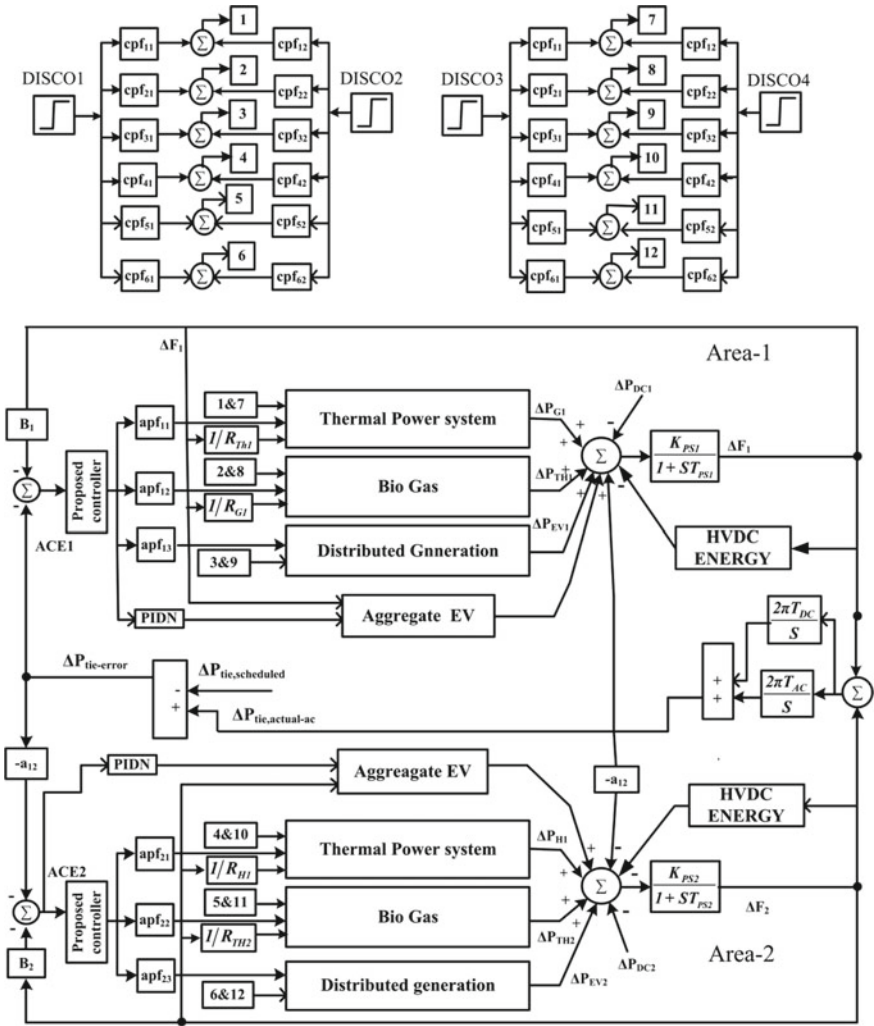


Fig. 1 Two area test system

first scenario, there is no AC/DC link and HVDC energy, while in the second scenario there is AC/DC link and HVDC energy. All cases of deregulation are considered in the simulation.

Table 1 Rule for fuzzy membership

ACE	ACE						
	LN	MN	SN	Z	SP	MP	LP
LN	LP	LP	LP	MP	MP	SP	Z
MN	LP	MP	MP	MP	SP	Z	SN
SN	LP	MP	SP	SP	Z	SN	MN
Z	MP	MP	SP	Z	SN	MN	MN
SP	MP	SP	Z	SN	SN	MN	NL
MP	SP	Z	SN	MN	MN	MN	NL
LP	Z	SN	MN	MN	NL	NL	NL

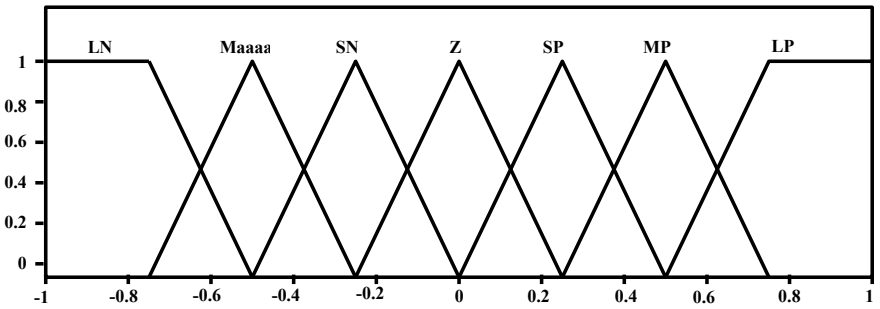


Fig. 2 Membership function for input and output of FLC

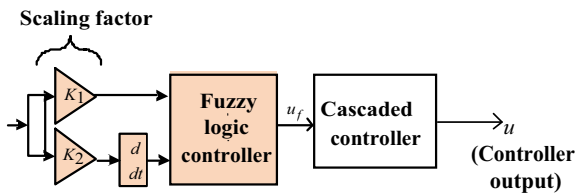


Fig. 3 Fuzzy cascaded controller

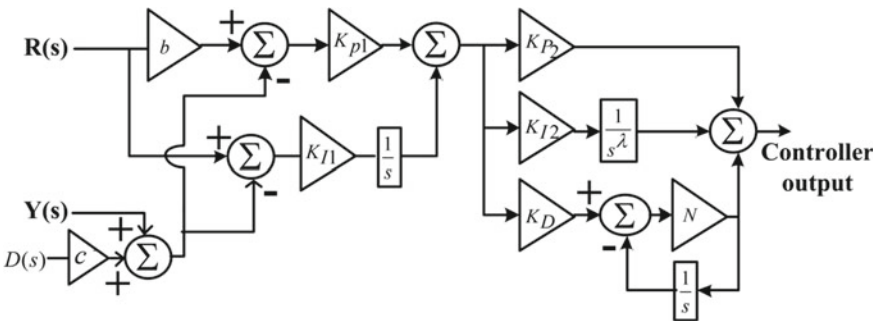


Fig. 4 Proposed three-degree-of-freedom cascaded controller

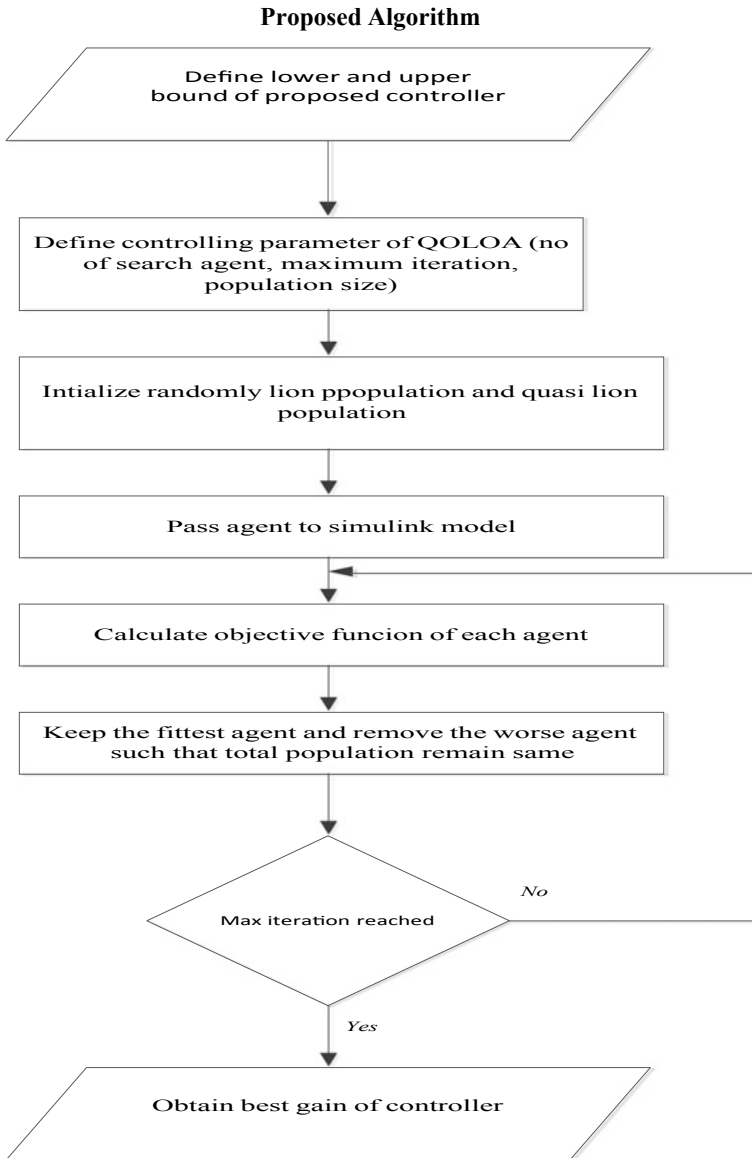


Fig.5 Procedure for QOLOA

4.1 Polco-Based Transation (PBT) Case

In the event of PBT, DISCO can obtain power from GENCO in the area where DISCO is located. In this case, one area’s load disturbance is 1%, while the other area’s load

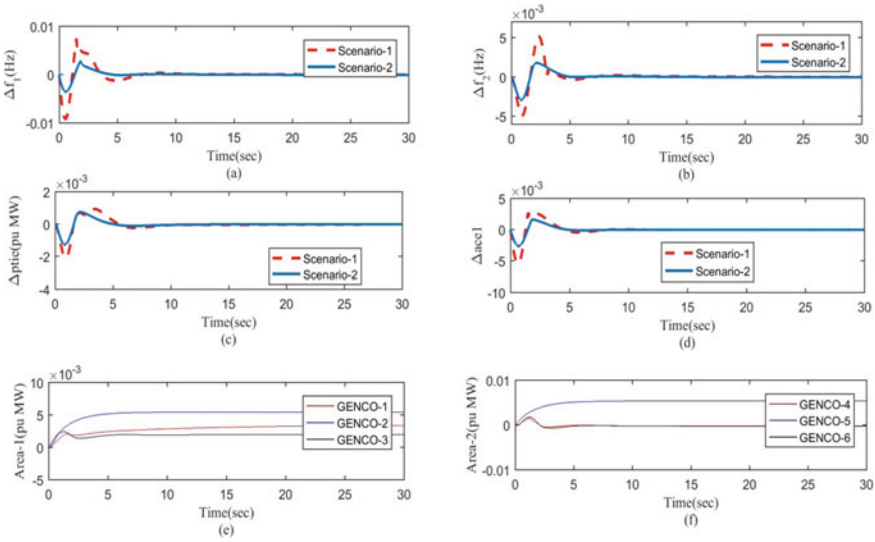


Fig. 6 System response for PBT Case **a** Δf_1 fluctuation **b** Δf_2 fluctuation **c** ΔP_{ite} fluctuation **d** Δace_1 fluctuation **e** Area -1 Generator output **f** Area -2 Generator output

disturbance is 0%. The fuzzy controller in Cascaded with $(PI-FOPIDN)$ makes up the control unit. The controller gain is optimized using QOLOA. PBT response is shown in Fig. 6.

4.2 Bilateral-Based Transition (BBT) Case

In the BBT scenario, the DISCO can draw power from any GENCO. The load disturbance in each location is 1% in this scenario. The fuzzy controller in Cascaded with $(PI-FOPIDN)$ makes up the control unit. The controller gain is optimized using QOLOA. BBT response is shown in Fig. 7.

4.3 Contract Violation Transition (CVT) Case

In this case, DISCO takes more power than what it has contracted for. The un-contracted power is taken from GENCO, in which area DISCO is situated. The load disturbance in area -1 is 1%, and the un-contracted load is 0.001 pu. The fuzzy controller in Cascaded $(PI-FOPIDN)$ makes up the control unit. The system response for the CVT case is shown in Fig. 8.

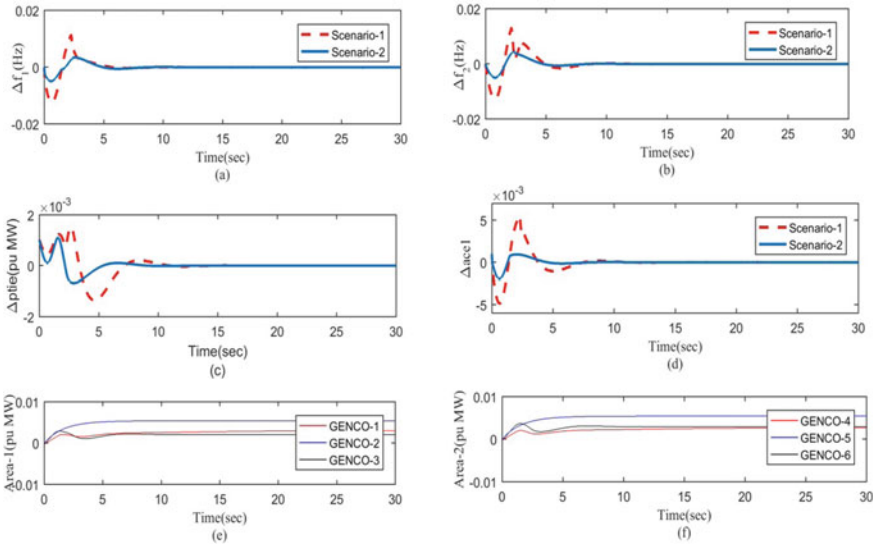


Fig. 7 System response for BBT Case **a** Δf_1 fluctuation **b** Δf_2 fluctuation **c** ΔP_{ite} fluctuation **d** Δace_1 fluctuation **e** Area-1 generator output **f** Area-2 generator output

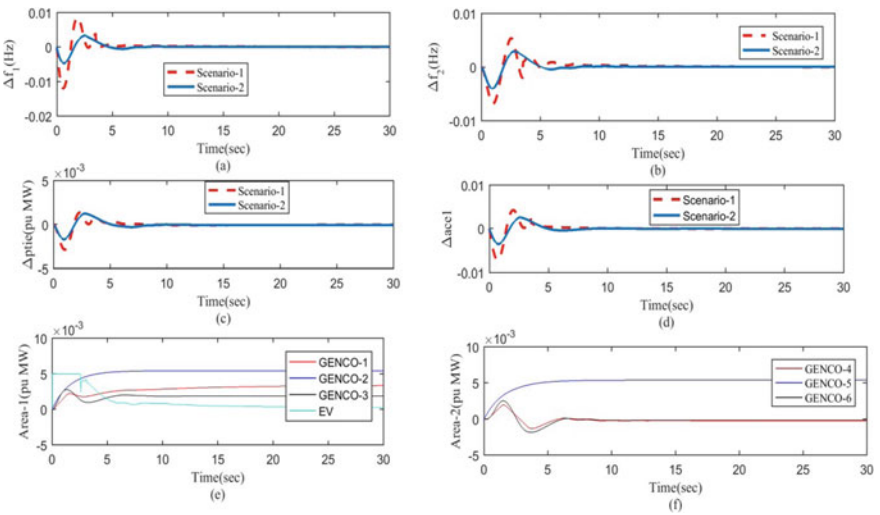


Fig. 8 System response for CVT Case **a** Δf_1 fluctuation **b** Δf_2 fluctuation **c** ΔP_{ite} fluctuation **d** Δace_1 fluctuation **e** Area-1 generator output **f** Area-2 generator output

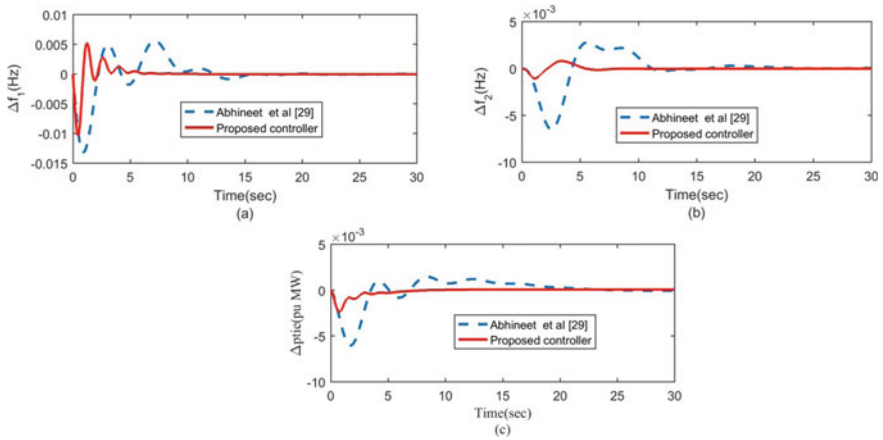


Fig. 9 System response for PBT Case a Δf_1 deviation b Δf_2 deviation c ΔP_{ite} deviation

4.4 Comparison with Previous Literature on the Same Platform

The paper simulated result for the PBT case is compared with a recent paper on AGC by [30] on the same platform. As demonstrated in Fig. 9, the suggested controller excels in settling time and deviation.

5 Conclusion

A new fuzzy controller cascaded with three-degree-of-freedom (3-DOF-PI-FOPID^λDN) controller is proposed. The result of the proposed controller improves with respect to the classical controller. In the presence of HVDC energy and AC/DC link, the system response of the test system improves in all three cases of deregulation. System response also improves in the presence of EV and DG.

References

1. Tan W, Chang S, Zhou R (2017) Load frequency control of power systems with nonlinearities. IET Gener, Transm & Distrib 11(17): 4307-4313
2. Daraz A, Suheel AM, Hazile M, Ulhaq I, Zafer F, Nurulfiqah NM (2020) Improved-fitness dependent optimizer based FOI-PD controller for automatic generation control of multi-source interconnected power system in deregulated environment. IEEE ACCESS 8: 197757–197775
3. Saha A, Saikia LC (2018) Combined application of redox flow battery and DC link in restructured AGC system in the presence of WTS and DSTS in distributed generation unit. IET Gener, Transm & Distrib 12(9): 2072–2085

4. El-Hameed MA, Elkholy MM, El-Fergany AA (2019) Efficient frequency regulation in highly penetrated power systems by renewable energy sources using stochastic fractal Optimizer. *IET Renew Power Gener* 13(12): 2174–2183
5. Shankar R, Chatterjee K, Bhushan R (2016) Impact of energy storage system on load frequency control for diverse sources of interconnected power system in deregulated power environment. *Electr Power Energy Syst* 79, 11–26
6. Bhatt P, Roy R, Ghoshal SP (2010) Optimized multi area AGC simulation in restructured power systems. *Electr Power Energy Syst* 32: 311–322
7. Debbarma S, Dutta A (2017) Utilizing electric vehicles for LFC in restructured power systems using fractional order controller. *IEEE Trans Smart Grid* 8(6): 2554–2564
8. Khooban MH, Niknam T, Blaabjerg F, Dragicevic T (2017) A new load frequency control strategy for micro-grids with considering electrical vehicles. *Electr Power Syst Res* 143: 585–598
9. Oshnoei A, Khezri R, Muyeen SM, Oshnoei S, Blaabjerg F (2019) Automatic generation control incorporating electric vehicles. *Electr Power Compon Syst* 0(0): 1–13
10. Rocha Almeida PM, Soares FJ, Pec JA, as Lopes (2015) Electric vehicles contribution for frequency control with inertia emulation. *Electr Power Syst Res* 127: 141–150
11. Sbordone D, Bertini I, Di Pietra B, Falvo MC, Genoveseb A, Martirano L (2015) EV fast charging stations and energy storage technologies: A real implementation in the smart micro grid paradigm. *Electr Power Syst Res* 120: 96–108
12. Rakhshani E, Rouzbehi K, Elsharty MA, Rodriguez Cortes P (2017) Heuristic optimization of supplementary controller for VSC-HVDC/AC interconnected grids considering PLL. *Electr Power Compon Syst* 45(3): 288–301
13. Zhu J, Guerrero JM, Hung W, Booth CD, Adam GP (2014) Generic inertia emulation controller for multi-terminal voltage-source-converter high voltage direct current systems. *IET Renew Power Gener* 8(7): 740–748
14. Prakash A, Murali S, Shankar R, Bhushan R (2019) HVDC tie-link modeling for restructured AGC using a novel fractional order cascade controller. *Electr Power Syst Res* 170: 244–258
15. Saikia LC, Sahu SK (2013) Automatic generation control of a combined cycle gas turbine plant with classical controllers using Firefly Algorithm. *Electr Power Energy Syst* 53: 27–33
16. Pan I, Das S (2015) Fractional-order load-frequency control of interconnected power systems using chaotic multi-objective optimization. *Appl Soft Comput* 29: 328–344
17. Pan I, Das S (2016) Fractional order AGC for distributed energy resources using robust optimization 7(5): 2175–2186
18. Debbarma S, Saikia LC, Sinha N (2014) Robust two-degree-of-freedom controller for automatic generation control of multi-area system. *Electr Power Energy Syst* 63: 878–886
19. Li M, Zhou P, Zhao Z, Zhang J (2016) Two-degree-of-freedom fractional order-PID controllers design for fractional order processes with dead-time. *ISA Trans* 61: 147–154
20. Rahman A, Saikia LC, Sinha N (2015) Load frequency control of a hydro-thermal system under deregulated environment using biogeography-based optimised three- degree-of-freedom integral-derivative controller. *IET Gener Transm Distrib* 9(15):2284–2293. <https://doi.org/10.1049/iet-gtd.2015.0317>
21. Dash P, Saikia LC, Sinha N (2015) Automatic generation control of multi area thermal system using Bat algorithm optimized PD–PID cascade controller. *Electr Power Energy Syst* 68: 364–372
22. Zamani A, Barakati SM, Yousofi-Darmian S (2016) Design of a fractional order PID controller using GBMO algorithm for load–frequency control with governor saturation consideration. *ISA Trans* 64: 56–66
23. Tang Y, Cui M, Hua C, Li L, Yang Y (2012) Optimum design of fractional order $PI^\lambda D^\mu$ controller for AVR system using chaotic ant swarm. *Expert Syst Appl* 39:6887–6896
24. Chatterjee S, Mukherjee V (2016) PID controller for automatic voltage regulator using teaching–learning based optimization technique. *Electr Power Energy Syst* 77: 418–429
25. Mohanty B (2015) TLBO optimized sliding mode controller for multi-area multi-source nonlinear interconnected AGC system. *Electr Power Energy Syst* 73, 872–881

26. Shankar R, A Kumar, Raj U, Chatterjee K (2018) Fruit fly algorithm-based automatic generation control of multiarea interconnected power system with FACTS and AC/DC links in deregulated power environment. *Int Trans Electr Energy Syst.* e2690
27. Panda S, Mohanty B, Hota PK (2013) Hybrid BFOA–PSO algorithm for automatic generation control of linear and nonlinear interconnected power systems. *Appl Soft Comput* 13: 4718–4730
28. Dahiya S, Parmar KPS (2021) A novel fractional order proportional integral derivative plus second-order derivative controller for load frequency control. *Int J Sustain Energy* 40(3): 235–252
29. Yazdani M, Jolai F (2016) Lion optimization algorithm (LOA): A nature-inspired metaheuristic algorithm. *J Comput Des Eng* 3: 24–36
30. Prakash A, Kumar K, Parida SK (2020) PIDF(1+FOD) controller for load frequency control with SSSC and AC–DC tie-line in deregulated environment. *IET Gener, Transm & Distrib* 14(14): 2751–2762

Harmonic Performance Analysis for Different Loads with and Without PV



Aakriti Khanna, Anjali Garg, and Sreedhar Madichetty

1 Introduction

In recent years, we are aware that due to environmental factors and the ever-increasing demand for energy, fossil fuel energy generation has decreased to a great extent. As an alternative approach, renewable energy sources (RES) are coming into play which include solar energy, wind energy, bio energy and hydro energy. Solar energy can be used by means of a photovoltaic (PV) system; this system converts solar radiations into electricity. PV systems are categorized into standalone and grid-connected PV systems. Grid-connected systems are more widely used; in these, the PV source is integrated into the electrical grid via power electronic technology [1–4]. Power electronic technology used for the integration of source to the grid is the inverter. Various topologies for renewable systems and some current control strategies have been presented for the control of the converter [5].

Current controller is an important part of the control unit. Only when the current controller is proper, adjustment of DC link voltage and the study of system stability while connecting to grid is feasible. Many current controllers which are used to track the reference currents include the PI controller, sliding mode controller, hysteresis current controller, fuzzy logic controller, etc. Various techniques have been compared in [6–9]. A few hybrid and conventional PV array configurations have been modeled in this which compares the configurations for efficiency and economic purpose [10].

A. Khanna (✉) · A. Garg
Department of EECE, The NorthCap University, Gurugram, India
e-mail: aaki.0502@gmail.com

A. Garg
e-mail: anjalineerajgarg867@gmail.com

S. Madichetty
Department of EEE, Mahindra University, Hyderabad, India
e-mail: sreedhar.madichetty@mahindrauniversity.edu.in

The harmonic control loop plays an important role in grid-connected systems so that the system functions properly; various harmonic performance and control methods are presented in [11–14].

In this paper, this section gives an introduction to renewable energy sources and grid-connected systems, Sect. 2 gives a description of the system explaining its basic components, Sect. 3 presents the waveforms for voltage and current for simulation models in MATLAB/Simulink software, Sect. 4 compares the system with and without PV in terms of Total Harmonic Distortion (THD) for different types of loads and Sect. 5 concludes the paper.

2 System Description

The system consists of various components which include a source, inverter, control technique for the inverter, grid and loads. The system block diagram is shown in Fig. 1.

2.1 Source

The source here produces DC voltage. We are considering a DC voltage source from the Simulink library and PV Array which produces equivalent DC voltage. The DC voltage used for the simulation purpose is 850 volts.

2.2 Inverter

An inverter is a device which takes the DC value as its input and converts it into AC value so that it can be fed into the electric utility grid. Figure 2 shows the circuitry for a three-phase inverter used in a Grid connection. The inverter does the synchronization of frequency and limits the voltage in such a way that it does not exceed the grid voltage. An inverter plays a dual role: first, it converts DC to AC, and, second, it does

Fig. 1 System block diagram

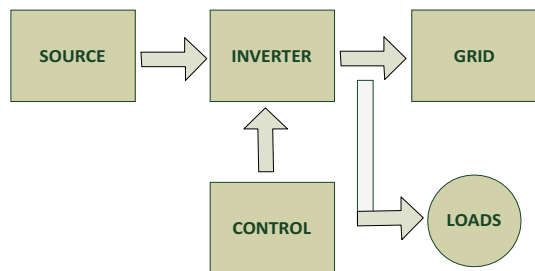
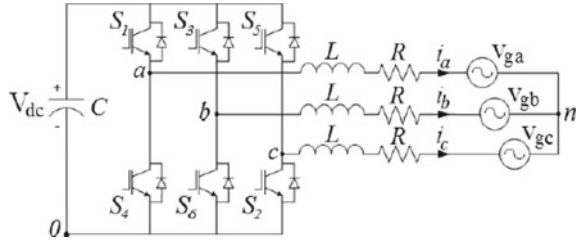


Fig. 2 Three-phase grid-connected inverter [15]



the job of synchronization, thereby maintaining a constant DC link voltage. The topology here assumes that the switches used are ideal, the voltages are balanced and DC link voltage used is constant. The inverter here includes six IGBT switches which are connected in a bridge configuration.

2.3 Inverter Control

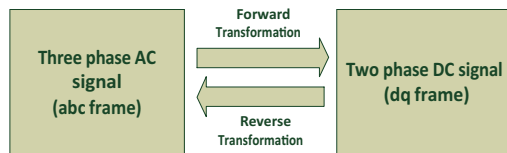
Control of an inverter is designed using the dq-axis theory or synchronous reference frame technique (SRF technique) which involves the principle of DQ rotation frame transformation. This converts the AC sinusoidal signals to DC, performs the operation on these values and then transforms these back to AC domain. The transformations include three-phase AC signals to two-phase DC signals in forward transformation; the operations are then performed on these two-phase DC signals, and these are then converted back to three-phase AC signals in reverse transformation. The transformations are shown in Fig. 3.

With this control technique, the reference currents are generated, which further are used for the control signal generation. PLL, Phase locked loop, generates the angle between the two axes for the transformation process. Hysteresis current controller performs the comparison of actual values and reference values generating the error signal which is then controlled via a Proportional Integral (PI) loop resulting in the generation of the switching pulses for the inverter.

The equations involved in the process of transformation are based on Clarke and Park transformations.

The Clarke transformation handles the conversion between three-phase AC signals and two-phase AC signals.

Fig. 3 Transformations in control technique



abc frame \rightarrow $\alpha\beta$ frame is represented in (1) and $\alpha\beta$ frame \rightarrow abc frame is represented in (2).

$$\begin{bmatrix} I_\alpha \\ I_\beta \end{bmatrix} = \frac{2}{3} \begin{bmatrix} 1 & -\frac{1}{2} & -\frac{1}{2} \\ 0 & \frac{\sqrt{3}}{2} & -\frac{\sqrt{3}}{2} \end{bmatrix} \begin{bmatrix} I_a \\ I_b \\ I_c \end{bmatrix} \quad (1)$$

$$\begin{bmatrix} I_a \\ I_b \\ I_c \end{bmatrix} = \frac{3}{2} \begin{bmatrix} \frac{2}{3} & 0 \\ -\frac{1}{3} & \frac{1}{\sqrt{3}} \\ -\frac{1}{3} & -\frac{1}{\sqrt{3}} \end{bmatrix} \begin{bmatrix} I_\alpha \\ I_\beta \end{bmatrix} \quad (2)$$

The Park transformation handles the conversion between two-phase AC signals and two-phase DC signals.

$\alpha\beta$ frame \rightarrow dq frame is represented in (3) and dq \rightarrow frame \rightarrow $\alpha\beta$ frame is represented in (4)

$$\begin{bmatrix} I_d \\ I_q \end{bmatrix} = \begin{bmatrix} \cos \rho & \sin \rho \\ -\sin \rho & \cos \rho \end{bmatrix} \begin{bmatrix} I_\alpha \\ I_\beta \end{bmatrix} \quad (3)$$

$$\begin{bmatrix} I_\alpha \\ I_\beta \end{bmatrix} = \begin{bmatrix} \cos \rho & -\sin \rho \\ \sin \rho & \cos \rho \end{bmatrix} \begin{bmatrix} I_d \\ I_q \end{bmatrix} \quad (4)$$

where ρ is the angle by which dq coordinate system is displaced from $\alpha\beta$ coordinate system.

2.4 Harmonics and THD

Harmonics are signals which have integral multiple frequencies of the fundamental frequency. The harmonics can pose a major problem in the power quality of electrical systems. These are caused by the non-generation of sinusoidal waves from inverters and the types of loads connected in a system.

Total Harmonic Distortion (THD) is a measure of observing the harmonics in the system. It is the ratio of total harmonics (the sum of all harmonic components which are present in the signal) to the fundamental frequency as given in (5). Various methods are available to calculate THD:

$$\text{THD} = \frac{\sqrt{V_2^2 + V_3^2 + V_4^2 + \dots}}{V_1} \quad (5)$$

where,

V_1 is the signal amplitude (rms volts),

V_2 is the second harmonic component (rms volts),

V_3 is the third harmonic component (rms volts) and so on.

3 Simulations and Results

The simulations for a grid-connected system with and without PV for different load conditions is done using the Simpower system Simulink toolbox in MATLAB R2020.

3.1 Grid-Connected DC Voltage Source with Linear Load

The voltage and current waveforms for grid and load respectively for a grid-connected DC voltage source with linear load are shown in Fig. 4.

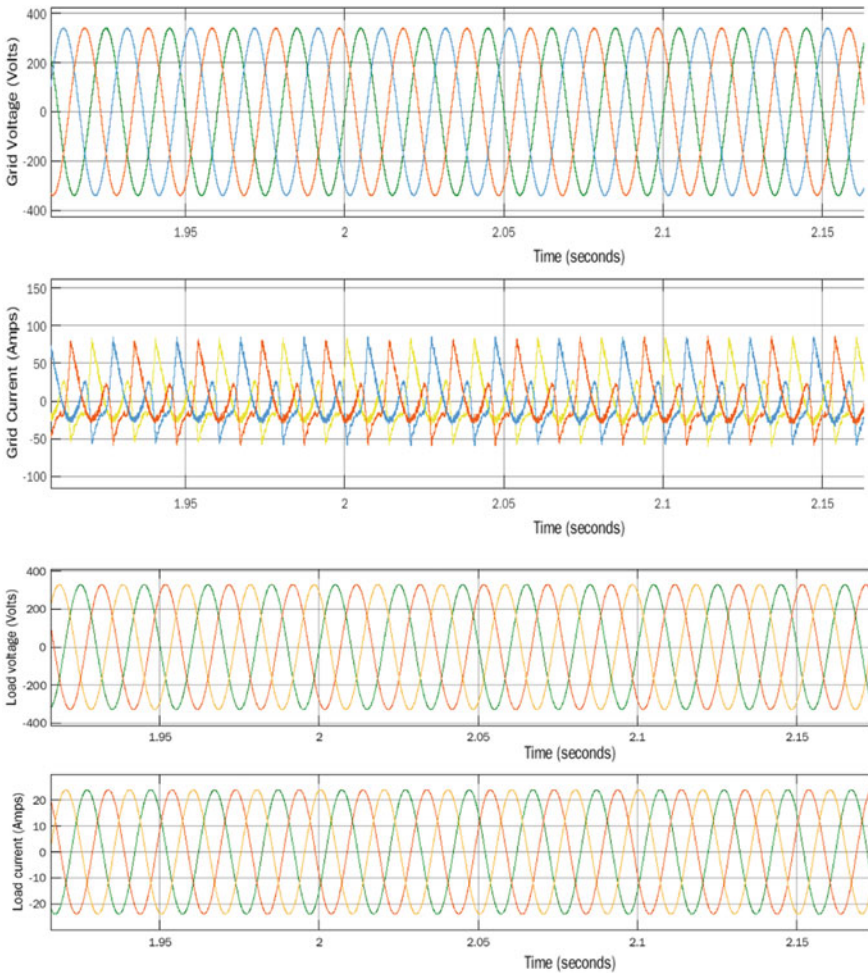


Fig. 4 Voltage and current waveforms for grid and load respectively for grid-connected DC voltage source for linear load

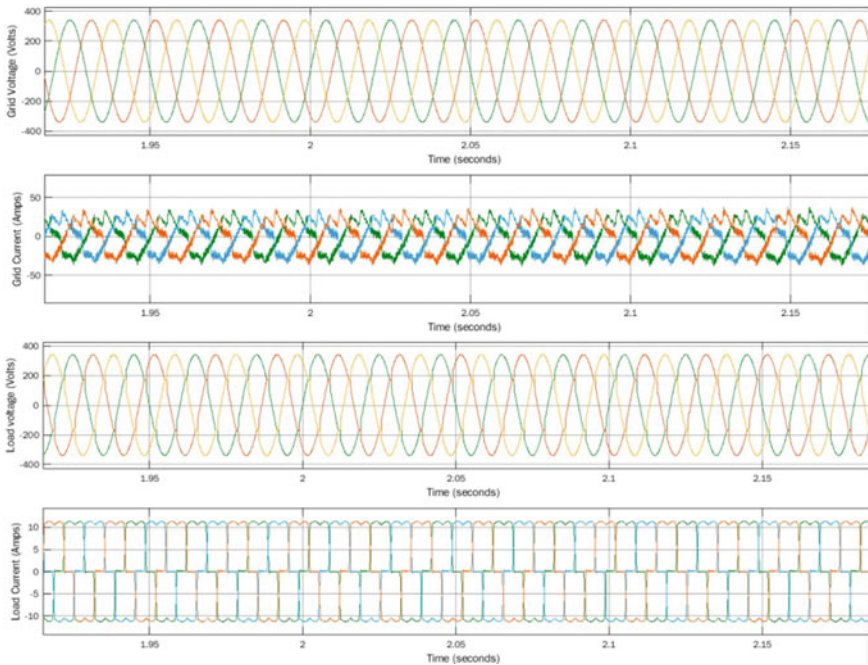


Fig. 5 Voltage and current waveforms for grid and load respectively for grid-connected DC voltage source for non-linear load

3.2 Grid-Connected DC Voltage Source with Non-linear Load

The voltage and current waveforms for grid and load respectively for a grid-connected DC voltage source with non-linear load are shown in Fig. 5.

3.3 Grid-Connected PV Source with Linear Load

The voltage and current waveforms for grid and load respectively for grid-connected PV voltage source with linear load are shown in Fig. 6.

3.4 Grid-Connected PV Source with Non-linear Load

The voltage and current waveforms for grid and load respectively for a grid-connected PV voltage source with non-linear load are shown in Fig. 7.

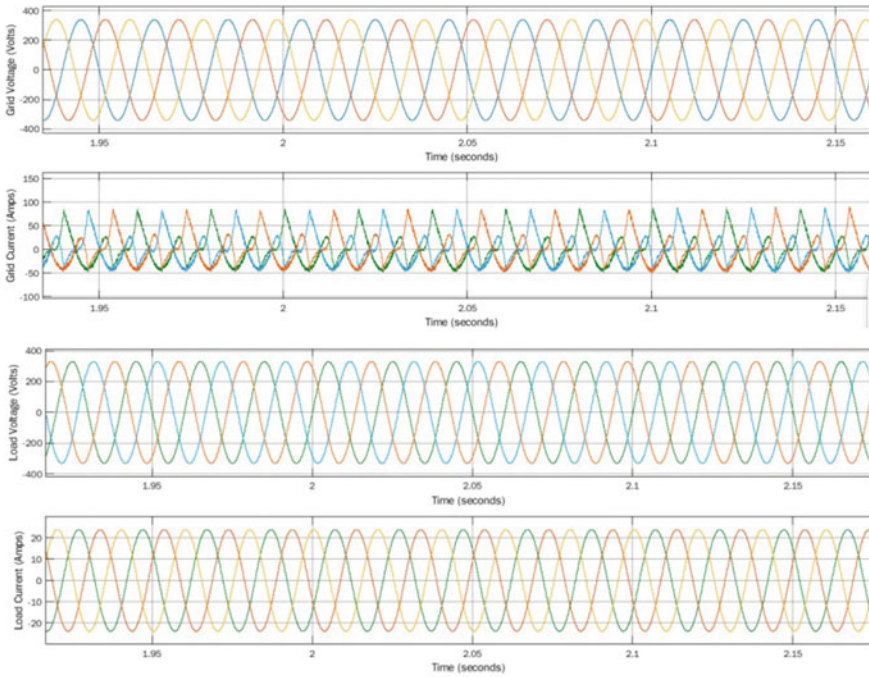


Fig. 6 Voltage and current waveforms for grid and load respectively for grid-connected PV voltage source for linear load

3.5 Grid-Connected DC Source with Linear and Non-linear Load

The voltage and current waveforms for grid and load respectively for a grid-connected DC voltage source with both linear load and non-linear load are shown in Fig. 8. The connection of loads is such that before 1.5 s, only non-linear load is connected, from 1.5 to 2 s, both linear and non-linear loads are connected, from 2 to 2.2 s, only linear load is connected, and from 2.2 to 3 s, both loads are open and after that only non-linear load is connected. The change in current waveforms is clearly observed in Fig. 8.

3.6 Grid-Connected PV Source with Linear and Non-linear Load

The voltage and current waveforms for grid and load respectively for a grid-connected PV voltage source with both linear load and non-linear load are shown in Fig. 9.

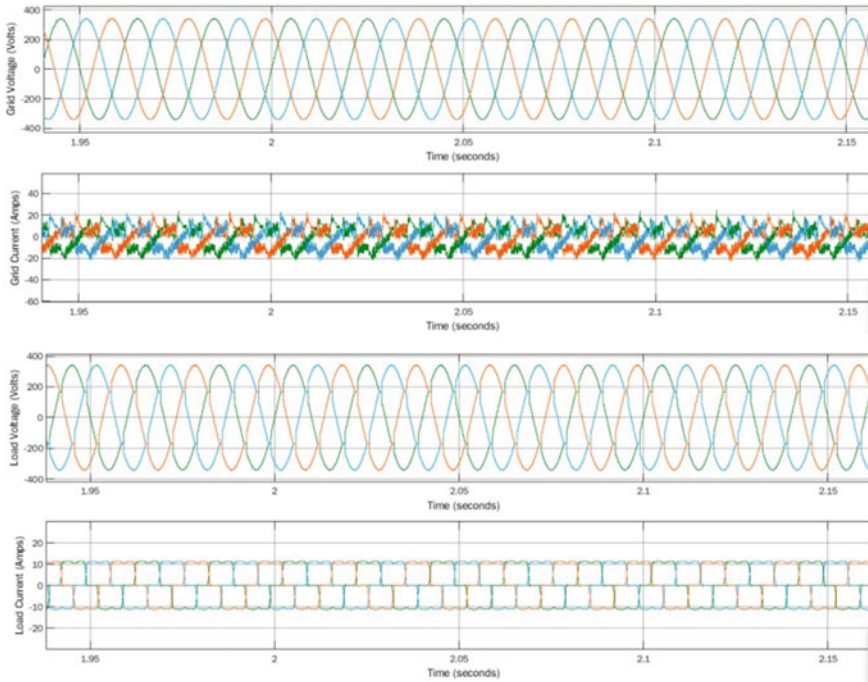


Fig. 7 Voltage and current waveforms for grid and load respectively for grid-connected PV voltage source for non-linear load

The connection of loads is such that before 1.5 s, only non-linear load is connected, from 1.5 to 2 s, both linear and non-linear loads are connected, from 2 to 2.2 s, only the linear load is connected, from 2.2 to 3 s, both loads are open and after that only the non-linear load is connected. The change in current waveforms is clearly observed in Fig. 9.

4 Comparison of System with and Without PV in Terms of THD

Table 1 presents the total harmonic distortion comparison for a grid-connected models with a DC voltage source and PV array as a source with separate linear and non-linear loads. Table 2 presents THD for grid-connected models with a DC voltage source and PV array as source (Figs. 8 and 9) with both linear and non-linear load in the same model.

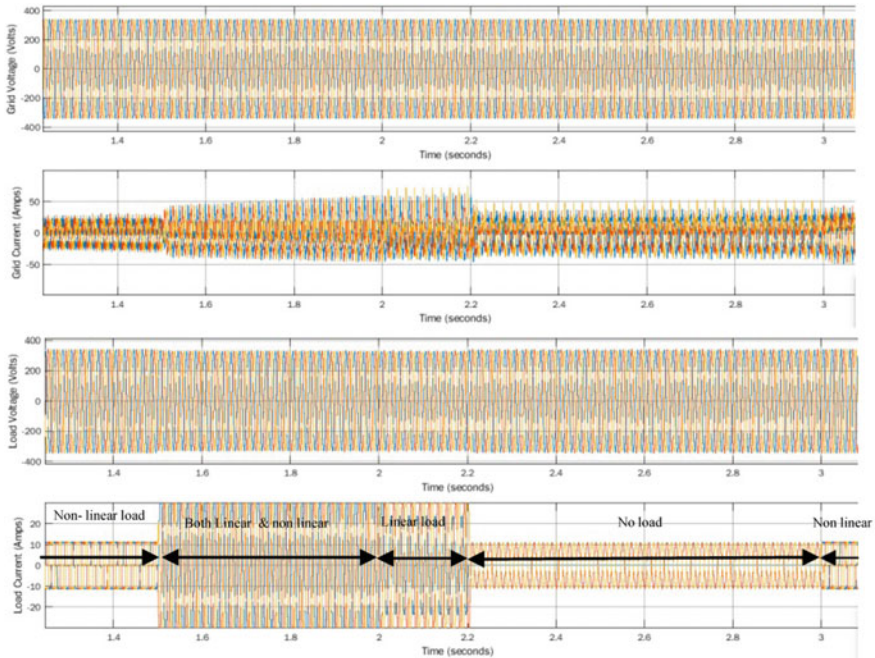


Fig. 8 Voltage and current waveforms for grid and load respectively for grid-connected DC source with both linear and non-linear load

5 Conclusion

According to the results, when only the linear load is connected and the DC voltage source is replaced with a PV source, the grid current THD decreases whereas the other THDs remain the same. When only a non-linear load is connected and the DC voltage source is replaced with a PV source, the grid current THD increases, and a slight change is noticed in load voltage THD while other THDs remain the same.

When both, the linear and non-linear loads, are connected in the same model, we observe that grid current THD increases. Therefore, it is concluded that grid current THD increases for all cases, i.e. linear load, non-linear load and combined linear and non-linear loads when the DC voltage source is replaced by PV source whereas the rest THDs remain approximately the same.

From the observations, it can be said that harmonics mostly arise out of non-linear loads, and grid current THD is affected the most.

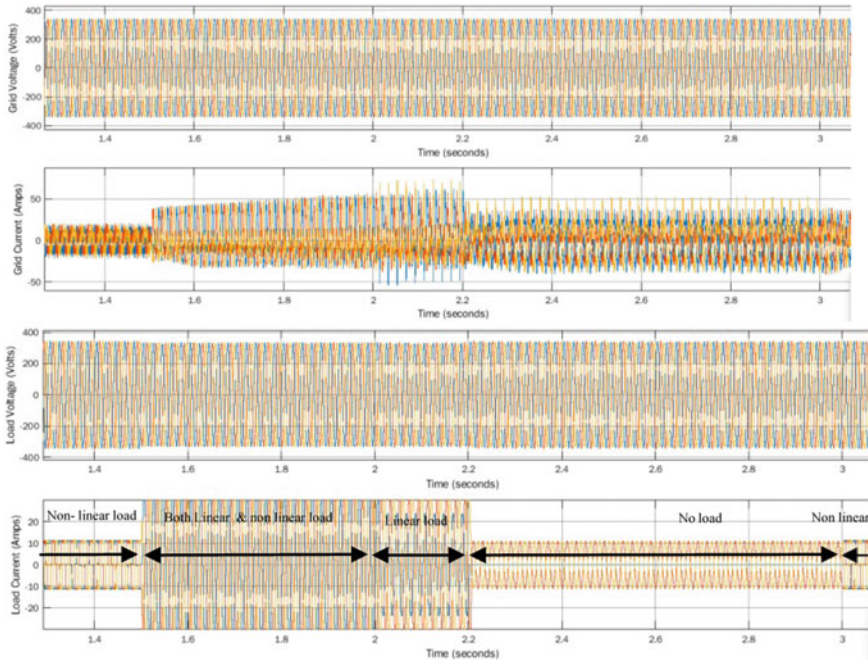


Fig. 9 Voltage and current waveforms for grid and load respectively for grid-connected PV source with both linear and non-linear load

Table 1 THD Comparison for linear and non-linear load separately

Type of load	Grid voltage THD (%)		Grid current THD (%)		Load Voltage THD (%)		Load current THD (%)	
	DC voltage	PV	DC voltage	PV	DC voltage	PV	DC voltage	PV
Linear load	0.35	0.40	168.02	150.34	0.33	0.33	0.06	0.06
Non-linear load	0.40	0.40	27.81	62.82	5.31	5.33	26.64	26.64

Table 2 THD comparison when both linear and non-linear loads in same model

Type of load	Grid voltage THD (%)		Grid current THD (%)		Load voltage THD (%)		Load current THD (%)	
	DC voltage	PV	DC voltage	PV	DC voltage	PV	DC voltage	PV
Linear load	0.37	0.39	103.9	120.87	0.35	0.38	0.04	0.04
Non-linear load	0.39	0.39	34.37	58.11	5.31	5.32	26.64	26.65
Both loads	0.36	0.39	93.06	121.05	5.07	5.07	8.55	8.55

References

1. Sahan B, Araújo SV, Nöding C, Zacharias P (2011) Comparative evaluation of three-phase current source inverters for grid interfacing of distributed and renewable energy systems. *IEEE Trans Power Electron* 26(8):2304–2318
2. Carrasco JM et al (2006) Power-electronic systems for the grid integration of renewable energy sources: a survey. *IEEE Trans Ind Electron* 53(4):1002–1016
3. Kouro S, Leon JI, Vinnikov D, Franquelo LG (2015) Grid-connected photovoltaic systems: an overview of recent research and emerging PV converter technology. *IEEE Ind Electr Mag* 9(1):47–61
4. Deng F, Wang Q, Liu D, Wang Y, Cheng M, Chen Z (2019) Reference submodule based capacitor monitoring strategy for modular multilevel converters. *IEEE Trans Power Electr* 34(5):4711–4721
5. Teodorescu R, Liserre M, Rodriguez P (2011) Grid converters for photovoltaic and wind power systems. John Wiley & Sons
6. Singh B, Al-Haddad K, Chandra A (1999) A review of active filters for powerquality improvement. *IEEE Trans Ind Electr* 46(5):960–971
7. Timbus A, Liserre M, Teodorescu R, Rodriguez P, Blaabjerg F (2009) Evaluation of current controllers for distributed power generation systems. *IEEE Trans Power Electr* 24(3):654–664
8. Ruan X, Wang X, Pan D, Yang D, Li W, Bao C (2018) Control techniques for LCL-type grid-connected inverters. Springer, Singapore
9. Gupta SK, Ahlawat A, Gupta D (2018) Comparison between inverter control techniques in grid connected solar photovoltaic systems. *J Electr Eng* 12(2)
10. Bonthagorla PK, Mikkili S (2020) Performance investigation of hybrid andconventional PV array configurations for grid-connected/standalone PV systems. *CSEE J Power Energy Syst*
11. Liu K et al (2021) Admittance modeling, analysis, and reshaping of harmonic control loop for multiparalleled SAPFs system. *IEEE Trans Industr Inf* 17(1):280–289
12. Sidrach-de-Cardona M, Carretero J (2005) Analysis of the current total harmonic distortion for different single-phase inverters for grid-connected pv-systems. *Sol Energy Mater Sol Cells* 87(1–4):529–540
13. Jia K, Chen J, Zhao G, Yang B, Bi T (2021) Second harmonic injection-basedrecovery control of PV DC boosting integration system. *IEEE Trans Smart Grid* 12(2):1022–1032
14. Yanarates C, Zhou Z (2021) Symmetrical pole placement method-based unityproportional gain resonant and gain scheduled proportional (PR-P) controller with harmonic compensator for single phase grid-connected PV inverters. *IEEE Access* 9:93165–93181
15. Isen E, Bakan AF (2016) Development of 10 kW three-phase grid connected inverter. *Automatika* 57(2): 319–328

Intelligent Planning of Multiple DG with Practical Load Models Using Metaheuristic Methods



Bikash Kumar Saw , Aashish Kumar Bohre , and Tushar Kanti Bera 

1 Introduction

The intelligent optimal planning of multiple distributed generations (DGs) is considered as both active power and reactive power source based upon the power supply and consumption capability of DG. Here the optimal planning of different types of DGs [1–4] at optimal power factor is presented with different models of loads like constant, industrial, residential, commercial, and mixed loads [2–11]. The assumption of constant load in the distribution system planning may mislead the exact assessment of the system performance [12–20]. Therefore, the different load models are considered based on voltage dependency for the intelligent optimal planning of different DGs in the system. Intelligent allocation of multiple-DG with real load models based on minimization technique using metaheuristic methods like GA, PSO, and BF-PSO are presented. The proposed work is explained in sections, namely, this section is about the introduction, formulation of the problem is given in Sect. 2, modelling loads are discussed in Sect. 3, in Sect. 4, the result analysis is presented, and in Sect. 5, conclusion is given.

B. K. Saw (✉) · A. K. Bohre · T. K. Bera
Department of Electrical Engineering, NIT Durgapur, Durgapur, India
e-mail: bks.18ee1105@phd.nitdgp.ac.in

A. K. Bohre
e-mail: aashishkumar.bohre@ee.nitdgp.ac.in

T. K. Bera
e-mail: tusharkanti.bera@ee.nitdgp.ac.in

2 Problem Formulation

The multiple-objective function (FMO)-based fitness problem is used for intelligent allocation of multiple-DG with real load models using GA, PSO, and BF-PSO methods is explained as:

$$F_{MO} = r_1 PLI + r_2 QLI + r_3 VDI + k_4 RI \quad (1)$$

where, $\sum_{i=1}^4 r_i = 1$.

Where r_1, r_2, r_3 , and r_4 , are the weighting factors of indices. PLI, QLI, VDI, and RI is the active power loss, reactive power loss, voltage deviation, and reliability index of the system separately.

3 Load Modelling

The residential, industrial, and commercial real load models depend on voltage are illustrated in [2, 19] has implemented in this work, and their expression in mathematical form is as follows:

$$P_{Loadi} = P_{Doi} \left(a_1 (V')^{\alpha o} + b_1 (V')^{\alpha i} + c_1 (V')^{\alpha r} + d_1 (V')^{\alpha c} \right) \quad (2)$$

$$Q_{Loadi} = Q_{Doi} \left(a_2 (V')^{\beta o} + b_2 (V')^{\beta i} + c_2 (V')^{\beta r} + d_2 (V')^{\beta c} \right) \quad (3)$$

where, P_{Loadi} and Q_{Loadi} are real and reactive power load at the bus “i”, P_{Doi} and Q_{Doi} are the operating points active power and reactive power load at the bus “i”, operating points voltage is V_o and voltage at the bus “i” is V_i , $V' = V_i/V_o$. Whereas α & β are the active and reactive power exponents for real load models, viz constant, industrial, residential, and commercial whose subscript in the Eqs. (2) and (3) are written as o, i, r , and c separately.

4 Result Analysis

The IEEE 15-bus network has been considered to validate the proposed algorithm with 100 MVA base. The MFO problem given in equation (1) is minimized to allocate the multiple DGs intelligently with real load models using metaheuristic techniques. Based on the obtained optimum value of the MFO problem, the multiple using metaheuristic techniques DGs are allocated in the proposed algorithm, and

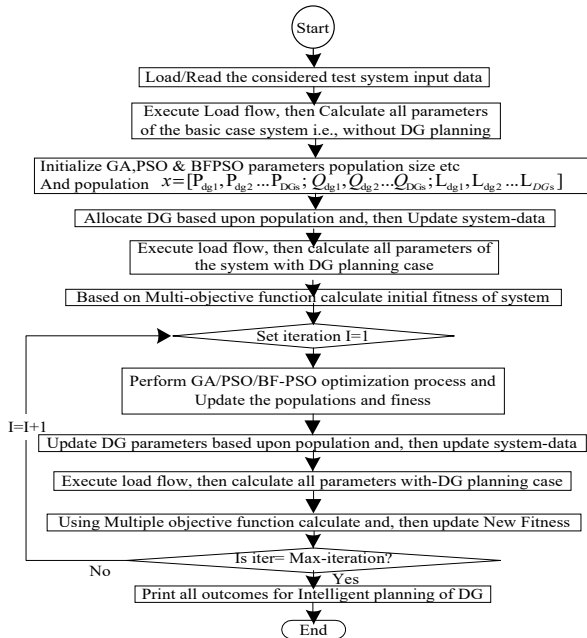


Fig. 1 Flow chart for intelligent planning of multiple DGs using GA, PSO, and BF-PSO

indexes for different real load models are obtained. For the constant, industrial, residential, commercial and mixed different real load models, the achieved outcomes are presented after intelligent planning of multiple DGs. The base load case of the system is assumed for the system consisting of constant loads. This part of analysis is about the planning of multi DGs intelligently in the IEEE 15-bus network with different real load models using metaheuristic techniques GA, PSO, and BF-PSO. The results for intelligent optimal planning of multiple DGs using optimization techniques are given in Figs. 1, 2, 3, and Tables 1, 2.

The voltage profile results are given in Fig. 1, where an improved system voltage profile is found with multiple DGs. From the obtained voltage profile of IEEE 15-bus network, it can be said that the different real load models have different effects on it.

The variation of active and reactive power loss results for the IEEE 15-bus network with different real load models using GA, PSO, and BF-PSO are given in Figs. 2 and 3, respectively. These losses are more efficiently reduced with multiple DGs as compared to the base system using optimization technique, and also vary with different load models while planning the optimal allocation of multiple DGs. The best results for loss reduction are obtained by BF-PSO while considering the optimal planning of multi DGs. The optimal size and locations of multi DGs (i.e. three DGs) including the constant load model for BF-PSO are 0.6034 MW and 0.5653 MVar at bus 4, 0.3350 MW and 0.3799 MVar at bus 7, 0.1938 MW and 0.2479 MVar at

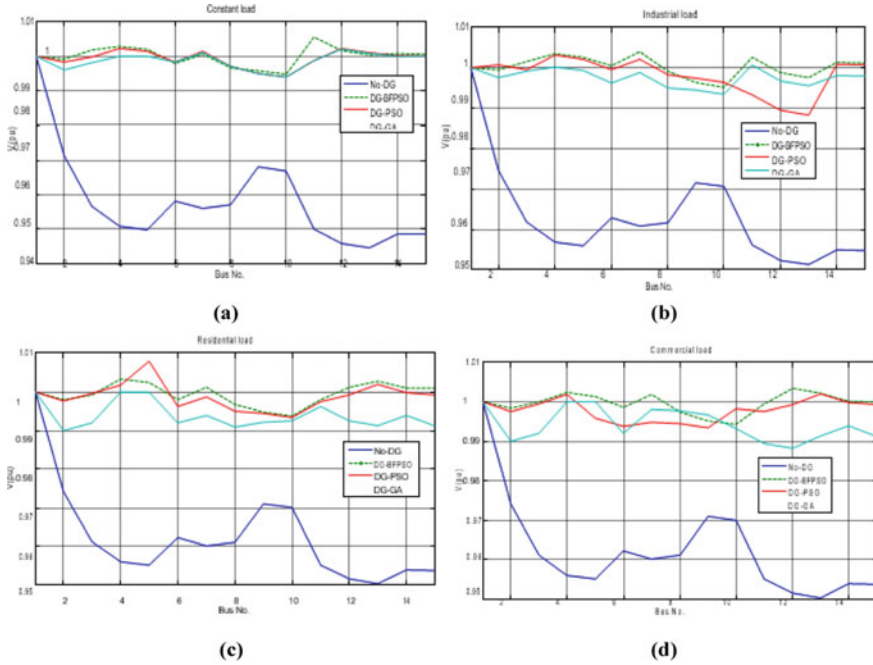


Fig. 2 IEEE 15-bus network voltage profile with multiple DGs; **a** Constant, **b** Industrial, **c** Residential, and **d** Commercial

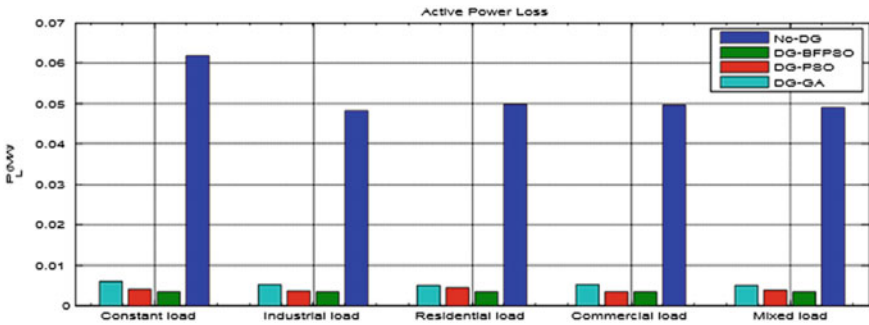


Fig. 3 Loss in active power of IEEE 15-bus network with multiple DGs for real load models

bus 12, for PSO are 0.2993 MW and 0.3491 MVar at bus 7, 0.3835 MW and 0.5685 MVar. at bus 4, 0.4307 MW and 0.3681 MVar at bus 11, and for GA 0.2539 MW and 0.2525. MVar at bus 2, 0.2881 MW and 0.3352 MVar at bus 7, 0.7507 MW and 0.7241 MVar. at bus 4 separately. The active and reactive power loss of the IEEE 15-bus network with multiple DGs using optimization techniques are given in Table 2 (Fig. 4).

Table 1 DG size and locations for IEEE 15-bus radial network with multiple DGs

Load type	DG-1 P (MW) & Q (MVAR)		DG-2 P (MW) & Q (MVAR)		DG-3 P (MW) & Q (MVAR)		Optimal location	Technique
	P	Q	P	Q	P	Q		
Constant	0.6034	0.5653	0.3350	0.3799	0.1938	0.2479	4, 7, 12	BF-PSO
	0.2993	0.3491	0.3835	0.5685	0.4307	0.3681	7, 4, 11	PSO
	0.2539	0.2525	0.2881	0.3352	0.7507	0.7241	2, 7, 4	GA
Industrial	0.5223	0.5612	0.3135	0.2813	0.3616	0.4096	4, 11, 7	BF-PSO
	0.2704	0.3755	0.5921	0.3578	0.2443	0.4164	7, 4, 11	PSO
	0.2986	0.2704	0.3048	0.3429	0.6683	0.6537	2, 7, 4	GA
Residential	0.3283	0.3890	0.2099	0.2090	0.5626	0.5998	7, 12, 4	BF-PSO
	0.1665	0.1725	0.3672	0.2257	0.6513	0.6792	13, 7, 4	PSO
	0.4227	0.5059	0.4658	0.3380	0.3632	0.3758	3, 4, 7	GA
Commercial	0.5567	0.5906	0.2522	0.2120	0.3407	0.3861	4, 12, 7	BF-PSO
	0.5783	0.6762	0.2975	0.3054	0.2407	0.1564	4, 6, 12	PSO
	0.3444	0.2766	0.2977	0.3277	0.6435	0.6659	2, 7, 4	GA

Table 2 Active and reactive power losses for IEEE 15-Bus distribution network with multiple DGs

Load type	Losses (MW/MVAr)		No-DG	DG-BFPSO	DG-PSO	DG-GA
Constant load	PL		0.0617	0.0034	0.004	0.0061
	QL		0.0572	0.0026	0.0029	0.0046
	Loss reduction (%)	PL	–	94.49%	93.52%	90.11%
		QL	–	95.46%	94.93%	91.96%
Industrial load	PL		0.0482	0.0035	0.0036	0.0053
	QL		0.0447	0.0025	0.0027	0.0039
	Loss reduction (%)	PL	–	92.74%	92.53%	89.01%
		QL	–	94.41%	93.96%	91.28%
Residential load	PL		0.0497	0.0034	0.0045	0.0051
	QL		0.0461	0.0025	0.0035	0.0036
	Loss reduction (%)	PL	–	93.16%	90.95%	89.74%
		QL	–	94.58%	92.41%	92.19%
Commercial load	PL		0.0496	0.0034	0.0036	0.0053
	QL		0.046	0.0025	0.0027	0.0039
	Loss reduction (%)	PL	–	93.15%	92.74%	89.32%
		QL	–	94.57%	94.13%	91.52%

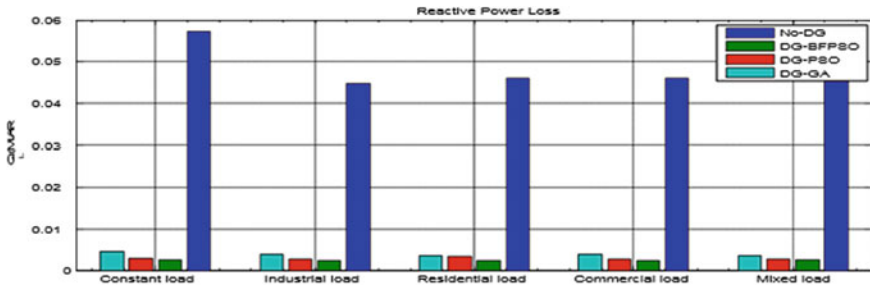


Fig. 4 Loss in reactive power of IEEE 15-bus network with multiple DGs for real load models

The value of active and reactive power loss reduction including the constant load model are 94.49 and 95.46% for BF-PSO, 93.52 and 94.93% for PSO, and 90.11 and 91.96% for GA with respect to No-DG case. Similarly, the system performances of the IEEE 15-bus radial distribution network with multiple DGs for industrial, residential, and commercial different real load models can be analyzed and the waves of different real load models on the optimal intelligent planning of multiple DGs can be described.

5 Conclusion

The intelligent allocation of multi DG with real load models based on the minimization technique using metaheuristic methods such as GA, PSO, and BF- PSO is presented with a multi-objective function for IEEE 15-bus radial network. The result analysis explains that the proposed technique is effective with respect to the power loss reduction (active and reactive) and enhancement in the profile of system voltage. The relative result analysis of the proposed system is also offered, which evidently specifies that the planned method is effective with BF-PSO optimization. Hence, based on the overall analysis, it can be summarized that the projected procedure offers additional technical as well as economic profits related to the other approach.

References

1. Kumar A, Rizwan M, Nangia U (2019) Optimal sizing of renewable energy resources in a microgrid for a distributed generation system. In: International symposium on advanced electrical and communication technologies (ISAECT). IEEE
2. Bohre AK, Ganga A, Dubey M (2016) Optimal sizing and sitting of DG with load models using soft computing techniques in practical distribution system. *IET Gener Trans Distrib* 10(11):2606–2621
3. Bohre AK et al (2015) Impacts of the load models on optimal planning of distributed generation in distribution system. *Adv Artif Intell* 2015(16877470)

4. Bohre AK, Agnihotri G, Dubey M (2015) The optimal distributed generation placement and sizing using novel optimization technique. *Middle-East J Sci Res (MEJSR)* 23(6):1228–1236
5. Bohre AK, Agnihotri G, Dubey M (2014) Hybrid butterfly based particle swarm optimization for optimization problems. In: *First international conference on networks & soft computing (ICNSC2014)*. IEEE
6. Bohre AK et al (2014) A novel method to find optimal solution based on modified butterfly particle swarm optimization. *Int J Soft Comput Math Control* 3(4):1–14
7. Bohre AK, Ganga A, Dubey M (2015) The butterfly-particle swarm optimization (butterfly-PSO/BF-PSO) technique and its variables. *Int J Soft Comput Math Control (IJSCMC)* 4(3)
8. Bohre AK et al (2015) Impacts of the load models on optimal sizing and siting of distributed generation in distribution system. *World Appl Sci J* 33(7):1197–1205
9. Dubey M, Agnihotri G, Bohre AK (2016) Distributed generation planning including load models using different optimization techniques. *J Electr Eng* 16(1):12–12
10. Bohre AK et al (2015) Assessment of intricate DG planning with practical load models by using PSO. *Electr Comput Eng Int J (ECIJ)* 4(2):15–22
11. Bohre AK, Agnihotri G, Dubey M (2015) The optimal planning of distributed generation using OPF and butterfly-pso (BF- PSO) technique. *J Electr Eng* 15(4):12–12
12. El-Khattam W, Salama MMA (2004) Distributed generation technologies, definitions and benefits. *Electr Power Syst Res* 71(2):119–128
13. Viral R, Khatod DK (2012) Optimal planning of distributed generation systems in distribution system: a review. *Renew Sustain Energy Rev* 16(7):5146–5165
14. Georgilakis PS, Hatziargyriou ND (2013) Optimal distributed generation placement in power distribution networks: models, methods, and future research. *IEEE Trans Power Syst* 28(3):3420–3428
15. Bayod-Rújula AA (2009) Future development of the electricity systems with distributed generation. *Energy* 34(3):377–383
16. Kalambe S, Agnihotri G (2014) Loss minimization techniques used in distribution network: bibliographical survey. *Renew Sustain Energy Rev* 29:184–200
17. Singh D, Misra RK, Singh D (2007) Effect of load models in distributed generation planning. *IEEE Trans Power Syst* 22(4):2204–2212
18. Liu MB, Canizares CA, Huang W (2009) Reactive power and voltage control in distribution systems with limited switching operations. *IEEE Trans Power Syst* 24(2):889–899
19. El-Zonkoly AM (2011) Optimal placement of multi-distributed generation units including different load models using particle swarm optimization. *Swarm EvolComput* 1(1):50–59
20. Kumar B, Saw BS, Bohre AK (2020) Optimal distribution network reconfiguration to improve the system performances using PSO with multiple-objectives. In: *International conference on computational intelligence for smart power system and sustainable energy (CISPSSE)*. IEEE

Modeling and Simulation of a Single-Phase Single-Stage Grid Connected PV System



Rachna Dhir

1 Introduction

With the ever-increasing demand for electricity across the globe and challenges posed by the depleting fossil fuels in recent years, renewable energy sources have gained ground in recent years. Among all the renewable energy systems, Photovoltaic (PV) energy stands out due to its tremendous potential in energy conversion. However, due to dependency on the weather conditions, the ratio of price/efficiency of PV systems is not really impressive [1] which calls for the necessity of having a high-performance power electronic converter in order to connect it to the main utility grid for power sharing. The typical PV converter is based on a two stages converter [2, 3].

Normally, the first stage is a DC-DC boost type converter which along with MPPT control, extracts the maximum power from the panel and boosts the PV voltage to a value higher than the peak of the grid voltage. This facilitates the availability of optimum voltage at the second stage. The second stage is a DC-AC inverter that generates a sinusoidal current to be injected into the grid. The association of the two converters results in a two-stage power conversion which suffers from inherent drawbacks of high cost, sluggish response and high conduction losses [4]. Due to the necessity of reducing the cost and increasing the efficiency of the systems at the same time, the interest in single-stage conversion has grown in recent years [5, 6]. The single-stage PV topologies must carry out two functions: Drawing maximum power from the panel and injection of a sinusoidal current waveform into the grid. To realize the two functions in a single-stage topology, it is necessary to identify an effective MPPT control and current control for the inverter. In both single-stage and two-stage configuration, we have an inverter connected to the main grid. In order to ensure optimum working, there should be a minimum voltage across the dc bus

R. Dhir (✉)

J. C. Bose University of Science and Technology, YMCA, Faridabad, India

e-mail: rachna@jcbouseust.ac.in

which equals the peak value of voltage including voltage drop across the filter. If the voltage across the multitude of panels in series and in parallel is greater than the dc link voltage, it can be directly connected to the inverter without using any additional circuits. This kind of arrangement is known as single-stage conversion. On the other hand, if the number of solar panel strings is less, and the output voltage is less than the dc link voltage, then the PV panels cannot be directly connected to the inverter. A boost converter needs to be connected in order to raise the voltage to the minimum voltage level required at the input of the inverter known as two-stage conversion.

2 System Description

The connection of a dc source with the main grid requires a power electronic interface which can be categorized into single-stage conversion system and two-stage conversion system. The single-stage conversion system involves only a dc-ac converter as the power conditioning circuit, while the two-stage conversion system constitutes a dc-dc converter followed by a dc-ac converter as the power conditioning circuit.

Figure 1 shows the schematic of single-phase single-stage grid connected photovoltaic system.

Typically grid connected PV systems require a two-stage conversion vis-à-vis dc-dc converter followed by a dc-ac inverter. But these types of systems require additional circuits which result in conduction losses, sluggish transient response and higher cost [7].

An alternative could be eliminating the dc-dc converter and connecting the PV output directly to the inverter and then to the main grid. In this case, PV array can be chosen as a string of PV panels in series or in parallel in order to make the voltage reach the minimum voltage levels required at the inverter side. Besides,

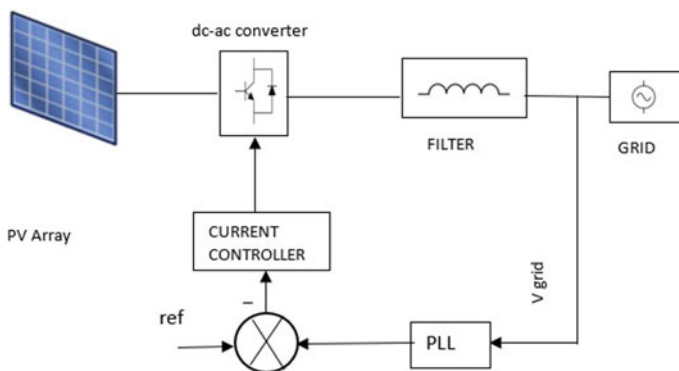


Fig. 1 Schematic of the photovoltaic system under consideration

single-stage converter offers the advantage of lower costs, good efficiency and simple implementation.

3 Control Structure

3.1 MPPT Control

Despite having tremendous potential in generating energy, because of dependency on the amount of solar irradiation, temperature, and other weather conditions, photovoltaic systems offer low energy conversion efficiency and high initial costs. The PV system has non-linear P-V and I-V characteristics that continuously vary with temperature and irradiation.

In order to operate PV systems at higher efficiencies, it is imperative that these work at their maximum power point (MPP). To fulfil this objective, a number of techniques have been suggested in many research papers [8–10]. These are broadly categorized as—Perturb and Observe (P&O), Incremental Conductance method, constant voltage method among others. But the first two remain popular and are commonly implemented due to the number of advantages offered by them.

The purpose of MPPT is to continuously tune the system in order to extract maximum power from the PV array regardless of weather conditions. In Perturb and Observe technique, a perturbation is given to the array voltage, and the corresponding output power is compared with its previous value. If power increases, the perturbation is continued in the same direction. On the other hand, if power decreases, the perturbation is reversed. This process continues until a maximum power point is reached. In P and O technique, the operating point keeps revolving around MPP. Nonetheless, this technique is simpler and the equilibrium point is reached rapidly.

While in Incremental Conductance technique, the algorithm is able to determine when the maximum power point has reached and hence the perturbation can be stopped. But this method is complex besides taking a good amount of computational time [11].

The PV system under consideration is simulated using P and O algorithm for maximum power tracking and is tested for different irradiance and temperature values. The scheme of P and O technique is shown below (Fig. 2).

3.2 Grid Tied Inverter

Grid tied inverter holds a significant position in the photovoltaic-grid arrangement. The energy conversion from dc to ac side is made by a single-phase voltage source inverter. PV inverter system consists of a solar array and a dc link capacitor C, on the input dc side with an output ac filter (LCL), and grid connection on the ac side. The

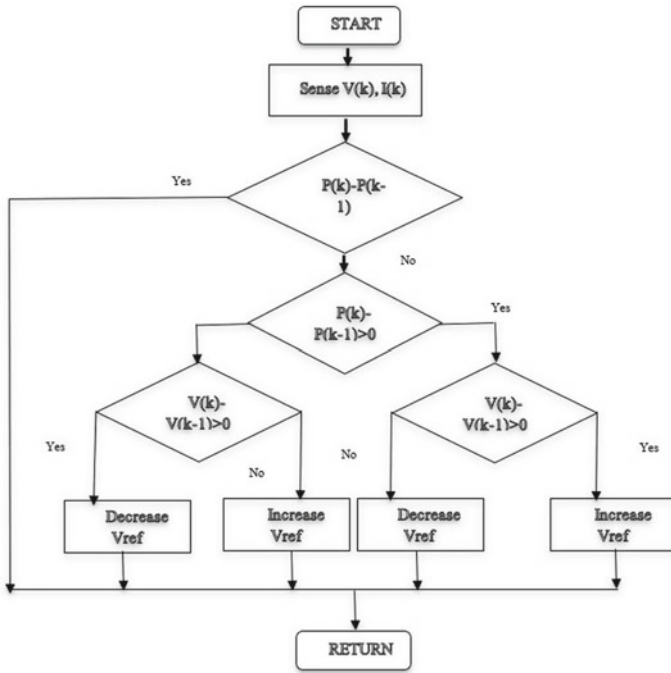


Fig. 2 Flowchart of perturb and observe algorithm

number of panels in the string has to ensure a dc voltage higher than the ac voltage peak of all time [12].

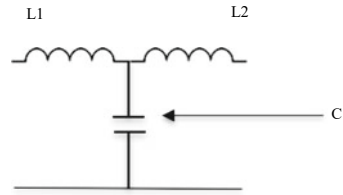
Besides advancing to the corresponding ac value, the grid inverter is synchronized with the grid to operate at a power factor close to unity. Synchronization is also needed to improve inverter efficiency and monitor both inverter and grid.

Several synchronization methods have been proposed in various research works [13, 14]. Among them, the phase locked loop (PLL) algorithms have proved to be the most effective, robust and simple. A PLL is a closed loop feedback control system that synchronizes inverter output signals with that of the grid.

3.3 Filter

Typically, L filters are employed in grid connected arrangements but LCL filters are found to have shown promising results [15] as they have higher (3rd) order and have improved performance leading to a compact design. Though their usage results in resonance and stability issues for which a special control circuit is required (Fig. 3).

Fig. 3 LCL filter



The values considered are as under:

$L_1 = 4.06 \text{ Mh}$	$K_p = L/\tau = 27.066$
$L_2 = 4.35 \text{ Mh}$	$K_r = 100$
$C = 6.0175 \text{ }\mu\text{F}$	
Time constant, $\tau = 150 \text{ }\mu\text{s}$	

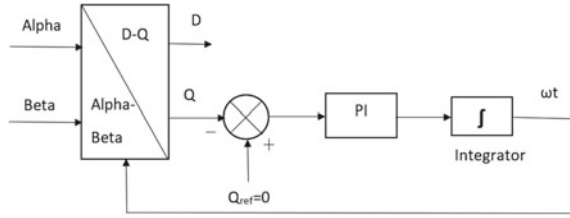
3.4 Phase Locked Loop (PLL)

The active current sent by the inverter to the main grid should be in phase with the grid voltage. The output current of the inverter is synchronized with the grid voltage to give a sinusoidal reference current leading to unity power factor operation. The purpose of phase locked loop (PLL) is to generate the reference for the implementation of current controller in grid connected inverter. Similarly, for reactive power sent to the main grid, phase locked loop generates a signal which is 90 out of phase with the actual voltage [16].

Phase locked loop (PLL) system with PI regulation is used to track grid voltage and to obtain amplitude and frequency values at the grid. Mainly there are three types of phase-locked loop systems for phase tracking-Zero crossing, Stationary reference frame and Synchronous Rotating Reference Frame based Phase locked loop. In the considered system, a synchronous reference frame (SRF) is used. The SRF-based PLL is one of the best, performances wise under non-ideal grid conditions [17, 18]. The basic idea of phase locked loop is to track the phase angle. The 3- Φ grid voltage is fed as input to the PLL and output is the phase angle of one of three phases.

Since there will be one inverter leg available at the substation, so only one phase is tracked. A 120-degree shift for each of the other two phases is done to get the required amount of tracking.

Fig. 4 Phase locked loop (PLL) structure



First, alpha-beta voltages are obtained by passing through low pass filters and necessary gain. After Alpha-beta to d-q transformation, the error is calculated between Q and Qref. This error is fed to a PI controller. Output of the PI controller gives the information about the angle. The (ωt) signal is obtained from angle information and is fed to alpha-beta to d-q transformation block (Fig. 4).

4 Simulink Model

The model is simulated using MATLAB and run for 3.5 s (Fig. 5 and Table 1).

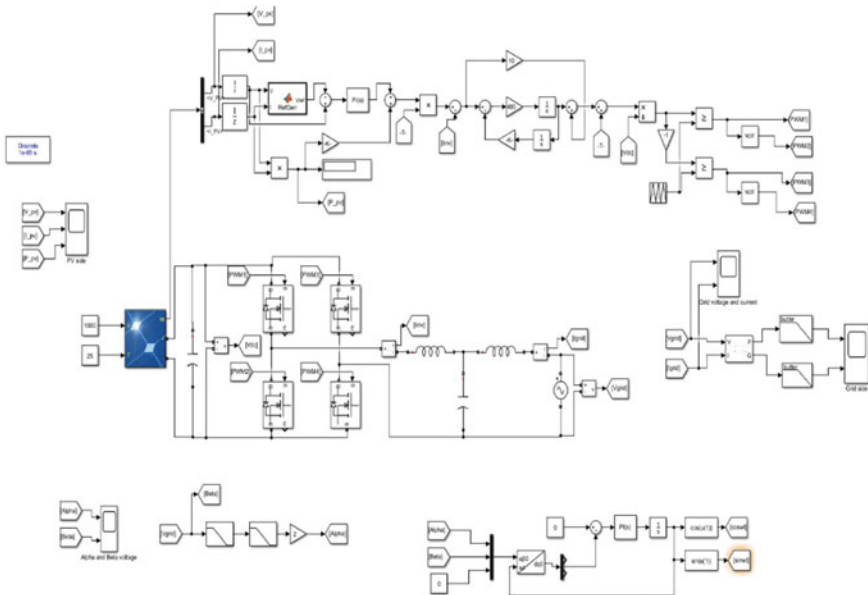


Fig. 5 SIMULINK model of system under consideration

Table 1 Simulation parameter values

S.no	Parameter	Value
PV side		
1	Ns	11
2	Np	01
3	V _{oc}	493.5 V
4	V _{mppt}	400–500 V
5	F _{sw} (switching frequency)	10 kHz
Filter		
6	L ₁	4.06 mH
7	L ₂	4.35 mH
8	C	6.23 μF
9	V _{grid}	230 V(rms)
10	Frequency	50 Hz
11	Rated power	2 kW

5 Results and Discussion

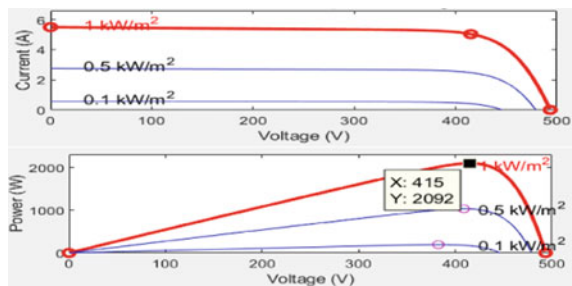
In Fig. 6, the PV and I-V characteristics have been demonstrated for various irradiance values and a constant temperature of 25 °C, where it can be deduced that as irradiation increases, the power also increases in the same proportion.

The maximum power which can be reached is around 2 kW. The grid side parameters have been shown in Figs. 7 and 8.

For PLL, the obtained waveforms for alpha-beta voltages are shown in Fig. 9, the two waveforms are 90 degrees apart which is further useful when fed to alpha- beta to d-q transformation block in order to achieve proper synchronization of inverter and grid.

Further PV side parameters behaviour is evident from waveforms shown in Fig. 10. The voltage at PV output is sufficient to directly connect it to the inverter for synchronization and control.

Fig. 6 PV and IV characteristics of PV array



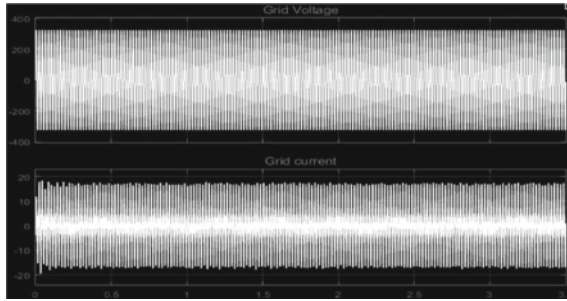


Fig. 7 Grid side voltage and current

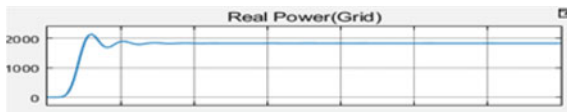


Fig. 8 Grid side real power

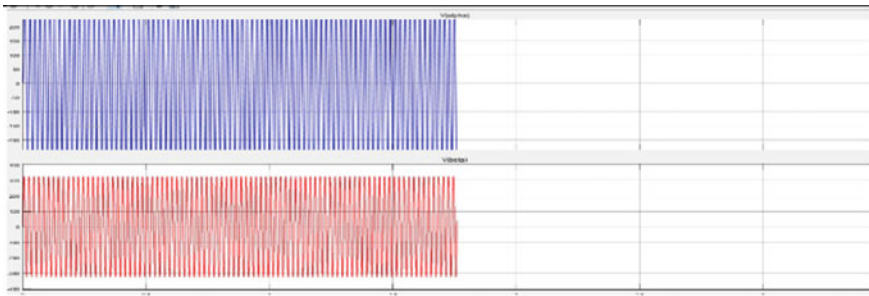
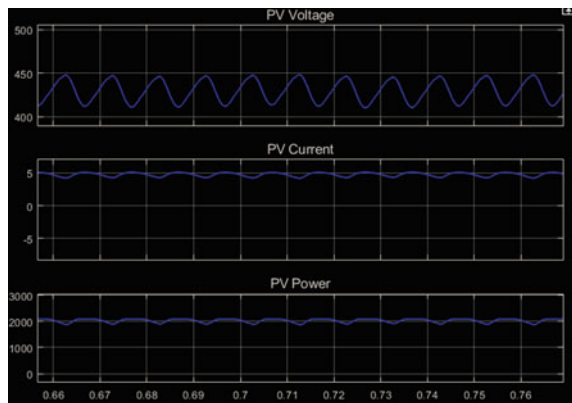


Fig. 9 Alpha-beta voltage

Fig. 10 PV side voltage, current and power



6 Conclusion

This paper presented a single-phase grid connected PV system and the objective behind this work is to use understand the behaviour of PV energy conversion in grid connected condition. The interface with the grid is carried out through a single-stage conversion topology. The PV system is modelled for maximum power using P and O algorithm. The output from PV system is directly connected to PWM inverter which synchronizes the operation with the help of Phase locked loop. The modelling of phase locked loop in the synchronously rotating reference frame is shown and the necessary signal is sent to the current controller for the required synchronization. The entire system is modelled in MATLAB and results are shown for the voltage and power levels at the PV side, inverter, and grid side. Further harmonic analysis could be done on the system, and a proper tuning circuit is realized accordingly.

References

1. Kazmierkowski M, Krishnan R, Blaabjerg F (2002) Control in power electronics, selected problems. Academic Press, ISBN 0-12-402772-5
2. Cecati C, Dell'Aquila A, Liserre M, Monopoli VG (2003) Design of H-bridge multilevel active rectifier for traction systems. *IEEE Trans Ind App* 39:1541–1550
3. Yuan X, Merk W, Stemmler H, Allmeling J (2002) Stationary-frame generalized integrators for current control of active power filters with zero steady-state error for current harmonics of concern under unbalanced and distorted operating conditions, *IEEE Trans Ind App* 38(2):523–532
4. Zmood DN, Holmes DG (2003) Stationary frame current regulation of PWM inverters with zero steady-state error. *IEEE Trans Power Electron* 18(3):814–822
5. Teodorescu R, Blaabjerg F, Liserre M, Borup U (2004) a new control structure for grid-connected pv inverters with zero steady-state error and selective harmonic compensation. In: *Proceedings of APEC'04*, vol. 1, pp 580–586
6. Hohm DP, Ropp ME (2000) Comparative study of maximum power point tracking algorithms using and experimental, programmable, maximum power point tracking test bed. In: *Proceedings of photovoltaic specialists conference*, pp 1699–1702
7. Kuo YC, Liang TJ (2001) Novel maximum-power-point-tracking controller for photovoltaic energy conversion system. *IEEE Trans Ind Electron* 48(3):594–601
8. Liserre M, Blaabjerg F, Hansen S (2005) Design and control of an LCL-filter based active rectifier. *Proc IAS'01* 1:299–307
9. Enslin JHR, Wolf MS, Snyman DB, Swiegers W (1997) Integrated photovoltaic maximum power point tracking converter. *IEEE Trans Ind Electron* 44(6)
10. Kjaer SB, Pedersen JK, Blaabjerg F (2005) A review of single- phase grid-connected inverters for photovoltaic modules. *IEEE Trans Ind Appl* 41(5)
11. Schimpf F, Norum LE (2008) Grid connected converters for photovoltaic, state of the art, ideas for improvement of transformerless inverters. In: *Nordic workshop on power and industrial electronics*
12. Fortunato M, Giustiniani A, Petrone G, Spagnuolo G, Vitelli M (2008) Maximum power point tracking in a one-cycle-controlled single-stage photovoltaic inverter. *IEEE Trans Ind Electron* 55(7):2684–2693
13. Kuo Y-C, Liang T-J, Chen J-F (2001) Novel maximum- power-point-tracking controller for photovoltaic energy conversion system. *IEEE Trans Power Electron* 48(3):594–601

14. Chen Y, Smedley KM (2004) A cost-effective single-stage inverter with maximum power point tracking. *IEEE Trans Power Electron* 19(5):1289–1294
15. Gonzalez R, Lopez J, Sanchis P, Marroyo L (2007) Transformer-less inverter for single-phase photovoltaic systems. *IEEE Trans Power Electron* 22(2):693–697
16. Ribeiro H, Silva F, Pinto S, Borges B (2009) Single stage, inverter for PV applications with one cycle sampling technique in the MPPT algorithm. In: *IECON Porto 2009*
17. Fernández A, Sebastián J, Hernando MM, Arias M, Pérez G (2006) Single stage inverter for a direct AC connection of a photovoltaic cell module. In: *Power electronics specialists conference 2006, PESC'06*, 18, pp 1–6
18. Ciobotaru M, Teodorescu R, Blaabjerg F (2005) Control of single-stage single-phase PV inverter. In: *European conference on power electronics and applications*, 10p. <https://doi.org/10.1109/EPE.2005.219501>

Grid Integration of 3P3W Single-Stage Solar PV System Using Modified Digital Filter Control



Pushendra Sharma, Abhishek Kumar, and Rashmi Agarwal

1 Introduction

The non-renewable sources of energy (kerosene oil, petrol, diesel, wood, coal, natural gas, and many others) are the conventional source of energy that is depleting in a very fast manner and combustion of these sources is used to generate electricity. These non-renewable sources of energy release toxic gases like nitrogen dioxide which affects ozone, carbon dioxide and causes global warming, sulphur dioxide causes acid rain [1]. Therefore, it shows the harmful impact on the environment and all living beings. However, there is a need for such types of sources which provide solutions to the problem related to conventional sources. There are many renewable energy sources like solar, biofuel, wind, etc., The dominancy of solar energy among others is because installation time is very less as compared to other alternatives. The resource is available free of cost, i.e., sunlight, which is pollution-less and requires less maintenance.

The solar PV (Photovoltaic) system is classified as a standalone system and grid interfaced system. Standalone system requires batteries. Hence, they are more costly than grid-connected system. Thus, grid interfaced solar PV system is alluring more attention nowadays and becomes superior to a standalone system. Solar PV characteristics are varying in nature. Solar PV power changes with changes in surrounding condition. Hence, MPPT (Maximum Power Point Tracking) technique is needed for the extraction of maximum output from solar PV array. There are various existing MPPT techniques such as INC (incremental conductance), AI (Artificial Intelligence), fuzzy-based MPPT, etc., are reported in the literature. INC-based MPPT technique is easy to implement and simple. Moreover, it has a swift response and high

P. Sharma (✉) · A. Kumar · R. Agarwal
Department of Electrical Engineering, J. C. Bose University of Science & Technology, YMCA,
Faridabad, Haryana 121006, India
e-mail: Kukku.tiwari28@gmail.com

tracking efficiency. However, the abovementioned MPPT techniques are complex to implement [2, 3].

There is tremendous available control algorithms based on reactive power theory (RPT) and SRF (Synchronous Reference Frame) theory, which has been explained in the literature, basically used for harmonic elimination, grid current balancing, and maximum power extraction from the interconnected grid system. These control techniques enhance system power quality because the non-linear load is connected at PCC (Point of Common Coupling) [4, 5] explains the improvement of power quality for 3P3W (Three-Phase Three-Wire) systems and using PLL (Phase locked Loop) algorithm, respectively. Non-linear load and load unbalance conditions are subjected to create harmonics. For grid voltage variation, an adaptive controller has been developed and discussed in the literature [6]. But these systems also don't have non-linear load and unbalanced load conditions, hence not being discussed in it. Grid tied inverter is interfaced by an artificial neural network controlled non-conventional source, used is discussed in [7]. This proposed algorithm is very compatible with controlling the switching of inverter and for the elimination of harmonics, whereas the disadvantage of the conventional technique is its computational time which is more as compared to MDF (Modified Digital Filter) technique. MDF technique provides the advantage of reduced computational time and fast dynamic behavior with reduced and efficient steady-state error. MDF has defeated the limitations of the present DF (Digital Filter) algorithm, which provides less computational processing concern and has a quick dynamic behavior with addition to competent steady-state precision. However, the MDF generates a sinusoidal fundamental load component. This, in-phase sinusoidal fundamental load component, is required for extraction of the active load component of each phase and grid reference currents component [8–10].

Moreover, the latest research is going in the field of solar PV systems, hybrid systems, and smart electricity grid including the advantages of nanotechnology, solar PV integrated LED's for automatic lightening, water pumping, power forecasting estimation, etc [11–14]. The proposed MDF algorithm is able to extract reference grid current components from load current, which is further used to generate VSC switching. The paper consists of an introduction which is explained in Sect. 1, Sect. 2 describes the proposed 3P3W solar PV system employing M-LWDF control algorithm, Sect. 3 presents the INC-based MPPT and M-LWDF control algorithm. In Sect. 4, results have been explained for steady state, unbalanced load condition, and under varying insolation level. Section 5 consists of final conclusion.

2 System Layout

Figure 1 shows 3P3W (Three-Phase Three-Wire) solar PV system using the MDF algorithm which consists of solar PV array, coupling inductor (L_f), VSC (Voltage Source Converter), ripple filter (RC), non-linear load, etc. An IGBT's-based three-phase, VSC converts DC input into AC output. The grid current ripples are reduced

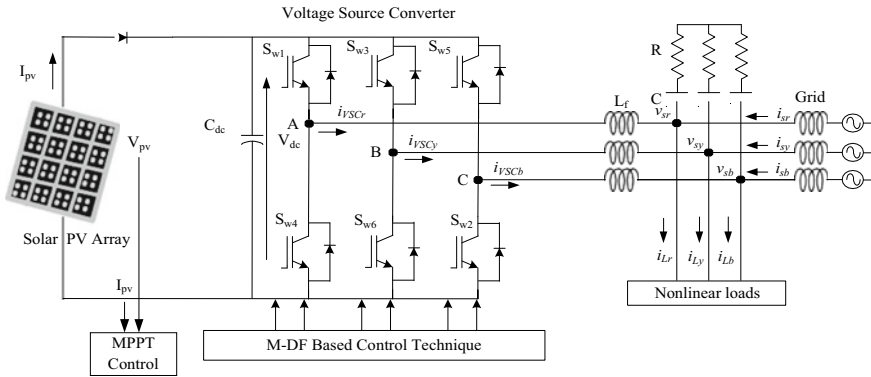


Fig. 1 3P3W solar photovoltaic system

by the coupling inductor (L_f). For reducing the switching ripples from VSC, a ripple filter. For load unbalancing, the load of phase ‘a’ is disconnected by using a switch.

3 Control Approach

The MDF-based control approach is subdivided into VSC control and MPPT control. The VSC-based MDF control approach provides reactive power compensation, harmonic mitigation, and load balancing. MPPT control extracts peak PV power. The details of the control algorithm are explained as given below.

3.1 MPPT Control

INC-based MPPT technique extracts the peak power. This technique extracts the maximum power point by comparing the rate of conductance from the conductance. The INC technique tracks the maximum point using PV current (I_{pv}) and PV voltage (V_{pv}) based on the equation which is mentioned as

$$-\frac{I_{pv}}{V_{pv}} = \frac{\partial P_{pv}}{\partial V_{pv}} = 0, \text{ at MPP} \tag{1}$$

$$-\frac{I_{pv}}{V_{pv}} \left\langle \frac{\partial P_{pv}}{\partial V_{pv}}, -\frac{I_{pv}}{V_{pv}} \right\rangle 0, \text{ shift to rightward} \tag{2}$$

$$-\frac{I_{pv}}{V_{pv}} > \frac{\partial P_{pv}}{\partial V_{pv}}, -\frac{I_{pv}}{V_{pv}} < 0, \text{ shift to leftward} \tag{3}$$

3.2 VSC Control

Figure 2 shows the control algorithm. VSC Control consists of unit template extraction, fundamental current extraction, and reference grid currents extraction. This control is explained below.

3.2.1 Unit Template Extraction

Amplitude of voltage (V_t) at PCC (Common Coupling Point) is calculated by [14]

$$V_t = \{2(v_{sr}^2 + v_{sy}^2 + v_{sb}^2)/3\}^{1/2} \tag{4}$$

The line voltages (v_{ry}, v_{yb}) to phase voltage transformation (v_{sr}, v_{sy}, v_{sb}), which is expressed as [14],

$$\begin{bmatrix} v_{sr} \\ v_{sy} \\ v_{sb} \end{bmatrix} = \frac{1}{3} \begin{bmatrix} 2 & 1 \\ -1 & 1 \\ -1 & -2 \end{bmatrix} \begin{bmatrix} v_{ry} \\ v_{yb} \end{bmatrix} \tag{5}$$

In-phase unit, vector are calculated by

$$w_{pr} = \frac{v_{sr}}{V_t}, w_{py} = \frac{v_{sy}}{V_t}, w_{pb} = \frac{v_{sb}}{V_t} \tag{6}$$

The quadrature voltage unit vectors estimation

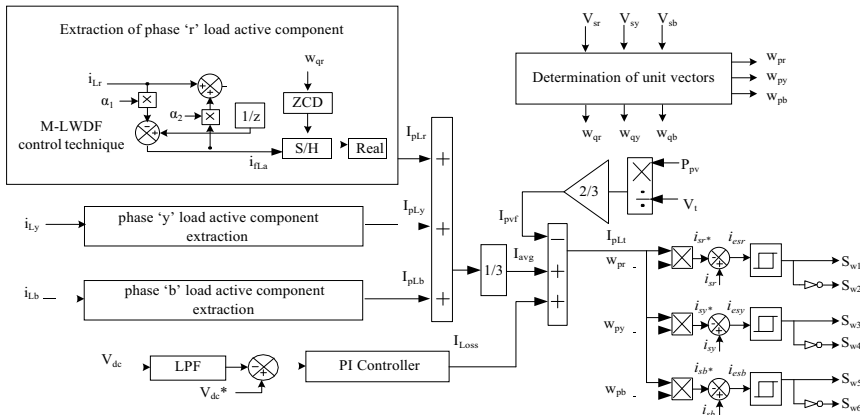


Fig. 2 MDF-based control technique

$$w_{qy} = \frac{(3w_{pr} + w_{py} - w_{pb})}{2\sqrt{3}}, \quad (7)$$

$$w_{qb} = \frac{(-3w_{pr} + w_{py} - w_{pb})}{2\sqrt{3}} \quad (8)$$

3.2.2 Relationship Between i_{Lr} and i_{flr} in MDF

Relationship between i_{Lr} and i_{flr} in the MDF control technique is mentioned as given below,

$$\frac{i_{Lr}}{i_{fLr}} = (i_{Lr} + \alpha_2 i_{fLr})z^{-1} - \alpha_1 i_{Lr} \quad (9)$$

$$= i_{Lr}(1 - \alpha_1 z^{-1}) + \alpha_2 i_{fLr} z^{-1} \quad (10)$$

Here, α_1 and α_2 are filter coefficients.

i_{Lr} = load current component.

i_{flr} = fundamental load current component.

From the above equation, the relation between the i_{Lr} and i_{flr} can be computed as,

$$\frac{i_{Lr}}{i_{fLr}} = \frac{(1 - \alpha_1 z^{-1})}{-\alpha_2 z^{-1}} \quad (11)$$

$$i_{fLr} = i_{Lr} \left[\frac{-\alpha_2 z^{-1}}{(1 - \alpha_1 z^{-1})} \right] \quad (12)$$

Moreover, i_{flr} is passed to S&H (sample and hold) logic circuit for achieving the reference grid current.

3.2.3 Reference Grid Current Extraction

Average weight active component (I_{pLavg}) is estimated as,

$$I_{pLavg} = \frac{1}{3} [I_{pLr} + I_{pLy} + I_{pLb}] \quad (13)$$

The DC link voltage (V_{dc}) is controlled by using a PI controller. The output of PI controller is DC current loss component (I_{loss}) which is calculated as given by,

$$I_{loss}(m) = I_{loss}(m-1) + k_p \{V_{dce}(m) - V_{dce}(m-1)\} + k_i V_{dce}(m) \quad (14)$$

In the above equation, V_{dce} is given as,

$$V_{dce} = V_{dc} * -V_{dc} \quad (15)$$

PV feed forward component (I_{pvf}) is used to handle the changing surrounding conditions, which is expressed by,

$$I_{pvf} = \frac{2}{3} \left[\frac{P_{pv}}{V_{pv}} \right] \quad (16)$$

Net fundamental component is expressed as,

$$I_{pLt} = I_{pLavg} + I_{loss} - I_{pvf} \quad (17)$$

Reference grid currents are extracted as

$$\begin{aligned} i_{sr}^* &= I_{pLt} * w_{pr}, \\ i_{sy}^* &= I_{pLt} * w_{py}, \\ i_{sb}^* &= I_{pLt} * w_{pb}, \end{aligned} \quad (18)$$

The current errors estimation is given by

$$\begin{aligned} i_{esr} &= i_{sr}^* - i_{sr}, \\ i_{esy} &= i_{sy}^* - i_{sy}, \\ i_{esb} &= i_{sb}^* - i_{sb}, \end{aligned} \quad (19)$$

Switching sequences for 3-leg VSC are done by using the current error.

4 Simulation Results

Grid-integrated solar PV system with MDF control technique is modeled and results are analyzed in MATLAB/Simulink under different conditions. Non-linear loads, having value $R = 20 \Omega$ and $L = 200 \text{ mH}$ are selected.

4.1 Steady State Condition

Figure 3 depicts the system behavior under steady-state condition. Figure 3a shows the sinusoidal grid current (i_{sryb}) and load current (i_{Lryb}) are distorted. The DC link voltage (V_{dc}) is constant. Figure 3b shows that solar PV current (I_{pv}) and PV power

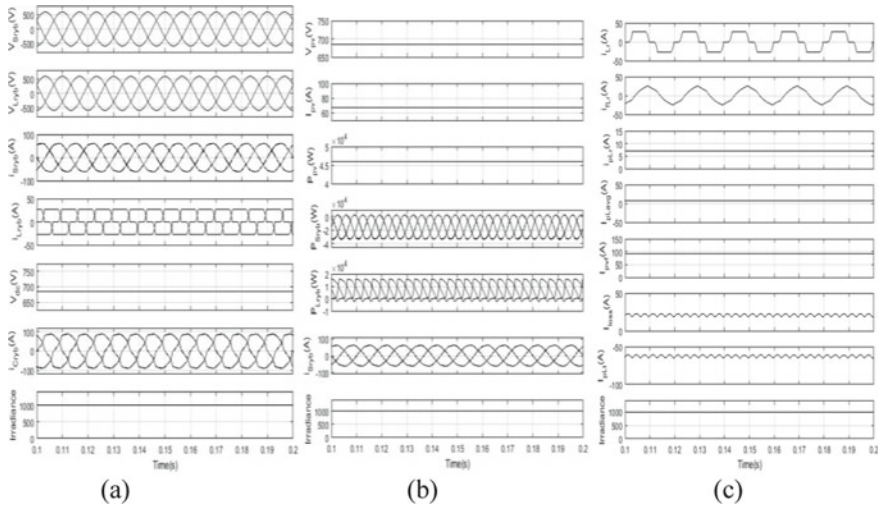


Fig. 3 Simulated results for steady state **a** V_{Sryb} , V_{Lryb} , i_{Sryb} , i_{Lryb} , V_{dc} , i_{Cryb} , Irradiance **b** V_{pv} , i_{pv} , P_{pv} , P_{Sryb} , P_{Lryb} , i_{Sryb} **c** i_{Lr} , i_{LrL} , i_{pLr} , i_{pLavg} , i_{pLv} , i_{loss} , i_{pLt}

(P_{pv}), PV voltage (V_{pv}) are maintained constant. Moreover, the solar PV array is providing the power to load and surfeit PV power is fed to the grid. Therefore, grid power (P_{sryb}) is negative. Figure 3c illustrates the internal signal of the proposed control algorithm. All the internal signals like i_{pLr} , i_{pLavg} , i_{pLv} , i_{loss} , and i_{pLt} are maintained near a fixed value.

4.2 Unbalanced Non-linear Load Condition

Figure 4 depicts the system behavior under unbalanced non-linear load conditions. The load of phase ‘r’ is disconnected between the interval $t = 0.2-0.3$ s. Figure 4a illustrates that grid currents have incremented. The VSC current is compensating for the load current. Hence, sinusoidal grid currents are noticed. The DC link voltage shows constant. Figure 4b depicts the increase in grid active power because the required load power has decreased. Solar PV current (I_{pv}) and PV power (P_{pv}), PV voltage (V_{pv}) are maintained constant. Figure 4c illustrates that i_{Lr} and i_{Lr} are maintained near zero value under an interval of disconnection of load. However, i_{pLr} , i_{pLavg} , i_{loss} , and i_{pLt} have decreased after load removal. Moreover, i_{pLv} , is maintained constant.

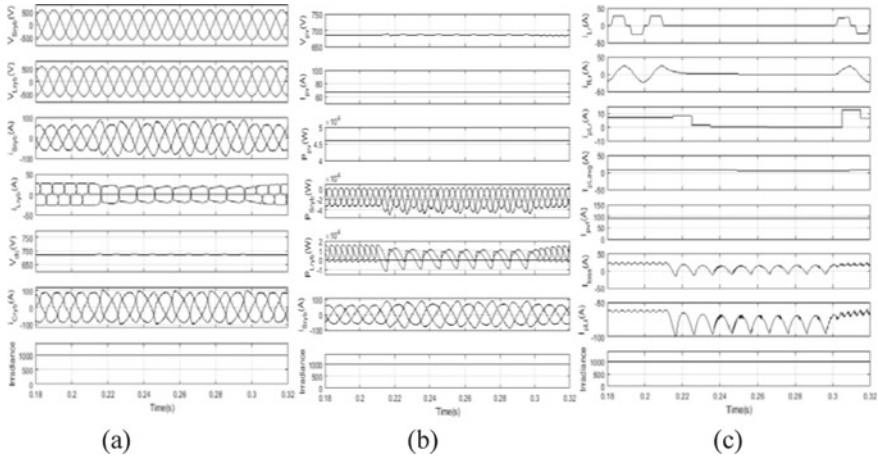


Fig. 4 Simulated results for load unbalancing **a** V_{Sryb} , V_{Lryb} , i_{Sryb} , i_{Lryb} , V_{dc} , i_{Cryb} , Irradiance **b** V_{pv} , i_{pv} , P_{pv} , P_{Sryb} , P_{Lryb} , i_{Sryb} , and **c** i_{Lr} , i_{fLr} , i_{pLr} , I_{pLavg} , I_{pvf} , I_{loss} , and I_{pLt}

4.3 Response Under Varying Insolation Level

Figure 5 illustrates the system response under varying insolation levels between intervals of 0.5–0.6 s. Figure 5a depicts reduction in VSC currents has been noticed because insolation levels have reduced. As a result, a decrease in grid currents has been noticed. The load current is unchanged. Figure 5b shows that solar PV current (I_{pv}) and PV power (P_{pv}), PV voltage (V_{pv}) are decreased under the decreased insolation level. Hence, lesser power is supplied to the grid. Figure 5c shows that i_{Lr} , i_{fLr} , i_{pLr} , and I_{loss} are unaffected by varying insolation. However, I_{pvf} and I_{pLt} have decreased under varying insolation level.

4.4 THD Analysis

Figure 6 shows the load current THD and grid current. The load current THD and grid current THD are 41.00% and 1.42%, respectively. Hence, the MDF algorithm shows a good capability of compensating load current containing high harmonics. As a result, grid current THDs are well maintained below 5% within in IEEE-519 standard.

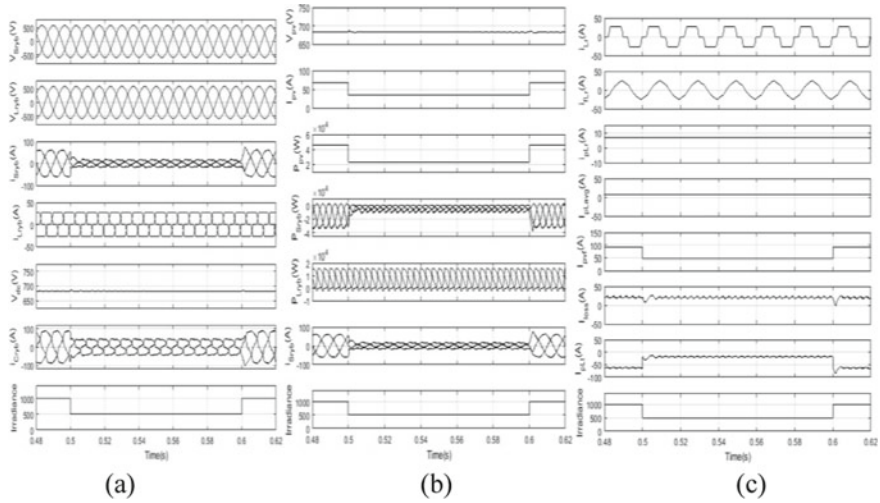


Fig. 5 Simulated results for varying insolation **a** V_{Sryb} , V_{Lryb} , i_{Sryb} , i_{Lryb} , V_{dc} , i_{cryb} , Irradiance **b** V_{pv} , i_{pv} , P_{pv} , P_{Sryb} , P_{Lryb} , i_{Sryb} , and **c** i_{Lr} , i_{Lr} , i_{pLr} , I_{pLavg} , I_{pvf} , I_{loss} , I_{pLt}

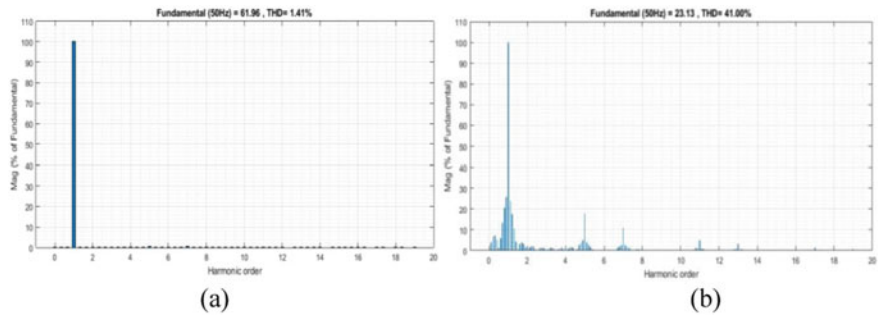


Fig. 6 Harmonic Spectra and THD **a** grid current **b** load current

5 Conclusion

Simulated results have shown a good response of the proposed system using MDF control technique under various conditions. VSC provides reactive power compensation, harmonic mitigation, and load balancing. The VSC has provided active power to the load and surfeit power is injected into the grid. The MDF-based control is able to maintain the THDs of grid current near 1.42%, which is well within recommended IEEE-519 limits.

References

1. Solanki CS (2015) Solar photovoltaics: fundamentals, technologies and applications. PHI Learning, New Delhi
2. Liu Y, Lu Z, Yang F (2018) The investigation of solar PV models. In: IEEE power & energy society innovative smart grid technologies conference (ISGT), pp 1–5
3. Julien S, Sajadi A, Hodge BM (2022) Hierarchical control of utility-scale solar PV plants for mitigation of generation variability and ancillary service provision. *IEEE Trans Sustain Energy*
4. Chau TK, Yu SS, Fernando T, Iu HH (2018) Demand-side regulation provision from industrial loads integrated with solar PV panels and energy storage system for ancillary services. *IEEE Trans Ind Inf* 14(11):5038–5049
5. Patel ND, Naik AP (2018) A low jitter–low phase noise wideband digital phase locked loop in nanometer cmos technology. *IJECET* 9(3):1–12
6. Xu S, Shao R, Cao B, Chang L (2021) Single-phase grid-connected PV system with golden section search-based MPPT algorithm. *Chin J Electr Eng* 7(4):25–36
7. Shabat MM, El-Amassi DM, Abu Shaar Kh Kh, Schaadt DM (2019) Design of solar cell structure based on Au nanoparticles. In: IEEE 7th Palestinian international conference on electrical and computer engineering (PICECE), IEEE2019
8. Alam MJE, Muttaqi KM, Sutanto D (2016) Effective utilization of available PEV battery capacity for mitigation of solar PV impact and grid support with integrated V2G functionality. *IEEE Trans Smart Grid* 7(3):1562–1571
9. Singh S, Kewat S, Singh B, Panigrahi BK, Kushwaha MK (2022) A multifunctional three-phase grid coupled solar PV energy conversion system using delayed μ -law proportionate control for PQ improvement. *IEEE Trans Ind Appl* 58(1):554–564
10. Vorobyov A, Hennemann C, Dallemagne Ph (2019) Solar cell antenna for IoT and wearable applications. In: 13th European conference on antennas and propagation (EuCAP), IEEE 2019
11. Bagheri-Farahbakhsh M, Cross A, Strickland D, Morris P, Martin T, Lakin T (2019) Hybrid PV/battery-storage unit for residential applications. *J Eng IET* (17)
12. Shukl P, Singh B (2020) Multifunctional control of weak grid inertia solar PV system with synchronization capability. In: International conference on power, instrumentation, control and computing (PICCC), pp 1–6
13. Sharma A, Gupta TN, Rawat MS (2021) Grid connected solar PV fed constant power water pumping system. In: International conference on intelligent technologies (CONIT), pp 1–6
14. Singh B, Chandra A, Haddad KA (2015) Power quality: problems and mitigation techniques. Wiley, London

Multi Terrain Motion Control Vehicle



Oomang Bishnoi, Preeti, and Sansh Bir Dagar

1 Introduction

Gestures can arise through physical motion, however, they mostly arise from the hand or face [1, 2]. Individuals can put in gestures to govern or have interaction with gadgets. Many strategies were made for the usage of cameras and computer imaginative and prescient logics to interpret the signal. A robot is a device that can carry out a few tasks assigned to it mechanically. Robots can sustain on their own or even can be controlled remotely. Robots have arisen to such a scale that they are able to mimic a human being and can also take decisions by themselves. The main aspect of a robot is the way it interacts with humans which is through Human–Machine Interface [3, 4]. In the past few years, robotic communication has developed massively which was not easy in the early years and thus requires a lot of hard work. With the advancement of robots, gesture control came into existence. Gestures arise from any movement done by our body part, however, they basically arise from our palm or face. Gestures recognised are analysed by computer and output is generated, which is considered a form of human interface language [5–7]. With gesture recognition into play, there is a lot less need for textual content interfaces. A gesture is a motion that needs to be viewed by a person and has to bring a few pieces of data. Human–robot interaction relies heavily on hand gesture recognition (HRI). For people who are disabled or disadvantaged, signal language is the most natural manner of communication.

The focus of this work is to apprehend hand motions and utilise them to move a vehicle car wirelessly. An accelerometer sensor is used for steering and is a controlled variable. The idea presented in this article may be useful to physically challenged

O. Bishnoi · Preeti (✉) · S. B. Dagar
Skill Faculty of Engineering and Technology, Shri Vishwakarma Skill University, Palwal,
Haryana, India
e-mail: preetiednith@gmail.com

people at large who can easily control their movement by wearing the sensor-based gloves and moving the wheelchair as per their requirement. Further, the idea may find applications in military implementations of using a robot, medical implementations for using robots for surgeries, robots used at building sites, in industries to operate carts, etc.

The following is how the paper is structured. The introduction to the current work is presented in Sect. 1. Section 2 presents the design of a gesture controlled vehicle followed by the description of components in Sect. 3. Section 4 depicts the results obtained using Arduino code, and at the end, the conclusion and future scope of the work are presented in Sect. 5.

2 Design of Gesture Controlled Car

The targeted gesture controlled robot operates on the basis of MPU 6050, which detects a human gesture, analyses the data, and delivers it to Arduino UNO, where the appropriate voltage is applied (both 3V or 0V). MPU 6050 is a similar sensor that is used in our mobile phones to use the auto-rotate feature. We will use this module to sense the gesture and then these signals will tell the Robot over the Radio Frequency by using RF Module to tell the Robot in which direction to go [8–10]. As a controller, the Arduino UNO is used. The data is subsequently passed into an Encoder (HT 12E), which prepares it for transmission via an RF transmitter. RF434 is the RF module in use here. The RF receiver obtains the statistics at the receiving end, which is then passed on to the decoder (HT 12D). The encoder data is fed into the motor motive force IC (L293D), which controls the cars in a unique configuration to move the bot in different directions. Figure 1 depicts the overall system's block diagram.

The circuit diagram of transmitter (Fig. 1) and receiver (Fig. 2) [1] of the gesture controlled vehicle is described as follows:

- (a) Transmitter: It sends data to the RF 434 TX module in the form of voltage levels, which are fed into the SDA and SCL pins of the Arduino UNO, which calculates the gesture movements of the hand and determines the data to be conveyed.
- (b) Receiver: The data pin generates the serial data received at the receiver (Rx434) and connects it to the decoder (HT 12D).

The accelerometer, MPU 6050, was calibrated with the help of an Arduino UNO software. All of the conditions meeting the requirement of the desired direction of movement have been calibrated, and the MPU 6050's X and Y directions will only be evaluated if the Z direction condition is met (Fig. 3).

The values of four data pins on the Arduino UNO are set or reset based on the conditions found in MPU 6050. On the basis of the parameters, the Arduino code is developed for the desired movement of the vehicle robot.

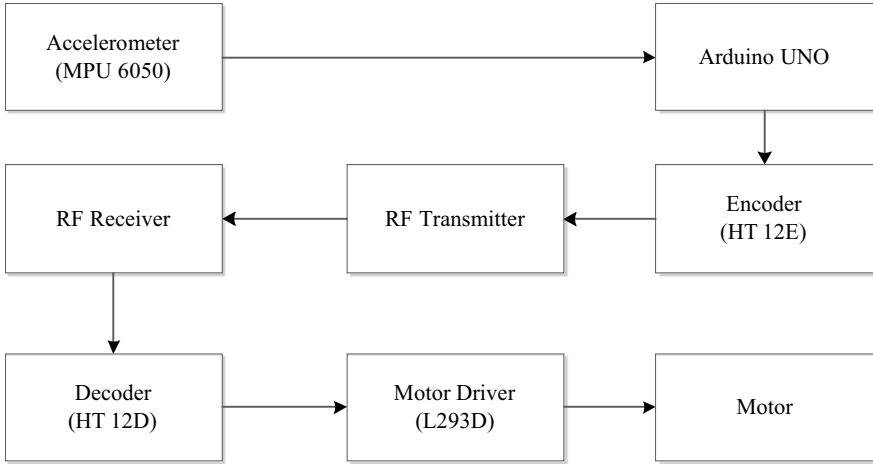


Fig. 1 Block diagram of gesture controlled vehicle

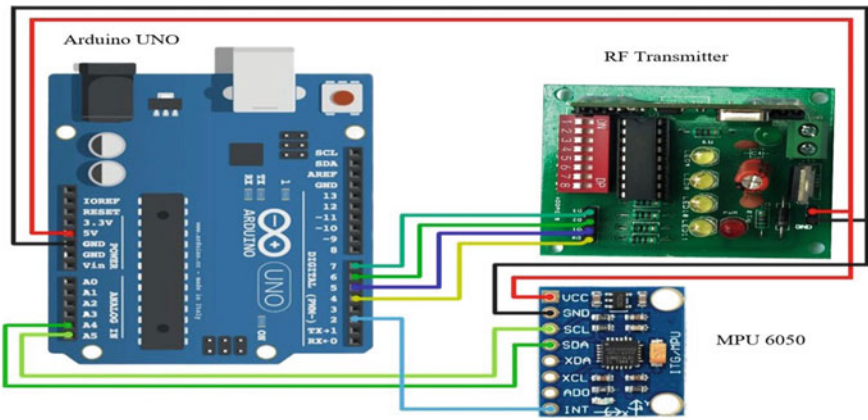


Fig. 2 Circuit diagram of gesture control remote module

3 Components of Gesture Controlled Vehicle

The entire system is split into two parts: the transmitter and the receiver part [11]. The transmitter and receiver comprise the following.

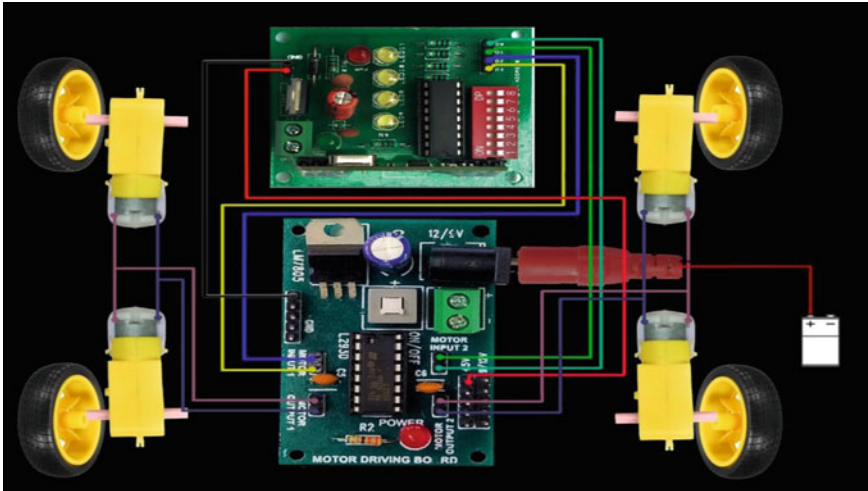


Fig. 3 Circuit diagram of gesture control robot

3.1 Accelerometer and Arduino UNO

Because it can measure minute activities, the accelerometer is utilised as a sensing instrument. MPU 6050 is a six-DOF (degrees of freedom) accelerometer, which means it can output six values: three from the accelerometer and three from the gyroscope. However, the best accelerometer readings were used in this study. To reduce the mission's worth, the most efficient microcontroller or controller was utilised. The Arduino UNO is utilised for the transmitter, while the RF module is used for data transmission. A three-axis accelerometer and three-axis gyroscope are included in the MPU 6050. We can now measure acceleration, rotational displacement, and a range of other motion-related metrics using this method. To detect gestures, this will be connected to an Arduino UNO.

3.2 Encoder

With 212 encoders, the HT12E is an encoder-integrated circuit (IC). They'll be employed in far-flung managed device applications using the 212 series of decoders. It's primarily used to link RF and IR circuits together. The encoder/decoder pair should be compatible in terms of address range and data format. The address of encoder IC and decoder IC must be matched for secure and complete data transmission.

3.3 RF Transmitter and Receiver

A radio frequency module (RF module) is a typically tiny electrical device that transmits and receives radio signals between pieces of equipment. Wireless communication with all other tools in an embedded machine is frequently acceptable. Optical or radio frequency (RF) communication can be used to complete this wi-fi conversation.

3.4 Decoder

The HT12D is a decoder integrated circuit from the 212 family of decoders. Remote-controlled device programmes, including burglar alarms, vehicle door controllers, and security systems, are commonly utilised with this type of decoder. It's designed to link RF and infrared circuits only.

3.5 Motor Driver

The L293D is a circuit that incorporates two H-bridge motor driving forces (IC). Motor drivers act like modern amplifiers because they take a low-today-day manipulating signal and provide a better- today-day signal. The automobiles are driven by this superior cutting-edge indication.

Two H-bridge driving force circuits are included in the L293D. DC motors can be pushed forward and backward at the same time in their most common mode of operation. Common sense can be entered at pins 2 and 7, as well as pins 10 and 15, to control vehicle motor operations.

3.6 Gear Motors

A gear motor is an electric motor with a low horsepower or low speed output that is designed to create high torque. Geared vehicles come in a range of shapes and sizes, and they're probably likely used in a variety of household gadgets. Can openers, storage door openers, washing machines, time manipulation knobs, and even electric driven alarm clocks all use gear motors. Clinic beds, business jacks, and cranes are all common commercial programmes for a tool motor. They all work in the same way, regardless of the type of tool motor you're working with. When a system is necessary to apply an excessive amount of pressure in order to circulate a very heavy object, gear cars are widely used in commercial packages (Fig. 4).

Fig. 4 DC gear motor

4 Results and Discussions

It is observed from the results obtained that with acceleration orientation of $+y$, $-y$, $-x$, and $+x$, the vehicle is taking the direction forward, reverse, left, and right, respectively, and when the vehicle is required to be stopped, the accelerometer orientation needs to be at rest.

It is also observed that the five positions of the hand are exactly matched with the directions of movement of the vehicle.

5 Conclusion

The primary goal of this work was to create a vehicle that could run utilising hand movements captured by the Accelerometer MPU 6050 and wireless RF connection. An Arduino UNO R3 was utilised as a microcontroller for this project. The vehicle makes the appropriate movements for the pre-programmed and calibrated hand signals. With the help of the accelerometer, data from hand motions is supplied into the Encoder HT 12E via the Arduino UNO, and the values are then communicated via Tx 434. The values are received by Rx 434 and decoded

by a Decoder HT 12D before being transmitted to the motor driving component L293D. The information collected from the component operating the motor is then used to control these motors. The limitations of the current work, such as the small battery and limited range of operation of the RF module, could be overcome in the future by employing more powerful batteries and a GSM module for wi-fi signal transmission. A camera can also be mounted on the vehicle to monitor its movement.

The accelerometer of a mobile phone can also be used for controlling the movement of the vehicle which will reduce the hardware cost of the project and will give a basic understanding of interfacing technology tools with vehicles.

References

1. Mahesh B, Aruloli S, Sambhavi A (2015) Robotic control by using virtual method. In: 2015 Online international conference on green engineering and technologies (IC-GET)
2. Wu XH, Su MC, Wang PC (2010) A hand-gesture-based control interface for a car-robot. In: Proceedings of 2010 IEEE/RSJ international conference on intelligent robots and systems, Taipei, Taiwan, 18–22 Oct 2010
3. McAllistel G, McKenna SJ, Ricketts IW. Towards a non-contact driver vehicle interface. In: Proceedings of 2000 IEEE intelligent transportation systems conference proceedings. Dearborn (MI), USA 1–3 Oct 2000
4. Zobl M, Geigel M, Schullec B, Lang M, Rigoll G (2003) A real time system for hand gesture-controlled operation of in-car devices. In: Proceedings of 2003 IEEE, ICME 2003
5. Bannach D, Amft O, Kunze KS, Heinz EA, Troster G, Lukowic P (2007) Waving real hand gestures recorded by wearable motion sensors to a virtual car and driver in a mixed-reality parking game. In: Proceedings of the 2007 IEEE symposium on computational intelligence and games (CIG 2007)
6. Pickering CA, Burnhamt KJ, Richardson MJ (2007) A research study of hand gesture recognition technologies and applications for human vehicle interaction. Jaguar and Land Rover Technical Research, UK, Jaguar Cars, Engineering Centre, Whitley, Coventry. Coventry University, UK, Control Theory and Applications Centre, Priory Street
7. Luo RC (2012) Confidence fusion based human-robot interaction with hand gesture and emotion recognition for service robotics. In: Proceedings of CINTI 2012, 13th IEEE international symposium on computational intelligence and informatics, 20–22 Nov 2012, Budapest, Hungary
8. Zhao S, Li S, Chen L, Ding Y, Zheng Z, Pan G (2013) iCPS-Car: an intelligent cyber- physical system for smart automobiles. In: Proceedings of 2013 IEEE. 10.11.09
9. Jia Qi H, Santoso M (2013) Immersive driving car simulation for children using natural user interface controller. In: Proceedings of 2013 IEEE. 10.11.09/ISUVR.2013.17
10. Parada-Loira F, González-Agulla E, Alba-Castro JL (2014) Hand gestures to control infotainment equipment in cars. In: Proceedings of 2014 IEEE intelligent vehicles symposium (IV), Dearborn, Michigan, USA, 8–11 June 2014
11. Bano A, Kundu M, Jana A, Pal SK (2019) Gesture control interface of a robot-car using raspberry PI. Project Report, Instrumentation engineering, RCC Institute of Information Technology, Maulana Abul Kalam Azad University of Technology

Optimal Frequency Control of Micro-Grid System Using IPD–(1 + I) Controller



Yogendra Arya and Kavita Singh

1 Introduction

Modern power strategies demand power generation solutions with the least greenhouse gases and carbon emissions. The interest in renewable units (RUs) has increased due to the depletion of fossil sources to fulfill the energy demand and the use of promising strategic policies [1]. In this circumstance, an islanded micro-grid system integrated with renewable energy sources (RESs) is accepted to be an economical solution owing to the smaller scale, power security, and on-site distribution of power which helps to provide a sustainable carbon-neutral electrified society.

Therefore, the higher penetration of RESs with variable consumer demands causes surplus deviation in the system frequency [2]. In fact, the gap between power generation and demand might usually occur in the micro-grid subsystem which prompts energy and frequency disturbance.

Wide employment of diversified storage units (SUs), such as batteries, flywheels, and ultra-capacitors (UCs), has been leveraged to smoothen the system performance as well as to reduce the pressure on the diesel units [3]. To conserve desired performance during sudden disturbances, a collection of different controllers and algorithmic techniques has been introduced by many researchers in the past [4]. Authors in [5] the targeted load frequency regulation assignment has been analyzed by PI/PID controllers tuned by genetic algorithm (GA). The authors in [6] have depicted a very commonly used FOPID controller tuned by Imperialist competitive algorithm (ICA)

Y. Arya

Department of Electrical Engineering, J.C. Bose University of Science and Technology, YMCA, Faridabad, Haryana 121006, India

K. Singh (✉)

Department of Electronics and communication Engineering, Rawal Institute of Engineering and Technology, Tikri Khara, Faridabad, Haryana 121004, India

e-mail: kavitasingh.jamia@gmail.com

algorithm. The application of cascaded PI with PD controller-based flower pollination optimization (FPO) for the frequency response model of micro-grid system has been discussed in [7]. In [8], the utilization of FOPID controller for reducing the system ΔF in a random and nonlinear model of a micro-grid has been shown. In [9], a cascade fractional-order controller that consists of 3 design variables proportional-integral derivative controllers was proposed. While the objective is to control the system frequency in a much better way, these techniques have drawbacks like higher-order controller structure, complexity in implementations, and prove unsuitable for all operating conditions. An alternative way of solving the issues is to use an effective evolutionary algorithmic technique like GA [5], Jaya [10], ICA [11, 12], WOA [13], etc. In order to enhance the dynamic responses effectively with fewer control parameters, in this paper, a maiden integral-proportional-derivative with one plus integral (IPD-(1 + I)) controller structure has been implemented. Owing to the advantage of the proposed control stratagem, this study proposed the ICA technique to select the gains of the (IPD-(1 + I)) controller so that the frequency deviations will be minimized, and the frequency stability will be enhanced under different operating conditions.

The remaining manuscript is structured as follows. The mathematical modeling of a micro-grid system is demonstrated in Sect. 2. This is observed by a depiction of the advocated controller strategy and optimization algorithm in Sects. 3 and 4. The obtained simulation outcomes from the considered micro-grid are given in Sect. 5, pursued by the conclusions in Sect. 6.

2 System Configuration

The proposed micro-grid consists of wind power system, solar power system, aqua electrolyser (AE), fuel cell (FC), diesel engine generator (DEG), flywheel energy storage subsystem (FESS), battery energy storage subsystem (BESS), and ultra-capacitor (UC) as shown in Fig. 1. In actual systems, DEG, FC generators, and AE are higher-order systems with nonlinearities. However, in this study, only the lower-order frequency domain has been considered to control. Therefore, in this paper, we represent DEG, FC, FESS, BESS, and UC by simple first-order transfer functions. AE is exploited to reduce the promptly changing yield power from wind and solar power systems and produce hydrogen as fuels for FCs. The power relationship among different components of the micro-grid is expressed as (1 and 2) [5]

$$P_t = P_W + P_{PV} - P_{AE} \quad (1)$$

$$P_s = P_t + P_{DEG} + P_{FC} \pm P_{FESS} \pm P_{BESS} \pm P_{UC} \quad (2)$$

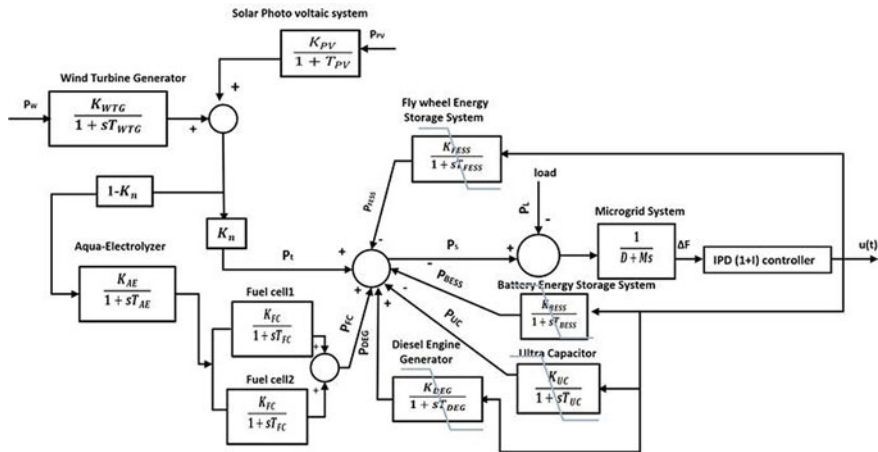


Fig. 1 Block diagram of suggested micro-grid model

2.1 Power Deviations

To maintain the load demand balance, generated power must be tuned since the yield power of RES varies with time. This is regulated as per the difference between supply and demand load as given in (3) [5]

$$\Delta P_e = P_s - P_L \Delta P_e = P_s - P_L \tag{3}$$

2.2 Frequency Deviations

The frequency variation in the power system is signified as follows (4) [5]:

$$\Delta f = \frac{\Delta P_e}{K_{sys} + D} \Delta F = \frac{\Delta P_e}{K_{sys} + D} \tag{4}$$

where, ΔP_e ΔP_e represents changes in generating energy subsystem, and K_{sys} is the power subsystem as constant frequency response. Thus, micro-grid system model transfer function can be expressed as (5) [5]

$$G_{sys} = \frac{\Delta F}{\Delta P_e} = \frac{1}{Ms + D} \tag{5}$$

In Eq. 5, M/D represent inertia constant and load damping constant, respectively.

3 Control Strategy

The nominal PID controller has been employed in several industries and power system fields. At the moment, to meet up the tasks of frequency regulation in a stable and adaptable way, two-stage controllers are at the forefront of analytical trends. That’s due to their robustness and better adjustment of controller parameters than classical PID controllers. The general stratagem of the proposed IPD–(1+I) controller is shown in Fig. 2. The control is accomplished by employing the input ΔF signal. It is expressed in transfer function form as (6)

$$U_c(s) = \Delta F \left(\frac{K_{I1}}{s} + K_P + K_d s \right) \left(1 + \frac{K_{I2}}{s} \right) \tag{6}$$

3.1 Fitness Function

To tune the design variables of the controller, the integral of the square of the Δf is selected as the fitness function (7) [4].

$$J = \int_0^T (\Delta e(t))^2 \tag{7}$$

Minimizing J , Subjected to $K^{\min} \leq K \leq K^{\max}$.

where K represents the different gains of the proposed controller and K^{\min} and K^{\max} represent the lower and upper limits of gain value.

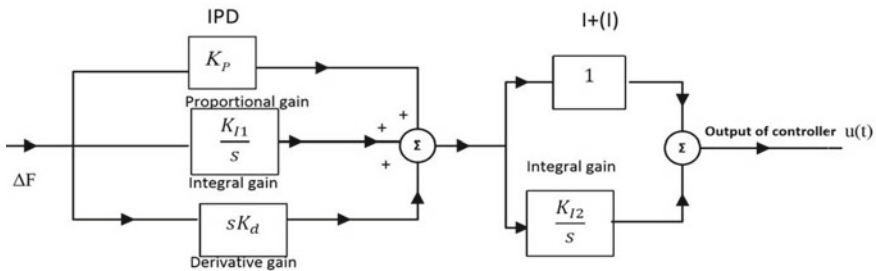


Fig. 2 IPD (1+I) Controller structure

4 Imperialist Competitive Algorithm (ICA)

ICA starts with a primary populace having nations where the finest nations are considered as imperialist states [12]. The remaining nations work as the colonies of related imperialist states. The related colonies of primer nations are distributed to imperialists in view of their assets. The nation's energy which is corresponding to its fitness value is connected contrariwise to its 'J'. The colonialist states with their colonies lay out certain empires. When making a primer empire, the colonies in all of them start continuing close to their suitable colonialist country. This moving system is named adaptation. Related to this manner; the colony with higher power might replacement of the imperialist. All through the imperialistic contest; their strong empires endeavor to increase their powers however the lesser strong lose each of their states to other people as well as got rid of their optimization issue. Toward the finish of ICA, the arrangement is engaged at the highest level of a strong empire. Finally, the imperialistic rivalry meets in a state where just 1 domain wins, and every one of its colonies or imperialists will enjoy the indistinguishable area and power. All the considered parameters for this algorithm have been taken from [11] and for further details refer [12].

5 Simulation Results and Analysis

A hybrid micro-grid system has been developed to analyze the capabilities of the proposed controller (IPD (1+I)) with two RESs (wind and solar). Two different types of loads are used to analyze the efficacy of the proposed controller. In this study, we have considered two cases as mentioned below:

1. The dynamic response investigation of the subsystem by considering step load perturbations.
2. Dynamic response investigation of the subsystem by contemplating random load perturbations.

5.1 Simulation Results of Case 1

For this situation, during $0 < t < 35$ s, the wind/solar power energy is considered 0.45 p.u/0.35 p.u separately. Load is considered 1 p.u through $0 < t < 80$ s. After 35-s, WT power and solar PV are abruptly diminished to 0.4 p.u and 0.19 p.u individually. At the $t = 80$ s, the associated load is abruptly raised from 1 to 1.1 p.u. The variation in load, as well as generation, is regulated by FC, BESS, FESS, UC, and DEG through the control signal since the WTPG and solar PV create consistent power. The power control framework frequency vacillates because of these abrupt fluctuations in power distribution generation by RES and load requirements. This Δf is constrained through

the proposed controller as well as the outputs response of framework parameters is changed in accordance with relating values to such an extent that the gap in supply and load is less. Figure 3 reveals the progression variations in wind power, solar power, and demanded load.

Whenever wind turbine power diminished from 0.45 to 0.4 pu, solar PV power decreased from 0.35 to 0.19 pu after 35 s, and the associated load changed from 1 to 1.1 pu abruptly at 80 s, the resulted yields of the FC, FESS, UC, BESS, and DEG are changed. Consequently, the gap between supply and load is decreased. At last, the ΔF comes to a steady state. The design variables values of various control structure got using the ICA method are given in Table 1. The power results of the fuel cell, Flywheel subsystem, ultracapacitor, BESS, and DEG are introduced in Fig. 4. Figure 5 shows the ΔF of the proposed micro-grid system. It very well might be seen that the response of the proposed regulator is awesome among PI and PID regulators used for investigation as far as peak transient deviation and settling the time.

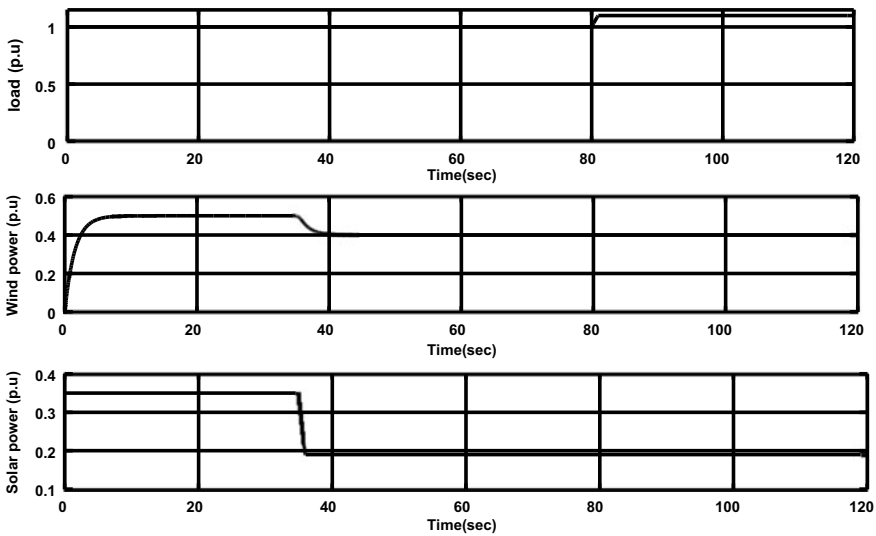


Fig. 3 Demanded load, wind power, and solar power profiles in case-1

Table 1 Design variables of considered controller optimized by ICA

Variables	PI	PID	IPD(1+I)
K_p	4.7	5.21	5.5
I K_{I1}	2.1	3.22	4.67
K_d	–	6.23	5.81
I K_{I2}	–	–	3.5

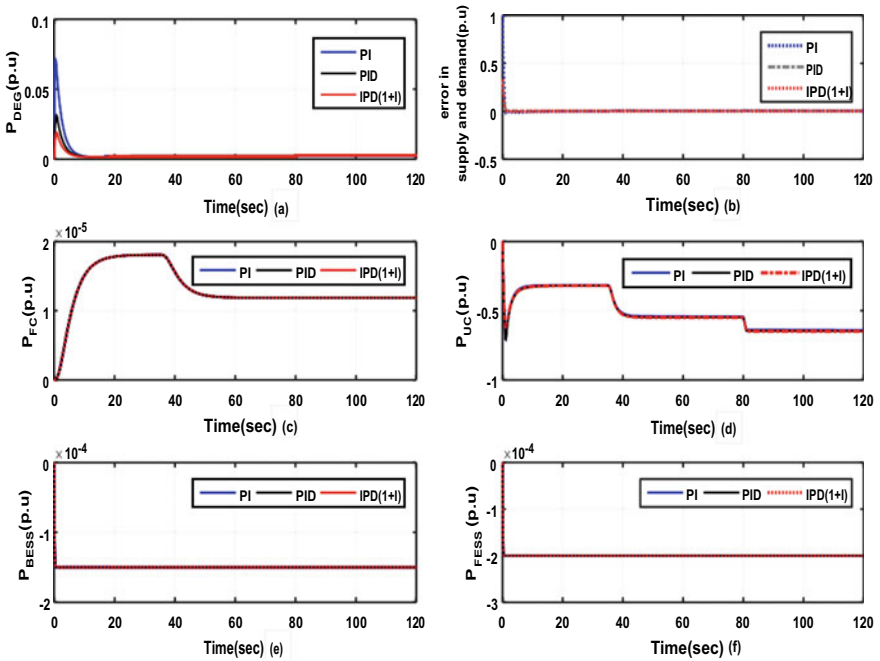


Fig. 4 Power output of different components under case-1

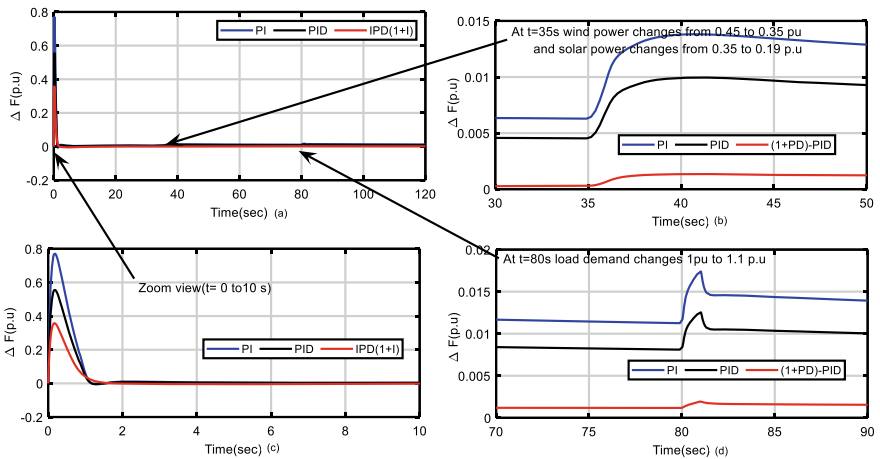


Fig. 5 Frequency deviation in the system under case-1

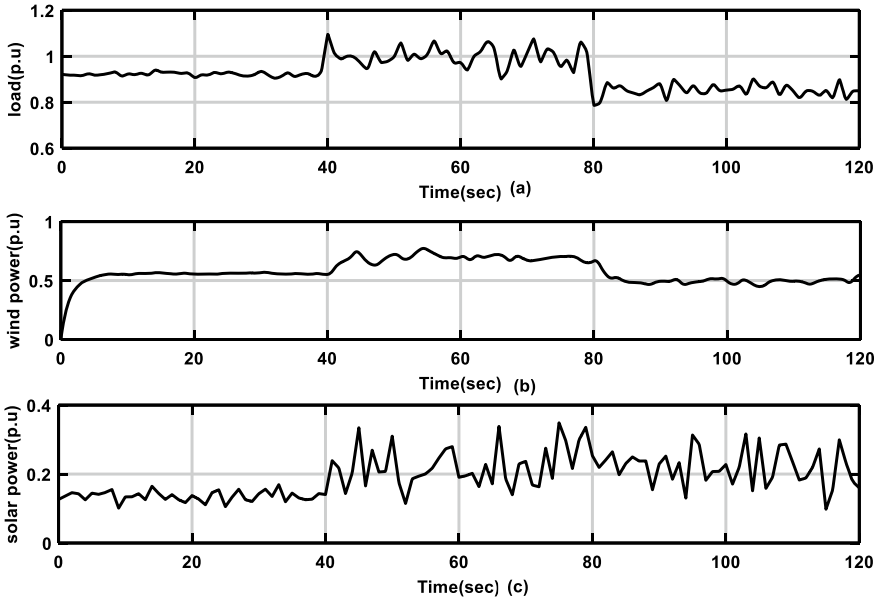


Fig. 6 Demanded load, wind power, and solar power profiles in case-2

5.2 Simulation Results of Case 2

In this case, the random load perturbation (RLP), random wind, and solar are considered for the realistic scenario as displayed in Fig. 6. Figure 7 gives the profile of ΔF , under abrupt changes as discussed above. To corroborate the effectiveness of the advocated control technique, its transient response is compared with PI/PID control techniques, and the attained results are shown in Fig. 7. The power yields of different components are displayed in Fig. 8, which again shows the superior performance of IPD (1+I) controller over PI/PID.

6 Conclusions

In this study, an effective control stratagem is developed by optimizing a two-stage (IPD-(1+I)) controller structure with an imperialistic competitive algorithm (ICA) for the frequency regulation of micro-grid. The amalgamation of sustainable power sources like wind, solar thermal, and conventional sources like DEG, FC, FESS, BESS in addition to UC is studied. As novelty, the development of the (IPD-(1+I)) controller is applied for a frequency response model through the ICA

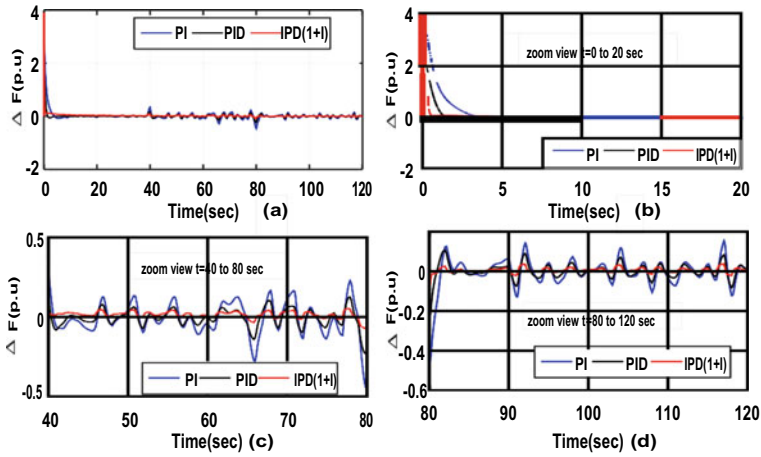


Fig. 7 Frequency deviation in the system under case-2

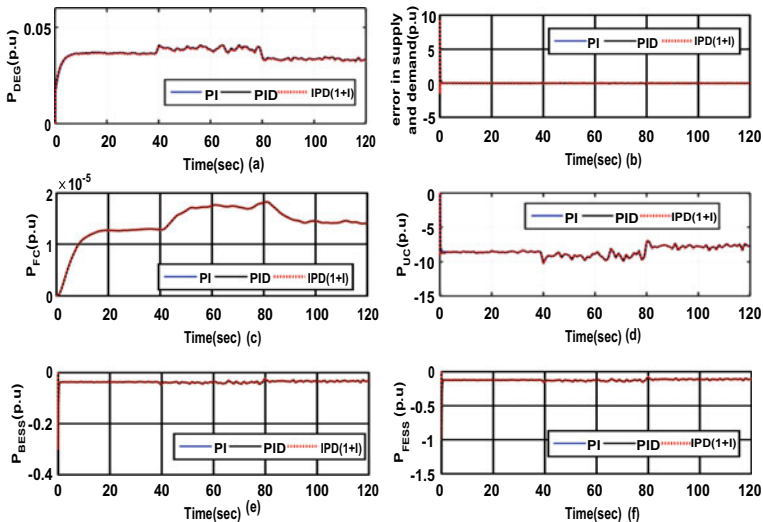


Fig. 8 Power output of different components under case-2

technique and the dynamic response is presented and compared with other traditional controllers (PI/PID). It was noticed that the (IPD-(1+I)) controller can manage system disturbances and enable the required power sharing between sub-systems.

References

1. Almeshqab F, Ustun TS (2019) Lessons learned from rural electrification initiatives in developing countries: insights for technical, social, financial and public policy aspects. *Renew Sustain Energy Rev* 102:35–53. <https://doi.org/10.1016/j.rser.2018.11.035>
2. Rakhshani E, Remon D, Mir Cantarellas A, Rodriguez P (2016) Analysis of derivative control based virtual inertia in multi-area high-voltage direct current interconnected power systems. *IET Gener Transm Distrib* 10:1458–1469 <https://doi.org/10.1049/iet-gtd.2015.1110>
3. Singh K, Amir M, Ahmad F, Refaat SS (2021) Enhancement of frequency control for stand-alone multi-microgrids. *IEEE Access* 9:79128–79142. <https://doi.org/10.1109/ACCESS.2021.3083960>
4. Alhelou H, Hamedani-Golshan ME, Zamani R, Heydarian-Forushani E, Siano P (2018) Challenges and opportunities of load frequency control in conventional, modern and future smart power systems: a comprehensive review. *Energies* 11:2497. <https://doi.org/10.3390/en11102497>
5. Das DC, Roy AK, Sinha N (2012) GA based frequency controller for solar thermal–diesel–wind hybrid energy generation/energy storage system. *Int J Electr Power Energy Syst* 43:262–279. <https://doi.org/10.1016/j.ijepes.2012.05.025>
6. Singh K, Amir M, Ahmad F, Khan MA (2021) An integral tilt derivative control strategy for frequency control in multimicrogrid system. *IEEE Syst J* 15:1477–1488. <https://doi.org/10.1109/JSYST.2020.2991634>
7. Dash P, Saikia LC, Sinha N (2016) Flower pollination algorithm optimized PI-PD cascade controller in automatic generation control of a multi-area power system. *Int J Electr Power Energy Syst* 82:19–28. <https://doi.org/10.1016/j.ijepes.2016.02.028>
8. Pan I, Das S (2015) Kriging based surrogate modeling for fractional order control of microgrids. *IEEE Trans Smart Grid* 6:36–44. <https://doi.org/10.1109/TSG.2014.2336771>
9. Guha D, Roy PK, Banerjee S (2021) Equilibrium optimizer-tuned cascade fractional-order 3DOF-PID controller in load frequency control of power system having renewable energy resource integrated. *Int Trans Electr Energy Syst*. 31. <https://doi.org/10.1002/2050-7038.12702>
10. Singh SP, Prakash T, Singh VP, Babu MG (2017) Analytic hierarchy process based automatic generation control of multi-area interconnected power system using Jaya algorithm. *Eng Appl Artif Intell* 60:35–44. <https://doi.org/10.1016/j.engappai.2017.01.008>
11. Arya Y (2018) Automatic generation control of two-area electrical power systems via optimal fuzzy classical controller. *J Franklin Inst* 355:2662–2688. <https://doi.org/10.1016/j.jfranklin.2018.02.004>
12. Atashpaz-Gargari E, Lucas C (2007) Imperialist competitive algorithm: an algorithm for optimization inspired by imperialistic competition. In: 2007 IEEE congress on evolutionary computation, pp 4661–4667. IEEE (2007). <https://doi.org/10.1109/CEC.2007.4425083>
13. Zaheeruddin KS, Amir M (2021) Intelligent fuzzy TIDF-II controller for load frequency control in hybrid energy system. *IETE Tech Rev* 1–17. <https://doi.org/10.1080/02564602.2021.1994476>

Study of Polarization Effect in WDM Channels Network



Vikash Kumar Dahiya and Sandeep K. Arya

1 Introduction

Wavelength division multiplexing (WDM) is an Optic fiber communications technique that multiplexes the multiple carrier signals in a fiber. It accomplishes this by employing distinct wavelengths for each transmission and may be used on single-mode or multimode fibers through lasers. Figure 1 displays a simple WDM system, illustrating how easy the WDM infrastructure is. WDM is frequently composed of WDM transmit modules that every other operate at a separate wavelength. Multiplexer—a passive device that merges several light sources together into a blended one, fibre architecture, demultiplexer—a passive device that separates the combined light source into individual ones, and WDM receiving modules [1].

Polarization effects were found during early fiber optic transmission testing. Polarization events in fiber optics were once considered a research curiosity. Several research institutions focused on these repercussions throughout the 1990s communications boom. The effects of fiber optic polarization and their interplay become increasingly vital as the bit rates of fibre optic channel increases. These effects must be overcome in order to deploy with over 10 Gb/s transmissions in wavelength across fibre optic in long-haul optical communication [2]. When the fibre facilities were developed by 1998, it could be a serious limitation in systems. The internal birefringence of contemporary fibre plants is minimal. External birefringence, like twists and external tension exerted on optical fibre, adds polarization effects significantly. Polarization effects have become increasingly important in understanding signal transmission in today's long-distance lightwave communication networks.

V. K. Dahiya (✉) · S. K. Arya (✉)

Department of Electronics and Communication Engineering, GJUS&T, Hisar, HR, India

e-mail: dvikash42@gmail.com

S. K. Arya

e-mail: aryasandeep@gmail.com

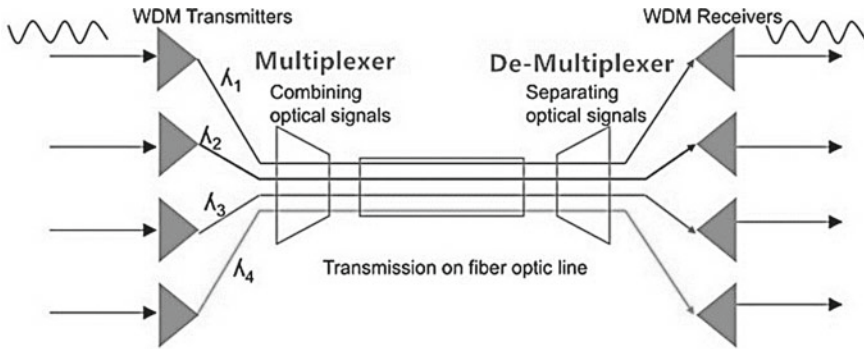


Fig. 1 Simple WDM system [1]

1.1 Research Gap and Motivation

The early optical fiber transmission tests revealed polarization effects. Polarization phenomena in optical fibre have hitherto been regarded as a laboratory curiosity. Several research organizations focused on these repercussions during the telecom boom in the 1990s. The effects of optical fibre polarization and their interplay become increasingly important as the information rate of a single optical channel increases. These effects must be overcome in order to deploy more than 10 Gb/s transmissions in a single wavelength via fibre plants in long-haul optical networks. When fibre plants were developed by 1998, it might be a serious limitation in systems. Internal birefringence, core asymmetry, and built-in stress are all present in these aged fibers. Internal birefringence is minimal in current fibre plants. Polarization effects are considerably enhanced by external birefringence, such as twists and external strain applied to optical fibre [2].

In today's long-distance lightwave communication networks, polarization effects are becoming increasingly important in understanding signal propagation. The following topics will be covered in this study: polarized light description, polarization phenomena in the WDM channel network, modeling of polarization phenomena, and polarizing components.

2 Theory

A light beam is made up of two orthogonal electrical vector field elements which fluctuate in amplitude and frequency. Polarized light arises during which the phase or amplitude of these two components differs. Polarization in optical fiber had thoroughly investigated, and a range of approaches for minimizing or exploiting the phenomena are available.

2.1 Manifestation of Polarization in Optical Fiber

Optical Fiber Birefringence:

Birefringence is defined as a behavior that happens in some components, causing light to be separated into two distinct channels. Since these indices of refraction of some materials alter based on the polarization optical path, this phenomenon occurs.

Birefringence can also be seen in fiber optics as a result of minor irregularity in the cross-section of the fiber core along its length and external factors such as bending. Stress-induced birefringence trumps geometry-induced birefringence in general.

Polarization Maintaining Fiber:

Polarization Maintaining (PM) Fiber is a customized fiber that creates a constant birefringence characteristic throughout its course on purpose, preventing coupling between the two orthogonal polarization orientations. The shape of the fiber and the materials employed in any design provides a substantial amount of stress in one direction, resulting in significant birefringence when subjected to random birefringence.

Poincare Sphere:

The Poincare Sphere is a traditional manner for expressing an EM wave's polarization and changes in polarization as it propagates. It allows you to forecast how any particular retarder can modify the polarization shape. Each polarization state equates to a certain spot upon that sphere. The sphere's two poles symbolize left and right circularly polarized light. Dots upon that equator display linear polarizations. The elliptical polarization stages indicate by all other places on the sphere. Horizontal linear polarization is designated by imaginary point H on the equator, and vertical linear polarization is designated by the diametrically opposite point V.

x , y , and z are Cartesian coordinate axes, as are the spherical orientation and ellipticity angles, and P is a point on the sphere's surface, as shown in Fig. 2a. It's worth noticing that the digits 2 and 2 represent the angles on the sphere. The equation translates Cartesian coordinates to spherical coordinates for a unit sphere.

$$\begin{aligned}x &= \cos(2\chi) \cos(2\psi), \quad 0 \leq \psi < \pi, \\y &= \cos(2\chi) \sin(2\psi), \quad -\pi/4 < \chi \leq \pi/4 \\z &= \sin(2\chi)\end{aligned}$$

where $x^2 + y^2 + z^2 = 1$.

The coordinate pair in the above equation can represent any polarization state. LHP(0° , 0°), L+45P($+90^\circ$, 0°), LVP(180° , 0°), L-45P(270° , 0°), RCP(0° , $+90^\circ$), and LCP(0° , -90°) are the degenerate polarization states on the Poincare sphere. The degenerate states on the x , y , and z axes are described in Fig. 2b. The equator has all linear polarization states, whereas the north and south poles have right and

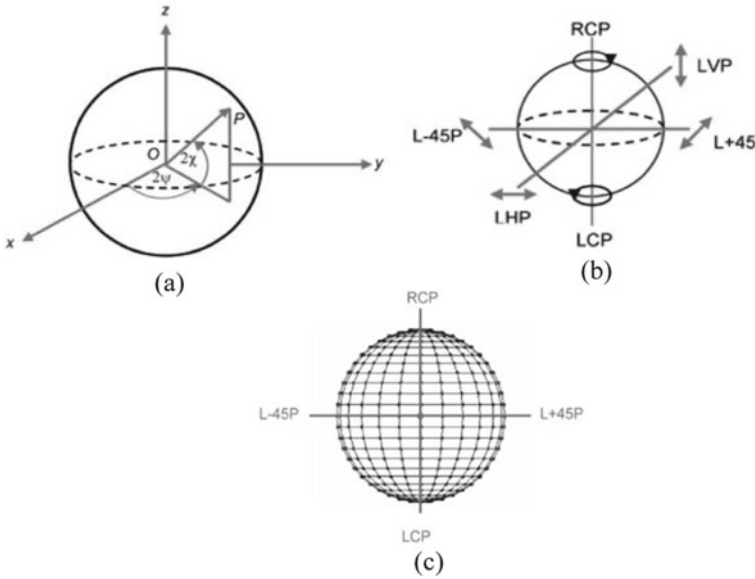


Fig. 2 The polarization states are represented by a poincare sphere [2]

left circular polarization states, respectively [3]. On the rest of the sphere’s surface, elliptically polarized states are depicted. The polarization states are depicted in Fig. 2c at each junction of the 7.5° latitude and 15° longitude lines [2].

Characteristics of Measurable Polarization:

1. DOP

The description of degree of polarization (DOP) is:

$$DOP = I_{pol} / (I_{pol} + I_{unp}),$$

in which I_{pol} and I_{unp} seem to be polarized and unpolarized light intensities, accordingly. Light is considered to be unpolarized when $DOP = 0$, and completely polarized when $DOP = 1$. Partially polarized light is used in intermediate conditions.

2. PER

The Polarization Extinction Ratio (PER) seems to be the decibel (dB) fraction of the least to greatest polarized power. This value will be specified as a specification by any polarization component.

3. PDL

Polarization Dependent Loss (PDL) seems to be the highest variation in insertion loss when sourcing polarization changes among every stage given as decibels (dB).

4. PMD

Material dispersion is a type of PMD. A mode, which has two orthogonal polarization modes, may be accommodated with an SM fiber. The optical fiber core should be completely circular. However, the core is not entirely round in reality, and mechanical forces such as bending induce birefringence in the fiber. This generates optical pulse dispersion by causing one of its orthogonal polarization modes to move quicker than the other. Differential Group Delay (DGD) is the largest difference in mode propagation periods driven by this dispersion, and its unit is commonly stated in $1e-12$. Due to its dynamic features, PMD exhibits a range of DGD readings throughout time rather than a single, stable value for a particular piece of fiber.

3 Simulation Setup and Configuration

This model’s goal is to show how the polarization states of neighboring channels in a WDM system impact channel performance. This phenomenon is induced by nonlinear interactions (XPM, FWM, Raman gain) between channels that are polarization-dependent. OptSim simulation software, which provides an environment with a nearly precise physical model of a system, is used for this purpose. The simulation configuration is depicted in Fig. 3. This system is made up of three main components: the transmitter, the fiber component, and the reception component.

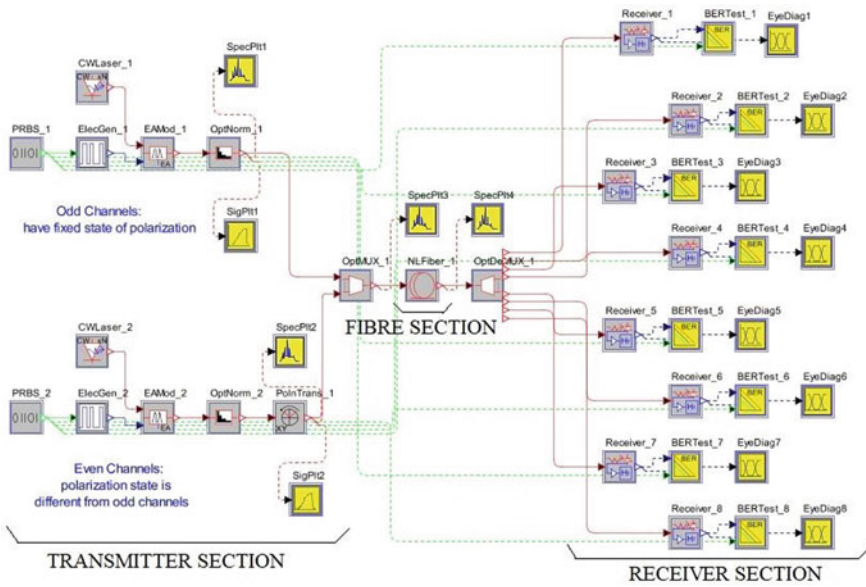


Fig. 3 Simulation setup

3.1 Transmitter Section

A PRBS generates a bit sequence at a rate of 10 Gbps in the transmitter. This bit sequence is passed into the Bit Error Rate (BER) Tester and the Electrical Signal Generator (which turns an input binary signal into an output electrical signal). The output of an electrical generator is sent to an electro-absorption modulator. We can directly define the extinction ratio of the output optical signal when voltage scaling is enabled. It has two input ports and one output port; the first accepts an optical signal that is modulated to produce the output optical signal, and the second accepts an electrical signal. To reach the required extinction ratio at the output, the modulator adjusts the input modulating voltage signal. By attenuating the input optical signal(s) to the provided average output power level, the Optical Power Normalizer normalizes the power of the optical signal. It is used to regulate the input optical power at the receiver while creating a BER versus receiving optical power curve graphic. It can also be used to dampen all input optical signals to the same level, despite their varying average input strengths. This is a setup with two types of channels (odd and even). The odd channel uses the polarization transformer concept, which alters the incoming optical signal(s) based on the parameters supplied. This model employs the transformation mode “rotation” to change the polarization of incoming signals. The polarization is rotated by the set angle in the Rotation mode. An optical WDM multiplexer is referred to as an optical multiplexer. It receives two optical signals (odd and even) at its input port and produces a WDM optical signal that includes all of the input WDM optical signals.

3.2 Fiber Section

The optical transmission is carried out over a 75-km cable. Based on the simulation settings, the fiber characteristics are reconfigured and summarized in Table 1.

Table 1 Parameters value

S. no	Parameters	Values
1.	Length	75e3 m
2.	Loss	0.23 dB/km
3.	Diameter	8.2e−6 m
4.	Effective_mode_area_normalized_by_core_area	1.425
5.	Constant_nonlinear_refractive_index_value	2.6e−20 m ² /W
6.	Raman strength model	Absolute
7.	Peak_raman_gain_at_reference_pump_wavelength	0.98e−13 m/W
8.	Reference_pump_wavelength_for_raman_gain	1.0e−6 m

3.3 Receiver Section

WDM demultiplexer processes fiber output. At its input port, it receives a WDM optical input and generates 8 single-channel optical outputs, one channel per port, at its output ports. Eight optical receivers receive the optical signal. A photodetector, a preamplifier, and a post-amplifier/filter complex are just a few of the components that make up an optical receiver. An optical input is transformed into an electrical current by the photodetector design. This photocurrent then being sent to the preamplifier module, which transforms it into voltage. Lastly, this post-amplifier design incorporates a series of baseband filters to modify the output wave. The photoreceiver noise elements are likewise computed by the model.

4 Results and Discussion

The configuration (Fig. 3) consists of eight channels deployed on a single optical length. The channel spacing is 50 GHz, and it is generated by 2 pseudo-random bit sequence generators, ES Generators, and Constant Wave laser sources in groups of odd and even channels (each with 4×100 GHz-spaced wavelengths). At first, every channel was polarized in the same manner. All even channels were being routed via Polarization Shifter before becoming multiplexed alongside odd channels, which spins the polarization status by angle “polAngle”. The Polarization Shifter parameter settings are shown in Fig. 4. The signal is launched into a channel once it has been multiplexed into the fiber, demultiplexed, then supplied to eight receivers, accompanied by a BER Tester to measure channel performance for a certain polarization state distinction among nearby channels.

This experiment comprises 2 topology files. Both have identical configurations (see Fig. 4), with the only change being the polarization angle processing in the parameter scan configuration:

- “WDM orthogonal polarization. moml”—in this file, the polarization angle is examined in 10° increments between 0° and 180° and the Q-factor is determined as a function of the polarization angle. Figure 5 depicts the outcomes for the odd channel (channel3) and even channel (channel6). The Q-factor is lowest at polarization angles of 0° or 180° , in other words, when every channel exhibits aligned polarization states, with the maximum for polarization angles of 90° , that is when neighboring channels’ polarization states are orthogonal with one another. The main distinction between maximum and minimum Q for these circumstances is 0.4–0.6 dB.
- “WDM random polarization. moml”—in this case, the polarization angle is an arbitrarily shifting value with uniform statistics inside a range of -180° to $+180^\circ$.

Parameter	Value	Units	Range	Std. Dev.	Distribution
mode	"Rotation"				
loss	0.0	dB	[0, 1e+032]	0.0	None
angle	polAngle	degree	[-180, 180]	103.9	Uniform
azimuth	0.0	degree	[-90, 90]	0.0	None
ellipticity	0.0	degree	[-45, 45]	0.0	None
symmetryFactor_x	0.0	none	[-1e+032, 1e+032]	0.0	None
symmetryFactor_y	1.0	none	[-1e+032, 1e+032]	0.0	None
coef11r	1.0	none	[-1e+032, 1e+032]	0.0	None
coef11i	0.0	none	[-1e+032, 1e+032]	0.0	None
coef12r	0.0	none	[-1e+032, 1e+032]	0.0	None
coef12i	0.0	none	[-1e+032, 1e+032]	0.0	None
coef21r	0.0	none	[-1e+032, 1e+032]	0.0	None
coef21i	0.0	none	[-1e+032, 1e+032]	0.0	None
coef22r	1.0	none	[-1e+032, 1e+032]	0.0	None
coef22i	0.0	none	[-1e+032, 1e+032]	0.0	None

Fig. 4 Polarization shifter parameter configuration

Figure 6 depicts the outcomes for configuration scan simulations for fifty statistical runs for Q-factor for the odd channel (channel3) and even channel (channel6) channel. The dots show the Q's of independent runs, whereas the solid line constitutes the average Q across fifty statistical runs. The minimum Q of ch.3 is 14.86 dB, and the maximum Q is 15.48 dB, with an average Q of 15.13 dB and a standard deviation of 0.21 dB. Channel 6 has a minimum Q of 14.75 dB, a maximum Q of 15.20 dB, an average Q of 14.90 dB, and a standard deviation of 0.18 dB.

5 Conclusion

The light signal is conveyed to the destination using optical fiber as a route in optical communication. The main benefits of optical communication systems are their high capacity, high security, greater BW, and low BER. Wavelength division multiplexing is a method used to increase the capacity of an optical system. However, the WDM suffers from the nonlinear impact, lowering overall performance. The results show that system penalties depend on the polarization state, with the worst-case scenario corresponding to every channel being aligned to the identical polarization condi-

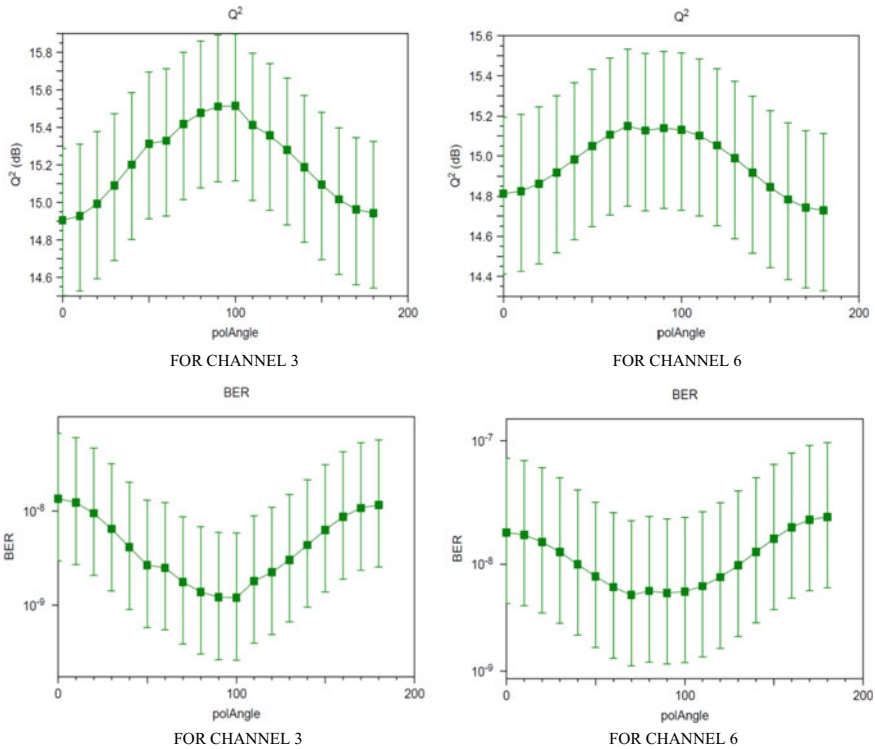


Fig. 5 a Shows the relationship between channel performance and polarization angle between neighboring channels: (left) example of an odd channel (ch.3); (right) example of an even channel (ch.6). **b** Shows the relationship between BER and polarization angle between neighboring channels: (left) example of an odd channel (ch.3); (right) example of an even channel (ch.6)

tion before being launched to fiber. Polarization scrambling (where all channels’ polarization states change randomly over time) can increase system performance by a few tenths of dB in our study. If nearby channels are launched with orthogonal polarization relative to one other, the best performance outcomes (the lowest penalties) will be obtained. In our sample, we saw a 0.4–0.5 dB increase in performance over the worst-case scenario.

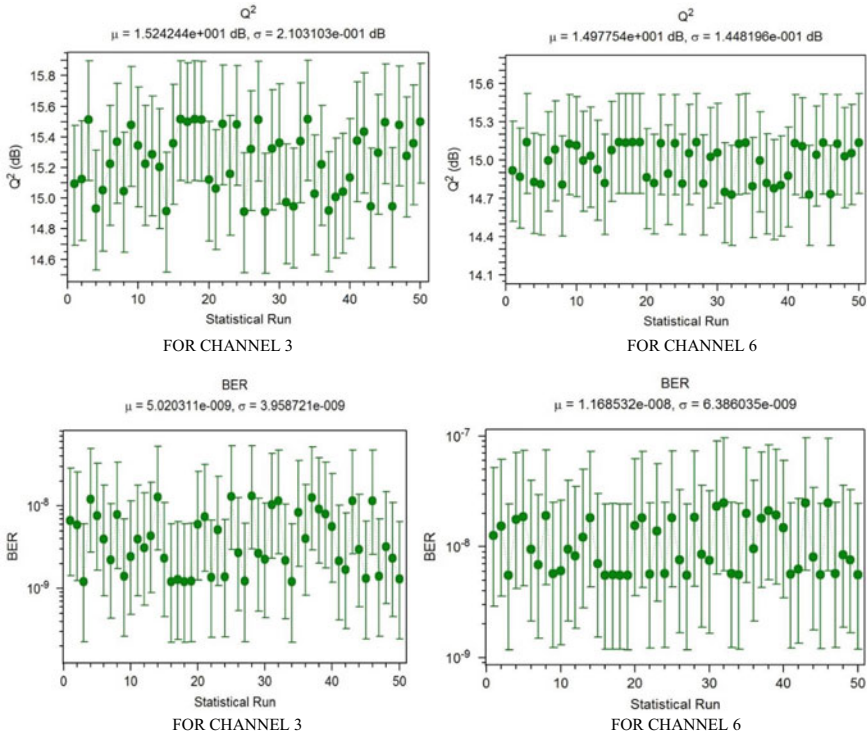


Fig. 6 a Channel performance for randomly varying polarization angles between adjacent channels: (left) example of an odd channel (ch.3); (right) example of an even channel (ch.6). **b** shows the relationship between BER and polarization angle between neighboring channels: (left) example of an odd channel (ch.3); (right) example of an even channel (ch.6)

References

1. How to use WDM for fiber capacity expansion?, Fiber Optic Solutions (2022). <https://www.fiber-optic-solutions.com/use-wdm-fiber-capacity-expansion.html>. Accessed 27 Apr 2022
2. Perlicki K (2015) Polarization effects in optical fiber links. In: Advances in optical fiber technology: fundamental optical phenomena and applications. IntechOpen, London, United Kingdom. <https://www.intechopen.com/chapters/47749>
3. Steve Yao X, Chen XJ (2022) Polarization effects unique to optical fiber systems. In: Polarization measurement and control in optical fiber communication and sensor systems, pp. 37–62. <https://doi.org/10.1002/9781119758488>

Bibliography

4. Nain H, Jadon U, Mishr V (2016) Evaluation and analysis of non-linear effect in WDM optical network. In: IEEE international conference on recent trends in electronics, information, & communication technology(RTEICT)
5. Singh S, Singh S (2017) Limitations on hybrid WDM/OTDM multicast overlay system imposed by nonlinear polarization effect and its mitigation. *IEEE Photonics J* 9:1–11
6. Zhang S, Liu Y, Liu Y, Dorren HJS (2012) All-optical sampling exploiting nonlinear polarization rotation in a single semiconductor optical amplifier. *Opt Commun* 285:1001–1004
7. Yaman F, Li G (2010) Nonlinear impairment compensation for polarization-division multiplexed WDM transmission using digital backward propagation. *IEEE Photonics J* 2(5):816–831
8. Lee J, Park K, Kim C, Chung Y (2002) Effects of nonlinear crosstalk in optical PMD compensation. *IEEE Photonics Technol Lett* 14(8):1082–1084
9. Shao Y, Chi N (2012) High spectral-efficiency 100 Gb/s transmission using DRZ, DQPSK and PolSK three-dimension orthogonal modulation. *Opt Commun* 285(6):1049–1052
10. Yu J et al (2009) 400 GB/s (4×100 Gb/S) Orthogonal PDM-RZ-QPSK DWDM signal transmission over 1040 km SMF-28. *Opt Exp* 17(20):17928–17933
11. Singh S, Singh S (2016) Performance analysis of hybrid WDM-OTDM optical multicast overlay system employing 120 Gbps polarization and subcarrier multiplexed unicast signal with 40 Gbps multicast signal. *Opt Commun* 385:36–42
12. Xie C (2009) Inter-channel nonlinearities in coherent polarization-division-multiplexed quadrature-phase-shift-keying systems. *IEEE Photonics Technol Lett* 21(5):274–276
13. Shao Y et al (2008) Novel optical orthogonally modulation schemes for superimposing DPSK signal on dark RZ signal. *Opt Commun* 281(4):3658–3667
14. Casillas DG, Stepanov S (2010) Polarization insensitive homodyne detection of optical phase modulation by two-wave mixing in saturable ER-doped fiber. *Opt Commun* 283:1134–1137
15. Charlet G, Renaudier J, Bertran Pardo O, Tran P, Mardoyan H, Bigo S (2008) Performance comparison of singly polarized and polarization—multiplexed at 10 Gbaud under nonlinear impairments. In: Presented at the optical fiber communication conference/National fiber optic engineers conference, San Diego, CA, USA, Paper OThU8
16. Zhang Y, Deng N, Chan CK, Chen LK (2008) A multicast WDM-PON architecture using DPSK/NRZ orthogonal modulation. *IEEE Photonics Technol Lett* 20(17):1479–1481
17. Xie X-P, Zhang J-G, Zhao W, Wen Y (2008) Analysis of polarization dependence for OTDM demultiplexers based on four wavelength mixing in semiconductor optical amplifier. *Opt Commun* 281:958–964
18. Samiul Habib M, Ahmad R, Selim Habib M, Razzak SMA (2014) Maintaining single-polarization and dispersion compensation with modified rectangular microstructure optical fiber. *Optik* 125:4030–4034
19. Zhou H, He J, Cao Z, Chen L (2013) All-optical wavelength conversion scheme to reduce the crosstalk among the two multiplexed channels for polarization multiplexing system. *Opt Fiber Technol* 19:549–555
20. Lin M, Zhang Y, Zhang J, Yuan X, Zhang M, Huang Y (2011) Mitigation of nonlinear effects in 112-Gb/s transmission at 50-GHz channel spacing with multi-rate neighbors. In Proceedings international conference SPIE-OSA-IEEE Asia communications and photonics, vol 8309, pp 83092V-1–83092V-6
21. Bock C, Prat J (2005) WDM/TDM PON experiments using the AWG free spectral range periodically to transmit unicast and multicast data. *Opt Exp* 13(8):2887–2891
22. Liu X et al (2009) Experimental demonstration of joint SPM compension in 44 Gb/s PDM-OFDM transmission with 16 QAM subcarrier modulations. In: Proceedings of 25th European conference on optical communication, Paper 2.3.4
23. Singh S, Singh S, Kaur R, Kaler RS. Performance investigation of optical multicast overlay system using orthogonal modulation format. *Opt Commun* 338:58–63, 2015. 4–68, 2016.

24. Agrawal GP (2007) Nonlinear fiber optics, 4th edn. Academic, San Diego, CA, USA
25. Agrawal GP (2002) Fiber-optic communication system, 3rd edn. Wiley, Singapore
26. The Poincaré Sphere, Spie.org (2022). https://spie.org/publications/fg05_p10-11_poincare_sphere?SSO=1. Accessed 27 Apr 2022

The Accomplishment of Quantum Key Distribution via BB84 Protocol with Optical Simulator



Prakash Singh Gill and Sandeep K. Arya

1 Introduction

Measurements in quantum mechanics cause a disturbance that can be used to detect eavesdroppers. This makes key distribution provably secure. [1] Key value stored in a key space K , the message in a message space M , the ciphertext in a ciphertext space C , and the encryption and decryption algorithms E/D make up cryptographic systems. It has been shown that symmetric cryptosystems work if the keys for encryption and decryption are the same, if the key length is alike the message length, and if only once can the random key be used. By the doctrines of quantum mechanics, entanglement, uncertainty, and no-replicating, Quantum cryptography can offer unconditional security.

In Quantum key distribution, a key is produced and distributed but no message data is transmitted. By using the key in combination with any chosen encryption algorithm, a message can be encrypted (and decrypted), which can then be sent over an ordinary communication medium. The one-time pad (OTP) is the algorithm most commonly linked with QKD. The key bits and message bits are XORed together to encrypt messages. Because the secret key can only be used once, the scheme is often referred to as OTP. A shared key must have a size exceeding or identical to the message's span. This has prevented OTP encryption from being widely used. Most commonly, QKD protocols use discrete variables (DVs) based on photon polarization; though continuous-variable (CV) protocols are also developed and demonstrated based on real amplitude measurements instead of discrete events (Fig. 1).

P. S. Gill (✉) · S. K. Arya

Department of Electronics and Communication Engineering, Guru Jambheshwar University of Science and Technology, Hisar 125001, Haryana, India

e-mail: Prakash1751@gmail.com

S. K. Arya

e-mail: Sandeeparya@just.org

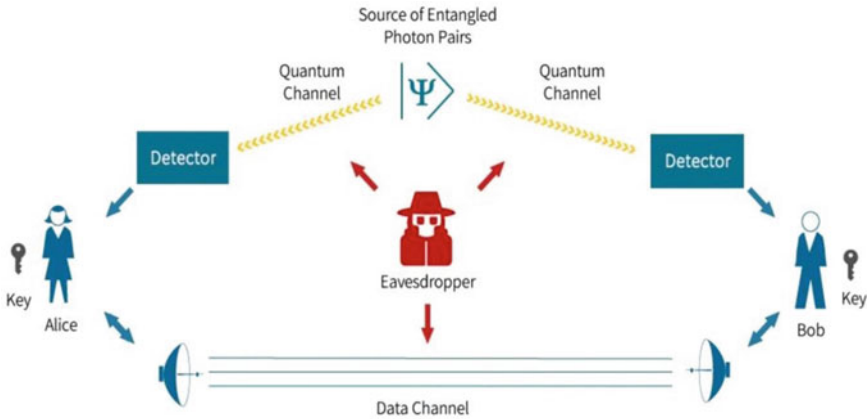


Fig. 1 Demonstrates—In QKD, we use two channels: one for sharing encrypted data and another for sharing decrypting keys between transmitter and receiver. We can detect the presence of an eavesdropper in a quantum channel due to a disturbance in the phase state of photons [2]

1.1 Research Gap and Motivation

There is currently a significant gap in the field of highly secure communication with minimal noise impact. As we know, quantum mechanics is the best option for resolving these two issues. As a result, we studied the QKD BB84 protocol and obtained these important observations on OptSim software.

Indian govt institute DRDO successfully tested a secured QKD implementation between two labs 12 km apart in December 2020, and now recently, DRDO with IIT Delhi collaboration has successfully tested QKD technology between two cities Prayagraj and Vindhyachal which are 100 km apart in February 2022. This has been my motivation for doing this paperwork.

2 Theory

BB84 encrypts every bit from Alice’s arbitrary key in one of the four polarization statuses based on her prepare and measure-procedure (Table 1).

Table 1 Four polarization orientations

Polarization planes	Dirac symbol	Basis	Bit-value
Horizontal-plane	$ H\rangle$	H or V (+)	0
Vertical-plane	$ V\rangle$	H or V (+)	1
Diagonal-plane	$ D\rangle$	D or A (x)	0
Anti-diagonal-plane	$ A\rangle$	D or A (x)	1

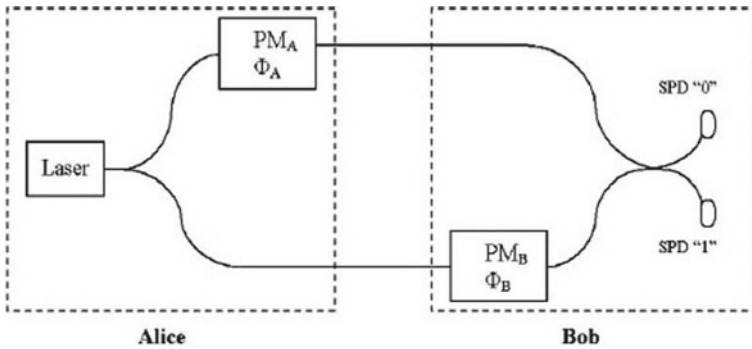


Fig. 2 Setup for BB84 phase coding with QKD. SPD stands for Single photon detector, while PM stands for Phase modulator [3]

2.1 QKD Protocol (BB84) Undertakes the Below Three Stages

1. **Raw Key Interchange:** The quantum channel is Alice’s way of encoding and transmitting each bit of the arbitrary key using polarization orientation encrypting over to Bob. Alice then uses an arbitrary number generator to create an arbitrary key. Every photon Bob measures is produced at random, in either an x or a+ basis, which she records.
2. **Key Selecting:** Alice and Bob talk via a classical channel about their basis choices. The measurements that are not matched basis (about half) are discarded.
3. **Classical Post-Processing:** Bob and Alice execute fault correction and privacy magnification with the classical communication medium. When the QBER exceeds the security edge, the sifted key gets cast off and the BB84 protocol is revived.

Figure 2 shows the BB84 protocol with phasing encoding. It is made up of an interferometer and two-phase modulators, one for Alice and the other for Bob. If the interferometer’s pathways are equal and the laser’s intensity is decreased to a single photon, the strengths at the two single photon detectors (SPDs) are: $I_0 = (\frac{1}{2})(1 + \cos(\varphi_A - \varphi_B))$ and $I_1 = (\frac{1}{2})(1 - \cos(\varphi_A - \varphi_B))$.

When the phase difference between the signal and reference pulses is 0 (bit 0), SPD0 acts and SPD1 acts when the phase difference is r (bit 1).

2.2 Theorems

- I. **Heisenberg Uncertainty Theorem** Even theoretically, it is impossible to calculate both the position and the velocity of an object alongside. A wave-particle duality underpins this principle.

- II. **Quantum Entanglement Theorem** Quantum Entanglement is a property of quantum pairs. When pairs are produced that pretend to be a single entity, these pairs are also called EPR pairs. Each quantum possesses what is known as a “spin”: the spin of one quantum may be up, while the spin of another is down, so the total spin is null, but it is unknown to which pair of quantum the measurement should be attributed until it is made. The wave function of one pair collapses in the opposite state when measured apart.
- III. **Quantum No-Replicating Theorem** Wootters, Zurek, and Dieks identified the quantum no-replicating theorem as a way to prevent duplicates of unfamiliar quantum states from getting made. An observer would be able to accurately measure the copies of a quantum state by copying unknown quantum states and so avoiding the limitations of Heisenberg Uncertainty theorem. Therefore, quantum measuring error improvement routines can’t use backup replicas of quantum states. Also, a quantum signal sent along a quantum channel can’t be amplified by an eavesdropper.

2.3 Photon Polarization

Waves of electromagnetic energy, such as light, produce a magnetic field, which vibrates during their travel. As photons pass through a filter, they are polarized by rotating electromagnetic fields, known as polarization. As a consequence of Heisenberg’s Uncertainty Principle, we cannot know both photons’ values simultaneously if one is measured and its value is affected. Two photons are conjugate when the polarization of one is randomized by the other. Setting up filters 0° and 90° forms one basis, whereas setting filters 45° and 135° forms its conjugate. As photos pass over the polarized beam splitter (PBS), they emerge initially vertically or horizontally before shifting to diagonally polarized photons. When the conjugate basis has been applied, 45° or 135° polarizations will occur with an approximately 1/2 percent probability (Table 2).

Table 2 BB84 implementation with phase encoding

Alice			Bob		Detection
Encoded bit	Alice’s basis	θ_a	θ_b	Bob’s basis	Decoded bit
1	0	π	0	0	1
0	1	$\pi/2$	$\pi/2$	1	0
0	1	$\pi/2$	0	0	?
1	0	π	0	0	0
0	0	0	$\pi/2$	1	?
1	1	$3\pi/2$	$\pi/2$	1	1
1	1	$3\pi/2$	0	0	?
0	0	0	$\pi/2$	1	?

3 Quantum Key Distribution System

Through the use of the simulation package OptSim, this model trades through the BB84 protocol. OptSim tool delivers a diversity of optical communication simulation and modeling. OptSim comprises a diversity of elements linked to photonic telecom elements.

3.1 Simple QKD Configuration

Our central aim is to replicate the QKD experiment with OptSim, which doesn't have built-in components that correlate with QKD operations but seems simpler in shallow. As a passive component of the QKD, the Polarization Beam Splitter functions to permit incoming light depending on its phase. However, OptSim splits photons based on two different angles and cannot be used. There are some elements within the OptSim library that don't perform as QKD elements. In these instances, the components will have to be altered or created.

The OptSim simulation program contains several other libraries that can be incorporated into a simulation as visualizers, such as Power Meters, Polarization Analyzers, and Detectors. The telecommunications system is divided into three major categories, which are transmitter, channels, and receivers. Transmitter blocks are based on photon sources, and OptSim provides a wide array of optical sources with numerous indivisible characteristics. It is essential to attenuate photon pulses in QKD to excerpt their single photon levels. Polarization of the photon is achieved using a polarizer, which adjusts its direction angle to fit the desired direction.

3.2 BB84 Implementation

Utilizing the four polarization states of the quantum channel form to implement the BB84 protocol. As a standard component in OptSim, optical fibers are well-known for channel classification. Incoming photons can be selected via PBS or via random selection using "select". During QKD experiments, the photons are sent to the receiver polarized randomly. When measuring an incoming photon, the receiver also selects a random polarization. In the end, detectors responding to the polarization will activate. Alice and Bob discuss all measurements of photon values in the public channel, explaining the QKD scenario in general. A discrete function can be used to obtain randomness by selecting just the right values for the random index, the least value, the extreme value, and the delta parameters. The true values for these parameters can then be chosen in order to produce correct randomness.

A QKD simulation of the BB84 protocol is shown in Fig. 4.

Table 3 QKD components (Y—Yes and N—No)

QKD_Parameters	Evaluation	
	Availability	Rectifications
Continuous wave laser	Y	N
Bit_seq_generator	Y	N
Modulator (Mod)	Y	N
Opt_attenuator	Y	N
Polarizer_Monitor	Y	Y
Fiber_channel	Y	N
Polarizer beam splitter (PBS)	Y	Y
OptMUX1 (Select)	Y	Y
Receiver1 (RX)	Y	Y

As revealed in Table 3, the components of the QKD are evaluated on various parameters.

4 Results

Figure 5 depicts the input spectrum acquired at the spectrum analyzer (specplt1) in Figs. 3 and 4 of OptSim’s setup of QKD and BB84 protocol implementations.

The input spectrum before polarization is shown in Fig. 5.

Figure 6 shows that after polarization, there is Little interference and T.I.R within the quantum medium.

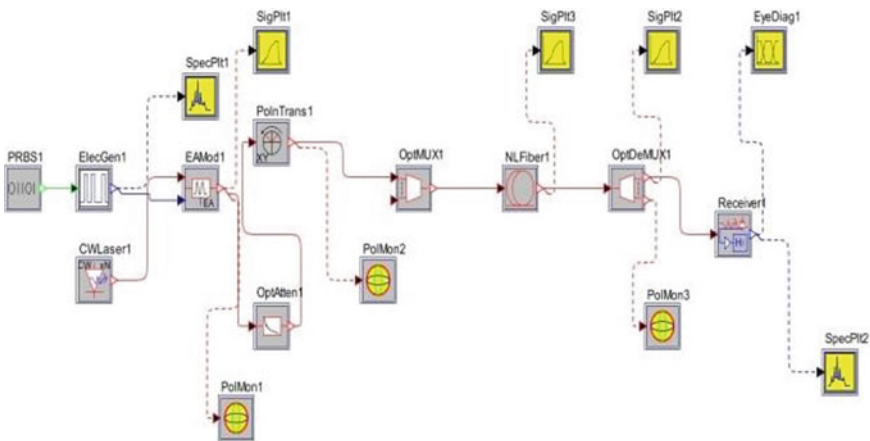


Fig. 3 Setup of the QKD system

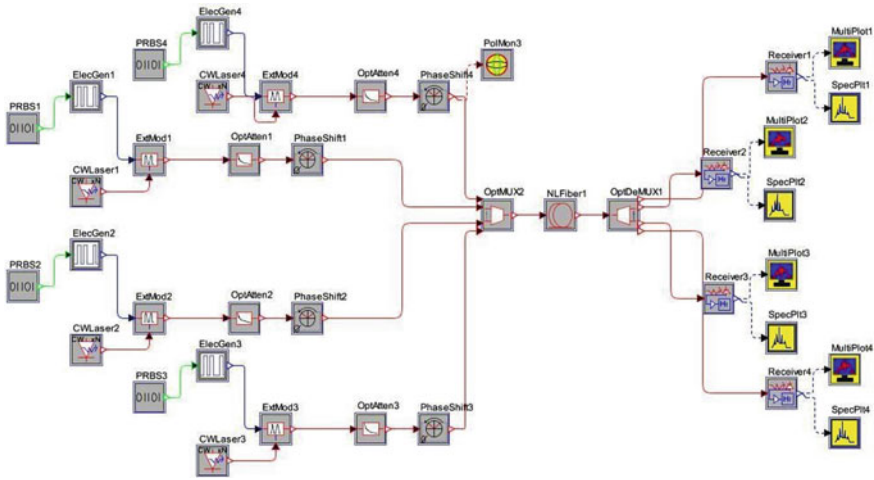


Fig. 4 BB84 QKD setup

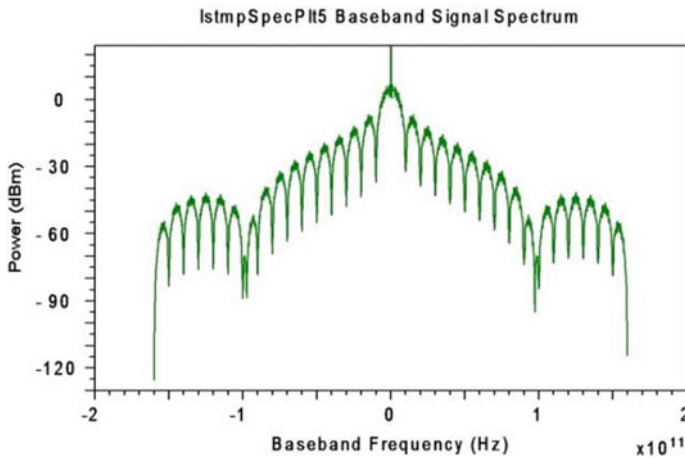


Fig. 5 BB84 and QKD input spectrum

Figure 7 depicts the spectrum of the output quantum channel later key dissemination with a single channel QKD setup. This setup shows that noise has a lower impact on the center band but a greater impact on the sidebands.

In Fig. 8, we demonstrate key distribution on OptSim using the QKD four-channel BB84 protocol setup. This setup shows the noise impact on the frequency sidebands, and the significant center band has been significantly reduced when compared to a single channel QKD setup.

After considering the two spectrums of Figs. 7 and 8, the BB84 protocol in the key distribution procedure has a limited influence on input noise.

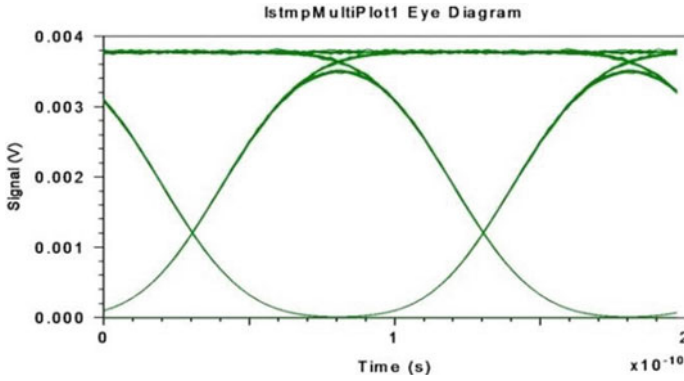


Fig. 6 Eye diagram of QKD

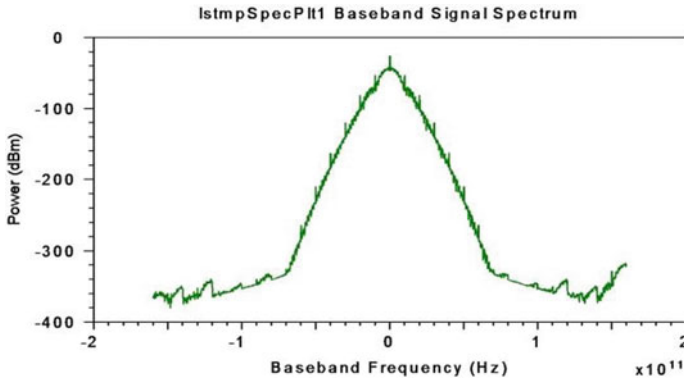


Fig. 7 QKD output spectrum

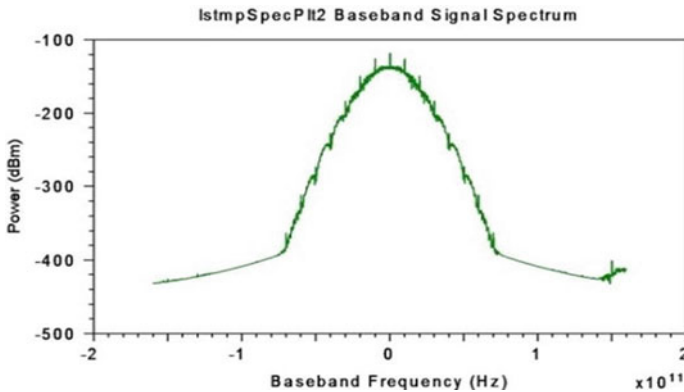


Fig. 8 BB84 output spectrum

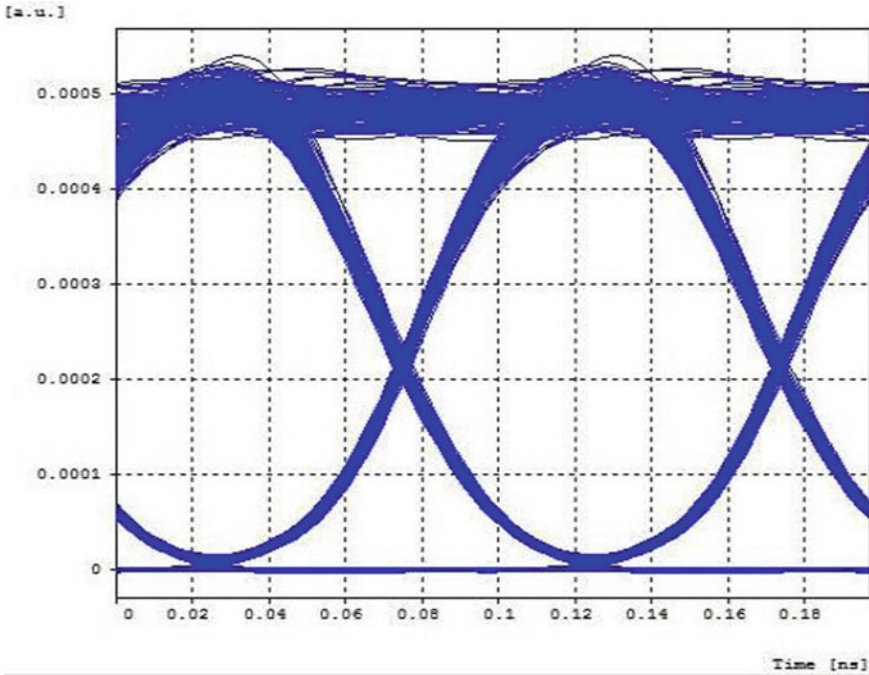


Fig. 9 100 km eye diagram

Figure 9 showing signal amplitude w.r.t time when we take optical fiber length of exactly 100 km.

Figure 10 showing Noise Impact when we take fiber length of 130 km through Eye Diagram.

5 Conclusion

Carrying out the QKD setup using OptSim simulation software and Noise Impact with distance covered is the focus of this paper. At present, QKD networks are available over distances of up to 200 km. To make communication easier, this range needs to be improved. QKD, as mentioned previously, provides unconditional security for key distribution using a protocol paradigm. For effective understanding and study of the QKD protocols, it is necessary to accurately evaluate both paradigms. A component modification is emulated in our paper. In order to determine the best value for each component, we can alter the parameter settings. Among the main advantages is the simplicity of the integration and the fact that any network devices or protocol modifications are not necessary. Choosing appropriate components correctly reduces

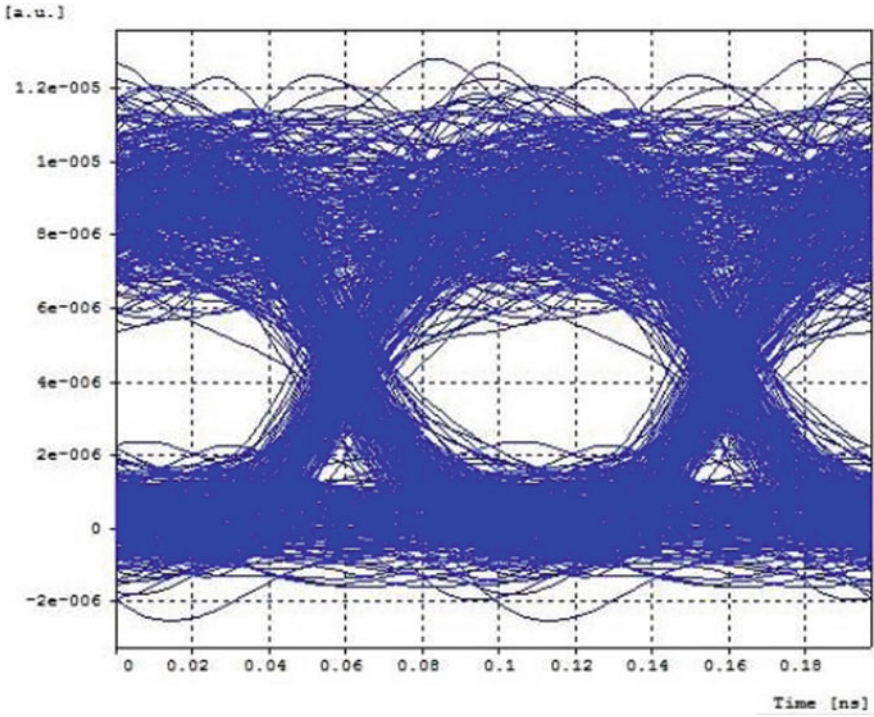


Fig. 10 130 km eye diagram

implementation cost using this simulation framework. A sophisticated Eve’s attack and detector problem can be added to this simulation.

References

1. Dent AW (2008) A brief history of provably-secure public-key encryption. In: Lecture notes in computer science
2. Duplinskiy A, Ustimchik V, Kurochkin Y (2017) Low loss QKD optical scheme for fast polarization encoding
3. The impact of quantum computing on present cryptography, ETSI (2018)

Bibliography

4. Winiarczyk P, Zabierowski W (2011) BB84 analysis of operation and practical considerations and implementations of quantum key distribution systems. In: CADSM'2011, Polyana-Svalyava (Zakarpattya), Ukraine, pp. 23–25
5. Wang Y, Wang H, Li Z, Huang J (2009) Man-in-the-middle attack on BB84 protocol its defence. In: IEEE international conference, pp. 438–439
6. Sharma A, Lakshmanaraj OV, Lenka, SK Security of entanglement based version of BB84 2010.protocol for Quantum Cryptography. In: Computer science and information technology (ICCSIT)
7. Archana B, Krithika S. Implementation of BB84 quantum key distribution using OptSim” IEEE ICECS 2015
8. Lo H-K, Ma X, Chen K (2005) Decoy state quantum key distribution. *Phys Rev Lett* 94:230504
9. Zhao Y, Qi B, Ma X, Lo H-K, Qian L (2006) Simulation and implementation of decoy state quantum key distribution over 60km telecom fiber. In: Proceedings of 2006 IEEE ISIT, pp. 2094–2098
10. Buhari A, Zukarnain ZA, Subramaniam SK (2012) An efficient modeling and simulation of quantum key distribution protocols using OptiSystem. In: Industrial electronics and applications, IEEE symposium, pp. 83–89
11. Poppe A, Schrenk B, Martin V, Aleksic S (2014) QKD in classic optical networks: two different worlds forever? (invited). In: Presented at the international workshop on quantum communication networks leeds, UK
12. Ralph TC (1999) Continuous variable quantum cryptography. *Phys Rev A* 61
13. Grosshans F, Grangier P (2002) Continuous variable quantum cryptography using coherent states. *Phys Rev Lett* 88:057902
14. Tang X, Wonfor A, Kumar R, Penty R, White I (2018) Quantum-safe metro network with low-latency reconfigurable quantum key distribution. *J Lightwave Technol* 36:5230–5236
15. Maroy O, Lydersen L, Skaar J (2010) Security of quantum key distribution with arbitrary individual imperfections. *Phys Rev A* 82:32337
16. Abruzzo S, Kampermann H, Mertz M, Bruß D (2011) Quantum key distribution with finite resources: secret key rates via Rényi entropies. *Phys Rev A* 84:32321
17. Renner R (2005) Security of quantum key distribution, PhD thesis, ETH Zurich
18. Cederlof J (2005) Authentication in quantum key growing, PhD thesis, Linköping University
19. Braunstein SL, Pirandola S (2012) Side-channel-free quantum key distribution. *Phys Rev Lett* 108:130502
20. Gisin N, Ribordy G, Tittel W, Zbinden H (2002) Quantum cryptography. *Rev Mod Phys* 74:145–195
21. da Silva TF, Xavier GB, Temporão GP, von der Weid JP (2014) Impact of Raman scattered noise from multiple telecom channels on fiber-optic quantum key distribution systems. *member,ieee*, vol 32, no 13
22. Waks E, Zeevi A, Yamamoto Y (2002) Security of quantum key distribution with entangled photons against individual attacks. *Phys Rev A* 65:052310
23. Cai QY (2006) Eavesdropping on the two-way quantum communication protocols with invisible photons. *Phys Lett A* 351:1–2
24. Martinez-Mateo J, Ciurana A, Martin V (2014) Quantum key distribution based on selective post-processing in passive optical networks. *IEEE Photonics Technol Lett* 26(9)
25. Eraerds P, Walenta N, Legré M, Gisin N, Zbinden H (2010) Quantum key distribution and 1 Gbps data encryption over a single fiber. *New J Phys* 12

Grid Fault Ride Through Control of a Permanent Magnet Synchronous Generator based Wind Energy Conversion System



Arika Singh  and Kirti Pal 

1 Introduction

Wind energy is being pushed as an important source of renewable energy. The installed capacity and production of electricity through WECS are growing tremendously fast and are expected to grow further as the entire globe is looking for sustainable and clean electricity generation. With the passage of time, the capacity of wind farms has started increasing exponentially and has reached a worldwide total cumulative installed capacity of 750 GW. Wind turbines have now become highly cost-effective with enhanced power ratings even up to 20MW of a unit. As the installed capacity of Wind Turbines is rising, it is becoming important to have a well-proven technology for WECS.

1.1 Literature Review

With the large-scale penetration of wind energy, especially with large independent production centers, possible disconnection of the wind farm due to a temporary fault on the grid side has become a serious concern for grid operators, and therefore, the grid codes are being made stricter. Fault Ride Through (FRT) is an area of active research that has gained considerable importance of late. Paper [1] presents a study on significant electrical aspects of PMSG-based WECS. An inclusive analysis of

A. Singh (✉) · K. Pal
Gautam Buddha Technical University, Greater Noida, Uttar Pradesh, India
e-mail: arikaahuja@gmail.com

A. Singh
KIET Group of Institutions, Ghaziabad, Uttar Pradesh, India

© The Author(s), under exclusive license to Springer Nature Singapore Pte Ltd. 2023
P. Singhal et al. (eds.), *Recent Developments in Electrical and Electronics Engineering*,
Lecture Notes in Electrical Engineering 979,
https://doi.org/10.1007/978-981-19-7993-4_37

445

converter topologies for WTs, digital control schemes, grid integration, FRT compliance methods, and upcoming trends are presented. Ahuja and Kumar [2] presented a review of the different methods used in PMSG FRT. The work is concentrated on the back-to-back VSC-based topology.

When the low voltage fault occurs at the grid side, the grid side converter (GSC) is left incapable of delivering power to the grid side, whereas the machine side converter (MSC) remains unaffected by the fault on the grid side. This is due to the fact that the two converters are interlinked by means of the dc link and the power being injected into the dc link from the MSC keeps on accumulating during the fault. This is due to the fact that wind turbine is producing power but the grid is incapable to take it. This causes the DC link voltage to reach prohibitively high values within a very short duration [3]. All the FRT schemes, therefore, strive to address this issue and try to bring the DC link voltage under control. The most rudimentary method for this would be to use a brake chopper on the dc link side and on detecting a fault, dissipate the extra power from the generator using a brake resistor [4]. However, this method is highly wasteful and thus some form of cross-coupling between the control loops of the GSC and MSC is being introduced in [5]. Herein, on detecting a fault, the power reference of the MSC would essentially be decreased by some form of droop control which is termed the de-loading of the MSC. However, while the MSC is being de-loaded, there is an imbalance of power with respect to the turbine and the machine side. Due to the extra power being supplied to the machine by the turbine, the rotor accelerates and it is possible that speed reaches excessive values. If this happens, pitch control of the blades is brought in, where by the mechanical power injected by the turbine itself is brought down [6]. Many devices, such as SVCs, dynamic voltage restorers, STATCOM, etc., have been shown to improve the FRT of WECS, but they also increase the overall cost of the system [7, 8], especially in WECS with FRC. Akrama Khan et al. [9] and Kim et al. [10] have described the LVRT of WECS by suppressing the overvoltage appearing at the DC link and the active power limitation during an unbalanced fault using the control of positive sequence component through GSC.

1.2 Research Gap and Motivation

The review highlights the lack of a clear consensus on the control of power electronic converters used for various WECS and an inadequate treatment of dynamic issues related to their operation. The variable speed WECS models are more or less generic, and there is still a requirement for well-developed (more accurate) models along with their control capabilities to study the dynamic behavior of WECS under varying wind speed and load conditions. FRT of WTs is becoming an important area of research. The literature available for FRT for fully rated back-to-back converter system is not significant. A complete coordinated control of converters and pitch mechanisms during grid fault conditions would be an interesting topic. LVRT is an important characteristic that a wind farm in a weak power system should possess.

Thus, appropriate controls should be developed to achieve this. Development of advanced wind farms having control capabilities equivalent to conventional power plants is to be done. Their reliability and protective features are to be enhanced. These problems have not been adequately addressed and continue to pose challenges to the control community. WECS control issues are, therefore, important since new grid code requirements are becoming harder day by day. After critically examining the existing literature, it is also realized that the methods for FRT, invariably use some extra control mechanism that kicks in when a fault is detected. The additional circuit is being used in many WECS to control the condition during fault. In almost all the methods, the control of MSC is done for MPPT while GSC is controlled for Grid integration and FRT.

1.3 Contribution

The contribution of this work includes (i) The presentation of a novel control strategy in which the dc link voltage control is taken care of by MSC and MPPT by the GSC. The control of fault is done effectively and the response is made quicker with the proposed FRT method (ii) The proposed method is more effective with no use of any external component while providing the fault ride through.

The proposed FRT method is discussed further in detail in the forthcoming sections with the paper organized as follows. In Introduction Section 1, the basic concepts of FRT have been discussed. Section 2 discusses the system configuration of the conventional and the presented systems. Section 3 looks into the control strategy adopted for the GSC and MSC for the conventional as well as the presented method. Section 4 presents the results of the simulation which is followed by a short inference cum discussion in Sect. 5. Finally, Sect. 6 concludes the work.

2 System Configuration

Figure 1 shows the general configuration of a back-to-back fully rated VSC-based WECS using PMSG. The WECS essentially has two control loops [11]. One is to make sure that the maximum available power is extracted from the wind, and the other is to control the amount of power injected into the grid in a manner that the dc link voltage is stabilized. In other words, conventionally, MPPT is taken care of by the MSC, and dc link voltage stabilization by the GSC.

However, as mentioned before, such a control structure requires additional control measures on the occurrence of a fault. It has been shown that it is quite possible to exchange the functions of the two converters and still be able to get the desired performance along with desirable operation during grid side fault. This methodology has been adopted in this paper to get desirable operation from a PMSG-based WECS during normal and grid fault conditions. In conventional control, when the dc link

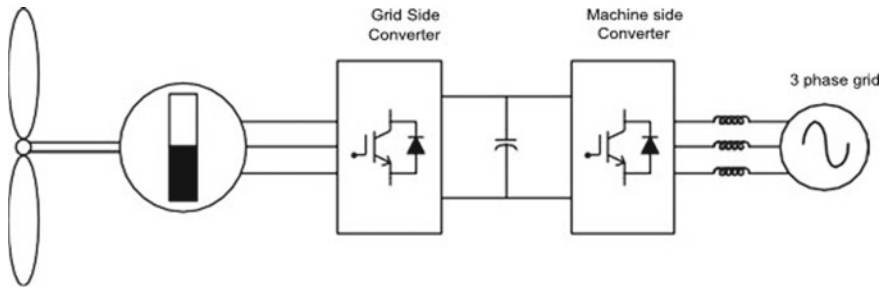


Fig. 1 PMSG-based WECS configuration

voltage rises up, the control loop for dc voltage stabilization essentially increases the active power injection into the grid, thus bringing the dc voltage back to normal [11].

On similar lines, dc voltage regulation may also be done, by taking injected power into the dc link as the controlled parameter. In conventional control, for MPPT, the power injected to the dc link from PMSG is fixed at a particular value depending upon the wind velocity and wind turbine characteristics. However, the same may be affected indirectly by controlling the grid power since the losses during the transfer of power is calculable. Thus is the crux of the logic used for this exchange of roles of the two converters—namely, GSC and MSC—in this method.

3 Control Strategy

3.1 DC Link Voltage Control

The conventional control loop is shown in Fig. 2. The synchronous reference frame is usually used so that the parameters to be controlled become dc values and thus PI controllers may be used. The V_{dc}^* is fixed depending on the magnitude of the grid voltage. The error, ΔV_{dc} is fed to the PI controller, the output of which is deemed to be the I_d^* component of the current to be injected into the grid. This is assuming that the voltage vector is in line with the q-axis of the synchronous reference frame.

The q-axis current component is decided by the amount of reactive power exchange required with the grid. The reference reactive power (Q^*) may further be derived from a grid voltage magnitude controller. A large number of different current control techniques are available in the literature [12].

In the novel control strategy, for dc link voltage control, P_g , the power injected from the machine side may be selected as the control parameter. It may be represented in Fig. 3.

From the basic PMSG modeling equations, we know that

Fig. 2 Conventional control loop for dc link voltage control

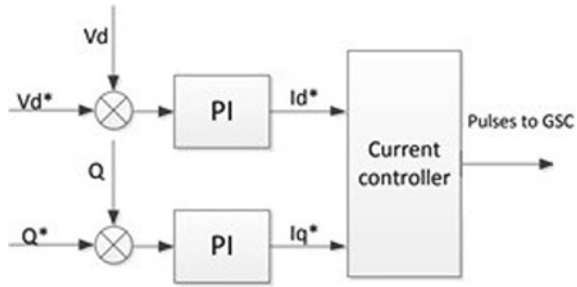
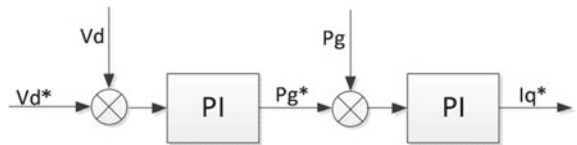


Fig. 3 Control loop for the presented control method



$$T_g = \frac{3}{2} \frac{P}{\omega} \lambda_f i_{qs} \tag{1}$$

where P is the no. of rotor poles, λ_f is the PM flux and i_{qs} is the q-axis stator current. It may also be noted that the above equation is valid only if L_d and L_q are nearly the same. In the case of a surface mount PMSM, assuming these to be equal is a reasonable approximation. It may be noted that the above equation will result only when the d-axis is aligned with the PM flux of the machine, λ_f .

It may also be written as

$$P_g = T_g \omega_r \tag{2}$$

where P_g is the Power injected by the PMSG into the DC link, T_g is the torque generated by the PMSG, and ω_r is the rotor speed. Thus, for controlling P_g , one may control the q-axis current of the PMSG.

3.2 Control for MPPT

The output power of a wind turbine is given by

$$P_t = \frac{1}{2} \zeta A C_p(\lambda, \beta) v_{wind}^3 \tag{3}$$

where ζ is the air density, A is the area swept by the blades, C_p is the power conversion coefficient and v_{wind} is the wind velocity in ms^{-1} . The power conversion coefficient is a function of the tip speed ratio, λ and pitch angle, β and λ is given by

$$\lambda = \frac{w_r R}{v_{wind}} \tag{4}$$

The typical characteristics of a wind turbine are plotted in Fig. 4 [10]. From the curve, it is clear that a particular w_m exists for each wind speed at which maximum power would be extractable from the wind. In other words, in order to maximize C_p , one needs to maintain an optimum tip speed ratio, λ_{opt} . Thus, the turbine speed should be varied linearly with the wind speed.

The conventional method to do this is to find the torque reference for the PMSG [13] and depending on this, find i_q^* (from (1)). An alternate method is to calculate w_r^* for a given wind velocity and compute T_g^* as shown in Fig. 5.

Thus indirectly the power P_g injected into the dc link (from (2)) is being controlled. In the novel method, P_g^* is determined by a similar approach which is as follows. From (3), the maximum power of the wind turbine may be calculated as

$$P_{r \max} = K_{opt} w_{m \text{ opt}}^3 \tag{5}$$

where

$$K_{opt} = \frac{1}{2} \zeta A C_{p \max} \left(\frac{R}{\lambda_{opt}} \right) \tag{6}$$

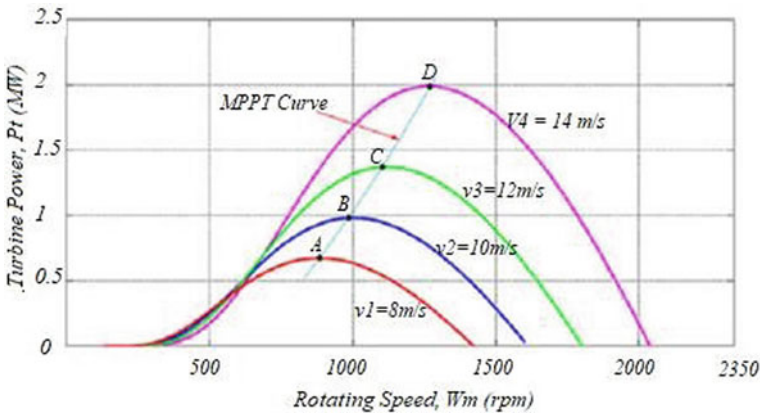
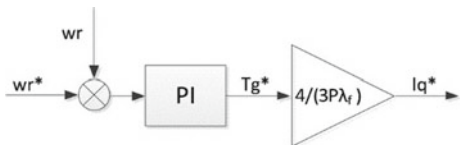


Fig. 4 Typical wind turbine characteristics

Fig. 5 Conventional MPPT control loop



Now, if the PMSG is made to extract P_{\max} from the wind turbine, the machine will be forced to operate at the maximum power point. Thus

$$P_g^* = K_{\text{opt}} w_m^3 \quad (7)$$

In the new control strategy adopted in this paper, MPPT control is done by the GSC. The power injected into the grid can be optimized by estimating the losses in the converters, the DC link, and inertial losses, and subtracting these from the generator power P_g^* at a given wind velocity. Thus

$$P_{\text{grid}}^* = P_g^* - J w_r \frac{d w_r}{dt} - C V_{dc} \frac{d V_{dc}}{dt} - P_{\text{loss}} \quad (8)$$

where J is the moment of inertia, V_{dc} is the dc link voltage and C is the dc link capacitor and P_{loss} is the loss occurring when the power is transferred through the converter across the dc link. Thus on injecting P_{grid}^* , one is able to indirectly control the power being extracted from the wind and MPPT is achieved.

4 Results and Discussion for Normal Conditions

Simulation of the abovementioned method is being done using MATLAB® SIMULINK. For comparison purposes, the conventional method was also simulated without any kind of cross-coupling or brake chopper. The idea is to observe the effectiveness of the new method. Hysteresis current controller has been used for both the converters in both the conventional and the new control methodologies, although voltage oriented control using constant switching frequency could also have been used.

Figure 6 shows the performance of the MPPT of the method. Wind velocity is made to increase in short steps of 0.4 ms^{-1} every 2s as shown in Fig. 6a. Along with the wind velocity, the rotor speed is observed to be increasing in Fig. 6b. The change in rotor speed is proportionate to the change in wind velocity. The active power being proportional to the rotor speed is also trending to increase as demonstrated in Fig. 6c. To demonstrate the linearity between the change in wind velocity and the generator speed, the ratio of wind velocity to rotor speed has also been plotted in Fig. 6d. The optimal ratio for MPPT has been calculated to be $3.33e^{-3}$ and has been shown as a black dashed line in the same figure. The actual ratio is found to closely follow this even with continuous variations in the wind velocity.

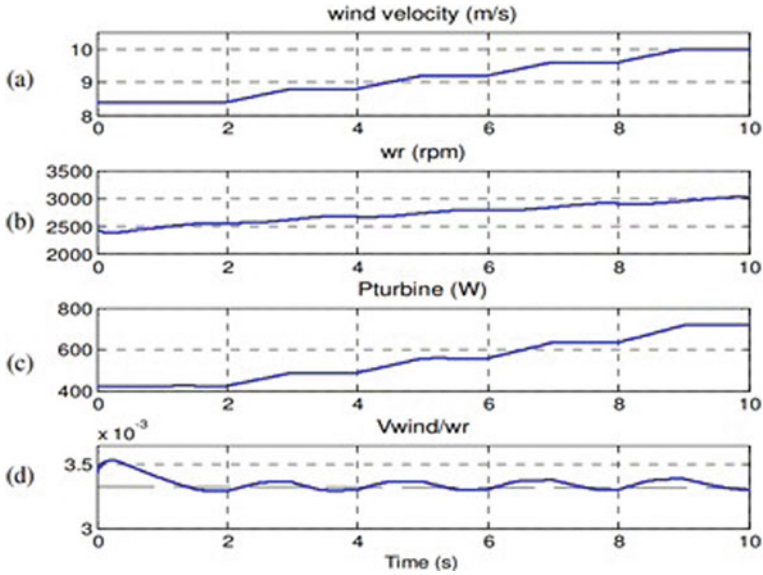


Fig. 6 MPPT performance of the presented method

5 Results and Discussion for Dynamic Conditions

Figure 7 shows the performance of the method under a grid fault condition. A three-phase symmetrical fault has been assumed. Figure 7a shows the phase A voltage at the grid side. Fault duration is between 5 and 5.2 s. Before the fault, the system is stable, as a constant wind velocity of 10.8 ms^{-1} has been assumed at the wind turbine side. The three-phase fault being a symmetrical fault affected the voltage badly and the voltage dropped to 0.1 pu as illustrated. As apparent through Fig. 7b, the dc link is seen to stabilize to its reference value of 700 V. On the occurrence of the fault, the dc link voltage is seen to rise but the variation is seen to be less than 2%. This shows the effectiveness of the controller and its quick action during fault. In Fig. 7c, clearly turbine power does not change much during the fault. However, due to the fault, the grid power has gone down to a very low value. In order to stabilize the dc link voltage, the control algorithm reduces P_g^* in the machine side converter and thus P_g reduces following P_{grid} .

Since, P_{turbine} remains the same throughout, the rotor speed increases as is seen clearly in Fig. 7d. If the rotor speed increase to exceedingly high values, it would be required to decrease the mechanical power being injected by the turbine, itself. Thus, the pitch control mechanism would have to be activated at high rotor speeds

Figure 8 shows the response for a similar fault happening on the grid side for a conventional control algorithm without any cross-coupling or any brake chopper. The idea is to observe how large the variation of the dc link voltage (see Fig. 8a) can be if proper control measures are not taken. The fault is for the same duration

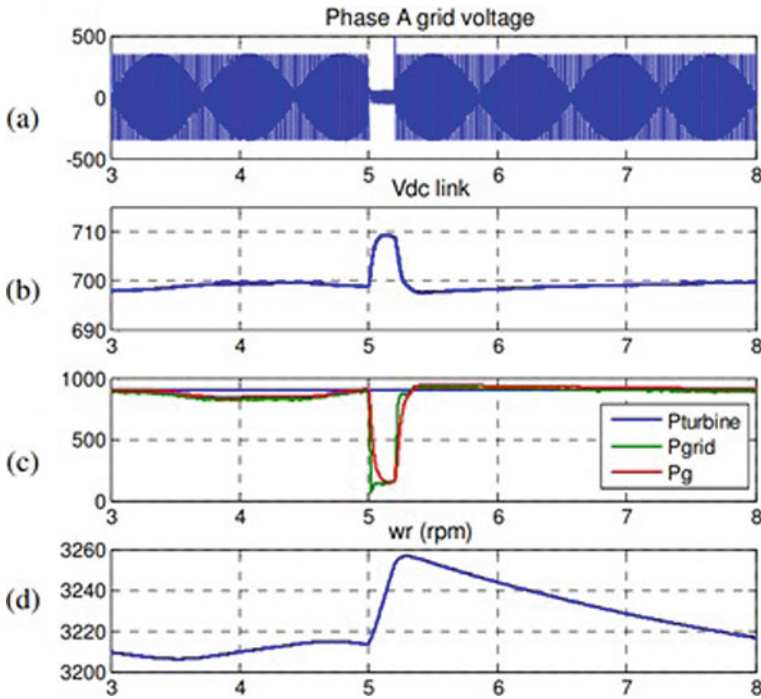


Fig. 7 Performance during grid side fault

as in the case of Fig. 7. DC link voltage V_{dc} is seen to rise up to around 770 V. This variation is as large as 10%. Also, from Fig. 8b, it is seen that the machine power, P_g does not decrease, during the fault, which is of course the reason why the dc link voltage has increased. Also, the P_{grid} is observed to have large oscillation which is highly undesirable. $P_{turbine}$ is seen to be constant just as in the last case. The rotor speed in Fig. 8c is seen to be roughly constant during the fault as the machine side converter is unaffected by the fault. On the whole, it is to be understood from the results of both simulations that during grid side fault, when the dc link voltage increase is prevented as in the new method, the rotor speed would increase, whereas in the conventional method, dc link voltage increases when the rotor speed is largely unaffected. However, typically, for PMSG-based WECS, the rating of the machine being large (order of MW), the moment of inertia of the machine-turbine set would as well be quite large. Thus, for short-duration faults, it is reasonable to assume that the rotor would not run away to exceedingly high speeds and that the need to use a pitch control mechanism would be minimum during faults which clears itself in a short duration.

Transfer function between the dc link voltage and machine injected power, P_g , is highly nonlinear. Thus, using a PI controller for the same creates a high probability for the system to produce limit cycles or chaotic oscillations. Such oscillations were also observed initially. The parameters of the PI controller were tuned by the Modulus

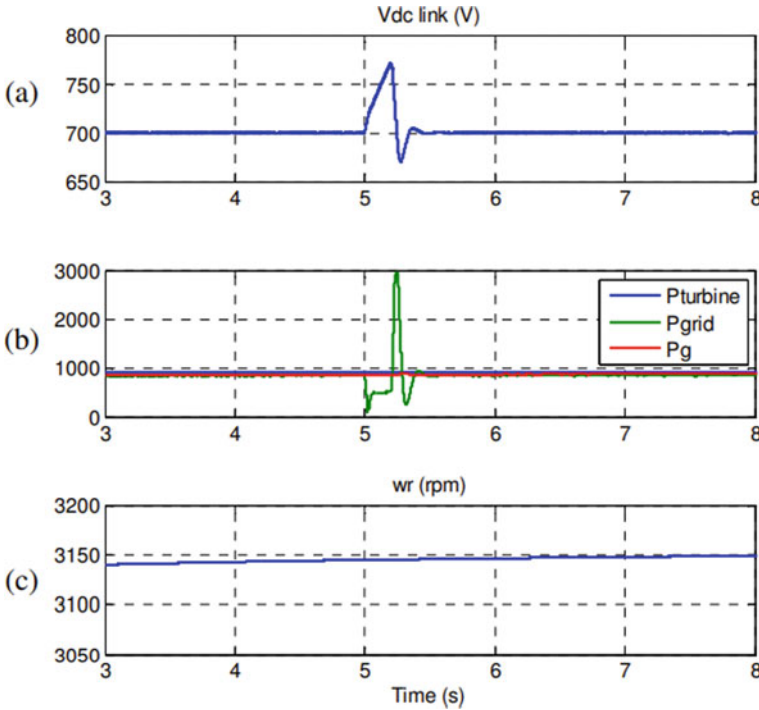


Fig. 8 Conventional method during grid side fault

optimum method. The problem was circumvented by putting a saturation block at the output of the $J \cdot dw/dt$ term (3). This limit had to be dynamically set as well since a very low limit would have made the MPPT response sluggish and a high limit would have caused limit cycle oscillations. The dynamic limit was set by observing the ratio of wind velocity to rotor speed. Until this ratio approaches a previously defined optimum value, a higher saturation limit was used and once the ratio is within a pre-defined band, the limit is reduced to a lower value. This method effectively helped to improve the response of MPPT as well as to reduce the limit cycle oscillations without using any feedback linearization techniques.

6 Conclusion

A novel method of control, with the role reversal of MSC and GSC, of fully rated back-to-back connected VSCs-based WECS has been presented. In conventional control, for MPPT, the power injected to the dc link from PMSG is fixed at a particular value depending upon the wind velocity and wind turbine characteristics. However, it is realized that the same may be affected indirectly by controlling the grid power since

the losses during the transfer of power are calculable. This is the crux of the logic used for this exchange of roles of the two converters—namely, GSC and MSC—in this method. To observe the control method's effectiveness in tackling the problem of dc link voltage rise during symmetrical grid fault, the proposed strategy and simulations have been demonstrated. The control strategy adopted also takes care of MPPT during normal operation under varying wind velocity conditions. Response of the MPPT has been made faster using an adaptive saturation limit used inside the control algorithm although simple PI controllers are adopted in both GSC and MSC control loops. The same method is equally applicable for Squirrel cage induction machine-based WECS using back-to-back VSC as well, though this work has considered a PMSG-based system.

References

1. Ramesh Babu N, Arulmozhiarman P (2013) Wind energy conversion systems—atechnical review. *J Eng Sci Technol* 8(4):493–507
2. Ahuja H, Kumar P (2019) A novel approach for coordinated operation of variable speed wind energy conversion in smart grid applications. *Elsevier Comput Electr Eng* 77:72–87
3. Brando G, Coccia A, Rizzo R (2004) Control method of a braking chopper to reduce voltage unbalance in a 3-levelchopper. In: *IEEE international conference on industrial technology ICIT*, vol 2, pp 975–978
4. Heng N, Jiao L, Peng Z, Yikang H (2008) Improved control strategy of an active crowbar for directly-driven PM wind generation system under grid voltage dips. In: *IEEE conference on electrical machines and systems*, pp 2294–2298
5. Junyent-Ferre A, Prieto Araujo E, Gomis Bellmunt O, Bianchi F (2011) Voltage sag ride through of PMSG wind turbines using droop control stabilization. In: *Power electronics and applications*, pp 1–8
6. Ahuja H, Bhuvaneshwari G, Balasubramanian R (2012) Ride through of grid faults for permanent magnet synchronous generator based wind energy conversion systems. In: *IEEE international conference on industrial and information systems, ICIIS*
7. Mosaad MI (2018) Model reference adaptive control of STATCOM for grid integration of wind energy systems. *IET Electr Power Appl* 12(5):605–613
8. Nasiri M, Milimonfared J, Fathi SM (2015) A review of low-voltage ride-through enhancement methods for permanent magnet synchronous generator basedwind turbines. *Renew Sustain Energy Rev* 47:399–415
9. Khan A, Ahmad H, Ahsan SM, Gulzar MM, Murawat S (2021) Coordinated LVRT support for a PMSG based wind energy conversion system integrated in to a weak AC-grid. *Energies* 14(20):6588–6599
10. Kim KH, Jeung YC, Lee DC, Kim HG (2012) LVRT Scheme of PMSG Wind Power Systems Based on Feedback Linearization. *IEEE trans on power electronics*, 27
11. Chinchilla M, Arnaltes S, Burgos JC (2006) Control of permanent-magnetgenerators applied to variable-speed wind-energy systems connected to the grid. *IEEE Trans Power Electron* 21
12. Tryznadlowski AM (1996) An overview of modern PWM techniques for three phase voltage controlled voltage source inverters. In: *Proceedings of the IEEE international symposium on industrial electronics*, vol 1, pp 25–39
13. Nakamura T, Morimoto S, Sanada M, Takeda Y (2002) Optimum control of iPMSG for wind generation system. In: *Proceedings of the power conversion conference, Osaka*, vol 3, pp 1435–1440

DTMOS Based Squarer Circuit and Its Application in Controllable Gaussian Function Generator



Sanjeev Kumar Yadav, Shweta Kumari, Maneesha Gupta,
and Ritu Raj Singh

1 Introduction

Low voltage application is becoming a new concern in the modern electronic world of low-power circuits. Sustaining the pattern of reducing more and more voltage and using less power becomes quite a difficult task. To cope with the challenge, low voltage techniques such as selfcascode, bulk driven, level shifters, sub-threshold, floating gate, and DTMOS [1–8] can be used. DTMOS concept is one of the key techniques that comes with the idea of tying bulk and gate of the transistor together. The dynamic threshold voltage MOSFET circuit fulfills the need for lowering the threshold voltage of a MOSFET. Signal levels can also be shifted by the use of varying threshold voltage property of DTMOS and even work below the operational values specified for a particular technology.

In this paper, proposed analog squarer circuit is used for designing of GFG. The squarer circuit has input voltage and output current. It has high input impedance and good compatibility to match with other topologies. The GFG circuit is the application of the proposed squarer circuit. The Gaussian function is the distributive function which shows the distribution of the random variable in a bell shape curve. It has been greatly used in data classification, on chip diffusion profile, matching pattern algorithms and neural networks and its application. Silicon area and power dissipation

S. K. Yadav (✉) · M. Gupta · R. R. Singh

Department of Electronics and Communications, Netaji Subhas University of Technology,
Dwarka, New Delhi, India

e-mail: sanjeevk.ev20@nsut.ac.in

R. R. Singh

e-mail: rituraj.singh@nsut.ac.in

S. Kumari

Department of Electronics and Communications, Bharati Vidyapeeth's College of Engineering,
New Delhi, India

reduces due to the implementation of GFG on analog hardware circuits. A Gaussian function based upon the second-generation current controlled current conveyor (CCCII) is implemented in Refs. [9, 10] which is based on a differential coupled amplifier (using two differential pairs). The FGMOS-based Gaussian circuit in Ref. [11] is implemented by replacing the MOSFETs in the conventional CMOS circuit, which are used as variable resistors. Reference [12] is also an implementation of the Gaussian function which includes the current mirror configuration, biased in the weak inversion, serially connected with voltage-controlled MOS transistors working as resistors in linear operation mode. But they have the problem of MOS transistor mismatching and only half part of the Gaussian function curve can be obtained. Analog squarer of Refs. [13, 14] is a good choice but more high input impedance is desirable. Therefore, the proposed squarer serves the purpose and by using this, the application of GFG is implemented.

This paper is arranged in 5 sections: Sect. 1 contains the introduction, and the proposed analog squarer circuit is described in Sect. 2. Controllable Gaussian function generator (GFG) based on the proposed squarer circuit is mentioned in Sect. 3. Several simulation results are conducted to test the effectiveness of the proposed and application circuit. They are described in Sect. 4 and in the last section, conclusions are made.

2 The Proposed Analog Squarer

2.1 Proposed Analog Squarer Principle

The proposed analog squarer is the modified form of the squarer circuit used in Ref. [13]. It consists of seven MOS transistors, operating in the saturation region. MOS Transistors M_1 and M_2 in Fig. 1 are used in the current mirror configuration that uses the DTMOS principle in which the gate and bulk of respective transistors are connected together Ref. [15]. The expression of V_{th} is given as:

$$v_{th} = v_{t0} + \gamma \left(\sqrt{|2\phi_F| + v_{SB}} - \sqrt{|2\phi_F|} \right) - \eta VDS \quad (1)$$

where V_{th} is the threshold voltage (when $V_{SB} \neq 0$), V_{t0} is the threshold voltage when no body bias is taken. γ is the body effect coefficient which depends on intrinsic parameters of the device. ϕ_F is surface potential at threshold (typically $|2\phi_F|$ equals 0.6 V). V_{SB} is the source-to-body voltage. The term ηVDS represents the effect of drain induced barrier lowering (DIBL) in which η is DIBL coefficient [15] and it is in the range of 0.02–0.1. The implementation of DTMOS on a squarer circuit, lowers V_{th} when high input is applied during the ON state of the transistor and when low input is applied then V_{th} becomes high. It also prevents leakage current and high

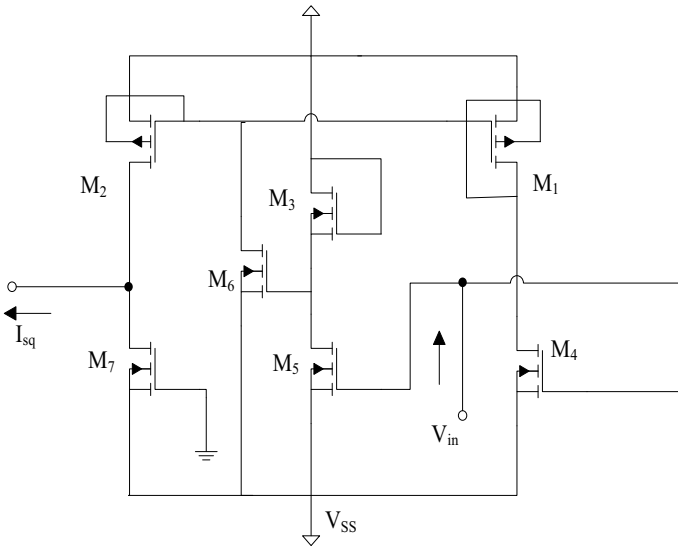


Fig. 1 The proposed squarer circuit

power consumption. The threshold voltage of analog squarer is changed according to the input applied and become a very effective technique to be used in low power application. The overall DTMOS gate capacitance is much larger than conventional MOS gate capacitance, but a larger driving current overcomes this problem and makes DTMOS enhanced circuit works faster. The bulk of rest transistors inside the proposed squarer circuit is tied to its respective sources, preventing body effect. M₃ and M₅ are arranged as a unity gain inverting amplifier, ignoring channel length modulation effects. All transistors have the same transconductance parameter k_n except M₇ is taken as $2k_n$. Drain currents of M₄, M₆ and M₇ are expressed as

$$I_{D4} = \frac{1}{2}k_n(v_{in} - v_{SS} - v_{TN})^2, \tag{2}$$

$$I_{D6} = \frac{1}{2}k_n(-v_{in} - v_{SS} - v_{TN})^2, \tag{3}$$

$$I_{D7} = k_n(-v_{SS} - v_{TN})^2, \tag{4}$$

Hence, the final output current (I_{out}) of the proposed analog squarer is obtained as follows:

$$I_{out} = I_{D4} + I_{D6} - I_{D7} \tag{5}$$

$$= k_n(v_{in})^2 \tag{6}$$

From Eq. (6), the floating branch, where output (I_{out}) is taken, directly proportional to V_{in}^2 by a factor of proportionality constant (k_n). The following condition must be satisfied to operate the circuit in the usual mode.

$$V_{SS} + V_{TN} < V_{in} < \frac{V_{TN}}{2} \quad (7)$$

3 Application: Gaussian Function Generator

Gaussian Function is implemented when the exponential function is applied to the quadratic function. The input to the quadratic function is taken as variable x and raising it to the negative power of an exponential, gives the expression of gaussian function y which is expressed as

$$y = Ae^{\frac{-x^2}{2\sigma^2}} \quad (8)$$

where 'A' is the amplitude of the Gaussian function and standard variance (σ) defines the base of the gaussian function. If the logarithm of the function is taken, the resulting term is a quadratic function of input. The input voltage of squarer circuit is first get squared. The squarer circuit uses current–voltage square law characteristics of the transistors in the saturation region. The output of squarer feeds as an input to the current mirror configuration operated in the weak inversion region for a generation of exponential characteristics of GFG.

3.1 Gaussian Function Generator Principle Designed Using Proposed Squarer

In Fig. 2 all transistors from M_8 – M_{11} constitute an exponential part of the GFG. M_8 and M_9 is in the current mirror configuration with two serially connected gate voltage-controlled resistors using transistors M_{10} and M_{11} attached to the sources of transistors of M_8 and M_9 respectively. When the squarer current I_{sq} is zero and the MOS implemented resistors are identical to each other, then current I_r will be the same as I_{out} . I_r is the reference current set at a very low value that enables MOS transistors M_8 and M_9 to operate in the weak inversion region. The drain current of M_8 and M_9 can be expressed as [12]

$$I_r = I_{D0} e^{\left(\frac{-v_{GS}}{nV_T}\right)} \left(e^{\left(\frac{-v_{SS}}{V_T}\right)} - e^{\left(\frac{-v_{DS}}{V_T}\right)} \right) \quad (9)$$

$$I_{OUT} = I_{D0} e^{\left(\frac{-v_{GS}}{nV_T}\right)} \left(e^{\left(\frac{-v_{S9}}{V_T}\right)} - e^{\left(\frac{-v_{D9}}{V_T}\right)} \right) \quad (10)$$

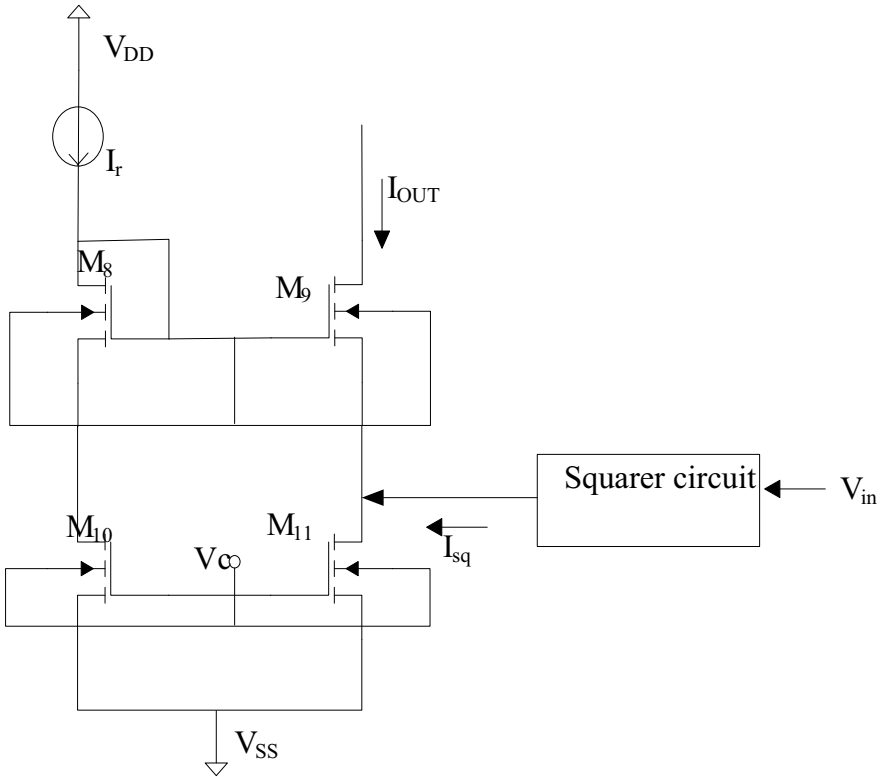


Fig. 2 Circuit diagram of the GFG using proposed squarer

Where $V_t = kT/q$, η is the subthreshold slope factor, I_{D0} is the process dependent parameter which depends on the threshold voltage and source-bulk voltage (V_{SB}). The condition under which M_8 and M_9 are in the weak inversion. It can be approximated as [6]

$$V_{GS8}, V_{GS9} < V_{T8,9} + \eta V_T \tag{11}$$

Since V_{D8}, V_{D9} are much greater than V_T , Eqs. (9) and (10) can be reduced to (12) and (13) respectively.

$$I_r \cong I_{D0} e^{\left(-\frac{v_{G8}}{\eta v_T}\right)} e^{\left(-\frac{v_{S8}}{v_T}\right)} \tag{12}$$

$$I_{OUT} \cong I_{D0} e^{\left(-\frac{v_{G9}}{\eta v_T}\right)} e^{\left(-\frac{v_{S9}}{v_T}\right)} \tag{13}$$

Again $V_{G8} = V_{G9}$ (Fig. 2), So, combining (12) and (13) leads to

$$I_{OUT} \cong I_r e^{\left(\frac{v_{S8}-v_{S9}}{v_T}\right)} \tag{14}$$

From Fig. 2, it is evidently clear that sources of M_8 and M_9 are in contact with the drain of M_{10} and M_{11} respectively. Putting the value of V_{S8} and V_{S9} in Eq. (14) gives

$$I_{OUT} \cong I_r e^{\left\{\frac{(I_r/g_{ds10})-(I_{OUT}/g_{ds11})-(I_{sq}/g_{ds11})}{v_T}\right\}} \tag{15}$$

where g_{ds10} and g_{ds11} are the output conductance of transistors M_{10} and M_{11} respectively.

Assume I_r is greater than I_{OUT} and I_{sq} is greater than both the former and the latter. Very small reference current I_r is used to bias the current mirror in weak inversion so that the output current can be approximated as

$$I_{OUT} \cong I_r e^{\left\{\frac{-(I_{sq}/g_{ds11})}{v_T}\right\}} = I_r e^{\left(-\frac{v_{S9}}{v_T}\right)} \tag{16}$$

From above expression, output current (I_{OUT}) of GFG is directly proportional to negative exponential of the output for squarer circuit (I_{sq}). It linearly modifies the voltage (V_{S9}) of M_9 transistor. Considering the source grounded, V_c is the control voltage that makes the transistor M_{10} and M_{11} to work in the linear region. The current expression in the linear region for transistor M_{11} is as follows.

$$I_D = \beta_{11} v_{D11} \left[v_C - v_{T11} - \frac{v_{D11}}{2} \right] \tag{17}$$

The control gate voltage (V_c) determines the output conductance of M_{11} . Its expression can be approximated as

$$g_{ds11} \cong \beta_{11} (v_c - v_{T11}) \tag{18}$$

For linear operation, the condition is

$$(v_c - v_{T11}) \gg v_{D11}, v_{S9} \tag{19}$$

Putting the expression of g_{ds11} and I_{sq} in (16), the final output function of the GFG is approximated as

$$I_{OUT} \cong I_r e^{\frac{(kv_{in})^2}{v_T \beta_{11} (v_c - v_{T11})}} \tag{20}$$

where I_r is the reference DC current of the exponential part of GFG used for biasing the circuit, V_T is the temperature volt equivalent and V_{in} is the input voltage of the squarer.

Equations (20) and (8) are similar and Eq. (20) has taken the form, provided $x = (kv_{in})$. Control input v_C defines the sigma value (σ) in (8). It also decides the width of the Gaussian function. For the lower limit calculation of I_{OUT} , maximum input currents I_{sq} sets the upper limit for the V_{S9} and the minimum value of V_C is obtained. So (16) can be rewritten as

$$I_{out\ min} = I_r e^{\frac{v_{S9\ max}}{v_T}} \quad (21)$$

The upper limit of $V_{S9\ max}$ can be determined while considering 10-bit precision over the output current. It is given as

$$I_{out\ min} = \frac{-I_r}{2^{10}} = I_r e^{\frac{v_{S9\ max}}{v_T}} \quad (22)$$

$$V_{S8\ max} = V_T \ln(1024) \quad (23)$$

To satisfy (19), the value ($V_{cmin} - V_{T11}$) should be greater than 180 mV and the maximum value should be the supply voltage.

The conductance g_{ds11} is varied in the given condition as

$$\beta_{11}(v_{DD} - v_{T11}) \geq g_{ds11} \geq \beta_{11}(v_{Cmin} - v_{T11}) \quad (24)$$

Using (8) and (24), the maximum swing of sigma (σ) can be expressed as

$$\frac{\sigma_{max}}{\sigma_{min}} = \sqrt{\frac{g_{ds11\ max}}{g_{ds11\ min}}} = \sqrt{\frac{(v_{DD} - v_{T11})}{(v_{Cmin} - v_{T11})}} \quad (25)$$

4 Simulation Results

Simulation results of the proposed circuits are obtained using 0.18 μ m CMOS technology under ± 0.4 V supply voltage. The dimensional sizes of used transistors in the proposed circuits (Figs. 1 and 2) are tabulated in Table 1. The functionality and performance of the GFG circuit are verified through various simulation results. Figure 3 shows DC response of the proposed squarer output and all simulations are done when input V_{in} is swept from the range of ± 0.3 V. In the GFG circuit, V_C can be varied from 0.1 to 0.3 V. At a supply voltage of 0.095 V, transistor M_{11} traverse from the linear region to the saturation region.

Figure 4 shows variations in the peak of the Gaussian curve with respect to a bias reference current (I_r), varying from 50 to 150 nA. Figure 5 shows variation in the width of Gaussian output with respect to different values of control voltage (V_C). In Table 2, the reference current I_r is varied from 0.050 to 0.150 μ A with the step increase of 0.050 μ A. Table 2 gives relative error (%) in Gaussian output current for

Table 1 Transistor’s aspect ratio of Figs. 1 and 2

Transistors	W (μm)	L (μm)
M1	100.0	1.0
M2	100.0	1.0
M3	10.0	1.0
M4	10.0	1.0
M5	10.0	1.0
M6	10.0	1.0
M7	20.0	1.0
M8	0.9	0.18
M9	0.9	0.18
M10	0.9	0.18
M11	0.9	0.18

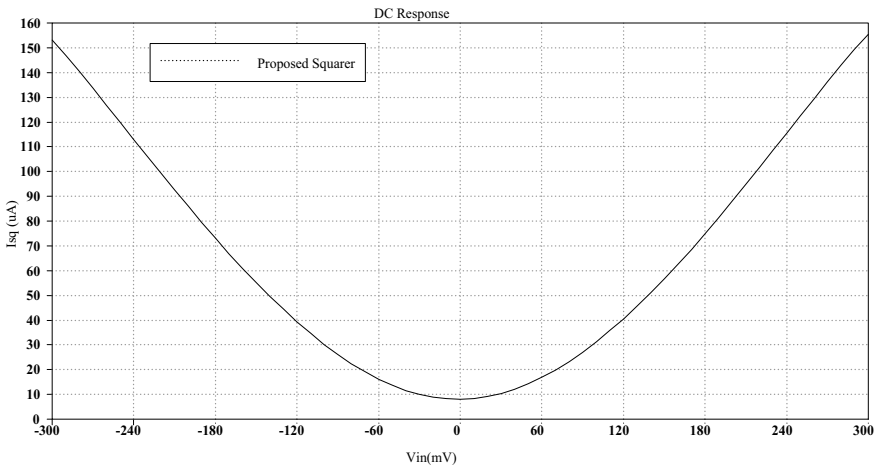


Fig. 3 The proposed squarer output when V_{in} ranges from -300 to $+300$ mV

different values of the control voltage (V_C) and reference current (I_r) fixed at 50 nA for best Gaussian curves. The percentage relative error in output current is stated as

$$E_r = \frac{I_{out} - I_r}{I_r} \times 100\% \tag{26}$$

It has been found that the percentage error is 0.19% at $V_C = 0.101$ V which is very low when compared with the work mentioned in Table 3 and constitutes a good implementation of the Gaussian application. From comparison Table 3, it can be concluded that all mentioned references have high operating voltage which consumes more power and does not fit in the low voltage application designs. In

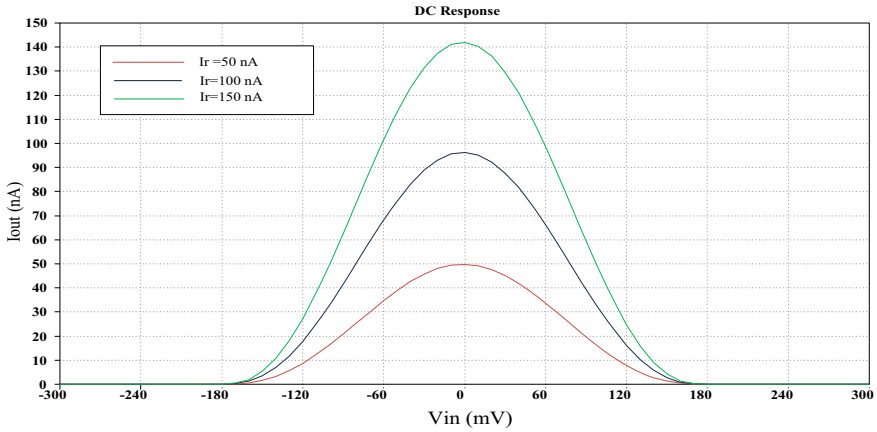


Fig. 4 Gaussian profile with the controllable peak for different I_r

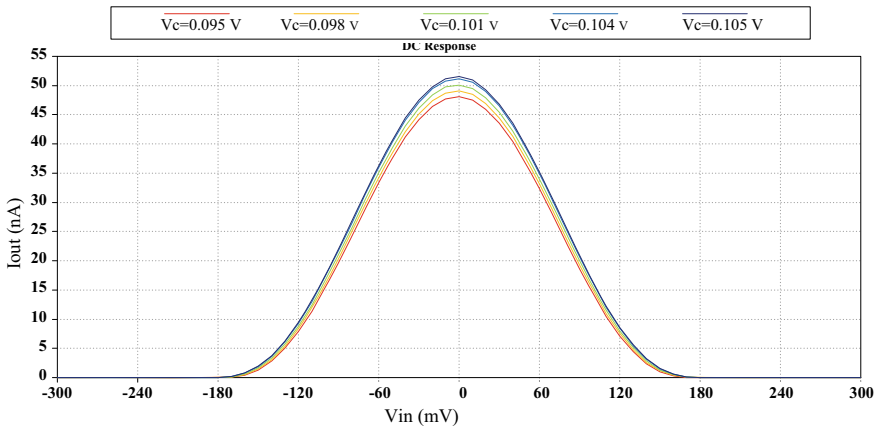


Fig. 5 Gaussian profile with the controllable width

Table 2 Relative error in output for different control voltage at $I_r = 50$ nA

I_r (nA)	50				
V_c (V)	0.095	0.098	0.101	0.104	0.105
I_{out} (nA)	48.11	49.09	50.10	51.17	51.53
E_r (%)	-3.92	-1.85	0.19	2.28	2.96

comparison with Refs. [9, 10, 12], they are using more bias currents or voltages. To operate the circuit in the weak inversion region, I_r is taken between 35 nA and 5 μ A. The dissipated power of the proposed circuit is 0.197 mW which is comparatively low.

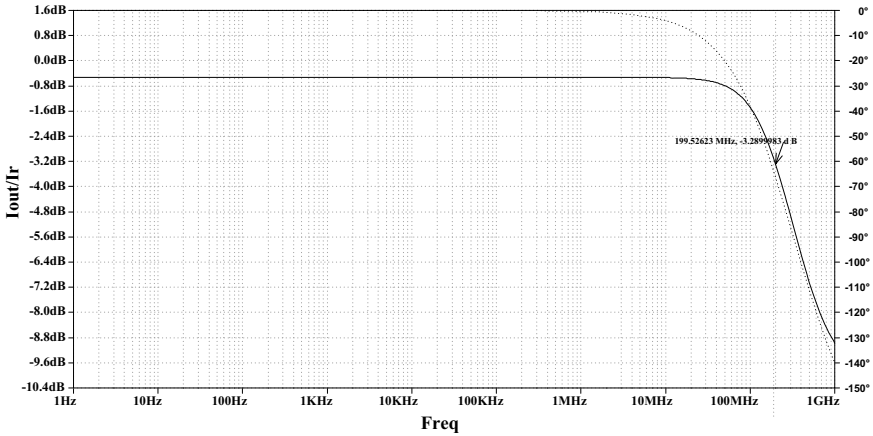


Fig. 6 Frequency response of GFG designed using proposed squarer

Figure 6 shows the frequency response of the exponential part of GFG. It can be seen that 3 db bandwidth of approximately 200 MHz is achieved which is also higher than Ref. [16] and other work mentioned in Table 3.

5 Conclusion

In this paper, a voltage squarer circuit has been proposed which is used to implement the fully programmed GFG. The input voltage of the squarer is squared and its equivalent current as the output is fed into the current mirror operated in weak inversion mode. This work is efficiently good as compared to previously reported work. The GFG consumes 0.197 mW operated at ± 0.4 V and, has -3 dB bandwidth approximately of 200 MHz. Both peak and mean of the Gaussian circuit can be controllable independently. The high output impedance of the proposed squarer circuit, makes it suitable to become highly cascadable for other topologies such as the current mirror to work in accordance with the squarer circuit and to use it for implementing the application such as the Gaussian circuit.

Table 3 Performance comparison of previously reported work and this work

	Technology (nm)	Supply voltage (V)	Bias current/voltage	Bandwidth (MHz)	Error (%)	DC power dissipation (μ w)	In-Out signals	No. of transistors
Pour and Mashoufi [9]	350	3.3	9 μ A	–	–	220	Voltage-Current	14
Abuelma'atti and Al-Abbas [10]	–	\pm 1.2	60 μ A	–	2.74	–	Voltage-Current	21
Srivastava et al. [11]	250	3.3	–	277.686	–	214	Voltage-Current	5
Madrenas et al. [12]	3000	5	1 μ A	–	0.18 at $V_c =$ 4.05 V	–	Voltage-Current	5
This Work	180	\pm 0.4	50 mA	199.52	0.19 at $V_c =$ 0.101 V	197	Voltage-Current	11

References

1. Gupta M, Pandey R (2011) Low-voltage FGMOS based analog building blocks. *Microelectron J* 42(6):10
2. Rajput SS, Jamuar SS (2002) Low voltage analog circuit design techniques. *IEEE CAS Mag* 2(1):18
3. Lande TS, Wisland DT, Soether T, Berg Y (1996) FLOGIC-Floating gate logic for low-power operation. In: 3rd IEEE international conference on electronics, circuits and systems, Rhodes, Greece
4. Gupta M, Pandey R (2010) FGMOS based voltage-controlled resistor and its applications. *Microelectron J* 41(1):8
5. Pandey R, Gupta M (2010) FGMOS based tunable grounded resistor. *Analog Integr Circ Sig Process* 65(3):7
6. Allen PE, Holberg DR (2004) *CMOS analog circuit design*. Oxford University Press
7. Aggarwal B, Gupta M, Gupta AK (2013) Analysis of low voltage bulk-driven self-biased high swing cascode current mirror. *Microelectronics* 44(3):11
8. Pandey R, Gupta M (2009) A novel voltage-controlled grounded resistor using FGMOS technique. In: IEEE international conference on multimedia, signal processing and communication technologies, Aligarh, India
9. Pour ME, Mashoufi B (2011) A low power consumption and compact mixed-signal Gaussian membership function circuit for neural/fuzzy hardware. In: IEEE 2011 international conference on electronic devices, systems and applications (ICEDSA), Kuala Lumpur, Malaysia
10. Abuelma'atti MT, Al-Abbas SR (2016) A new analog implementation for the Gaussian function. In: 2016 IEEE industrial electronics and applications conference (IEACon), EleKota Kinabalu, Malaysia
11. Srivastava R, Singh U, Gupta M (2011) Analog circuits for Gaussian function with improved performance. In: 2011 World congress on information and communication technologies, Mumbai, India
12. Madrenas J, Verleysen M, Thissen P, Voz JL (1996) A CMOS analog circuit for Gaussian functions 43:5
13. Yucel F, Yuce E (2018) Analog squarers using only seven MOS transistors and a four quadrant analog multiplier application. *J Circ Syst Comput* 27(2018):13
14. Yuce E, Yucel F (2014) A new cascaded CMOS voltage squarer circuit and its application: four quadrant analog multiplier. *Indian J Eng Mater Sci* 21:8
15. Niranjana V, Gupta M (2009) Low voltage four-quadrant analog multiplier. *Microelectron Int* 26:6
16. Weste NHE, Harris D, Banerjee A (2006) *CMOS VLSI design-a circuits and systems perspective*, 3rd edn. Dorling Kindersley India for Pearson Education, Boston, South Asia

Low-Voltage Low-Power DTMOS Based Second Generation Voltage Conveyor: Features and Design



Dhanuj Kumar Sharma, Shweta Kumari, and Maneesha Gupta

1 Introduction

In recent past, demand for low-power high performance analog integrated circuits has increased rapidly in VLSI design. But due to this requirement, there is an increase in the size and density of chips which aids in heat generation, thus limiting the performance of the circuit. Therefore, power dissipation has turned into a critical factor in low-voltage designs. This poses the need for a constant drop in supply that is suitable for digital circuits, as reduction in supply decreases the power dissipation of a digital circuit. But in analog circuits, as supply reduces, there is no reduction in threshold in harmony with the decrease in supply. Also, there are some trade-offs between gain–bandwidth, linearity, dynamic ranges when reducing the supply. Hence, to fulfil the low voltage operation of an analog integrated circuit, several techniques can be utilized to overcome this limitation. Some of the available techniques are bulk driven, DTMOS [1], floating gate, subthreshold technique, FVF (flipped voltage follower) and quasi floating gate techniques [2–5]. In this paper, the modification of voltage conveyors using DTMOS technique is proposed. Voltage conveyors (VCII) are the dual of current conveyors (CCII) [6]. As voltage conveyor has a voltage output terminal, it is more appropriate for the applications utilizing

D. K. Sharma (✉) · M. Gupta
Department of Electronics and Communications, Netaji Subhas University of Technology,
Dwarka, New Delhi, India
e-mail: dhanujk.ev20@nsut.ac.in

M. Gupta
e-mail: maneeshapub@gmail.com

S. Kumari
Department of Electronics and Communications, Bharati Vidyapeeth's College of Engineering,
New Delhi, India
e-mail: shwetagupta20009@gmail.com

voltage signals. By employing voltage conveyors in a design, the complexity of a circuit can be reduced and wider frequency operation of the circuit can be observed. For these advantages, researchers have now started operating on voltage conveyors as a building block. The design of the voltage conveyor proposed in previous research papers [7, 8] had some limitations in power consumption and dynamic ranges. These circuits were consuming high power and their dynamic ranges were not showing linearity as well. So in these proposed circuits, DTMOS technique has been implemented on PMOS transistors as it becomes well-matched with single-well technology that could be utilized in a regular CMOS with no need for any extra cost. Proposed circuit-I is supplied with a dual rail supply of ± 0.4 V and its power consumption is observed to be $45 \mu\text{W}$, much lesser than the previous work done. The proposed circuit-II is supplied with ± 0.6 V and the power consumed was observed as $24 \mu\text{W}$. Moreover, the output impedance of both the proposed circuits has increased which further increases its gain. Also, the dynamic ranges observed in the simulations were more linear as compared to previous work. Therefore, the DTMOS is measured to be most favourable for low-power applications. So, in this paper, two designs of second-generation voltage conveyors (VCII) are introduced operating at low voltage of ± 0.4 V and ± 0.6 V respectively mapped onto 180 nm CMOS technology using DTMOS technique.

This paper is organised as follows: Sect. 1 defines the VCII characteristics; Sect. 1.2 defines DTMOS; Sect. 2 introduces two new DTMOS-based voltage conveyors; Sect. 3 displays the simulation results of the circuit and Sect. 4 concludes the work.

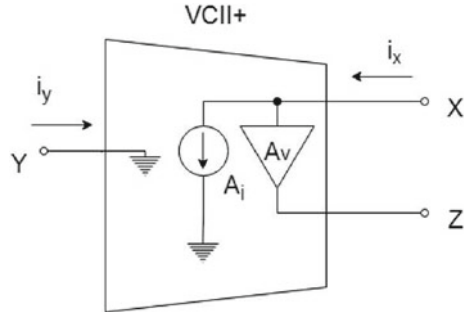
1.1 VCII Characteristics

Figure 1 shows a common electrical symbol of voltage conveyor [8] with parasitic components at their ports. This is a three-port block. All three ports are represented by X , Y , and Z terminals. Terminals Y and Z exhibits low impedance nearly taken as zero while terminal X shows high impedance ideally taken as infinite. Here, the voltage conveyor consists of a current buffer between Y and X ports and a voltage buffer between X and Z ports.

As shown in Fig. 1, voltage gain is calculated among X and Z terminals whereas current gain is calculated among Y and X terminals. If $\beta = +1$, it is considered as a VCII+ whereas for $\beta = -1$, it is taken as VCII-.

$$\begin{bmatrix} i_x \\ v_y \\ v_z \end{bmatrix} = \begin{bmatrix} 0 & \beta & 0 \\ 0 & 0 & 0 \\ \alpha & 0 & 0 \end{bmatrix} \begin{bmatrix} v_x \\ i_y \\ i_z \end{bmatrix}$$

Fig. 1 VCII symbol



1.2 Dynamic Threshold Mos Transistor

In this technique [4], the bulk region and the gate of a CMOS transistor are tied together. Fig. 2 shows the p-type MOS with DTMOS enabled technique and its representation. The variation of threshold voltage (V_{th}) in the DTMOS enabled transistor is proportional to the variation in the voltage at body terminal with the variation in the voltage at gate terminal. Its threshold voltage (V_{th}) decreases when source to body voltage (V_{SB}) rises with increase in voltage at the gate terminal as given in Eq. (1). [9]

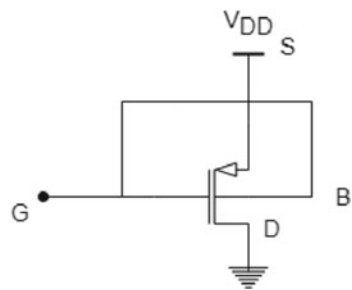
$$V_{th} = V_{th0} - \gamma \left(\sqrt{2|\phi_F|} - \sqrt{2|\phi_F| - V_{SB}} \right) \tag{1}$$

where V_{th0} specified in Eq. (2) is the V_{th} at zero bias $\gamma = \sqrt{2qN_a \epsilon_s / C_{OX}}$ is the bulk parameter, ϕ_F is inversion layer potential.

$$V_{th0} = 2|\phi_F| + V_{FB} + \sqrt{2qN_a \epsilon_s 2|\phi_F| / C_{ox}} \tag{2}$$

Moreover, to keep leakage currents small, V_{SB} should be smaller than or equal to $2\phi_F$. If $V_{SB} = 2\phi_F$, then it produces least V_{th} as presented in Eq. (3)

Fig. 2 DTMOS enabled PMOS



$$V_{th, \min} = 2|\phi F| + V_{FB} \quad (3)$$

This decreased V_{th} surges current at drain terminal, thereby offering greater DTMOS transconductance as displayed in Eq. (4). here g_m is gate whereas g_{mb} is body transconductance of a MOS.

$$G_{md} = g_m + g_{mb} \quad (4)$$

Moreover, for designing CMOS circuits based on DTMOS technique, triple well technology is required. As the effective transconductance increases by this technique, it helps in enhancing the gain of the proposed circuit too.

2 Circuit Diagrams of Proposed Voltage Conveyors

The two circuits proposed in this paper are voltage conveyors, both of which are implemented using DTMOS technique. This technique had been used in the past and proved to be efficient in reducing the power consumption of the circuit at low voltages. There are multiple other techniques to reduce the power consumption of a circuit but as stated above, DTMOS among them comes out to be the best alternative for voltage conveyors for reasons stated above. Following are the proposed circuits.

2.1 Proposed-I VCH

The second generation voltage conveyor [7] designed using the DTMOS technique is presented in Fig. 3.

In this circuit, M4–M7, M10 and M11 transistors are employed with DTMOS technique. This circuit is realised by series combination of current buffer (M₁–M₇) and voltage buffer (M₈–M₁₂) [7]. In current buffer, negative feedback loop formed with M₂–M₅ transistors offers low impedance on the Y port. Through simple current mirror composed of M₆ and M₇, the current at the input is transferred from port X to port Z. Similarly, voltage applied at port X is conveyed to port Z by a voltage buffer designed by M₈–M₁₂ MOS transistors. Due to the negative feedback loop formed by MOS transistors M₈–M₁₁, low impedance is observed at terminal Z. Finally, MOS transistors M_{B0}–M_{B5} are used for biasing. DTMOS technique is applied to all the PMOS transistors of this circuit. The simulation of this circuit is given in the further section.

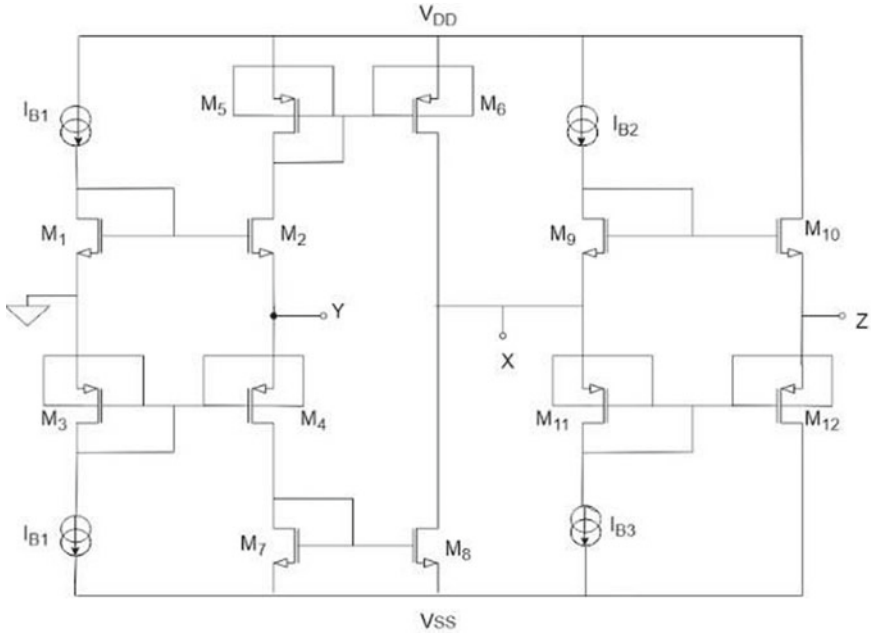


Fig. 4 Circuit diagram of proposed-II VCI

3 Simulations

Simulations of the proposed circuit-I are performed using 180nm technology at a voltage of $\pm 0.4V$. The W/L ratios of transistors (NMOS, PMOS) are taken as $13.6 \mu\text{m}/0.55 \mu\text{m}$ and $40.6 \mu\text{m}/0.54 \mu\text{m}$ respectively for proposed circuit-I. The value of bias currents (I_{B0} and I_{B1}) are taken as $25 \mu\text{A}$.

Simulations of proposed circuit-II are performed using 180 nm CMOS technology at a voltage of $\pm 0.6 V$. The aspect ratios (W/L) of transistors are given in Table 1 for proposed circuit-II. The voltages and the bias currents (I_{B1} , I_{B2} , I_{B3}) are $\pm 0.6 V$ and $20 \mu\text{A}$ respectively.

As shown in waveform Fig. 5, a test voltage of 100 mV is applied at terminal X and the voltage output is observed at terminal Z. Fig. 5a, b represents the DC responses

Table 1 W/L ratios for proposed circuit- II

MOSFETs	Aspect ratio ($\mu\text{m}/\mu\text{m}$)
M1–M2, M9–M10	3/0.3
M3–M4, M11–M12	10/0.3
M5–M6	30/0.9
M7–M8	9/0.9

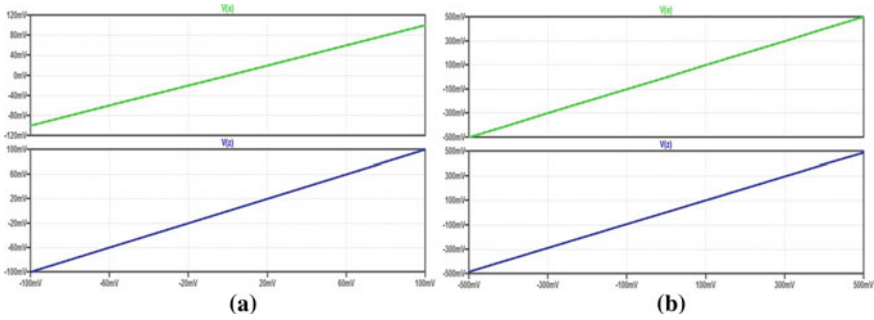


Fig. 5 DC response V_x versus V_z of **a** proposed-I and **b** proposed-II circuits

of proposed-I and proposed-II circuits respectively. The error between them was observed to be less than 1%.

In Fig. 6, transients of voltage signals are represented by applying a sinusoidal wave of 100 mV as voltage signals applied at terminal X and output is observed at terminal Z. Fig. 6a, b represents the transient waveforms of proposed-I and proposed-II circuits respectively.

Figure 7 shows the sinusoidal waveforms of test current 20 μ A applied at terminal Y and output current observed at terminal X. Fig. 7a, b represents the transient waveforms of proposed I and II circuits respectively.

Figure 8 shows the AC analysis of both proposed circuits as 8a and 8b respectively where the input is applied at terminal Y and voltage is observed at terminal Z. The gain of the proposed circuit I and II are observed to be 72 dB and 59 dB and -3 dB bandwidth are observed as 89 MHz and 84 MHz respectively. Table 2 presents a comparative analysis of proposed circuits with previously reported circuits. From Table 2 observations, the gain and bandwidth of proposed circuit-I is greater than proposed-II. Proposed circuit-I consumes less power as compared to proposed circuit-II. Both the proposed circuits outperform the previous work done in terms of power dissipation.

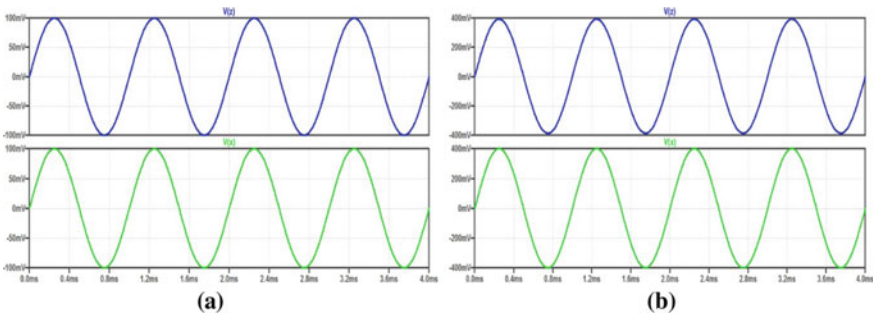


Fig. 6 Transients V_x versus V_z of **a** proposed-I and **b** proposed-II circuits

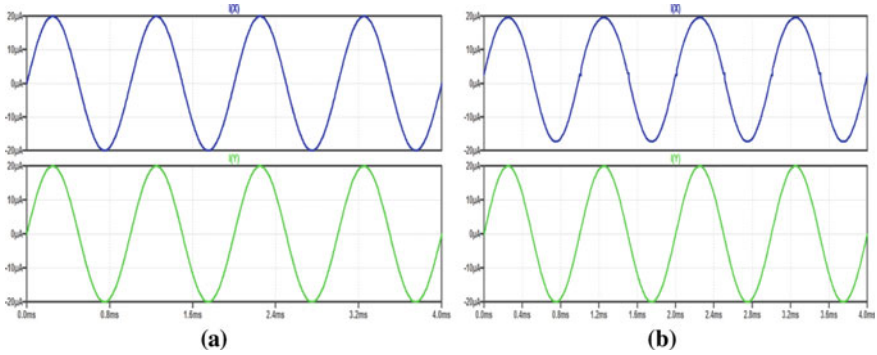


Fig. 7 Transients I_y versus I_x of **a** Proposed-I and **b** Proposed-II circuits

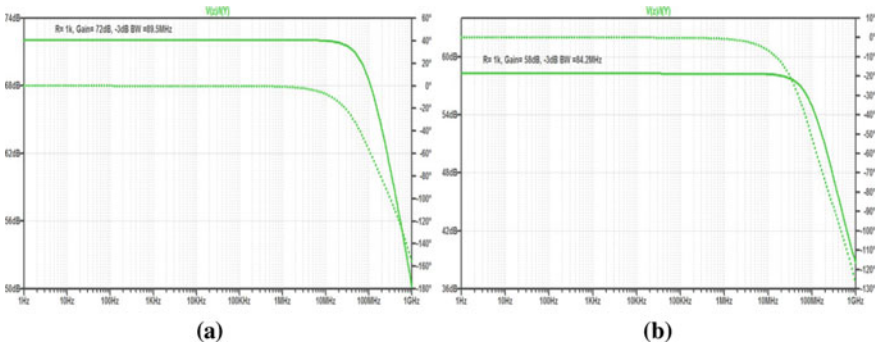


Fig. 8 AC analysis of I_y versus V_z of **a** proposed-I and **b** proposed-II circuits

Table 2 Comparison of proposed circuits with previously reported work

Parameters	Ref. [10]	Ref. [8]	Proposed circuit-I	Proposed circuit-II
Technology	0.18 μm	0.18 μm	0.18 μm	0.18 μm
Supply voltage	$\pm 0.1.65$ V	± 0.9 V	± 0.4 V	± 0.6 V
Bias current I_B	NA	20 μA	25 μA	20 μA
Current gain (I_x/I_y) (no load)	NA	1	0.9921	0.997
Voltage gain (V_x/V_y) (no load)	NA	0.987	0.998	1.021

(continued)

Table 2 (continued)

Parameters	Ref. [10]	Ref. [8]	Proposed circuit-I	Proposed circuit-II
Current range (I_X/I_Y) (no load)	NA	± 1.22 mA	± 1.17 mA	± 1.19 mA
Voltage range (V_X/V_Y) (no load)	NA	± 0.89 V	± 0.732 V	± 0.52 V
<i>-3 db bandwidth</i>				
I_X/I_Y	200 MHz	167 MHz	89 MHz	84 MHz
V_Z/V_X	217 GHz	100 GHz	76 GHz	114 GHz
<i>Offset voltage</i>				
V_{OY}	NA	-0.463 mV	-0.127 mV	-0.278 mV
V_{OX}		-81.82 mV	-73.24 mV	-96.24 mV
V_{OZ}		-80.48 mV	-65.44 mV	-93.46 mV
<i>Parasitic parameter</i>				
R_Y, L_Y	6.7 Ω , 1.5 μ H	1.88 k Ω , 20.8 nH	1.46 k Ω , 15 nH	1.46 k Ω , 15 nH
$R_X, C_X R_Z, L_Z$	1.2 M Ω , 30 fF	273.8 Ω , 64 fF	574 Ω , 45 fF	574 Ω , 45 fF
$R_X, C_X R_Z, L_Z$	0.7 Ω , 9 μ H	1.75 k Ω , 5.77 nH	0.99 k Ω , 9.12 nH	0.99 k Ω , 9.12 nH
1% THD I_X for input I_Y @ 1 MHz	0.1% @ 100 μ A _{p-p}	2.44 mA _{p-p}	1.81 mA _{p-p}	2.12 mA _{p-p}
1% THD V_Z for input V_X @ 1 MHz	0.068% @ 1V _{p-p}	1.78 V _{p-p}	1.01 V _{p-p}	1.65 V _{p-p}
Static power dissipation (μ W)	330	179	45	24

4 Conclusion

This paper proposed two circuits, both circuits of voltage conveyors based on the DTMOS technique supplied at low voltage of ± 0.4 and ± 0.6 V and designed using 180 nm CMOS technology. In this work, improvements in the power consumption, dynamic ranges and output impedances were observed as compared to the previous work done. The key factor of power consumption is reduced in both the circuits. Proposed circuit-II offered more reduction in power consumption as compared to proposed circuit-I. Major improvements were observed in linear ranges of both current and voltages and power consumption. Simulations confirm the effective performances of these circuits. Moreover, the workability of these proposed circuits confirms them to be capable of working at low supply voltages.

References

1. Assaderaghi F, Sinitsky D, Parke S, Bokor J, Ko PK, Hu C (1997) Dynamic threshold-voltage MOSFET (DTMOS) for ultra-low voltage VLSI. *IEEE Trans Electron Devices* 44(3):414–422
2. Khatab F, Bay S, Dabbous A, Vlassis S (2013) A survey of non-conventional techniques for low-voltage, low-power analog circuits design. *Radioengineering* 22(2):415–427
3. Ferreira LHC, Pimenta TC, Moreno RL (2007) An ultra-low-voltage ultra-low-power CMOS Miller OTA with rail-to-rail input/output swing. *IEEE Trans Circ Syst II Express Briefs* 54(10):843–847
4. Rakús M, Stopjaková V, Arbet D (2017) Design techniques for low-voltage analog integrated circuits. *J Electr Eng* 68(4):245–255
5. Sedra A, Smith K (1970) A second generation current conveyor and its applications. *IEEE Trans Circ Theor CT-17*:132–134
6. Toumazou C, Lidgley J, Haigh D (1990) *Analogue IC design: the current mode approach*. Peter Pererinus, London, UK
7. Safari L, Yuce E, Minaei S, Ferri G, Stornelli V (200) A second-generation voltage conveyor (VCII)-based simulated grounded inductor
8. Kumngern M, Torteanchai U, Khateb F (2019) CMOS class AB second generation voltage conveyor
9. Razavi B (2018) *Design of analog CMOS integrated circuits*. Mc Graw Hill Education, Chennai
10. Safari L, Barile G, Stornelli V, Ferri G (2018) An overview on the second generation voltage conveyor: features, design and applications. *IEEE Trans Circ Syst II Express Briefs*

A Novel Method to Power Losses Reduction in Radial Distribution System: A Multiobjective Generalized Particle Swarm Optimization (MOGEP SO)



Sapna Ladwal , Anil Kumar , and Avantika Sethi

Abbreviations

DG	Distribution Generator
RES	Renewable Energy Resources
EDS	Electrical Distribution System
MOO	Multiobjective Optimization
ES	Energy Storage Units
ACO	Ant colony optimization
RRA	Runner Root Algorithm
ANN	Artificial Neural Network
SFLA	Improved Shuffled Frog Leaping Algorithm
WOA	MSA and Whale optimization algorithm
GWO	Grey Wolf Optimization
MOGOA	Multiobjective Grass Hopper Optimization
3D-GSO	Three-dimensional Group Search Optimization
EPC	Epsilon Constrained
MMFF	Minimum-Maximum Fuzzy Satisfying
EP	Evolutionary Programming
FF	Fitness Function

S. Ladwal (✉) · A. Kumar
Department, of Electrical Engineering, Deen Bandhu Chhotu Ram University of Science and Technology, Murthal, Sonapat, Haryana, India
e-mail: 20001902006sapnaladwal@dcrustm.org

A. Kumar
e-mail: Anil.ee@dcrustm.org

A. Sethi
Department, of Electrical Engineering, University Institute of Engineering and Technology, Panjab University, Chandigarh, India

FODPSO	Fractional-order Darwinian PSO
GA	Genetic algorithm
GEPHO	General particle swarm optimization
GP	Genetic programming
IPSO	Immune PSO
LS-DF-PSO	Line search-based derivative-free PSO
NC	Natural computing
NPSO	Negative PSO
PSO	Particle swarm optimization
SMO-DSR	Stochastic Multiobjective Distribution System Reconfiguration
EPC-MMF	Epsilon Constrained (EPC) method with minimum–maximum fuzzy satisfying (MMF)
BPSO	Binary Particle Swarm Optimization
HAS	Harmony Search Algorithm algorithms
MOPSO	Multiobjective Particle Swarm Optimization
MOGEPHO	Multiobjective Generalized Particle Swarm Optimization

1 Introduction

1.1 Motivation and Incitement

Network reconfiguration is a required procedure in order to get the best possible design for the power system. The reconfiguration of tie switches ensures that the radial structure of the power system network is not disrupted. Among the components of a distribution system are feeders, switches, lines, and generating units. During the network reconfiguration process, the locations of the open and closed switches are altered. During the reconfiguration of the radial distribution system, the system is encountering certain difficulties. The three stages that are accessible in the network add to the network's complexity. The unbalanced load condition occurs as a result of the connecting of several loads to a single phase of electricity. The load distribution between the feeders and the DG units is not equal across the board. Because of the little data available from the distribution system, there is less actual monitoring and control. Because the network's existing devices are interconnected with one another, the failure of a single device can have a negative impact on the performance of the others. When designing an effective network setup, the power quality, price, and equipment configuration should all be taken into consideration. The automatic network reconfiguration takes care of all the duties, such as lowering power loss, lowering the price, increasing dependability, and maintaining voltage profile stability. The appropriate placement of devices in the distribution network can help to improve voltage stability while also reducing power loss.

An extra set of auxiliary energy sources is added to a network in order to compensate for the load's imbalance situation. In the current DNR system, renewable energy

resources (RES) and energy storage units (ES) are frequently utilized in combination. DNR provides the distribution system with energy management services for renewable energy sources and charging/discharging schedules for electric vehicles. In an overvoltage condition, the nodes (buses) and branches of a network are underperforming [1]. Because of the overvoltage, an imbalanced load condition develops in the network, which may be prevented by inserting a DG unit on the specified bus routes. The sensitivity analysis of buses [2] can be used to determine the best position for the DG unit. The addition of power electronics devices such as DSTATCOM [3, 4] and a compensator [5] can help enhance the stability and voltage profile and reactive power. The network reconfiguration and electrical device allocation processes allow for more efficient network reconfiguration and power loss reduction than previously available methods. The optimization algorithm can make a decision on the reconfiguration of tie-switches or open switches based on their current configuration. Network reconfiguration is accomplished through the use of cutting-edge techniques such as ant colony optimization (ACO) [3], RRA (Runner Root Algorithm) [6], improved shuffled frog leaping algorithm (SFLA) [7], MSA and Whale optimization algorithm (WOA) [8], Genetic Algorithm (GA) [9], and Grey Wolf Optimization (GWO) [10].

A number of multiobjective optimization methods are also employed in the design of a distribution network's DNR. Network reconfiguration techniques for the distribution system are very frequently utilized, and multiobjective optimization approaches are one of the most common. In order to increase DG profit while decreasing business costs, a stochastic multiobjective distribution system reconfiguration (SMO-DSR) is utilized [11]. A multiobjective problem is converted into a single-objective optimization problem using the SMO-DSR objective function, which is used to solve the constraint method using the constraint technique. Multiobjective Grass Hopper Optimization (MOGOA) [12], 3D-GSO (three-dimensional group search optimization) [13], and the epsilon constrained (EPC) method with minimum-maximum fuzzy satisfying (MMFF) EPC-MMF [14] are all methods for improving the reliability and power loss of a distribution system network. It is also utilized for network reconfiguration and DSTATCOM deployment [4], which are both accomplished using multiobjective particle swarm optimization (MOPSO). Heuristic GA [15] is used to optimize the voltage profile stability and power loss of a system. The mathematical and heuristic approaches for network reconfiguration are among the state-of-the-art methods available today. The primary objectives of the techniques described above are the reduction of power loss, the balancing of load, and the reduction of costs.

1.2 Literature Review

The previous work in this area can be categorized into single-objective and multiobjective optimization. In a single objective problem, either only one objective is optimized or weighted addition of multiobjective is used as a single objective. Whereas, in the multiobjective category, this article only considers the Pareto optimal solutions.

Various scientific studies for the demand response reconfiguration network were offered as state-of-the-art. The author addresses several objectives such as the best-distributed generator positioning, energy loss, network costs, security indexes and dependability [1, 3, 6, 7, 11–13, 16–19]. The appropriate DG positioning and loss of energy reduction boosted ISFLA's accuracy and convergence rate. By the best selection of DG allocation and EES parameters [1, 20], the costs of DG units, the customer interruption and distribution efficiency increased. The GA technique is used to optimize the position of the integrated DG units [9]. For the optimum network configuration, a hybrid heuristic genetic algorithm [15] is also presented. By combining his method of heurism with genetic algorithms, the convergence time is improved. For network reconfiguration, an all-round method for the optimization of teaching-learning harmony (CLTHSO) is proposed [21]. The combination of the TLBO and HSO approach is the CLTHSO method. The hybrid technique offered the optimum assignment and simultaneous reconfiguration of DG units.

Using the Binary Particle Swarm Optimization (BPSO) and Harmony Search Algorithm (HSA) algorithms, we provide multiobjective network reconfiguration and DG allocation [22]. Applicable to IEEE-33 and PG&E-69 bus models. The network reconfiguration minimizes the dispersed network's real power loss and overload. A genetic algorithm (GA) is used to reposition DG units in a network [2]. The GA-based network reconfiguration achieved optimal DG positioning and fixed capacitor bank position in dispersed networks. The overall cost of the IEEE 69 bus distributed network reconfiguration is reduced. For network reconfiguration, a mixed-integer second-order cone programming model is used [23]. The suggested technique based on GAMS optimization software is tested on the IEEE 33 bus radial system network. That increases reliability and reduces costs. The HSA technique is used to reorganize an imbalanced distribution network [24]. The HSA technique is used to test the two major conditions with and without DG units on IEEE 25 buses. The suggested HSA technique obtains the optimum radial network reconfiguration. An IS-BPSO method for radial distributed network reconfiguration is described [25]. The IS-BPSO technique has a fast convergence rate and minimizes power loss. A multiobjective optimization algorithm is constructed for optimum network reconfiguration using the epsilon constrained (EPC) technique and the MMFF trade-off conditions [14]. The multiobjective model reduces power loss and improves voltage profile. The IEEE 33 bus system model is optimized with GAMS. The pareto optimum approach solves a multiobjective network reconfiguration issue [5]. The pareto front concept optimizes active power loss, carbon emissions, and operating costs. The fuzzy decision-making algorithm gets the best Pareto answer. The Pareto ideally based approach achieves effective and optimum network reconfiguration. The multiobjective PSO method is presented for selecting DSTATCOM position and parallel capacitor bank size [4]. MOPSO's objective function is the cost of the voltage profile, voltage stability, and losses. The best placement of DER with capacitor C is accomplished by two multiobjective optimization algorithms (MSA and WOA) [8].

1.3 Contribution

MO algorithms are seen in many real-world scenarios so to the background research. The MO algorithms converged quickly on the issue formulation. This study uses Multiobjective Generalized Particle Swarm Optimization to handle network reconfiguration (MOGEP SO). Sensitivity analysis determines DG placement on buses. This study considers three objective functions: active power loss, DG installation cost, and proximity. MOCPSO simultaneously optimizes each of these objective functions.

1.4 Paper Organization

The paper is arranged as follows: Sect. 2 contains the statement of the problem. Section 3 has a thorough explanation of the MOGEP SO, Sect. 4 contains a summary of the results, and Sect. 5 contains concluding thoughts on the subject.

2 Problem Formulation

The Swarm network reconfiguration is a process for altering the structure and topological conditions of the distribution consists of three components like feeders, sectionalize switches, and tie switches. It can manage the overload condition by transferring the load from heavy load feeders to light load feeders. A radial distribution system has several advantages like minimum short circuit current, simple switching, protection scheme, and low cost. The reliability of a radial distribution system is low, which can be improved by the optimal reconfiguration. Some factors like increasing demand, intermittent generation, deregulation of the power system, and climate changes are affecting the power system stability.

The efficient and reliable power system is obtained by implementing the control and measurement system policies. These policies may include the optimal tie switch locations, DG placement on buses. The allocation of the DG units on the critical nodes improves the stability and minimizes the branch losses of the power network. In previous studies [6, 11–13, 16, 17], multiobjective optimization is used to enhance the voltage and power stability of a network, considering power loss and cost as the primary objective function. The power system reconfiguration is constrained by the voltage and power flow limits. The active and reactive power flow information is considered to measure the centrality of the network. The closeness centrality of a node is defined as the sum of its entire closest path available a bus to every other bus in the network. During the overvoltage condition, the DGs are placed at sensitive buses. The critical buses are identified by sensitivity analysis. This paper suggests power loss minimization, DG installation cost reduction, and topological

measurement (closeness) as the objective function for the MOCPSO optimization algorithm.

The single objective optimization achieves the optimal tuning of continuous, integer, and binary variables. The searching ability of a single-objective optimization algorithm is degraded in terms of convergence and provides local optima solution. The multiobjective optimization algorithm provides a global optima solution by considering the Pareto environment. The following objective functions are

$$\text{Min}(F_1) = P_{\text{Loss}}(Z) \tag{1}$$

$$\text{Min}(F_2) = IC_{DG} \tag{2}$$

$$\text{Min}(F_3) = C_c(m) \tag{3}$$

Subject to

Power flow constraints

$$P_i^{\min} \leq P_i^{\text{loss}} \leq P_i^{\max} \tag{4}$$

$$V_i^{\min} \leq V_i \leq P_i^{\max} \tag{5}$$

DG constraints

$$P_{DG}^{\min} \leq P_{DG}^i \leq P_{DG}^{\max} \tag{6}$$

$$Q_{DG}^{\min} \leq Q_{DG}^i \leq Q_{DG}^{\max} \tag{7}$$

Radial constraints

The node n_b is radial if the solution $(n_b - 1)$ is available in the circuit and connected to other nodes. The total numbers of substation nodes are denoted by n_{bs} . The electrical distribution system (EDS) is radial if its transfer node is not terminal, and two circuits must be leaving the transfer node. The use of the transfer node is defined by a matrix y_i , and the determinant of matrix y_i is equal to 1, else the determinant of the matrix is 0. The radial constraints equations formulate as

$$\sum_{(ij) \in \Omega_l} x_{ij} = n_b - n_{bs} - \sum_{j \in \Omega_{bp}} (1 - y_j) \tag{8}$$

$$x_{ij} \leq y_j \quad \forall (ij) \in \Omega_l, \forall j \in \Omega_{bp} \tag{9}$$

$$x_{ji} \leq y_j \quad \forall (ji) \in \Omega_l, \forall j \in \Omega_{bp} \tag{10}$$

$$\sum_{(ij) \in \Omega_l} x_{i,j} + \sum_{(ji) \in \Omega_l} x_{ji} \geq 2y_j \quad \forall j \in \Omega_{bp} \tag{11}$$

$$|y_j| \in \{0, 1\} \quad \forall j \in \Omega_{bp} \tag{12}$$

The constraints from 8 to 12 avoid loop generation caused by transfer nodes, and terminal transfer nodes prevent from the distribution system. The constraints are known as the radial constraint [26]. The transfer node utilization is depending on the determinant of matrix $|y_j| = 1$ and $|y_j| = 0$

$$|y_j| = 1 \quad \forall (ij) \in \Omega_l, \forall j \in \Omega_{bp} \tag{13}$$

$$|y_j| = 0 \quad \forall (ji) \in \Omega_l, \forall j \in \Omega_{bp} \tag{14}$$

Active power loss

Losses in the electrical power distribution system affect the operating cost of the network. The total power loss of a radial-type distribution network is defined as the summation of all line segment losses.

The formulation of power loss is as

$$P_{Loss}(Z) = \sum_{j=1}^{Nbr} R_j \times \left(\frac{P_j^2 + Q_j^2}{V_j^2} \right) \tag{15}$$

DG installation cost

The installation and operation cost of the distributed generators is calculated as

$$IC_{DG} = \sum_j^{ndg} (IC_j \cdot P_{int-j}) \tag{16}$$

In Eq. 16, IC_j represents the one-time installation cost. The size of the j th DG installation is denoted by the P_{int-j} .

Closeness

Radial type distribution network is represented by a graph containing a set of vertices (and thus a set of edges). The graph nodes represented by the vertices and the transmission line impedance provide their corresponding interconnection. The undirected graph of two adjacent nodes with the connected graph of order N and size is

denoted by $\mathcal{G} = \{\mathcal{N}, E, Z\}$. Here $\mathcal{N} = \{i | i \in \mathcal{N}^N\}$ has all the nodes of the distribution network and set $E = \{e_{ij} | e_{ij} \in E^l \cap i, j \in \mathcal{N}^N\}$ shows the transmission line connecting them.

The summation of all shortest path nodes which can be used for the evaluation of rapid power injected into the system nodes is known as the closeness centrality. The mathematical formulation of closeness is

$$C_c(m) = \sum_{n=1}^N d_{mk} = \sum_{k=1}^N \sum_{n=1}^N \frac{P_{nm}(k)}{P_{nm \max}} \tag{17}$$

Sensitivity Analysis

In-network reconfiguration, the optimal location of DG technologies is selected by the sensitivity analysis. The sensitivity of a power system network is defined as the power loss derivative with respect to the busload, and the factor is called the Low Sensitivity Factor (LSF). The sensitivity factor of the buses is used to determine the location of the DG units in the power system network. The formulation of sensitivity factor as;

$$\frac{\partial P_{Loss,K} (K + 1)}{\partial P_k} = 2 \frac{P_k R_k}{V_k^2} \tag{18}$$

For calculating sensitivity factors at each bus are presented in the power system sequence network and arranged in ascending order. The potential buses are considered as the DG placement location in the power system network [2].

3 Multiobjective Generalized Particle Swarm Optimization

The network reconfiguration is achieved by minimizing the power loss from Eq. 15, DG installation cost from Eq. 16, and closeness centrality from Eq. 18. The classical three objective functions have to be reduced simultaneously with tuning variables. The state-of-the-art methods in evolutionary multiobjective optimization algorithms are suffered by the local optimum solution and early convergence [16]. Researchers [11, 12, 16–18] have implemented a MOO solution for network reconfiguration via 2 or 3 objective functions. Many researchers use single MOO like MOGO [12], MO-NSGA [16], MO-PDNSGA [17], and MOIHNS [18]. In [27] a cellular automata concept is integrated into the PSO (Particle swarm optimization) algorithm, which explores the closest position of every swarm to reach the solution. A MOPSO (Multiobjective PSO) algorithm is presented for the higher dimensional variable solution with fixed constraints [23]. The MOPSO algorithm still performs poorly in finding a globally optimal solution. We proposed a low-level hybrid optimization scheme MOCPSO for the network reconfiguration of a power system.

The optimization algorithm is characterized by the exploration and exploitation phases. The suggested approach, multiobjective cellular automata particle swarm optimization (MOCPSO), is tried to minimize the maximum of three objective functions. The exploration phases performed search space solutions, and the exploration phase tries to converge the search agents quickly. The metaheuristic approaches cannot improve the issue of premature convergence [9, 10, 15]. The hybrid multiobjective optimization algorithms are not implemented for the network reconfiguration. The MOPSO and Cellular Automata brief description is given below. The proposed MOCPSO algorithm can achieve a global optimum solution of network reconfiguration objective function.

3.1 Multiobjective PSO Algorithm

The particle swarm optimization is inspired by the food-searching behavior of the swarms. The flock birds' behavior for searching the food is the basic principle of the PSO algorithm. The optimal solution is considered as the searching food, and birds are the particles for search space. The implementation of PSO is simple and has better optimization capability. The formulation of the position of the birds and optimal solution are evaluated in Eqs. 19 and 20.

$$V_i^{t+1} = V_i^t + c_1 \cdot r_1 (p_i^t - X_i^t) + c_2 \cdot r_2 (p_g^t - X_i^t) \tag{19}$$

$$X_i^{t+1} = X_i^t + V_i^{t+1} \tag{20}$$

The velocity and position of each particle are updated in each iteration. The velocity formulates in Eq. 19, and the location of particles derive from 20. The real constants values are represented by c_1 and c_2 , and r_1 and r_1 are the random numbers lie between 0 and 1. The best position evaluation of particle provides the best position update solution for the fitness function score. The leaders' particles are equipped with the best objective fitness at the respective objective functions. In MOPSO, the Pareto optimal test provides a pareto optimum solution front of the multiobjective functions [23]. The Pareto two-level ranking scheme can handle the MOO problem reliably. An external archive controller and grid for is stored to the best area of the search space of the particle. The archive has two main functions: selecting of leaders and storing them in the external archive of best non-dominated solutions.

For new version of multiobjective problems adopts the Pareto ranking scheme is added to the PSO algorithm. Multiobjective optimization problems are compared to single-objective optimization by considering two solutions in a precise sense. A solution is said to be dominated if $\forall_i \in \{1, 2, \dots, K\}, f_i(\vec{\mathbf{u}}) < f_i(\vec{\mathbf{v}})$. A decision vector $\vec{\mathbf{u}}$ is non-dominate $\vec{\mathbf{v}}$ if and only if $\forall_i \in \{1, 2, \dots, K\}, f_i(\vec{\mathbf{u}}) < f_i(\vec{\mathbf{v}})$ and $\exists_i \in \{1, 2, \dots, K\}, f_i(\vec{\mathbf{u}}) < f_i(\vec{\mathbf{v}})$.

The non-dominated solution is tracked by the archive of the external repository. Non-dominated solution are achieved to store iteratively obtained set of the entire feasible decision for better solution [23]. If first stage is empty of an external archive, the update mechanism solution is saved and copied. Dominance of archive solution is better than the current solution, then the offspring new solution is deleted and non-dominated solutions saved.

Hybrid Mogeptoalgorithm

The exploration stage of MOPSO is updated by concept selecting the random position from the set of local best positions of swarms and the weightage of it is used to update the velocity. MOGEPSo algorithm is used here to estimate the performance of a distributed network under the reconfiguration. Each swarm particle is supposed to be a solution containing tie switches locations and DG capacity. The three objective functions considered for the network reconfiguration are minimization of active and reactive power losses, each DG set installation cost and closeness centrality of nodes. The population is sorted by non-dominated solution and the algorithm achieves an optimal solution. The initial dimension of each population is equal to the number of variables. MOGEPSo generates a range of solutions, but all solutions do not prominently satisfy all conditions of constraints.

The designed objective function is as stated in Eqs. 1, 2 and 3. These are computed and stored in the temporary memory of each swarm particle. In order to find, the exact neighbors in the niche of a swarm, the surrounding area is manifested. The evaluation of each objective function is also carried out for the neighbors. The fitness of each swarm is compared with the next immediate neighbor and the current fitness values replace the least values stored. The best position is considered the current position of the swarm.

The exploitation phase follows the traditional velocity and position update of the PSO algorithm. The weight parameter is added using Eq. 18 and computes the best velocity value. The process of the MOGEPSo algorithm is iterative, so different sets of neighbors are calculated in each iteration.

$$V_i^{t+1} = \psi [w_1 V_i^t + w_2 c_1 \cdot r_1 (p_i^t - X_i^t) + w_3 \alpha_1 c_2 \cdot r_2 (p_g^t - X_i^t) + w_4 \alpha_2 c_3 \cdot r_3 (p_{\text{rand}}^t - X_i^t) + w_5 \alpha_3 c_4 \cdot r_4 V_{\text{rand}}^t] \quad (21)$$

where $\psi = \frac{2}{|2 - (c_2 + c_3)|^2 - 5(c_2 + c_3)}$

4 Experiment Study

The proposed algorithm is tested on IEEE 33 radial bus system with 32 sectionalize switches and 5 tie switches. The position of tie switches can be changed within Kirchoff's current loop (KCL), respectively. Five tie switches create 5 KCLs. The bus diagram of the IEEE 33 bus system is shown in Fig. 1. Sensitivity analysis helps

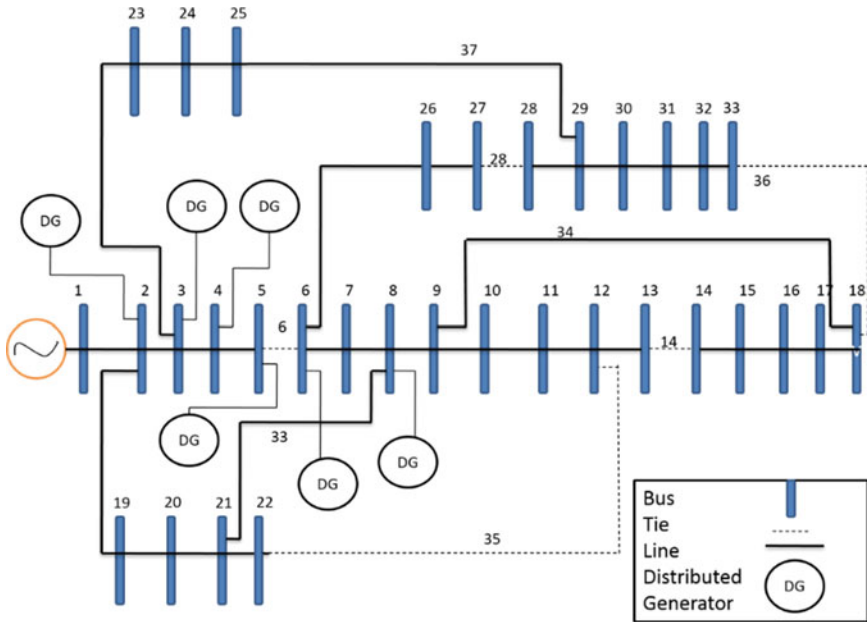


Fig. 1 IEEE 33 radial bus system with tie switches

to select the most sensitive buses which have the highest power losses. In this work, 6 DG’s has been selected to place in the network, so 6 topmost sensitive buses are selected. These are 2, 3, 4, 5, 6, 8. The multiobjective GEPSO algorithm selects the DG capacity and changes the tie switches position to minimize the active power losses.

The normal load scenario is considered for the simulation. A voltage constraint of 0.8–1.1 p.u. is selected. The population size of 20 and 50 iterations of the MOGEP SO algorithm are considered. The multiobjective function contains three objective functions as DG installation cost, active and reactive power loss, and closeness centrality optimized with the MOGEP SO approach. The convergence plot of MOGEP SO with the three objective functions is shown in Fig. 2. The solution in the repository is considered as the final optimum solution. These are non-dominated particles and set at the optimal objective function values for minimum power losses, node’s closeness and DG installation cost.

After the optimization, the network is reconfigured and change their status of switches with tie switches from 33, 34, 35, 36, 37 to 6, 14, 28, 34, and 36. We have analyzed the effect of change in tie switch position without DG placement and reduction in power losses with tie switch reconfiguration along with DG. Table 1 lists the comparison. The initial power loss in the IEEE 33 bus system is 603.43 KW with minimum operated voltage 0.83 pu. The power loss reduces to 39.73% in the case of MOGEP SO with tie switches and DG units. The power loss in the PSO case optimized with tie switches and DG units is only 4.03% which is much lower

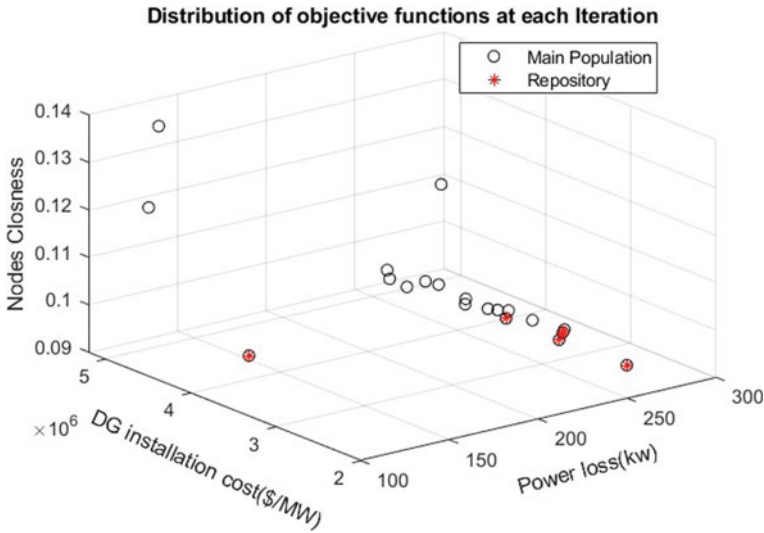


Fig. 2 Convergence trend of MOGEP SO for objective functions

than the proposed MOGEP SO method. Figure 3 shows the voltage profile plot for the proposed method with MOP SO and the unoptimized case for both scenarios: tie switch only and tie switch and DG placement. It is validated from the graph that none of the method has violated the voltage limit constraint. Maintaining the constraint, the lowest voltage magnitude per unit is with MOGEP SO is 0.9739 with both tie switches and DG, whereas it is 0.9659 with MOP SO and 0.90378 for the unoptimized case. An improvement of 0.82% is achieved by the proposed scheme than MOP SO for the minimum voltage.

The total active and reactive power losses in all lines are shown in Fig. 4. The bar plot represents the decrease in active power loss by 39.73%. The power loss is minimized by using the optimization algorithm. The branches' normal power loss is reduced to 147.28 kW for the PSO algorithm with tie switches and tie switches plus DG units. Further the real power loss is minimized to 103.33 kW range in case of MOGEP SO optimized IEEE 33 radial bus system with tie switches and tie switches plus DG units.

5 Conclusion

The active power losses are minimized in IEEE 33 radial bus system with the proposed multiobjective generalized particle swarm optimization algorithm. This article tested the algorithm under two scenarios for normal load conditions: tie switch reconfiguration only: tie switch and DG placement. Three objectives for minimization are simultaneously solved by MOGEP SO. An improvement of 39.73% in active power

Table 1 Power loss and voltage per unit comparison between unoptimized, MOPSO and MOGEPFO optimized network reconfiguration

Model	Position of tie switches	DG location	DG capacity	Power loss (kW)	Power loss reduction (%)	Minimum voltage (p.u)
Normal IEEE 33 model	33, 34, 35, 36, 37	-	-	210.9876	-	0.90378
PSO+Tie-Switches+DG Network Reconfiguration	11, 7, 34, 36, 28	2, 3, 4, 5, 6, 8	DG(2) = 29.53 DG(3) = 25.76 DG(4) = 22.64 DG(5) = 45.29 DG(6) = 64.51 DG(8) = 44.10	147.2873	30.19	0.9659
PSO+Tie-Switches Network Reconfiguration	11, 7, 34, 36, 28	-	-	164.0407	22.13	0.9637
MOGEPFO+Tie-Switches+DG Network Reconfiguration	6, 14, 29, 35, 36	2, 3, 4, 5, 6, 8	DG(2) = 53.7375 DG(3) = 14.4234 DG(4) = 11.5624 DG(5) = 52.3895 DG(6) = 23.4081 DG(8) = 69.9998	103.335	51.0	0.9739
MOGEPFO+TieSwitches Network Reconfiguration	6, 14, 29, 35, 36	-	-	107.9161	49.14	0.9730

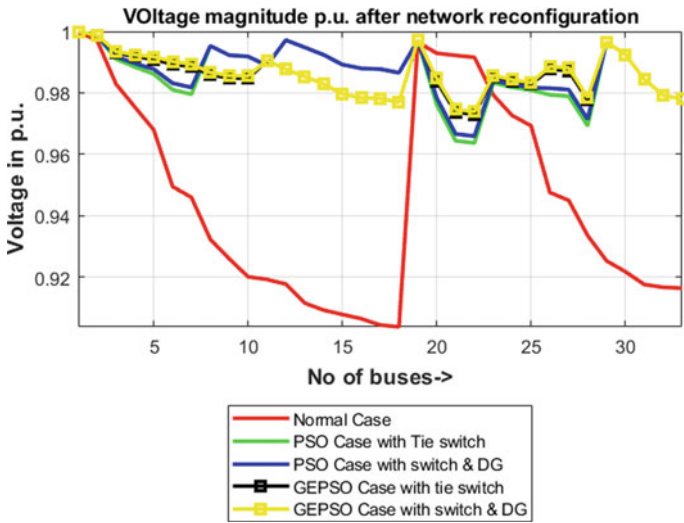


Fig. 3 Voltage magnitude of IEEE 33 bus system under normal load condition

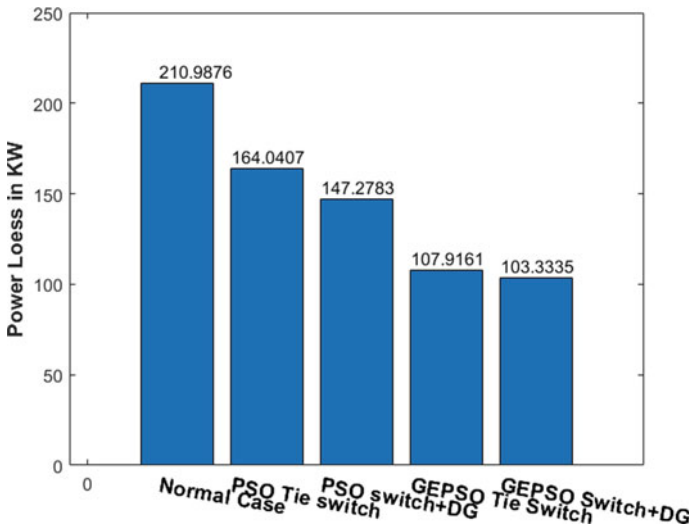


Fig. 4 Comparison of power loss among different strategies

losses and 7.5% in minimum voltage p.u. from the unoptimized case is achieved by the proposed scheme.

The proposed study concluded with remarks as

- An optimal network reconfiguration revises the power flow path, which reduced the power loss of a distribution network.

- By adding the distributed generator unit to the distribution network, the power flow in the sectionalizes switches minimizes, which reduced the power loss.
- Simultaneously performed network reconfiguration and deployment of DG units can provide a better solution than individually implemented schemes.

In the future, the scheme will be rigorously tested on higher bus systems with multiple load conditions.

The MINLP model is used to solve the commercial issues of DSR operation [12]. Total network power loss and voltage variation are optimized in a single objective and multi-objective manner. The MSA and WOA achieve efficient network reconfiguration. The location of integrated DG units is optimally selected by the GA method [28]. The GA optimization achieves different configurations of the distribution network. The proposed GA optimization improves the stability of the voltage-sensitive buses. The DSTATCOM allocation in the distribution system and network reconfiguration is achieved by the multi-objective grey wolf optimization (MO-GWO) algorithm [29]. The GWO algorithm establishes the size and allowance of DSTATCOM. The GA optimized distribution networks are IEEE 33, 39, and real-time 31 bus distribution systems. A hybrid heuristic genetic algorithm is also proposed for the optimal network reconfiguration [30]. The convergence time is improved, and computational time is reduced by the combination of the heuristic approach and genetic algorithm. A comprehensive teaching-learning harmony search optimization algorithm (CLTHSO) is proposed for the network reconfiguration [31]. The CLTHSO method is the combination of the TLBO and HSO method. The suggested approach, multi-objective cellular automata particle swarm optimization (advanced MOPSO), is used to minimize the three objective functions. The exploration phases performed search space solution, and the exploration phase tries to converge the search agents quickly. The met heuristic approaches cannot improve premature convergence [28–30]. The hybrid method provided the simultaneous reconfiguration and optimal allocation of DG units.

References

1. Azizivahed A, Arefi A, Jirsaraie SG, Shafie-khah M, Li L, Zhang J, Catalao JPS (2019) Energy management strategy in dynamic distribution network reconfiguration considering renewable energy resources and storage. *IEEE Trans Sustain Energy*
2. Esmaeili D, Zare K, Mohammadi-Ivatloo B, Nojavan S (2015) Simultaneous optimal network reconfiguration, DG and fixed/switched capacitor banks placement in distribution systems using dedicated genetic algorithm. *Majlesi J Electr Eng* 9(4):31–41
3. Oloulade A, Imano AM, Fifatin X, Vianou A, Tamadaho H, Badarou R (2019) Multiobjective optimization of the safe operation of the electrical distribution system by placing D-FACTS and network reconfiguration. *J Power Ener Eng* 7(9):94–113
4. Zeinalzadeh A, Estebarsari A, Bahmanyar A (2019) Simultaneous optimal placement and sizing of DSTATCOM and parallel capacitors in distribution networks using multiobjective PSO. In: 2019 IEEE Milan PowerTech, pp 1–6. IEEE

5. Hamida IB, Salah SB, Msahli F, Mimouni MF (2019) A new short-term planning strategy for multiobjective distribution network reconfiguration and optimal DG insertion. *Arab J Sci Eng* 44(8):6813–6868
6. Nguyen TT, Nguyen TT, Truong AV, Nguyen QT, Phung TA (2017) Multiobjective electric distribution network reconfiguration solution using runner-root algorithm. *Appl Soft Comput* 52:93–108
7. Siahbalaee J, Rezanejad N, Gharehpetian GB (2019) Reconfiguration and DG sizing and placement using improved shuffled frog leaping algorithm. *Electric Power Compon Syst* 47(16–17):1475–1488
8. Saleh, AA, Mohamed AA, Hemeida AM (2019) Optimal allocation of distributed generations and capacitor using multiobjective different optimization techniques. In: 2019 international conference on innovative trends in computer engineering (ITCE), pp 377–383. IEEE
9. Aravinth NA, Vatul VA, Narayanan K (2019) A multi objective framework for optimal installation of distributed generator units using genetic algorithm. In: 2019 IEEE innovative smart grid technologies-Asia (ISGT Asia), pp 1347–1351. IEEE
10. Selvaraj G, Rajangam K (2019) Multiobjective grey wolf optimizer algorithm for combination of network reconfiguration and D-STATCOM allocation in distribution system. *Int Trans Electr Energy Syst* 29(11):e12100
11. Nikkhah S, Rabiee A (2019) Multiobjective stochastic model for joint optimal allocation of DG units and network reconfiguration from DG owner's and DisCo's perspectives. *Renew Energy* 132:471–485
12. Tavakoli Ghazi Jahani MA, Nazarian P, Safari A, Haghifam MR (2019) Multiobjective grasshopper optimization algorithm based reconfiguration of distribution networks. *J Oper Autom Power Eng* 7(2):148–156
13. Zhan J, Liu W, Chung CY, Yang J (2020) Switch opening and exchange method for stochastic distribution network reconfiguration. *IEEE Trans Smart Grid*
14. Tavakoli Ghazi Jahani MA, Nazarian P, Safari A, Haghifam MR (2019) Multiobjective optimization model for optimal reconfiguration of distribution networks with demand response services. *Sustain Cities Soc* 47:101514
15. Jakus D, Čadenović R, Vasilj J, Sarajčev P (2020) Optimal reconfiguration of distribution networks using hybrid heuristic-genetic algorithm. *Energies* 13(7):1544
16. Teive RCG, Rese ALR, Parreira JP (2019) Distribution network reconfiguration considering multiple objectives-a strategic approach. In: 2019 IEEE PES innovative smart grid technologies conference-Latin America (ISGT Latin America), pp 1–6. IEEE
17. Sun R, Liu Y, Zhu H, Azizipanah-Abarghooee R, Terzija V (2019) A network reconfiguration approach for power system restoration based on preference-based multiobjective optimization. *Appl Soft Comput* 83:105656
18. Mohamadi MR, Abedini M, Rashidi B (2020) An adaptive multiobjective optimization method for optimum design of distribution networks. *Eng Optim* 52(2):194–217
19. Teimourzadeh H, Mohammadi-Ivatloo B (2020) A three-dimensional group search optimization approach for simultaneous planning of distributed generation units and distribution network reconfiguration. *Appl Soft Comput* 88:106012
20. Guo S, Lin J, Zhao Y, Wang L, Wang G, Liu G (2020) A reliability-based network reconfiguration model in distribution system with DGs and ESSs using mixed-integer programming. *Energies* 13(5):1219
21. Quadri IA, Bhowmick S (2019) A hybrid technique for simultaneous network reconfiguration and optimal placement of distributed generation resources. *Soft Comput* 1–22
22. Liu K-Y, Sheng W, Liu Y, Meng X (2017) A network reconfiguration method considering data uncertainties in smart distribution networks. *Energies* 10(5):618
23. Hooshmand E, Rabiee A (2019) Energy management in distribution systems, considering the impact of reconfiguration, RESS, ESSs and DR: a trade-off between cost and reliability. *Renew Energy* 139:346–358
24. Roosta A, Eskandari H-R, Khooban M-H (2019) Optimization of radial unbalanced distribution networks in the presence of distribution generation units by network reconfiguration using harmony search algorithm. *Neural Comput Appl* 31(11):7095–7109

25. Pegado R, Ñaupari Z, Molina Y, Castillo C (2018) Radial distribution network reconfiguration for power losses reduction based on improved selective BPSO. *Electr Power Syst Res* 169:206–213
26. Lavorato M, Franco JF, Rider MJ, Romero R (2011) Imposing radiality constraints in distribution system optimization problems. *IEEE Trans Power Syst* 27(1):172–180
27. Coello CAC, Pulido GT, Lechuga MS (2004) Handling multiple objectives with particle swarm optimization. *IEEE Trans Evol Comput* 8(3):256–279
28. Guerra G, Martinez-Velasco JA (2017) Evaluation of MATPOWER and OpenDSS load flow calculations in power systems using parallel computing. *J Eng* 2017(6):195–204
29. Kong X, Yong C, Wang C, Li P, Li Y, Chen Y (2020) Multiobjective power supply capacity evaluation method for active distribution network in power market environment. *Int J Electr Power Energy Syst* 115:105467
30. Mureddu M, Caldarelli G, Damiano A, Scala A, Meyer-Ortmanns H (2016) Islanding the power grid on the transmission level: less connections for more security. *Sci Rep* 6:34797
31. Gutierrez F, Barocio E, Uribe F, Zuniga P (2013) Vulnerability analysis of power grids using modified centrality measures. *Discrete Dyn Nat Soc*

The Uprising of Blockchain Technology in the Energy Market Industry



Nishkar R. Naraindath , Ramesh C. Bansal , and Raj M. Naidoo 

1 Introduction

1.1 Literature Review

Coal-based power plants have been the predominant form of energy production worldwide due to benefits such as large-scale generational capacity, stable power production and their relatively lower construction costs and periods [1]. The global call for progressively reducing carbon emissions has offset research efforts from fossil fuel energy production to more environmentally friendly options, with photovoltaic and wind systems being popular choices [2]. This drive has been further enforced by the European Commission through the precise formulation of binding environmental targets set for the near future (2030) [3]. The possible extent of decarbonisation of the power sector can be undoubtedly enhanced by promoting localised renewable energy generation. Power network providers often employ traditional financial incentives for prosumers, such as feed-in tariffs. This holistic approach does not adequately account for decentralised energy ecosystems [4]. Another practical approach to promote localised energy production is by rewarding prosumers through subsidies, which

N. R. Naraindath (✉) · R. C. Bansal · R. M. Naidoo
Department of Electrical, Electronic and Computer Engineering, University of Pretoria, Pretoria,
South Africa
e-mail: nrnaraindath@gmail.com

R. C. Bansal
e-mail: raj.naidoo@up.ac.za

R. M. Naidoo
e-mail: rcbansal@ieee.org

R. C. Bansal
Department of Electrical Engineering, University of Sharjah, Sharjah, United Arab Emirates

places unnecessary financial strain on governments and policymakers [5]. Shifting toward transactive energy through energy exchange mechanisms can overcome these shortcomings.

Energy market facilitation is not without challenges. Firstly, they rely heavily on market parties, e.g., transmission system operators, to purchase and coordinate ancillary services for additional support to the system [6]. Secondly, considerable uncertainty is introduced into energy management systems. This uncertainty results in local imbalances, attributed to the reliance on estimation techniques for generation and demand energy profiles. The extent of localised energy imbalances increases with the incorporation of distributed resources, especially renewable energy generators. Ancillary service providers collaborate with grid operators to provide on-demand energy compensation in exchange for financial remuneration [7]. Thirdly, traditional market mechanisms are centralised, which presents a single point of attack jeopardising data and operational security.

1.2 Research Gap and Motivation

Blockchain technology exhibits the potential to address some of the challenges of energy market facilitation by eliminating the need for intermediaries. The technology offers additional advantages of enhanced security, immutability and transparency. However, several barriers hinder its official adoption, such as the apparent lack of deployable infrastructure for scalable applications, the unsustainable energy consumption of some consensus mechanisms, the unmet regulatory implications, insufficient incentive for large-scale entity collaboration, the distinct lack of governance, the risk of rogue distributed autonomous agents and the elevated risks of privacy infringement and illegal usage. These barriers can be addressed with increased awareness, public incentive, policy inducement and extensive research. This paper aims to promote awareness regarding blockchain technology and its role in transforming the energy market industry.

1.3 Contributions

1. Provide a comprehensive overview of the fundamentals, principles and opportunities of blockchain technology in the energy market industry
2. Perform a conceptual simulation of the conventional approach to smart contract integration in facilitating energy exchange transactions
3. Identify opportunities for future research.

1.4 Paper Organisation

In Sect. 2, the concept of blockchains is introduced from a foundation’s perspective, with various design principles provided. Section 3 presents the emergence of smart contracts by discussing their essential purpose and other fundamentals. Section 4 provides an overview of the need for energy markets by highlighting their suitability for achieving sustainable demand management. Section 5 evaluates the current applications of blockchain technology in energy ex-changes in a unified approach and presents a conceptual blockchain-based energy exchange simulation. Section 6 presents the essential findings and conclusions.

2 The Fundamentals of Blockchains

2.1 Defining a Blockchain

A blockchain is a complex data structure described as a distributed and immutable digital ledger. Each ledger record typically represents a specific block on the blockchain, whereas the cryptographical links serve as the continuous chain [8]. Furthermore, direct copies of the blockchain are equitably distributed across numerous independent nodes (active users of the network) to increase the reliability and transparency of the system. These essential characteristics improve the fundamental integrity and security of the system.

A generic blockchain is illustrated in Fig. 1. It typically contains four elements: valuable data, timestamp, hash and previous hash. The data can be in any digital form; however, data capacity limitations exist. Timestamps indicate when a specific block was appended to the chain. Unix timestamps are frequently employed due to their versatility across various digital systems. The hash may be traditionally regarded as an encrypted identifier for data obtained from a hashing algorithm. Lastly, the previous block’s hash is contained in a block for enhanced security. This distinctive feature presents a challenge to subtly altering a block without having an apparent mismatch to the hash record stored in the subsequent block [9].

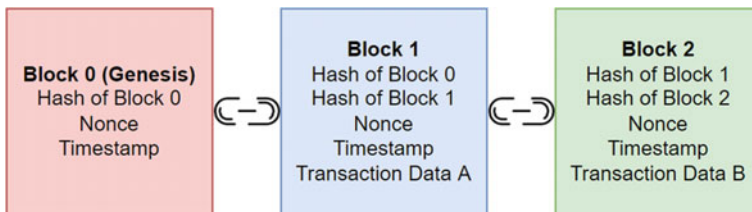


Fig. 1 An example of a blockchain consisting of numerous blocks

2.2 *Types of Blockchains*

Four types of blockchain exist [10]. The first type is the public blockchain which is accessible by the public. These chains are popular as they enable anyone to actively participate in the network without permission from an authority. Transparency increases trust and may be regarded as a strategic asset; however, it may also be perceived as a strategic risk. For instance, marketing and trading strategies may be imitated by competitors. This form of transparency may jeopardise an organisation. As a result, private blockchains may be employed. These blockchains enforce restrictions on access to the network [11]. It also does not require a trusted protocol to make transparency a design choice and is commonly governed by centralised authorities such as the government [12]. Hybrid blockchains are less popular blockchains that combine characteristics of public and private blockchains. The last blockchain type is sidechains. This form of technology serves as an accessory to the blockchain as they run parallel to the main chain. They enhance the efficiency and scalability of the system [13].

2.3 *The Key Principles of Blockchains*

The original Bitcoin white paper highlighted the potential application of a particular protocol; however, several key principles for general blockchain technology can be implicitly identified [14]. These principles enable general blockchains to regulate, validate and secure transactions efficiently. Various aspects of some of the principles are discussed as follows.

Network Integrity Four values are necessary for ensuring a network's integrity is not breached—honesty, accountability, deliberation, and transparency. Transparency is a prevalent trait of blockchain implementation since it provides an effective means to counter corruption and fraud [14]. Conventional systems contain centralised registries with a lack of trust among immediate parties, resulting in the dependence of third parties' involvement as intermediaries. A distributed ledger can counter this as it is naturally transparent and reliable. It typically achieves this by equitably distributing extensive knowledge in the system and enhancing attribution, such as asset origins and ownership history [15]. The other three values can be ensured by applying reliable consensus mechanisms among independent nodes in the network. This powerful feature ensures the consistency and validity of the blockchain [16].

Distribution of Power There is an intrinsic risk of malicious attacks in digital networks, particularly centralised ones. Consequently, a blockchain network should be able to defend against network attacks relentlessly. Blockchains can achieve this by operating in a decentralised manner with a distribution of network control. This feature rapidly improves the strength of defence and reliability of a network since there is no single point of attack [15]. Mass collaboration among independent network

facilitators is therefore required to maintain the blockchain. The resiliency and reliability of the network are increased when there is an expansion in the distribution of power. Furthermore, modern mining algorithms incorporate more innovative techniques requiring application-specific integrated circuits, cloud mining and mining pools [17].

Privacy Every individual is justly entitled to their privacy; however, the digital age has taken away the control of each user's privacy with the user's private information gathered and made readily available. Blockchain enables users to have control of their unique identity by conventionally representing individuals pseudonymously in the form of public addresses. In doing so, no personal information is required from the network's users [18].

Incentivise Commitment Due to the decentralisation of a blockchain, independent network facilitators (miners) should be committed to steadfastly maintaining the integrity and security of the network. For this key concept to function efficiently, there must be value established as a direct incentive [19]. This value is typically enforced through a digital token such as bitcoin. Independent miners are then incentivised to faithfully serve the network by ensuring the secure and effective functioning of the system. Collaboration is naturally encouraged as a direct result. Monetary policies are developed in software to control these rewards issuing. Effective strategies such as reward halving can also be incorporated to promote deflation and increase the token's monetary value, further contributing to an enhanced incentive for users [20].

Security There are numerous security threats to digital systems in the modern-day, such as hacking and phishing [16]. It is, therefore, imperative that systems can prevent these potential threats by incorporating security as a design principle. This fundamental principle is responsible for providing confidentiality, non-repudiation and authenticity of the network. Cryptography is typically utilised to ensure the security of the blockchain is withheld [21].

Inclusion A blockchain network should promote the participation of any individual with no discrimination. This essential characteristic can be achieved by eliminating the specific need for personal information such as the unique identity of a user [14].

3 The Emergence of Smart Contracts

3.1 *Improving the Traditional Contract*

Contracts are an essential aspect of legal-binding agreements. They are responsible for governing rights and duties among multiple parties. It achieves this by clearly defining the specific terms of agreements whilst depicting rewards and possible penalties. Traditional contracts are written or oral form. Challenges naturally arise in executing the agreements without enforcement, occasionally requiring litigation [22]. As a result, there is unnecessary consumption of valuable resources. The novel

concept of smart contracts has been introduced to address this challenge by ensuring compliance with a contract [23]. It can achieve automatic and impartial execution due to its inability to be revoked or stopped. These revolutionary contracts are intended as complementary tools to improve the judicial system progressively and should be used in synergy with traditional contracts [24].

3.2 The Inner Workings of Smart Contracts

Smart contracts are executable computer programmes that are typically deployed on blockchain ledgers [25]. They reliably enforce the terms of contracts by making usage of independent and distributed nodes. By eliminating intermediaries, ancillary costs (from administration and services) and potential risks of tampering can be significantly reduced [26]. Various benefits naturally arise from utilising these contracts, primarily improved computational input, predictability and security. Smart contracts are utilised for three essential purposes. Firstly, they rigorously enforce contractual terms. Secondly, they eliminate the need for an intermediary by enabling a reliable and unbiased interaction. In doing so, a cost-benefit arises. Lastly, they ensure that the moral integrity of both parties is upheld [27].

A smart contract is guaranteed to act in the same manner and is auto-executable. It achieves this by transferring the contract terms into software capable of automatically executing once all conditions have been adequately met [22]. Necessary conditions are continuously monitored with advanced algorithms and sophisticated sensors. The usage of programming logic promotes impartiality in its execution, whereas traditional contracts rely on human judgement. Impartiality is achieved by incorporating programming languages characterised by uniform computational logic and successful execution regardless of external factors. Furthermore, the consensus algorithms employed on distributed blockchains mitigate the potential risks from deliberate manipulation or false contract execution. The shared database enables key nodes to validate the conditions and actions of the contract [28].

3.3 Operational Phases in Smart Contracts

There are four operational phases when considering generic smart contracts from a practical perspective. These distinct phases can be classified as search, negotiation, performance and post-performance incentives. During the search phase, parties discover and survey each other. This phase is followed by negotiation, which entails creating the agreed-upon terms and conditions of the contract. The committed parties then proceed to the performance phase. During this phase, performance is ensured by managing collaterals such as money, service, guarantee or product. In the previous phase, post-performance incentivising is performed by rating the opposing party. This phase is necessary for promoting the desirable outcome and can be achieved

with a specific control structure—the structure assists in predicting the contract’s outcome dynamically.

3.4 Smart Contract’s Lifecycle

Four stages can describe a smart contract’s lifecycle: creation, deployment, execution, and completion [29]. In the creation stage, negotiation is performed among parties to determine the contract’s terms. These terms are then transferred into the software before validating by the parties. The finalised smart contract is stored on a blockchain in the subsequent stage, and digital assets related to the contract are frozen. The execution stage occurs after that, which entails evaluating the conditions of the contract and automatically executing the contract when compliance has been fulfilled. Lastly, the state of the contract is updated with the digital assets released to the appropriate parties.

4 Demand Management Through Energy Markets

4.1 The Need for Localised Energy Trading

Increasing demand for sustainable energy usage has led to more significant adoption rates for renewable energy sources in distribution networks. Energy management systems are therefore necessary to counter the intermittence of renewable energy [30]. Peer-to-peer (P2P) energy management is a promising approach as it offers more considerable flexibility and convenience than traditional approaches such as centralised and multi-agent management [31]. P2P energy trading encourages more significant interaction between energy suppliers, consumers and prosumers. Power system users are incentivised to explore alternative forms of energy production. As a result, the penetration of renewable energy in a power network can be increased, improving the stability and efficiency of a network. Sophisticated bidding strategies can further be employed to optimise profitability and service delivery in these markets as proposed in [32].

4.2 Technical Barriers Hindering P2P Trading

Numerous technical barriers hinder P2P trading systems. One of the most prominent barriers is the rigidity of traditional distribution networks. These networks cannot accommodate bidirectional energy flow [33]. Furthermore, centralised network configurations result in users accessing the power network at different sections

[31]. Active distribution networks can overcome these barriers. These controllable energy systems accommodate distributed power generation, energy storage, and bidirectional energy flow [34]. Incorporating energy hubs can further enhance the involvement of energy ecosystem participants by interconnecting energy producers, prosumers, and consumers. Energy hubs accommodate the multi-generation nature of energy markets [35]. Multiple energy carriers in energy markets can be optimally coordinated within these hubs through stochastic and probabilistic approaches as described in [36] and [37], respectively. These game-theoretic approaches enhance the viability of integrated energy markets in energy hubs whilst presenting an opportunity for risk aversion.

5 Blockchain Technology in Energy Markets

5.1 Present Research Development

Blockchain technology can address the concerns of energy monopolisation and lack of transparency in energy exchanges. The technology can enable peer-to-peer energy exchanges in a decentralised manner [38]. It can facilitate energy exchanges in a secure, unbiased and reliable manner [39]. The concept of peer-to-peer (P2P) energy trading through blockchain technology has been implemented in a Brooklyn microgrid located in New York. A framework for developing an efficient energy market in a microgrid has been proposed in [40]. Upon evaluation of the Brooklyn microgrid, it was partially compliant with the framework.

A wide variety of blockchain solutions are being developed at the moment. A blockchain selection procedure has been proposed in [11] to assist organisations in determining which technology is best suited to their needs. A layered approach to protocol integration is recommended in complex systems requiring scalability, decentralisation, and practicality. Layer 1 protocols represent the base architecture of networks, whereas layer 2 operates on layer 1 to improve the functionality and interoperability of the system [41]. This layered approach has been incorporated into a novel sharing system [42]. The blockchain ecosystem consists of a blockchain (layer 1), lightning network (layer 2) and smart contracts (layer 2). Specialised solutions are also being developed. For instance, a novel decentralised digital currency (NRGcoins) has been proposed in [43]. The currency has been developed to improve the feasibility and reliability of open currency exchange markets by employing a hybrid machine-learning algorithm. There is a concentrated focus on deploying smart contracts for peer-to-peer energy markets facilitated on blockchains [44]. Smart contracts, commonly de-ployed by centralised power management systems, are incorporated to automate the transfer of funds in the network [45]. A blockchain system was proposed in a study of a game theory model, including energy storage demand-side management [46]. A consortium blockchain based on Zig-Ledger was developed as a rudimentary technological framework for energy exchanges. Smart

contracts containing energy bids were then manually deployed on the blockchain. The system can be improved through the implementation of a decentralised application.

A modest energy offer-based blockchain solution, without smart contracts, can also be employed for smaller-scale systems such as the one discussed in [47].

Furthermore, energy markets are being established, with public blockchains predominant. This approach presents a challenge to the supervision capabilities of power organisations as users can freely interact with the system. In addition, personal data is exposed. On the other hand, energy management performed on consortium blockchains addresses concerns of exposure privacy at the risk of malicious nodes registering false accounts and entering the system. A private blockchain system can address these concerns whilst enabling reduced communication delays; however, there is centralisation. An example of this approach has been deployed on a Hyperledger Fabric [31]. Another application of a private blockchain, built through Multi-Chain, is explored in [22], with a machine-to-machine transaction management method proposed.

5.2 Conceptual Simulation of a P2P Energy Exchange

The concept of blockchain technology in facilitating a simplified energy exchange between an arbitrary prosumer and consumer is simulated on MATLAB. The algorithm has been adapted from the pseudocode provided in [48] to account for insufficient consumer eWallet balances. The capability of the smart contract is evaluated by modelling the contract's terms as a function as depicted in Fig. 2. The smart contract successfully coordinates energy exchange transfers and balance updates for two scenarios—an energy surplus and an energy deficit. A summary of the simulation results is provided in Table 1.

6 Conclusion

Blockchain technology possesses the potential to revolutionise the digital age. In synergy with smart contracts, blockchains enable applications to be facilitated in a transparent, reliable, and immutable environment. The present research developed has been focused on modest applications from a predominantly transactive perspective, as demonstrated in the conceptual simulation performed on MATLAB. With more significant integration efforts, Blockchain technology can enable fully autonomous and decentralised energy ecosystems. Recommended opportunities for research are in the decentralisation of energy scheduling, intellectual property control, licensing, maintenance management, power flow monitoring, power quality regulation and resource management.

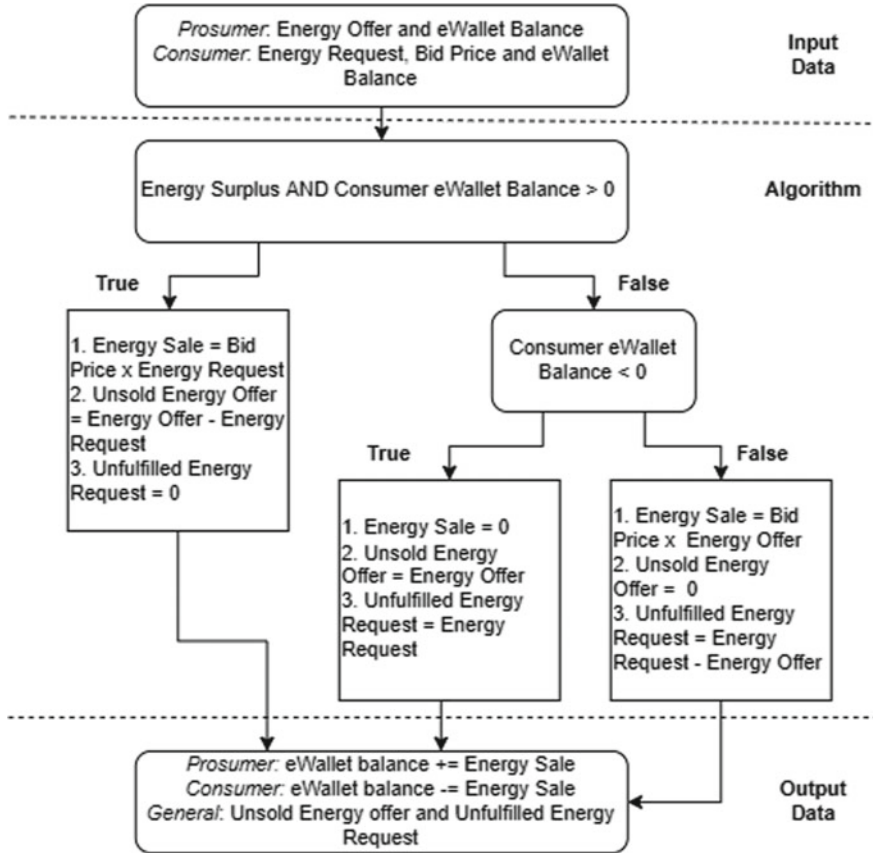


Fig. 2 Methodology for simulating a P2P energy exchange on MATLAB

Table 1 Simulation results under various energy conditions

Time interval (ms)	0 < t < 1		1 < t < 2		2 < t < 3		3 < t < 4	
Energy condition	Excess	Deficit	Excess	Deficit	Excess	Deficit	Excess	Deficit
Energy offer (kWh)	45.21	30.31	42.80	27.80	40.34	25.34	41.57	26.57
Bid price (ZAR)	6.647	8.647	5.886	7.886	5.106	7.106	5.497	7.497
Energy request (kWh)	32.60	32.60	31.40	31.40	30.17	30.17	30.79	30.79
Consumer eWallet (ZAR)	783.30	738.80	598.40	519.50	444.40	339.40	275.10	140.20
Prosumer eWallet (ZAR)	316.70	361.20	501.60	580.50	655.60	760.60	824.90	959.80
Unsold energy (kWh)	12.60	0	11.40	0	10.17	0	10.79	0
Unfulfilled energy (kWh)	0	2.395	0	3.598	0	4.832	0	4.214

References

1. Liu X, Bansal R (2014) Integrating multi-objective optimization with computational fluid dynamics to optimize boiler combustion process of a coal fired power plant. *Appl Energy* 114:658–669
2. Bansal RC, Zobaa AF (2022) Handbook of renewable energy technology systems. World Scientific Publisher, UK
3. Knopf B, Nahmmacher P, Schmid E. The European renewable energy target for 2030—an impact assessment of the electricity sector. *Energy Policy* 85:50–60, 10
4. Lesser JA, Su X (2008) Design of an economically efficient feed-in tariff structure for renewable energy development. *Energy Policy* 36(3):981–990
5. Heras S, Palanca J (2016) Smart grid demonstration platform for renewable energy exchange. *Adv Pract Appl Scalable Multi-agent Syst* 1:277–280
6. King W, Scarpellini P (2000) Connection rules for generation and management of ancillary services. *EURELECTRIC*, vol 1, no. May
7. Hijgenaar S, Erkin Z, Keviczky T, Siemons J, Bisschops R, Verbraeck A (2018) A decentralised energy trading architecture for future smart grid load balancing. In: *IEEE international conference on smart grid communications*, vol 1, no. October, pp 77–82
8. Pilkington M (2016) Blockchain technology: principles and applications. In: *Research handbook on digital transformations*, pp 225–253
9. Crosby M, Pattanayak P, Verma S, Kalyanaraman V (2016) Blockchain technology: beyond bitcoin. *Appl Innov Rev* June(2):7–19
10. de Kruijff J, Weigand H. Understanding the blockchain using enterprise ontology. In: *Lecture notes in computer science*, pp 29–43
11. Lai R, LEE Kuo Chuen D (2018) Blockchain—from public to private. In: *Handbook of blockchain, digital finance, and inclusion*, 1st edn., vol 2, pp 145–177. Elsevier
12. Sabry SS, Kaittan NM, Ali IM (2019) The road to the blockchain technology: concept and types. *Periodica Eng Nat Sci* 7(4):1821–1832
13. Abdi AI, Eassa FE, Jambi K, Almarhabi K, Al-Ghamdi ASAM (2020) Blockchain platforms and access control classification for IOT systems. *Symmetry* 12(10):1–17
14. Tapscott D, Ticoll D, Lowy A (2016) Blockchain revolution: how the technology behind bitcoin is changing money, business, and the world
15. Gupta S, Sinha S, Bhushan B (2020) Emergence of blockchain technology: fundamentals, working and its various implementations. *SSRN Electron J* 1:1–5
16. Zhao Y. Research on the consensus mechanisms of blockchain technology. In: *International conference on economics, finance, business, and development (ICEFBD)*, pp 289–293. Francis Academic Press
17. Banafa A (2020) Blockchain technology and applications, pp 1–154
18. Feng Q, He D, Zeadally S, Khan MK, Kumar N (2019) A survey on privacy protection in blockchain system. *J Netw Comput Appl* 126:45–58
19. He Y, Li H, Cheng X, Liu Y, Yang C, Sun L (2018) A blockchain based truthful incentive mechanism for distributed P2P applications. *IEEE Access* 6(1):27324–27335
20. Bhaskar ND, Chuen DLK (2015) Bitcoin mining technology. Elsevier Inc.
21. Halpin H, Piekarska M (2017) Introduction to security and privacy on the blockchain. In: *Proceedings—2nd IEEE European symposium on security and privacy workshops, EuroS and PW*, pp 1–3
22. Huang Y, Bian Y, Li R, Zhao JL, Shi P (2019) Smart contract security: a software lifecycle perspective. *IEEE Access* 7:150184–150202
23. Szabo N (1996) Smart contracts: building blocks for digital transformation. *J Transhumanist Thought* 16:1–14
24. Sayeed S, Marco-Gisbert H, Caira T (2020) Smart contract: attacks and protections. *IEEE Access* 8:24416–24427
25. Zheng Z, Xie S, Dai HN, Chen W, Chen X, Weng J, Imran M (2020) An overview on smart contracts: challenges, advances and platforms. *Future Gener Comput Syst* 105:475–491

26. Ante L (2020) Smart contracts on the blockchain—a bibliometric analysis and review. *Telematics Inform* 57(April):101519
27. Wang S, Yuan Y, Wang X, Li J, Qin R, Wang FY (2018) An overview of smart contract: architecture, applications, and future trends. In: *IEEE intelligent vehicles symposium, proceedings*, vol June, no 4, pp 108–113
28. Zou W, Lo D, Kochhar PS, Le XBD, Xia X, Feng Y, Chen Z, Xu B (2021) Smart contract development: challenges and opportunities. *IEEE Trans Softw Eng* 47(10):2084–2106
29. Sillaber C, Waltl B (2017) Life cycle of smart contracts in blockchain ecosystems. *Datenschutz und Datensicherheit - DuD* 41(8):497–500
30. Hirsch A, Parag Y, Guerrero J (2018) Microgrids: a review of technologies, key drivers, and outstanding issues. *Renew Sustain Energy Rev* 90(March):402–411
31. Wang L, Jiao S, Xie Y, Mubaarak S, Zhang D, Liu J, Jiang S, Zhang Y, Li M (2021) A permissioned blockchain-based energy management system for renewable energy microgrids. *Sustainability (Switzerland)* 13(3):1–19
32. Saxena A, Kumar R, Bansal RC, Mahmud M (2021) Bidding strategies of a power producer in power market: measurement indices and evaluation. In: *Uncertainty in modern power systems*, pp 635–652. Elsevier
33. Shang Y, Liu M, Shao Z, Jian L (2020) Internet of smart charging points with photovoltaic Integration: a high-efficiency scheme enabling optimal dispatching between electric vehicles and power grids. *Appl Energy* 278(July):115640
34. Núñez-Mata O, Palma-Behnke R, Valencia F, Mendoza-Araya P, Jiménez-Estévez G (2018) Adaptive protection system for microgrids based on a robust optimization strategy. *Energies* 11(2)
35. Mohammadi M, Noorollahi Y, Mohammadi-ivatloo B, Yousefi H (2017) Energy hub: from a model to a concept—a review. *Renew Sustain Energy Rev* 80(November 2016):1512–1527
36. Heidari A, Bansal RC, Hossain J, Zhu J (2022) Strategic risk aversion of smart energy hubs in the joined energy markets applying a stochastic game approach. *J Clean Prod* 349(March):131386
37. Heidari A, Bansal RC (2021) Probabilistic correlation of renewable energies within energy hubs for cooperative games in integrated energy markets. *Electric Power Syst Res* 199(May):107397
38. Mengelkamp E, Notheisen B, Beer C, Dauer D, Weinhardt C (2018) A blockchain-based smart grid: towards sustainable local energy markets. *Comput Sci Res Dev* 33(1–2):207–214
39. Foti M, Vavalis M (2019) Blockchain based uniform price double auctions for energy markets. *Appl Energy* 254(July):113604
40. Mengelkamp E, Gartner J, Rock K, Kessler S, Orsini L, Weinhardt C (2018) Designing microgrid energy markets: a case study: The Brooklyn microgrid. *Appl Energy* 210:870–880
41. Aniello L, Baldoni R, Gaetani E, Lombardi F, Margheri A, Sassone V (2017) A prototype evaluation of a tamper-resistant high performance blockchain-based transaction log for a distributed database. In: *Proceedings—13th European dependable computing conference, EDCC*, pp 151–154
42. Qi L, Li X, Qi B, Wang H (2017) Shared economy model of charging pile based on block chain ecosystem. *Electric Power Constr* 38(9):1–7
43. Mihaylov M, Jurado S, Van Moffaert K, Avellana N, Nowé A (2014) NRG-X-change a novel mechanism for trading of renewable energy in smart grids. In: *SMART-GREENS—Proceedings of the 3rd international conference on smart grids and green IT systems*, pp 101–106
44. Brilliantova V, Thurner TW (2019) Blockchain and the future of energy. *Technol Soc* 57:38–45
45. Wu X, Duan B, Yan Y, Zhong Y (2018) M2M blockchain: the case of demand side management of smart grid. In: *Proceedings of the international conference on parallel and distributed systems—ICPADS*, vol December, pp 810–813
46. Noor S, Yang W, Guo M, van Dam KH, Wang X (2018) Energy demand side management within micro-grid networks enhanced by blockchain. *Appl Energy* 228(July):1385–1398

47. Sikorski JJ, Haughton J, Kraft M (2017) Blockchain technology in the chemical industry: machine-to-machine electricity market. *Appl Energy* 195:234–246
48. Kirli D, Couraud B, Robu V, Salgado-Bravo M, Norbu S, Andoni M, Antonopoulos I, Negrete-Pincetic M, Flynn D, Kiprakis A (2021) Smart contracts in energy systems: a systematic review of fundamental approaches and implementations. *Renew Sustain Energy Rev* 158:112013

Performance of Nichrome/p-Si Schottky Diode



Ekta Sharma, Reena Rathi, and Vamshi Krishna Dasarraju

1 Introduction

Metal-Semiconductor contacts are the base of all semiconductor devices which may be rectifying (Schottky) or Ohmic in nature. Schottky contacts have important applications like in high-frequency devices, high switching devices, metal base transistor, nuclear particle detector, varactor diode, temperature sensors (from cloud physics to harsh environment), gas sensors, etc. [1, 2]. For use in harsh environment like gas sensing applications, particle detection, temperature sensor, etc. a rectifying contact must be non-corrosive, antioxidant, easy to fabricate, compatibility with device and should be of low cost [3–6]. Additionally, the interface between metal and semiconductor should be good so that device can give desired results. Various techniques have proposed to improve the interface between metal-semiconductor contacts [7–9].

Furthermore, contact should be proper because the accuracy of results depends upon M-S interface properties like their adhesion, reactivity and native oxide effect. Researchers discuss the problems associated with commonly used elemental metals as Schottky contact on silicon [1, 2]. Ageing effect, oxidation in open atmosphere and low-temperature reaction of Al excludes it for making good Schottky contact. While the drawbacks of gold as Schottky contact include diffusion of silicon into gold and its poor adhesion [10–12]. Although many metals like Ti, Cr was used as diffusion barriers but these do not provide satisfactory results. Pt was also used as Schottky contact metal, but it is costly and not compatible with the CMOS process.

Silicides of many metals were also incorporated to make abrupt junctions, but they also have some problems associated with them. Cobalt silicide exhibit interface

E. Sharma · Reena Rathi (✉)
Chaudhary, Ranbir Singh University, Jind 126102, India
e-mail: rekharathi0441@gmail.com

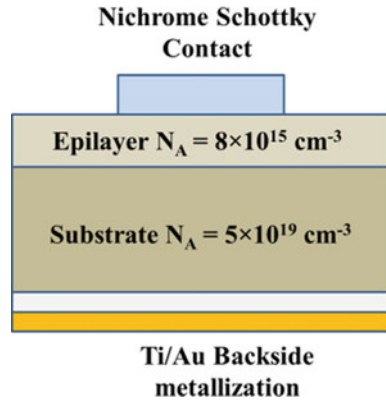
V. K. Dasarraju
Illinois University, Northern, Dekalb, IL 60115, USA

roughness problem which leads to junction leakage. Moreover, high temperature is required for the formation of the CoSi₂ phase, which affects the redistribution of activated implanted impurities in material [12]. Additionally, Pd metal was found to be very reactive and forms amorphous silicide with silicon even at room temperature. A silicide interface is rarely having similar crystal matching to that of the silicon crystal structure without any stresses. Stress may cause cracking of the layer. When compositions of silicides of Hf, Zr, Mn, Ni, Rh approaches nearly equal to silicon, barrier heights will decrease as compared to elemental metals. The same decrease in barrier height was observed with metals like Cr, Mo, Pt and W. Rare earth metals and their disilicides, needs an additional passivation layer to prevent their oxidation. Most of the transition metals like Mo, Ni, Cr, and Cu get oxidized in the open environment [2, 7, 13–17]. In order to probe metal-Silicon system more closely e.g., to control the barrier heights, making of shallow junctions and to understand chemistry of interaction of binary alloy systems with silicon, some alloys like NiPt, PtSi, PdSi, GdPt, GdV, PbEr, TiW, etc. have been also reported [18–23]. To the best of our knowledge, not much work has been reported on nichrome alloy as Schottky contact metal. Nichrome alloy has distinctive properties like antioxidant, non-corrosive, high thermal stability, low cost and device compatibility [16, 24, 25]. These properties may prove a milestone in future electronic devices used in harsh environment like gas sensing, particle detection, temperature sensing, etc. In this paper, nichrome alloy-based Schottky diode on p-type silicon wafer was fabricated by using E-beam deposition process. Electrical characteristics of fabricated diodes were explored on the basis of space charge limiting current, Poole-Frenkel and Ohmic conduction mechanisms.

2 Experimental

Initially, p/p+-Si<100> epitaxial wafer with resistivity 2 ± 0.2 ohm-cm were used for fabrication of Schottky diode. Before metal deposition, wafers were degreased using warm TCE, Acetone and Methanol. Furthermore, wafers were cleaned using standard RCA cleaning technique, in which organic and inorganic contaminants removed by NH₄OH:H₂O₂:H₂O (1:1:5 volume at 600 °C) and HCl:H₂O₂:H₂O (1:1:6 volume at 85 °C) solutions, respectively. Subsequently, silicon wafers were given a dip in 5% HF solution to remove native oxide. For making Schottky contact, nichrome wire having composition Ni-80 wt%:Cr-20 wt % was used as a source. Nichrome wire was turned into a circular shape and placed into crucible within the e- beam chamber. A vacuum of the order of 2×10^{-7} Torr was maintained using ion pumps and subsequently, nichrome was evaporated using e-beam. Diodes of different sizes i.e., 0.5 mm were fabricated by using a metal mask. The film thickness of nichrome was measured using Tally Step and came out approximately 2 μm. For making Ohmic contact, a composite layer of Ti/Au was deposited on the backside of the silicon wafers. Current–Voltage (I–V) characteristics of the diode were measured

Fig. 1 A schematic of the fabricated Nichrome/p-Silicon Schottky diode



using Keithley 236 I-V analyzer at room temperature. A schematic representation of fabricated Nichrome/p-silicon Schottky diode has been depicted in Fig. 1.

3 Results and Discussion

The forward bias electrical characteristics of nichrome/p-Si Schottky diodes were observed at room temperature and illustrated in Fig. 2a. The I-V characteristics were achieved by sweeping the DC bias voltage ranging from 0 to 0.6 V with a step of 1 mV. The intercept and slope of the straight-line portion of semi-logarithmic J-V graph were used to determine barrier height and ideality factor. Values of the ideality factor of devices were observed to be greater than unity ($\eta > 1$), which means that there exists conduction mechanism other than thermionic emission.

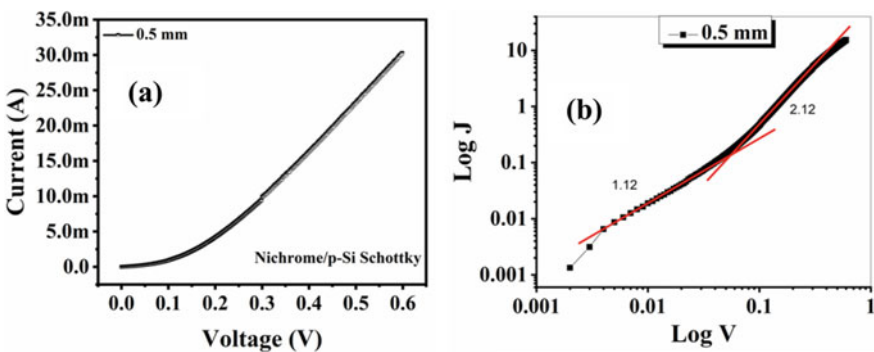


Fig. 2 a Current-voltage characteristics of nichrome/n-Si Schottky barrier diodes of size 0.5 mm in diameter. b Log (J) versus Log (V) characteristics of the device for investigation of current conduction mechanism

Many researchers have pointed out that non-ideality is a cause of Schottky emission, Pool-Frenkel mechanism, space charge limiting current, etc. [17, 26]. Therefore, to describe the forward characteristics of diode; a logarithmic scale was used. The consistencies of curves were probed using power-law type relationship $I \propto V^m$. Dominancy among the above-said mechanisms was interpreted in terms of value of power (m) of $\log J$ - $\log V$ graph in Fig. 2b.

When value of $m = 1$, Ohmic conduction mechanism will be dominated whereas $m > 2$ indicates space charge limiting current conduction mechanism. Furthermore, the value of m lies in between 1 and 2 implies that the conduction would be either by Schottky or Poole-Frenkel conduction mechanism.

3.1 Conduction Mechanism in Fabricated Diode

We have probed the prevailing dominancy of above said conduction mechanisms in p-type fabricated diode. Two linear regions were observed in $\log J$ - $\log V$ curve of Nichrome/p-Si Schottky diodes of size 0.5 mm in diameter, shown in Fig. 2b. These regions were classified as the lower electric field region where the power is $1 < m < 2$ and other is the higher electric field region, where the power is $m > 2$. The value of m lies in between $1 < m < 2$ in the lower electric field region implies that current conduction mechanism could be either by Schottky emission or by Poole-Frenkel effect. Theoretical calculated value of β was 1.1×10^{-5} for the Schottky effect and 2.19×10^{-5} for the PF effect.

The slope of Fig. 2b in the lower electric field region was found 1. It indicates that current conduction mechanism is Ohmic in nature, which is due to the presence of thermal equilibrium free charge carriers. Whereas, in the higher electric field region, the slope was found 1.51, which implies that current conduction mechanism could be either by Schottky emission or by Poole-Frenkel effect. The experimentally calculated value of β comes out to be 2.75×10^{-5} for 0.5 mm diameter diode size which shows that current conduction is due to the PF effect. The experimental values of β for both the diodes are in close agreement with theoretically calculated values of β in the PF conduction mechanism. These results indicate that the common mechanism of current conduction among p-type silicon Schottky diode is ohmic in the lower electric field region and PF in the high electric field region. This gives impression that there are deep defect states present within the reference material due to dirt, swirl in substrate, misfit dislocations, oxygen, carbon, etc. [2, 27]. These defect states may be contributed in the re-emission of charge carriers via Poole-Frenkel effect in the low electric field region. In high electric field region, the concentration of charge carriers will be very high, and starts filling up the shallow trap states. These shallow traps present near semiconductor-metal interface will limit the current to flow via space charge limiting current [28].

4 Conclusion

Anti-oxidant, anti-corrosive and low-cost nichrome (Ni-80 wt%:Cr-20 wt%) alloy-based Schottky on p-type silicon diode was successfully fabricated and characterized. It requires no extra adhesive layer and found compatible with standard silicon fabrication technology. Nichrome film was deposited using the e-beam evaporation metallization system. In fabricated Schottky diodes, it was observed that there exist two regions namely the low electric field region and the high electric field region. The slopes of LogJ-LogV graph reveal that in low electric field region, current conduction mechanism will be ohmic whereas in high electric field region, conduction mechanism will be PF limiting current. These curves conclude that there exist some deep level defects states in reference material, which emits charge carriers in low electric field via Poole-Frenkel conduction. In high electric field regions, charge carriers will be very high due to Poole-Frenkel emitted and electrode injected charge carriers. These carriers will contribute in current conduction in the high electric field region via space charge limiting current.

References

1. Tyagi MS (1984) Physics of Schottky barrier junctions. In: Metal-semiconductor Schottky barrier junctions their applications, pp 1–60. https://doi.org/10.1007/978-1-4684-4655-5_1
2. Kumar V, Maan AS, Akhtar J (2014) Barrier height inhomogeneities induced anomaly in thermal sensitivity of Ni/4H-SiC Schottky diode temperature sensor. *J Vac Sci Technol B Nanotechnol Microelectron Mater Process Meas Phenom* 32(4):041203. <https://doi.org/10.1116/1.4884756>
3. Kumar V, Pawar S, Maan AS, Akhtar J (2015) Diameter dependent thermal sensitivity variation trend in Ni/4H-SiC Schottky diode temperature sensors. *J Vac Sci Technol B Nanotechnol Microelectron Mater Process Meas Phenom* 33(5):052207. <https://doi.org/10.1116/1.4929890>
4. Kumar V, Verma J, Maan AS, Akhtar J (Dec.2020) Epitaxial 4H-SiC based Schottky diode temperature sensors in ultra-low current range. *Vacuum* 182:109590. <https://doi.org/10.1016/j.vacuum.2020.109590>
5. Petersson S, Mgbenu E, Norde H, Tove PA (1977) Evaluating PtSi front contact to surface barrier detectors. Elsevier
6. Hiraki A (1983) Low temperature reactions at Si/metal interfaces; What is going on at the interfaces? *Surf Sci Rep* 3(7):357–412. [https://doi.org/10.1016/0167-5729\(84\)90003-7](https://doi.org/10.1016/0167-5729(84)90003-7)
7. Kumar V, Kumar S, Maan AS, Akhtar J (2020) Interface improvement of epitaxial 4H-SiC based Schottky diodes by selective heavy ion irradiation. *Appl Nanosci* 1–8. <https://doi.org/10.1007/s13204-020-01608-3>
8. Kumar V, Maan AS, Akhtar J (2022) Defect levels in high energy heavy ion implanted 4H-SiC. *Mater Lett* 308:131150. <https://doi.org/10.1016/J.MATLET.2021.131150>
9. Kumar V, Maan AS, Akhtar J (2013) Selective SHI irradiation for mesa type edge termination in semiconductor planar junction. *J Phys Conf Ser* 423(1):012057. <https://doi.org/10.1088/1742-6596/423/1/012057>
10. Card HC (1976) Aluminum—Silicon Schottky barriers and ohmic contacts in integrated circuits. *IEEE Trans Electron Devices* 23(6):538–544. <https://doi.org/10.1109/T-ED.1976.18449>

11. Kumar V, Maan AS (2018) Improvement in reverse bias leakage current of Ni/4H-nSiC Schottky barrier diodes via MeV selective ion irradiation. In: IOP conference series: materials science and engineering, vol 331, no 1, p 012016. <https://doi.org/10.1088/1757-899X/331/1/012016>
12. Kumar V, Kaminski N, Maan AS, Akhtar J (2016) Capacitance roll-off and frequency-dispersion capacitance-conductance phenomena in field plate and guard ring edge-terminated Ni/SiO₂/4H-nSiC Schottky barrier diodes. *Phys status solidi* 213(1):193–202. <https://doi.org/10.1002/pssa.201532454>
13. Kumar V, Maan AS, Akhtar J (2020) Electronic transport in epitaxial 4H–SiC based Schottky diodes modified selectively by swift heavy ions. *Mater Sci Semicond Process* 115:105108. <https://doi.org/10.1016/J.MSSP.2020.105108>
14. Kumar V, Kumar S, Maan AS, Akhtar J (2021) Interfacial and structural analysis of MeV heavy ion irradiated SiC. *Appl Nanosci* 1–8. <https://doi.org/10.1007/s13204-021-01921-5>
15. Kumar V, Maan AS, Akhtar J (2018) Tailoring surface and electrical properties of Ni/4H-nSiC Schottky barrier diodes via selective swift heavy ion irradiation. *Phys status solidi* 215(5):1700555. <https://doi.org/10.1002/PSSA.201700555>
16. Petrovic S et al (2006) Structure and surface composition of NiCr sputtered thin films. *Sci Sinter* 38(2):155–160. <https://doi.org/10.2298/SOS0602155P>
17. Yakuphanoglu F, Tugluoglu N, Karadeniz S (2007) Space charge-limited conduction in Ag/p-Si Schottky diode. *Phys B Condens Matter* 392(1–2):188–191. <https://doi.org/10.1016/J.PHYSB.2006.11.018>
18. Thomas S, Terry LE (1976) Composition profiles and Schottky barrier heights of silicides formed in NiPt alloy films. *J Appl Phys* 47(1):301–307. <https://doi.org/10.1063/1.322316>
19. Nava F, Mantovani S, Pignatelli G, Queirolo G, Celotti G (1982) The interaction of Ni-Pt alloy with silicon. *Thin Solid Films* 89(4):381–386. [https://doi.org/10.1016/0040-6090\(82\)90315-7](https://doi.org/10.1016/0040-6090(82)90315-7)
20. Eizenberg M, Foell H, Tu KN (1981) Formation of shallow Schottky contacts to Si using Pt-Si and Pd-Si alloy films. *J Appl Phys* 52(2):861–868. <https://doi.org/10.1063/1.328850>
21. Thompson R, Eizenberg M, Tu KN (1981) Schottky contacts of Gd-Pt and Gd-V alloys on n-Si and p-Si. *J Appl Phys* 52(11):6763–6768. <https://doi.org/10.1063/1.328629>
22. Ottaviani G, Tu KN, Thompson RD, Mayer JW, Lau SS (1983) Interaction of Pd–Er alloys with silicon. *J Appl Phys* 54(8):4614–4622. <https://doi.org/10.1063/1.332617>
23. Aboelfotoh MO (1987) Schottky-barrier behavior of a Ti–W alloy on Si(100). *J Appl Phys* 61(7):2558–2565. <https://doi.org/10.1063/1.337933>
24. Rölke J (1981) Nichrome thin film technology and its application. *Electrocompon Sci Technol* 9(1):51–57. <https://doi.org/10.1155/APEC.9.51>
25. Weiser K (1970) *Semiconductor technique: current injection in solids*. Murray A. Lampert and Peter Mark. Academic Press, New York, vol xiv, 354 pp, illus. \$18. Electrical science series. *Science* (80-) 170(3961):966–967. <https://doi.org/10.1126/science.170.3961.966.b>
26. Yüksel ÖF, Kuş M, Şimşir N, Şafak H, Şahin M, Yenel E (2011) A detailed analysis of current-voltage characteristics of Au/perylene-monoimide/n-Si Schottky barrier diodes over a wide temperature range. *J Appl Phys* 110(2):024507. <https://doi.org/10.1063/1.3610394>
27. Yoon Y, Yan Y, Ostrom NP, Kim J, Rozgonyi G (Nov.2012) Deep level transient spectroscopy and minority carrier lifetime study on Ga-doped continuous Czochralski silicon. *Appl Phys Lett* 101(22):222107. <https://doi.org/10.1063/1.4766337>
28. Verma J, Pant S, Kumari S, Belwanshi V, Dalal J, Kumar A (2022) Trench termination in Ga₂O₃-based power device: a simulation-based study. *Appl Nanosci* 2021:1–7. <https://doi.org/10.1007/S13204-021-02219-2>

Behaviour of SiC Schottky Diode Temperature Sensors in 200–600 K



Jaya, Bhavya Sinhmar, Vamshi Krishna Dasarraju, and Sudhir Dalal

1 Introduction

To attain best quality and yield, the electronic devices demand for best monitoring of temperature levels. In integrated circuits (ICs), real-time monitoring of temperature at critical locations helps in predicting the failure of vital parts of the system in a timely fashion, which ultimately reduces the maintenance cost and even damage to the system. To lessen the industrial influence on environment, energy efficiency and explicit temperature control provides the optimum research area which exerts increasing demands from temperature sensors. All monitoring applications, demand for temperature sensors disregarding their probed settings. Therefore, the basic need of industrial sector is reliable, precise and accurate temperature sensors. Their technological advancement needs the development of sturdy, low-cost reproducible and easily ICs integrated temperature sensors [1–3].

Owing to their quick response time, broad range of temperature and good accuracy, thermocouples are preferred for stunning temperature sensing. Common industrial working conditions include strong vibrations, high heat, erosion (cetera), corrosion, etc., which collectively decreases the thermocouple dependability and limit their lifespan [4]. Looking into above needs, temperature sensors based on commonly used semiconductors like Si, GaAs, etc., have been developed and implemented in various applications [5, 6]. However, extreme environments like space exploration

Jaya · B. Sinhmar (✉)
Chaudhary Ranbir Singh University, Jind 126102, India
e-mail: bhavyasinhmar@gmail.com

V. K. Dasarraju
Northern Illinois University, Dekalb, IL 60115, USA

S. Dalal
AI Jat HM College, Rohtak 124001, India

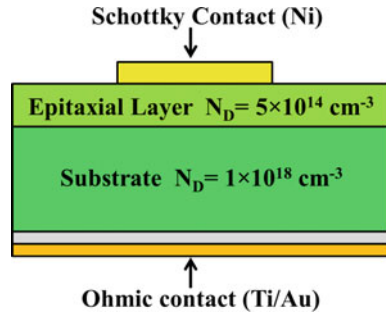
missions, terrestrial applications, etc. needs broad temperature operational and radiation robust temperature sensors. Low working temperature and susceptibility to radiation damage exclude the applicability of conventionally semiconductor-based (i.e., Si, GaAs, etc.) sensors in above mentioned applications.

Utilization of wide bandgap semiconductors like SiC, GaN, diamond, etc. has suggested as an alternative. However, owing to advancement in the crystal quality as well as ease of access in the market makes SiC of utmost importance. It has a wide range of excellent properties, such as a wide band gap, a high thermal coefficient, a low intrinsic carrier concentration, a high breakdown electric field, and a high chemical inertness, making it a promising candidate for use in extreme environments. As a consequence, researchers are continuously working on the development of SiC-based various devices and their improvement in their performance [1, 3, 5, 7–11]. Recently, Schottky diodes are developed and the most cost-effective devices among all SiC fabricated devices, with significant commercial purposes in power and sensing applications [2, 4, 12–15]. Higher switching performance, power density, efficiency and lower system costs, ease of fabrication are just a few benefits that make Schottky diodes of prime interest in temperature sensing applications. SiC Schottky diodes are therefore good candidates for high-temperature monitoring in challenging industrial environments because of their simple structure, extremely small size, low cost, ease of fabrication. Reported literature reveals that SiC-based SBD temperature sensors have been characterized at high temperature [2, 13]. However, a little attention is paid to their low-temperature behavior, which is imperative for their utilization in space exploration and terrestrial applications. Therefore, the present work reports thermal sensing characteristics of SiC-based Schottky diode temperature sensors at low temperatures i.e., in 200–600 K. The sensitivity value and stability is governed by forward behavior and parameter extraction.

2 Device Design

Simulation of devices gives useful information about devices that cannot be predicted in real-time. The atlas module of SILVACO TCAD software facilitates the design of the device and its simulation for getting electrical characteristics, which gives more insight into physical behaviour in the device under operation. This software has the capability of modelling various devices made up of crystalline to amorphous materials and dc and ac characteristics, etc. This tool is having a bunch of semiconductor equations to model various phenomena in the devices. Using the above capabilities, accurate modelling of any device can be performed. Moreover, the exactness of the findings depends on the correctness of the parameter inputs. The main parameters in the present work are the bandgap of SiC, its intrinsic carrier concentration, mobility of electrons and holes, electron affinity, permittivity, doping of the substrate, device dimensions, diffusion lengths, etc. A schematic representation of the simulated structure in the existing work is depicted in Fig. 1. The structure contained a substrate, which is selected as n+ SiC in the present work, with a height of 20 μm and doping

Fig. 1 Schematic of the fabricated device with dimensions. The material parameters are as per purchased wafer



of $1 \times 10^{18} \text{ cm}^{-3}$. The top layer on the substrate is an epitaxial layer or drift layer with a thickness of $10 \mu\text{m}$ having a doping of $= 5 \times 10^{14} \text{ cm}^{-3}$. The Schottky metal in the present work was chosen of metal having work function 5.1 eV . The main parameters for dielectric are its permittivity and thickness as these parameters impact reverse breakdown voltage mainly. The backside contact was made as an ohmic contact. For SiC, following parameters have been used; band gap = 3.2 eV , electron affinity = 4.12 eV , Schottky metal work function = 4.8 V , permittivity = 9.6 , conduction band density of states = $1 \times 10^{19} \text{ cm}^{-3}$, valence band density of states = $1.2 \times 10^{19} \text{ cm}^{-3}$ and the temperature $T = 300 \text{ K}$. Numerous models like FD statistics, Selberherr impact ionization, SRH and Auger recombination, parallel and concentration field-dependent mobility, etc. have used.

3 Results and Discussion

The forward bias characteristic of the designed device has been shown in Fig. 2. It can be seen in Fig. 2 that the forward voltage drop in the device is decreasing with increasing the temperature. Moreover, the current is increasing exponentially within applied voltage range.

Fig. 2 Current–voltage characteristics of the fabricated device within specified temperature range

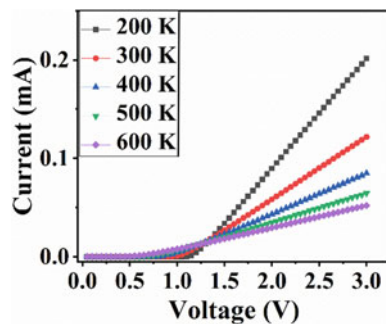
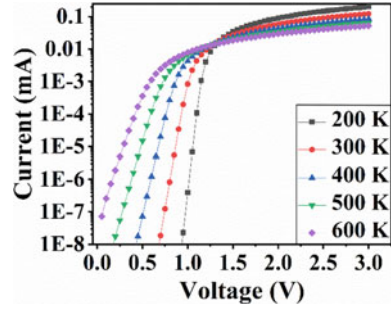


Fig. 3 Semi-logarithmic current–voltage plot of the fabricated device within specified temperature range



The corresponding semi-logarithmic forward bias current–voltage characteristics of the fabricated sensor, within a specified temperature range, are shown in Fig. 3. The linearity in the low bias range of Fig. 3 reveals that thermionic emission current flow mechanism dominates over other current conduction mechanisms. Moreover, at high-bias regions, the curves start bending which reveals that the series resistance effect comes into play.

It is shown in Fig. 3 that at current transportation it started at lower bias as temperature is increasing. Such temperature-dependent current transport is discussed in terms of thermionic emission model as [16, 17]:

$$I_f = I_s \exp\left(\frac{q(V_f - I_f R_s)}{\eta k T}\right) \tag{1}$$

where

$$I_s = AA^* T^2 \exp\left(\frac{q\Phi_b}{kT}\right) \tag{2}$$

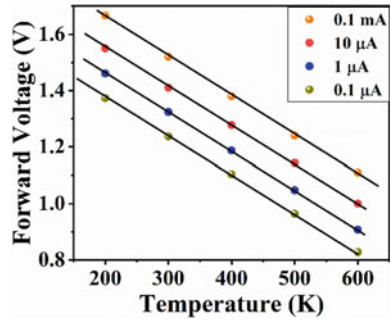
is the saturation current in the device.

In Eqs. 1 and 2, R_s is the series resistance of the device, k is the Boltzmann constant (1.38×10^{-23} J/K), T is the measurement temperature, q is the electronic charge, A is the Schottky contact area of the device and A^* is the effective Richardson constant ($146 \text{ A/cm}^{-2} \text{ K}^{-2}$). Moreover, η and Φ_b are the ideality factor and the device’s barrier height. Barrier height and ideality factor are important device characteristics whose values and stability are intrinsically related to the technological process. The slope and intercept of linear \ln at each temperature investigated (J) versus V plots can be determined. Rearranging Eq. (1) for forward voltage (V_f) will give rise to:

$$V_f = \eta\Phi_b + I_f R_s + \frac{\eta k T}{q} \ln\left(\frac{I_f}{AA^* T^2}\right) \tag{3}$$

Equation (3) shows that current forward voltage or on-voltage is inversely dependent on the temperature. The same trend is followed by fabricated devices at elevated

Fig. 4 Variation in the forward voltage (V_f) as a function of temperature at specified current levels



temperatures as shown in Fig. 3. Using Fig. 3, the variation in forward voltage with temperature, at specified current levels (i.e., 20 to 1 μA) is measured, and shown in Fig. 4.

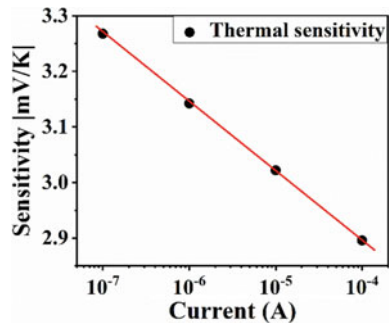
It is shown in Fig. 4 that forward voltage is almost a linear function of temperature at each selected current level, which shows their relevancy for use in temperature sensing. Analytically, the absolute value of the thermal sensitivity of the fabricated sensor can be expressed as [13]:

$$|S| = \left| \frac{dV_f}{dT} \right| = \left| \frac{\eta K}{q} \left[\ln \left(\frac{I_f}{AA^*T^2} \right) - 2 \right] \right| \tag{4}$$

Experimentally, the thermal sensitivity of the fabricated sensor is determined using the slope of forward voltage drop versus temperature (see Fig. 4) and shown in Fig. 5.

As shown in Fig. 5 the thermal sensitivity of the fabricated sensors is increasing with a decrement in the measurement current level, which is in accordance with Eq. 4. Moreover, the maximum value of the sensitivity is calculated as 3.27 mV/K at 0.1 μA. These results suggest the applicability of silicon carbide-based Schottky diode thermal sensors in low-temperature applications. It can be seen in Fig. 4 that the thermal sensitivity is not perfectly linear within measure current range. Such findings have been excellently described [16, 17] in terms of barrier height inhomogeneties

Fig. 5 Absolute values of thermal sensitivity of the sensor at selected current levels. The thermal sensitivity is increasing with measurement current level



exist at the interface of fabricated Ni/4H-nSiC Schottky barrier diode temperature sensor. The nanometer-sized patches exist at the interface of fabricated device impede the flow of charge carriers at low current levels and hence forward voltage does not as it should be. Researchers currently focusing on development of techniques to improve the interface of SiC based Schottky structures [6, 8, 18]. On the other hand, at high current and temperature levels, existence of more charge carriers in higher energy states will facilitates the variation in forward voltage drop with temperature. Therefore, the forward voltage variation with temperature will follow the thermionic emission model.

4 Conclusions

In conclusion, SiC Schottky diode thermal sensor has been fabricated. Its current–voltage characteristic has been acquired in temperature range varied from 200 to 600 K. The device showed exponential increase in current with applied voltage. Moreover, the forward voltage drop showed decrement with increasing of temperature. It worth mention here that the forward voltage drops of the device found varying linearly with temperature. The absolute values of sensitivity of the fabricated devices are found increasing with decreasing the measurement current levels in the devices.

References

1. Baliga BJ (2006) Silicon carbide power devices. World Scientific. <https://doi.org/10.1142/5986>
2. Draghici F et al (2019) 400 °C sensor based on Ni/4H-SiC Schottky diode for reliable temperature monitoring in industrial environments. *Sensors (Basel)* 19:10. <https://doi.org/10.3390/S19102384>
3. Kranzer D et al (2018) Applications of SiC devices. In: Wide bandgap semiconductor power devices: materials, physics, design, and applications, pp 345–371. Elsevier. <https://doi.org/10.1016/B978-0-08-102306-8.00010-1>
4. Kumar V et al (2014) Barrier height inhomogeneities induced anomaly in thermal sensitivity of Ni/4H-SiC Schottky diode temperature sensor. *J Vac Sci Technol B Nanotechnol Microelectron Mater Process Meas Phenom* 32(4):041203. <https://doi.org/10.1116/1.4884756>
5. Kumar V et al (2016) Capacitance roll-off and frequency-dispersion capacitance-conductance phenomena in field plate and guard ring edge-terminated Ni/SiO₂/4H-nSiC Schottky barrier diodes. *Phys status solidi* 213(1):193–202. <https://doi.org/10.1002/pssa.201532454>
6. Kumar V et al (2022) Defect levels in high energy heavy ion implanted 4H-SiC. *Mater Lett* 308:131150. <https://doi.org/10.1016/J.MATLET.2021.131150>
7. Kumar V et al (2020) Electronic transport in epitaxial 4H–SiC based Schottky diodes modified selectively by swift heavy ions. *Mater Sci Semicond Process* 115:105108. <https://doi.org/10.1016/J.MSSP.2020.105108>
8. Kumar V et al (2020) Interface improvement of epitaxial 4H-SiC based Schottky diodes by selective heavy ion irradiation. *Appl Nanosci* 1–8. <https://doi.org/10.1007/s13204-020-01608-3>

9. Kumar V et al (2013) Selective SHI irradiation for mesa type edge termination in semiconductor planar junction. *J Phys Conf Ser* 423(1):012057. <https://doi.org/10.1088/1742-6596/423/1/012057>
10. Kumar V et al (2018) Tailoring surface and electrical properties of Ni/4H-nSiC Schottky barrier diodes via selective swift heavy ion irradiation. *Phys Status Solidi* 215(5):1700555. <https://doi.org/10.1002/PSSA.201700555>
11. Kumar V, Maan AS (2018) Improvement in reverse bias leakage current of Ni/4H-nSiC Schottky barrier diodes via MeV selective ion irradiation. In: *IOP conference series materials science and engineering*, vol 331, no 1, pp 012016. <https://doi.org/10.1088/1757-899X/331/1/012016>
12. Kumar V et al (2015) Diameter dependent thermal sensitivity variation trend in Ni/4H-SiC Schottky diode temperature sensors. *J Vac Sci Technol B Nanotechnol Microelectron Mater Process Meas Phenom* 33(5):052207. <https://doi.org/10.1116/1.4929890>
13. Kumar V et al (2020) Epitaxial 4H-SiC based Schottky diode temperature sensors in ultra-low current range. *Vacuum* 182:109590. <https://doi.org/10.1016/j.vacuum.2020.109590>
14. Senesky DG (2013) Wide bandgap semiconductors for sensing within extreme harsh environments. *ECS Trans* 50(6):233–238. <https://doi.org/10.1149/05006.0233ecst>
15. Zhang N et al (2014) Temperature sensor based on 4H-silicon carbide pn diode operational from 20 °C to 600 °C. *Appl Phys Lett* 104(7):073504. <https://doi.org/10.1063/1.4865372>
16. Rhoderick EH (1982) Metal-semiconductor contacts. In: *IEE proceedings I solid state electron devices*. <https://doi.org/10.1049/ip-i-1.1982.0001>
17. Tyagi MS (1984) Physics of Schottky barrier junctions. In: *Metal-semiconductor Schottky barrier junctions and their applications*. https://doi.org/10.1007/978-1-4684-4655-5_1
18. Kumar V et al (2012) Simulation based analysis of temperature effect on breakdown voltage of ion implanted Co/n-Si Schottky diode 4(4):04009(4pp)

Investigation on Trench Edge Termination in SiC Based Power Device



Reena Rathi, Ekta Sharma, and Vamshi Krishna Dasarraju

1 Introduction

The medical, transportation and industrial sector of modern life has increased demand for high frequency and voltage devices. The conventionally used silicon- based devices in the above-said applications have reached their maximum potential. So, SiC, Ga₂O₃, GaN, diamond, etc., have come into the picture which are wide bandgap semiconductors [1–3]. Their performances are far better than silicon counterparts for implementation in the abovementioned applications. Moving forward, the current agenda is to increase the performance and reliability of wide bandgap semiconductors [4–15]. Instead of easy availability of SiC in the market, it provides high crystal quality which makes it a strong candidate in comparison to other materials for its use in devices with high power and frequency [16]. SiC is an artificially fabricated crystalline compound, made up of atoms of silicon (Si) and Carbon (C). Thermal conductivity (3–5 W/cm °C), breakdown electric field (2.6×10^6 V/cm), band gap (3.3 eV), high saturation electron velocity (2.7×10^7 cm/s) and high stability are some significant features of SiC which ascribes to its usage in the manufacturing of numerous devices [5, 7, 8, 17]. Furthermore, SiC can be leveraged to manufacture devices of high power accompanying thin and heavy doped drift layers due to its high breakdown electric field strength [5, 8]. The minority charge carrier storage gets reduced by using these thin drift layers and also these increase the switching frequency of SiC-based bipolar devices. The properties like wider bandgap and high thermal conductivity of SiC have steered the growth of high temperature (i.e., up to 350 °C) and power efficient operational devices. As a consequence, SiC materials

Reena Rathi · E. Sharma (✉)
Chaudhary Ranbir Singh University, Jind 126102, India
e-mail: ektasharma9797@gmail.com

V. K. Dasarraju
Northern Illinois University, Dekalb, IL 60115, USA

can be used to fabricate lightweight, cost efficient and compact devices [17, 18]. The most mature among existing power devices is a Schottky diode (SD) [19]. These devices do not have minority carrier storage issues, and thus are best suitable for fast switching action [20–22]. The vertical Schottky diodes have high power capability than lateral structures as in former ones; there is a complete backside ohmic contact which facilitates high current capability [23]. However, the electric field congesting at the boundaries of the SDs generates a reliability issue. Due to the lower area on the border of the SDs, the electric field has been observed very high as compared to the rest of the device, which owes to the congestion of electric field there.

Moreover, the existence of edge electric fields in devices leads to early breakdown of the device at lower applied fields on the reverse bias. The most common area of interest is along the periphery of the device, where the electric field is high compared to an area beneath the junction. Minimization of such high electric fields at the periphery of the junction is known as edge termination. Without edge termination, the breakdown in the device is roughly ~20% of the ideal value. There have been various strategies adopted to minimize the edge terminations in the devices [24]. For SiC and GaN, different techniques have been developed to minimize the fields at the edges of the gadgets, like ion implantation, field plate, guard rings and selective swift heavy ion irradiation [6, 11–15, 24]. Nevertheless, many issues are afflicted with existing techniques for SiC. For instance, without using any additional photolithography step, the guard ring can be easily achieved. In spite of it, lower blocking voltage efficiency, higher surface electric field and intensified width of the edge can be accomplished by this technique. While junction termination extension technique (JTE) can be executed, it requires the dopant activation procedure that considerably constricts the process window. Moreover, in order to reduce the edge effect in gadgets, ion implantation induced field limiting ring was employed [25–29]. Anyhow, the manufacturing process of FLR get complexed due to mask formation for ion shielding, the requirement of multiple beam ion implantation and supplementary procedures like ion activation at high temperature. Primarily, a specific thermal treatment is necessary to achieve a cleaned surface devoid of any impurity. Various research groups have mentioned multiple floating rings, trench and bevel JTE as alternatives to edge effect alleviating methods. Nevertheless, a comparatively larger edge width is required for these techniques. In essence, straightforward and cheap technology is the need of the hour for creating high power devices [1, 30–32]. Furthermore, interface of the device also plays major role in determining the breakdown characteristics of the device. Researchers are putting efforts towards improvement in the interface of the SiC based devices [33–35].

Additionally, advancements in current technology need low-cost and high area efficient devices. It has been reported that trench termination is the most effective and area-efficient structure in edge termination. Therefore, this work optimized the trench parameters of the SiC-based SDs to get maximum breakdown voltage. The device was simulated using Silvaco TCAD software. The trench was designed at the boundary of the gadget under discussion. The trench was filled with a dielectric material and simulated for maximum breakdown voltage. Additionally, the unterminated devices were also simulated and compared with terminated ones.

2 Device Structure

Simulation of devices gives useful information about devices that cannot be predicted in real-time. The atlas module of the software SILVACO TCAD facilitates the design of the device and its simulation for getting electrical characteristics, which gives more insight into physical behavior in the device under operation. This software has the capability of modelling various devices made up of crystalline to amorphous materials and dc and ac characteristics, etc. This tool is having a bunch of semiconductor equations to model various phenomena in the devices. Using the above capabilities, accurate modelling of any device can be performed. Moreover, the exactness of the findings depends on the correctness of the parameter inputs. The main parameters in the present work are the bandgap of SiC, its intrinsic carrier concentration, mobility of electrons and holes, electron affinity, permittivity, doping of the substrate, device dimensions, diffusion lengths, etc. [34]. A schematic representation of the simulated structure in the existing work is depicted in Fig. 1.

The structure contained a substrate, which is selected as n+ SiC in the present work, with a height of 20 μm and the doping of $5 \times 10^{19} \text{ cm}^{-3}$. The top layer on the substrate is an epitaxial layer or drift layer with 10 μm thickness having a doping of $= 5 \times 10^{16} \text{ cm}^{-3}$. The Schottky metal in the present work was chosen of metal having work function 4.8 eV. The designed trench is of dimension 10 μm width and 300 nm height. SiO_2 is the dielectric which is used to fill the trench. The main parameters for the dielectric are its permittivity and thickness as these parameters impact reverse breakdown voltage mainly. The backside contact was made as an ohmic contact. For SiC, the following parameters have been used; band gap = 3.2 eV, electron affinity = 4.12 eV, Schottky metal work function = 4.8 V, permittivity = 9.6, density of states of conduction band = $1 \times 10^{19} \text{ cm}^{-3}$, density of states of valence

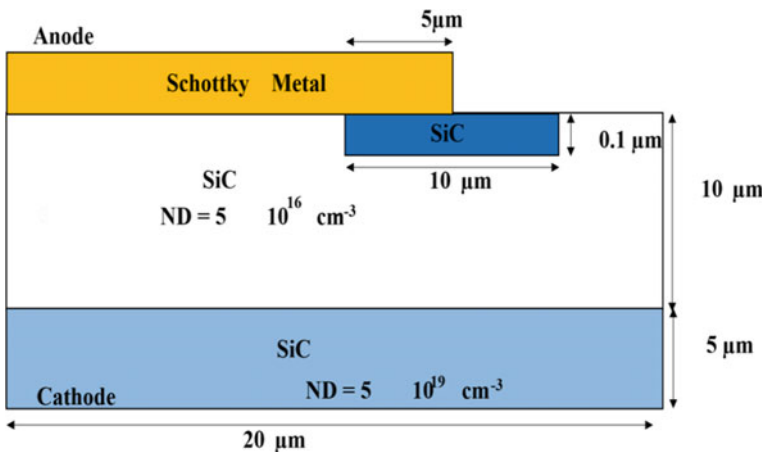


Fig. 1 Schematic of the manufactured device with dimensions. The parameters of the material are as per purchased wafer

band = $1.2 \times 10^{19} \text{ cm}^{-3}$ and temperature $T = 300 \text{ K}$. Numerous models like FD statistics, Selberherr impact ionization, SRH and Auger recombination, parallel and concentration field-dependent mobility, etc. have been used. Moreover, the meshing of the device was selected cautiously so that it does not lead to misleading results. Additionally, the mesh spacing was chosen as a smooth variation to minimize the solution convergence issue in the device [34].

3 Results and Discussion

Figure 2 depicts the potential profile in the un-terminated gadget. It is shown in Fig. 2a at point A, the potential is at extreme, which is the edge of the device. Owing to this high potential, the electric field will also be very high there as shown in the graphical representation of Fig. 2a. Such extreme electric field will avail energy to the free charge carriers, which caused an increase in impact ionization. As a result of this, avalanche breakdown happens in the device and the device will breakdown as lower reverse voltages. It must be mentioned here that in real devices, other factors like defects in the material could also cause premature breakdown of the devices. However still, the edge effect caused breakdown dominates. In case of un-terminated devices, the breakdown voltage was obtained as 160 V.

To lessen the edge electric field crowding in the device, the implemented trench termination strategy is shown in Fig. 1. Previous studies revealed that the dielectric material in the trench should be chosen such that the electric field does not exceed its breakdown strength. Therefore, a couple of dielectric materials have been used demonstrated with varying permittivity as reported in the literature and their breakdown is determined [30, 36–38]. In the present work, SiO₂ is used due to maturity

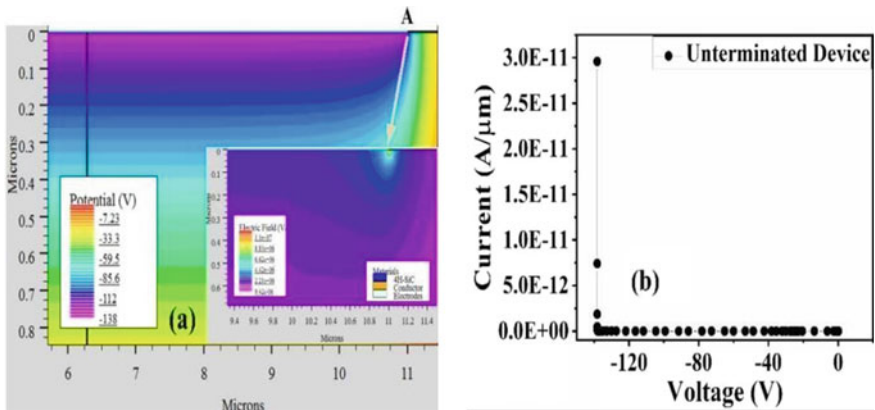


Fig. 2. a The potential distribution in the un-terminated device the with highest value at point A, which is the edge of the device and corresponding electric field has been shown in its inset; b The simulated value of breakdown voltage in un-terminated device

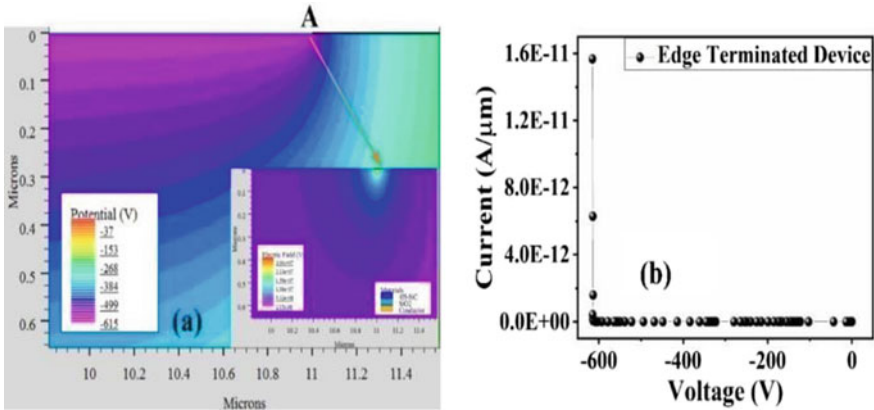


Fig. 3. a The potential distribution in the edge terminated device with highest value at point A, which is the device’s edge and corresponding electric field (EF) has been shown in its inset. It can be seen that EF which was at point B previously has been shifted to point A after edge termination b The simulated value of the breakdown voltage in edge terminated device

in its deposition and processing technology in the manufacturing industry. The used metal as a field plate will shift the high electric field at the edges away from it and the reverse breakdown voltage of the device is improved. Using above facts, the distribution of potential in the above-mentioned device is shown in Fig. 3.

Figure 3 shows that using trench termination in Ga₂O₃, the potential at its corner “A” has been minimized compared to the un-terminated structure and shifted to point “B” which is inside the dielectric material: SiO₂. This will lead to a minimization of crowding of the electric field at corners of the structure and increase the reverse breakdown voltage of the device as depicted in the inset of Fig. 3a. The simulation performed in this work estimated the reverse breakdown in the device as 640 V.

4 Conclusion

In conclusion, trench induced edge termination in SiC-based SDs have been investigated. The SiC-based SD are simulated with and without edge termination using Silvaco TCAD simulation software. The un-terminated device structures have shown maximum electric field at its edges, which leads to early breakdown of the device at 160 V. However, with the SiO₂ filled trench structures, the electric field at boundary of the structure is found relaxed. This leads to an increment in the breakdown voltage of the structure to 640 V. These findings reveal that the usage of the trench termination structures could be beneficial in decrement of edge width in structures and therefore the size of the structure.

References

- Baliga BJ (2006) Silicon carbide power devices. World Scientific
- DiMarino CM, Burgos R, Dushan B (2015) High-temperature silicon carbide: characterization of state-of-the-art silicon carbide power transistors. In: IEEE industrial electronics magazine, vol 9, no 3, pp 19–30. Institute of Electrical and Electronics Engineers Inc.
- Tsao JY et al (2018) Ultrawide-Bandgap semiconductors: research opportunities and challenges. *Adv Electron Mater* 4(1):1600501. <https://doi.org/10.1002/AELM.201600501>
- Kumar V, Maan AS, Akhtar J (2014) Barrier height in homogeneities induced anomaly in thermal sensitivity of Ni/4H-SiC Schottky diode temperature sensor. *J Vac Sci Technol B Nanotechnol Microelectron Mater Process Meas Phenom* 32(4):041203. <https://doi.org/10.1116/1.4884756>
- Kumar V, Pawar S, Maan AS, Akhtar J (2015) Diameter dependent thermal sensitivity variation trend in Ni/4H-SiC Schottky diode temperature sensors. *J Vac Sci Technol B Nanotechnol Microelectron Mater Process Meas Phenom* 33(5):052207. <https://doi.org/10.1116/1.4929890>
- Ueda T (2019) GaN power devices: current status and future challenges. *Jpn J Appl Phys* 58(SC):804. Institute of Physics Publishing. <https://doi.org/10.7567/1347-4065/ab12c9>
- Kumar V, Kumar S, Maan AS, Akhtar J (2020) Interface improvement of epitaxial 4H-SiC based Schottky diodes by selective heavy ion irradiation. *Appl Nanosci* 1–8. <https://doi.org/10.1007/s13204-020-01608-3>
- Kumar V, Kaminski N, Maan AS, Akhtar J (2016) Capacitance roll-off and frequency-dispersion capacitance-conductance phenomena in field plate and guard ring edge-terminated Ni/SiO₂/4H-nSiC Schottky barrier diodes. *Phys status solidi* 213(1):193–202. <https://doi.org/10.1002/pssa.201532454>
- Jones EA, Wang FF, Costinett D (2016) Review of commercial GaN power devices and GaN-based converter design challenges. *IEEE J Emerg Sel Top Power Electron* 4(3):707–719. <https://doi.org/10.1109/JESTPE.2016.2582685>
- Kumar V, Verma J, Maan AS, Akhtar J (2020) Epitaxial 4H-SiC based Schottky diode temperature sensors in ultra-low current range. *Vacuum* 182:109590. <https://doi.org/10.1016/j.vacuum.2020.109590>
- Kumar V, Maan AS (2018) Improvement in reverse bias leakage current of Ni/4H-nSiC Schottky barrier diodes via MeV selective ion irradiation. *IOP Conf Ser Mater Sci Eng* 331(1):012016. <https://doi.org/10.1088/1757-899X/331/1/012016>
- Kumar V, Maan AS, Akhtar J (2013) Selective SHI irradiation for mesa type edge termination in semiconductor planar junction. *J Phys Conf Ser* 423(1):012057. <https://doi.org/10.1088/17426596/423/1/012057>
- Mishra UK, Shen L, Kazior TE, Wu YF (2008) GaN-based RF power devices and amplifiers. *Proc IEEE* 96(2):287–305. <https://doi.org/10.1109/JPROC.2007.911060>
- Kumar V, Maan AS, Akhtar J (2018) Tailoring surface and electrical properties of Ni/4H-nSiC Schottky barrier diodes via selective swift heavy ion irradiation. *Phys status solidi* 215(5):1700555. <https://doi.org/10.1002/PSSA.201700555>
- Kumar V, Maan AS, Akhtar J (2020) Electronic transport in epitaxial 4H-SiC based Schottky diodes modified selectively by swift heavy ions. *Mater Sci Semicond Process* 115:105108. <https://doi.org/10.1016/J.MSSP.2020.105108>
- Singh R (2006) Reliability and performance limitations in SiC power devices. *Microelectron Reliab* 46(5–6):713–730. <https://doi.org/10.1016/j.microrel.2005.10.013>
- Kimoto T, Cooper JA (2014) Fundamentals of silicon carbide technology, vol 9781118313. Wiley Singapore Pte. Ltd, Singapore
- Kranzer D, Hensel A, Thoma J, Armbruster C, Hercegfi P, Schönberger S (2018) Applications of SiC devices. In: Wide bandgap semiconductor power devices: materials, physics, design, and applications, pp 345–371. Elsevier
- Verma J, Pant S, Kumari S, Belwanshi V, Dalal J, Kumar A (2022) Trench termination in Ga₂O₃-based power device: a simulation-based study. *Appl Nanosci* 2021:1–7. <https://doi.org/10.1007/S13204-021-02219-2>

20. Millan J, Godignon P, Perpina X, Perez-Tomas A, Rebollo J (2014) A survey of wide bandgap power semiconductor devices. *IEEE Trans Power Electron* 29(5):2155–2163. <https://doi.org/10.1109/TPEL.2013.2268900>
21. Bahat-Treidel E et al (2012) Fast-switching GaN-based lateral power schottky barrier diodes with low onset voltage and strong reverse blocking. *IEEE Electron Device Lett* 33(3):357–359. <https://doi.org/10.1109/LED.2011.2179281>
22. Oh S, Yang G, Kim J (2017) Electrical characteristics of vertical Ni/ β -Ga₂O₃ Schottky barrier diodes at high temperatures. *ECS J Solid State Sci Technol* 6(2):Q3022–Q3025. <https://doi.org/10.1149/2.0041702jss>
23. Yang J, Ahn S, Ren F, Peartorn SJ, Jang S, Kuramata A (2017) High breakdown voltage (\sim 201) β -Ga₂O₃ Schottky rectifiers. *IEEE Electron Device Lett* 38(7):906–909. <https://doi.org/10.1109/LED.2017.2703609>
24. Pérez Rodríguez R (2006) Planar edge terminations and related manufacturing process technology for high power 4H-SiC diodes
25. Sheridan DC, Niu G, Merrett JN, Cressler JD, Ellis C, Tin CC (2000) Design and fabrication of planar guard ring termination for high-voltage SiC diodes. *Solid State Electron* 44(8):1367–1372. [https://doi.org/10.1016/S0038-1101\(00\)00081-2](https://doi.org/10.1016/S0038-1101(00)00081-2)
26. Onose H, Oikawa S, Yatsuo T, Kobayashi Y (2000) Over 2000 V FLR termination technologies for SiC high voltage devices. In: 12th international symposium on power semiconductor devices & ICs proceedings (Cat. No.00CH37094), pp. 245–248. <https://doi.org/10.1109/ISPSD.2000.856817>
27. Perez R, Tournier D, Perez-Tomas A, Godignon P, Mestres N, Millan J (2005) Planar edge termination design and technology considerations for 1.7-kV 4H-SiC PiN diodes. *IEEE Trans Electron Devices* 52(10):2309–2316. <https://doi.org/10.1109/TED.2005.856805>
28. Mahajan A, Skromme BJ (2005) Design and optimization of junction termination extension (JTE) for 4H-SiC high voltage Schottky diodes. *Solid State Electron* 49(6):945–955. <https://doi.org/10.1016/j.sse.2005.03.020>
29. Hiyoshi T, Hori T, Suda J, Kimoto T (2008) Simulation and experimental study on the junction termination structure for high-voltage 4H-SiC PiN diodes. *IEEE Trans Electron Devices* 55(8):1841–1846. <https://doi.org/10.1109/TED.2008.926643>
30. Liu Y et al (2019) Design and characterization of the deep-trench, U-shaped field-plate edge termination for 1200-V-Class SiC devices. *IEEE Trans Electron Devices* 66(10):4251–4257. <https://doi.org/10.1109/TED.2019.2931638>
31. Zhao JH, Alexandrov P, Li X (2003) Demonstration of the first 10-kV 4HSiC Schottky barrier diodes. *IEEE Electron Device Lett* 24(6):402–404. <https://doi.org/10.1109/LED.2003.813370>
32. Brunt EV et al. (2014) 22 kV, 1 cm², 4H-SiC n-IGBTs with improved conductivity modulation. In: Proceedings of the international symposium on power semiconductor devices and ICs, pp 358–361. <https://doi.org/10.1109/ISPSD.2014.6856050>
33. Kumar V, Maan AS, Akhtar J (2022) Defect levels in high energy heavy ion implanted 4H-SiC. *Mater Lett* 308:131150. <https://doi.org/10.1016/J.MATLET.2021.131150>
34. Kumar V, Akhtar J, Singh K, Maan AS (2012) Simulation based analysis of temperature effect on breakdown voltage of ion implanted Co/n-Si Schottky diode, vol 4, no 4, p 4009. <https://essuir.sumdu.edu.ua/handle/123456789/30266>. Accessed Jul 31, 2021
35. Kumar V, Kumar S, Maan AS, Akhtar J (2021) Interfacial and structural analysis of MeV heavy ion irradiated SiC. *Appl Nanosci* 1–8. <https://doi.org/10.1007/s13204-021-01921-5>
36. Theolier L, Mahfoz-Kotb H, Isoird K, Morancho F, Assie-Souleille S, Mauran N (2009) A new junction termination using a deep trench filled with BenzoCycloButene. *IEEE Electron Device Lett* 30(6):687–689. <https://doi.org/10.1109/LED.2009.2020348>
37. Sasaki K et al (2017) First demonstration of Ga₂O₃ trench MOS-type schottky barrier diodes. *IEEE Electron Device Lett* 38(6):783–785. <https://doi.org/10.1109/LED.2017.2696986>
38. Wang H et al (2018) Trench termination With SiO₂—encapsulated dielectric for near-ideal breakdown voltage in 4H-SiC devices. *IEEE Electron Device Lett* 39(12):1900–1903. <https://doi.org/10.1109/LED.2018.2874471>